OUTER-SPHERE EFFECTS ON THE COPPER SITES OF PSEUDOMONAS AERUGINOSA AZURINS

Thesis by

Kyle M. Lancaster

In Partial Fulfillment of the Requirements for the

degree of

Doctor of Philosophy

CALIFORNIA INSTITUTE OF TECHNOLOGY

Pasadena, California

2011

(Defended August 18, 2010)

..
ii

This one's for Mom and Dad.

ACKNOWLEDGEMENTS

I owe a great many people a great many thanks. Please bear with me.

My folks, Catherine and Wayne Lancaster, have made everything possible for me; without their love, support, and genetics I would have nothing and be nowhere. Accordingly, they get first billing.

Life would be very different if John Brennan had not kindled my love affair with the personal computer. So, if my parents get a healthy dose of the credit for the path my life has taken, John too should receive his fair share.

The top brass come next:

The Commander, Harry B. Gray, taught me how to not only be a scientist but to be a human being who sciences. I have been many wonderful places, met many wonderful people, and learned many wonderful things all because of Harry. I aspire to pay it forward many times over!(!!)

Lord John H. Richards was a wise counselor, a voice of reason, and a very good friend to me from the very beginning. I also very much enjoyed serving as his operative on various research black ops.

Jay R. Winkler made many useful suggestions that were always considered and sometimes followed. He also taught me to be far more critical as a scientist than I was "fresh out of the box" as a new recruit.

On to my crack team of collaborators:

Serena DeBeer showed me the light of the synchrotron, and my eyes have been open ever since. I look forward to our continuing collaboration and friendship. (Even though it requires me to leave my precious Southern California.)

Alejandro Vila, "Professor Malbec," put me up and put up with me for a month in Rosario, Argentina. He enriched my life with an appreciation not only for the power and utility of NMR when leveled at paramagnetic metalloproteins, but also for the central role of a grill in one's household.

Maria Eugenia "Ogi" Zaballa was my partner in Rosario. I could not imagine working with a more meticulous and skilled NMR spectroscopist. Her time and instruction are gratefully acknowledged.

Frank Neese fueled not only my desire to dig in to electronic structure (and to have fun with ORCA!), but has inspired me to remain sharply dressed while doing so.

Tony Vlcek provided sanction to my moonlighting as a synthetic inorganic chemist. He also taught me that a glass of wine goes very well with excited state photophysics.

Karl Wieghardt gave me great advice over a beer in Ithaca, in addition to hosting me for a few weeks in his spectroscopic playground. Someday I will get him that iridium dithiolene…

The Ambassador from Mülheim, Stephen Sproules, is kindly thanked for his unique sense of humor, a lot of Q-band EPR spectra, and for keeping me well-supplied with German confectionery and artificial sweetener.

The Three Wise Men of Rehovot: I was privileged to have the help of Scot Wherland, Ole Farver, and Geheimerat Israel Pecht with my research. It is humbling to have worked with these pioneers of blue copper and biological electron transfer. Israel is thanked individually for hosting me in the Holy Land, proofreading portions of this thesis, and for serving as an unofficial member of my committee.

Daniella Goldfarb and Alexey Potapov provided electron paramagnetic reinforcement to the study of type zero copper. While I hope someday to understand pulsed EPR techniques, for the time being I thank them for their beautiful work and laudable patience.

Edward Jerome Crane, III predated Harry by many years in being the person to not say "no." E.J. really gave me my start in the biz, and it was a delight to keep working together.

Matthew Sazinsky gave me some useful hints with protein crystallography, and he let me monopolize his anaerobic chamber for several days.

Oh, and Daniel J. O'Leary: I came home. Thanks for pushing me in the right direction.

Next, I thank the two gentlemen who taught me almost everything I know about synthesis:

Rev. Dr. James B. Gerken and I had many eventful nocturnal musical and/or chemistry-related evenings. He also almost prevented three of the biggest catastrophes incurred during the production of this thesis.

Theis Brock-Nannestad is a man who knows how to live. He taught me that making anything on less than the gram, or as I now call it, the "Danish" scale is hardly worth the time.

My contemporaries in the Gray Nation are thanked as a whole; I could not imagine a more colorful collection of characters with whom to endure the indentured servitude of graduate school.

Corporal Brian S. Leigh taught me everything I needed to get me off the ground, and then some. From azurin to Zeeman, Brian knew everything.

Joshua H. Palmer was my brother-in-arms. Between our shared affinity for rems and heavy metals I am not certain how long our friendship and collaboration will last, but it will never grow tiresome.

Gretchen Keller and Morgan Cable are the two sisters I have never had. I think that requires no further elaboration.

Alec Durrell endured my company in 314 BI for four years. For this he should be applauded, not merely acknowledged. Also, his assent to being recruited for pimH and general willingness to serve as spectroscopic mercenary deserve special thanks.

Melanie Pribisko Yen was my own personal safety officer. She is thanked for early synthetic guidance, late night trips to dinner and/or Huntington Hospital, and her inspirational perseverance.

Keiko Yokoyama is the golden girl of electrochemistry. It has been a delight sharing azurin with her for the past several years. Domo!

Charlotte Whited kept me on my toes, since I never knew what zinger was next. I am very grateful for her friendship and willingness to let me bum around on her couch when I was feeling lazy.

Jillian Dempsey is a role model for everyone. She's also as gifted in the kitchen as the laboratory; it has been a pleasure working with her as well as hosting dinner parties.

Lionel "Lucky Pierre" Cheruzel brought a very French je ne sais quoi to the Gray Nation. I hope he never changes.

Don Walker helped me out with a lot of stuff in lab, but more importantly he ensured that I held my gastronomic standards sky-high. I think the final score wound up in my favor, though.

Matthew Hartings and I got our starts in the Nation together. Paths diverged, but I remain grateful to him for helping me acclimate to Caltech during those first few months of Aß-42.

John Magyar shared his bountiful inorganic chemistry library with me, and in doing so really pointed me in the right direction.

The denizens of the sub-basement: Heather, Maraia, Nicole, Peter, Bert, Gitrada, and Astrid – thank you for bringing some cheer to our subterranean domain. While I cannot promise that I will miss the SB, I will miss its inhabitants.

Allison Saltzman was my first and only undergraduate. A lot of sass, but plenty of savvy, too. She has a bright future in science if she chooses.

Yuling Sheng provided occasional supplements to my protein supplies. Often these came just in the nick of time; her impressive yields of azurin are acknowledged with gratitude.

Scott Ross and Dave Vandervelde helped me collect early NMR spectra, and both tempted me with international NMR meetings I should have attended.

Larry Henling, Mike Day, Jens Kaiser, and Pavle Nikolovski provided crystallographic expertise. Jens in particular helped me with some more troubling datasets. It was almost worth the abuse.

Bruce Brunschwig is thanked for the odd bit of advice, his sense of humor, and for introducing me to my favorite unit of energy.

Catherine May and Rick Jackson ran a tight ship in the BI, but thankfully turned a blind eye to my coffee theft. Catherine always had the right "fix" for any "problem"; I am very glad I was never one of the latter in her eyes. Rick's POETS meetings were intellectually and hepatically stimulating.

My extended Pomona College family – Alicia, Alix, Andrew, Brooke, Charles, Colleen, Courtney, Ganesh, Jason, Jennifer, John, Nils, and Yianni – your warm friendship and unflagging support over the last few years were indispensible. Thank you also for being participants in the experiments in entropy that were repeated cleanings of The Holliston preceding its immediate rampage.

Two Sagehens get extra credit:

David D. Lydon, Esq. contributed directly to the science contained herein: he provided his couches, his shower, and his entertainment center on several runs to SSRL. Of course, his company, friendship, support, and refreshments were also enjoyed.

Justin Durivage contributed his scholastic prowess with an 11th hour reading of the azurin review. It was great to have a reputable historian inspect my historical narrative!

Occasionally I stepped outside for a breath of fresh air -

Elizabeth Lester gave me a life outside the lab. I am a richer person for her friendship.

Philip Evans and Jason "Orence" Blackader taught me that the great outdoors are best enjoyed with many kilowatts of bass. The future is LOUD!

Finally, to everyone else I have neglected to mention explicitly whom I encountered within the concrete jungle of Los Angeles, thank you for keeping life interesting!

ABSTRACT

This thesis reports explorations into the mechanisms by which the $Cu^{II/I}$ reduction potential is tuned within a protein coordination matrix comprised exclusively of hard ligands, *i.e.* N- and O- donors. The base scaffold for this work is the type 2 copper binding C112D azurin from *Pseudomonas aeruginosa*. Further mutations to the axial methionine at position 121 were effected, as substiutions at this position have been found to dramatically alter the reduction potentials of the type 1 center of the wild-type protein.

Chapter 1 contextualizes the work carried out in the preparation of this thesis by surveying the last fifty years of investigations into the biophysics, spectroscopy, reactivity, modification, and application of azurins.

Chapter 2 initiates the study by introducing C112D/M121X (X = M, E, H, and L) azurins. The C112D/M121E azurin is found to have a surprisingly high reduction potential at neutral pH ($E^{o}_{1/2}$ ~ 290 mV vs NHE), despite the presence of an axial carboxylate. Spectroscopic (EPR, UV/vis, XAS), structural (X-ray diffraction), and electrochemical studies reveal that a rack mechanism imposes a constraint on the active site whereby the rigidty of H46 at pH ≤ 8 prevents coordination of Cu^{II} by E121; this structural frustration destabilizes the Cu^{II}, imparting an elevated reduction potential. When this constraint is released by deprotonation of H35, the Cu^{II} can be coordinated by E121, resulting in a ~ 200 mV drop in reduction potential. While a similar mechanism may be at work in C112D/M121H, structural evidence has not been forthcoming in support of this explanation for its ~ 300 mV potential in the presence of a strong axial ligand.

The C112D/M121L mutation gives rise to a Cu^{II} site that exhibits spectroscopic properties similar to type 1 copper. It and similar mutants C112D/M121X (X = L and F) are the subject of Chapter 3, which again combines EPR, UV/vis, XAS, X-ray diffraction, and electrochemistry to indicate that these azurins comprise a novel class of copper protein, now referred to as "type zero copper." Interestingly, crystal structures reveal a restoration of the outer sphere coordination from the wild type protein, as N47 and F114 backbone amides

donate hydrogen bonds to the non-coordinated carboxyl oxygen of D112. This was offered initially as a qualitative explanation for enhanced electrochemically-measured electron transfer activity in these proteins.

MCD, pulsed EPR, NMR, and DFT studies are detailed in Chapter 4, with their focus being the comparison of type zero proteins to the type 2 C112D azurin. Interestingly, these proteins show wide variation in their Cu^{II} electron spin relaxation characteristics, allowing for the observation of several directly coordinated ligands by ^{1}H NMR with resolution on par with type 1 centers. This has enabled measurement of proton hyperfine interactions that, in concert with pulsed EPR studies, show that electron delocalization over the site histidines is similar to wild type azurin. However, no evidence is found for metal-ligand covalency on par with a type 1 center. Subtle variations within the type zero series are observed that are explained in terms of varied tetrahedral distortion within these sites. DFT calculations suggest that the spectroscopic properties of these sites, like type 1 sites, require the establishment of outer sphere coordination, namely the "rack" network of hydrogen bonds to residue 112. Thus type zero copper may be legitimately considered a type 1 site *sans* sulfur.

Finally, in Chapter 5 activation studies and Marcus theoretical analyses of stopped flow and pulse radiolysis kinetics are combined with structural evidence from XAS studies. These experiments demonstrate that the electron transfer enhancement of the type zero centers owes to outer sphere structural constraints imparting a dramatically reduced reorganization energy compared to the type 2 C112D protein. The availability of a high-potential, electron transfer efficient hard-ligand copper site now affords the promise of engineering robust oxidation catalysts without concern for irreversible deactivation by oxidation of soft, sulfur-based ligands.

TABLE OF CONTENTS

LIST OF ILLUSTRATIONS AND/OR TABLES

ID ***Page***

NOMENCLATURE AND ABBREVIATIONS

4,7-dmphen: 4,7-dimethyl-1,10-phenanthroline
BCP: blue copper protein
bpy: 2,2'-bipyridine
CD: circular dichroism
CV: cyclic voltammetry
CW: continous wave
cytc$_{551}$: cytochrome c_{551}
DFT: density functional theory
DSC: differential scanning calorimetry
ED-NMR: ELDOR-detected NMR
EDTA: ethylenediaminetetraacetic acid
ELDOR: electron electron double resonance
ENDOR: electron nuclear double resonance
EPR: electron paramagnetic resonance
ESE: electron self-exchange
ESEEM: electron spin echo envelope modulation
ESI-MS: electrospray ionization mass spectrometry
e.s.u.: estimated standard uncertainty
ET: electron transfer
EXAFS: extended X-ray absorption fine structure
EXSY: exchange spectroscopy
FPLC: fast protein liquid chromatography
FWHM: full-width at half-maxium
Hcy: homocysteine
HYSCORE: hyperfine sublevel correlation
IPTG: ß-D-isopropyl-thiogalactopyranoside
kK: kilokaiser (1 x 10^3 cm^{-1})
LB: Luria-Bertani (broth)
LF: ligand field
LLCT: ligand to ligand charge transfer
LMCT: ligand to metal charge transfer
MCD: magnetic circular dichroism
MCO: multicopper oxidase
mK: millikaiser (1 x 10^{-3} cm^{-1})
MLCT: metal to ligand charge transfer
MM: molecular mechanics
MQ-H_2O: Milli-Q water
NaOAc: sodium acetate
NaP_i: sodium phosphate
NHE: normal hydrogen electrode
NiR: nitrite reductase
NMR: nuclear magnetic resonance
NQR: nuclear quadrupole resonance
ORC: oxidation-reduction cycle
phen: 1,10-phenanthroline
PR: pulse radiolysis
SAM: self-assembled monolayer
SCF: self-consistent field
SDM: site-directed mutagenesis
SDS-PAGE: sodium dodecyl sulfate polyacrylamide gel electrophoresis
Sec: selenocysteine
STD: saturation transfer difference
TB: Terrific broth
QM: quantum mechanics
UV/vis: ultraviolet/visibile
XAS: X-ray absorption spectroscopy
XPS: X-ray photoelectron spectroscopy

Chapter 1

FIFTY YEARS OF AZURIN

INTRODUCTION

The story of blue copper proteins (BCPs) is neither short nor simple. It is a branching, twisted journey through myriad scientific disciplines; it is an assortment of controversies, their resolutions, and their replacements. Beginning *in medias res* with a discussion of new directions in the engineering and characterization of BCPs would be foolhardy; moreover, the motivations behind many of the experiments to be described herein would seem confusing if not arbitrary. To inform the reader and to pay tribute to the legions of investigators who have charted the waters of the BCPs, we must start at the beginning and progress from the BCP as biochemical curiosity to scientific mainstay.

The azurin family of cupredoxins represents a central focus in the BCP narrative. Among the first to be discovered and characterized, azurins remain workhorses in many research arenas including the studies of protein folding and stability, biological electron transfer (ET), bioinorganic spectroscopy, and protein engineering. Though other BCPs, *e.g.* plastocyanins, stellacyanins, rusticyanins, fungal laccases, *etc.* have yielded investigators important insights, we can narrow our discussion to azurin without too many glaring omissions. Comparisons will be drawn where illuminating, but the reader is directed to a recent review by Dennison for an appreciation of the diversity among BCPs.[1] While certainly interesting, an exhaustive review of the entire BCP superfamily would exceed the scope of this work and likely span several volumes!

HISTORICAL PERSPECTIVE

As early as 1956 a blue protein was identified by biochemists isolating components of the bacterial metabolome. This protein was isolated with heme-containing cytochromes *c* from various gram-negative bacteria, including members of the *Bordetella*, *Pseudomonas*, and *Alcaligenes* genii.[2] Convention at the time dictated that this curious protein be named for its distinguishing coloration, thus Sutherland and Wilkinson dubbed it "azurin."[3-4]

Prudently, the pioneering azurin work focused on characterization, both of physical/spectroscopic properties as well as its interactions with putative reaction partners. These efforts were restricted to the study of native protein as isolated from host organisms. A typical "classical" azurin preparation is included as appended material (Appendix 1-A).

The recombinant DNA revolution marked an explosive period in the study of azurin. 1987 saw the amplication and cloning of the *Pseudomonas aeruginosa* azurin gene from genomic DNA by Canters.[5] Shortly thereafter Karlsson and co-workers reported the expression and purification of recombinant protein from *Escherichia coli*.[6] In 1991, the Richards lab synthesized a codon-optimized *P. aeruginosa* azurin gene.[7] The Richards and Karlsson systems afforded not only convenient modes of isolating copious quantities of azurin, but also served as scaffolds for the construction by cassette mutagenesis of protein variants ranging from simple point mutants to azurins with wholly replaced metal binding loops. (Both expression systems remain in use by laboratories worldwide; future researchers are urged to verify their system before embarking on any azurin undertaking.) With this newfound genetic malleability, azurin was thrust into the spotlight of metalloprotein research. Investigators could approach previously untenable questions regarding the nature of BCP metal coordination, biophysics, and electron transfer through the application of site directed mutagenesis.

Now is the time to move from straight history to facts and figures. Separation of broad areas of focus has been attempted, but clean compartmentalization with concomitant maintenance of logical flow is untenable for such a storied protein. Where necessary the

interdisciplinary implications of studies will be acknowledged, but in-depth discussions will be reserved for their respective sections. With this disclaimer we shall now proceed to sequential discussion of the structure and biophysics, electronic structure, electron transfer reactivity, engineering, and applications of azurin.

THE AZURIN ROADMAP

Not unreasonably, informed discussion of any chemical species demands an intricate understanding of its molecular structure. X-ray diffraction data for *Achromobacter denitrificans* (formerly *Alcaligenes denitrificans*) azurin was available by 1969,[8] but it was not until 1978 that Adman and Jensen released the first 3D azurin structure.[9] This structure came somewhat after the release of the first BCP structure, that of plastocyanin by Hans Freeman.[10] The 3 Å Adman and Jensen structure for the *P. aeruginosa* protein was ultimately refined to 2.7 Å.[11] Since these initial investigations, over seventy crystal structures have been deposited in the PDB running the gamut of alterations made to the azurins from metal substitution to ligand loop replacements.

We start with the primary sequence. Azurins are small proteins (14 kDa) comprised of approximately 130 residues. The first azurin sequence, that of *P. aeruginosa* (then *fluorescens*) azurin was reported in 1967.[12] This number has exploded; today 740 primary azurin sequence results are returned from a search of the National Center for Biotechnology Information protein database; while there are many duplications this highlights the ubiquity of azurins, particularly in denitrifying bacteria.[13] Multiple sequence alignment of ten of these proteins reveals the expected high degree of homology (Figure 1.1). From this alignment, a consensus sequence for the metal-binding loop is determined as NH_2-C(S/T)FPGHXXXM-COOH. In addition to the metal-binding cysteine, the proteins include two other conserved cysteines that constitute a structural disulfide. As these are periplasmic proteins, their genes encode preproteins with N-terminal periplasmic translocation tags. These tags are ultimately cleaved during localization to the periplasm, resulting in mature azurins. Thus the oft-reported "14.6 kDa" molecular mass for *P. aeruginosa* azurin is in error, as this corresponds to the preprotein with its 2080 Da leader seqeuence.

To familiarize ourselves with the protein, we shall examine in detail the various features of the 1.9 Å, pH 5.5 crystal structure of the *P. aeruginosa* azurin reported by Nar and co-workers (Figure 1.2, PDBID: 4AZU).[14] This represents the highest-resolution unmodified, Cu^{II} *P. aeruginosa* structure and thus affords the most informed discussion of subtle interactions such as hydrogen bonding. This structure was collected in tandem with one at pH 9.0; the reasoning behind and implications of this study are better left for later discussion. Where useful, we will draw comparisons to structures from other species, such as the *A. denitrificans* azurin structure refined to 1.8 Å.[15] It should be noted that most azurin studies have focused on the *P. aeruginosa* variant.

We shall immediately focus on "the interesting part," the Cu binding site, which is located at the "north pole" of the protein and consists of a distorted trigonal bipyramid with ligation from sidechains within the 34-48 and 111-122 loops (Figure 1.2). The three equatorial ligands consist of two histidine N_δ's and one cysteine thiolate. Weak axial interactions complete the arrangement; there is a backbone carbonyl oxygen at the "north pole" and a methionine thioether at the "south pole." One histidine, the cysteine, and the methionine are all positioned on one loop; in *P. aeruginosa* azurin, this occurs from residue 112 to 121. Extending to the secondary coordination sphere, hydrogen bonds are formed between two backbone amides and the cysteine sulfur atom (Figure 1.3). Interestingly, the coordination environment is unperturbed by metal ion removal or substitution (by *e.g.*, Zn^{II}).[16-17] This is a consequence of this outer coordination sphere, it is the so-called "rack" effect (also referred to as an entatic state).[18-19]

We shall now move to a less focused view of the protein and appreciate the elegance of its entire molecular structure. Azurin has served as a fertile test bed for biophysical investigations. As a result of work primarily by the Malmström and Wittung-Stafshede labs, a detailed picture has evolved illustrating the roles of hydrophobic packing and cofactor binding on the folding mechanism as well as native-state stability. These factors cannot be discussed in a mutually exclusive manner, as metalation-state and type *i.e.* Cu^{I}, Cu^{II}, Zn^{II} all dramatically affect the biophysical properties of the protein. It should be noted that Zn^{II} binding, despite lacking

physiological relevance (except in the context of recombinant protein expression)[6,17] has facilitated many investigations of folding dynamics and stability.

The tertiary structure of *P. aeruginosa* azurin consists of a Greek-key ß-sandwich motif[20] characteristic of the cupredoxins.[1] The azurins feature, in addition to their cupredoxin fold, a long α-helix which in the case of *P. aeruginosa* azurin comprises residues 54-67. This α-helix is among the features that distinguish azurin from other cupredoxins, and has been implicated in stabilizing the folded protein,[21] though its deletion does not disturb the overall protein fold and only minutely perturbs the metal binding site. A structural comparison of *P. aeruginosa* azurin with azurin from *A. denitrificans* (PDBID: 2AZA) demonstrates a high degree of structural conservation, with a C_α root-mean-square deviation (RMSD) of 0.6 Å (Figure 1.4).[15]

The ß-sandwich is built around a core consisting of eight conserved hydrophobic residues,[22] V31, L33, W48, L50, V95, F97, Y108, and F110 using the numbering of *P. aeruginosa* azurin (Figure 1.6). These residues have been shown to participate in forming the interlocked-pair supersecondary structure characteristic of the ß-sandwich motif.[23] Steady state and kinetic analyses of alanine point mutations have revealed that half of these residues, L50, V31, L33, and V95, serve mechanistic roles as they form native-like interactions in the folding transition state, whereas I7, F15, W48, and F110 do not appear to participate in the folding pathway but rather serve to stabilize the folded protein.[24]

The azurin protein fold can be monitored by several techniques: UV-vis of the blue copper center (relevant only to the Cu^{II} form, *vide infra*), circular dichroism (CD) to monitor secondary structure, and fluorescence spectroscopy to monitor the local folding environment around W48. Thus, these methods each report in a location-specific manner allowing assessment of folding mechanism, *e.g.* "two-state" versus a folding mechanism involving multiple discrete intermediate states. *P. aeruginosa* azurin has been shown through equilibrium unfolding experiments with guanidine hydrochloride to have a folded state that is substantially stabilized ($\Delta\Delta G_U$ = 23 kJ/mol) by Cu^{II} binding.[25] Cu^{I} and Zn^{II} binding also result in stabilized folds (Table 1.1). Apo azurin folds with tau ~ 7 ms, while azurin in the presence of Cu folds in a biphasic manner (tau 1 = 10 ms, 85%, tau 2 = 200 ms, 15 %).[26-27]

Extended X-ray absorption fine structure (EXAFS, *vide infra*) measurements of Cu^{II} and Cu^{I} in the unfolded state,[28] along with electrochemistry[29] have demonstrated that Cu in either oxidation state remains bound to the unfolded protein. Subsequent experiments with histidine to glycine variants, as well as experiments with Zn^{II} protein showed these to be the ligands from the metal-binding loop (C-H-M).[30] The metal-protein interaction is only slightly weakened in the unfolded state (Table 1.1). For example, at pH 7.0 and at 293 K, the K_D for Cu^{II} is 25 fM in the folded state; the K_D is 300 fM in the unfolded state.[31] Zn^{II} is bound far less strongly in either folding state (82 nM, F; 5.1 μM, U); this has been attributed to the non-interaction of M121 with this metal, an assertion that is supported by the aforementioned EXAFS measurements.[28,23] Cu^{II} binding rates have been measured for *P. aeruginosa* azurin at pH 7.0, 293 K: in unfolded protein the metal binds on the submillisecond timescale; in folded protein full metal uptake takes several minutes.[26-27]

P. aeruginosa azurin unfolding has been demonstrated in apo- and Zn^{II} forms to be reversible and proceed through a "two-state" mechanism. However, the irreversible aerobic oxidation of the cysteine thiolate by Cu^{II} has precluded to date more detailed studies of this form of the protein.[29] Likewise aerobic oxidation of Cu^{I} azurin likely has precluded folding investigations. That said, substantial effort has been expended elucidating the mechanisms of folding of apo- and Zn^{II}-azurin. As mentioned, these studies have focused on the eight "hydrophobic core" residues V31, L33, W48, L50, V95, F97, Y108, and F110 as well as active-site and secondary coordination sphere mutants. Combined steady-state, stopped-flow, and theoretical investigations have verified a two-state folding mechanism for apo-protein and have characterized its transition state.[32-33] Apo-azurin folds around a native-like core comprised of V31, L33, L50 (Figure 1.5). This finding was corroborated by earlier work on C112S azurin.[34] Meanwhile, W48, Y108, and F110 do not participate in the transition state nucleus but stabilize the folded state (*vide supra*).

Zn^{II} azurin is a more complicated case, although it has yielded many insights into the effects of cofactor ligation on protein folding. It also folds via a "two-state" mechanism, and as mentioned retains the metal (bound to C112 and H117 in *P. aeruginosa* azurin) in the unfolded state. However, the folding transition state moves with denaturant concentration.[35]

Studies of folding kinetics by Wilson and Wittung-Stafshede allowed reconstruction of "snapshots" of the Zn^{II} azurin folding event.[36] Early during folding, diffuse interactions exist, though there is some clustering of residues around L50, V31, and V95. Native-like structure then forms around L50 presumably involving A82 and F97 (found nearby in the folded protein). Next, V31 and I81 join the folding nucleus. At this point, the investigators proposed the protein to "zip up," with native-like interactions achieved by residues I20, V22, W48, L50, I81, A82, V95, and V97. The investigators concluded from their work that Zn^{II} flattens a sharp activation barrier in the folding reaction coordinate. Finally, it was proposed that Zn^{II} does not participate in the folding process although it affects the folding energy landscape. Further, theoretical studies (calibrated to experiment) on the folding of Zn^{II} azurin focused on the mechanism by which the free energy barrier to folding is affected by the metal.[37] These studies found that the aforementioned "rack" forms early in the folding process, imparting a considerable entropic penalty on the process. Bond breakage of the G45 carbonyl and H46 imidazole ligation (the residues in *P. aeruginosa* azurin not bound to metal in the unfolded state) leads to a kinetic bottleneck that perturbs the folding of Zn^{II} (and presumably Cu) azurin relative to apoprotein.

All told, azurins are very robust proteins. The free energy of unfolding determined from guanidine titrations of *P. aeruginosa* azurin is 52 ± 3 kJ/mol in the Cu^{II} form, 40 ± 3 kJ/mol in Cu^{I}, and as mentioned 29 ± 2 kJ/mol as the apoprotein. Thermal stabilities provide the biophysically disinclined with more tangible numbers; these were reported in 1986 by Engeseth and McMillin in an investigation combining calorimetry and spectroscopy. They report an unfolding temperature, T_M, of 80° C for Cu^{II} azurin, 90° C for Zn^{II} azurin, and transitions at 62° C and 86° C for apoazurin.[38] Also reported are values for other metal derivatives (Table 1.2). These values have seen repetition in the literature in comparisons to various engineered azurins (*vide infra*).[39-42]

Before leaving the tertiary structure of the protein and its constituent hydrophobic core residues, we would be remiss in neglecting to mention *P. aeruginosa* azurin W48 (and, by extension, its analogues throughout the azurin family), a residue of both structural and purportedly functional consequence (Figure 1.5). W48 imparts 21 kJ/mol of stability to the apoprotein (as assessed by the W48A mutation).[32] Notably, W48 possesses a highly blue-

shifted emission band from its indole sidechain, with λ_{em} = 306-308 nm.[43] This band possesses fine structure[44] and is quenched with varying efficiencies by metal ions in the active site.[45] The emission is relatively long lived, with lifetimes at pH 8.0, 298 K of 4.7 ns in apoprotein and having a biphasic emission decay in Cu^{II} protein with 0.2 and 4.5 ns components.[46-47] These biphasic decay kinetics have been ascribed to conformational heterogeneity of W48.[48-51] Site-directed mutagenesis (SDM) studies[47] revealed that the high-energy emission is a consequence of a highly hydrophobic enviroment. These studies further relate photophysics to interaction of the indole with proximal residues. Thus, W48's utility in the aforementioned folding studies is clear – the position of the emission band is a sensitive reporter of hydrophobic core integrity.

Azurin possesses a disulfide bond near the N-terminus at its "southern" end between C3 and C26 (Figure 1.6). This feature is not universal to BCPs; it is absent in amicyanin and plastocyanin, and occurs in a radically different location in stellacyanin (near the protein north pole, by its metal center). Substitutions C3S and C26S were carried out individually and in concert.[52] Single C to S mutants maintain the overall fold of the protein and preserve the electronic structure of the type 1 copper. The double mutant has a vastly perturbed fold with the conversion of type 1 to type 2 copper. These initial studies demonstrated that the disulfide is not necessary for the proper fold and function of azurin, but that the fold is sensitive to non-native interactions installed at this location.

Further studies, these on the C3A/C26A mutant, sought a more quantitative description on the role of the disulfide in folding and stability. With the disulfide replaced by alanines, azurin adopts its proper fold and there appears to be minor, if any perturbation to the T1 copper (as probed by UV/vis and EPR).[53] However, the overall stability of the protein is lowered by the removal of the disulfide; by UV/vis, fluorescence, and differential scanning calorimetry (DSC), C3A/C26A azurin was shown to lose 20 ºC of thermal stability, unfolding at 60 ºC. The investigators posited that the disulfide stabilizes the folded protein by decreasing conformational entropy of the folded state and maximizing solvent exposure of hydrophobic residues in the unfolded state. Artificial disulfides have been introduced into *P. aeruginosa* azurin; their effects on folding and stability have been investigated and discussed.[54] It should

be noted that biophysical studies concerning the azurin disulfide have been limited to the steady state. Folding kinetics data are not available for mutants of the disulfides - their role in the transition states of azurin folding should be of interest.

P. aeruginosa azurin possesses two surface histidines, H35 and H83, which are not involved in metal cofactor binding (Figure 1.8). However, these residues are notable for functional and functionalizational reasons. H35 has been implicated as a conformational switch: it participates in a pH-dependent hydrogen bonding interaction with the protein backbone [pK_a (Cu^{II}-form) ~ 5.9-6.2, pK_a (Cu^{I} form) = 7.1].[55] Thus we now address the issue of the pH dependence study of the WT *P. aeruginosa* azurin 3D structure. At pH 5.5, the protonated H35 imidazole amine hydrogen bonds with the backbone carbonyl of P36.[14] At pH 9.0, the now-deprotonated histidine is hydrogen bound to the backbone amide of G37 as a result of a peptide backbone flip.[14] The active site remains essentially unperturbed as a consequence of this structural rearrangement, this has however been invoked to explain the pH-dependence of electron transfer reactivity and the $Cu^{II/I}$ reduction potential (*vide infra*). Its conditional participation as an outer-sphere determinant of Cu ligation will be presented in Chapter 2.

H83, while also ionizable, is more surface exposed and thus does not appear to modulate any pH-dependent structural perturbations. However, it deserves specific attention for two reasons. First, H83 was the first residue in azurin to be labeled with transition metal electron-transfer agents.[56] Subsequent mutagenesis studies have allowed the Gray lab to conduct remarkable studies of intramolecular protein electron transfer using azurin as the workhorse. These will be discussed in more detail later. Second, H83 has been found to modulate crystal contacts by coordination to an extra metal ion.[57] The resulting crystal form of azurin has allowed for determination of many 3D structures, including those reported in Chapters 2 and 3.

Having now extensively toured the "azurin road-map," we are well-equipped to discuss in detail the functional implications of the various structural features. We proceed immediately to the electronic structure of bound Cu^{II}; the factors contributing to its notable spectroscopic properties will provide a useful introduction to several methods that will be discussed in more detail in subsequent chapters.

SPECTROSCOPIC STUDIES: THE "BLUE COPPER PROTEIN QUESTION" AND BEYOND

The azurin copper binding site gives rise to a host of interesting spectroscopic features of complex origin. However, one cannot ignore the elephant in the dining room: solutions of azurin are intensely blue, with the most prominent component of its absorption spectrum being a band centered at 15.85 kilokaisers (kK = 1 x 10^3 cm^{-1}) (630 nm) with an extinction coefficient of 5700 $M^{-1}cm^{-1}$ (Figure 1.8).[58] The path to elucidating the origins of this and other peculiar spectroscopic features of blue copper proteins was fraught with controversy, but consensus seems to have been achieved.

Initial debates focused on the oxidation state of the copper chromophore. Cu^I complexes were known with intense coloration, particularly those involving donation from oxygen ligands.[59] This prompted R.J.P. Williams to postulate a chromophoric Cu^I ion as the eponymous blue center.[60]

Blue proteins other than azurin were known by 1960. It was two such proteins, ceruloplasmin and laccase, which were first shown to exhibit an atypically narrow axial hyperfine splitting ($A_{||}$) in their electron paramagnetic resonance (EPR, *vide infra*) spectra.[61] Such values typically range from 12 to 16 millikaiser (1 mK = 10^{-3} cm^{-1}) for tetragonal Cu^{II} complexes.[62] Ceruloplasmin and laccase display $A_{||}$ values of 8 and 9 mK, respectively. Assigning this spectroscopic feature to and thus establishing blue copper as arising from a bound Cu^{II} ion proved initially difficult, as quantitative EPR demonstrated this aberrant signal accounted for only approximately half of the stoichiometric copper in these proteins.

Enter azurin – one bound blue copper; one EPR spectrum with a narrow $A_{||}$ of ~ 6 mK (Figure 1.9).[63] These measurements correlated the chromophore with this now characteristic EPR feature. As such the blue coloration and narrow $A_{||}$ could be combined as a fingerprint that quantitatively established BCPs as belonging to a unique class of proteins with a signature electronic structure – Malmström thus proposed a nomenclature system that labeled normal, tetragonal "non-blue" Cu^{II} as "type 2" copper and blue copper as "type 1" copper.[64] Now

came the challenge of firmly establishing the type 1 electronic structure. Tetrahedral Cu^{II} complexes were known to exhibit narrow $^{63,65}Cu$ hyperfine splittings. These include $CuCl_4$,[65] the Cu^{II} complex of ($\alpha\alpha$'bromo-)dipyrromethene,[66] and Cu^{II}-doped dichlorobis(triphenylphosphine oxide)Zn^{II} [67] with $A_{||} \leq 2.0$ mK and $A_{||} = 2.5$ mK, and 2.0 mK, respectively. However, complexes of this variety lacked the intense blue absorption. Indeed, although compounds such as those reported by Holland, Tolman, and coworkers[68-69] come close, no model compounds could replicate (or have replicated) the full spectroscopic features of blue copper. This logic led Bo Malmström to propose that blue copper arose due to some strong influence from protein ligation.[70] The proposition that protein backbone modulation strongly influences protein cofactor reactivity had been circulating for several years;[18] Malmström thus went on to propose such a "rack" effect at play in blue copper. Around this time, R.J.P. Williams entered into the discussion the proposal of an energetically frustrated or "entatic" state that gave rise to the spectroscopic properties and activities of blue copper proteins.[19,71]

As mentioned, 1978 was an exciting year for azurin; Elinor Adman provided the world with a 3.0 Å resolution crystal structure of the active site that would later be refined to 2.7 Å (Figure 1.2).[9,11] Like plastocyanin,[10] the active site structure was shown to contain an inner coordination sphere consisting of two imidazole nitrogens from H46 and H117, as well as thiolate ligation from C112 with a curiously short 2.1 Å Cu-S(C112) bond.[72] The coordination sphere was complemented by weak axial interactions at the "north pole" from the backbone carbonyl of G45 (2.84 Å) and at the "south pole" from the thioether of M121 (3.18 Å distance). With this working model (and that of plastocyanin), spectroscopists had something into which to sink their teeth.

Two of these spectroscopists included Harry Gray and Ed Solomon, who may be regarded among the heroes of blue copper spectroscopy, as they solved the "blue copper protein question." In a comprehensive study combining CD, magnetic circular dichroism (MCD, *vide infra*), and low temperature electronic absorption spectroscopy, Solomon, Gray, and co-workers dissected the visible spectra of azurin, plastocyanin, and stellacyanin[73] as an extension to earlier work[74] applying similar methodologies to BCPs. They concluded that the blue

copper absorption arose principally from charge transfer from the imidazole and thiolate ligands, with the more intense "blue band" a product of the latter interaction.

Solomon then proceeded to clean house with the type 1 electronic structure, with on-going investigations interrogating subtleties arising among BCP variants. These studies have been progressively well-reviewed,[75-77] though we will focus on some of the most significant findings of these related investigations. This will provide a convenient introduction to techniques that will be employed in the studies described later in this dissertation.

Having given a nod to the historical background and controversy originally surrounding the assignment of the spectroscopic origin of eponymous feature of blue copper, we shall now examine the spectrum in detail. Our launchpad shall be the previously mentioned work of Solomon and Gray,[73] and our initial picture shall be the electronic absorption, or, UV/visible spectrum of azurin. As applied to transition metal complexes, this technique measures the energies at which electrons are excited between metal d-orbital levels (ligand field or LF transitions), from d-orbitals to ligand orbitals (metal to ligand charge transfer or MLCT transitions), from ligand orbitals to d-orbitals (ligand to metal charge transfer or LMCT transitions), or from ligand to ligand orbitals (LLCT). (While we shall not concern ourselves here with such matters, transitions can occur as mixtures of the aforementioned categories.) The selection rules governing the intensities of UV/vis absorption features are discussed in many textbooks, though the author recommends the work of Harris and Bertolucci[78] as an accessible entree to the field. Aficionados are encouraged to consult the works of Griffith,[79] Ballhausen,[80] and Figgis[81] for more advanced treatments.

The UV/vis spectrum of azurin in hand, we immediately note 3 features. The first is the intense and slightly asymmetric "blue band" at 15.85 kK with an extinction coefficient of 5700 $M^{-1}cm^{-1}$. Gaussian deconvolution of the spectrum reveals three other bands at 20.79, 17.65, and 12.83 kK. Initial assignments were based on LF treatments of Cu^{II} in a pseudo-tetrahedral ligand field environment and comparison to model Cu^{II} complexes. It should be noted that these initial treatments were subject to the occlusive fog-of-war of a noisy electron density map for *P. aeruginosa* azurin.

Nevertheless, substantial progress was made toward definitive assignment of the blue copper absorption spectrum. These absorption measurements were aided by room temperature CD and MCD measurements. CD spectroscopy measures light absorption of different polarizations by optically active species. MCD spectroscopy makes similar measurements but relies not on intrinsic optical activity but makes use of the Faraday effect, or the magnetic-field induction of optical activity. In depth discussion of the theory behind these techniques is beyond the scope of this review; the reader is instead directed to an excellent chapter by M.K. Johnson.[82] This now said, the combination of CD and MCD allowed resolution of additional features at 10.50 and 5.80 kK that were assigned as $^2B_2 \rightarrow {}^2B_1$ and $^2B_2 \rightarrow {}^2E$ LF transitions in the tetragonally flatted tetrahedral MO scheme. LF assignments were facilitated by the selection rules of MCD; specifically, LF transitions are far more intense in MCD than CD due to magnetic dipole intensity mechanisms.

The initial assignment of the charge transfer bands was intentionally omitted above; correct assignment required more sophisticated methodology. By measurement of single crystal absorption spectra, transition polarizations can be established. Assignments made by Solomon and coworkers using data from plastocyanin[83] can be extended to azurin. The intense charge transfer bands at 15.85 and 12.83 kK, by polarization, originate from the Cu-S interaction. Low-temperature MCD revealed reversed energy and intensity orderings of Sπ-Cu and with respect to a D_{4h}, type 2 copper complex.[84] The 15.85 kK band in azurin then is the Sπ-Cu LMCT, the 17.65 kK band is the S$\sigma\rightarrow$Cu. The 20.79 kK band is His N$\pi\rightarrow$Cu LMCT. The 12.83 kK band is a LF absorption; presumably $3d_{x2-y2}$ to $3d_{xz/yz}$ by analogy to Solomon's MO scheme for blue copper. In plastocyanin an additional LMCT, assigned as methionine S $\rightarrow$ Cu LMCT, is present at 23.34 kK. This band is not observed in *P. aeruginosa* azurin; this is likely a consequence of a longer S(M)-Cu distance relative to plastocyanin (3.18[14] vs 2.78 Å[85] at 1.9 Å resolution).

The other and arguably more intriguing spectroscopic feature of blue copper, as has been mentioned, is the narrow Cu $A_{||}$ measured by EPR (Figure 1.9). Determination of the origin of this feature required extensive investigation. In the process, this has led to the development and biological application of powerful spectroscopic methods. Ultimately the combined efforts towards resolving the mystery of the narrow $A_{||}$ led to a well-defined electronic

structure for blue copper. (It should be noted that much of the work addressing this issue involved studies of plastocyanin, however our discussion of the electronic structure of blue copper would be incomplete without this story!)

To allow full appreciation of the search for the narrow $A_{||}$'s origin, we need to develop EPR in slightly more detail than we have for previously covered techniques. We have treated the electronic structure of azurin's blue copper thus far without resorting to quantum mechanics and its requisite mathematical treatment; the fun need not stop - we may still proceed in our pseudo-qualitative fashion. As with the previously mentioned methods the reader is directed to the plentiful works covering the application of EPR to transition metals, from the highly accessible introduction by Palmer[86] to more in-depth treatments such as that by McGarvey[87] and, for the pathologically interested, the discourse of Neese and Solomon[88] as well as the tome of Abragam and Bleaney.[89]

The power of EPR, to distill the technique to its essence, is its ability to localize unpaired electrons (these unpaired electrons can be referred to as spins). In short, it answers the questions "where are they," "who are they interacting with," and "how seriously are they involved with those entities." The first question is addressed by the shape of the magnetic field created by the unpaired electron as it flits about its molecular orbital; this is manifested in the magnitudes of the deviations of the cartesian components of the *g*-tensor from the free electron value $g_e = 2.0023$. The energies effecting these transitions are field-dependent; EPR at multiple frequencies can thus be used to separate g-tensor contributions to EPR spectra from hyperfine and quadrupolar splittings. The transition energy levels probed by the EPR experiment are perturbed by the interaction of the unpaired spin(s) with nuclear spins of proximal atoms. In the case of transition metal complexes, these interactions are largely dominated by the interaction of the unpaired electron with its host transition metal nucleus; the multiplicities of these "hyperfine interactions" address the "who." Electron interaction with nuclei from non-parent (*e.g.* ligand) atoms result in "superhyperfine" splitting. Finally, the magnitudes of the hyperfine interactions, represented by the energy separations of the hyperfine lines, can give an indication of the strength with which the unpaired electron interacts with these nuclei.

The hyperfine interaction has three major contributors: the Fermi contact term, and the through-space spin and orbital dipolar terms. The first term arises from direct interaction between the electron and the nucleus; with a node at the nucleus it would seem that the Fermi contact term would amount to nothing for an unpaired transition metal electron localized in some d orbital. However, mixture of s-character into the ground state molecular orbital allows some probability at the nucleus, leading to non-zero Fermi contact. This term is isotropic. The spin dipolar term arises from interaction between the spin component of the electron's magnetic moment and the nuclear moment; localization of the unpaired electron to different d-orbitals leads to variable contributions of this term along different directions in the Cartesian coordinate; thus the spin dipolar term is anisotropic and sensitive to the orbital makeup of the unpaired electron's parent molecular orbital. Finally, there is the orbital dipolar term arising from an orbital contribution to the electron's magnetic moment; this term is also anisotropic and may be estimated by measurable deviations from g_e of the components of the g tensor.

Readily apparent in the azurin EPR spectrum is the interaction between the unpaired electron and $^{63/65}$Cu. This is the 4-line pattern observed at the lower end of the magnetic field sweep – it, finally and explicitly, is $A_{||}$. The splitting is 6.5 mK. The other feature we may note is the axial character of the spectrum; that is, $g_z > g_x = g_y$. EPR spectroscopy conducted at W-band (95 GHz) on a single crystal of *P. aeruginosa* azurin has established not only very precise values for the principal components of the g-tensor (g_x=2.0393 ± 0.0004, g_y=2.0658 ± 0.0007, and g_z=2.273 ± .004), but has also established the orientation of their corresponding axes with respect to the copper ligands (Figure 1.11, Table 1.4).[90] The magnetic z-axis is 15º off of the Cu-S(M121) bond. The x-y axes are placed roughly in the H46/H117/C112 plane. It should be noted that the slight site rhombicity and magnetic axis orientation highlight the peril of attempting to treat protein metal binding sites with strict group theory – Nature is not bound by character tables!

EPR at low microwave frequencies allows deconvolution of features arising due to hyperfine splittings from those arising due to g-anisotropy. A combined S- (3.4 GHz) and L-band (1.2 GHz) allowed accurate determination of hyperfine splittings from $^{63/65}$Cu as well as ^{14}N (Table 1.3).[91] This study also demonstrates the magnetic inequivalence of the imidazole

N's, a feature of blue copper that has been rigorously investigated with pulsed EPR techniques (*vide infra*).

The magnitudes of $A_{||}$ and g_z have been used as fingerprints of copper sites in proteins, establishing not only the type 1/type 2 regime, but also have permitted spectroscopists to predict the coordination of copper.[62] Azurin is, of course a type 1 protein, with representative g_z and $A_{||}$ values. The initial hypothesis pursued by Solomon for the narrow $A_{||}$ was a spin-dipolar mechanism. Mixing of sufficient (~12 %) $4p_z$ character into the blue copper frontier MO would lead to a spin dipolar contribution sufficient, given calculated Fermi contact[92] and an estimate from g-values of orbital dipolar contribution, to account for the low $A_{||}$.

X-ray absorption spectroscopy (XAS) provided an answer to the spin-dipolar question. X-ray absorption spectroscopy can be thought of as simply an extension of electronic absorption spectroscopy to very high (~0.050 – 80 keV) energies; it probes the promotion of core (*i.e.* 1/2s, 2p) electrons to frontier orbitals and into the continuum. Part of its power lies in its specificity: XAS can be targeted to specific elements. Moreover, features can be used to precisely determine metal oxidation states.[93] Thus XAS can be classified by both the atom and the orbital from which the electron is excited. Promotion from 1s is referred to as K-edge spectroscopy, for example. Beyond the so-called "edge," where electrons are ejected to the continuum, interference patterns can be measured arising from the scatter of photoelectron waves off atoms proximal to the absorbing atom. These are EXAFS, and from them can be extracted precise (moreso even than X-ray diffraction) interatomic distances. A useful treatment of XAS including EXAFS is available from Scott.[94]

Cu K-edge XAS of Cu^{II} complexes generally display two pre-edge (E < 9.02 keV) features.[95-96] (The pre-edge spectrum is referred to as the X-ray absorption near edge spectrum or XANES.) The lowest energy feature is the 1s to 3d absorption. This feature is a useful measure of distortion from octahedral and D_{4h} symmetry, as in these point groups it is electronic dipole forbidden (though it gains intensity through quadrupolar mechanisms).[97] This feature can gain intensity by the mixing of 4p character into the frontier 3d orbital; thus, it serves as an experimental measure of p-mixing. Indeed, in plastocyanin (and azurin, Figure

1.12) this feature gains intensity relative to D_{4h} copper model complexes.[95] However, single crystal XAS experiments showed that this mixing is $4p_{x,y}$, whose contribution to the spin-dipolar term would raise $A_{||}$.[96,98]

The narrow $A_{||}$ of blue copper is not due to a spin dipolar contribution. Another possibility was examined: the simple removal of electron density from the Cu nucleus. Thus the covalency of the Cu site was probed by a combination of methods. The direct measurement of Cu character in the ground state of blue copper was achieved by L-edge (2p/2s → continuum) XAS.[99] Comparison of plastocyanin Cu^{II} $L_{2,3}$ edge peak intensities to Cu^{II} model complexes indicated a ground state wavefunction for blue copper containing ~41% copper character. Mystery solved: the hyperfine splitting is narrow because the electron-nuclear interaction is attenuated by delocalization.

But whence? Previous studies had implicated the histidines as dominant contributors to the ligand field splitting of blue copper,[73,83] although there was also the issue of the short Cu-S(C) bond. Small superhyperfine splitting (~ 2 mK) from nitrogens in blue copper as measured by pulsed EPR (*vide infra*) contraindicated substantial delocalization over the histidines. Lacking nuclear spin, natural abundance sulfur could not be probed for superhyperfine interaction. However, returning to the hutch, the S K-edge could be used to determine the delocalization over the sulfur. Again comparing intensities to model complexes, 38% Sπ character was found in the ground state blue copper wavefunction.[96] No electron density was assigned to the methionine thioether. Based on SCF-Xα calculations (*vide infra*), 8% of electron density was assigned symmetrically to the histidines. So, to finish the current story: electron delocalization from S to Cu^{II} in the blue copper site results in high covalency with narrow $A_{||}$.

It would seem from the aforementioned discussion that azurin has played but a small role in the study of the electronic structure of blue copper. This is, of course, false. If we pursue our present course and chase down the remainder of the site electron density, we will find azurin back in the limelight. Moreover, we now finally encounter an area concerned with the electronic structure of blue copper undergoing active investigation. With that, we shall

immediately turn to more specialized magnetic resonance methods: pulsed EPR and NMR of paramagnetic molecules.

Pulsed EPR techniques include electron nuclear double resonance spectroscopy (ENDOR), electron spin echo envelope modulation (ESEEM), and the 2D hyperfine sublevel correlation spectroscopy (HYSCORE). These techniques allow the spectroscopist to measure hyperfine couplings that would fall within the linewidths of more conventional, CW-EPR techniques. While these techniques will be developed slightly and applied in Chapter 4, the reader is directed to a chapter by Chasteen and Snetsinger, as well as a recent review from Prisner and coworkers.[100-101]

A pioneering investigation combining W-band single-crystal ENDOR and X-band solution ESEEM spectroscopies on *P. aeruginosa* azurin confirmed asymmetry in the delocalization of the blue copper unpaired electron over the noncoordinated N_ε's of H46 and H117.[102] An ESEEM study confirmed this asymmetry and identified a third N which was thought to be a backbone amide.[103] A more thorough treatment by the same investigators repeating their single crystal work at W-band with ^{15}N-labeled crystals provided isotropic superhyperfine couplings for the noncoordinated H46-$^{14}N_\varepsilon$ (0.029 mK) and H117-$^{14}N_\varepsilon$ (0.043 mK).[104] These correspond, assuming localization to N sp^2 hybrid orbitals, to 0.24 and 0.47 % of the spin density. Not surprisingly, substantially more electron density is located on the coordinated N_δ's of H46 and H117. Again asymmetry is observed, with 4.9 % on H46 and 9.4 % on H117. Additionally, two further N signals were identified (for a total of five). ESEEM at X-band of the H117G variant provided further confirmation of these assignments and in particular the observed asymmetry.[105] Additional work by Goldfarb and coworkers proposed an ENDOR-visible ^{14}N to be the backbone amide of H46, coupled to the copper through G45 – a proposition implying G45 behaves as a *bona fide* ligand as opposed to merely providing an electrostatic perturbation, though based on investigations from Groenen and coworkers, in addition to further work by Goldfarb (Chapter 4), this N is far more likely to be the backbone amide from C112.[106]

Deuterium ENDOR studies at W-band have attempted to quantify spin density over C112. This study displayed appreciable agreement with Solomon's L-edge and S K-edge measurements, yielding 45 % spin density on Cu and 30 % on S.[107] However, the point of the exercise – quantification of delocalization over the cysteine ß-protons – would not come to fruition until a later study that showed an uneven distribution over the two protons of 1.6 and 1.3 % spin density.[108] To date no study has appeared attempting to measure ^{33}S superhyperfine coupling in the blue copper site. This is likely a cost/benefit issue, as electron delocalization afforded by ligand K-edge as well as indirectly through measurement of co-residual superhyperfine coupling provides consistent values; meanwhile, the price of ^{33}S is not inconsequential.

NMR investigations proceeded in parallel with these studies. This technique can also be used to measure superhyperfine couplings. However, owing to drastic broadening effects, NMR is incredibly sensitive to the spin relaxation time of unpaired electrons of paramagnetic species. Typically these relaxation times are prohibitively long for Cu^{II}, however type 1 copper electron spin relaxation times are orders of magnitude shorter than those of type 2 copper. Combined with the development of specialized methods for the detection of quickly relaxing resonances,[109-111] paramagnetically shifted signals corresponding to atoms within the inner coordination sphere of Cu^{II} can be observed. Furthermore, if electron transfer is sufficiently rapid between Cu^{II} and Cu^{I} forms of the protein (as it is for azurin, *vide infra*), exchange spectroscopy (EXSY) and saturation transfer difference (STD) experiments may be conducted to assign the paramagnetically shifted resonances, assuming prior knowledge of the chemical shifts of residues in the Cu^{I} form of the protein. Informed by such studies as well as EPR investigations, one may use NMR to quantify the extent of Fermi contact (*vide supra*) and thus extract hyperfine terms. The power of NMR is thus evident in its ability to site-specifically pinpoint electron delocalization near a paramagnetic center. Moreover, information from dipolar and contact shifts has served as valuable structural refinement constraints that permit the structural characterization of metalloproteins.[112] For more further discussion of the origins, interpretation, and application of the NMR of paramagnetic speices, the reader is directed to works by Ming[113] and Bertini.[114] A detailed description appears in Chapter 4, as well.

The first paramagnetically shifted Cu^{II} ^1H signals in BCPs were reported simultaneously for *P. aeruginosa* azurin, amicyanin, and some amicyanin variants.[109] Furthermore, EXSY experiments could correlate these resonances to previously assigned Cu^{I} signals.[115-116] This permitted the Canters lab to not only assess electron delocalization over active site protons in a site-specific manner, but more significantly they definitively established the presence of electron density over the axial methionine in the blue copper coordination sphere. Bertini and coworkers used this work as a springboard to conduct a study that, aided by a larger 800 MHz spectrometer, included a comprehensive assignment of the Cu^{II} *P. aeruginosa* proton spectrum, complete with pseudocontact-corrected hyperfine terms for not only ligand protons, but the C_α and amide protons of N47 as well.[112] The measurement of spin delocalization over N47 highlights the influence of the "rack" over the electronic structure of the type 1 site. The investigators also compared the hyperfine couplings to cysteine C_β protons among azurin, plastocyanin, and stellacyanin; they suggested that among these BCPs, azurin possesses the "most covalent" Cu-S(C112) bond. Their proposal that the G45 carbonyl's influence on maintanence of Cu co-planarity with the N-N-S ligand triad (by balancing the attractive influence of M121) appears valid in light of a similar analysis by the Canters group concerning Cu-S(M) interactions and site rhombicity in their aforementioned study.[109]

Investigations of hyperfine couplings to azurin ligand carbons via ^{13}C direct-detected NMR are currently underway in Vila's laboratory. ^{15}N couplings may also be measured, but are more technically challenging.[117] Moreover, for azurin it would seem that pulsed EPR techniques have finished the job *viz.* site nitrogens.

Before we leave experimental investigations of the electronic structure of blue copper, we shall survey vibrational studies of metal-ligand bonding. Little time was spent discussing efforts toward establishing the nature of the type 1 coordination sphere; however, the contributions of Raman spectroscopy will be highlighted as they have ultimately led to insights beyond simply answering the now silent clamor of "Why is it blue?" (Although Raman spectroscopists certainly joined the din!)[118-120] Raman spectroscopists have gleaned from azurin a detailed understanding of the nature of Cu-S(C) ligation in BCPs, including insights into tuning of this ligand by outer-sphere coordination by "rack" amides (*vide infra*).

Raman spectroscopy is a vibrational technique that measures the loss in photon enegy from inelastic scattering of light with molecular species. These losses in energy, referred to as Raman shifts, correspond to molecular vibrational frequencies. Moreover, their intensities may be used to probe excited state structural deviations. Resonance Raman spectra are produced when the probe light spectrally overlaps with an absorption band exhibited by the molecule of interest. In this case, the intensities of Raman shifts corresponding to vibrations of atoms related to the chromophore are enhanced. For in-depth discussion, the reader is directed to the several available treatments.[121-123]

Excitation into either the blue copper Sπ- or Sσ-Cu^{II} LMCT's produces a rich resonance Raman spectrum exhibiting several strong fundamental vibrations between 250 and 500 cm^{-1}. [118-120,124-125] Assignment of this spectrum required substantial effort, including temperature dependence studies,[126-127] normal coordinate analysis,[128] and production of ^{2}H, ^{15}N, ^{34}S, and $^{63/65}Cu$ isotopologs.[129-134] The prevailing wisdom dictates that these features arise primarily from the ligated cysteine. Assignments of the *P. aeruginosa* azurin resonance Raman spectrum from Ref. 133 are reproduced in Table 1.5.

Among the aforementioned experiments, the resonance Raman spectroscopy of azurin reconstituted with Cu^{II} in D_2O deserves special attention. Blue copper Raman spectra recorded by exchanging holoprotein into D_2O typically produced minor, ~1 cm^{-1} shifts in observed bands.[129-130] By now, NMR spectroscopists had observed that the amide protons of N47 and F114 in *P. aerugniosa* holoazurin did not exchange for ^{2}H – only in the case of apoprotein was exchange observed.[115,136] However, much larger isotope shifts on the order of 5 cm^{-1} were observed when azurin was reconstituted in D_2O.[135] These effects were attributed to hydrogen bonds from the N47 and F114 amide protons to the cysteine sulfur being coupled to Cu-S vibrational modes. These findings lend yet further credence to the importance of the N47-C112-F114 hydrogen bond network in defining the type 1 electronic structure. As the authors state, these interactions must be included in any complete electronic structural description of azurin, and by extension, all BCPs.

Resonance Raman spectroscopy has also served as a probe of BCP active site geometry. The Cu-S(C) stretch is highly sensitive to geometric distortions. This allows one to distinguish

between trigonal type 1 sites (where the Cu is neatly in the N-N-S plane) from tetrahedrally distorted sites. In the former case the Cu-S(C) Raman shifts occur between 430 and 405 cm^{-1}, whereas in the latter case they are shifted to lower energy, exhibiting values from 405 to 355 cm^{-1}.[137] Resonance Raman intensities also provide structural information, in that intensity patterns are sensitive to the size and conformation of the metal-binding loop.[130] This information, combined with the insensitivity of the intensities to metal ion identity support the assertion that BCPs exert substantial biophysical control (the "rack") over the electronic structure of their cysteine thiolate ligand.

As spectroscopy and theory can be regarded as perfect bedfellows (particularly in bioinorganic chemistry), we shall briefly chronicle azurin's adventures *in silico* before making our departure from the blue copper site. Early computational investigations of blue copper were limited by something fairly evident: BCPs are big molecules. However, early computational limitations could be overcome by focusing on either model complexes or minimal active site models. Using self-consistent field-Xα (SCF-Xα) scattered-wave calculations,[138] Solomon was able to inform many of his earlier studies of blue copper with computational results leading to estimates of electron density distributions that have since been verified by experiment.[83,95,139]

More recent computational investigations have sought to establish the link between the divergent structures among BCPs and their spectroscopic features. *Ab initio* studies, again on active site models, have suggested that for trigonal type 1 proteins such as azurin, the Cu-S(C) bond consists mostly of S-π character, whereas tetrahedrally distorted BCPs have increasing amounts of S-σ character in these bonds.[140] This result comprises some of the theoretical support for Solomon's "coupled distortion" model, where this change to a strongly S-σ bond results in the conversion to type 2 copper; recently this configurational shift has been shown to rely upon protein-imposed constraints over axial ligation - in nitrite reductase the lack of constraint allows transition between type 1 and type 2 copper; in BCPs such as azurin no such fluxionality exists owing to the "rack" constrained active site.[141]

Further computational studies have sought to produce electronic structural descriptions of blue copper that reproduce the abundant EPR/NMR hyperfine data. Including only the H-H-C sidechains along with the copper, the experimental g tensor and ^{14}N hyperfine tensors could be reproduced.[142] Density functional theory (DFT)[143] has also been applied to this problem; with DFT inclusion of axial ligation in this case was not computationally prohibitive.[144] Although experimental EPR parameters could be reproduced, the electronic structural description was found to be highly functional dependent.

Of course, the BCP electronic structure relies on far more than simply the inner coordination sphere. The combination of quantum mechanics (QM) with molecular mechanics (MM) into the QM/MM approach[145-146] allows the inclusion of secondary and "beyond secondary" coordination effects on the electronic structure of blue copper. This approach, while not trivial, is computationally tractable. Sinnecker and Neese demonstrated the importance of inclusion of not only the full protein, but also its aqueous solvation cage for the accurate reproduction of plastocyanin's spectroscopic properties and by extension its proper electronic structural description.[147] The importance of solvation has been further investigated in a study on azurin wherein the QM Hamiltonian was polarized by solvent modeled as point charges.[148] This work suggests that the discrete solvation of azurin and by extension all metalloproteins is critical to spectroscopic properties and function.

ELECTRON TRANSFER: THE WHY, THE WHERE, AND THE HOW

In chemistry as much as any other scientific discipline, form follows function. A rich discussion has preceded of the interplay of biophysics and physical inorganic chemistry. Now the physiological function of azurins deserves equal billing, and we note at the outset that experiments in this area have had impacts that extend far beyond simply answering "Why does the bug need this little blue wonder?" So, we shall shift gears briefly to biology before returning to the comfort of more physical ground.

It should be appreciated by this point that there are many species that produce azurins. *Methylobacillus flagelattum*, a methylotrophic anaerobic bacterium, has been shown by gene deletion to require its azurin for optimal growth on methylamine.[149] However, more commonly the organismal role for azurin is the subject of speculation. As has been our *modus operandi* we take *P. aeruginosa* as our prime example. Early work implicated its azurin in denitrification (reuduction of nitrate to nitrite).[150-152] Evidence for such participation included correlation of expression levels with anaerobic incubation in the presence of nitrate, as well as the observation of electron transfer *in vitro* with nitrate reductase. Moreover, the co-isolation with cytochrome c_{551} and observation of *in vitro* electron transfer suggested a role for this protein as a redox partner.[2,153] However, molecular biologists have demonstrated that *Pa* is not necessary for nitrate reduction; *P. aeruginosa* strains from which the azurin gene is disrupted show little difference in viability when grown anaerobically in the presence of nitrite or nitrate.[154] This work did propose a role for *P. aeruginosa* azurin in oxidative stress response, however the exact nature of this participation awaits elucidation. Interestingly, after half a century we still do not know the physiological role of one of our most studied molecules.

As alluded to, far more important than "What *does* it do?" is "What *can* it do?" *P. aeruginosa* azurin *can* participate in electron transfer (ET) with the organism's cytochrome c_{551},[153] its cytochrome *c* peroxidase,[154] and its nitrite reductase (at one point regarded to possibly be a cytochrome *c* oxidase).[155] Studies of reactions between azurin and these redox partners opened the door to azurin's participation in investigations of biological ET.

This threshold was first passed in 1970. Eraldo Antonini and coworkers, anticipating extended (and extant) debate regarding the mechanism of biological ET, reported the first kinetics data on azurin: this was the mixing experiment between the *P. fluorescens* azurin and its cytc_{551}.[156] Concomitant oxidation of one constituent was observed with reduction of the other, indicating ET between the proteins. Regardless of the direction, ET was rapid, with apparent second order rate constants on the order of 10^6 $M^{-1}s^{-1}$. Reactions between this azurin and mammalian cytochrome *c* were found to be three orders of magnitude slower; this was taken as evidence for physiological ET between the two bacterial proteins. Also noted was complicated concentration dependence – the reaction was not simply a second-order process.

Two camps sought to firmly establish the mechanism of ET from azurin to cytochrome *c*. Employing the temperature jump technique, Pecht and Rosen observed two kinetically distinct processes at pH 7.0. Preliminary analysis suggested that these arose from complex association and electron transfer steps.[157] Brunori and coworkers duplicated the first group's results, but differed in their interpretation of the data.[158] The faster of the two reactions was thought to be electron transfer from reduced *P. aeruginosa* cytc_{551} to oxidized azurin based on its concentration dependence behavior. The slower process, independent of reactant concentration, became the subject of further controversy. What was immediately apparent was that a simple A + B ↔ C + D picture did not apply to this reaction. Subsequent work led to the proposition that the mechanism involved equilibrium between redox-inactive forms of Cu^I azurin.[159] However, another treatment of the mechanism included a conformational equilibrium of Fe^{III} cytochrome c_{551}.[58] Interestingly, kinetics measured several years later substituting the *Alcaligenes faecalis* azurin for that of *P. aeruginosa* in the reaction with *P. aeruginosa* cytc_{551} were best modeled lacking the redox-inactive Cu^I azurin equilibrium.[160]

NMR spectroscopists provided an explanation for this peculiar behavior. A pH-titratable histidine was observed in the NMR spectrum of *P. aeruginosa* azurin.[136,161-162] The pK_a of this histidine (~7) was consistent with the equilibrium constant for the inactive azurin conformer proposed by Pecht and Rosen. This histidine was ultimately identified as H35. Moreover, NMR studies of the *A. faecalis* azurin showed its H35 to have a pK_a much lower, as it could not be protonated.[163] (Subsequent crystallographic work has revealed that H35 in *A. faecalis*, like *A. denitrificans* is buried deeper in the protein than in *P. aeruginosa*, *vide supra*).[15,164] Thus evidence

was mounting in favor of H35 as the residue responsible for the redox inactive form of the Cu^{I} *Pa* azurin.

Final proof awaited the recombinant DNA revolution. Gerard Canters, one of the master azurin sculptors, directed the systematic replacement of *P. aeruginosa* azurin's H35 with non-ionizable residues F, L, and Q.[165] Kinetics experiments, again mixing with *cyt* c_{551}, showed obviation of the "slow phase." Thus, H35's protonation equilibrium was the factor leading to the complicated kinetics. Soon after, structural work would demonstrate that the H35 protonation state dictated the backbone torsion of P36/G37.[14] The kinetics battle between the Pecht and Brunori camps occurred at ~ pH 7, near the pK_a of H35 - with its Cu oxidation-state dependent pK_a, the conformational flip leads to a condition where site rigidity is compromised and thus electron transfer reactivity is rendered less efficient by a transiently increased reorganization energy (*vide infra*).

The azurin-cytochrome mixing experiments would provide still more insights into biological ET. In addition to the lively debate from which we just departed, there was also discussion of the nature of the ET-competent complex between the two proteins. The reaction was thought to be outer sphere in nature, based on the solvent inaccessibility of the blue copper site. However, the path from electron donor to electron acceptor required elucidation. Farver and Pecht reported in 1981 a technique to label plastocyanin with Cr^{III}.[166] The application of this technique to *P. aeruginosa* azurin indicated the existence of two electron transfer sites on azurin; Cr^{III} labeled azurin reacted slowly with cytochrome c_{551}, yet showed unperturbed kinetics with nitrite reductase.[167-168] The Cr^{III} was proposed, based on the now-available crystal structure, to occupy a hydrophobic patch near H117 consisting of residues M13, V43, M44, M64, F114, P115, G116, H117, A119, and L120 (Figure 1.11). This experiment demonstrated elegantly interface-specificity of interprotein electron transfer. However, Canters would go on to propose that Cr^{III} disrupted ET with nitrite reductase by changing the reduction potential of azurin, rather than disrupting the pathway.[165] Nevertheless, this experiment did support the Farver/Pecht proposition of the H117 "hydrophobic patch" as the site of interaction with cytochrome c_{551}.

In parallel with the early protein-protein experiments, investigations mostly by the Gray laboratory explored the ET reactivity of *P. aeruginosa* azurin with coordination complexes. These studies applied the theoretical framework of Marcus to compare the ET reactivities of a range of metalloproteins. Before discussing the implications of this work, we shall briefly develop the Marcus theory.

The semiclassical Marcus expression for electron transfer rates is given by Eq. (1.1):[169]

$$k_{ET} = \sqrt{\frac{4\pi^3}{h^2 \lambda k_B T}} H_{AB}^2 \exp\left\{ -\frac{\left(\Delta G^\circ + \lambda\right)^2}{4\lambda k_B T} \right\} \tag{1.1}$$

In Eq. (1), h is Planck's constant, k_B is Boltzmann's constant, T is the temperature (K), H_{AB} is the electronic coupling between reactants, $-\Delta G^\circ$ is the driving force for electron transfer (typically calculated from the reduction potentials of the donor and acceptor), and λ is the reorganization energy. When the driving force of the reaction equals the total reorganization energy the rate constant reaches its maximum value, k_{MAX}. H_{AB}^2 decays exponentially with the separation distance; as such we can estimate k_{MAX} by Eq. (1.2):

$$k_{MAX} = 1 \times 10^{13} \exp\left\{ -\beta (r - r_0) \right\} \text{ s}^{-1} \tag{1.2}$$

where r is the donor-acceptor distance and r_0 is the value of r for donor and acceptor in direct (van der Waals) contact; the generally accepted value for r_0 is 3.0 Å. ß then is a metric for the strength of coupling between donor and acceptor, with smaller values indicating greater coupling.

Another special case is that of electron self-exchange (ESE), *e.g.* ET from Cu^I azurin to Cu^{II} azurin. In this case, $\Delta G^\circ = 0$, so ET rates are largely regulated by λ. Thus ESE provides a measure of a molecule's intrinsic ET reactivity; this is a convenient metric for comparing closely related species for which the electronic coupling can be assumed to be approximately the same.

Because there is no net formation of product/loss of reactant, ESE would seem to be a difficult quantity to measure. However, arising from the Marcus theory is the Marcus cross-relation, Eq. (1.3):[169]

$$k_{12} = \sqrt{K_{12}k_{11}k_{22}f_{12}} \tag{1.3}$$

Thus from the knowledge of the ET rate constant of a bimolecular reaction such as that between azurin and cytochrome *c*, the equilibrium constant K_{12} (calculated from ΔG^o) and with knowledge of the ESE rate constant k_{nn} of one of the species, the ESE rate of the remaining species may be calculated. The remaining term, f_{12}, is typically assumed to be 1, with this approximation approaching validity as K_{12} approaches 1. Even without defined ESE rate constants, comparisons among the same reaction could be used to define *relative* rate constants among the varied reagent. We elaborate on this discussion in Chapter 5, but for now we are poised to continue our narrative.

These tools in hand, the Gray contingent began mixing metal complexes with a host of ET proteins: cytochromes, laccases, azurins, plastocyanins, *etc.*[170-175] Some representative data, mostly to highlight the discrepancies in calculated ("apparent") ESE rate constants, appear in Table 1.6. The variation within the magnitudes of apparent ESE rate constants calculated using results from the range of redox agents suggested different binding modalities and thus different donor-acceptor coupling among the proteins studied. That stellacyanin displayed the most consistent rate constants indicated a surface-exposed metal site, an assertion that would ultimately be verified by structural studies.[176]

The Gray effort was complemented by the Pecht lab, whose work with the ferri/ferrocyanide couple invoked entropic arguments to explain several rate discrepancies; differences in donor-acceptor coupling, explained as a more "buried" reaction center in azurin vs plastocyanin, led to different calculated ESE rates.[177] Moreover, the Pecht study lent further credence to the notion that putative physiological partners display enhanced bimolecular reaction constants owing to interfacial optimization. Further validation of the Marcus approach to protein ET kinetics would come from Wherland and Pecht's return to

BCP/cytochrome couples.[178] This landmark study demonstrated the ability to model 13 experimentally observed reaction rates using only six ESE rate constants; notably, the value calculated for ESE rate constant of *P. aeruginosa* azurin, 9.9 x 10^5 $M^{-1}s^{-1}$, agrees well with directly determined values (*vide infra*).

To further investigate the intrinsic ET reactivity of *Pa* azurin, the Canters group developed methods to measure its ESE rate. Two methods were evaluated in parallel: one being freeze-quench EPR mixing ^{63}Cu azurin with the ^{65}Cu isotopolog[179] and the other being the measurement of Cu^{II} concentration dependence of the T_2 relaxation times of Cu-proximal ^{1}H NMR shifts in a largely Cu^{I} azurin sample.[180-181] The rate from the EPR experiment, 2.4 ± 1 x 10^6 $M^{-1}s^{-1}$ (corrected to room temperature), agreed with the results from the NMR experiment, 0.4 – 1.4 x 10^6 $M^{-1}s^{-1}$. The NMR experiment, owing to its relative ease and lower cost has become a standard technique for the measurement of BCP ESE rate constants. Importantly, it also demonstrated that the low and high pH forms of azurin are equally reactive, with measured rate differences largely attributed to ionic strength variations.

The NMR experiment also had the last word in the discussion of the site of azurin ESE reactivity. The M64E substitution introduced pH-inducible negative charge in the hydrophobic patch (*vide supra*).[182] At low pH, with the hydrophobic patch still devoid of net charge, ESE reactivity, 1 x 10^6 $M^{-1}s^{-1}$, was unperturbed relative to wild-type. However, once deprotonated, E64's negative charge slowed ESE to 1.6 x 10^4 $M^{-1}s^{-1}$, almost two orders of magnitude. Thus, the hydrophobic patch also mediates ESE. This information was exploited by Farver and coworkers to establish the pathway of ESE.[183] It was observed in the 1991 Nar structure that azurin formed a homodimeric face at the hydrophobic patch (Figure 1.12).[14] Interestingly, two water molecules were located in this interface. Calculations employing many-electron wavefunctions (*vide infra*) demonstrated these water molecules to be crucial in a well-coupled ET pathway, with adjustments in their position propagating to orders of magnitude differences in H_{AB}.

Bimolecular azurin ET reactions were also employed to investigate long-range electron transfer (LRET). Initial work reanalyzing the data from the aforementioned metal studies sought to establish the distance-dependence of ET rates.[184] However, it was clear that precise

donor-acceptor distances were a requirement for rigorous analysis. Structural studies informed the study of the Cr^{II} reduction of plastocyanin and azurin by localizing the binding sites,[185-186] but it was the work of Farver and co-workers on azurin and stellacyanin that ultimately confirmed that the ET and labeling sites of Cr^{III} on BCPs were identical.[187] A long-distance locus of interaction between azurin and the photoexcitable complexes $Cr(bpy)_3^{3+}$ and $Ru(bpy)_3^{2+}$ was modeled by docking simulations; acceptable agreement between the extracted distance and the kinetics measured at concentrations amenable to formation of the remotely-bound complex was found within the Marcus theoretical framework.[188]

While reasonable predictions of donor-acceptor distances could be extracted from these transition metal mixing studies, a new direction was due. Of course electrons still went from donor to acceptor, but these electrons would not be leaving their molecule of origin. The Cr^{III} labeling of BCPs by Farver and Pecht[166-168] provided an inspiration for what would become landmark protein ET experiments. Ultimately, this scheme proved unsatisfactory owing to the substitutional lability of the Cr^{II} ET product. However, the Gray lab found a winner in Ru-labeled proteins.

Jay Winkler delivered the flash heard around the world in 1982.[189] The target was a solution containing $Ru(bpy)_3^{2+}$, ethylenediaminetetraacetic acid, and cytochrome *c* labeled at H33 with $Ru^{III}(NH_3)_5$. The excited $Ru(bpy)_3^{2+}$ would deliver electrons to both the Fe^{III}-heme and the $Ru^{III}(NH_3)_5$, but ET could also be observed from the Ru label to the heme. Subsequent work would allow exploration of the distance dependence of LRET.

Azurin joined the Ru-labeled LRET party in 1983 with a similar experimental scheme involving the *P. aeruginosa* protein labeled at H83 (*vide supra*).[190] Analysis of the thermodynamics of LRET from H83 to the Cu revealed a very low $\Delta H^{\ddagger}$, suggestive of very low λ as a characteristic effecting efficient ET in the blue copper site.[191] This analysis would be complemented some years later by a combined temperature- and driving-force dependence study employing a series of different labels at H83 that would provide a solid $\lambda = 0.82$ eV for *P. aeruginosa* azurin.[192] This λ agreed with that calculated by LRET studies of Farver and Pecht (*vide infra*).

Weighing in to the still-contentious issue of distance and medium dependence would prove the first of azurin's major triumphs in LRET. Again, it was the recombinant DNA revolution that would empower major strides. The issue of medium dependence of LRET demanded an answer. Studies of various cytochromes *c* labeled at various positions had provided a wealth of information, but lacking in the analysis was a systematic study of increased separation between ET donor and acceptor along defined secondary structure.[193] Using the Richards synthetic gene for *P. aeruginosa* azurin, H83 was conservatively mutated to Q. The Gray group generated single mutants stationing a histidine at 122, 124, and 126 along the same ß-strand. Ruthenium labeling with agents suitable for activationless ($\Delta G^o = 0$, Eq.(2)) ET followed by laser flash-quench studies revealed an exponential distance dependence of electron transfer with a $\beta = 1.1$ A^{-1} (Figure 1.13).[194] That these rates corresponded to ET involving tunneling through the protein backbone was conclusively demonstrated by the repetition of these experiments in single crystals of Ru/Os-sensitized azurin.[195]

These experimental studies supported the development of a new theoretical framework for donor-acceptor coupling in LRET. Global analysis of data from a series of ET reactions led Dutton and coworkers in 1992 to propose a one-dimensional square tunneling barrier model with a uniform ß of 1.4 $Å^{-1}$.[196] Put simply, the intervening medium is inconsequential to the kinetics – ET is "as the crow flies" through a protein. Such a physical description was inadequate to describe the ET of ruthenated proteins as measured by the Gray contingent. Beratan and Onuchic had proposed the so-called "pathway" model, wherein LRET couplings are modeled as a chain of repeat units whose contributions to the distance decay are specific to their nature.[197-200] Intuitively, covalent bonds represent a strongly-coupled unit, with hydrogen bonds and through-space jumps contributing respectively greater attenuations to the coupling. The pathway model was employed successfully to correlate the rates of ET in ruthenated cytochromes.[201] Electrons, it would seem, are ants following a trail. They are not crows.

The pathway model would find further success when applied to the ET kinetics of ruthenated azurins. The pathway model was elaborated upon in 1995 to more intimately treat the issue of disparate contributions from different types of bonds.[202] Furthermore, the pathways treatment was modified to take into account the anisotropic covalency of the blue copper site; so-called "Solomon weights" were applied to the azurin ligands based on

electronic structural calculations from the Solomon lab.[139,203-204] In this scheme, metal-ligand coupling diminished in strength with the H46/H117 nitrogen's worth about 0.25 the C112 sulfur, and the G45 carbonyl and M121 thioether worth 0.1 the weight of C112. This treatment, applied to the analysis of the H122/124/126-Ru and H83-Ru azurins, demonstrated the importance of explicitly modeling hydrogen bonding networks along ET pathways.

Along with Gray and coworkers, Pecht and Farver developed their own scheme for studying LRET.[205] This technique would not require any special modification of azurin. We return now to one of the features that distinguishes azurin among the BCPs – the south-pole disulfide. Pulse radiolytically generated CO_2^- radicals were used in a manner similar to $Ru(bpy_3)^{2+}$: initial rapid bimolecular reduction of both the disulfide to the radical anion (SS^-) and Cu^{II} to Cu^{I} may take place, however, under conditions of excess protein over reducing CO_2 radicals only a few azurin molecules are reduced at both sites. Hence a slow, concentration independent reduction of remaining Cu^{II} coupled to SS^- oxidation could also be seen. This kinetics phase was LRET from SS^- to Cu^{II}.

Farver and Pecht have made substantial contributions concerning medium effects on LRET from this experiment. Early on the team compared *P. aeruginosa* azurin to the *A. faecalis, A. species* and *P. fluorescens* proteins.[205-206] The measured rates of ET from SS^- to Cu^{II} at 298 K, pH 7.0 were 44 ± 7, 11 ± 2, 28 ± 1.5, and 22 ± 3 $M^{-1}s^{-1}$, respectively. From this work it was supposed that differences in ET path were the dominant contributors to the disparate kinetics. A major difference among the azurins was the substitution in *A. faecalis* and *P. fluorescens* of V and L for W48, respectively. This implicated W48 in electronically coupling the Cu to the disulfide. However, theoretical work by Broo and Larsson favored a structural rather than electronic role for W48.[207] Application of the Beratan/Onuchic pathways model implicated two possible pathways through *P. aeruginosa* azurin in the Farver/Pecht ET experiment (Figure 1.14).[208-209] One has been referred to as the "W48" path, which makes a through-space jump from V31 to W48, and the other is a largely covalent-bond path terminating with a hydrogen bond from N10 to H46. Application of the "Solomon weights" to these paths renders them roughly equivalent in contribution to the observed ET rates.

Site-directed mutagenesis stimulated the Farver and Pecht studies to a similar degree as the Gray work. H35Q, M44K, and M121L mutants would allow studies of the driving force dependence on ET kinetics, though these effects could not easily be decoupled from simultaneous perturbations to reorganization energy.[210-211] Mutations directly to the inner coordination sphere, H46G, H117G, and M121H, produced concerted perturbations to driving force, reorganization energy, donor-acceptor distance, and donor-acceptor coupling.[212] The influence of W48 on the kinetics was probed by working on a host of azurin variants. Its substitution by A, F, S, Y, L, and M would have only slight effects on the ET kinetics.[211,213] However, that all of these mutations and more produced kinetics with correlated activation parameters demonstrated consistency in the ET mechanism, *i.e.* ET proceeded through the W48 and H46 pathways. By extension, in all cases the kinetics were inconsistent with the Dutton model.

It should be noted that although it appears W48 plays a small role in the pulse radiolysis kinetics of wild-type protein, a recent report demonstrated its capacity for ET to Cu in azurin, confirming suggestions from years of fluorescence quenching studies.[45] Photochemically generated $W48^{\bullet}$ was observed by excited state ET from W48 to Cu^{II} with concomitant indole deprotonation, generating W48 neutral radical. Species identity was confirmed by EPR and resonance Raman, with comparison to previously characterized tryptophan radical species.[214] That ET is possible from W48 in this case but that it is not necessary for rapid LRET in the PR experiments implies that either the H46 path can become preferential and thus destructive pathway interference is lifted, or that the driving force is not available in the case of the PR experiments to generate the $W48^{\bullet}$ intermediate necessary to enhance the kinetics.

Before moving on, we should highlight two particularly interesting results reported from the pulse radiolysis studies that are relevant to ongoing research. First, deuterium isotope effect studies showed a k_H/k_D of 0.7 at 298 K in *P. aeruginosa* azurin.[215] The more rapid kinetics in D_2O were a result of a more favorable (less negative) activation entropy. This was explained in terms of greater thermal protein expansion in H_2O. The implications of this explanation, particularly in terms of the effects of medium dynamics along ET pathways, are under investigation.

The other, and arguably more striking observation, was the enhancement of ET in the V31W variant.[213] The rapid kinetics were explained by structural studies and modeling invoking π-stacked indole rings enhancing donor-acceptor coupling. This would seem at odds with the assertion that W48 does not participate in enhancing D-A coupling in the PR experiments; unless, that is, one considers the operation of destructive pathway interference leading to slower than expected W48-promoted kinetics. In any case, such behavior has striking implications for ET, particularly in the context of recently reported aromatic-residue mediated "electron hopping." Hopping through aromatic sidechains has long been invoked to explain the unexpectedly rapid ET across otherwise prohibitively long distances in systems such as photosystem II and ribonucleotide reductase.[216-217] Electron hopping was experimentally observed in an engineered azurin variant where a tryptophan was installed at position 124 with a $Re^{I}(CO)_3$(4,7-dimethyl-1,10-phenanthroline) photosensitizer attached to a histidine at position 126 (Figure 1.15).[218] π-stacking between the diimine ligand and W124 was thought to enhance coupling between W and the Re, likely enabling the hopping.

A relatively recent development has been the application of electrochemistry to the study of biological ET. Efforts largely on the part of the Ulstrup group have resulted in the measurement of electrode-mediated azurin ET. Initial studies measured electrochemical responses from *P. aeruginosa* azurin adsorbed on monocrystalline Au(111) surfaces;[219] electron microscopy showed that azurin on such surfaces forms well-ordered, closely packed monolayers.[219-220] X-ray photoelectron spectroscopy (XPS) revealed thatthese layers form via sulfur linkages – that is, azurin is bound via the south-pole disulfide. Protein-electrode ET was established by differential pulse voltammetry showing peaks near the solution ΔE^{o}; ET rates of 30 s^{-1} were measured by electrochemical impedance spectroscopy. These values agreed with the Farver/Pecht measurements (44 s^{-1}), indicative of ET from the disulfide-electrode interface to the copper. However, as these rates were measured with no overpotential, they implied a drastically lower λ for the electrode than the disulfide, a logical assertion. Azurin, long known to be highly stable, demonstrated retention of electrochemical activity even with a disrupted disulfide and packed into monolayers on an electrode surface.

Further work was inspired by an electrochemical study of azurin adsorbed on alkanethiol self-assembled monolayers (SAMs).[221] Again employing imaging and electrochemical techniques the Ulstrup group showed the retention of ET functionality by azurin on SAM-modified monocrystalline Au(111) electrodes.[222] Rates were shown to be exponentially dependent on SAM chain length between 11 and 17 alkyl groups. With fewer than 11 alkyl groups the rates demonstrated saturation; the origin of this saturation is still not clear. Work by Gray and co-workers has suggested the requirement of W48 for observation of electrochemical signals, though this work was conducted with a highly engineered variant of azurin whose aromatic amino acid complement had been entirely substituted to phenylalanine.[223] Nevertheless, this work offers the intriguing possibility of an ET route from electrodes through N47; the influence of this residue on ET reactivity is under investigation.

TAILOR-MADE AZURINS: METAL-SUBSTITUTED AND GENETICALLY ENGINEERED VARIANTS

The engineering of azurin by metal substitution and/or genetic manipulation has fueled many of the aforementioned studies; discussion of the biophysics, spectroscopy, and ET reactivity of exclusively the wild-type variants would have necessitated omission of many critical results and left many stories without satisfying conclusions. Nevertheless, there remain unmentioned many fascinating cases of azurin being bent to will and creativity that will continue to highlight its staggering utility to the broad scientific community.

Nature, of course, was the first to produce azurin variants. We have made mention where relevant of the differences among azurin species and so will pass over detailed enumeration of the subtle variations between *e.g.* the azurins from *P. aeruginosa* and *A. faecalis*. They will only be brought up now because, before recombinant DNA technology scientists had at first largely used these pre-existing variants to explore structural effects over ET, spectroscopy, *etc.* However, some mileage was to be had from metal-substitution studies: an impressive representation of the transition block has found its way into azurin's Cu binding site. Zn^{II} has been discussed extensively (*vide supra*); its role in probing the folding and stability of azurin, as

well as in demonstrating the protein's control over active site geometry (the rack) should by now be quite clear.

Removing Cu^{II} from azurin is relatively straightforward: dialysis against 0.5 M KCN for eight hours ensures that your material is absolutely, positively apoprotein. From there, if the metal will go in (and stay in!), you are free to derivatize. This was used to the advantage of spectroscopists seeking to answer the "blue copper protein question," with early guesses as to the nature of the ligand set informed by Co^{II} substitution.[45,224-225] More significantly, the favorable NMR properties of Co^{II} have been exploited to probe metalloprotein coordination environments.[226-227] The Ni^{II} derivatives of the azurins have been subject to a similar series of studies.[227-228]

Investigations of Co^{II} and Ni^{II} azurins have been informed by crystal structures of each derivative.[229-230] The coordination geometry in *P. aeruginosa* azurin is slightly perturbed upon substitution of Cu^{II} by Co^{II} and Ni^{II}. The Cu-O(G45) distance decreases with concomitant increase of the Cu-S(M121) distance, though the metal is not substantially removed from the N-N-S equatorial plane. Resonance Raman studies demonstrate decreased Cu-thioether stretching frequencies, in accord with these observations. Interestingly, comparative resonance Raman studies between *P. aeruginosa* and *A. denitrificans* azurins reveal substantial differences in the spectra of Ni^{II} variants; the Cu^{II} proteins demonstrate high degrees of similarity.[231-232] These results imply that outer-sphere coordination is directed in part by the bound metal ion. Recently, X-ray MCD experiments have supported the increased interaction between Ni^{II} and the G45 carbonyl.[233]

All told, it would appear that cofactor electronics can markedly influence the coordination environment of the azurins. Cu^{II} is optimal: its affinity for the G45 carbonyl and M121 thioether allows it to maintain its minimally redox reorganizing coordination geometry; meanwhile subtle electronic effects propagate to the outer sphere. The Ni-S(Cys) bond length in *P. aeruginosa* azurin is 2.39 Å; the Co-S(Cys) bond length is 2.20 Å. Decreased electron delocalization over the C112 thiolate would weaken the hydrogen bonding from N47 and F114 amides; anisotropy in the thiolate interactions with Co^{II} and Ni^{II} derivatives among

different azurin species may account for the observed deviation among the resonance Raman spectra of the Ni^{II} proteins. Cu-S(C112) interactions remain consistent among the azurin species. These subtleties require further investigation.

Metal derivatives have also seen use in photophysical investigations. Indirect evidence for the preparation of Mn^{II} was reported, as apoprotein incubated with Mn^{II} demonstrated quenched W48 fluorescence implying metalation.[45] However, this report has not been substantiated by any explicit characterization by analytical methods or additional spectroscopy. Co^{II} and Cu^{II} quenching studies have been supplemented with studies of Ag^{I}, Hg^{II}, and Cd^{II}.[45,234-235] Whereas these works concentrated on the study of W48 photophysics, Au^{I} substituted azurin has displayed metal-centered emission.[236]

Hg^{II} and Cd^{II} azurins have been studied to structurally characterize the metal binding site.[237-239] Cd^{II} azurin more closely resembles Cu^{II} in its active site geometry than Zn^{II}, with a distant 2.8 Å from the metal to the G45 carbonyl. Being isoelectronic with Cu^{I}, Cd^{II} has been proposed as a probe of properties intermediate between the two Cu oxidation states. Perturbed angular correlation spectroscopy, a gamma-ray technique, has been used as evidence that M121 acts to rigidify the metal site, despite the failure to observe direct interaction between M121 and the Cd^{II}.[240]

For all the information provided by these studies, there are only so many transition metals in the periodic table. Site-directed mutagenesis, as we have seen, has allowed an explosion of azurin variants. Concomitant with the synthetic gene for *P. aeruginosa* azurin, Richards reported the cassette mutagenesis of M121 to the entire set of natural amino acids.[7] Spectroscopic data were reported at this time for M121X (X = V, I, N, D, H), as well as the H46D protein. Casette mutagenesis of M121 was also carried out in the Lundberg lab.[241] Spectroscopic studies were carried out for Cu^{II} as well as Co^{II} and Ni^{II} variants of M121X (X = L, G, D, E) proteins from this lab.[242] More significantly, the effects of M121X substitutions as well as mutations proximal to the binding site were explored by detailed spectroelectrochemical (Table 1.8) and structural studies.[243-244] This work demonstrated a clear role for axial ligation in reduction potential tuning of blue copper, confirming previous hypotheses from ligand field theoretical considerations.[245]

The reduction potential of the $Cu^{II/I}$ couple in azurin has continued to receive attention. M121X substitutions with non-standard amino acids demonstrated a correlation between site hydrophobicity and reduction potential.[246] Electrochemical, structural, and reactivity studies of the F114P variant highlighted the importance of the F114 NH-S(C112) hydrogen bond, the disruption of which leads to a 90 mV drop in reduction potential and drastically reduced ET efficiency (as measured by ESE NMR experiments).[247] These observations were recently combined to demonstrate the additive effects of outer-sphere coordination and site hydrophobicity upon reduction potential, allowing Lu and coworkers to tune the $Cu^{II/I}$ couple in *P. aeruginosa* azurin over a 600 mV range.[248]

The effect of active site mutagenesis on the spectroscopic properties of Cu^{II} in azurin have been explored extensively. H46 was among the first residues to be probed by mutagenesis; among the results of these studies it was shown that type 1 character is retained by H46D but no other mutations.[249] Interestingly, H46D the reduction potential remains a high 297 mV even in the presence of a negatively charged carboxylate. The ET rate between $Ru(bpy)_2$(imidazole)(H83) and Cu drops almost two orders of magnitude; this is ascribed to a weakening of the Cu-S(C112) interaction.[250]

Further proof of the criticality of thiolate ligation to the type 1 Cu electronic structure was afforded by the "Mizoguchi mutant," the C112D variant.[251] This substitution produces a type 2 copper site. Moreover, the electron transfer efficiency of the protein is dramatically reduced. This has been ascribed to both reduced active-site covalency and an elevated reorganization energy. The latter explanation has been supported by EXAFS studies demonstrating a 0.2 Å expansion in the coordination sphere of the Mizoguchi mutant upon reduction.[252] Further data on the C112D azurin is reported in Chapters 2-5.

The only other Cu-binding C112X mutant reported has been the substitution to selenocysteine (SeC).[253] This variant exhibits a red-shifted LMCT and a doubled Cu $A_{||}$. Cu and Se EXAFS show an extended Cu-X112 bond to 2.30 Å, though this bond does not vary with oxidation state.[254] A 3D structure is not available for either oxidation state of C112SeC azurin, though as suggested by the investigators the rack mechanism likely accounts for this

behavior. ET data are not reported; such data would likely yield interesting insight into the relative contributions of coupling and reorganization in BCP ET reactivity.

As with C112D/SeC, wholly divergent electronic structures can be produced by axial substitutions. M121H/K/E azurins have been extensively studied; they give rise to a peculiar set of properties intermediate between type 1 and type 2 that are highly dependent on pH and temperature.[132,241,255-257] Such sites have appropriately enough been dubbed "type 1.5" copper sites. In the case of M121H and M121E, limiting structures have been identified corresponding to "ligand on" and "ligand off" states; these have been ascribed to the protonation states of the axial ligand.[258-260] In the case of the "ligand on" forms, the proteins display axial EPR spectra with $A_{||} \sim 10$ mK; at low pH the "ligand off" sites exhibit rhombic type 1 spectra. These azurins have been used as evidence against the rack mechanism of Cu binding, with detractors citing increased protein flexibility allowing the accommodation of axial ligation. However, we shall see in Chapter 2 that just because an axial ligand can bind (*i.e.* is deprotonated), it need not necessarily do so.

The M121Q variant has been constructed as a model of the stellacyanin blue copper site.[261-263] The spectroscopic properties of this azurin closely resemble those of stellacyanin, lending support to the notion that stellacyanin's active site contained an axial amide *in lieu* of the more ubiquitous thioether. This would ultimately be confirmed by the report of a stellacyanin crystal structure.[176] Interestingly, M121Q azurin displays degraded ET efficiency, the origin of which has been ascribed to higher site reorganization on the basis of large differences between the Cu^{II} and Cu^{I} structures. Outer-sphere coordination elements present in stellacyanin are likely not conserved upon translation of its ligand set into the azurin scaffold.

Recently Lu and coworkers reported a detailed structural and spectroscopic study of M121C and M121Hcy (Hcy = homocysteine) azurins.[264] In M121C azurin, there is a pH-dependent transition from a type 1 protein at low pH to a green type 2 protein when the pH is 7 or higher. M121Hcy is a red type 2 protein with pH independent spectroscopic properties. These mutants further support the Solomon "coupled distortion" model, where strong axial

coordination results in weaker equatorial cysteine ligation owing as the d_{x2-y2} orbital is rotated to favor overlap with Sσ versus Sπ *(vide supra)*.

The capacity for exogenous ligand binding has been studied in H46G and H117G azurins. Apoprotein stuctures of H46G and H117G are available; irreversible thiol oxidation has so far frustrated attempts at determining native structures.[265] In H117G azurin, a type 2 Cu protein, type 1 character can be restored by addition of ligands such as imidazole.[266-268] Electron transfer reactions of "type 1 reconstituted" H117G azurin are slower than those of wild-type protein;[269] structural studies have shown that the exogenous ligands are ejected upon Cu reduction with substantial bond length perturbations.[270] These observations led to the proposal of Cu^I geometric stabilization as a mechanism for elevated reduction potentials in the H117G "type 1 reconstituted" variants. Parallel studies performed on H46G azurin have yielded similar results, though equilibrium mixtures of type 1 and type 2 sites are common as opposed to pure species in the case of H117G.[271]

Exogenous ligands also bind to M121X mutants. The M121G mutant creates a cavity at the south pole that accommodates the binding of azide, thiocyanate, and cyanide.[272] This study was extended to M121X (X = A, V, L, D).[273-274] In this work, water was observed as a ligand in the M121G mutant; this water was observed to compete with exogenous ligands for Cu binding. Alcohol and exogenous carboxylate binding could also be observed spectroscopically. The crystal structures of M121A and the M121A adduct with azide have been reported; in the latter case the azide moves the Cu out of the NNS equatorial plane, resulting in a distorted tetrahedral geometry.[275] In the case of M121E, azide is able to displace the endogenous carboxylate.[276] The ability to bind exogenous ligands holds promise for future azurin design projects; appropriately engineered azurins with such binding pockets could conceivably be converted from ET proteins to enzymes.

Even more exotic variants of azurin have been produced to model the metal binding sites of heterologous proteins. Malmström demonstrated the high degree of similarity between the cupredoxin fold of azurin and the Cu_A domain of cytochrome *c* oxidase.[277] Lu and Richards, by substituting the putative metal-binding loop of the latter into the former, generated a hybrid

"purple azurin" containing a binuclear Cu_A site.[278] Spectroscopic studies have verified the classification of the site as Cu_A, albeit with slightly perturbed geometry relative to other known Cu_A domains; *e.g.* the Cu-Cu distance is the shortest observed at 2.39 Å.[279] A 1.65 Å crystal structure of "purple azurin" has been reported, allowing for analysis of subtle differences among the Cu_A family (Figure 1.16).[280] The azurin tertiary structure is preserved in the loop variant, with the major structural perturbations occurring, unsurprisingly, in the metal binding domain. The azurin south pole C3/C26 disulfide was exploited by Pecht and Farver to compare the ET reactivities of Cu_A and blue copper; the comparison of "purple" and native azurins indicated a markedly lower reorganization energy of 0.4 eV (relative to blue copper, 0.82 eV) for the Cu_A site.[281] As with WT azurin, site directed mutagenesis could be employed to probe effects of ligand substitution. Not surprisingly, C112S and C116S variants each result in highly perturbed electronic structures.[282] In keeping with XAS studies, the cysteines were found to be inequivalent; C112S results in two type 2 copper centers, while C116S retains a type 1 copper. "Purple azurin" is less sensitive to substitution at the histidines: H121X (X = A, D, G, or N) mutants retain largely unperturbed Cu_A sites.[283-284] Mutations at M121, interestingly, show very little effect over the reduction potential of the Cu_A site; whereas substitutions M121X (X = L, D, or E) are able to tune "blue azurin" through a 170 mV range, only a 24 mV range is exhibited in "purple azurin."[285]

A similar design scheme was employed by Canters and Dennison to explore commonalities among the cupredoxins. In seminal work, the ligand-containing Cu-binding loop of *Thiobacillus versutus* amicyanin (residues 93-99) was replaced by the corresponding loop of poplar plastocyanin, generating a redox-competent BCP.[286] This work was extended by transferring the loops of *P. aeruginosa* azurin, *A. faecalis* pseudoazurin, and *P. aureofaciens* nitrite reductase, all to similar effect.[287] In all these cases, including "purple azurin," the C-H-M ligand loop was extended. Azurin, with its stable ß-sandwich structure and relatively long metal binding loop, afforded an excellent testing ground for "the other direction:" loop-contraction also allowed the construction of novel, chimeric BCPs.[288-291] Interestingly, the structures adopted by the metal binding sites are dictated not by the scaffold protein but by the transplanted loops; *e.g.* the plastocyanin loop on azurin will produce an protein with a plastocyanin metal binding site structure. Furthermore, these studies revealed a minimal

domain for the blue copper site: CTPHPM. Moreover, the Dennison menagerie demonstrated an interesting feature of the ligand loop: its structure is sequence-independent.[292] Rather, the lengths dictate the structure; amino acid composition fixes the $Cu^{II/I}$ reduction potential. As in the case of M121X mutants,[246] loop hydrophobicity correlates with potential. As these loops have been demonstrated to be the sites of intramolecular ET, this affords the promise of engineering novel specific protein-protein interactions, which in turn could lead to new ET pathways in azurins (or any redesigned BCP) to be used as electron relays in biomolecular electronic devices (*vide infra*).

Superstructural azurin variants have also been designed. These constructs arose as further specimens for ET studies. The first set comprised *P. aeruginosa* azurins crosslinked by disulfide bridges at position 42.[293-295] These proteins were used to further demonstrate the importance of medium effects on LRET. Another disulfide-mediated dimer formed from S118C azurins has also been constructed; this construct demonstrates anti-cooperativity in its redox in that the semi-oxidized state is structurally stabilized relative to the fully oxidized state.[296] A divergent strategy for construction of superstructural azurins is the addition of imidazole-terminated linkers to H117G azurins.[297]

Generally, these engineered azurins have been produced to study some fundamental property of the protein, whether ET, spectroscopy, or biophysics. However, azurin has also been extended from a molecular laboratory to a component of medical therapy as well as bioelectronics.

BUT CAN IT CURE CANCER: SOLVING THE WORLD'S PROBLEMS WITH AZURIN

Yes, azurin can cure cancer (*vide infra*). This well-studied protein holds practical promises that have not been lost on scientists outside the biophysical and bioinorganic realms. Knowing now what makes azurin tick and having an appreciation for its forgiving nature towards the imaginations of protein engineers, we may survey some of the recent developments wherein azurin has been put to task.

Recently oncologists have enlisted the help of pathogenic bacteria in the fight against cancer. Among these microbiological mercenaries, *P. aeruginosa* showed particular promise. Initially it was observed that excreted *P. aeruginosa* proteins, among them ATP-dependent kinases, exhibit cytotoxic activity toward macrophages.[298] However, ATP was not required for cytotoxicity. Interestingly, a secretory fraction containing azurin and cytochrome c_{551} was found to also destroy macrophages. Of the two, azurin was identified as the major player in effecting cell death.[299] Moreover, experiments with apoazurin and mutants incapable of copper binding have determined that redox/ET is not the causative factor; however, mutations to the hydrophobic patch at M44 and M64 resulted in decreased cytotoxicity.[300] Azurin-treated macrophages displayed higher concentrations of the apoptosis-signaling p53 protein than untreated, leading to the suggestion that azurin somehow binds to p53 and stabilizes it.[299] GST-pulldown assays later confirmed an azurin-p53 interaction.[301] Further studies have not only quantified the binding affinity (nM), but have revealed a 4:1 azurin:p53 stoichiometry, indicating that azurin may act to shield p53 from proteolysis in the cell.[302]

Macrophages, however, are not the enemy. While providing an explanation for *P. aeruginosa* pathogenicity and immuno-evasion, the p53 binding behavior indicated a possible application in cancer therapy. This was first demonstrated in melanoma cells, wherein apoptosis was induced by incubation with azurin.[303] Interestingly, azurin was found to enter the cells of its own accord; moreover, p53 was demonstrated to transport azurin to the nuclei. The tumor regression activity was later demonstrated in breast and prostate cancer cells.[304-305]

Despite being an exciting prospect for our venerable blue protein, the use of a full protein in cancer treatment raises several troubling issues, among them organismal immune response. As an answer, investigations have shown that there is a minimal domain that produces this cancer-remediating activity. Residues 50-77, comprising the alpha-helix and flanking loop regions, not only induces apoptosis, but it is the domain responsible for cellular translocation.[306] Residues 50-67 comprise the translocational portion, while residues 65-77 are responsible for antiproliferative activity toward tumor cells.[307-308] So, while it has yet to save a life, azurin (or parts of it, at least) holds remarkable promise as a potential chemotherapeutic agent in humanity's ongoing pitched battle against cancer.

Bionanotechnologists have also recognized azurin's utility. In 1994, Canters and coworkers proposed potential applications of redox proteins, azurin among them, in bioelectronic devices.[309-312] The immobilization of azurin to an electrode by wiring the H117G mutant via an imidazole-terminated linker was pursued as a possible strategy for redox-mediated electrical signal transduction. Of interest is that a functional sensor for superoxide has been tested using Au-immobilized azurin.[313]

Self-assembly has been pursued as another route toward azurin-based bioelectronic devices. Ordered and disordered layers of azurin between Au electrodes on Si/SiO_2 substrates can behave as biological diodes or transistors depending on orientation and device configuration.[314-320] As should not come as a surprise given our lengthy discussion of azurin's stability, minimal changes are observed in W48 emission on surface adsorption and dehydration; moreover, full solution reconstitution was observed after a month.[321] This work has been extended recently to indium tin oxide, wherein structural integrity is again preserved concomitant with high degrees of electronic coupling to the substrate.[322]

All these studies have established that azurin could be a functional element for nanocomputation – promise that is now coming to fruition. The first reported protein-based biomemory device was inspired by work from Ulstrup and coworkers; it consisted of azurin immobilized to Au electrodes by engineered cysteines.[323] This device demonstrated requisite "read," "write," and "erase" functions. Moreover, the device could achieve 500,000 cycles. This device was improved by creation of discrete Au immobilization sites on a Si substrate, with a more stable azurin variant created by attachment to Au by new surface cysteine introduced by the K92C mutation.[324-325] Further sophistication is achieved by addition of cytochrome *c*, which adds second read, write, and erase functions.[326] Single-molecule devices are currently being pursued and could make a considerable impact in the field.

Concluding Remarks

If we think of the azurins as nails, then extending the metaphor they have been hit with just about every hammer. Although their physiological purposes in many host organisms remain (curiously) mysterious, their generalized functionalities and behaviors have been explored extensively. The biophysicists have quantified and rationalized stability, empowering protein engineers to tinker with the azurins to the limits of imagination. Thanks to the combined efforts of spectroscopists, very little remains to learn about the blue copper site; this has informed the kineticists probing azurin ET reactivity with lessons that apply generally to BCPs. The thorough characterization of this one, small, now not-so-curiously blue protein has provided the background necessary for application in contexts such as medical research and nanotechnology.

The saga of azurin is far from over.

REFERENCES

1) Dennison, C. *Coord. Chem. Rev.* **2005**, *249*, 3025-3024.
2) Horio, T. *J. Biochem.* **1958**, *45*, 267-279.
3) Sutherland, I.W.; Wilkinson, J.F. *Biochem. J.* **1962**, *84*, 43.
4) Sutherland, I.W.; Wilkinson, J.F. *J. Gen. Microbiol.* **1963**, *30*, 105-112.
5) Canters, G.W. *FEBS Lett.* **1987**, *212*, 168-172.
6) Karlsson, B.G.; Pascher, T.; Nordling, M.; Arvidsson, R.H.A.; Lundberg, L.G. *FEBS Lett.* **1989**, *246*, 211-217.
7) Chang, T.K.; Iverson, S.A.; Rodrigues, C.G.; Kiser, C.N.; Lew, A.Y.; Germanas, J.P.; Richards, J.H. *Proc. Natl. Acad. Sci. U.S.A.* **1991**, *88*, 1325-1329.
8) Strahs, G. *Science* **1969**, *165*, 60-61.
9) Adman, E.T.; Stenkamp, R.E.; Sieker, L.C.; Jensen, L.H. *J. Mol. Biol.* **1978**, *123*, 35-47.
10) Colman, P.M.; Freeman, H.C.; Guss, J.M.; Murata, M.; Norris, V.A.; Ramsahw, J.A.M.; Venkatappa, M.P. *Nature* **1978**, *272*, 319-324.
11) Adman, E.T.; Jensen, L.H. *Isr. J. Chem.* **1981**, *21*, 8-12.
12) Ambler, R.P.; Brown, L.H. *Biochem. J.* **1967**, *104*, 784-825.
13) NCBI – Proteins. http://www.ncbi.nlm.nih.gov/protein
14) Nar, H.; Messerschmidt, A.; Huber, R.; van de Kamp, M.; Canters, G.W. *J. Mol. Biol.* **1991**, *221*, 765-772.
15) Baker, E.N. *J. Mol. Biol.* **1988**, *203*, 1071-1095.
16) Nar, H.; Messerschmidt, A.; Huber, R.; van de Kamp, M.; Canters, G.W. *FEBS Lett.* **1992**, *306*, 119-124.
17) Nar, H.; Huber, R.; Messerschmidt, A.; Fillippou, A.C.; Barth, M.; Jaquinod, M.; van de Kamp, M.; Canters, G.W. *Eur. J. Biochem.* **2005**, *205*, 1123-1129.
18) Eyring, H.; Lumry, R.; Spikes, J.D. "Kinetic and Thermodynamic Aspects of Enzyme-Catalyzed Reactions" in *The Mechanism of Enzyme Action* (McElroy, W.D and Glass, B.; eds.) **1954**, pp. 123-136, The Johns Hopkins Press, Baltimore.
19) Williams, R.J.P. "The Selective Interactions of Metal Ions and Protein Groups" in *Molecular Basis of Enzyme Action and Inhibition* (Desnuelle, P.A.E., ed) **1963**, pp 133-149, Pergamon Press, Oxford.
20) Clothia, C.; Hubbard, T.; Brenner, S.; Barns, H.; Murzin, A. *Ann. Rev. Biophysics. Biomol. Struct.* **1997**, *26*, 597-627.
21) Manetto, G.D.; Grasso, D.M.; Milardi, D.; Pappalardo, M.; Guzzi, R.; Sportelli, L.; Verbeet, M.P.; Canters, G.W.; La Rosa, C. *ChemBioChem* **2007**, *8*, 1941-1949.
22) Engman, K.C.; Sandberg, A.; Leckner, J.; Karlsson, B.G. *Protein Sci.* **2004**, *13*, 2706-2715.
23) Kister, A.E.; Finkelstein, A.V.; Gelfand, I.M. *Proc. Natl. Acad. Sci. U.S.A.* **2002**, *99*, 14137-14141.
24) Wilson, C.J.; Wittung-Stafshede, P. *Proc. Natl. Acad. Sci. U.S.A.* **2005**, *102*, 3984-3987.
25) Marks, J.; Pozdnyakova, I.; Guidry, J.; Wittung-Stafshede, P. *J. Biol. Inorg. Chem.* **2004**, *9*, 281-288.
26) Pozdnyakova, I.; Wittung-Stafshede, P. Biochemistry **2001**, *40*, 13728-13733.
27) Pozdnyakova, I.; Wittung-Stafshede, P. *J. Am. Chem. Soc.* **2001**, *123*, 10135-10136.
28) DeBeer, S.; Wittung-Stafshede, P.; Leckner, J.; Karlsson, G.; Winkler, J.R.; Gray, H.B.; Malmström, B.G.; Solomon, E.I.; Hedman, B.; Hodgson, K. *Inorg. Chim. Acta* **2000**, *297*, 278-282.
29) Wittung-Stafshede, P; Hill, M.G.; Gomez, E.; Di Bilio, A.; Karlsson, G.; Leckner, J.; Winkler, J.R.; Gray, H.B.; Malmström, B.G. *J. Biol. Inorg. Chem.* **1998**, *3*, 367-370.
30) Pozdnyakova, I.; Guidry, J.; Wittung-Stafshede, P. *J. Biol. Inorg. Chem.* **2001**, *6*, 182-188.
31) Blasise, C.A.; Berg, J.M. *J. Am. Chem. Soc.* **2003**, *125*, 6866-6867.
32) Wilson, C.J.; Wittung-Stafshede, P. *Proc. Natl. Acad. Sci. U.S.A.* **2005**, *102*, 3984-3987.
33) Zong, C.; Wilson, C.J.; Shen, T.; Wolynes, P.G.; Wittung-Stafshede, P. *Biochemistry* **2006**, *45*, 6458-6466.
34) Engman, K.C.; Sandberg, A.; Leckner, J.; Karlsson, B.G. *Protein Sci.* **2004**, *13*, 2706-2715.

35) Pozdnyakova, I.; Wittung-Stafshede, P. *Biochim. Biophys. Acta* **2003**, *1651*, 1-4.
36) Wilson, C.J.; Wittung-Stafshede, P. *Biochemistry* **2005**, *44*, 10054-10062.
37) Zong, C.; Wilson, C.J.; Shen, T.; Wittung-Stafshede, P.; Mayo, S.L.; Wolynes, P.G. *Proc. Natl. Acad. Sci. U.S.A.* **2007**, *104*, 3159-3164.
38) Engeseth, H.R.; McMillin, D.R. *Biochemistry* **1986**, *25*, 2448-2455.
39) La Rosa, C.; Milardi, D.; Grasso, D.; Guzzi, R.; Sportelli, L. *J. Phys. Chem.* **1995**, *99*, 14864-14870.
40) Guzzi, R.; La Rosa, C.; Grasso, D.; Milardi, D.; Sportelli, L. *Biophys. Chem.* **1996**, *60*, 29-38.
41) Guzzi, R.; Sportell, L. *J. Phys. Chem. B.* **1998**, *102*, 1021-1028.
42) Sandberg, A.; Leckner, J.; Shi, Y.; Schwarz, F.P.; Karlsson, B.G. *Biochemistry* **2002**, *41*, 1060-1069.
43) Finazzi-Agrò, A.; Rotilio, G.; Avigliano, L.; Guerrieri, P.; Boffi, V.; Mondovì, B. *Biochemistry*, **1970**, *9*, 2009-2014.
44) Burstein, E.A.; Permyakov, E.A.; Yashin, V.A.; Burkhanov, S.A.; Finazzi-Agrò, A. *Biochim. Biophys. Acta* **1977**, *491*, 155-159.
45) Tennent, D.L.; McMillin, D.R. *J. Am. Chem. Soc.* **1979**, *101*, 2307-2311.
46) Grinvald, A.; Steinberg, I.Z. *Biochim. Biophys. Acta* **1976**, *427*, 663-678.
47) Gilardi, G.; Mei, G.; Rosato, N.; Canters, G.W.; Finazzi-Agro, A. *Biochemistry* **1993**, *33*, 1425-1432.
48) Grinvald, A.; Schlessinger, J.; Pecht, I.; Steinberg, Z. *Biochemistry* **1975**, *14*, 1921-1929.
49) Munro, I.; Pecht, I.; Stryer, L. *Proc. Natl. Acad. Sci. U.S.A.* **1979**, *76*, 56-60.
50) Szabo, A.G.; Stepanik, T.M.; Wayner, D.M.; Young, N.M. *Biophys. J.* **1983**, *41*, 233-244.
51) Kroes, S.J.; Canters, G.W.; Gilardi, G.; van Hoek, A.; Visser, A.J.W.G. *Biophys. J.* **1998**, *75*, 2441-2450.
52) Bonander, N.; Karlsson, B.G.; Vänngård, T. *Biochim. Biophys. Acta* **1995**, *1251*, 48-54.
53) Guzzi, R.; Sportelli, L.; La Rosa, C.; Milardi, D.; Grasso, D.; Verbeet, M. Ph.; Canters, G.W. *Biophys. J.* **1999**, *77*, 1052-1063.
54) Tigerström, A.; Schwarz, F.; Karlsson, G.; Ökvist, M.; Álvarez-Rúa C.; Maeder, D.; Robb, F.T.; Sjölin, L. *Biochemistry* **2004**, *43*, 12563-12574.
55) Corin, A.F.; Bersohn, R.; Cole, P.E. *Biochemistry* **1983**, *22*, 2032-2038.
56) Margalit, R.; Kostic, N.M.; Che, C.M.; Blair, D.F.; Chiang, H.J.; Pecht, I.; Shelton, J.B.; Shelton, J.R.; Schroeder, W.A.; Gray, H.B. *Proc. Natl. Acad. Sci. U.S.A.* **1984**, *81*, 6554-6558.
57) Faham, S.; Mizoguchi, T.J.; Adman, E.T.; Gray, H.B.; Richards, J.H.; Rees, D.C. *J. Biol. Inorg. Chem.* **1997**, *2*, 464-469.
58) Rosen, P.; Pecht, I. *Biochemistry* **1976**, *15*, 775-786.
59) Orgel, L.E. Enzyme-metal-substrate Complexes as Co-ordination Compounds, in *Metals and Enzyme Activity* (Crook, E.M., ed) **1958**, pp. 8-20, The University Press, Cambridge.
60) Williams, R.J.P. The Selective Interactions of Metal Ions and Protein Groups, in *Molecular Basis of Enzyme Action and Inhibition* (Desnuelle, P.A.E., ed) **1963**, pp 133-149, Pergamon Press, Oxford.
61) Malmström, B.G.; Vänngård, T. *J. Mol. Biol.* **1960**, *2*, 118-124.
62) Peisach, J.; Blumberg, W.E. *Arch. Biochem. Biophys.* **1974**, *165*, 691-708.
63) Broman, L.; Malmström, B.G.; Aasa, R.; Vänngård, T. *Biochim. Biophys. Acta* **1963**, *75*, 365-376.
64) Malkin, R.; Malmström, B.G. *Adv. Enzymol. Relat. Areas Mol. Biol.* **1970**, *33*, 177-244.
65) Sharnoff, M. *J. Chem. Phys.* **1965**, *42*, 3383-3395.
66) Bates, C.A.; Moore, W.S.; Standley, K.J.; Stevens, K.W.H. *Proc. Phys. Soc.* **1962**, *79*, 73-83.
67) Bencini, A.; Gatteschi, D.; Zanchini, C. *J. Am. Chem. Soc.* **1980**, *102*, 5234-5237.
68) Holland, P.L.; Tolman, W.B. *J. Am. Chem. Soc.* **1999**, *121*, 7270-7271.
69) Randall, D.W.; DeBeer George, S.; Holland, P.L.; Hedman, B.; Hodgson, K.O.; Tolman, W.B.; Solomon, E.I. *J. Am. Chem. Soc.* **2000**, *122*, 11632-11648.
70) Malmström, B.G. Two Forms of Copper in Copper-Containing Oxidases, in *Oxidases and Related Redox Systems* (King, T.E., Mason, H.S. and Morrison, M., eds) **1965** vol. 1, pp-207-216, Wiley, New York.
71) Vallee, B.L.; Williams, R.J.P. *Proc. Natl. Acad. Sci. U.S.A.* **1968**, *59*, 498-505.
72) Tullius, T.D.; Frank, P.; Hodgson, K.O. *Proc. Natl. Acad. Sci. U.S.A.* **1978**, *75*, 4069-4073.
73) Solomon, E.I.; Hare, J.W.; Dooley, D.M.; Dawson, J.H.; Stephens, P.J.; Gray, H.B. *J. Am. Chem. Soc.* **1980**, *102*, 168-178.
74) Solomon, E.I.; Hare, J.W.; Gray, H.B. *Proc. Natl. Acad. Sci. U.S.A.* **1976**, *73*, 1389-1393.
75) Solomon, E.I.; Baldwin, M.J.; Lowery, M.D. *Chem. Rev.* **1992**, *92*, 521-542.

76) Solomon, E.I.; Szilagyi, R.K.; DeBeer George, S.; Basumallick, L. *Chem. Rev.* **2004**, *104*, 419-458.
77) Solomon, E.I. *Inorg. Chem.* **2006**, *45*, 8012-8025.
78) Harris, D.C.; Bertolucci, M.D. *Symmetry and Spectroscopy: An Introduction to Vibrational and Electronic Spectroscopy.* 1st ed.; Dover: New York, **1989**.
79) Griffith, J.S. *The Theory of Transition-Metal Ions.* 1st ed.; Camrbidge: Cambridge, **1961**.
80) Ballhausen, C.J. *Introduction to Ligand Field Theory.* 1st ed.; McGraw-Hill: New York, **1962**.
81) Figgis, B.N. *Introduction to Ligand Fields.* 1st ed.; Wiley: New York, **1966**.
82) Johnson, M.K. CD and MCD Spectroscopy. In *Physical Methods in Bioinorganic Chemistry: Spectroscopy and Magnetism;* Que, L. Jr., Ed. University Science Books: Sausalito, **2000**, pp 233-286.
83) Penfield, K.W.; Gay, R.R.; Himmelwright, R.S.; Eickman, N.C.; Norris, V.A.; Freeman, H.C.; Solomon, E.I. *J. Am. Chem. Soc.* **1981**, *103*, 4382-4388.
84) Desjardins, S.R.; Penfield, K.W.; Cohen, S.L.; Musselman, R.L.; Solomon, E.I. *J. Am. Chem. Soc.* **1983**, *105*, 4590-4603.
85) Fields, B.A.; Bartsch, H.H.; Bartunik, H.D.; Cordes, F.; Guss, J.M.; Freeman, H.C. *Acta Cryst. D.* **1994**, *50*, 709-730.
86) Palmer, G. Electron Paramagnetic Resonance of Metalloproteins. In *Physical Methods in Bioinorganic Chemistry: Spectroscopy and Magnetism;* Que, L. Jr., Ed. University Science Books: Sausalito, **2000**, pp 121-186.
87) McGarvey, B.R. *Trans. Met. Chem.* **1967**, *3*, 89-201
88) Neese, F.; Solomon, E.I. Interpretation and Calculation of Spin-Hamiltonian Parameters in Transition Metal Complexes. In *Magnetism: Molecules to Materials IV*; Miller, J.S.; Drillon, M.; Eds. Wiley-VCH: Weinheim, **2003**, pp 345-466.
89) Abragam, A.; Bleaney, B. *Electron Paramagnetic Resonance of Transition Ions*; Clarendon: Gloucestershire, **1970**.
90) Coremans, J.W.A.; Poluektov, O.G.; Groenen, E.J.J.; Canters, G.W.; Nar, H.; Messerschmidt, A. *J. Am. Chem. Soc.* **1994**, *116*, 3098-3101.
91) Antholine, W.E.; Hanna, P.M.; McMillin, D.R. *Biophys. J.* **1993**, *64*, 267-272.
92) Freeman, A.J.; Watson, R.E. In *Magnetism*; Rado, G.T.; Suhl, H.; Eds.; Academic: New York, **1965**; Vol. 2A.
93) Berry, J.F.; Bill, E.; Bothe, E.; George, S.D.; Mienert, B.; Neese, F.; Wieghardt, K. *Science* **2006**, *312*, 1937-1941.
94) Scott, R.A. X-ray Absorption Spectroscopy. In *Physical Methods in Bioinorganic Chemistry: Spectroscopy and Magnetism;* Que, L. Jr., Ed. University Science Books: Sausalito, **2000**, pp 465-504.
95) Gewirth, A.A.; Cohen, S.L.; Schugar, H.J.; Solomon, E.I. *Inorg. Chem.* **1987**, *26*, 1133-1146.
96) Shadle, S.E.; Penner-Hahn, J.E.; Schugar, H.; Hedman, B.; Hodgson, K.O.; Solomon, E.I. *J. Am. Chem. Soc.* **1993**, *115*, 767-776.
97) Hahn, J.E.; Scott, R.A.; Hodgson, K.O.; Doniach, S.; Desjardins, S.R.; Solomon, E.I. *Chem. Phys. Lett.* **1982**, *88*, 595-598.
98) Scott, R.A.; Hahn, J.E.; Doniach, S.; Freeman, H.C.; Hodgson, K.O. *J. Am. Chem. Soc.* **1982**, *104*, 5364-5369.
99) George, S.J.; Lowery, M.D.; Solomon, E.I.; Cramer, S.P. *J. Am. Chem. Soc.* **1993**, *115*, 2968-2969.
100) Chasteen, N.D.; Snetsinger, P.A.; ESEEM and ENDOR Spectroscopy. In *Physical Methods in Bioinorganic Chemistry: Spectroscopy and Magnetism;* Que, L. Jr., Ed. University Science Books: Sausalito, **2000**, pp 187-232.
101) Lyubenova, S.; Maly, T.; Zwicker, K.; Brandt, U.; Ludwig, B.; Prisner, T. *Acc. Chem. Res.* **2010**, *43*, 181-189.
102) Coremans, J.W.A.; van Gastel, M.; Poluektov, O.G.; Groenen, E.J.J.; den Blaauwen, T.; van Pouderoyen, G.; Canters, G.W.; Nar, H.; Hammann, C.; Messerschmidt, A. *Chem. Phys. Lett.* **1995**, *235*, 202-210.
103) Coremans, J.W.A.; Poluektov, O.G.; Groenen, E.J.J.; Canters, G.W.; Nar, H.; Messerschmidt, A. *J. Am. Chem. Soc.* **1997**, *119*, 4726-4731.
104) Coremans, J.W.A.; Poluektov, O.G.; Groenen, E.J.J.; Canters, G.W.; Nar, H.; Messerschmidt, A. *J. Am. Chem. Soc.* **1996**, *118*, 12141-12153.
105) van Gastel, M.; Coremans, W.A.; Jeuken, L.J.C.; Canters, G.W.; Groenen, E.J.J. *J. Phys. Chem. A* **1998**, *102*, 4462-4470.

106) Kofman, V.; Farver, O.; Pecht, I.; Goldfarb, D. *J. Am. Chem. Soc.* **1996**, *118*, 1201-1206.
107) Fittipaldi, M.; Warmerdam, G.C.M.; de Waal, E.C.; Canters, G.W.; Cavazzini, D.; Rossi, G.L.; Huber, M.; Groenen, E.J.J. *ChemPhysChem* **2006**, *7*, 1286-1293.
108) Sottini, S.; Gast, P.; Blok, A.; Canters, G.W.; Cavazzini, D.; Rossi, G.L.; Groenen, E.J.J. *Appl. Magn. Reson.* **2010**, *37*, 219-227.
109) Kalverda, A.P.; Salgado, J.; Dennison, C.; Canters, G.W. *Biochemistry* **1996**, *35*, 3085-3092.
110) Bertini, I.; Ciurli, S.; Dikiy, A.; Gasanov, R.; Luchinat, C.; Martini, G.; Safarov, N. *J. Am. Chem. Soc.* **1999**, *121*, 2037-2046.
111) Abriata, L.A.; Ledesma, G.N.; Pierattelli, R.; Vila, A.J. *J. Am. Chem. Soc.* **2009**, *131*, 1939-1946.
112) Bertini, I.; Fernández, C.O.; Karlsson, B.G.; Leckner, J.; Luchinat, C.; Malmström, B.G.; Nerissian, A.M.; Pierattelli, R.; Shipp, E.; Valentine, J.S.; Vila, A.J. *J. Am. Chem. Soc.* **2000**, *122*, 3701-3707.
113) Ming, L.-J. Nuclear Magnetic Resonance of Paramagnetic Metal Centers in Proteins and Synthetic Complexes. In *Physical Methods in Bioinorganic Chemistry: Spectroscopy and Magnetism;* Que, L. Jr., Ed. University Science Books: Sausalito, 2000, pp 465-504.
114) *Solution NMR of Paramagnetic Molecules. Applications to Metallobiomolecules and Models.* Bertini, I.; Luchinat, C.; Parigi, G., Eds.; Current Methods in Inorganic Chemistry 2; Elsevier: Amsterdam, 2001.
115) Canters, G.W.; Hill, H.A.O.; Kitchen, N.A.; Adman, E.T. *Eur. J. Biochem.* **1984**, *138*, 141-152.
116) Van de Kamp, M.; Canters, G.W.; Wijmenga, S.S.; Lommen, A.; Hilbers, C.W.; Nar, H.; Messerschmidt, A.; Huber, R. *Biochemistry* **1992**, *31*, 10194-10207.
117) Balayssac, S.; Jiminez, B.; Piccioli, M. *J. Biomol. NMR* **2006**, *34*, 63-73.
118) Miskowski, V.; Tang, S.-P.W.; Spiro, T.G.; Shapiro, E.; Moss, T.H. *Biochemistry* **1975**, *14*, 1244-1250.
119) Siiman, O.; Young, N.M.; Carey, P.R. *J. Am. Chem. Soc.* **1976**, *98*, 744-748.
120) Ferris, N.S.; Woodruff, W.H.; Rorabacher, D.B.; Jones, T.E.; Ochrymowycz, L.A. *J. Am. Chem. Soc.* **1978**, *100*, 5939-5942.
121) Spiro, T.G.; Czernuszewicz, R.S. Resonance Raman Spectroscopy. In *Physical Methods in Bioinorganic Chemistry: Spectroscopy and Magnetism;* Que, L. Jr., Ed. University Science Books: Sausalito, 2000, pp 59-120.
122) Ferraro, J.R. *Introductory Raman Spectroscopy*, 2nd ed. Academic Press: London, 2002.
123) Nakamoto, K. *Infrared and Raman Spectra of Inorganic and Coordination Compounds. Part B. Applications in Coordination, Organometallic, and Bioinorganic Chemistry.* 6th ed. Wiley: Hoboken, 2009.
124) Siiman, O., Young, N.M.; Carey, P.R.; *J. Am. Chem. Soc.* **1974**, *96*, 5583-5585.
125) Ferris, N.S.; Woodruff, W.H.; Tennent, D.L.; McMillin, D.R. *Biochem. Biophys. Res. Commun.* **1979**, *88*, 288-296.
126) Woodruff, W.H.; Norton, K.A. *J. Am. Chem. Soc.* **1983**, *105*, 657-658.
127) Woodruff, W.H.; Norton, K.A.; Swanson, B.I.; Fry, H.A. *Proc. Natl. Acad. Sci. U.S.A.* **1984**, *81*, 1263-1267.
128) Thamann, T.J.; Frank, P.; Willis, L.J.; Loehr, T.M. *Proc. Natl. Acad. Sci. U.S.A.* **1982**, *79*, 6396-6400.
129) Mino, Y.; Loehr, T.M.; Wada, K.; Matsubara, H.; Sanders-Loehr, J. *Biochemistry* **1987**, *26*, 8059-8065.
130) Han, J.; Adman, E.T.; Beppu, T.; Codd, R.; Freeman, H.C.; Huq, L.; Loehr, T.M.; Sanders-Loehr, J. *Biochemistry* **1991**, *30*, 10904-10913.
131) Han, J.; Loehr, T.M.; Lu, Y.; Valentine, J.S.; Averill, B.A.; Sanders-Loehr, J. *J. Am. Chem. Soc.* **1993**, *115*, 4256-4263.
132) Andrew, C.R.; Yeom, H.; Valentine, J.S.; Karlsson, B.G.; Bonander, N.; van Pouderoyen, G.; Canters, G.W.; Loehr, T.M.; Sanders-Loehr, J. *J. Am. Chem. Soc.* **1994**, *116*, 11489-11498.
133) Dave, B.C.; Germanas, J.P.; Czernuszewicz, R.S. *J. Am. Chem. Soc.* **1993**, *115*, 12175-12176.
134) Andrew, C.R.; Han, J.; den Blaauwen, T.; van Pouderoyen, G.; Vijgenboom, E.; Canters, G.W.; Loehr, T.M.; Sanders-Loehr, J. *J. Biol. Inorg. Chem.* **1997**, *2*, 98-107.
135) van Gastel, M.; Nagano, Y.; Zondervan, R.; Canters, G.W.; Jeuken, L.J.C.; Warmerdam, G.C.M.; de Waal, E.C.; Groenen, E.J.J. *J. Phys. Chem. B* **2002**, *106*, 4018-4021.
136) Hill, H.A.O.; Smith, B.E. *J. Inorg. Biochem.* **1979**, *11*, 79-93.

137) Andrew, C.R.; Sanders-Loehr, J. *Acc. Chem. Res.* **1996**, *29*, 365-372.
138) Johnson, K.H. *Annu. Rev. Phys. Chem.* **1975**, *26*, 39-57.
139) Solomon, E.I.; Gewirth, A.A. *J. Am. Chem. Soc.* **1988**, *110*, 3811-3819.
140) Pierloot, K.; De Kerpel, J.O.A.; Ryde, U.; Olsson, M.H.M.; Roos, B.O. *J. Am. Chem. Soc.* **1998**, *120*, 13156-13166.
141) Ghosh, S.; Xie, X.; Dey, A.; Sun, Y.; Scholes, C.P.; Solomon, E.I. *Proc. Natl. Acad. Sci. U.S.A.* **2009**, *106*, 4969-4974.
142) van Gastel, M.; Coremans, J.W.A.; Sommerdijk, H.; van Hemert, M.C.; Groenen, E.J.J. *J. Am. Chem. Soc.* **2002**, *124*, 2035-2041.
143) Neese, F. *Coord. Chem. Rev.* **2009**, *253*, 526-563.
144) Remenyi, C.; Reviakine, R.; Kaupp, M. *J. Phys. Chem. B* **2007**, *111*, 8290-8304.
145) Gao, J. *Rev. Comp. Chem.* **1996**, *7*, 119-185.
146) Gao, J.; Truhlar, D.G. *Ann. Rev. Phys. Chem.* **2002**, *53*, 467-505.
147) Sinnecker, S.; Neese, F. *J. Comput. Chem.* **2006**, *27*, 1463-1475.
148) Kang, J.; Ohta, T.; Hagiwara, Y.; Nishikawa, K.; Yamamoto, T.; Nagao, H.; Tateno, M. *J. Phys.: Condens. Matter* **2009**, *21*, 1-8.
149) Gak, E.R.; Chistoserdov, A.Y.; Lidstrom, M.E. *J. Bacteriol.* **1995**, *177*, 4575-4578.
150) Barber, D.; Parr, S.R.; Greenwood, C. *Biochem. J.* **1976**, *157*, 431-438.
151) Silvestrini, M.C.; Tordi, M.G.; Colosimo, A.; Antonini, E.; Brunori, M. *Biochem. J.* **1982**, *203*, 445-451.
152) Zannoni, D. *Biochim. Biophys. Acta.* **1989**, *975*, 299-316.
153) Wilson, M.; Greenwood, C.; Brunori, M.; Antonini, E. *Biochem. J.* **145**, 449-457.
154) Vijgenboom, E.; Busch, J.E.; Canters, G.W. *Microbiology* **1997**, 2853-2863.
155) Silvestrini, M.C.; Falcinelli, S.; Ciabatti, I.; Cutruzzola, F.; Brunori, M. *Biochimie* **1994**, *76*, 641-654.
156) Antonini, E.; Finazzi-Agrò, A.; Avigliano, L.; Guerrieri, P.; Rotilio, G.; Mondovì, B. *J. Biol. Chem.* **1970**, *245*, 4847-4856.
157) Pecht, I.; Rosen, P. *Biochem. Biophys. Res. Commun.* **1973**, *50*, 853-858.
158) Brunori, M.; Greenwood, C.; Wilson, M.T. *Biochem. J.* **1974**, *137*, 113-116.
159) Wilson, M.T.; Greenwood, C.; Brunori, M.; Antonini, E. *Biochem. J.* **1975**, *145*, 449-457.
160) Rosen, P.; Segal, M.; Pecht, I. *Eur. J. Biochem.* **1981**, *120*, 339-344.
161) Ugurbil, K.; Norton, R.S.; Allerhand, A.; Bersohn, R. *Biochemistry*, **1977**, *16*, 886-894.
162) Ugurbil, K.; Bersohn, R. *Biochemistry*, **1977**, *16*, 3016-3023.
163) Mitra, S.; Bersohn, R. *Proc. Natl. Acad. Sci. U.S.A.*, **1982**, *79*, 6807-6811.
164) Sukumar, N.; Chen, Z.; Ferrari, D.; Merli, A.; Rossi, G.L.; Bellamy, H.D.; Chistoserdov, A.; Davidson, V.L.; Mathews, F.S. *Biochemistry*, **2006**, *45*, 13500-13510.
165) van de Kamp, M.; Silvestrini, M.C.; Brunori, M.; Van Beeumen, J.; Hali, F.C.; Canters, G.W. *Eur. J. Biochem.* **1990**, *194*, 109-118.
166) Farver, O.; Pecht, I. *Proc. Natl. Acad. Sci. U.S.A.* **1981**, *78*, 4190-4193.
167) Farver, O.; Pecht, I. *Isr. J. Chem.* **1981**, *21*, 13-17.
168) Farver, O.; Blatt, Y.; Pecht, I. *Biochemistry*, **1982**, *21*, 3556-3561.
169) Marcus, R.A.; Sutin, N. *Biochim. Biophys. Acta.* **1985**, *811*, 265-322.
170) Dawson, J.W.; Gray, H.B.; Holwerda, R.A.; Westhead, E.W. *Proc. Natl. Acad. Sci. U.S.A.* **1972**, *69*, 30-33.
171) Wherland, S.; Holwerda, R.A.; Rosenberg, R.C.; Gray, H.B. *J. Am. Chem. Soc.* **1975**, *97*, 5260-5262.
172) Rosenberg, R.C.; Wherland, S.; Holwerda, R.A.; Gray, H.B. *J. Am. Chem. Soc.* **1976**, *98*, 6364-6369.
173) McArdle, J.V.; Coyle, C.L.; Gray, H.B.; Yoneda, G.S.; Holwerda, R.A. *J. Am. Chem. Soc.* **1977**, *99*, 2483-2489.
174) Cummins, D.; Gray, H.B. *J. Am. Chem. Soc.* **1977**, *99*, 5158-5167.
175) Mauk, A.G.; Bordignon, E.; Gray, H.B. *J. Am. Chem. Soc.* **1982**, 7654-7657.
176) Hart, P.J.; Nersissian, A.M.; Herrmann, R.G.; Nalbandyan, R.M.; Valentine, J.S.; Eisenberg, D. *Protein Sci.* **1996**, *5*, 2175-2183.
177) Goldberg, M.; Pecht, I. *Biochemistry* **1976**, *15*, 4197-4208.
178) Wherland, S.; Pecht, I. *Biochemistry* **1978**, *17*, 2585-2591.

179) Groeneveld, C.M.; Dahlin, S.; Reinhammar, B.; Canters, G.W. *J. Am. Chem. Soc.* **1987**, *109*, 3247-3250.
180) Groeneveld, C.M.; Canters, G.W. *Eur. J. Biochem.* **1985**, *153*, 559-564.
181) Groeneveld, C.M.; Canters, G.W. *J. Biol. Chem.* **1988**, *263*, 167-173.
182) Van Pouderoyen, G.; Mazumdar, S.; Hunt, N.I.; Hill, H.A.O.; Canters, G.W. *Eur. J. Biochem.* **1994**, *222*, 583-588.
183) Mikkelsen, K.V.; Skov, L.H.; Nar, H.; Farver, O. *Proc. Natl. Acad. Sci. U.S.A.* **1993**, *90*, 5443-5445.
184) Mauk, A.G.; Scott, R.A.; Gray, H.B. *J. Am. Chem. Soc.* **1980**, *102*, 4300-4303.
185) Armstrong, F.A.; Driscoll, P.C.; Hill, H.A.O.; Redfield, C. *J. Inorg. Biochem.* **1986**, *28*, 171-180.
186) Cho, K.C.; Blair, D.F.; Banerjee, U.; Hopfield, J.J.; Gray, H.B.; Pecht, I.; Chan, S.I. *Biochemistry* **1984**, *23*, 1858-1862.
187) Skov, L.K.; Olsen, K.; Christensen, U.; Farver, O. *Inorg. Chem.* **1993**, *32*, 4762-4765.
188) Brunschwig, B.S.; DeLaive, P.J.; English, A.M.; Goldberg, M.; Gray, H.B.; Mayo, S.L.; Sutin, N. **1985**, *24*, 3743-3749.
189) Winkler, J.R.; Nocera, D.G.; Yocom, K.M.; Bordignon, E.; Gray, H.B. *J. Am. Chem. Soc.* **1982**, *104*, 5798-5800.
190) Kostic, N.M.; Margalit, R.; Che, C.-M. *J. Am. Chem. Soc.* **1983**, *105*, 7765-7767.
191) Margalit, R.; Kostic, N.M.; Che, C.-M.; Blair, D.F.; Chiang, H.-J.; Pecht, I.; Shelton, J.B.; Shelton, J.R.; Schroeder, W.A.; Gray, H.B. *Proc. Natl. Acad. Sci. U.S.A.* **1984**, *81*, 6554-6558.
192) Di Bilio, A.J.; Hill, M.G.; Bonander, N.; Karlsson, B.G.; Villahermosa, R.M.; Malmström, B.G.; Winkler, J.R.; Gray, H.B. *J. Am. Chem. Soc.* **1997**, *119*, 9921-9922.
193) Winkler, J.R.; Gray, H.B. *Chem. Rev.* **1992**, *92*, 369-379.
194) Langen, R.; Chang, I.-J.; Germanas, J.P.; Richards, J.H.; Winkler, J.R.; Gray, H.B. *Science* **1995**, *268*, 1733-1735.
195) Crane, B.R.; Di Bilio, A.J.; Winkler, J.R.; Gray, H.B. *J. Am. Chem. Soc.* **2001**, *123*, 11623-11631.
196) Moser, C.C.; Keske, J.M.; Warncke, K.; Farid, R.S.; Dutton, P.L. *Nature* **1992**, *355*, 796-802.
197) Beratan, D.N.; Onuchic, J.N.; Betts, J.N.; Bowler, B.E.; Gray, H.B. *J. Am. Chem. Soc.* **1990**, *112*, 7915-7921.
198) Beratan, D.N.; Betts, J.N.; Onuchic, J.N. *Science* **1991**, *252*, 1285-1288.
199) Betts, J.N.; Beratan, D.N.; Onuchic, J.N. *J. Am. Chem. Soc.* **1992**, *114*, 4043-4046.
200) Onuchic, J.N.; Beratan, D.N.; Winkler, J.R.; Gray, H.B. *Annu. Rev. Biophys. Biomol. Struct.* **1992**, *21*, 349-377.
201) Beratan, D.N.; Onuchi, J.N.; Winkler, J.R.; Gray, H.B. *Science* **1992**, *258*, 1740-1741.
202) Regan, J.J.; Di Bilio, A.J.; Langen, R.; Skov, L.K.; Winkler, J.R.; Gray, H.B.; Onuchic, J.N. *Chem. Biol.* **1995**, *2*, 489-496.
203) Lowery, M.D.; Solomon, E.I. *Inorg. Chim. Acta* **1992**, *200*, 233-243.
204) Solomon, E.I.; Lowery, M.D. *Science* **1993**, *259*, 1575-1581.
205) Farver, O.; Pecht, I. *Proc. Natl. Acad. Sci. U.S.A.* **1989**, *86*, 6968-6972.
206) Farver, O.; Pecht, I. Long-Range Intramolecular Electron Transfer in Azurins. *J. Am. Chem. Soc.* **1992**, *114*, 5764-5767.
207) Broo, A.; Larsson, S. *J. Phys. Chem.* **1991**, *95*, 4925-4928.
208) Farver, O.; Skov, L.K.; Gilardi, G.; van Pouderoyen, G.; Canters, G.W.; Wherland, S.; Pecht, I. *Chem. Phys.* **1996**, *204*, 271-277.
209) Farver, O.; Pecht, I. *J. Biol. Inorg. Chem.* **1997**, *2*, 387-392.
210) Farver, O.; Skov, L.K.; van de Kamp, M.; Canters, G.W.; Pecht, I. *Eur. J. Biochem.* **1992**, *210*, 399-403.
211) Farver, O.; Skov, L.K.; Pascher, T.; Karlsson, B.G.; Nordling, M.; Lundberg, L.G.; Vänngård, T.; Pecht, I. *Biochemistry* **1993**, *32*, 7317-7322.
212) Farver, O.; Jeuken, L.J.C.; Canters, J.W.; Pecht, I. *Eur. J. Biochem.* **2000**, *267*, 3123-3129.
213) Farver, O.; Skov, L.K.; Young, S.; Bonander, N.; Karlsson, B.G.; Vänngård, T.; Pecht, I. *J. Am. Chem. Soc.* **1997**, *119*, 5453-5454.
214) Shafaat, H.S.; Leigh, B.S.; Tauber, M.J.; Kim, J.E. *J. Am. Chem. Soc.* **2010**, *132*, 9030-9039.
215) Farver, O.; Zhang, J.; Chi, Q.; Pecht, I.; Ulstrup, J. *Proc. Natl. Acad. Sci. U.S.A.* **2001**, *98*, 4426-4430.
216) Nordlund, P.; Reichard, P. *Annu. Rev. Biochem.* **2006**, *75*, 681-706.

217) Barber, J. *Biochem. Soc. Trans.* **2006**, *34*, 619-631.
218) Shih, C.; Museth, A.K.; Abrahamsson, M.; Blanco-Rodriguez, A.M.; Di Bilio, A.J.; Sudhamsu, J.; Crane, B.R.; Ronayne, K.L.; Towrie, M.; Vlcek, A. Jr.; Richards, J.H.; Winkler, J.R.; Gray, H.B. *Science* **2008**, *320*, 1760-1762.
219) Chi, Q.; Zhang, J.; Friis, E.P.; Andersen, J.E.T.; Ulstrup, J. *Electrochem. Commun.* **1999**, *1*, 91-96.
220) Chi, Q.; Zhang, J.; Nielsen, J.U.; Friis, E.P.; Chorkendorff, I.; Canters, G.W.; Andersen, J.E.T.; Ulstrup, J. *J. Am. Chem. Soc.* **2000**, *122*, 4047-4055.
221) Gaigalas, A.K.; Niaura, G. *J. Colloid Interface Sci.* **1997**, *193*, 60-70.
222) Chi, Q.; Zhang, J.; Andersen, J.E.T.; Ulstrup, J. *J. Phys. Chem. B* **2001**, *105*, 4669-4679.
223) Fujita, K.; Nakamura, N.; Ohno, H.; Leigh, B.S.; Niki, K.; Gray, H.B.; Richards, J.H. *J. Am. Chem. Soc.* **2004**, *126*, 13954-13961.
224) McMillin, D.R.; Rosenberg, R.C.; Gray, H.B. *Proc. Natl. Acad. Sci. U.S.A.* **1974**, *71*, 4760-4762.
225) Solomon, E.I.; Rawlings, J.; McMillin, D.R.; Stephens, P.J.; Gray, H.B. *J. Am. Chem. Soc.* **1976**, *98*, 8046-8048.
226) Moratal, J.-M.; Salgado, J.; Donaire, A.; Jiménez, H.R.; Castells, J. *Inorg. Chem.* **1993**, 3587-3588.
227) Donaire, A.; Salgado, J.; Moratal, J.-M. *Biochemistry* **1998**, *37*, 8659-8673.
228) Blaszak, J.A.; Ulrich, E.L.; Markley, J.L.; McMillin, D.R. *Biochemistry* **1982**, *21*, 6253-6258.
229) Bonander, N.; Vänngård, T.; Tsai, L.-C.; Langer, V.; Nar, H.; Sjölin, L. *Proteins: Structure, Function, and Bioinformatics* **1997**, *27*, 385-394.
230) Moratal, J.M.; Romero, A.; Salgado, J.; Perales-Alarcón, A.; Jiménez, H.R. *Eur. J. Biochem.* **1995**, *228*, 653-657.
231) Czernuszewicz, R.; Franczkiewicz, G.; Zareba, A.A. *Inorg. Chem.* **2005**, *44*, 5745-5752.
232) Fitzpatrick, M.B.; Czernuszewicz, R.S. *J. Biol. Inorg. Chem.* **2009**, *14*, 611-620.
233) Funk, T.; Kennepohl, P.; Di Bilio, A.J.; Wehbi, W.A.; Young, A.T.; Friedrich, S.; Arenholz, E.; Gray, H.B.; Cramer, S.P. *J. Am. Chem. Soc.* **2004**, *126*, 5859-5866.
234) Strambini, G.B.; Gabellieri, E. *J. Phys. Chem.* **1991**, *95*, 4352-4356.
235) Klemens, F.K.; McMillin, D.R. *Photochem. Photobiol.* **1992**, *55*, 671-676.
236) McCleskey, T.M.; Mizoguchi, T.J.; Richards, J.H., Gray, H.B. *Inorg. Chem.* **1996**, *35*, 3434-3435.
237) Klemens, A.S.; McMillin, D.R.; Tsang, H.-T.; Penner-Hahn, J.E. *J. Am. Chem. Soc.* **1989**, *111*, 6398-6402.
238) Engeseth, H.R.; McMillin, D.R.; Otvos, J.D. *J. Biol. Chem.* **1984**, *259*, 4822-4826.
239) Blackwell, K.A.; Anderson, B.F.; Baker, E.N. *Acta Cryst. D.* **1994**, *50*, 263-270.
240) Danielsen, E.; Bauer, R.; Hemmingsen, L.; Andersen, M.-L.; Bjerrum, M.J.; Butz, T.; Tröger, W.; Canters, G.W.; Hoiting, C.W.G.; Karlsson, G.; Hansson, Ö.; Messerschmidt, A. *J. Biol. Chem.* **1995**, *270*, 573-580.
241) Karlsson, B.G.; Nordling, M.; Pascher, T.; Tsai, L.-C.; Sjölin, L.; Lundberg, L.G. *Prot. Eng.* **1991**, *4*, 343-349.
242) Di Bilio, A.J.; Chang, T.K.; Malmström, B.G.; Gray, H.B.; Karlsson, B.G.; Nordling, M.; Pascher, T.; Lundberg, L.G. *Inorg. Chim. Acta* **1992**, *198-200*, 145-148.
243) Pascher, T.; Karlsson, B.G.; Nordling, M.; Malmström, B.G.; Vänngård, T. *Eur. J. Biochem.* **1993**, *212*, 289-296.
244) Murphy, L.M.; Strange, R.W.; Karlsson, B.G.; Lundberg, L.G.; Pascher, T.P.; Reinhammar, B.; Hasnain, S.S. *Biochemistry* **1993**, *32*, 1965-1975
245) Gray, H.B.; Malmström, B.G. *Comments Inorg. Chem.* **1983**, *2*, 203-209.
246) Berry, S.M.; Ralle, M.; Low, D.W.; Blackburn, N.J.; Lu, Y. *J. Am. Chem. Soc.* **2003**, *125*, 8760-8768.
247) Yangisawa, S.; Banfield, M.J.; Dennison, C. *Biochemistry* **2006**, *45*, 8812-8822.
248) Marshall, N.M.; Garner, D.K.; Wilson, T.D.; Gao, Y.-G.; Robinson, H.; Nilges, M.J.; Lu, Y. *Nature* **2009**, *462*, 113-116.
249) Germanas, J.P.; Di Bilio, A.J.; Gray, H.B.; Richards, J.H. *Biochemistry* **1993** *32*, 7698-7702.
250) Regan, J.J.; Di Bilio, A.J.; Winkler, J.R.; Richards, J.H.; Gray, H.B. *Inorg. Chim. Acta* **1998**, *275-276*, 470-480.
251) Mizoguchi, T.J.; Di Bilio, A.J.; Gray, H.B.; Richards, J.H. *J. Am. Chem. Soc.* **1992**, *114*, 10076-10078.

252) DeBeer, S.; Kiser, C.N.; Mines, G.A.; Richards, J.H.; Gray, H.B.; Solomon, E.I.; Hedman, B.; Hodgson, K.O. *Inorg. Chem.* **1999**, *38*, 433-438.
253) Berry, S.M.; Gieselman, M.D.; Nilges, M.J.; van der Donk, W.A.; Lu, Y. *J. Am. Chem. Soc.* **2002**, *124*, 2084-2085.
254) Ralle, M.; Berry, S.M.; Nilges, M.J.; Gieselman, M.D.; van der Donk, W.A.; Lu, Y.; Blackburn, N.J. *J. Am. Chem. Soc.* **2004**, *126*, 7244-7256.
255) Canters, G.W.; Gilardi, G. *FEBS Lett.* **1993**, *325*, 39-48.
256) Kroes, S.J.; Andrew, C.R.; Sanders-Loehr, J.; Canters, G.W. *J. Inorg. Biochem.* **1995**, *59*, 661.
257) Kroes, S.J.; Hoitink, C.W.G., Andrew, C.R.; Ai, J.; Sanders-Loehr, J.; Messerschmidt, A.; Hagen, W.R.; Canters, G.W. *Eur. J. Biochem.* **1996**, *240*, 342-351.
258) Karlsson, B.G.; Tsai, L.-C.; Nar, H.; Sanders-Loehr, J.; Bonander, N.; Langer, V.; Sjölin, L. *Biochemistry* **1997**, *36*, 4089-4095.
259) Salgado, J.; Krose, S.J.; Berg, A.; Moratal, J.M.; Canters, G.W. *J. Biol. Chem.* **1998**, *273*, 177-185.
260) Messerschmidt, A.; Prade, L.; Kroes, S.J.; Sanders-Loehr, J.; Huber, R.; Canters, G.W. *Proc. Natl. Acad. Sci. U.S.A.* **1998**, *95*, 3443-3448.
261) Romero, A.; Hoiting, C.W.G.; Nar, H.; Huber, R.; Messerschmidt, A.; Canters, G.W. *J. Mol. Biol.* **1993**, *229*, 1007-1021.
262) Coremans, J.W.A.; Poluektov, O.G.; Groenen, E.J.J.; Warmerdam, G.C.M.; Canters, G.W.; Nar, H.; Messerschmidt, A. *J. Phys. Chem.* **1996**, *100*, 19706-19713.
263) Salgado, J.; Jiménez, H.R.; Moratal, J.M. *Biochemistry* **1996** *33*, 1810-1819.
264) Clark, K.M.; Marshall, N.M.; Sieracki, N.A.; Nilges, M.J.; Blackburn, N.J.; van der Donk, W.A.; Lu, Y. *J. Am. Chem. Soc.* **2010**, *132*, 10093-10101.
265) Hammann, C.; van Pouderoyen, G.; Nar, H.; Gomis, R.F.; Messerschmidt, A.; Huber, R.; den Blaauwen, T.; Canters, G.W. *J. Mol. Biol.* **1997**, *266*, 357-366.
266) den Blaauwen, T; van de Kamp, M.; Canters, G.W. *J. Am. Chem. Soc.* **1991**, *113*, 5050-5052.
267) den Blaauwen, T.; Canters, G.W. *J. Am. Chem. Soc.* **1993**, *115*, 1121-1129.
268) den Blaauwen, T.; Hoitink, C.W.; Canters, G.W.; Han, J.; Loehr, T.M.; Sanders-Loehr, J. *Biochemistry* **1993**, *32*, 12455-12464.
269) Gorren, A.C.F.; den Blaauwen, T.; Cantes, G.W.; Hopper, D.J.; Duine, J.A. *FEBS Lett.* **1996**, *381*, 140-142.
270) Jeuken, L.J.C.; Ubbink, M.; Bitter, J.H.; van Vliet, P.; Meyer-Klaucke, W.; Canters, G.W. *J. Mol. Biol.* **2000**, *299*, 737-755.
271) van Pouderoyen, G.; Andrew, C.R.; Loehr, T.M.; Sanders-Loehr, J.; Mazumdar, S.; Hill, H.A.O.; Canters, G.W. *Biochemistry* **1996**, *35*, 1397-1407.
272) Vidakovic, M.; Germanas, J.P. *Angew. Chem. Int. Ed.* **1995**, *34*, 1622-1624.
273) Bonander, N.; Karlsson, B.G.; Vänngård, T. *Biochemistry* **1996**, *35*, 2429-2436.
274) Frackzkiewicz, G.; Bonander, N.; Czernuszewicz, R.S. *J. Raman Spectrosc.* **1998**, *29*, 983-995.
275) Tsai, L.-C.; Bonander, N.; Harata, K.; Karlsson, G.; Vänngård, T.; Langer, V.; Sjölin, L. *Acta Cryst. D* **1996**, *52*, 950-958.
276) Strange, R.W.; Murphy, L.M.; Karlsson, B.G.; Reinhammar, B.; Hasnain, S.S. *Biochemistry* **1996**, *35*, 16391-16398.
277) Wittung, P.; Källebring, B.; Malmström, B.G. *FEBS Lett.* **1994**, *349*, 286-288.
278) Hay, M.; Richards, J.H.; Lu, Y. *Proc. Natl. Acad. Sci. U.S.A.* **1996**, *93*, 461-464.
279) Hay, M.T.; Ang, M.C.; Gamelin, D.R.; Solomon, E.I.; Antholine, W.E.; Ralle, M.; Blackburn, N.J.; Massey, P.D.; Wang, X.; Kwon, A.H.; Lu, Y. *Inorg. Chem.* **1998**, *37*, 191-198.
280) Robinson, H.; Ang, M.C.; Gao, Y.-G.; Hay, M.T.; Lu, Y.; Wang, A. H.-J. *Biochemistry*, **1999**, *38*, 5677-5683.
281) Farver, O.; Lu, Y.; Ang, M.C.; Pecht, I. *Proc. Natl. Acad. Sci. U.S.A.* **1999**, *96*, 899-902.
282) Hwang, H.J.; Nagraj, N.; Lu, Y. *Inorg. Chem.* **2006**, *45*, 102-107.
283) Wang, X.; Berry, S.M.; Xia, Y.; Lu, Y. *J. Am. Chem. Soc.* **1999**, *121*, 7449-7450.
284) Berry, S.M.; Wang, X.; Lu, Y. *J. Inorg. Biochem.* **2000**, *78*, 89-95.
285) Hwang, H.J.; Berry, S.M.; Nilges, M.J.; Lu, Y. *J. Am. Chem. Soc.* **2005**, *127*, 7274-7275.
286) Dennison, C.; Vijgenboom, E.; Hagen, W.R.; Canters, G.W. *J. Am. Chem. Soc.* **1996**, *118*, 7406-7407.
287) Buning, C.; Canters, G.W.; Comba, P.; Dennison, C.; Jeuken, L.; Melter, M.; Sanders-Loehr, J. *J. Am. Chem. Soc.* **2000**, *122*, 204-211.

288) Yanagisawa, S.; Dennison, C. *J. Am. Chem. Soc.* **2003**, *125*, 4974-4975.
289) Yanagisawa, S.; Dennison, C. *J. Am. Chem. Soc.* **2004**, *126*, 15711-15719.
290) Li, C.; Yanagisawa, S.; Martins, B.M.; Messerschmidt, A.; Banfield, M.J.; Dennison, C. *Proc. Natl. Acad. Sci. U.S.A.* **2006**, *103*, 7258-7263.
291) Li, C.; Banfield, M.J.; Dennison, C. *J. Am. Chem. Soc.* **2007**, *129*, 709-718.
292) Sato, K.; Li, C.; Salard, I.; Thompson, A.J.; Banfield, M.J.; Dennison, C. *Proc. Natl. Acad. Sci. U.S.A.* **2009**, *106*, 5616-5621.
293) van Amsterdam, I.M.C.; Ubbink, M.; Einsle, O.; Messerschmidt, A.; Merli, A.; Cavazzini, D.; Rossi, G.L.; Canters, G.W. *Nat. Struct. Biol.* **2001**, *9*, 48-52.
294) Farver, O.; Canters, G.W.; van Amsterdam, I.; Pecht, I. *J. Phys. Chem. A* **2003**, *107*, 6757-6760.
295) de Jongh, T.E.; Hoffmann, M.; Einsle, O.; Cavazzini, D.; Rossi, G.; Ubbink, M.; Canters, G.W. *Eur. J. Inorg. Chem.* **2007**, *2007*, 2627-2634.
296) van Amsterdam, I.M.C.; Ubbink, M.; Canters, G.W. *Inorg. Chim. Acta* **2002**, *331*, 296-302.
297) van Pouderoyen, G.; den Blaauwen, T.; Reedijk, J.; Canters, G.W. *Biochemistry* **1996**, *35*, 13205-13211.
298) Zaborina, O.; Dhiman, N.; Chen, M.L.; Kostal, J.; Holder, I.A.; Chakrabarty, A.M. *Microbiology* **2000**, *146*, 2521-2530.
299) Yamada, T.; Goto, M.; Punj, V.; Zaborina, O.; Kimbara, K.; Das Gupta, T.K; Chakrabarty, A.M. *Infect. Immun.* **2002**, *70*, 7054-7062.
300) Goto, M.; Yamada, T.; Kimbara, K.; Horner, J.; Newcomb, M.; Das Gupta, T.K.; Chakrabarty, A.M. *Mol. Microbiol.* **2003**, *47*, 549-559.
301) Punj, V.; Das Gupta, T.K.; Chakrabarty, A.M. *Biochem. Biophys. Res. Commun.* **2003**, *312*, 109-114.
302) Apiyo, D.; Wittung-Stafshede, P. *Biochem. Biophys. Res. Commun.* **2005**, *332*, 965-968.
303) Yamada, T.; Goto, M.; Punj, V.; Zaborina, O.; Chen, M.L.; Kimbara, K.; Majumdar, D.; Cunningham, E.; Das Gupta, T.K.; Chakrabarty, A.M. *Proc. Natl. Acad. Sci. U.S.A.* **2002**, *99*, 14098-14103.
304) Punj, V.; Bhattacharyya, S.; Saint-Dic, D.; Vasu, C.; Cunningham, E.A.; Graves, J.; Yamada, T.; Constantinou, A.I.; Christov, K.; White, B.; Li, G.; Majumdar, D.; Chakrabarty, A.M.; Das Gupta, T.K. *Oncogene* **2004**, *23*, 2367-2378.
305) Chaudhari, A.; Mahfouz, M.; Fialho, A.M.; Yamada, T.; Granja, A.T.; Zhu, Y.; Hashimoto, W.; Schlarb-Ridley, B.; Cho, W.; Das Gupta, T.K.; Chakrabarty, A.M. *Biochemistry* **2007**, *46*, 1799-1810.
306) Yamada, T.; Fialho, A.M.; Punj, V.; Bratescu, L.; Das Gupta, T.K.; Chakrabarty, A.M. *Cell. Microbiol.* **2005**, *7*, 1418-1431.
307) Yamada, T.; Mehta, R.R.; Lekmine, F.; Christov, K.; King, M.L.; Majumdar, D.; Shikaitis, A.; Green, A.; Bratescu, L.; Beattie, C.W.; Das Gupta, T.K. *Mol. Cancer Ther.* **2009**, *8*, 2947-2958.
308) Taylor, B.N.; Mehta, R.R.; Yamada, T.; Lekmine, F.; Christov, K.; Chakrabarty, A.M.; Green, A.; Bratescu, L.; Shilkaitis, A.; Beattie, C.W.; Das Gupta, T.K. *Cancer Res.* **2009**, *69*, 537-546.
309) Gilardi, G.; den Blaauwen, T.; Canters, G.W. *J. Contr. Rel.* **1994**, *29*, 231-238.
310) Albers, W.M.; Lekkala, J.O.; Jeuken, L.; Canters, G.W.; Turner, A.P.F. *Bioelectrochem. Bioenerg.* **1997**, *42*, 25-33.
311) Verbeet, M.P.; *et al. J. Inorg. Biochem.* **1999**, *74*, 327.
312) Gilardi, G.; Fantuzzi, A. *Trends Biotechnol.* **2001**, *19*, 468-476.
313) Shleev, S.; Wetterö, J.; Magnusson, K.-E.; Ruzgas, T. *Biosens. Bioelectr.* **2006**, *22*, 213-219.
314) Cingolani, R.; Rinaldi, R.; Maruccio, G.; Biasco, A. *Physica E* **2002**, *13*, 1229-1235.
315) Rinaldi, R.; Biasco, A.; Maruccio, G.; Cingolani, R.; Alliata, D.; Andolfi, L.; Facci, P.; De Rienzo, F.; Di Felice, R.; Molinari, E. *Adv. Mater.* **2002,** *14*, 1453-1457.
316) Rinaldi, R.; Biasco, A.; Maruccio, G.; Arima, V.; Visconti, P.; Cingolani, R.; Facci, P.; De Rienzo, F.; Di Felice, R.; Molinari, E.; Verbeet, M. Ph.; *App. Phys. Lett.* **2003**, *82*, 472-474.
317) Rinaldi, R.; Maruccio, G.; Biasco, A.; Visconti, P.; Arima, V.; Cingolani, R. *Ann. N.Y. Acad. Sci.* **2003**, *1006*, 187-197.
318) Maruccio, G.; Biasco, A.; Visconti, P.; Bramanti, A.; Pompa, P.P.; Calabi, F.; Cingolani, R.; Rinaldi, R.; Corni, S.; Di Felice, R.; Molinari, E.; Verbeet, M.P.; Canters, G.W. *Adv. Mater.* **2005**, *17*, 816-822.
319) Rinaldi, R.; Cingolani, R. *Physica E* **2004**, *21*, 45-60.

320) Alessandrini, A.; Salerno, M.; Frabboni, S.; Facci, P. *App. Phys. Lett.* **2005**, *86*, 133902.
321) Pompa, P.P.; Bramanti, A.; Maruccio, G.; del Mercato, L.L.; Cingolani, R.; Rinaldi, R. *Chem. Phys. Lett.* **2005**, *404*, 59-62.
322) Bizzarri, A.R.; Andolfi, L.; Taranta, M.; Cannistraro, S. *Biosens. Bioelectr.* **2008**, *24*, 204-209.
323) Choi, J.-W.; Oh, B.-K.; Kim, Y.J.; Min, J. *App. Phys. Lett.* **2007**, *91* 263902.
324) Kim, S.-U.; Yagati, A.K.; Min, J.; Choi, J.-W. *Thin Solid Films* **2009**, *518*, 682-687.
325) Yagati, A.K.; Kim, S.-U.; Min, J.; Choi, J.-W. *Biosens. Bioelectr.* **2009**, *24*, 1503-1507.
326) Lee, T.; Kim, S.-U.; Min, J.; Choi, J.-W. *Adv. Mater.* **2010** *22*, 510-514.
327) Holwerda, R.A.; Wherland, S.; Gray, H.B. *Annu. Rev. Biophys. Bioeng.* **1976**, *5*, 363-396.
328) Wood, P.M. *Biochim. Biophys. Acta* **1974**, *357*, 370.

Table 1.1. Metal binding constants for *P. aeruginosa* azurin. Values reproduced from References 28 and 31.

Metal	k_D (Folded)	k_D (Unfolded)
Cu^{II}	25 fM	0.3 nM
Cu^{I}	0.033 fM	3.0 fM
Zn^{II}	82 nM	5.1 ± 2 μM

Table 1.2. Dentaturation temperatures for *P. aeruginosa* azurin variants. The values for unfolding of Ni^{II} azurin are given in the presence of stoichiometric and superstoichiometric concentrations of Ni^{II}.

Form	T_m (ºC)	Method	Reference
Apoazurin	62 ± 2	DSC	38
Apoazurin (transition 2)	86 ± 2	DSC	38
Cu^{II}	80 ± 2	DSC	38
Cu^{II}	86.3 ± 0.5	DSC	39
Cu^{II}	80	Optical	40
Cu^{II}	86.30 ± 0.06	DSC	41
Cu^{II}	81.48 ± 0.08	Optical	41
Cu^{II} (D_2O)	86.46 ± 0.07	DSC	41
Cu^{II} (D_2O)	86.15 ± 0.05	Optical	41
Cu^{I}	85.4 ± 0.5	DSC	42
Co^{II}	82 ± 2	DSC	38
Ni^{II} (excess)	75 ± 2	DSC	38
Ni^{II} (excess, transition 2)	90 ± 2	DSC	38
Ni^{II}	68 ± 2	DSC	38
Ni^{II} (transition 2)	82 ± 2	DSC	38
Zn^{II}	90 ± 2	DSC	38
Zn^{II}	89.6 ± 0.1	DSC	42
Ag^{I}	78 ± 2	DSC	38
Hg^{II}	91 ± 2	DSC	38
Cd^{II}	93 ± 2	DSC	38

Table 1.3. EPR parameters of Cu^{II} *P. aeruginosa* azurin measured by single-crystal W-band (95 GHz)[90] and frozen solution L- (1.2 GHz) and S-band (3.4 GHz)[91] studies.

	Value	Reference
g_{xx}	2.0393 ± 0.0004	90
g_{yy}	2.0568 ± 0.0007	90
g_{zz}	2.273 ± 0.004	90
A_x (^{65}Cu, mK)	1.0	91
A_y (^{65}Cu, mK)	0.60	91
A_z (^{65}Cu, mK)	5.744	91
A^{N1}_x (mK)	0.90	91
A^{N1}_y (mK)	0.851	91
A^{N1}_z (mK)	0.90	91
A^{N2}_x (mK)	0.70	91
A^{N2}_y (mK)	0.60	91
A^{N2}_z (mK)	0.584	91

Table 1.4. Selected resonance Raman assignments of Cu^{II} *P. aeruginosa* azurin. Values from Reference 134.

Shift (cm^{-1})	**Assignment**
Fundamentals	
408	Cu^{II}-S (C112)
657	(C_{α}-N) (C112)
753	(S-C_{β}) (C112)
1226	(CNH) (C112)
1407	($HC_{\beta}H$) (C112)
Combination Bands	
693	408 + 284
780	408 + 372
809	408 + 400
836	408 + 428
1155	408 + 753

Table 1.5. ET rates for reactions of *P. aeruginosa* and *P. fluorescens* azurins with transition metal complexes. Values for k_{ese} were calculated by the Marcus cross relationship (Eq. 1.3).

Variant	Reagent	k_{12} ($M^{-1}s^{-1}$)	k_{ese} (Reagent, $M^{-1}s^{-1}$)	k_{ese} (Azurin, $M^{-1}s^{-1}$)	Reference
P. aeruginosa	$Fe(EDTA)^{2-}$	1.3×10^3	1×10^4 - 1×10^5	1×10^{-3} - 2×10^{-1}	171
P. aeruginosa	$Co(phen)_3^{3+}$	3.2×10^3	1.5×10^1 - 1.5×10^2	4×10^2 - 1×10^5	327
P. aeruginosa	cytc_{551} (Fe^{II})	6.1×10^6	1×10^{-1} - 1×10^8	4×10^3 - 1×10^{14}	58
P. fluorescens	$Fe(CN)_6^{3-}$	1.2×10^4	5×10^3 - 5×10^4	5×10^0 - 5×10^2	328
P. fluorescens	cyt*c* (Fe^{II})	3×10^3	2×10^2 - 1×10^3	2×10^3 - 2×10^5	328
P. fluorescens	cyt*f* (Fe^{III})	6×10^6	1×10^3 - 2×10^5	5×10^6 - 2×10^{10}	328
P. fluorescens	cytc_{551} (Fe^{II})	5×10^6	6×10^1 - 7×10^3	2×10^8 - 6×10^{11}	328
P. fluorescens	cytc_{553} (Fe^{II})	2×10^7	3×10^2 - 3×10^4	4×10^8 - 9×10^{11}	328

Figure 1.1. Multiple sequence alignment of azurin genes from ten species. Gene FASTA sequences were retrieved from the National Center for Biotechnology Information Protein database and aligned with ClustalW. Alignment was visualized in Jalview; sequence conservation is highlighted in blue, with darkness proportional to the degree of conservation. The *Kangiella koreensis* azurin lacks the conserved disulfide – however it does retain a high degree of sequence homology in the 56-67 (*P. aeruginosa* notation, 80-90 in the sequence alignment) α-helix region.

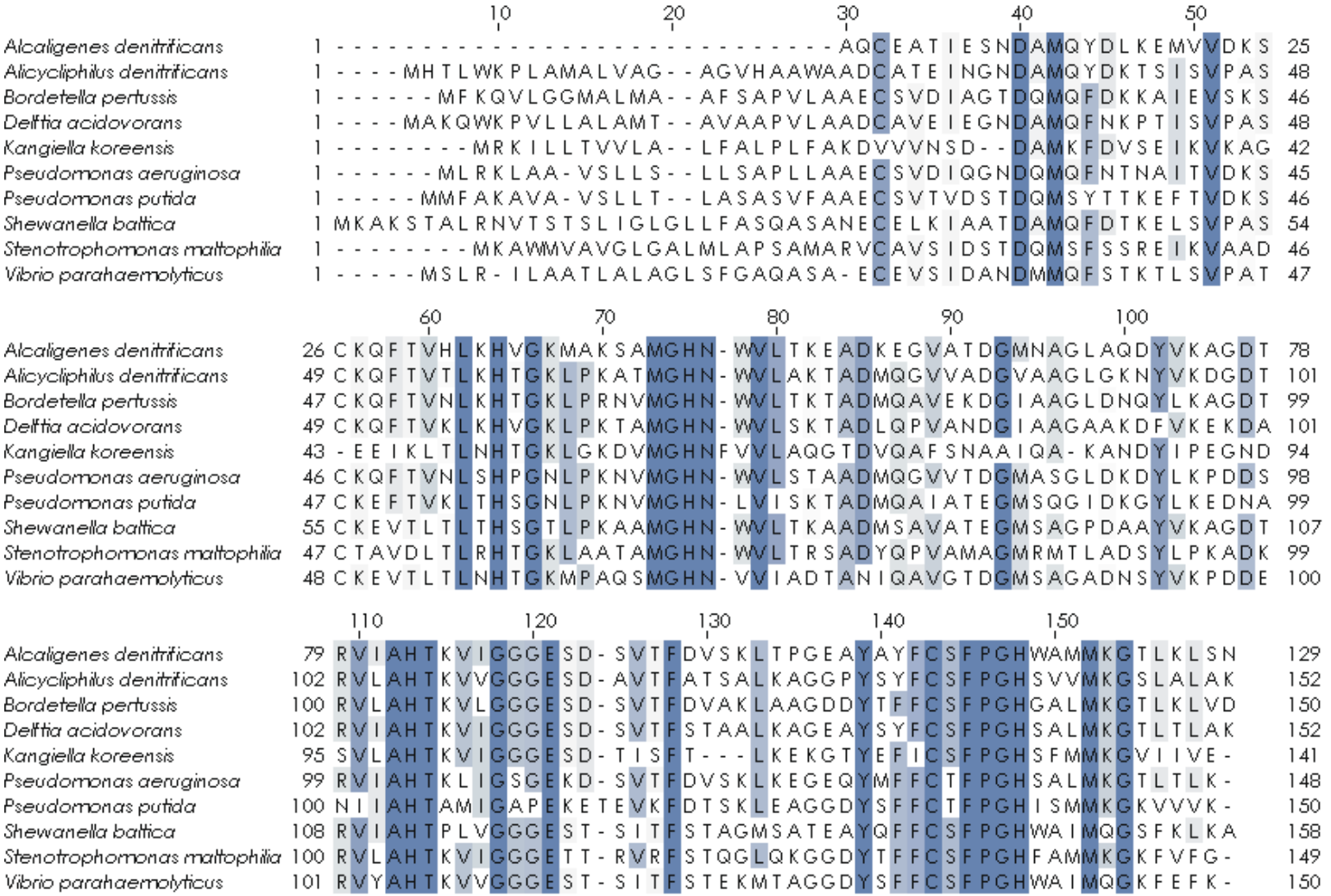
10 20 30 40 50
Alcaligenes denitrificans 1 - AQCEATIESNDAMQYDLKEMVVDKS 25
Alicycliphilus denitrificans 1 - - - - MHTLWKPLAMALVAG - - AGVHAAWAADCATEINGNDAMQYDKTSISVPAS 48
Bordetella pertussis 1 - - - - - - MFKQVLGGMALMA - - AFSAPVLAAECSVDIAGTDQMQFDKKAIEVSKS 46
Delftia acidovorans 1 - - - - MAKQWKPVLLALAMT - - AVAAPVLAADCAVEIEGNDAMQFNKPTISVPAS 48
Kangiella koreensis 1 - - - - - - - - MRKILLTVVLA - - LFALPLFAKDVVVNSD - - DAMKFDVSEIKVKAG 42
Pseudomonas aeruginosa 1 - - - - - - MLRKLAA - VSLLS - - LLSAPLLAAECSVDIQGNDQMQFNTNAITVDKS 45
Pseudomonas putida 1 - - - - - MMFAKAVA - VSLLT - - LASASVFAAECSVTVDSTDQMSYTTKEFTVDKS 46
Shewanella baltica 1 MKAKSTALRNVTSTSLIGLGLLFASQASANECELKIAATDAMQFDTKELSVPAS 54
Stenotrophomonas maltophilia 1 - - - - - - - - MKAWMVAVGLGALMLAPSAMARVCAVSIDSTDQMSFSSREIKVAAD 46
Vibrio parahaemolyticus 1 - - - - - MSLR - ILAATLALAGLSFGAQASA - ECEVSIDANDMMQFSTKTLSVPAT 47
60 70 80 90 100
Alcaligenes denitrificans 26 CKQFTVHLKHVGKMAKSAMGHN - WVLTKEADKEGVATDGMNAGLAQDYVKAGDT 78
Alicycliphilus denitrificans 49 CKQFTVTLKHTGKLPKATMGHN - WVLAKTADMQGVVADGVAAGLGKNYVKDGDT 101
Bordetella pertussis 47 CKQFTVNLKHTGKLPRNVMGHN - WVLTKTADMQAVEKDGIAAGLDNQYLKAGDT 99
Delftia acidovorans 49 CKQFTVKLKHVGKLPKTAMGHN - WVLSKTADLQPVANDGIAAGAAKDFVKEKDA 101
Kangiella koreensis 43 - EEIKLTLNHTGKLGKDVMGHNFVVLAQGTDVQAFSNAAIQA - KANDYIPEGND 94
Pseudomonas aeruginosa 46 CKQFTVNLSHPGNLPKNVMGHN - WVLSTAADMQGVVTDGMASGLDKDYLKPDDS 98
Pseudomonas putida 47 CKEFTVKLTHSGNLPKNVMGHN - LVISKTADMQAIATEGMSQGIDKGYLKEDNA 99
Shewanella baltica 55 CKEVTLTLTHSGTLPKAAMGHN - WVLTKAADMSAVATEGMSAGPDAAYVKAGDT 107
Stenotrophomonas maltophilia 47 CTAVDLTLRHTGKLAATAMGHN - WVLTRSADYQPVAMAGMRMTLADSYLPKADK 99
Vibrio parahaemolyticus 48 CKEVTLTLNHTGKMPAQSMGHN - VVIADTANIQAVGTDGMSAGADNSYVKPDDE 100
110 120 130 140 150
Alcaligenes denitrificans 79 RVIAHTKVIGGGESD - SVTFDVSKLTPGEAYAYFCSFPGHWAMMKGTLKLSN 129
Alicycliphilus denitrificans 102 RVLAHTKVVGGGESD - AVTFATSALKAGGPYSYFCSFPGHSVVMKGSLALAK 152
Bordetella pertussis 100 RVLAHTKVLGGGESD - SVTFDVAKLAAGDDYTFFCSFPGHGALMKGTLKLVD 150
Delftia acidovorans 102 RVIAHTKVIGGGESD - SVTFSTAALKAGEAYSYFCSFPGHSALMKGTLTLAK 152
Kangiella koreensis 95 SVLAHTKVIGGGESD - TISFT - - - LKEKGTYEFICSFPGHSFMMKGVIIVE - 141
Pseudomonas aeruginosa 99 RVIAHTKLIGSGEKD - SVTFDVSKLKEGEQYMFFCTFPGHSALMKGTLTLK - 148
Pseudomonas putida 100 NIIAHTAMIGAPEKETEVKFDTSKLEAGGDYSFFCTFPGHISMMKGKVVVK - 150
Shewanella baltica 108 RVIAHTPLVGGGEST - SITFSTAGMSATEAYQFFCSFPGHWAIMQGSFKLKA 158
Stenotrophomonas maltophilia 100 RVLAHTKVIGGGETT - RVRFSTQGLQKGGDYTFFCSFPGHFAMMKGKFVFG - 149
Vibrio parahaemolyticus 101 RVYAHTKVVGGGEST - SITFSTEKMTAGGDYSFFCSFPGHWAIMQGKFEFK - 150

Figure 1.2. 1.9 Å 3D crystal structure of *P. aeruginosa* azurin at pH 5.5 (PDBID: 4AZU). The CuII ion and amino acid residues involved in its ligation are explicitly modeled. Nitrogen atoms are dark blue, oxygen atoms are red, and sulfur atoms are yellow.

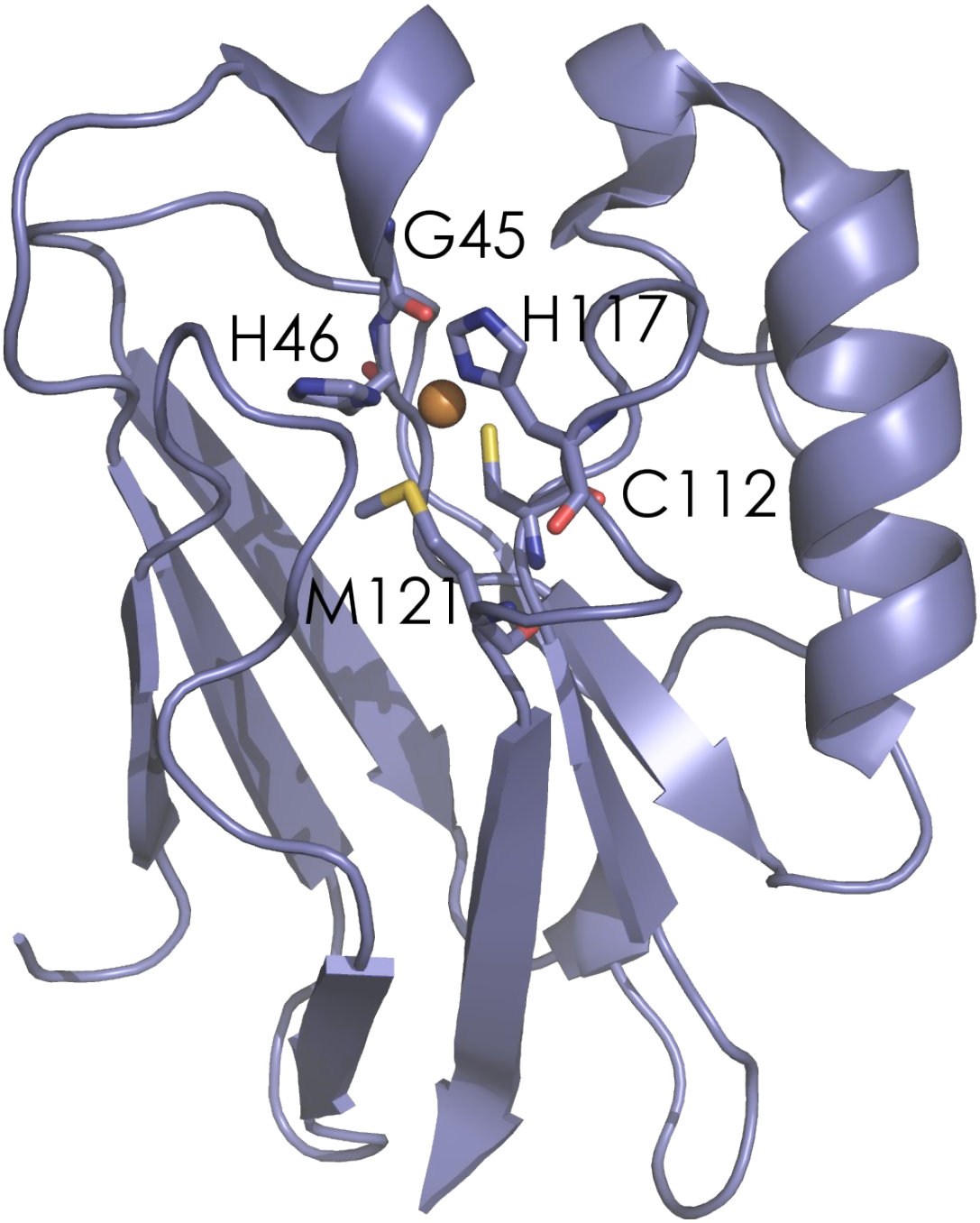
G45
H46
H117
C112
M121

Figure 1.3. 1.9 Å 3D crystal structure of P. aeruginosa azurin at pH 5.5 (PDBID: 4AZU), focused on the N47-C112-F114 hydrogen bond network. Heteroatom distances are printed in Å. Nitrogen atoms are dark blue, oxygen atoms are red, and sulfur atoms are yellow.

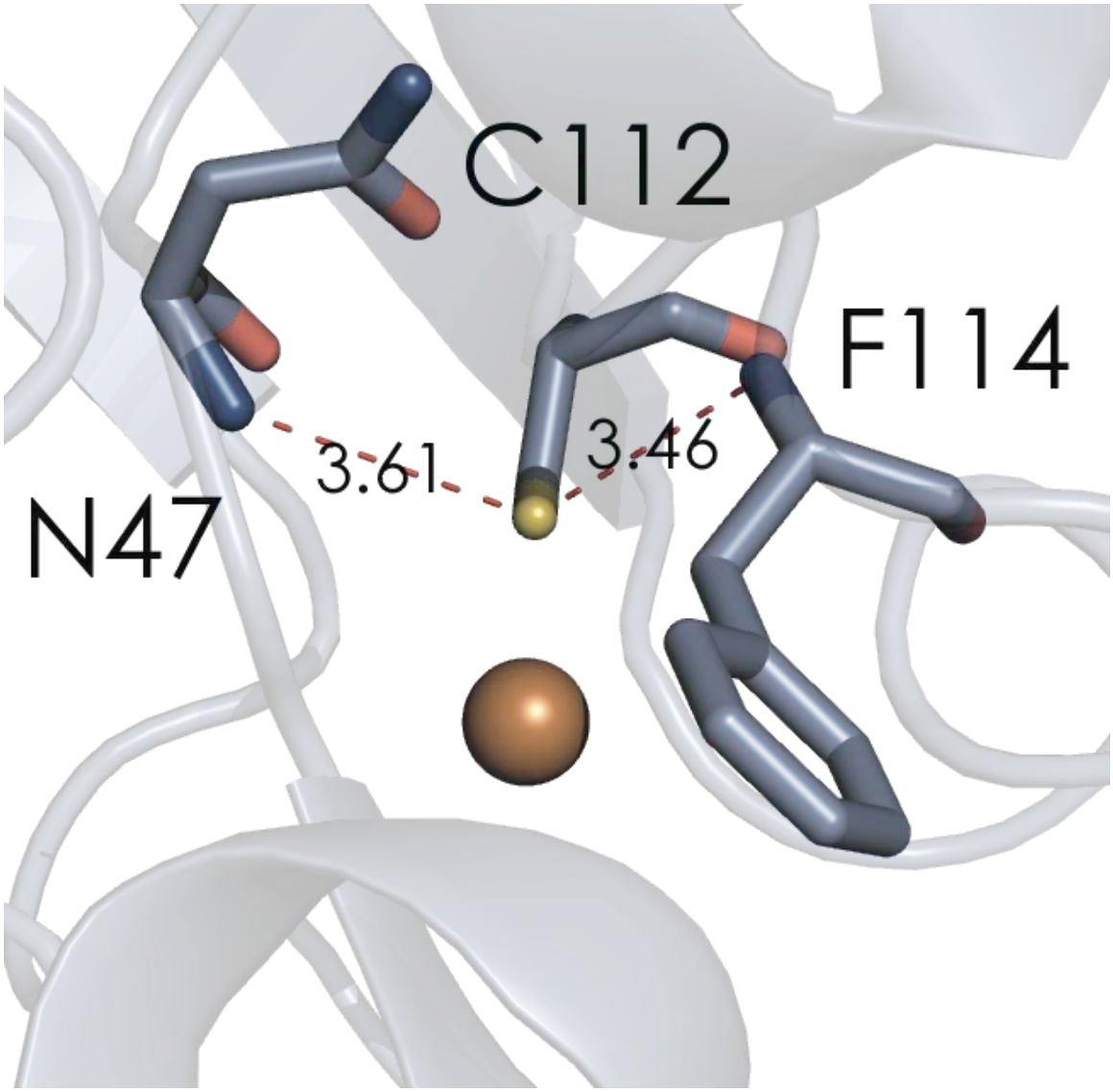
C112
F114
3.61
3.46
N47

Figure 1.4. C_α structural alignment of *P. aeruginosa* azurin (1.9 Å at pH 5.5, PDBID: 4AZU, periwinkle) with *A. denitrificans* azurin (1.8 Å PDBID: 2AZA, white).

Figure 1.5. 1.9 Å 3D crystal structure of P. aeruginosa azurin at pH 5.5 (PDBID: 4AZU). The eight residues forming the "hydrophobic core," V31, L33, W48, L50, V95, F97, Y108, and F110, have been highlighted. Nitrogen atoms are dark blue, oxygen atoms are red.

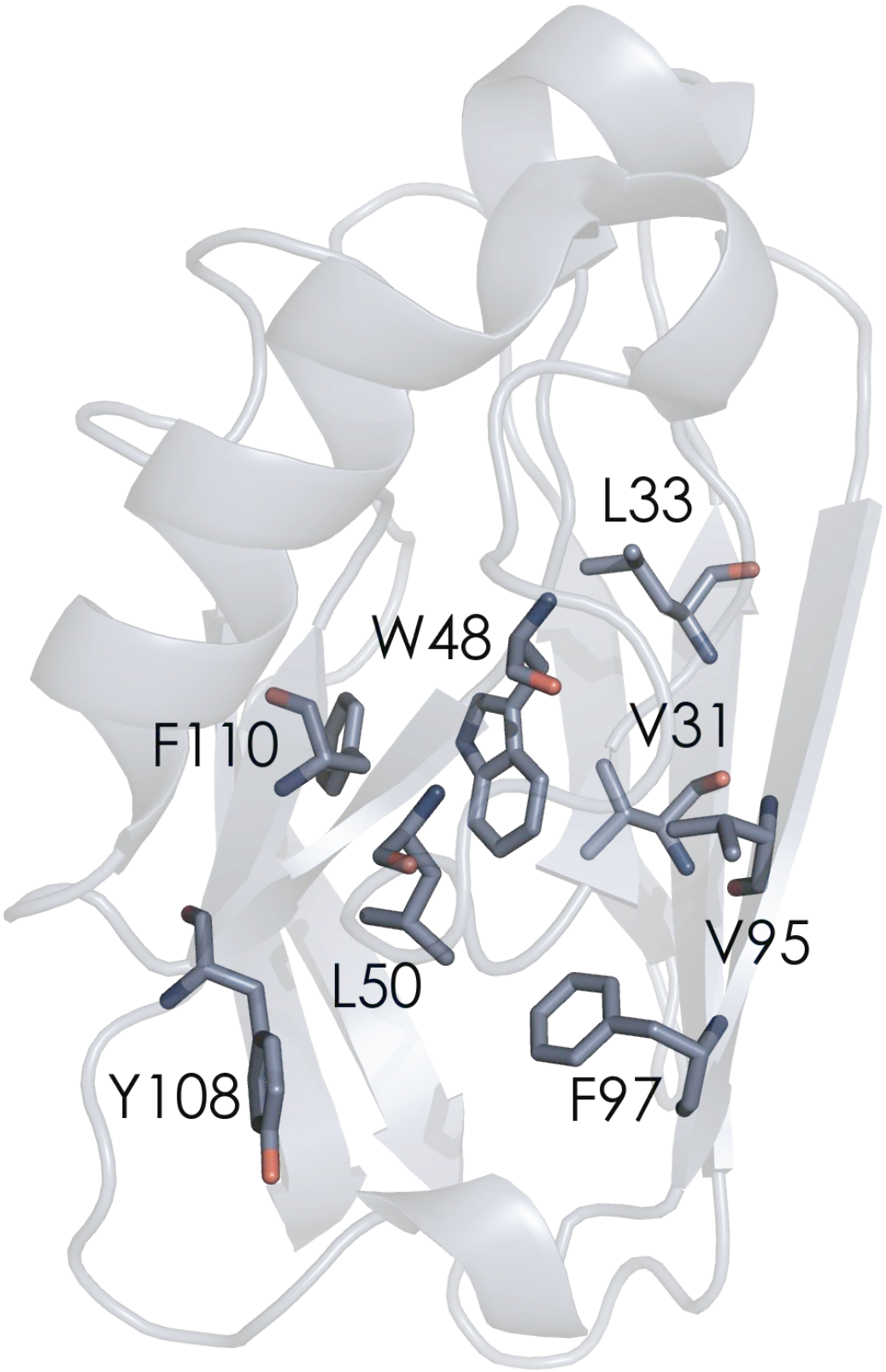
L33
W48
F110
V31
V95
L50
Y108
F97

Figure 1.6. 1.9 Å 3D crystal structure of *P. aeruginosa* azurin at pH 5.5 (PDBID: 4AZU). The C3-C26 disulfide bridge is highlighted. Nitrogen atoms are dark blue, oxygen atoms are red, sulfur atoms are yellow.

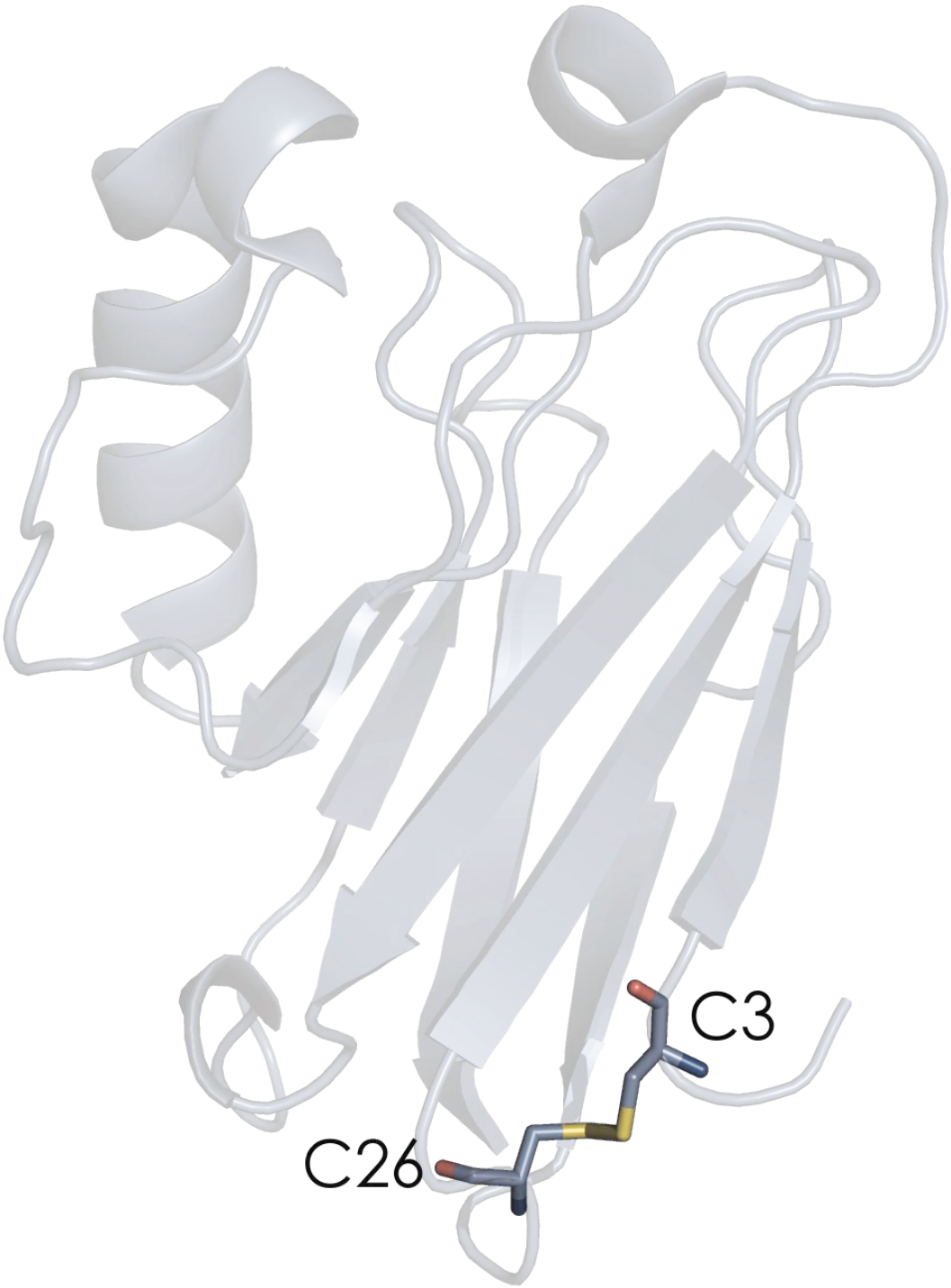
C3
C26

Figure 1.7. 1.9 Å 3D crystal structure of *P. aeruginosa* azurin at pH 5.5 (PDBID: 4AZU). H35 and H83 are highlighted. The metal binding site is also explicitly modeled for orientational reference. Nitrogen atoms are dark blue, oxygen atoms are red, sulfur atoms are yellow.

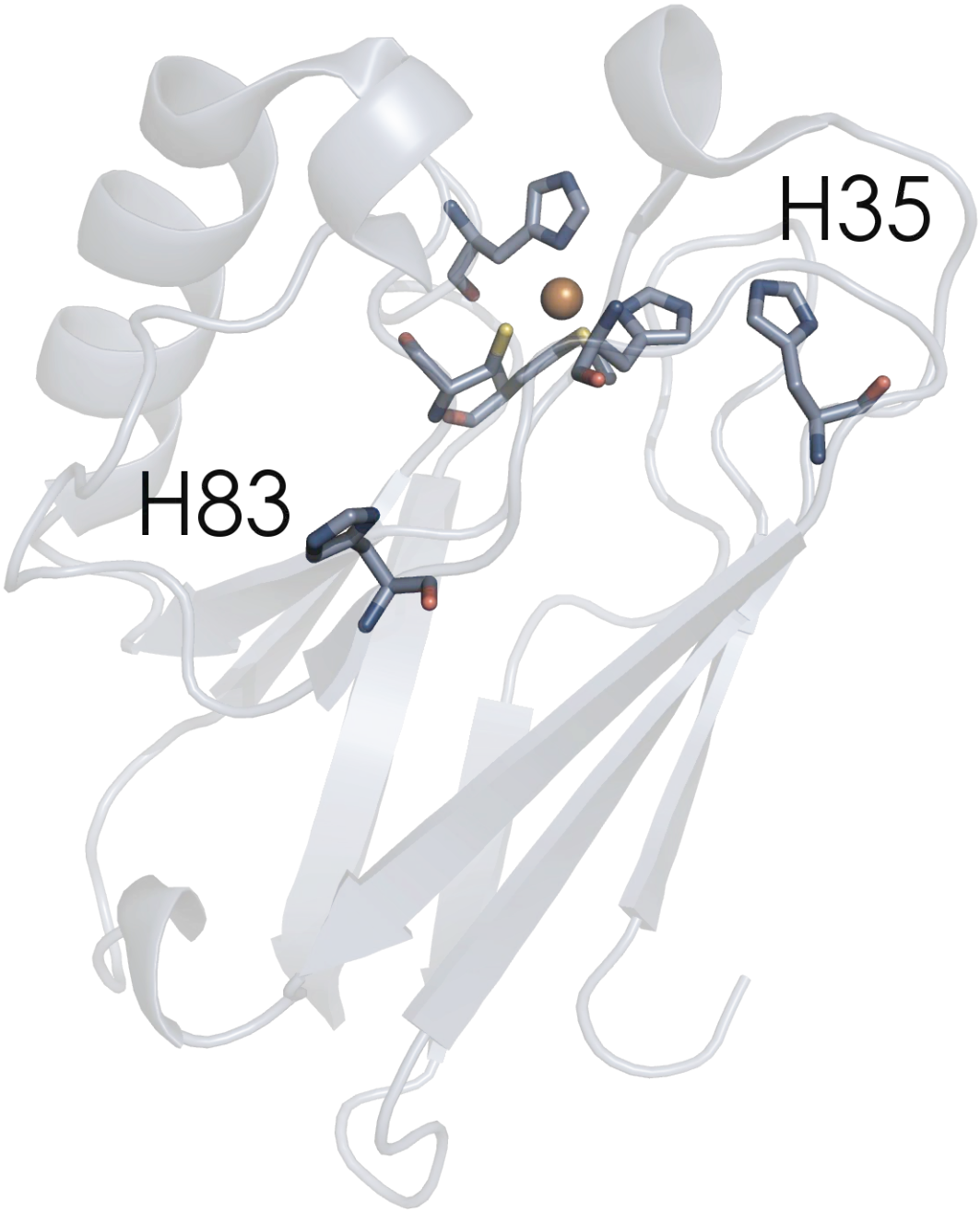
H35
H83

Figure 1.8. Electronic absorption spectrum of *P. aeruginosa* azurin recorded in 100 mM NaP_i, pH 7.0 at 298 K. The $S\pi(C112)\text{-}Cu^{II}$ LMCT is located at 15.85 kK, as indicated by John H. Richards.

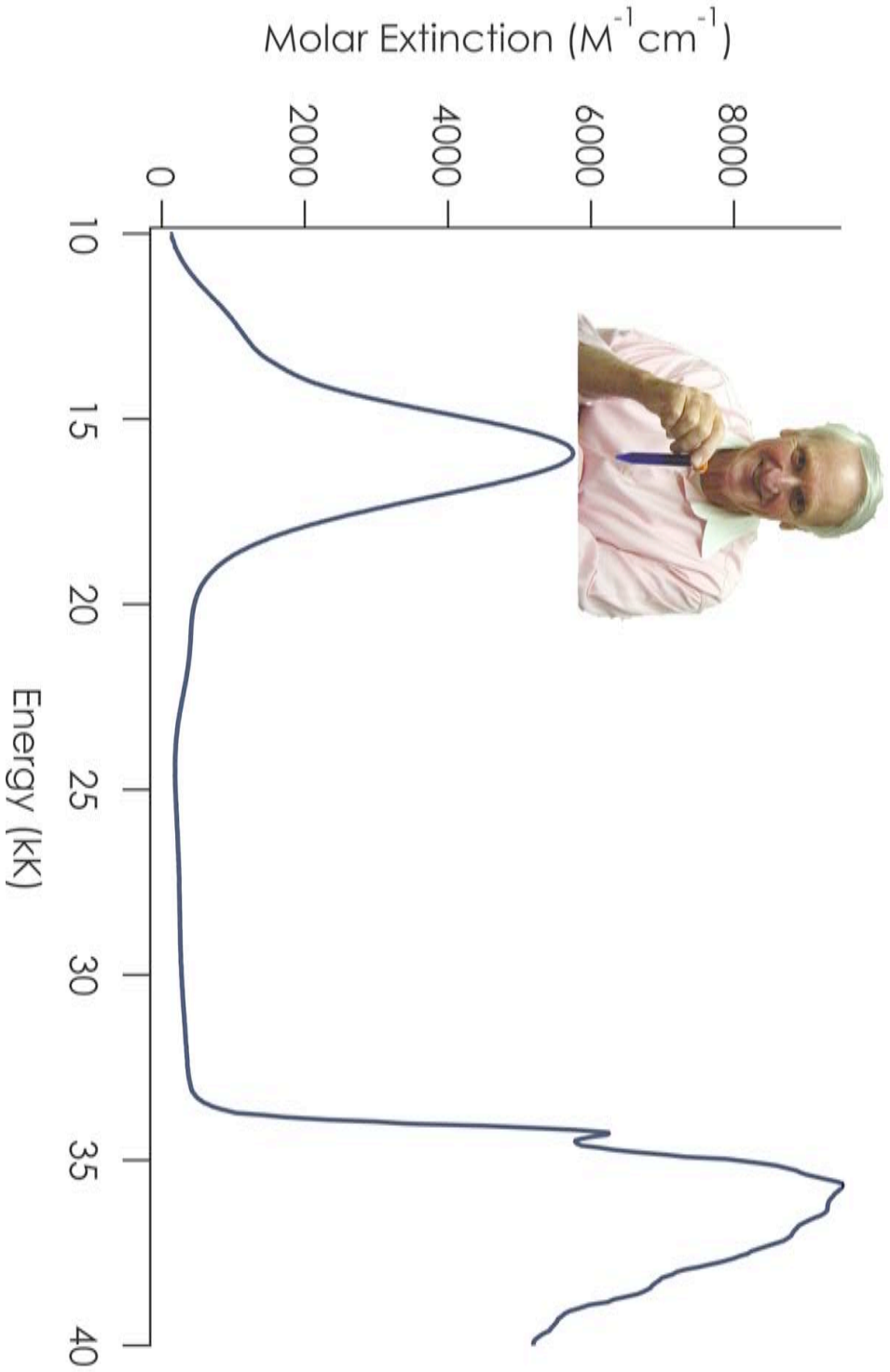
Molar Extinction ($M^{-1}cm^{-1}$)
0
2000
4000
6000
8000
10
15
20
25
30
35
40
Energy (kK)

Figure 1.9. X-band (9.5 GHz) EPR spectrum of *P. aeruginosa* azurin recorded in 77 K aqueous glass (50 mM NaP_i pH 7.0 containing 50% glycerol). Modulation amplitude was 5 G, microwave power was 6.2 mW.

2800
3000
3200
3400
3600
Magnetic Field (Gauß)

Figure 1.10. Principal axes of the magnetic g-tensor of *P. aeruginosa* azurin as determined by single-crystal W-band EPR.[90] The z-axis makes a ~ 15° angle with Cu-S(M121) and the x- and y-axes lie very nearly in the plane of the NNS equatorial triad. Axes are overlaid on the 1.9 Å 3D crystal structure at pH 5.5 (PDBID: 4AZU).

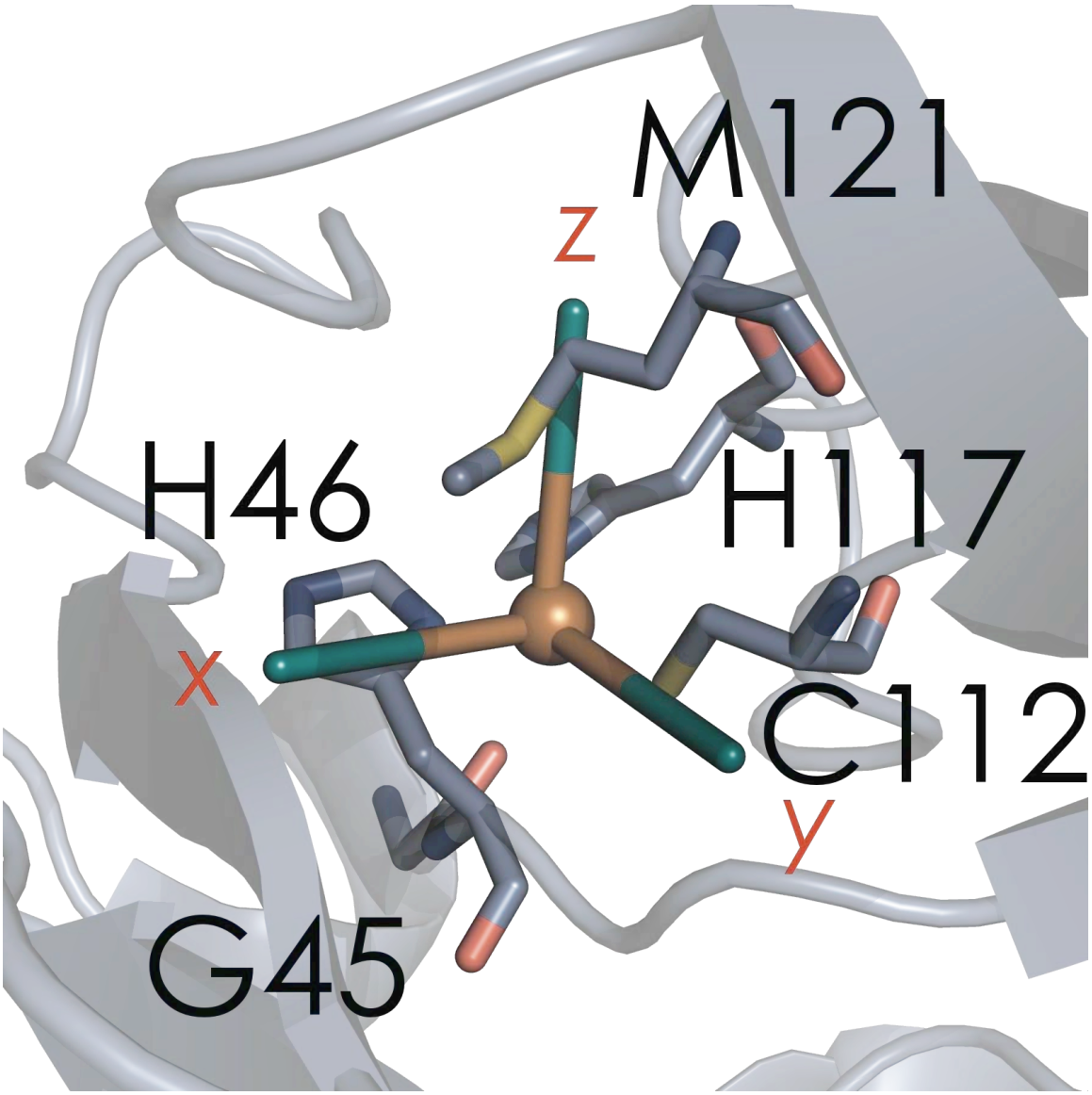
M121
z
H46
H117
x
C112
y
G45

Figure 1.11. 1.9 Å 3D crystal structure of *Pseudomonas aeruginosa* azurin at pH 5.5 (PDBID: 4AZU). Residues comprising the ET-mediating "hydrophobic patch" around H117 are highlighted. The metal binding site is also explicitly modeled for orientational reference. Nitrogen atoms are dark blue, oxygen atoms are red, sulfur atoms are yellow.

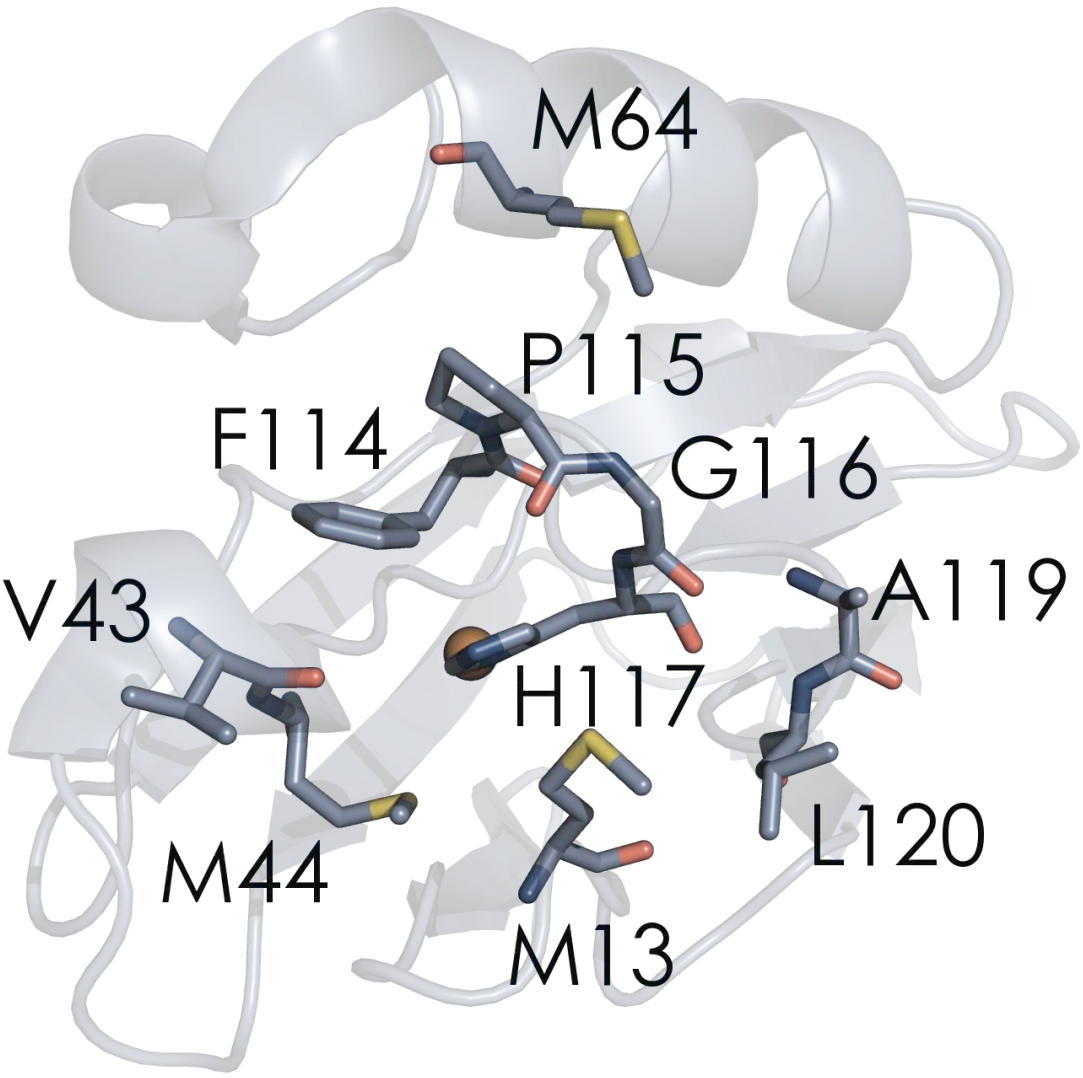
M64
P115
F114
G116
V43
A119
H117
L120
M44
M13

Figure 1.12. 1.9 Å 3D crystal structure of *P. aeruginosa* azurin at pH 5.5 (PDBID: 4AZU). Chains A and C are shown, demonstrating crystallization mediation by the H117 hydrophobic patch. Crystallographically observed water molecules within the interface are modeled as red spheres; these waters have been demonstrated to enhance the coupling between coppers in azurin ESE reactions. The metal binding site is also explicitly modeled for orientational reference. Nitrogen atoms are dark blue, oxygen atoms are red, sulfur atoms are yellow.

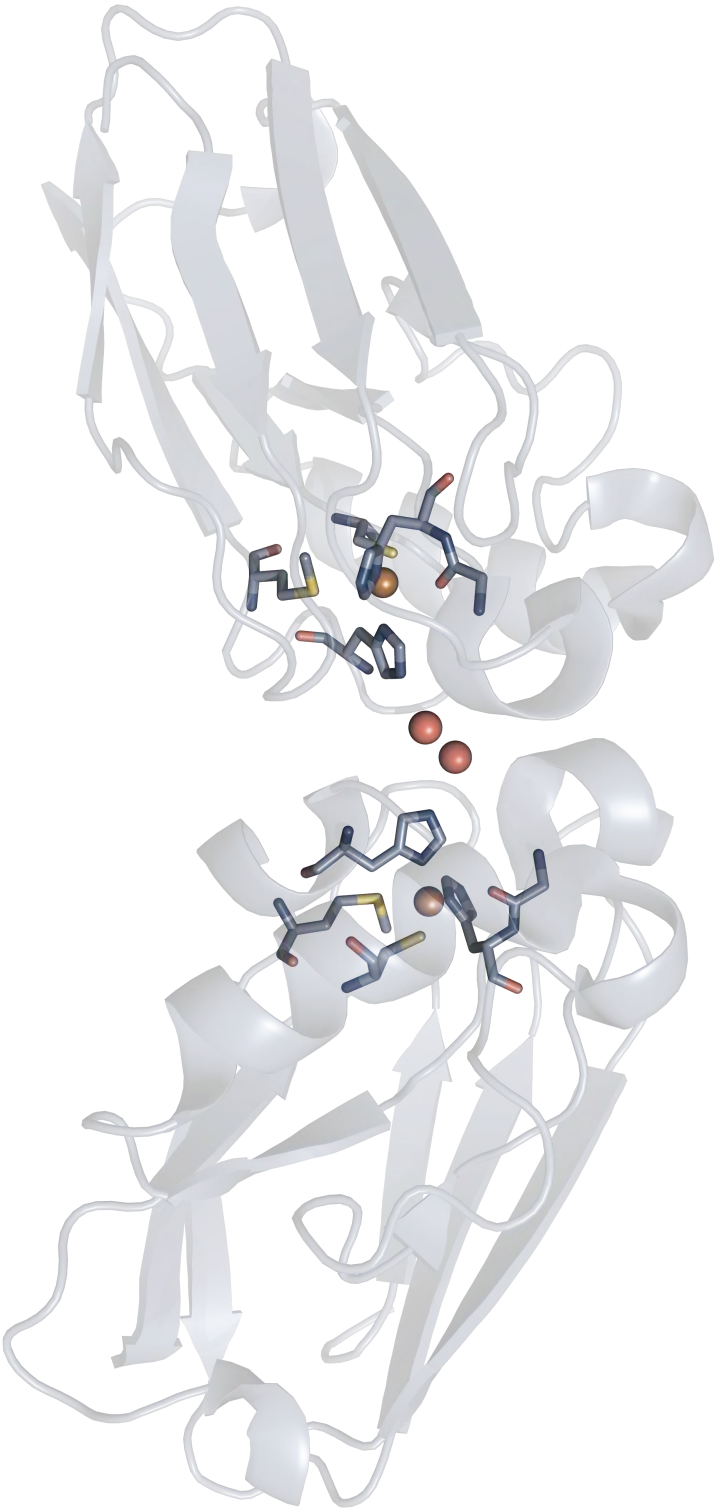

Figure 1.13. Plot of distance-dependence of electron transfer through a ß-strand as demonstrated by activationless tunneling through Ru^{II}-modified azurins. Distances are calculated by the Ru-Cu separation, subtracted by R_o, the close contact distance, which is taken to be 3.0 Å. The plot is fit to a line giving a ß for electron tunneling through a ß-stand of 1.1 $Å^{-1}$. The plot is displayed with a composite of structural models of $Ru(bpy)_2(imH)$-HX (X = 122, 124, 126) azurins generated in Pymol with the 1.9 Å 3D crystal structure of *Pseudomonas aeruginosa* azurin at pH 5.5 (PDBID: 4AZU). The metal binding site is explicitly modeled. Nitrogen atoms are dark blue, oxygen atoms are red, sulfur atoms are yellow. Plot adapted from Reference 194.

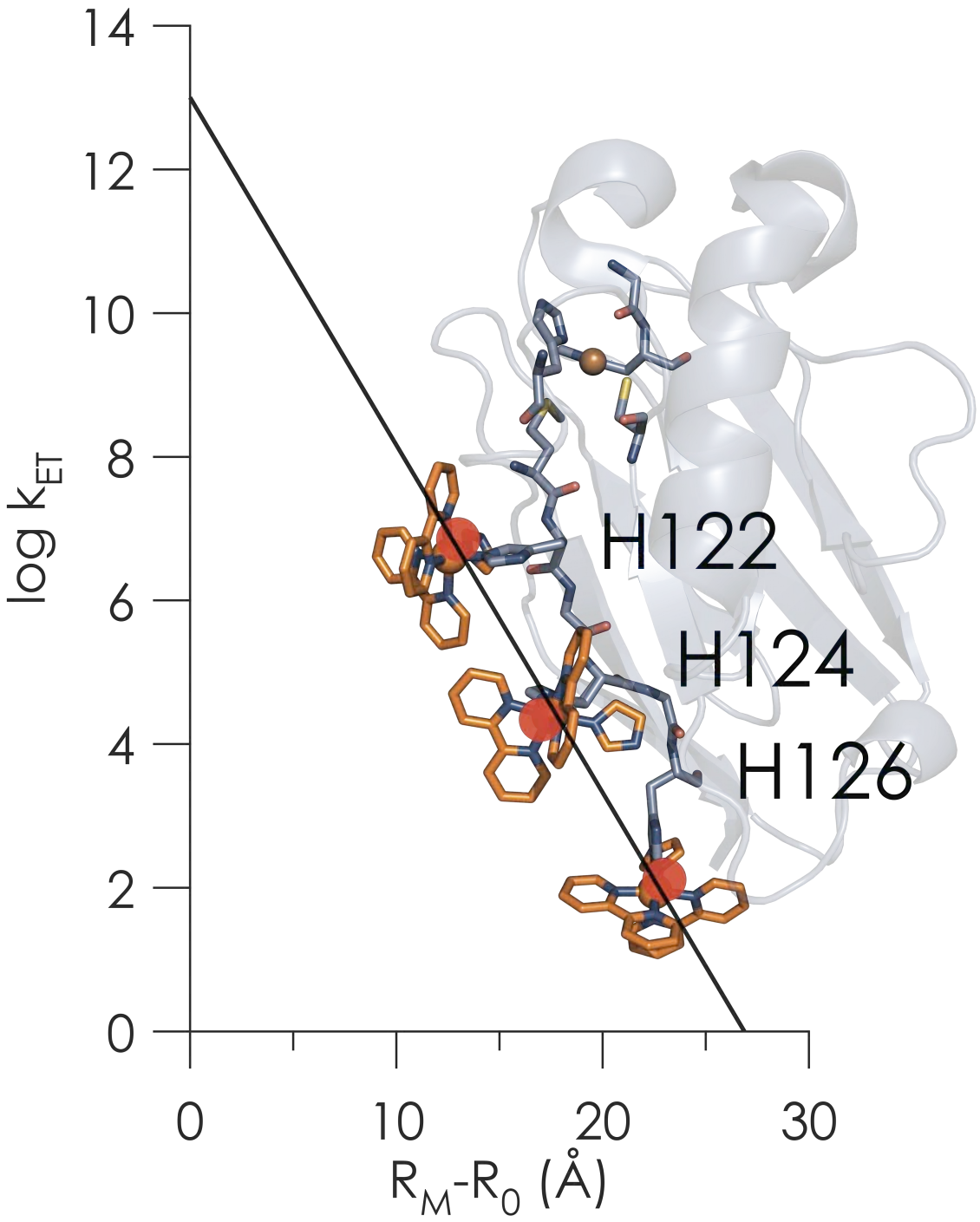
14
12
10
8
6
4
2
0
log k_{ET}
0
10
20
30
R_M-R_0 (Å)
H122
H124
H126

Figure 1.14. 1.9 Å 3D crystal structure of *Pseudomonas aeruginosa* azurin at pH 5.5 (PDBID: 4AZU). LRET pathways from the C3/C26 disulfide to the Cu are highlighted. The "W48 pathway" is indicated in white. The "H46 pathway" is indicated in magenta. Through space and hydrogen bonds marked with red dashed lines. Nitrogen atoms are dark blue, oxygen atoms are red, sulfur atoms are yellow. Figure adapted from Reference 213.

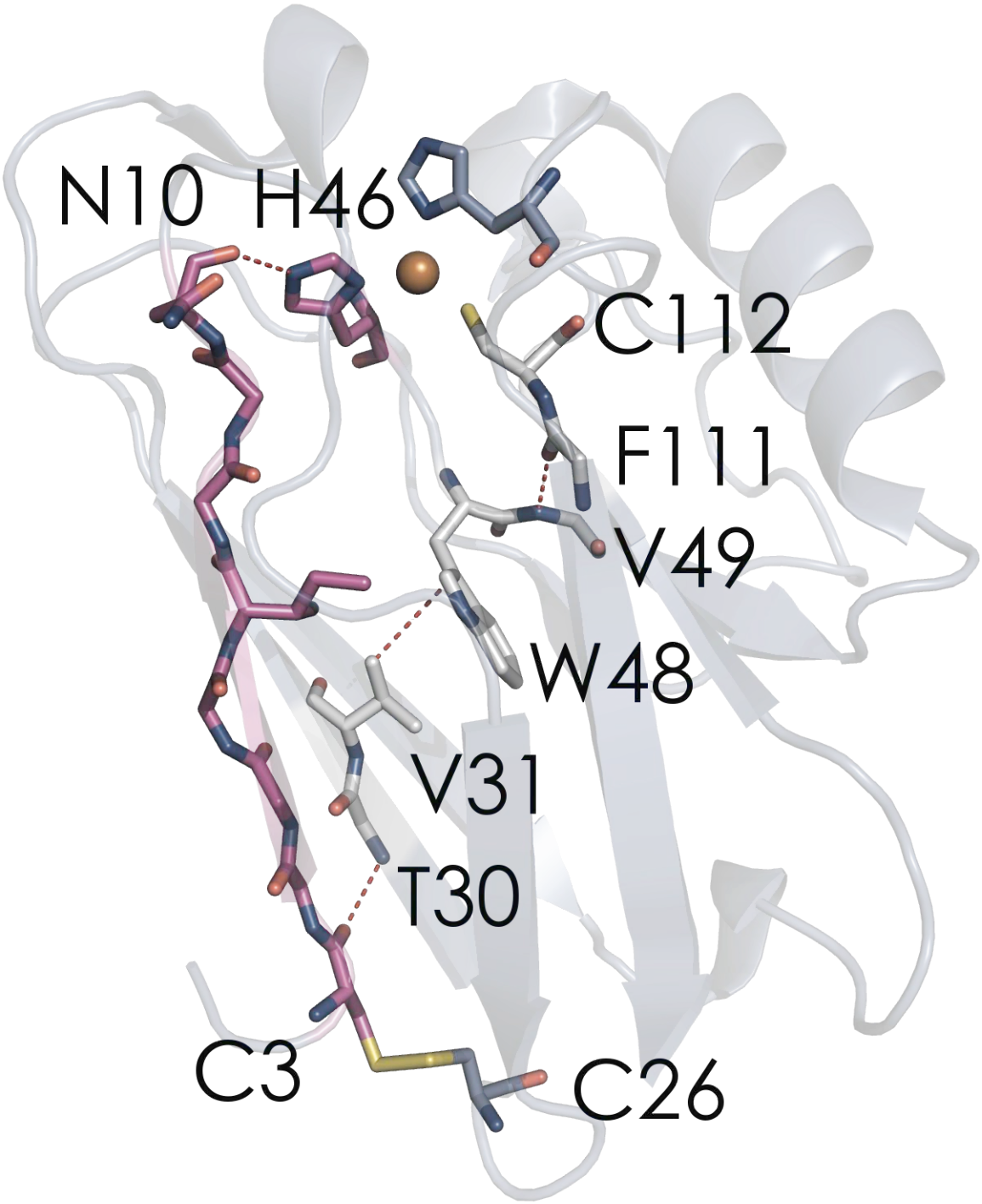
N10
H46
C112
F111
V49
W48
V31
T30
C3
C26

Figure 1.15. 1.5 Å crystal structure of $Re(CO)_3$(4,7-dimethyl-1,10-phenanthroline)(H124) H83N/K122W/T124H azurin (PDBID: 217O). Electron transfer is greatly accelerated through this mutant by "hopping" through the intervening tryptophan. π-stacking interactions between the indole and the phenanthroline rings are thought to enhance coupling between W122 and the Re photosensitizer. Figure adapted from Reference 218. Nitrogen atoms are dark blue, oxygen atoms are red, sulfur atoms are dark yellow, the photosensitizer is visualized in bright yellow.

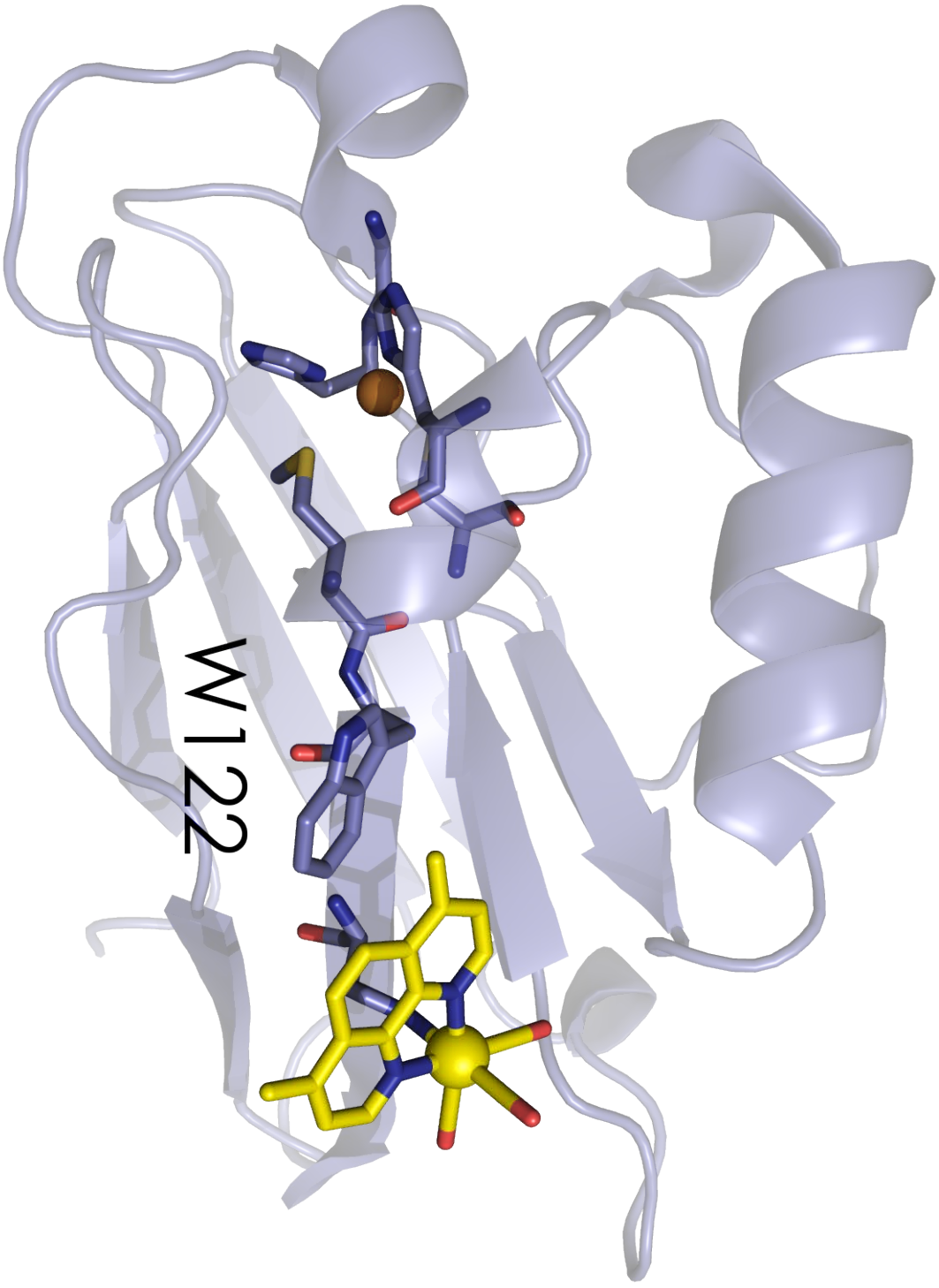
W122

Figure 1.16. 1.65 Å crystal structure of the Cu_A-loop substituted "purple azurin" (in purple, PBDID: 1CC3) overlaid over the pH 5.5 1.9 Å structure of WT *P. aeruginosa* azurin (in periwinkle, PDBID: 4AZU). The tertiary structure of the *P. aeruginosa* azurin is largely unperturbed by the loop subtitution, with an overall C_α RMSD of 0.65 Å. However, "purple azurin" may be reconstituted with 2 Cu atoms, forming the mixed-valence Cu_A site. Cu ligands are highlighted. Nitrogen atoms are dark blue, oxygen atoms are red, sulfur atoms are yellow.


C116
E114
G45
H120
H46
C112
M123

APPENDIX 1-A

Early purifications of azurin started with enormous (~350 L) cultures of *Pseudomonas aeruginosa*. From such grand quantities of this unfriendly organism could be expected pitiful quantities of protein. The purification described in Chapter 5 of this dissertation yields approximately 4 g of azurin from 8 L of relatively non-hazardous *Escherichia coli*. An example of one of the classical preparations is reproduced here from the Gray Nation's classical preparative bioinorganic chemistry text *Barry's Bible*, 2nd Edition. Relevant references for this preparation are:

1) Ambler, R.P. *Biochem. J.* **1963**, *89*, 341.

2) Ambler, R.P.; Brown, L.H. *Biochem. J.* **1967**, *104*, 784.

3) Ambler, R.P.; Wynn, M. *Biochem. J.* **1973**, *131*, 485.

4) Rosen, P.; Pecht, I. *Biochemistry* **1976**, *15*, 775.

Growth of Bacteria

1. Culture medium for *P. aeruginosa*.

   Per liter of culture:

   5.0 g sodium citrate (dihydrate)

   5.0 g $NaNO_3$

   1.0 g KH_2PO_4

   0.5 g $MgSO_4 \cdot 7\ H_2O$

   4.0 g Difco yeast extract

   10 mg $FeCl_3 \cdot 6\ H_2O$

   5 mg $CuSO_4 \cdot 5\ H_2O$

2. A freeze dried culture of *P. aeruginosa* is suspended by adding a few drops of sterile media and transferred to a culture tube containing about 10 mL of media. The tube was incubated at 37 ºC for 24-48 hours without aeration or agitation. Cells were routinely examined using a phase contrast microscope to confirm that they were motile rods typical of *P. aeruginosa*. (Note: No antibiotic resistance selection!)

3. The culture was streaked onto Petri dishes containing MacConkey agar (which suppresses the growth of Gram-positive organisms) and incubated for about 24 hours at 37 ºC under aerobic conditions in order to yield single colonies. The bacteria were stored on MacConkey agar slants in the refrigerator, but tended to lose their viability after only a month.

4. Starter cultures for a fermentor run were prepared by transferring a single bacterial colony into about 20 mL of sterile media and incubating at 37 ºC for about 24 hours. This culture was added to about 3 L of sterile media that was incubated overnight at 30-35 ºC in a water bath. Finally, the 3 L of culture were used to inoculate the 350 L fermentor.

5. Bacteria were grown in the fermentor for approximately 24 hours at 37 ºC without stirring or aeration, and open to room atmosphere pressure. No pressure buildup is allowed. After 24 hours, the pH of the culture was always between 8.0 and 8.5 and monitoring the pH was a convenient qualitative way to follow the growth of these organisms. Starting pH in the fermentor is 6.5. After bacteria have grown to 2 x 10^9 cells/ mL, pH is about 8. The medium may be modified as follows:

a. Increase yeast extract to 7.0 g/L.

b. Add Bacto-Peptone (Difco) 1-2 lbs/350 L.

c. Increase $CuSO_4 \bullet 5\ H_2O$ to 10 mg/L.

6. The contents of the fermentor are spun down using the Sharples centrifuge at a flow rate of approximately 60-90 L/hour. The tan colored cell paste should either be used within 24 hours of harvesting or frozen at -60 ºC for later use.

(The Caltech fermentor was an insulated stainless steel tank that could be sealed and pressurized. It had a working capacity of approximately 350 L with a jacket for steam sterilization, plumbing for temperature control, a sterile aeration system, and an overhead stirring motor with a sealed bearing. An industrial size Sharples centrifuge (type AS26) was used to sediment the contents of the fermentor. Commonly used in the dairy industry as a cream separator, this continous flow centrifuge had a three foot vertical hollow rotor with a maximum speed of 15,000 RPM and could efficiently pellet bacteria at a flow rate up to 100 L/h.)

Preparation of Acetone Powder

1. Small portions of bacterial paste (1 mL volume maximum) are thrown into cold acetone (-10 to -20ºC) with stirring. The acetone is kept cold by addition of powdered dry ice. Use 1 L acetone per 200 g of bacterial paste. Use an overhead mechanical stirrer. Stir for 1-2 hours after the bugs have been added or until the chunks have been broken up.

2. Filter the solids out with Whatman #1 paper in a large Büchner funnel (26 cm diameter) and a 4 L filter flask.

3. Resuspend the solids in a similar volume of cold acetone as before. Stir for about 1 hour. The bacteria should be broken up into a fine powder at this point.

4. Filter out solids using the large Büchner funnel from step 2.

5. Wash the powder in the Büchner funnel with cold acetone (2 L), then with 1 L cold ether.

6. Spread out the powder and allow to air dry.

7. Place the powder in a crystallization dish and then place the dish in a vacuum dessicator. Evacuate the dessicator with a mechanical pump (use two LN_2 traps)

until no volatiles come off. Up to 8 hours of pumping may be required. As much as 50-100 mL of ether, acetone, and water may be removed. Store under vacuum at 4 ºC if desired.

Cytochrome c_{551} and Azurin from P. aeruginosa Acetone Powder

1. Extraction of Azurin and Cytochrome c_{551} from Acetone Powder.

   a. 200 g of acetone powder are ground in a mortar and then suspended in 2 L of 0.1 M ammonium acetate buffer (pH 6.5, preheated to 45 ºC) using a Waring blender operating at the "high" setting. Blend for 1 minute and then let settle for 5-10 minutes. Blend for 1 minute. Repeat this procedure for another 200 g batch of acetone powder. The instructions outlined below are designed for a total of 400 g of acetone powder and should be scaled accordingly.

   b. Stir the thick brown suspension at 5 ºC. When the temperature is below 25 ºC, add 1-2 mg DNAse I in a few mL of buffer. This will reduce the viscosity of the suspension. Stir the mixture in the cold overnight.

   c. Centrifuge to remove solids. First centrifuge for 1 hour at 10,000 RPM using a GSA rotor. This will remove most of the solids. Then completely clear the solution by centrifuging for 1 hour at 20,000 RPM in the SS34 ultracentrifuge rotor. Alternatively, the high speed centrifugation might be avoided by use of a Whatman 3 MM chromatography paper mulch. Cut the paper into small pieces and mulch in a Waring blender with 0.1 M ammonium acetate. Then pack the pump into a large Büchner funnel (26 cm diameter) with a 4 L filter flask and an aspirator. The solution must be clear and free of "mucous" to avoid clogging the columns.

   d. The clear, golden-brown solution is dialyzed against 3 changes of a ten-fold volume exchess of 0.05 M ammonium acetate buffer (pH 4.0) at 5 ºC. Absolute pH of 4.0 at 5 ºC is critical for successful column chromatography.

   e. A white-brown precipitate will form during dialysis. Is is removed by centrifugation at 9000 RPM in the GSA rotor for 30-60 minutes.

   f. 300 mg of $K_3Fe(CN)_6$ are dissolved in a small amount of buffer and added to the supernatant. The pH of the supernatant is checked and adjusted to pH 4.0 at 5 ºC with dilute acetic acid if necessary. Cold distilled water is added to the supernatant to make the conductivity of the solution the same as that of the 0.05 M ammonium acetate (pH 4.0) buffer at 5 ºC.

   g. The resulting solution is loaded onto a 4.0 x 25 cm column of Whatman CM-52 cellulose that has been equilibrated with 0.05 M ammonium acetate (pH 4.0) buffer. Three distinct bands will form: 1) a red band at the top of the column (mostly cytochrome c_5 and cytochrome c_4); 2) a blue band in the center (azurin);

and 3) a faster-moving red band (cytochrome c_{551}). Wash the column with up to 10 L of starting buffer. The three bands will move and spread out slightly.

h. Elute the cytochrome c_{551} with 0.05 M ammonium acetate (pH 4.45 at 5 ºC) buffer. Concentrate using an Amicon YM-5 membrane. Dialyze into buffer of choice, if desired. Freeze in aliquots (-70 ºC).

i. Elute the azurin with 0.05 M ammonium acetate buffer (pH 4.65 at 5 ºC).

j. Elute the cytochrome c_5 and c_4 with higher pH buffer. Concentrate and freeze in aliquots (-75 ºC).

2. Purification of Azurin

a. Dialyze the protein against 0.01 M Tris (pH 8.7 at 5 ºC).

b. Load the protein onto a 1.5 – 2.5 x 20 cm column of DE-52 cellulose (Whatman) that has been equilibrated with 0.01 M Tris (pH 8.7 at 5 ºC). Wash the column with about 1 L of this buffer. Elute with 0.05 M Tris (pH 8.7 at 5 ºC). If this column does not operate properly in the cold, try at room temperature.

c. If the azurin requires further purification (likely), concentrate the azurin to 6 mL or less with YM-5 membrane and pass it over a 2.5 x 80 cm column of Sephadex G-75 that has been equilibrated with 0.01 M Tris buffer (pH 8.7 at 5 ºC).

Approximate yields:

Azurin – 400 mg / 400 g acetone powder

Cytochrome c_{551} – 200 mg / 400 g acetone powder

APPENDIX 1-B

Over 70 crystal structures of various azurins are deposited in the RCSB Protein Data Bank. They are tablulated here in order of their dates of deposition.

Species	Form	Mutations	Resolution (Å)	PDBID
P. aeruginosa	Cu^{II}	-	2.7	1AZU
A. denitrificans	Cu^{II}		1.8	2AZA
P. aeruginosa	Zn^{II}	N47D	2.4	1AZR
P. aeruginosa	Cu^{II}	H35L	1.9	2AZU
P. aeruginosa	Cu^{II}	H35Q	2.1	3AZU
A. denitrificans	Apo		2.2	1AZB
A. denitrificans	Apo		1.8	1AZC
A. denitrificans	Apo		1.8	1AIZ
P. aeruginosa	Cu^{II} pH 5.5		1.9	4AZU
P. aeruginosa	Cu^{II} pH 9		1.9	5AZU
P. aeruginosa	Cu^{II}	F114A	2.6	1AZN
P. aeruginosa	Ni^{II}	W48M	2.2	1NZR
P. aeruginosa	Cu^{II}	I7S	2.2	1ILS
P. aeruginosa	Cu^{II}	F110S	2.3	1ILU
P. aeruginosa	Cu^{II}	M121A	2.2	2TSA
P. aeruginosa	Cu^{II} + Azide	M121A	2.3	2TSB
P. aeruginosa	Co^{II}		1.9	1VLX
A. denitrificans	Cu^{II}	M121Q	1.94	1URI
P. aeruginosa	Cu^{II}	M121E	2.3	1ETJ
P. aeruginosa	Cu^{II}	C112D	2.4	1AG0
P. fluorescens	Apo		2.05	1JOI
P. putida	Cu^{II}		1.92	1NWO
P. putida	Cu^{II}		1.6	1NWP
A. denitrificans	Cu^{II}	M121H	1.89	1A4A
A. denitrificans	Cu^{II}	M121H	1.91	1A4B
A. denitrificans	Cu^{II}	M121H	2.45	1A4C
A. xylosoxidans	Azurin I, Cu^{II}		2.45	1RKR
P. aeruginosa	Cu^{II}, $Ru(bpy)_2(ImH)(H83)$		2.3	1BEX
P. aeruginosa	Cu_A	Loop	1.65	1CC3
A. xylosoxidans	Azurin II, Cu^{I}		1.75	1DZ0
A. xylosoxidans	Azurin II, Cu^{II}		1.75	1DYZ
P. aeruginosa	Cu^{II}	C3A/C26A	2	1EZL
P. aeruginosa	Apo		1.85	1E65
P. aeruginosa	Zn^{II}		2.14	1E67
P. aeruginosa	Cu^{I}		2	1E5Z
Methylomonas sp strain J	Cu^{II} Isomer-2		1.6	1CUO
P. aeruginosa	Cu^{II}, $Re(CO)_3(4,7\text{-dmphen})(H107)$	H83Q, Q107H	1.8	1I53
P. aeruginosa	Cu^{II}, $Ru(bpy)_2(ImH)(H83)$		1.6	1JZE
P. aeruginosa	Cu^{II}, Ru(tpy)(phen)(H83)		1.5	1JZF

P. aeruginosa	Cu^{I}, Ru(tpy)(phen)(H83)		1.7	1JZH
P. aeruginosa	Cu^{II}, $Re(CO)_3$(phen)(H83)		1.62	1JZI
P. aeruginosa	Cu^{II}, $Os(bpy)_2$(ImH)(H83)		1.8	1JZJ
P. aeruginosa	Cu^{II}, Crosslinked at 42 with bis-meleimidomethylether	N42C	2	1JVL
P. aeruginosa	Cu^{II}, Crosslinked at 42 by disulfide	N42C	2.75	1JVO
P. aeruginosa	Cu^{II}	C3S/S100P	1.8	1GR7
P. aeruginosa	Cu^{II}, $Re(CO)_3$(phen)(H107)	All F, Q107H	1.9	1R1C
Methylomonas sp strain J	Cu^{II} Isomer-2		1.9	1UAT
P. aeruginosa	Cu^{II}	D62C/K74C	1.5	1XB3
P. aeruginosa	Cu^{II}	K24R	1.82	1XB6
P. aeruginosa	Zn^{II}	D62C/K74C	2	1XB8
A. xylosoxidans	Azurin II, Cu^{I}		1.13	2CCW
P. aeruginosa	Cu^{II}	Loop Shortened	1.25	2FT6
P. aeruginosa	Cu^{I}, pH 6	Loop Shortened	1.4	2FT7
P. aeruginosa	Cu^{I}, pH 8	Loop Shortened	1.55	2FT8
P. aeruginosa	Cu^{II}	Loop Shortened	1.61	2FTA
P. aeruginosa	Cu^{II}	F114P	1.6	2GHZ
P. aeruginosa	Cu^{I}	F114P	1.7	2GI0
P. aeruginosa	Cu^{II}, $Re(CO)_3$(phen)(H109)	E2Q/H83Q/M109H	1.4	2FNW
A. faecalis	Cu^{II}, Complex with Aromatic Amine Dehydrogenase		2.5	2H3X
A. faecalis	Cu^{II}, Complex with Aromatic Amine Dehydrogenase		2.6	2H47
A. faecalis	Cu^{II}, Complex with Aromatic Amine Dehydrogenase		1.95	2IAA
P. aeruginosa	Cu^{II}, $Re(CO)_3$(phen)(H124)	H38Q/T124H	1.35	2I7S
P. aeruginosa	Cu^{II}	Loop Substitution	1.55	2HX7
P. aeruginosa	Cu^{I}, pH 5	Loop Substitution	1.6	2HX8
P. aeruginosa	Cu^{I}, pH 4	Loop Substitution	1.7	2HX9
P. aeruginosa	Cu^{I}, pH 3.5	Loop Substitution	2.21	2HXA
P. aeruginosa	Zn^{II}, with 1,1'-hexane-1,6-diylbis(1H-imidazole)	H117G	2.83	2IWE
P. aeruginosa	Cu^{II}, $Re(CO)_3$(4,7-dmphen)(H124)	H83N, K122W, T124H, All F	1.5	2I7O
P. aeruginosa	Cu^{II}, Crosslinked at 42 by disulfide	N42C, M64E	2.3	2OJ1
P. aeruginosa	Cu^{II}, Crosslinked at 42 with bis-meleimidomethylether	N42C, M64E	2.25	2IDF
P. aeruginosa	Cu^{II}	Ala Loop	1.05	3FS9
P. aeruginosa	Cu^{I}	Ala Loop	0.98	3FSA
P. aeruginosa	Cu^{II}	Ala Loop	2.3	3FSV
P. aeruginosa	Cu^{II}	Ala Loop	2	3FSW
P. aeruginosa	Cu^{II}	Ala Loop	2	3FSZ

P. aeruginosa	Cu^{I}	Ala Loop	1.8	3FT0
P. aeruginosa	Cu^{II}	F114P/M121Q	2.35	3IN0
P. aeruginosa	Cu^{II}	C112D/M121L	2.1	3FPY
P. aeruginosa	Cu^{II}	C112D/M21I	1.9	3FQ1
P. aeruginosa	Cu^{II}	C112D/M121F	1.91	3FQ2
P. aeruginosa	Cu^{II}	C112D	1.9	3FQY
P. aeruginosa	Cu^{II}	N47S/M121L	2.6	3IN2
P. aeruginosa	Cu^{II}	N47S/M121L	2.1	3JT2
P. aeruginosa	Cu^{II}	N47S/F114N	1.8	3JTB
P. aeruginosa	Cu^{II}, $Re(CO)_3(phen)$(H126)	E2Q/H83Q/T126H/All F	1.45	3IBO

Chapter 2:

REDUCTION POTENTIAL TUNING IN C112D/M121X (X = E, H, OR L) *PSEUDOMONAS AERUGINOSA* AZURIN

INTRODUCTION

Pages and pages later the question may be looming: "Is there really more for azurin?" Again, its electronic structure has been attacked with almost every esoteric spectroscopy imaginable, the ET reactivity has been thoroughly investigated, and pretty soon it might even be the inspiration of cancer therapy. However, azurin's potential application in renewable energy was purposefully (and hopefully conspicuously) omitted. A role for azurin in tackling this important challenge is the subject to which we now turn.

Humanity has benefited from Nature's early adoption of solar energy for over a century.[1] Billions of years worth of solar photons are now going up in smoke as the accumulated biomass from these eons of solar-driven carbon fixation fuel our modern existence. We refer here to photosynthesis, whereby solar energy is used to oxidize water to O_2 via the oxygen-evolving complex of photosystem II, ultimately shuttling electrons quantum-mechanically staggering distances in order to fix CO_2.[2-3] The reduced carbon ultimately goes to the grave with its producer, where given sufficient time humanity can burble it forth to satisfy its addiction to a "lights-on" existence. However Nature is not particularly smart, nor is nature particularly lucky – ages upon ages of rolling the dice and coming up with a winning number has a probabilistically high chance. As such, humans really owe the odds our thanks.

Humans, however, are smart – as such we can fix the game. So we may take inspiration from Nature, but to maintain our standard of living we must improve rather than merely emulate. Photosystem II, for all its efficacy, is a very large protein complex consisting of multiple subunits that are constantly replaced as they incur damage from its highly oxidative task. Proteins that catalyze the opposite reaction are fairly small – the multicopper oxidases (MCOs) are soluble proteins ~ 50 kDa that catalyze the 4 electron reduction of dioxygen to water through the concerted action of type 1, type 2, and binuclear type 3 copper sites.[4] These proteins are fairly robust; so much so that functional electrodes have been built incorporating

these proteins that offer promise for fuel cell applications.[5] Bacterial MCOs such as copper efflux oxidase (CuEO) can be recombinantly expressed and may be modified by site-directed mutagenesis.[6] Archaeal homologues to this protein have been identified; the hyperthermophilic archaeon *Thermus thermophilus HB27* encodes an MCO that has been shown to be highly thermostable (T_m > 95 ºC).[7] The principle of microscopic reversibility dictates that the reverse reaction within a MCO should proceed by the opposite mechanism.[8] Thus, by properly tuning the reduction potentials of CuEO or the *T. thermophilus* laccase, we can oxidize water. Their photosensitization should then be readily achieved by standard methods.[9] So, we can either drive the oxidation of water photochemically or electrochemically given a properly engineered MCO. Copying and ultimately besting photosystem II requires wielding precise control over tranisition metal reduction potentials. For this, we turn to azurin as a testbed.

We know that the $Cu^{II/I}$ reduction potentials of type 1 sites span a wide range, from +200 mV to +1.0 V (or even greater) vs. the normal hydrogen electrode (NHE). This tunability permits type 1 sites to participate in ET at favorable driving forces with many different redox partners. Many factors[10] have been invoked as contributors to this redox potential modulation, including: axial ligation;[11-14] site hydrophobicity;[14-16] outer-sphere coordination (hydrogen bonding);[17] and electrostatics.[18] Lu and coworkers recently demonstrated the additive nature of these effects in their work on a series of *P. aeruginosa* azurin mutants whose reduction potentials span a 600 mV window.[19]

We now report an extension of these studies to "hard-ligand" Cu binding sites. These are defined as sites providing ligation from exclusively N- and O- donors comprising imidazoles, carboxylates, and carbonyls. The "Mizoguchi mutant," C112D azurin, will serve as a scaffold for exploring the effects of amino acid substitutions at M121 on the reduction potential of a type 2 center.[20] Specifically, we investigated the effects on reduction potential of the installation of negatively (M121E) and positively (M121H) charged axial ligands, as well as the effect of abolishing axial ligation and elevating site hydrophobicity (M121L). Characterization of C112D azurin is reproduced and supplemented in order to effect ready comparison to the axial mutants. Initial spectroscopic and electrochemical characterization of the C112D/M121X (X = M, E, H, L) azurins was communicated in *Inorganic Chemistry*: Lancaster,

K.M.; Yokoyama, K.; Richards, J.H.; Winkler, J.R.; Gray, H.B. *Inorg. Chem.* **2009**, *48*, 1278-1280.

MATERIALS AND METHODS

All reagents were used without further purification. 18.2 MΩ Milli-Q water (MQ-H_2O) was used in the preparation of all buffers and solutions.

Site-Directed Mutagenesis

SDM was carried out using the QuikChange™ kit employing *Pyrococcus furiosus* Turbo® DNA Polymerase (Stratagene). Kit instructions were followed to the letter. The Richards synthetic azurin gene on a T7 RNA Polymerase controlled plasmid was used as template DNA.[21] Oligonucleotide primers for site directed mutagenesis were purchased from Operon; HPLC- or PAGE-purity primers were used in all cases. The following oligonucleotides and their reverse complements were used to create

C112D:

5'-GAACAGTACATGTTCTTC**GAT**ACTTTCCCGGGTCACTCC-3';

C112DM121H:

5'-CCCGGGCCACTCCGCGCTG**CAC**AAGGGTACCCTGACCCTGAAG-3';

C112DM121E:

5'-CCCGGGCCACTCCGCGCTG**GAA**AAGGGTACCCTGACCCTGAAG-3';

C112DM121L:

5'-CCCGGGCCACTCCGCGCTG**CTG**AAGGGTACCCTGACCCTGAAG-3';

where bold codons indicate the loci of mutagenesis. PCR products were transformed into Novablue strain *E. coli* (Novagen). Following incubation on plates of Luria Bertani (LB)/agar

containing 100 μg/mL ampicillin, three colonies were selected for overnight growth in 5 mL LB containing 100 μg/mL ampicillin. Plasmid DNA was isolated by miniprep using the Qiaprep kit (Qiagen). DNA was sequenced at the Beckman Institute or by Laragen.

Protein Overexpression and Purification

Plasmids containing the desired C112D/M121X azurin were transformed into BL21(DE3) *E. coli*. Cells were grown on plates of LB/agar containing 100 μg/mL ampicillin overnight (16 hours). Single colonies were picked to inoculate 5 mL Terrific Broth (TB) starter cultures containing 100 μg/mL ampicillin. These cultures were grown at 37° C with shaking until visibly turbid, ~ 4-6 hours. Cultures were pelleted at 3750 x g for 10 minutes. Supernatant was poured off to remove excreted ß-lactamase and 7 mL fresh TB was added per 5 mL starter culture.

Typical overexpression was carried out on the 6 L scale. 2 mL of resuspended starter culture were added to 2 L of TB containing 100 μg/mL ampicillin in 6 L Erlenmeyer flasks. Cells were allowed to grow overnight with shaking at 32° C. In the morning, overexpression was induced by addition of ß-D-isopropylthiogalactopyranoside (IPTG) to 1 mM. Incubation temperature was raised to 37° C and overexpression was allowed to proceed for 6 hours. No Cu^{II} was added to the growth at any stage.

Cells were harvested by repeated 10-minute centrifugations at 3750 x g in 250 mL centrifuge bottles. Protein isolation was effected by osmotic shock. Final cell pellets were thoroughly resuspended in a 20% sucrose solution buffered at pH 8.1 with 300 mM Tris and containing 1 mM ethylenediaminetetraacetic acid (EDTA). Volume was raised to ~ 400 mL divided evenly between two centrifuge bottles. Cells were permitted to osmotically equilibrate in this solution for 45 minutes, at which point the suspensions were spun for 20 minutes at 7500 x g. Supernatant was decanted and pellets were partially resuspended in the residual solution. Bottles were then transferred to an ice bucket. 50 mL of ice-cold MQ-H_2O containing 500 μM $MgCl_2$ were then added quickly to each bottle and pellets thoroughly resuspended. The suspensions were then transferred to one 250 mL beaker containing a magnetic stir bar, covered with Parafilm™, and allowed to stir gently at 4° C for 15 minutes. In some cases

whole cell lysis accompanied periplasmic extrusion; this is evidenced by thickening of the suspension to mucosal consistency. In such cases it was necessary to add 5 mg each of DNase I and RNase A and 200 μL 2 M $MgCl_2$ to digest genomic DNA; complete digestion is achieved upon return to a thin, watery consistency, usually requiring an additional 30 minutes. The suspension is then spun at 20,000 x g in Oak Ridge tubes for 30 minutes. Supernatant is decanted and preserved; this crude extract should be pale-yellow to orange brown.

Crude extract was concentrated to ~20 mL in a 350 mL Amicon concentrator (Millipore) fitted with a YM-10 membrane. Volume was raised to 300 mL with 50 mM Tris pH 7.8 containing 50 mM NaCl. The volume was again reduced to ~20 mL. This material was then loaded on a Q Sepharose FF batch column with a column volume of approximately 150 mL. The batch column was equilibrated with 50 mM Tris pH 7.8 containing 50 mM NaCl. Under these conditions, azurin (apo or metalated) does not adsorb to the column material; anionic impurities, among them some heme-containing material, remain stacked on the column. 50 mL fractions were collected and assayed for azurin by UV/vis; fractions containing the characteristic apo-protein absorption band with the sharply resolved 290 nm peak were pooled. Volume at this point was usually 200-250 mL.

This material was then concentrated in an Amicon to 20 mL. Buffer was changed to 10 mM diethanolamine•Cl (DEA•Cl) at pH 9.0 by HiPrep 26/10 Desalting FPLC column (GE Healthcare). This solution was subsequently loaded onto a HiPrep 26/10 Q FF FPLC (GE Healthcare) column equilibrated with 10 mM DEA•Cl pH 9.0. Protein was eluted by a linear gradient from 0 to 40% 10 mM DEA•Cl pH 9.0 containing 200 mM NaCl over 30 minutes at a flow rate of 5 mL/min. Zn^{II}-azurin begins to elute at a conductivity 3 mS/cm or at roughly 13% buffer B. A second population, apoazurin, elutes at 5-6 mS/cm conductivity, or at ~ 20% buffer B. Apoazurin and Zn-azurin are pooled separately. Purification to homogeneity was achieved by size-exclusion chromatography on a HiLoad 16/60 Superdex 75 FPLC column (GE Healthcare) equilibrated with 50 mM Tris pH 7.5 containing 150 mM NaCl. Protein purity was assessed by SDS-PAGE and identity verified by ESI-MS.

Apoprotein was reconstituted with Co^{II} or Cu^{II} by adding a 100 mM solution of $CoCl_2$ or $CuSO_4$ to apoazurin in 50 mM HEPES pH 7.5. Final metal ion concentration was 1.1-1.2

times the concentration of apoprotein by A_{280} (ε_{280} = 8800 $M^{-1}cm^{-1}$). Protein was then exchanged into desired experimental buffer by PD-10 desalting column to remove excess metal ion.

P. aeruginosa cytochrome c_{551} (cytc_{551}) was expressed recombinantly in dual-transformed *E. coli* BL21(DE3): one plasmid contained the periplasmically-tagged c_{551} gene while a second plasmid bore eight genes to facilitate protein biosynthesis.[22] A 50 mL starter culture in LB medium was incubated with shaking for 24 h at 37 ºC. This culture was harvested, resuspended in TB medium, and added to 6 L TB medium (3x 2 L cultures in 6 L Erlenmeyer flasks). The expression culture was incubated at 37 ºC with shaking for 15 h. Protein was extracted following culture harvesting by osmotic shock (*vide supra*). If harvested pellets are not bright pink, transformation and overexpression must be repeated. Extract was concentrated in an Amicon fitted with a YM-10 membrane and exchanged into 10 mM Tris pH 7.6 by repeated dilution/concentration. The solution was then loaded onto a batch column packed with DEAE Sepharose FF (GE Healthcare); protein was eluted with a stepwise gradient from 10-40 mM Tris. The solution was acidified with glacial acetic acid to pH 4.0 and precipitate isolated by centrifugation. Buffer was then exchanged to 25 mM sodium acetate pH 4.0 by desalting column. The solution was loaded onto a HiLoad 26/10 SP Sepharose HP FPLC column (GE Healthcare) and eluted by pH gradient from 4-7. The protein was determined to be homogeneous by silver-stained PAGE; identity was verified by UV/vis and ESI-MS. Concentrations were determined by UV/vis for Fe^{II} (ε_{520} = 1.73 x 10^4, ε_{551} = 3.0 x 10^4 $M^{-1}cm^{-1}$) and Fe^{III} (ε_{520} = 1.06 x 10^4, ε_{551} = 9.28 x 10^3 $M^{-1}cm^{-1}$) protein.

UV/vis Spectroscopy

UV/vis spectra were recorded on a Hewlett Packard 8453 Diode Array Spectrophotometer fitted with a Peltier for temperature control. Spectra were recorded in 1 cm quartz cells from Starna. Extinction coefficients for Co^{II}- and Cu^{II}- azurin were determined by titration of apoprotein with analytically prepared aqueous solutions of $CoCl_2$ and $CuSO_4$. Titrations were carried out at 298.15 K in 100 mM Tris, pH 7.0. pH dependences of the C112D/M121H and C112D/M121E Cu^{II} UV/vis spectra were recorded by exchange of holoprotein into appropriate buffer.

EPR Spectroscopy

CW X-band (9.5 GHz) EPR spectra were recorded at 77 K on a Bruker EMX Biospin fitted with a liquid nitrogen cold finger. Initial EPRs for characterization were recorded in 10 mM sodium phosphate (NaP_i) pH 7.0. pH-dependent EPRs for C112D/M121H azurin we recorded in Tris pH 7.15 – 9.0. pH-dependent EPRs for C112D/M121E were recorded in 50 mM MES (pH 5.5), 50 mM HEPES (pH 6.0 – pH 8.0), and 50 mM CHES (pH 9.0 – pH 10.0), all containing 50% glycerol to facilitate glassing. Sample concentrations were 1-2 mM.

CW Q-band spectra were measured by Stephen Sproules at MPI – Mülheim using a Bruker ESP-300E spectrometer with a Bruker Q-band cavity (ER5106QT) with Bruker flexline support and an Oxford Instruments helium cryostat (CF935). Microwave frequencies were measured with a Hewlett-Packard frequency counter (HP5352P), and the field control was calibrated with a Bruker NMR field probe (ER035M). Q-band samples were measured at pH 7.0 in 50 mM HEPES containing 50% glycerol Sample concentrations were 1-2 mM. Spectra were simulated in SpinCount.[23]

X-ray Absorption Spectroscopy

Cu K-edge XAS, including EXAFS, were collected at the Stanford Synchrotron Radiation Lightsource (SSRL) at beam line 7-3 under ring conditions of 3 GeV and 200 mA. A Si(220) double-crystal monochromator was used for energy selection and a Rh-coated mirror (set to an energy cutoff of 13 keV) was used for harmonic rejection. Internal energy calibration was performed by assigning the first inflection point of a Cu foil spectrum to 8980.3 eV. Samples were exchanged into appropriate buffer containing 38% glycerol and concentrated to ~ 2mM. Proteins were loaded into 2 mm Delrin (C112D/M121E) or Lucite (C112D/M121H) XAS cells with 38 μM Kapton windows and glassed by rapid immersion in liquid nitrogen. Data were collected in fluorescence mode (using a Canberra Ge 30-element array detector) windowed on the Cu K_α emission line. The sample was maintained at 10 K in an Oxford liquid helium flow cryostat. To minimize photoreduction of Cu^{II}, the incident beam intensity was attenuated by a factor of 3 with a four-layer aluminum Reynolds filter. Data were collected from 8660 to 9380 eV (k = 10 $Å^{-1}$) to reduce collection time and thus photoreduction. Only one scan per 1 mm x 10 mm spot was included in averaging per sample for XANES. Scans were averaged and processed using the MAVE and PROCESS modules of

the EXAFSPAK software package.[24] Splines were optimized using PYSPLINE.[25] EXAFS were modeled using scattering paths calculated by FEFF7[26,27] from structural coordinate derived from molecular modeling starting with the 3D structure of C112D azurin (PDBID: 1AG0). EXAFS were fit using OPT, a component of EXAFSPAK.

Redox Titrations

In a typical experiment, an aliquot of cytc_{551} was reduced by addition of sodium dithionite to 1 mM. This protein was then desalted into the appropriate buffer. To a 1 cm quartz cuvette was added buffer of appropriate pH and c_{551} to ~8 μM. Final solution volume was 2 mL. This solution was titrated with a ~ 500 μM solution of Cu^{II} C112D/M121X azurin in MQ-H_2O. Data were fit in Igor to the following expression:

$$[Fe^{III}] = \frac{1}{2\times(K_{eq}-1)}\times K_{eq}\left(\frac{V_{add}}{V_{add}+V_i}\times\left[Cu^{II}\right]_i+\frac{V_i}{V_{add}+V_i}\times\left[Fe^{II}\right]_i\right)- \left(K_{eq}^2\times\frac{V_{add}}{V_{add}+V_i}\times\left[Cu^{II}\right]_i+\frac{V_i}{V_{add}+V_i}\times\left[Fe^{II}\right]_i\right)^2- 4\times\left(K_{eq}-1\right)\times\left(K_{eq}\times\left(\frac{V_{add}}{V_{add}+V_i}\times\left[Cu^{II}\right]_i\times\frac{V_i}{V_{add}+V_i}\times\left[Fe^{II}\right]_i\right)^{1/2}\right) \quad (2.1)$$

where V_{add} is the volume of Cu^{II} C112D/M121X azurin added, V_i is the initial volume (2 mL), $[Fe^{II}]_i$ is the starting cyt c_{551} concentration, and $[Cu^{II}]_i$ is the concentration of the C112D/M121X azurin. Fe^{III} concentrations were calculated as the difference from the percentage of initial Fe^{II} concentration from the ratio of A_{520} to A_{551} according to Eq. (2.2):

$$\frac{A_{520}}{A_{551}} = 1.1427 + 0.55401(\%Fe^{II}) - 0.065012(\%Fe^{II})^2 \quad (2.2)$$

Azurin reduction potentials were then calculated by the Nernst equation, using pH dependent reduction potentials for cyt c_{551} taken from the literature.[28]

Electrochemistry

Voltammetry on SAM modified monocrystalline Au(111) bead electrodes was conducted primarily by Keiko Yokoyama. Electrodes were formed according to a literature procedure.[29] Electrodes were formed by melting 99.999% Au wire (Alfa Aesar) into spheres in a hydrogen flame. The spheres were heated until bright orange, at which point they were tempered in an aqueous 50% HCl solution. This was repeated three times. The electrodes were then placed in boiling concentrated H_2SO_4 for ~ 2 hours. The electrode is then cleaned by an oxidation-reduction cycle (ORC) in 1 M H_2SO_4 between -0.3 and 1.5 V vs. Ag/AgCl for 20 cycles at a scan rate of 20 mV/s until a well-defined Au(111) voltammogram was obtained.[29] Gold beads that did not achieve this characteristic shape were not used. Electrodes were rinsed with MQ-H_2O, sonicated in MQ-H_2O for 2 minutes, and re-rinsed with MQ-H_2O. Mixed SAMs on the electrodes were prepared by immersing the electrodes in 200 μM tinctures of 1:1 methyl- and hydroxy-terminated alkanethiols. Electrodes were left undisturbed for 3-5 hours in the dark to allow thiolation of the Au. Electrodes were then rinsed with MQ-H_2O and again cleaned by ORC between 0.5 and -0.2 V in 10 mM NaOAc pH 4.6 until a flat CV is achieved. Electrodes failing to produce a flat CV were discarded.

Azurin was adsorbed onto SAM-modified Au electrodes by immersion of the prepared electrodes in 100 μM solutions of protein in 10 mM NaP_i pH 7.0. Electrodes were left in these solutions overnight at 4 ºC. Electrodes were rinsed with MQ-H_2O prior to measurement of CV.

CV or SWV were measured under Ar blanket in an Ar-sparged 10 mM NaP_i pH 7.0 in an H-cell cleaned by immersion in boiling water. The counter electrode was a Pt coil cleaned by treatment with 50 % aqueous HCl solution and H_2 flame. The reference electrode was a saturated Ag/AgCl electrode (0.197 mV vs. NHE). All electrochemical measurements were made with a model 660 Electrochemical Workstation (CH-Instrument, Austin, TX) at room temperature.

X-ray Crystallography

Azurin crystals were grown by modification of a literature method.[20b] Sitting-drop crystallography trays were set up by mixing 3 μL of 10-20 mg/mL azurin in 100 mM sodium

acetate (NaOAc) buffer at pH 5.6 were with 1, 2, or 3 μL of well solutions containing 25 – 30% PEG-4000, 100 mM $LiNO_3$, 20 mM $CuCl_2$, and 100 mM Tris at either pH 7.0 or 8.0. These drops were allowed to equilibrate against 250 μL of well solution at room temperature. Crystals usually appeared within 3 days, growing to final size by approximately one week.

X-ray diffraction data were collected "in-house" at the Caltech Molecular Observatory. Crystals were mounted in 0.4-0.7 mm nylon loops and equilibrated against cryoprotectant solutions consisting of appropriate well solution containing 30% ethylene glycol. Crystals were mounted under an Oxford liquid N_2 cryostream at 100 K. Crystals were diffracted with 1.54 Å Cu K_α X-rays from a rotating anode generator. Images were collected by a Rigaku RX-4000 area detector operated by the CrystalClear software package. Reflections were integrated using MOSFLM;[30] data was scaled and merged with SCALA.[31] Structures were solved by molecular replacement as implemented by the program MOLREP;[32] the previously available structure of C112D azurin (PDBID: 1AG0), reduced to polyalanine, was used as the starting model. Model building was conducted in COOT. Coordinates were refined by maximum likelihood restrained refinement in REFMAC5.[32]

RESULTS

Protein Overexpression and Purification

SDM successfully produced plasmids encoding the gamut of C112D/M121X (X = M, E, H, or L) azurins. DNA sequences are included in Appendix 2-A. In all cases, protein could be overexpressed. Quantities of protein isolated typically saturated the instrument spectrophotometer at both A_{280} and A_{290} during the Q-FF column chromatography step. As this step was an initial, coarse purification, attempts to optimize detection were not undertaken. Chromatograms from this purification step reveal two azurin populations in C112D, C112D/M121E, and C112D/M121L preparations (Figure 2.1). In the case of C112D/M121H there is a shoulder to lower elution volume. Reports from Lundberg of early purification of recombinant wild-type *P. aeruginosa* azurin indicated the concomitant isolation of an un-reconstitutable azurin fraction that later was revealed to be the Zn^{II} derivative.[33] Indeed, the two fractions can be distinguished in their metal-binding affinity, as the later-eluting fraction demonstrates Co^{II} incorporation, while the earlier fraction does not. ESI-MS reveals, in the case of C112D/M121L azurin, that both of these fractions consist of the desired protein (Figure 2.2). Based on the un-reconstitutable fraction presenting lower binding affinity for the positively charged Q FF column, we conclude that in these cases these fractions correspond to Zn-C112D/M121X azurin. Protein is homogeneously pure following size-exclusion chromatography (Figure 2.3) as assessed by SDS-PAGE. Protein identity was confirmed in all cases by ESI-MS (Figure 2.4). The calculated and experimental masses for each protein are as follows: C112D/M121H: 13963 (calc.), 13961.6 (exp.); C112D/M121E: 13955 (calc), 13953.0 (exp.); C112D/M121L: 13939 (calc.), 13937.6 (exp.). Cytochrome c_{551} was also successfully purified to homogeneity (Figure 2.5). The calculated mass for holo-cytc_{551} is 9309, and the experimental value was 9310.2.

Initial Characterization

C112D/M121X (X = E, H, L) each bind a single Cu^{II} or Co^{II} in their active sites as determined by titration of apoprotein with appropriate metal solutions (Figures 2.6-2.8). The

spectra of C112D azurin is included for reference, metal titrations were performed by Mizoguchi. Extinction coefficients were calculated for each spectrum and appear in Table 1. The Cu^{II} spectra at pH 7.0 in 10 mM NaP_i buffer show two absorption systems: at higher energy there is a shoulder ~ 32.3 kK with $\varepsilon \sim 1500\ M^{-1}cm^{-1}$ that has previously been assigned as imidazole N to Cu^{II} LMCT (Figure 2.9).[20] At lower energies each protein has absorption from ligand field transitions.

The Co^{II} spectra indicate 4- or 5-coordinate ligation of the metal by each protein (Figure 10). As intensities for Co^{II} ligand field absorption bands are sensitive to geometry,[33] the C112D/M121X (X = M, L) azurins likely have very similar, tetragonal geometries. Meanwhile, the intensities of the C112D/M121X (X = H, E) proteins likely coordinate Co^{II} in a more tetrahedral manner.

The C112D, C112D/M121E, and C112D/M121H azurins display axial, type 2 Cu EPR spectra in 10 mM NaP_i, pH 7.0 at 77 K (Figure 2.11, Table 2.2).[34] The C112D/M121E spectrum shows some heterogeneity in $g_{||}$; this is resolved when spectra are recorded of glassed samples (*vide infra*). The C112D/M121L azurin EPR spectrum is atypical of type 2 copper; its axial hyperfine splitting ($A_{||}$) is 10.1 mK, which is midway between type 1 and type 2. Moreover, there is anisotropy in $g_{\perp}$, $\Delta g_{xy} = 0.06$ that is resolvable at X-band.

Redox Behavior

The CV of C112D azurin yields a midpoint potential of 180 mV (vs NHE), in agreement with the value reported by Mizoguchi from redox titration with cyt c_{551} (Figure 2.12).[35] Current amplitudes are roughly equal to WT azurin. The CV of C112D/M121E azurin is very weak, suggestive of poor coupling to the electrode. However, square wave voltammetry (SWV) produces far better signal to noise, yielding a potential of 270 ± 10 mV (Figure 2.13). The pH 7.0 redox titration yields a potential of 293 ± 3 mV (Figure 2.14). The CV of C112D/M121H azurin is irreversible, though it indicates a markedly higher potential than the single mutant of ~ 450 mV (Figure 2.15). The solution potential as determined by cytc_{551} titration at pH 7.0 is 305 ± 5 mV (Figure 2.16). CV of C112D/M121L azurin is weaker than C112D, but signal to

noise is high enough to yield a potential of 280 ± 10 mV (Figure 2.17). The solution potential is 281 ± 3 mV (Figure 2.18). These reduction potentials are collected in Table 2.3.

The C112D/M121E azurin $E^{o}_{1/2}$ appeared counterintuitively high considering the additional negative charge to the C112D site, so the potential was determined by redox titrations over the pH range from 5.5 to 10.0 (Figure 2.19). The pH range was chosen to make use of the noncoordinating buffers (MES, HEPES, and CHES) that avoid complications from buffer-driven metal coordination equilibria. Similar ionic strengths were used to minimize medium effects on equilibrium positions.

The unexpectedly high reduction potential of C112D/M121E azurin is maintained across the range pH 6.0 to 7.5. Below pH 6.0 the reduction potential begins to increase (319 ± 5 mV at pH 5.5). From pH 7.5 to 10.0 there is a precipitous drop in reduction potential from 292 ± 9 to 117 ± 1 mV with an apparent pK_a ~ 9. Since the pK_a of the glutamate carboxylate is 4.25,[36] it is unlikely that the dramatic drop arises from a simple on-off ligation effect due to E121 protonation state. Rather, we attribute the rise in potential beginning ~ pH 5.5 to protonation of nonligated E121. The 175 mV drop in potential then likely represents ligation of E121 to Cu^{II}. This explanation for the drop in reduction potential does not come as a surprise given previous work on M121E azurin, which demonstrated vast electronic structural perturbations upon deprotonation of the axial carboxylic acid; the implication being that this event is the sole barrier to axial ligation.[37-41] However, that the reduction potential remains as high as 290 mV in the presence of what should be a Cu^{II}-stabilizing axial carboxylate is puzzling, a subject to which we now turn.

C112D/M121E – Spectroscopic Behavior

The X-band (9.5 GHz) EPR spectrum of a glassed pH 7.0 solution of C112D/M121E azurin recorded at 77 K unveils a cluttered $g_{||}$ region (Figure 2.20a). A spectrum of the same sample recorded at Q-band by Stephen Sproules (34 GHz) separates this absorption into two field-dependent four-line patterns, indicating that the pH 7.0 X-band spectrum arises from a mixture of two Cu^{II} species (Figure 2.20b). This obviates the possibility of attributing the fine structure of the $g_{||}$ region to superhyperfine splitting from the carboxylate proton, thus

supporting ligation-state rather than protonation-state equilibrium modulation of the $Cu^{II/I}$ reduction potential.

X-band EPR spectra were recorded in noncoordinating buffers (MES, HEPES, CHES) across the pH range 5.5 to 10 (Figure 2.21). Spectra corresponding to single species observed at the extrema of this range were simulated using the SPINCOUNT[25] package (Table 2.4, Figure 2.22). Fine structure observed in $g_\perp$ arises from a mixture of Cu $A_\perp$ and $A_{N\perp}$;[42] within the limits of the X-band experiment their contributions cannot be deconvoluted and as such these spectroscopic features were not simulated. The pH 5.5 species has a typical axial type 2 Cu^{II} EPR signature. The pH 10.0 species also possesses a type 2 Cu^{II} spectrum, though it displays anisotropy in $g_\perp$. The axial component of the g-tensor (g_z) decreases from 2.311 ± 0.018 to 2.207 ± 0.047, and there is a substantial (4 mK) increase in axial hyperfine splitting (A_z) at higher pH. The wider hyperfine splitting in the pH 10.0 species is likely attributed to an enlarged orbital dipolar contribution to the hyperfine based on its smaller g_z.

Anisotropy in $g_\perp$ in a D_{4h}-type coordination environment can arise from either lifting of $3d_{xz/yz}$ degeneracy (as would be expected upon geometric distortion) or from mixing of $3d_{z2}$ character into the ground state wavefunction.[43] At pH 5.5, $g_\perp$ is isotropic within the precision of the X-band measurement. However, after accounting for error there is a substantial anisotropy observed upon raising pH to 10.0, with $\Delta g_{x,y} = 0.051$. Without directly observing the energies of the $3d_{x2-y2}$ to $3d_{xz}$ and $3d_{x2-y2}$ to $3d_{yz}$ LF transitions, the origin of this anisotropy is somewhat ambiguous. However, indirect evidence from X-ray diffraction studies suggests $3d_{z2}$ mixing is the operative mechanism (*vide infra*).

The electronic spectrum of C112D/M121E azurin at pH 5.5 displays a weak ($\varepsilon \sim 70\ M^{-1}cm^{-1}$) Cu^{II} LF absorption band at 12.3 kK; this feature blue shifts to 18.9 kK at pH 10 (Figure 2.23). The dramatically stronger LF at pH 10 most likely is attributable to E121 carboxylate coordination to Cu^{II}.

The Cu K-edge XANES of C112D/M121E azurin displays a pH dependence (Figure 2.24). The lowest energy feature is the ~8979 eV Cu 1s to 3d transition.[44] This transition is forbidden in D_{4h}/O_h symmetry (except for some quadrupolar intensity),[45] but can gain

intensity either through mixing of Cu 4p character into the ground state upon distortion to T_d symmetry. The 1s to 3d XANES band of C112D/M121E azurin gains no intensity across the observed pH range; rather, it remains very weak. This indicates minimal perturbation to site symmetry, indicating that 3d orbital energy orderings and by extension degeneracies are likely preserved. However, the transition maximum shifts ~ 0.7 eV or ~6 kK to higher energy as a consequence of elevating the pH, reflecting increased energy of the frontier Cu^{II} 3d orbital. This shift accords with that observed in the visible spectrum (6.6 kK). As the XANES band corresponds to a transition from the Cu^{II} 1s to the frontier, half-filled 3d orbital, the data suggest that the LF band in the visible spectrum corresponds to a transition from the lowest-energy 3d level to the highest, and that the observed energy change in the visible spectrum reflects a perturbation primarily of the frontier 3d level. The observed shifts in g_z in the EPR spectra are consistent with these 3d energy perturbations.

The second feature displaying a pH dependence is a ~ 8987 eV shoulder that has been assigned as a "shakedown" transition.[44,46] This transition arises due to orbital contraction resulting from core vacancies following electron promotion. The energy of this transition has been correlated with covalency; lower energy reflects a more covalent site (*i.e.*, one with less Cu^{II} and more ligand character in the ground state). The transition loses intensity and shifts to lower energy upon a rise in pH from 5.5 to 10.0.

Finally, the edge maximum (8995-9000 eV) also shows a pH dependence, which indicates a structural rearrangement of the copper binding site in more basic solutions. An increase in coordination number upon axial carboxylate ligation logically explains this finding.

C112D/M121E – Structural Studies

The redox and spectroscopic data show that C112D/M121E azurin adopts two conformations between pH 5.5 and 10.0 with a pK_a of approximately pH 9.0. A pH 7.0 C112D/M121E crystal structure (2.1 Å resolution) revealed one of these conformations (Figure 2.25a, Table 2.5). Attempts to determine the structure of the protein at pH 10 resulted in datasets with sub-par refinement statistics (R_{free} = 35.0% at 2.3 Å resolution) owing to disorder in the residue 10-15 loop region. This structure was not deposited in the PDB. A structure was obtained at pH 9.0 (2.25 Å resolution with acceptable refinement statistics; Figure 25b, Table 2.5), however there was again increased disorder as reflected by elevation of the average thermal factors from 34.733 $Å^2$ (pH 7.0) to 43.827 $Å^2$ (pH 9.0).

Increasing the pH from 7.0 to 9.0 triggers a rearrangement of the Cu^{II} binding site (Table 2.6). The closest O_ε(E121)-Cu^{II} distance decreases from 2.67 to 2.24 Å, indicating a bonding interaction at the higher pH. At pH 9.0, the amino nitrogen of H35 is deprotonated, which leads to a peptide bond flip at P36 as H35 changes from a hydrogen-bond donor (to a backbone carbonyl) to a hydrogen-bond acceptor (from a backbone amide proton). This flip transition occurs with a pK_a of 6.2 in WT azurin, whereas in C112D/M121E azurin, the H35 pK_a is elevated, likely due to close proximity to a neutral metal binding site (as opposed to the monocationic site of WT azurin). Thus, at pH 9.0, the H35-P36 hydrogen bonding network is disrupted, but the peptide bond flip is not observed (Figure 2.26). However, H35 is dislocated; this adjustment propagates to H46, which allows the Cu^{II} ion to "sink" towards E121, thus establishing ligation (Figure 2.27). Lengthening of the Cu^{II}-O(G45) distance from 2.62 to 3.24 Å is consistent with this interpretation; the protein is not "loosened" to allow E121 access to the Cu^{II} – rather, the constraint imposed by H46 is relaxed, allowing Cu^{II} access to E121. Concomitant with shortening of the Cu^{II}-O(E121) distance are decreases in Cu^{II}-N(H46/117) distances. These stronger Cu-imidazole interactions likely elevate the $3d_{x2-y2}$ level and thus produce the blue shifted XANES and electronic absorption spectra. This effect is likely a manifestation of Solomon's "coupled distortion" mechanism, whereby increased axial interaction strength in blue copper sites leads to a rotation of $3d_{x2-y2}$, resulting in increased overlap with $S\sigma$ over $S\pi$.[47] In the present case axial ligation may rotate $3d_{x2-y2}$, increasing

overlap with the imidazole N-donors. Such an assertion will require extended spectroscopic and computational validation.

The introduction of E121 as a *bona fide* ligand would definitively lead to overlap between the O 2p/2s orbital's of the carboxylate with the $3d_{z2}$ of Cu^{II}. The ensuing destabilization of $3d_{z2}$ would bring it closer to the frontier $3d_{x2-y2}$ orbital, promoting admixture. Thus the $g_{\perp}$ anisotropy observed in the pH 10.0 EPR spectrum is likely attributable to $3d_{z2}$ mixing into the frontier molecular orbital wavefunction.

C112D/M121H – Spectroscopic Behavior

X-band EPR spectra of C112D/M121H azurin were recorded across the pH range from 7.15 to 9.0 (Figure 2.28, Table 2.7). In all cases the EPR spectra are type 2 and axial (within the resolution limits of X-band). Heterogeneity in g_z is not observed, indicating that within this pH range only one species is present in solution. $A_{||}$ increases with increasing pH, concomitant with decreasing g_z (Figure 2.29). This behavior indicates that the orbital dipolar hyperfine term is responsible for the pH-dependence of $A_{||}$, obviating any contribution from covalency or spin dipolar terms (4p-mixing). The lack of pH effects on $g_{\perp}$ anisotropy combined with absence of spin dipolar effects on $A_{||}$ imply that site geometry is maintained across the pH range.

Excitation energies, however, are perturbed, leading to the decrease in g_z. This was observed by pH-dependent UV/vis (Figure 2.30). The band maximum blue shifts 2.5 kK when the pH is increased from 7.15 to 9.0. The lack of species heterogeneity in the EPR suggests that no change in coordination number occurs within this pH range for C112D/M121H azurin. It is likely that the spectroscopic effects reported thus far occur due to a pH-dependent increase in LF strength of the equatorial ligand set.

C112D/M121H – Structural Studies

Crystals of C112D/M121H were in every case of low quality. Typically clusters of plates formed; plates isolated from these formations diffracted minimally. Occasionally single crystals were produced. In one case a crystal diffracted to ~ 2.4 Å (Figure 2.31). A dataset was collected and the unit cell determined and refined (Table 2.8). However, all attempts to solve the structure by either molecular replacement or isomorphous replacement failed.

EXAFS were recorded as an alternative means to study the active site structure. Two initial XAS scans of C112D/M121H azurin were averaged to produce Cu^{II} K-edge XANES. The white line (E ~ 9 keV) structures of the pH 7.0 C112D/M121E and C112D/M121H azurin XANES are roughly identical; moreover, there is no significant difference in the 8979 1s to 3d features' intensities (Figure 2.32). These data indicate that the axial ligand is at most weakly coordinated and that the C112D/M121H azurin geometry is tetragonal.

8 total XAS scans were recorded out to k = 13.4 $Å^{-1}$ and averaged. A model of the C112D/M121H structure was built from the *A. denitrificans* azurin M121H pH 6.5 3D structure using PyMol (PDBID: 1A4A) (Figure 2.34).[48] Scattering paths were calculated from this model using FEFF7. EXAFS were fit to models of increasing complexity using these paths (Table 2.8, Figure 2.34). The 25% error in coordination number by EXAFS makes quantification of this value troublesome. Best fits are achieved by four inner-sphere N/O scatterers at 1.99 Å, with a fifth N/O at 2.56 Å. This later atom is likely the more distant O of the D112 carboxylate or the G45 carbonyl O; although a nitrogen from the axial imidazole cannot be ruled out as a possibility. Adding 3 C scatterers, corresponding to C_γ of D112 and the imidazole C_ε's, improves the fit slightly, but a fourth C dampens the Debye-Waller factor of this scatterer and fails to improve fitting statistics. Based on the XANES, EXAFS, and EPR data, it would appear that H121 is weakly-coordinated, if at all. The Cu^{II} remains in the plane of the trigonal NNO ligand set.

DISCUSSION

Rack Constraints on Axial Ligand Coordination in C112D/M121X (X = E, H) Azurin

The decrease in the reduction potential of C112D/M121E azurin at elevated pH is, not surprisingly, a consequence of enhanced ligand field strength originating in E121 coordination as well as stronger Cu^{II}-imidazole interactions. That said, the high (~ 300 mV) reduction potential measured between pH 5.5 and 7.5 – even in the presence of a deprotonated axial carboxylate – demands discussion. Previous work on the type 1/1.5 M121H protein[48] implicated protein flexibility as permitting ligation of the engineered axial histidine; in this case ligation was observed to be imidazole protonation state dependent. In short, when it is possible for H121 to ligate Cu^{II}, it will do so. In the present case, the deprotonated E121 is capable of ligating Cu^{II}, but does not. The H35/H46 interaction appears to impose a structural constraint on the protein; thus a rack mechanism is in operation.[2,41] This structural frustration must, as has been proposed time and again for *bona fide* blue copper sites, account for the elevated potential. Though not operating in M121H azurin, rack mechanisms cannot be entirely dismissed in reduction potential tuning of protein-bound copper.

A similar situation has been observed by Solomon and coworkers in *Rhodobacter sphaeroides* nitrite reductase (NiR).[47] In this protein, there is a temperature-dependent transition between a green type 1.5 copper protein and a blue type 1 copper protein. Thermodynamics were invoked to explain this phenomenon: the non-ligation of the axial methionine in this protein is entropically favored at temperatures greater than 215 K; below this temperature the negative enthalpy from methionine ligation dominates, energetically favoring coordination and thus forming type 1.5 copper. No such transition has been reported for azurin; here Solomon invokes rack effects – the methionine is constrained from interaction with the copper. The mechanism of C112D/M121E azurin's electronic structural transition may be operative – the H35/H46 interaction prevents the Cu site from distorting, allowing methionine coordination.

This then begs the question: why does H121 not coordinate in the Mizoguchi site architecture? Imidazole ligation should be substantially favored enthalpically over E121 coordination. Coulombic contributions could favor E121 coordination over H121. More

likely, however, torsional constraints prevent the coordination of H121. However, without 3D structural characterization, arguments remain speculative. The unavailability of a crystal structure of this protein precludes further discussion. Nevertheless, its elevated reduction potential is likely attributable to rack effects in addition to the presence of a positively-charged sidechain. A pH dependence study of the reduction potentials of C112D/M121H azurin will likely demonstrate this effect. Such a study has been left as an exercise.

The Anomalous EPR Spectrum of C112D/M121L Azurin

Detailed study of the C112D/M121L mutant, beyond its initial characterization, has been intentionally omitted here. Its redox behavior seemed initially intuitive, given the introduction of elevated hydrophobicity in the active site.[13] However, its EPR spectrum brings it well outside of the type 2 fingerprint region.[34] More extensive electronic and molecular structural perturbations are at work with this variant. These effects shall occupy attention for the remainder of this dissertation.

REFERENCES

1) Gray, H.B. Powering the Planet with Solar Fuel. *Nat. Chem.* **2009**, *1*, 7.
2) Ferreira, K.N.; Iverseon, T.M.; Maghlaoui, K.; Barber, J. *Science* **2004**, *303*, 1831-1838.
3) Barber, J. *Chem. Soc. Rev.* **2009**, *38*, 185-196.
4) Solomon, E.I.; Sundaram, U.M.; Machonkin, T.E. *Chem. Rev.* **1996**, *96*, 2563-2606.
5) Lee, C.-W.; Gray, H.B.; Anson, F.C.; Malmström, B.G. *J. Electroanal. Chem.* **1984**, *172*, 289-300.
6) Roberts, S.A.; Weichsel, A.; Grass, G.; Thalaki, K.; Hazzard, J.T.; Tollin, G.; Rensing, C.; Montfort, W.R. *Proc. Natl. Acad. Sci. U.S.A.* **2002**, *99*, 2766-2771.
7) Miyazaki, K. *Extremophiles* **2005**, *9*, 415-425.
8) Tolman, R.C. *The Principles of Statistical Mechanics*, Oxford University Press: London, **1938**.
9) Hilhorts, R.; Laana, C.; Veeger, C. *Proc. Natl. Acad. Sci. U.S.A.* **1982**, *79*, 3927-3930.
10) Li, H.; Webb, S.P.; Ivanic, J.; Jensen, J.H. *J. Am. Chem. Soc.* **2004**, *126*, 8010-8019.
11) Pascher, T.; Karlsson, B.G.; Nordling, M.; Malmström, B.G.; Vänngård, T. *Eur. J. Biochem.* **1993**, *212*, 289-296.
12) Hall, J.F.; Kanbi, L.D.; Strange, R.W.; Hasnain, S.S. *Biochemistry* **1999**, *38*, 12675-12680.
13) Berry, S.M.; Ralle, M.; Low, D.W.; Blackburn, N.J.; Lu, Y. *J. Am. Chem. Soc.* **2003**, *125*, 8760-8768.
14) Garner, D.K.; Vaughan, M.D.; Hwang, H.J.; Savelieff, M.G.; Berry, S.M.; Honek, J.F.; Lu, Y. *J. Am. Chem. Soc.* **2006**, *128*, 15608-15617.
15) Donaire, A.; Jiménez, B.; Moratal, J.-M.; Hall, J.F.; Hasnain, S.S. *Biochemistry* **2001**, *40*, 837-846.
16) Donaire, A.; Jiménez, B.; Fernández, C.O.; Pierattelli, R.; Niizeki, T.; Moratal, J.-M.; Hall, J.F.; Takamitsu, K.; Hasnain, S.S.; Vila, A.J. *J. Am. Chem. Soc.* **2002**, *124*, 13698-13708.
17) Yanagisawa, S.; Banfield, M.J.; Dennison, C. *Biochemistry* **2006**, *45*, 8812-8822.
18) Battistuzzi, G.; Borsari, M.; Loschi, L.; Menziani, M.C.; De Rienzo, F.; Sola, M. *Biochemistry* **2001**, *40*, 6422-6430.
19) Marshall, N.M.; Garner, D.K.; Wilson, T.D.; Gao, Y.-G.; Robinson, H.; Nilges, M.J.; Lu, Y. *Nature* **2009**, *462*, 113-116.
20) a) Mizoguchi, T.J.; Di Bilio, A.J.; Gray, H.B.; Richards, J.H. *J. Am. Chem. Soc.* **1992**, *114*, 10076-10078. b) Faham, S.; Mizoguchi, T.J.; Adman, E.T.; Gray, H.B.; Richards, J.H.; Rees, D.C. *J. Biol. Inorg. Chem.* **1997**, *2*, 464-469.
21) Chang, T.K.; Iverson, S.A.; Rodrigues, C.G.; Kiser, C.N.; Lew, A.Y.; Germanas, J.P.; Richards, J.H. *Proc. Natl. Acad. Sci. U.S.A.* **1991**, *88*, 1325-1329.
22) Russell, B.S.; Zhong, L.; Bigotti, M.G.; Cutruzzolà, F.; Bren, K.L. *J. Biol. Inorg. Chem.* **2003**, *8*, 156-166.
23) Golombek, A.P.; Hendrich, M.P. *J. Magn. Reson.* **2003**, *165*, 33-48.
24) George, G.N. *EXAFSPAK.* (Stanford Synchrotron Radiation Laboratory, Stanford Linear Accelerator Center, Stanford University: Stanford, CA).
25) Tenderholt, A. *PySpline.* (Stanford Synchrotron Radiation Laboratory, Stanford Linear Accelerator Center, Stanford University: Stanford, CA).
26) DeLeon, J.M.; Rehr, J.J.; Zabinsky, S.I.; Albers, R.C. *Phys. Rev. B* **1991**, *44*, 4146-4156.
27) Rehr, J.J.; DeLeon, J.M.; Zabinsky, S.I.; Albers, R.C. *J. Am. Chem. Soc.* **1991**, *113*, 5135-5140.
28) Moore, G.R.; Pettigrew, G.W.; Pitt, R.C.; Williams, R.J.P. *Biochim. Biophys. Acta* **1980**, *590*, 261-271.
29) Tanimura, R.; Hill, M.G.; Margoliash, E.; Niki, K.; Ohno, H.; Gray, H.B. *Electrochem. Solid-State Lett.* **2002**, *5*, E67-E70.
30) Leslie, A.G.W. *Joint CCP4 + ESF-EAMCB Newsletter on Protein Crystallography* **1992** *26*.
31) CCP4 *Acta Crystallogr., Sect D: Biol. Crystallogr.* **1994**, *50*, 760-763.
32) Murshudov, G.N.; Vagin, A.A.; Dodson, E.J. *Acta Crystallogr., Sect D: Biol. Crystallogr.* **1997**, *53*, 240-255.
33) Karlsson, B.G.; Pascher, T.; Nordling, M.; Arvidsson, R.H.A.; Lundberg, L.G. *FEBS Lett.* **1989**, *246*, 211-217.Cotton and Wilkinson Co spectra
34) Peisach, J.; Blumberg, W.E. *Arch. Biochem. Biophys.* **1974**, *165*, 691-708.
35) Mizoguchi, T.J. Ph.D. Thesis, California Institute of Technology, **1996**.
36) Nelson, D.L.; Cox, M.M. *Lehninger Principles of Biochemistry*, 3rd ed.; Worth: New York, **2003**.

37) Di Bilio, A.J.; Chang, T.K.; Malmström, B.G.; Gray, H.B.; Karlsson, B.G.; Nordling, M.; Pascher, T.; Lundberg, L.G. *Inorg. Chim. Acta* **1992**, 145-148.
38) Andrew, C.R.; Yeom, H.; Valentine, J.S.; Karlsson, B.G.; Bonander, N.; van Pouderoyen, G.; Canters, G.W.; Loehr, T.M.; Sanders-Loehr, J. *J. Am. Chem. Soc.* **1994**, *116*, 11489-11498.
39) Strange, R.W.; Murphy, L.M.; Karlsson, B.G.; Reinhammar, B.; Hasnain, S.S. *Biochemistry* **1996**, *50*, 16391-16398.
40) Karlsson, B.G.; Tsai, L-C.; Nar, H.; Sanders-Loehr, J.; Bonander, N.; Langer, V.; Sjölin, L. *Biochemistry* **1997**, *36*, 4089-4095.
41) Webb, M.A.; Kiser, C.N.; Richards, J.H.; Di Bilio, A.J.; Gray, H.B.; Winkler, J.R.; Loppnow, G.R. *J. Phys. Chem. B* **2000**, *104*, 10915-10920.
42) Antholine, W.E.; Hanna, P.M.; McMillin, D.R. *Biophys. J.* **1993**, *64*, 267-272.
43) Gewirth, A.A.; Cohen, S.L.; Schugar, H.J.; Solomon, E.I. *Inorg. Chem.* **1987**, *26*, 1133-1146.
44) Shadle, S.E.; Penner-Hahn, J.E.; Schugar, H.J.; Hedman, B.; Hodgson, K.O.; Solomon, E.I. *J. Am. Chem. Soc.* **1993**, *115*, 767-776.
45) Hahn, J.E.; Scott, R.A.; Hodgson, K.O.; Doniach, S.; Desjardins, S.R.; Solomon, E.I. *Chem. Phys. Lett.* **1982**, *88*, 595-598.
46) DeBeer, S.; Kiser, C.N.; Mines, G.A.; Richards, J.H.; Gray, H.B.; Solomon, E.I.; Hedman, B.; Hodgson, K.O. *Inorg. Chem.* **1999**, *38*, 433-438.
47) Ghosh, S.; Xie, X.; Dey, A.; Sun, Y.; Scholes, C.P.; Solomon, E.I. *Proc. Natl. Acad. Sci. U.S.A.* **2009**, *106*, 4969-4974.
48) Messerschmidt, A.; Prade, L.; Kroes, S.J.; Sanders-Loehr, J.; Huber, R.; Canters, G.W. *Proc. Natl. Acad. Sci. U.S.A.* **1998**, *95*, 3443-3448.

Table 2.1. Electronic absorption spectroscopic features of Cu^{II} and Co^{II} C112D/M121X (X = M, E, H, L) azurins in 10 mM NaP_i at pH 7.0. Error in band maxima are on the order of 0.1 kK. Parenthetical values represent molar extinction coefficients in units of $M^{-1}cm^{-1}$ determined by triplicate titration of apoazurin with $CuSO_4$ or $CoCl_2$. These values are correct to within 5% uncertainty. The abbreviation sh signifies that this band is visible as a shoulder.

X	CuII LF λ_{max} (kK)	CuII LMCT λ (kK)	CoII LF λ_{max} (kK)
M	13.26 (100)	32.26 (1950)	19.31 (210), 17.86 (330), 16.39 (280), 15.87 (650,sh)
E	11.43 (70)	32.26 (1250)	17.57 (270), 18.83 (330), 16.67 (330)
H	15.22 (70)	32.26 (560)	18.21 (210,sh), 17.33 (240), 16.45 (280), 15.87 (170)
L	12.53 (100)	32.26 (1650)	19.27 (170), 17.89 (170), 16.42 (220), 15.92 (170, sh)

Table 2.2. Principal components of spin Hamiltonian g-tensor and ^{63,65}Cu (I = 3/2, 100% abundance) magnetic hyperfine tensor (A, mK[a]) derived from SpinCount[23] simulations of 77 K frozen solution X-band (9.5 GHz) EPR spectra of C112D/M121X azurins. Linewidths were modeled by strain parameters, σ_g and σ_A; these are indicated by parenthetical values alongside their corresponding parameters.

X	g_x	g_y	g_z	$A_\perp$	$A_{\|\|}$
M	2.05 (1)	2.05 (1)	2.31 (1)	.158 (4)	15.1 (1)
E	2.06 (3)	2.070 (1)	2.32 (3)	.215 (1)	15.1 (1)
H	2.06 (2)	2.06 (5)	2.30 (3)	.4 (2)	16.5 (1)
L	2.05 (1)	2.11 (1)	2.39 (1)	1.507 (3)	10.1 (1)

Table 2.3. Reduction potentials of C112D/M121X azurins (mV vs NHE) at pH 7.0 as measured by SAM-mediated electrochemistry or in solution by redox titration.

X	SAM	Solution
M	180	180
E	270	289
H	450	305
L	280	281

Table 2.4. Principal components of spin Hamiltonian g-tensor and ^{63,65}Cu (I = 3/2, 100% abundance) magnetic hyperfine tensor (A, mK[a]) Derived from SpinCount[23] simulations of 77 K aqueous glass X-band (9.5 GHz) EPR spectra of C112D/M121E azurin at pH 5.5 and 10.0. Linewidths were modeled entirely by strain parameters, σ_g and σ_A. Base simulation linewidth was set to 5 G in keeping with a 5 G modulation amplitude used in the experiment.

pH	g_x	g_y	g_z	σg_x	σg_y	σg_z	A_z(mK)	σA_z(mK)
5.5	2.067	2.067	2.312	0.017	0.017	0.019	15.8	0.1
10	2.027	2.078	2.212	0.017	0.024	0.038	19.8	0.5

Table 2.5. Solution potentials of $Cu^{II/I}$ couple in C112D/M121E azurin determined by redox titration with cytc_{551} between pH 5.5 and 10.0. Errors represent one standard deviation of 3 titrations.

pH	E^o
5.5	319 ± 5
6	299 ± 4
6.5	298 ± 7
7	293 ± 3
7.5	279 ± 1
8	258 ± 3
8.6	213 ± 1
9	190 ± 1
9.5	158 ± 2
10	117 ± 1

Table 2.6. Crystallographic data collection statistics for C112D/M121E azurin at pH 7.0 and 9.0.

	pH 7.0	pH 9.0
PDBID	3NP3	3NP4
Space Group	C 2 2 2_1	C 2 2 2_1
A	48.86	48.41
B	54.24	55.03
C	94.23	94.58
α	90°	90°
ß	90°	90°
γ	90°	90°
Resolution	19.28-2.10 Å	33.93-2.25 Å
Reflections	7238 (534)	5614 (404)
Completeness	99.9% (99.8%)	94.1% (89.8%)
Multiplicity	4.9 (5.0)	3.3 (3.3)
I/sigmaI	6.4 (2.1)	8.7 (5.7)
Rwork	21.4% (23.8%)	21.6% (21.7%)
Rfree	26.5% (27.1%)	27.6% (22.5%)
e.s.u. (work)	0.174 Å	0.218 Å
e.s.u. (free)	0.216 Å	0.278 Å
$B_{average}$	34.733 Å^2	43.827 Å^2

Table 2.6. Heteroatom distances to Cu^{II} (Å) in pH 7.0 and 9.0 C112D/M121E azurin structures.

	pH 7.0	**pH 9.0**
O(G45)	2.62	3.24
N(H46)	1.96	1.76
$O_{\varepsilon 1}$(D112)	1.73	1.72
$O_{\varepsilon 2}$(D112)	3.25	3.55
N(H117)	2.06	1.99
$O_{\varepsilon 1}$(E121)	2.67	2.24
$O_{\varepsilon 2}$(E121)	3.94	3.37

Table 2.8. Principal components of spin Hamiltonian g-tensor and ^{63,65}Cu (I = 3/2, 100% abundance) magnetic hyperfine tensor (A, mK[a]) of C112D/M121H azurin from pH 7.2 to 9.0. Derived from SpinCount[23] simulations of 77 K aqueous glass X-band (9.5 GHz) EPR spectra. Linewidths were modeled entirely by the g-strain parameters, σ_g. A-strain was not included in the simulations. Base simulation linewidth was set to 6 G in keeping with a 5 G modulation amplitude used in the experiment.

pH	gx	gy	gz	σgx	σgy	σgz	Ax,y(mK)	Az(mK)
7.2	2.0618	2.062	2.295	0.0258	0.03	0.03	0.1	16.63
7.5	2.058	2.058	2.272	0.021	0.021	0.024	0.2	17.45
7.8	2.058	2.058	2.269	0.02	0.02	0.02	0.1	17.67
8	2.057	2.057	2.258	0.02	0.02	0.02	0.1	18.27
8.5	2.055	2.055	2.246	0.02	0.02	0.02	0.1	19.13
9	2.054	2.045	2.241	0.02	0.02	0.01	0.1	19.17

Figure 2.9. Unit cell parameters for the one diffraction-quality C112D/M121H azurin crystal.

Space Group	P 4_2 2_1 2_2
A	69.9821
B	69.9821
C	169.4228
α	90°
ß	90°
γ	90°

Table 2.10. C112D/M121H Cu^{II} K-edge EXAFS simulations. EXAFS were fit in OPT[24] using paths calculated by FEFF7[26-27]. Coordination numbers (CN) were held constant while distances (R) and Debye-Waller factors (σ^2) were allowed to float. Error in distances are estimated to be 0.02-0.03 Å and 25% for coordination numbers. Fits were performed over the entire (0 to 6.0 Å) Fourier transform window. Goodness of fit is measured by F, defined as $[(\sum_i^n [k_i^3(\mathrm{EXAFS_{obs}} - \mathrm{EXAFS_{calc}})_i])^2 / n]^{1/2}$. F could be dramatically improved by data smoothing, but only fits to raw data are reported.

Fit Number	Path	CN	R(Å)	s2	F
1	Cu to N/O	3	1.986	0.00204	0.53
2	Cu to N/O	4	1.986	0.00338	0.49
3	Cu to N/O	5	1.985	0.00458	0.49
4	Cu to N/O	2	1.9819	0.00046	0.6
	Cu to N/O	2	2.514	0.01227	
5	Cu to N/O	3	1.985	0.00204	0.52
	Cu to N/O	1	2.549	0.0058	
6	Cu to N/O	4	1.984	0.00337	0.48
	Cu to N/O	1	2.548	0.00483	
7	Cu to N/O	4	1.986	0.00341	0.46
	Cu to N/O	1	2.559	0.00418	
	Cu to C	2	3.0014	0.00439	
8	Cu to N/O	4	1.987	0.00341	0.46
	Cu to N/O	1	2.557	0.00418	
	Cu to C	3	2.998	0.00439	
9	Cu to N/O	4	1.987	0.00341	0.46
	Cu to N/O	1	2.557	0.00546	
	Cu to C	4	2.998	0.00636	
10	Cu to N/O	4	1.987	0.00337	0.45
	Cu to N/O	1	2.557	0.0062	
	Cu to C	3	2.998	0.00597	
	Cu to C	2	3.31	0.00346	
11	Cu to N/O	4	1.985	0.00338	0.46
	Cu to N/O	1	2.542	0.00594	
	Cu to C	3	2.996	0.00555	
	Cu to C	3	3.317	0.00663	
12	Cu to N/O	4	1.984	0.00334	0.43
	Cu to N/O	1	2.539	0.00694	
	Cu to C	3	2.987	0.00653	
	Cu to C	2	3.311	0.00231	
	Cu to N/O	3	4.19	0.0014	
13	Cu to N/O	4	1.988	0.00343	0.42
	Cu to N/O	1	2.557	0.00414	
	Cu to C	3	3	0.00413	
	Cu to C	4	3.914	0.00254	
	Cu to N/O	6	4.25	0.00922	

Figure 2.1. FPLC chromatograms from the purification of C112D/M121X (X = E: a; H: b; L: c) azurin with HiPrep Q FF 16/10 column. In all cases the protein was in 10 mM DEA•Cl pH 9.0 buffer and loaded onto the column equilibrated with this buffer. Protein was run against a gradient from 0 to 40% 10 mM DEA•Cl containing 200 mM salt over 30 minutes at a flow rate of 5 mL/minute. Bands corresponding to apoazurin are marked with asterisks.

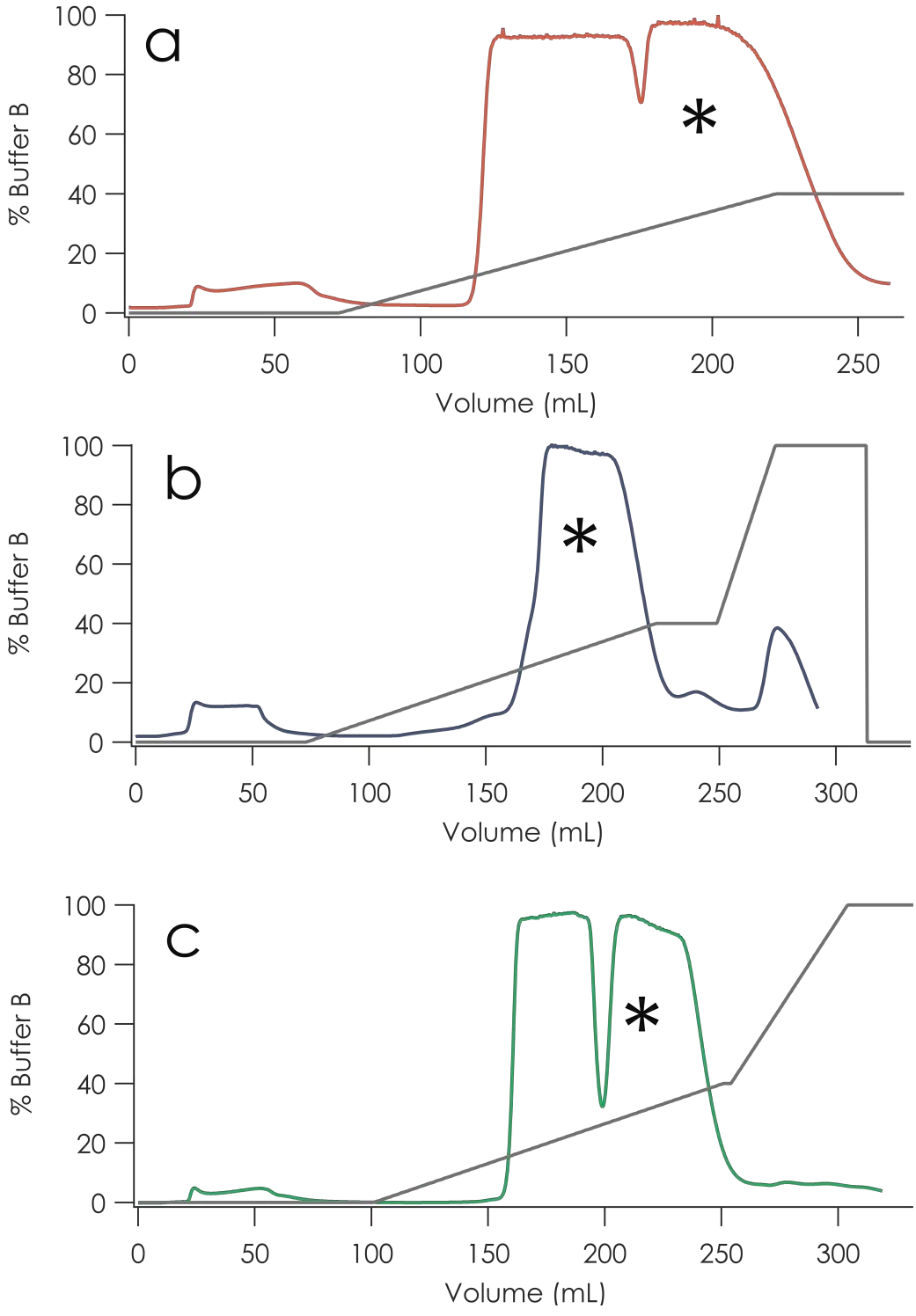
a
b
c
*
% Buffer B
Volume (mL)
0
20
40
60
80
100
0
50
100
150
200
250
300

Figure 2.2. ESI-MS of Zn^{II} fractions of **a)** C11D and **b)** C112D/M121L azurin preparations.

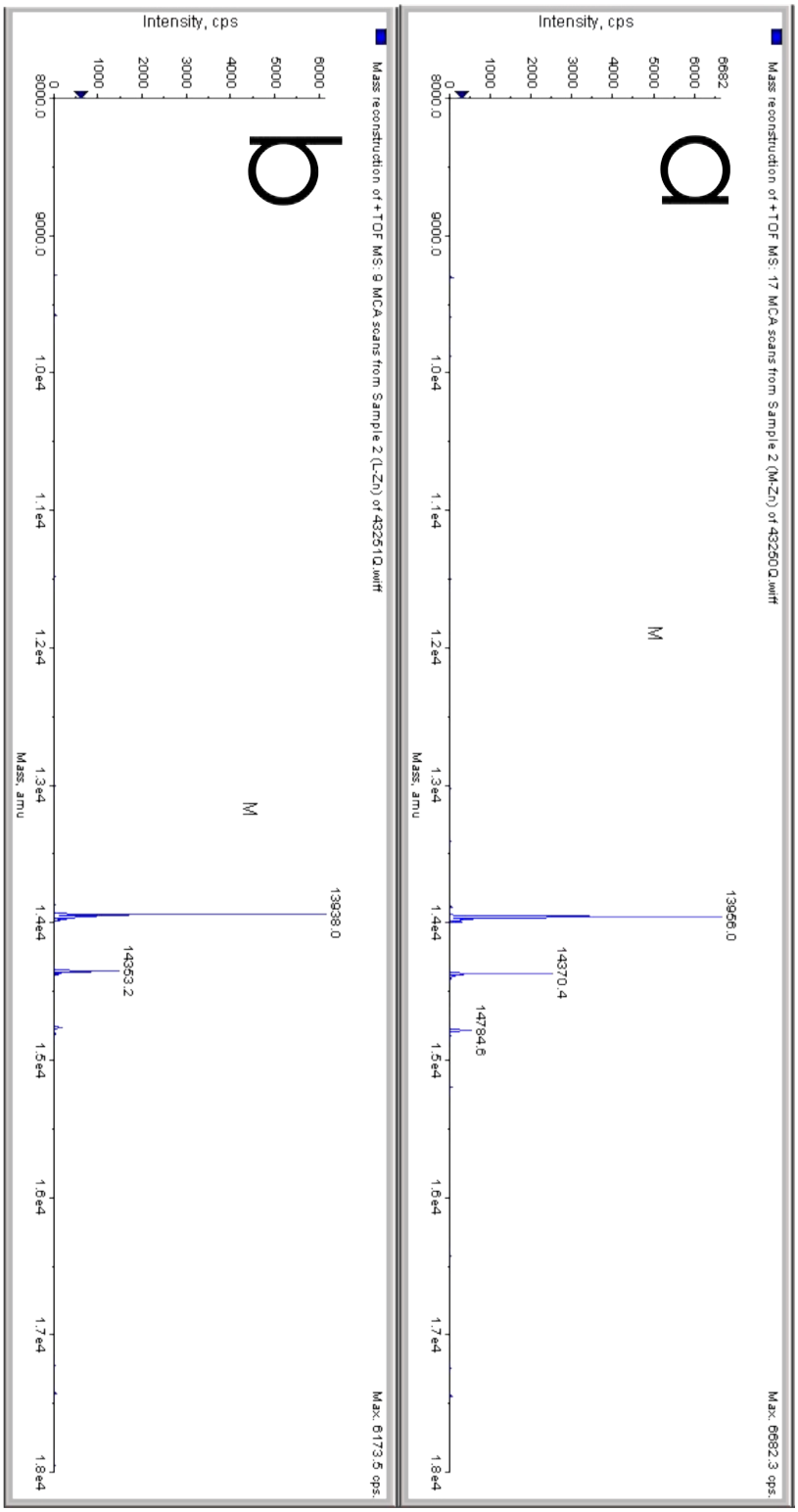
a
Mass reconstruction of +TOF MS: 17 MCA scans from Sample 2 (M-Zn) of 432560Q.wiff
Intensity, cps
Mass, amu
M
13956.0
14370.4
14784.8
Max: 6682.3 cps.
b
Mass reconstruction of +TOF MS: 9 MCA scans from Sample 2 (L-Zn) of 432551Q.wiff
Intensity, cps
Mass, amu
M
13938.0
14353.2
Max: 6173.5 cps.

Figure 2.3. FPLC chromatograms from the purification of apo C112D/M121X (X = E: a; H: b; L: c) azurin with HiLoad Superdex 75 16/60 column. In all cases the protein was in 50 mM Tris pH 7.5 buffer containing 150 mM NaCl and loaded onto the column equilibrated with this buffer. Bands corresponding to apoazurin are marked with asterisks.

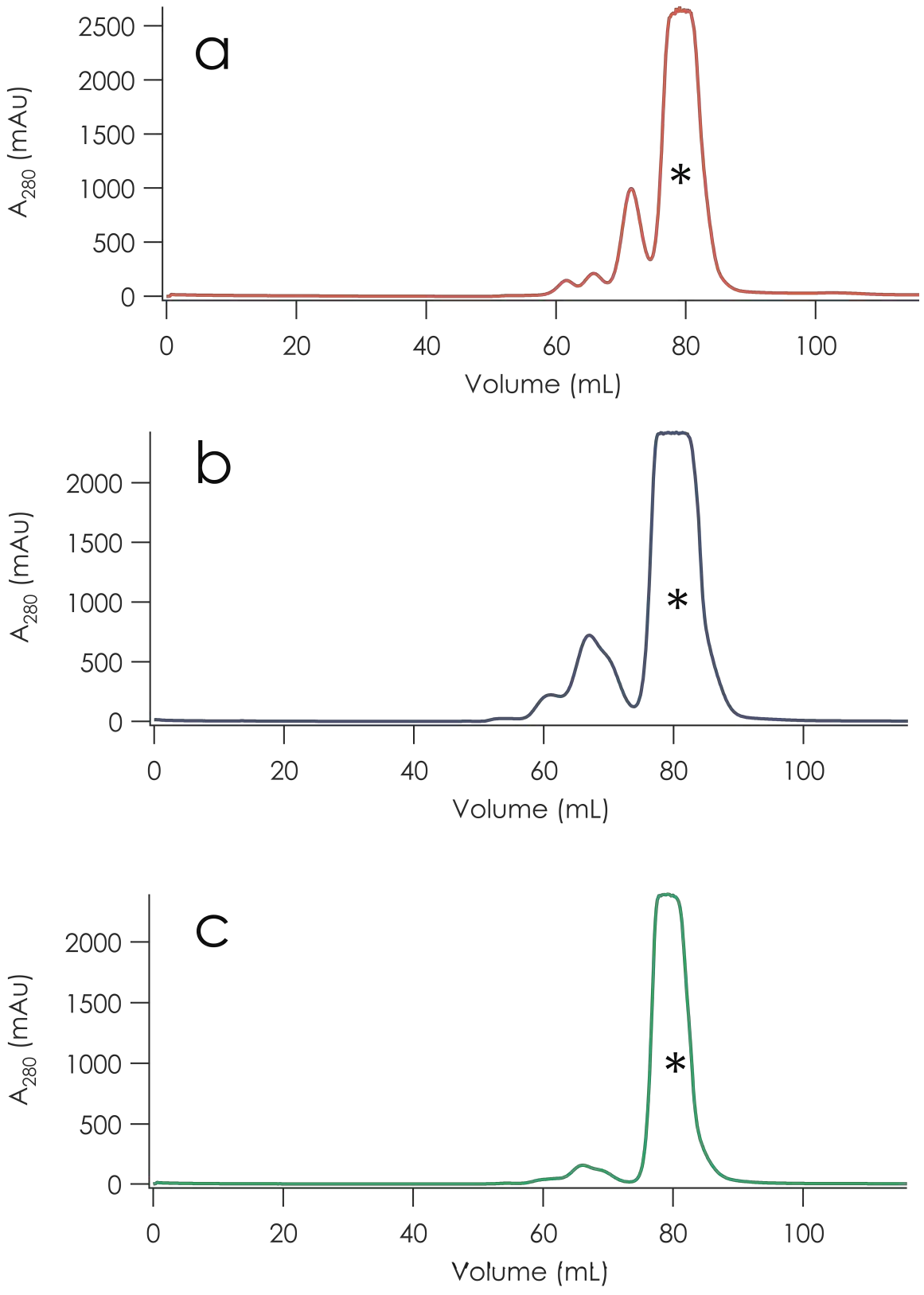
a
2500
2000
1500
1000
500
0
A_{280} (mAu)
*
0
20
40
60
80
100
Volume (mL)
b
2000
1500
1000
500
0
A_{280} (mAu)
*
0
20
40
60
80
100
Volume (mL)
c
2000
1500
1000
500
0
A_{280} (mAu)
*
0
20
40
60
80
100
Volume (mL)

Figure 2.4. ESI-MS of C112D/M121X (X = **a)** E, calc: 13955; **b)** H, calc: 13963; **c)** L, calc: 13939) azurins.

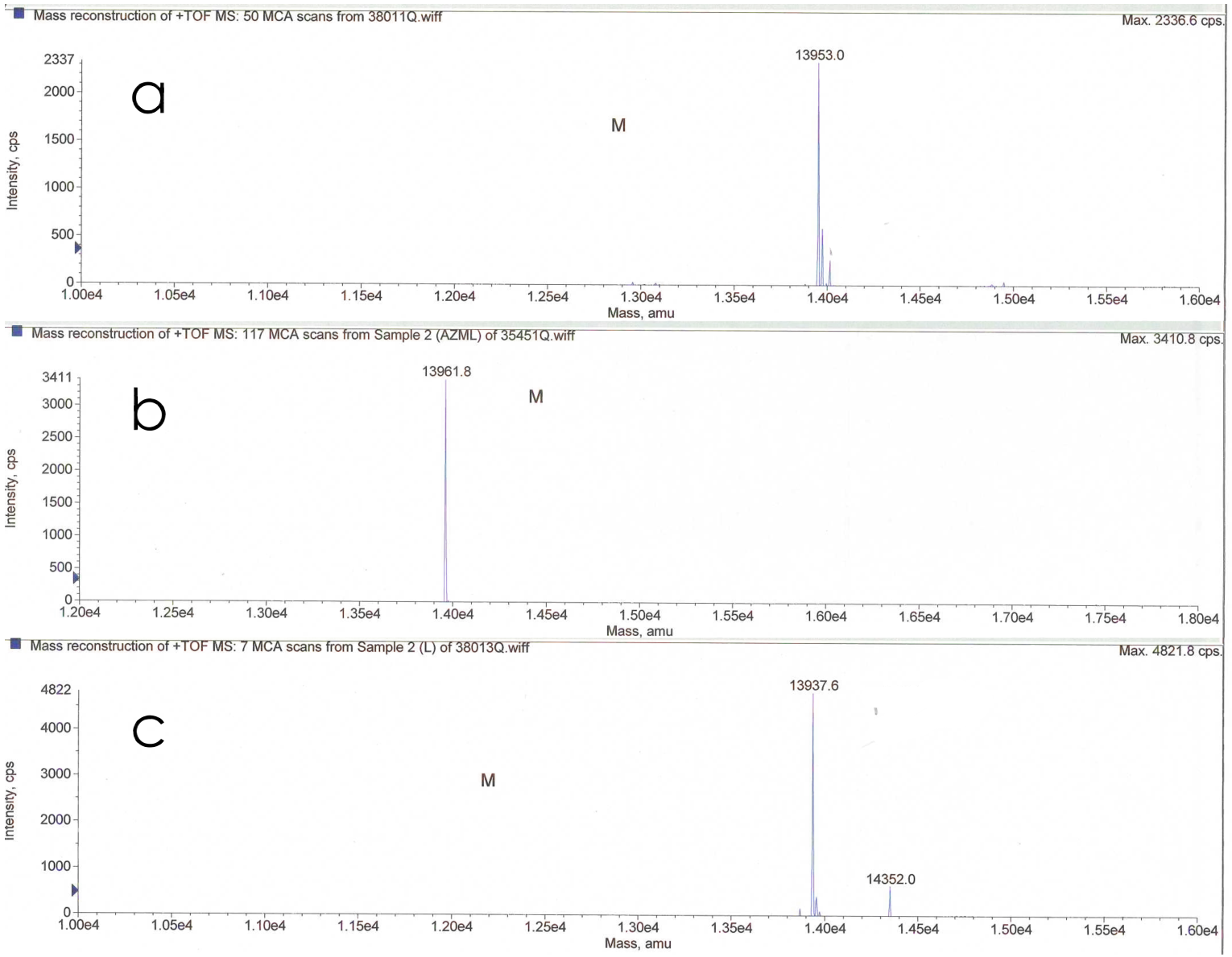
Mass reconstruction of +TOF MS: 50 MCA scans from 38011Q.wiff
Max. 2336.6 cps.
a
M
13953.0
Intensity, cps
Mass, amu
Mass reconstruction of +TOF MS: 117 MCA scans from Sample 2 (AZML) of 35451Q.wiff
Max. 3410.8 cps.
b
M
13961.8
Intensity, cps
Mass, amu
Mass reconstruction of +TOF MS: 7 MCA scans from Sample 2 (L) of 38013Q.wiff
Max. 4821.8 cps.
c
M
13937.6
14352.0
Intensity, cps
Mass, amu

Figure 2.5. ESI-MS of *P. aeruginosa* cytc_{551}. Calculated value for holoprotein: 9309.

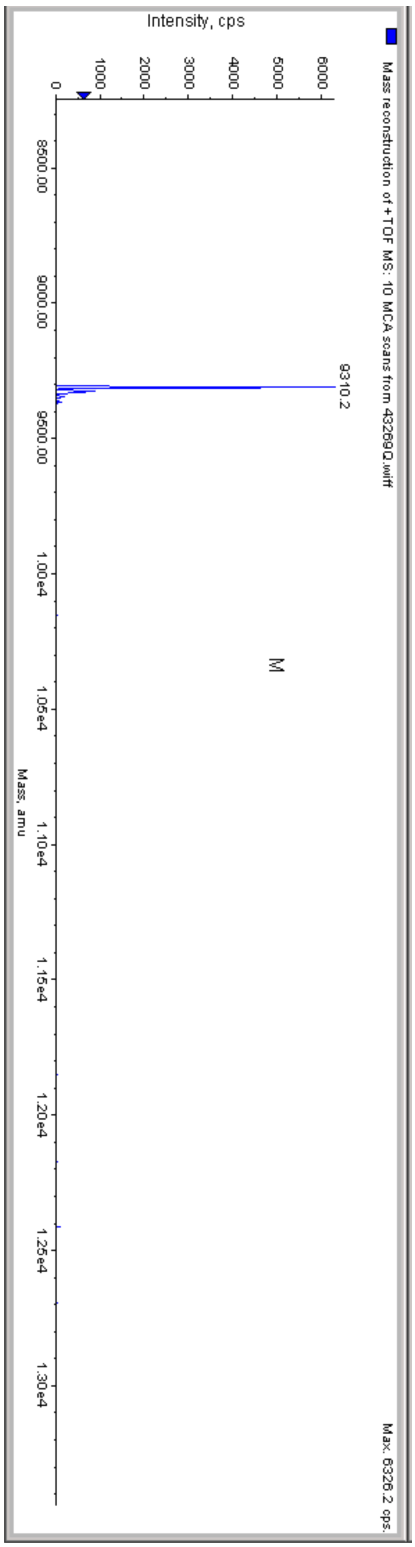
Intensity, cps
0
1000
2000
3000
4000
5000
6000
8500.00
9000.00
9500.00
1.00e4
1.05e4
1.10e4
1.15e4
1.20e4
1.25e4
1.30e4
Mass, amu
9310.2
M
Mass reconstruction of +TOF MS: 10 MCA scans from 43269Q.wiff
Max. 6326.2 cps.

Figure 2.6. Titration of 1 mL 310 μM apo C112D/M121E azurin in 100 mM Tris pH 7.0 with **a,b)** 50 μL aliquots of 1.018 mM $CuSO_4$ and **c)** 50 μL aliquots of 1 mM $CoCl_2$. Concentrations on the abcissa are corrected for dilution. Plots were fit to straight lines in the linear region to yield extinction coefficients for Cu^{II} and Co^{II} C112D/M121E azurin.

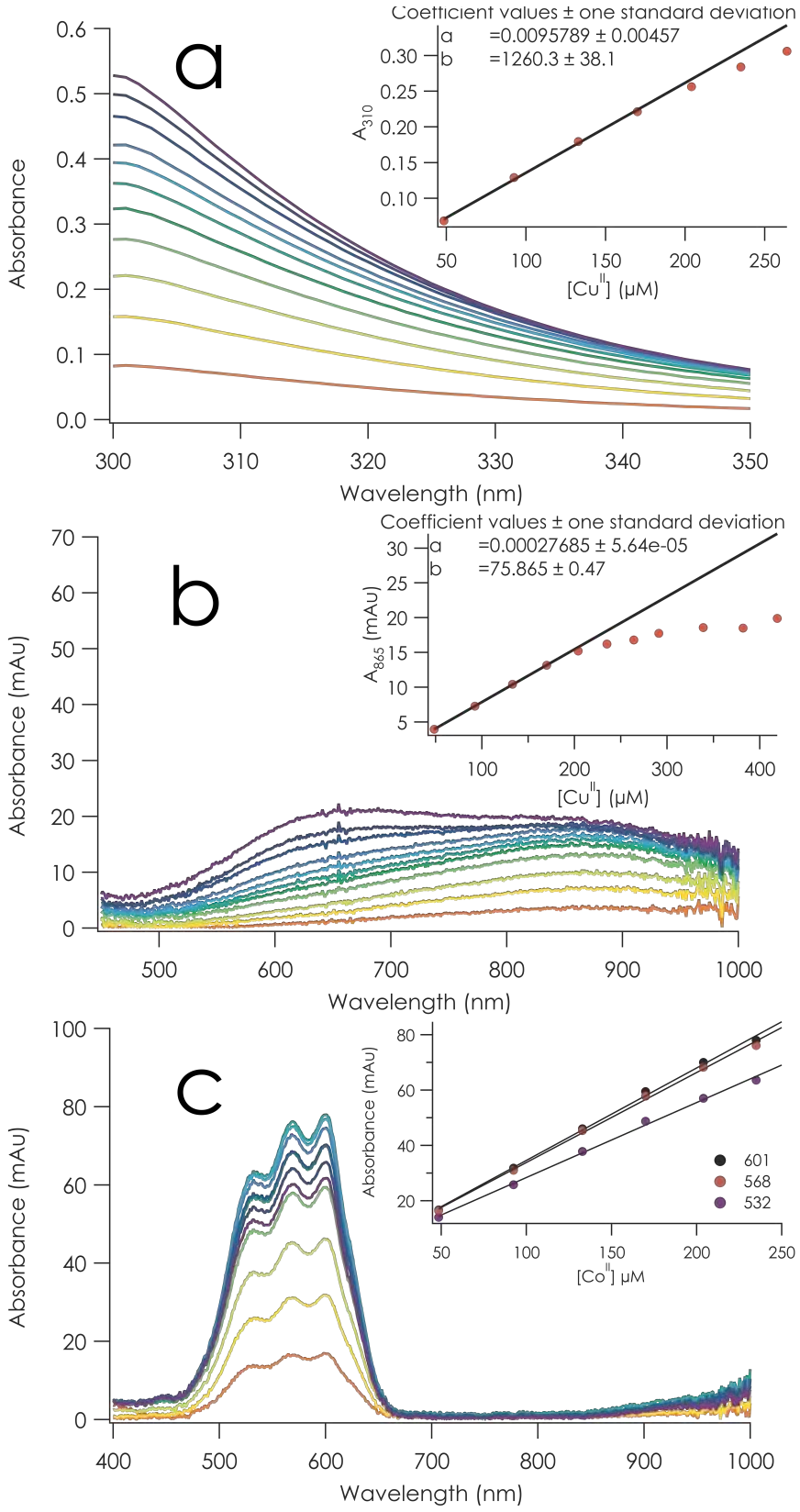
a
Coefficient values ± one standard deviation
a =0.0095789 ± 0.00457
b =1260.3 ± 38.1
A310
[Cu^II] (μM)
Absorbance
Wavelength (nm)
b
Coefficient values ± one standard deviation
a =0.00027685 ± 5.64e-05
b =75.865 ± 0.47
A865 (mAu)
[Cu^II] (μM)
Absorbance (mAu)
Wavelength (nm)
c
Absorbance (mAu)
601
568
532
[Co^II] μM
Absorbance (mAu)
Wavelength (nm)

Figure 2.7. Titration of 1 mL 1.25 mM apo C112D/M121H azurin in 100 mM Tris pH 7.0 with **a,b)** 10 μL aliquots of 10.18 mM $CuSO_4$ and **c)** 20 μL aliquots of 10 mM $CoCl_2$. Concentrations on the abcissa are corrected for dilution. Plots were fit to straight lines in the linear region to yield extinction coefficients for Cu^{II} and Co^{II} C112D/M121H azurin.

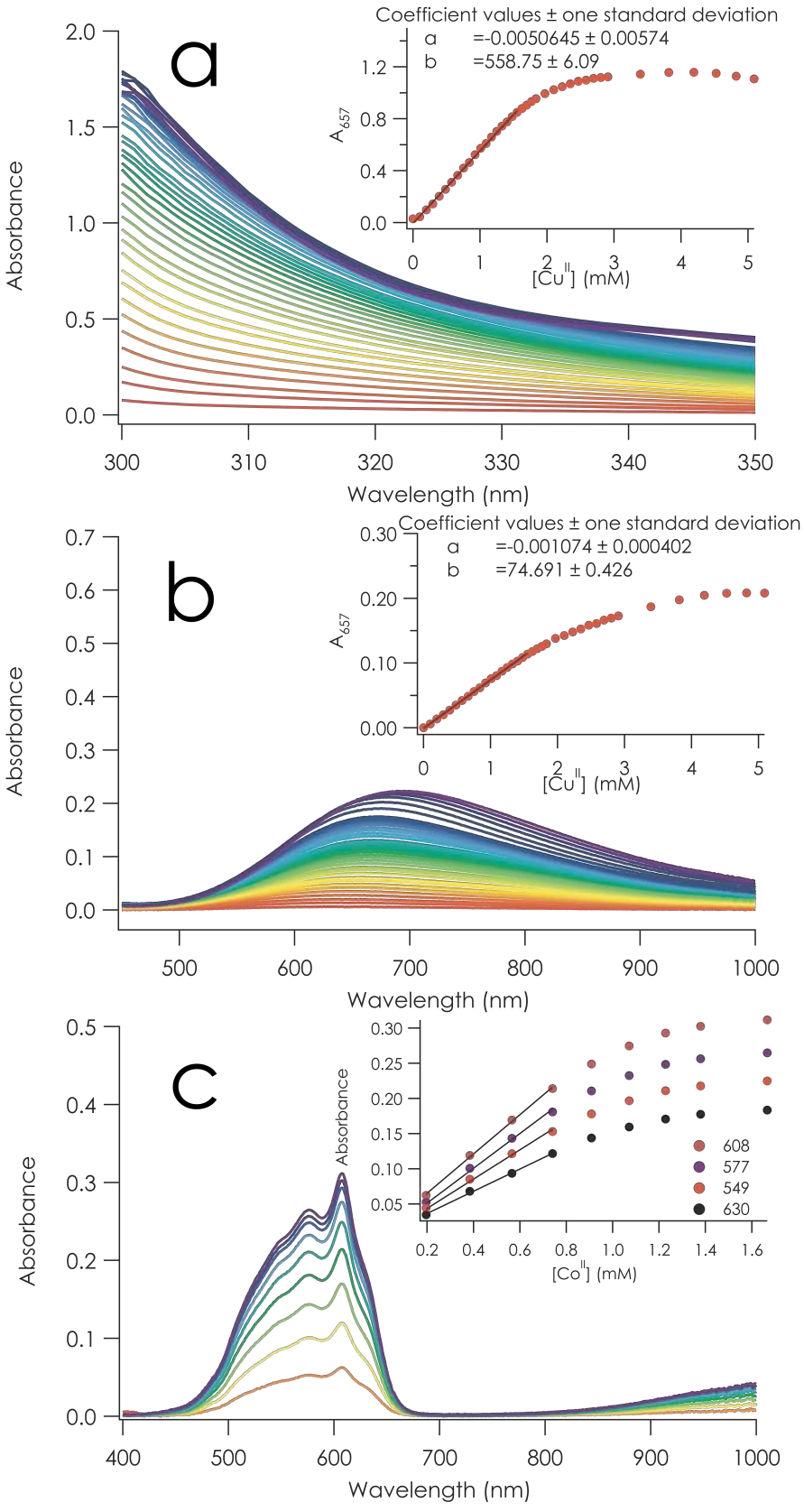
a
Coefficient values ± one standard deviation
a =-0.0050645 ± 0.00574
b =558.75 ± 6.09
A657
[Cu^II] (mM)
Absorbance
Wavelength (nm)
b
Coefficient values ± one standard deviation
a =-0.001074 ± 0.000402
b =74.691 ± 0.426
A657
[Cu^II] (mM)
Absorbance
Wavelength (nm)
c
Absorbance
608
577
549
630
[Co^II] (mM)
Absorbance
Wavelength (nm)

Figure 2.8. Titration of 1 mL 380 μM apo C112D/M121L azurin in 100 mM Tris pH 7.0 with **a,b)** 50 μL aliquots of 1.018 mM $CuSO_4$ and **c)** 1 mL 1.08 mM apo C112D/M121L azurin with 20 μL aliquots of 10 mM $CoCl_2$. Concentrations on the abcissa are corrected for dilution. Plots were fit to straight lines in the linear region to yield extinction coefficients for Cu^{II} and Co^{II} C112D/M121L azurin.

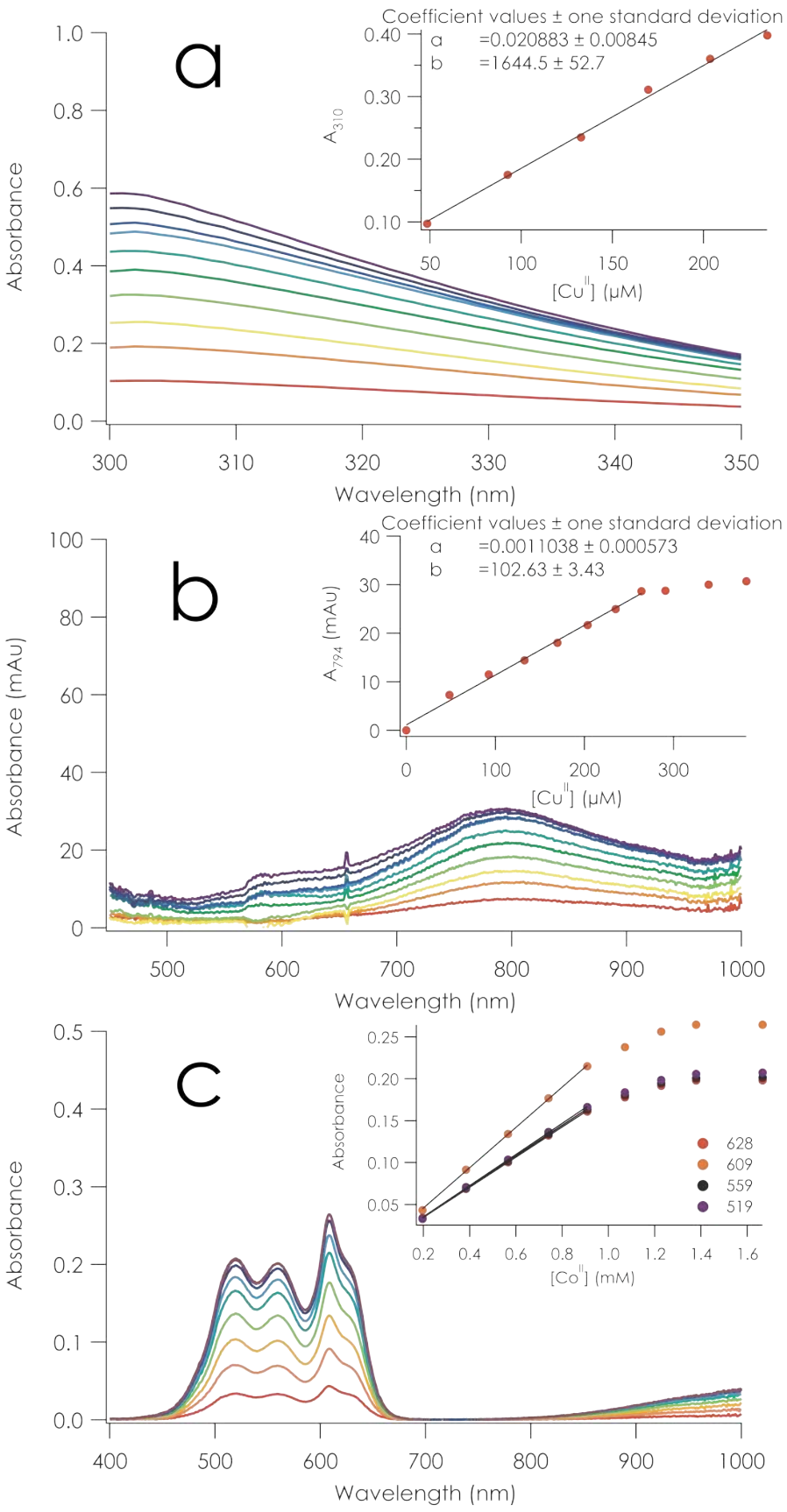
a
Coefficient values ± one standard deviation
a =0.020883 ± 0.00845
b =1644.5 ± 52.7
A310
[Cu^II] (μM)
Absorbance
Wavelength (nm)
b
Coefficient values ± one standard deviation
a =0.0011038 ± 0.000573
b =102.63 ± 3.43
A794 (mAu)
[Cu^II] (μM)
Absorbance (mAu)
Wavelength (nm)
c
Absorbance
628
609
559
519
[Co^II] (mM)
Absorbance
Wavelength (nm)

Figure 2.9. LF region of the electronic absorption spectra of Cu^{II} C112D/M121X azurins in 10 mM NaP_i pH 7.0. X = M (black), E (red), H (blue), L (green).

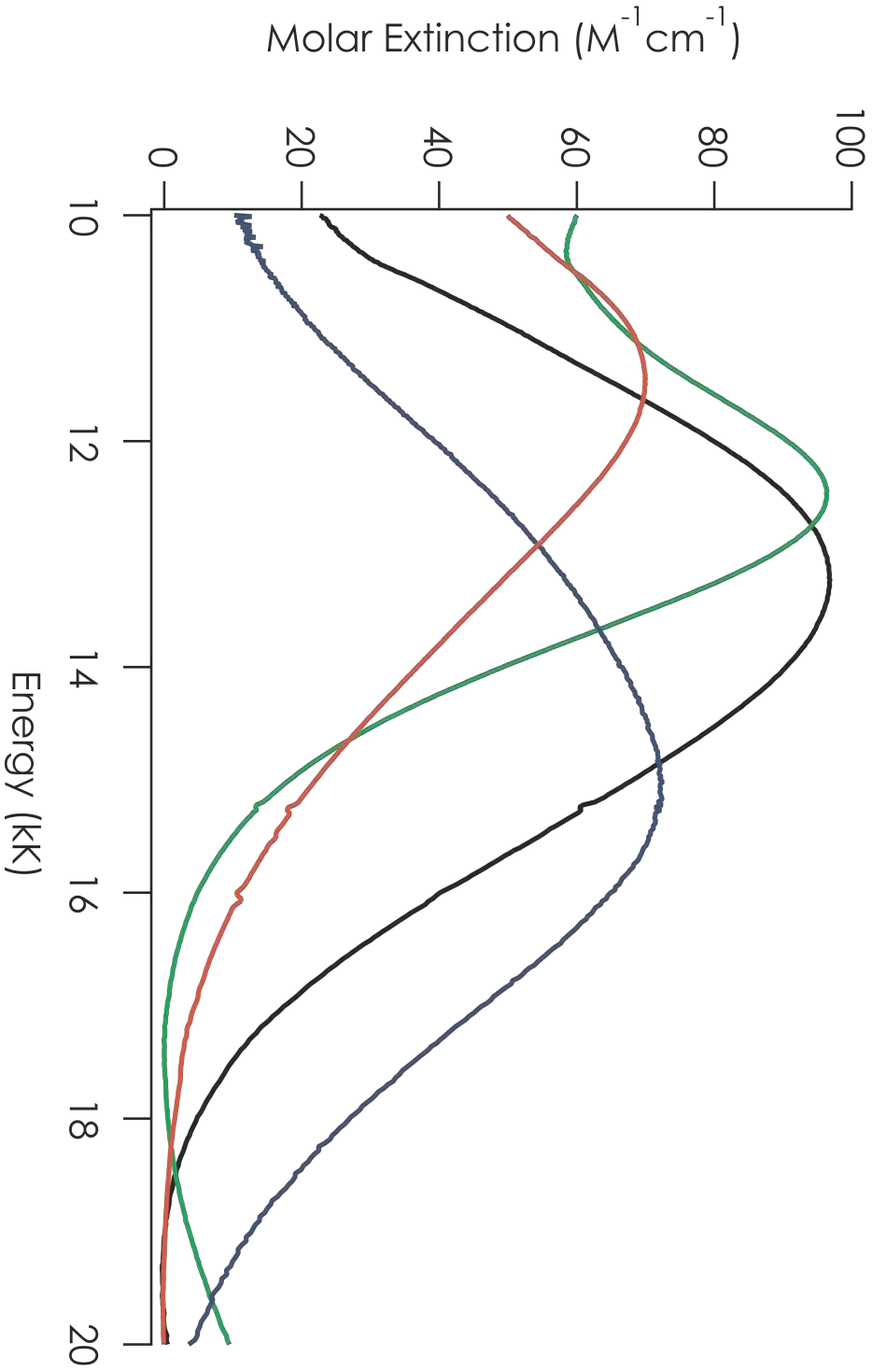
Molar Extinction ($M^{-1}cm^{-1}$)
0
20
40
60
80
100
10
12
14
16
18
20
Energy (kK)

Figure 2.10. LF region of the electronic absorption spectra of Co^{II} C112D/M121X azurins in 10 mM NaP_i at pH 7.0. X = M (black), E (red), H (blue), L (green).

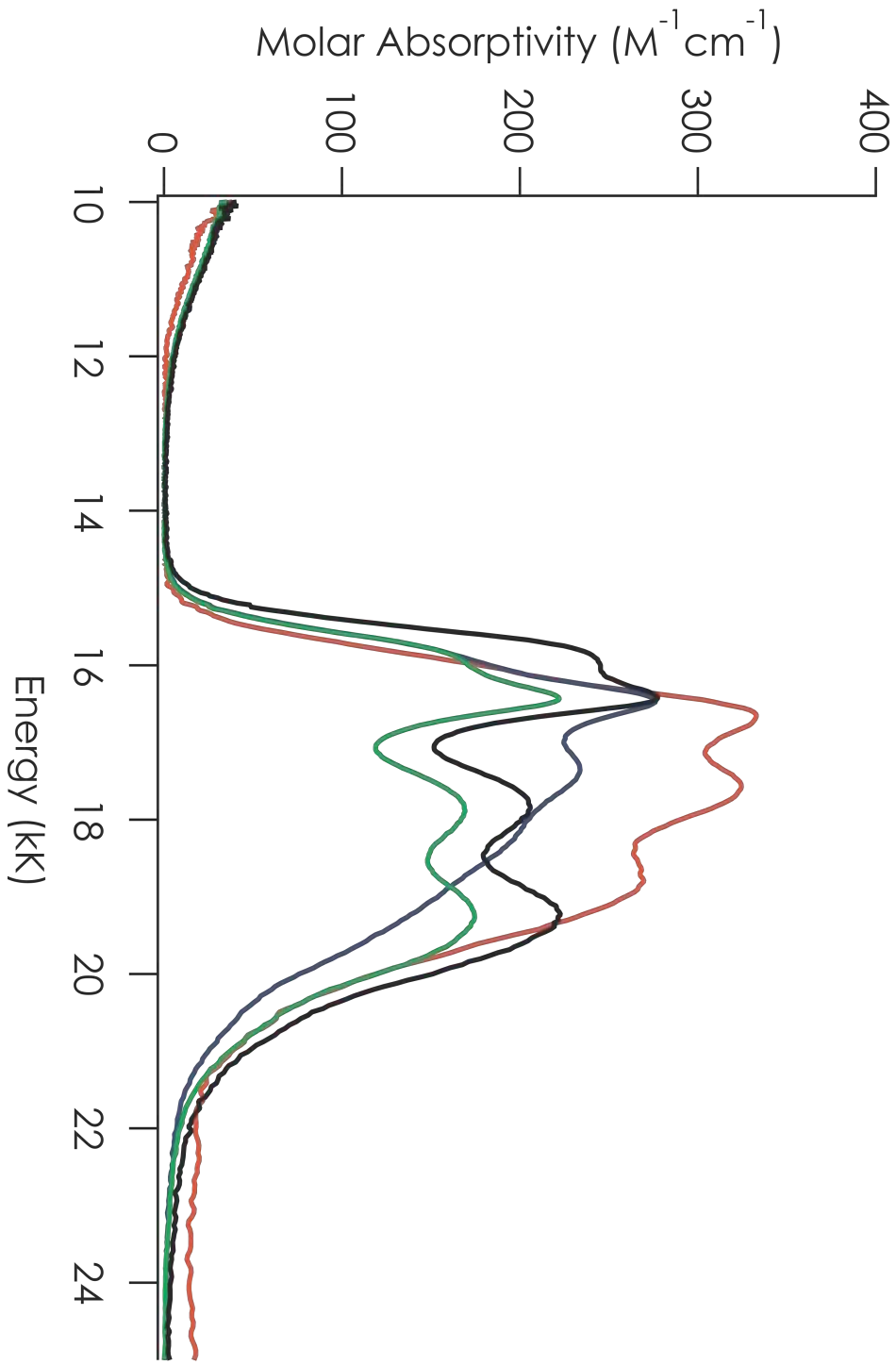
Molar Absorptivity ($M^{-1}cm^{-1}$)
0
100
200
300
400
Energy (kK)
10
12
14
16
18
20
22
24

Figure 2.11. 77 K frozen solution X-band (9.5 GHz) EPR spectra of C112D/M121X azurin in 10 mM NaP_i at pH 7.0. Spectra were recorded with a 5 G modulation amplitude and with 2 mW of microwave power. X = M (black), E (red), H (blue), L (green).

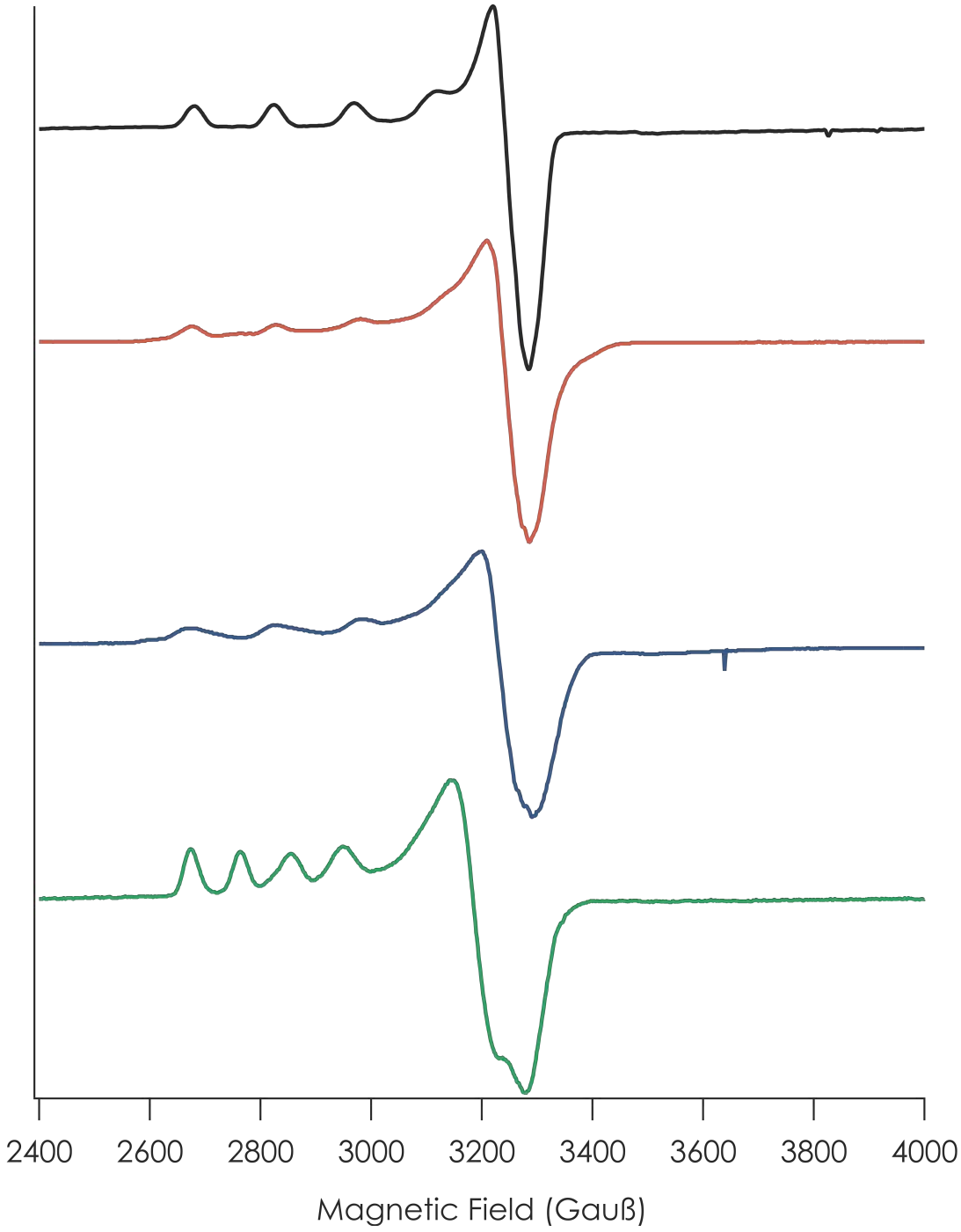
2400
2600
2800
3000
3200
3400
3600
3800
4000
Magnetic Field (Gauß)

Figure 2.12. CV of C112D azurin on SAM-modified Au(111) electrode in deaerated 10 mM NaP_i pH 7.0. CV was recorded under an Ar blanket at a scan rate of 50 mV/s and referenced to saturated Ag/AgCl (197 mV vs NHE). $E_{1/2}^{o}$ is 180 mV vs NHE.

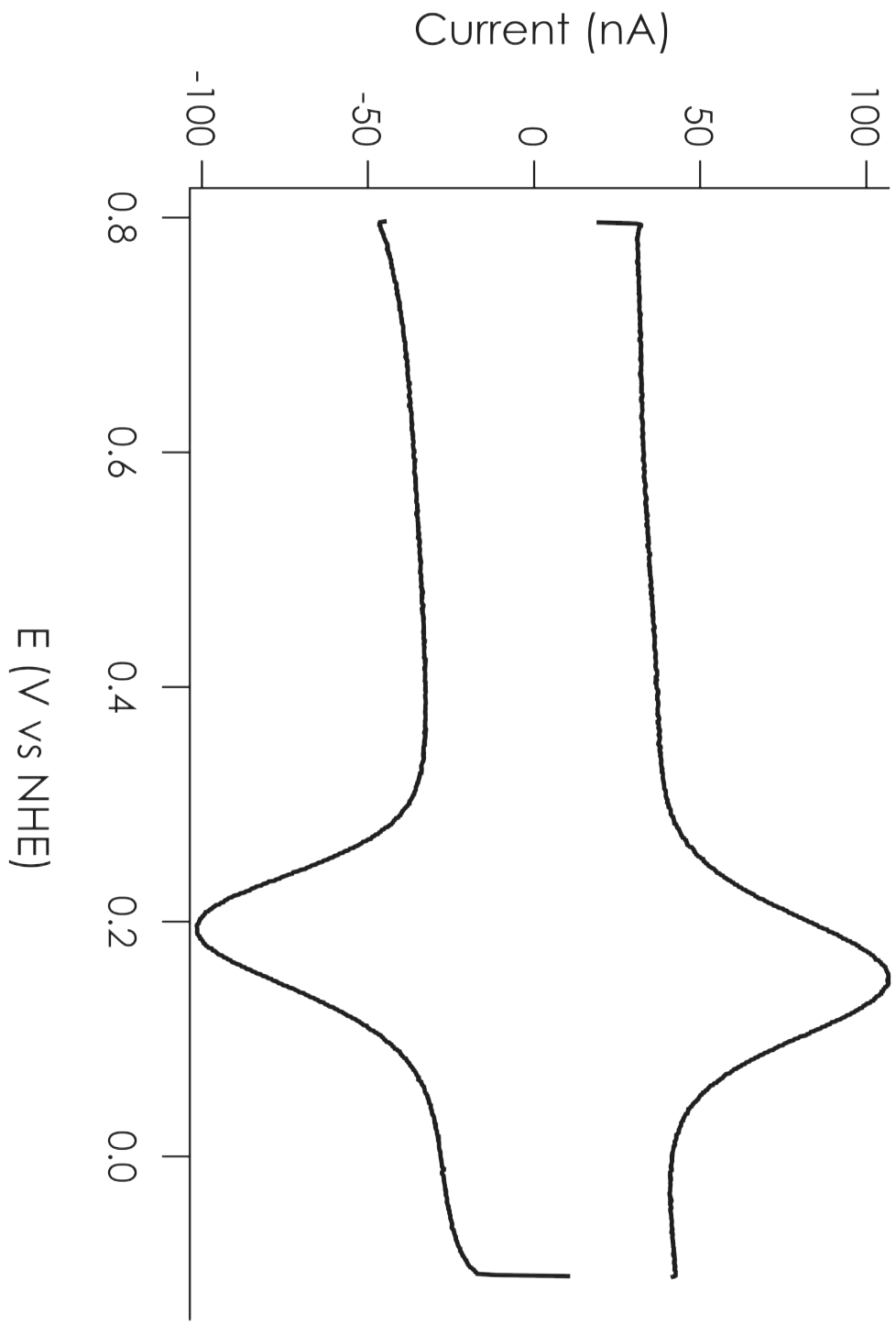
Current (nA)
-100
-50
0
50
100
0.8
0.6
0.4
0.2
0.0
E (V vs NHE)

Figure 2.13. SWV of C112D/M121E azurin on SAM-modified Au(111) electrode in deaerated 10 mM NaP_i pH 7.0. SWV was recorded under an Ar blanket with a square wave frequency of 8 Hz and referenced to saturated Ag/AgCl (197 mV vs NHE). $E_{1/2}°$ is 270 mV vs NHE.

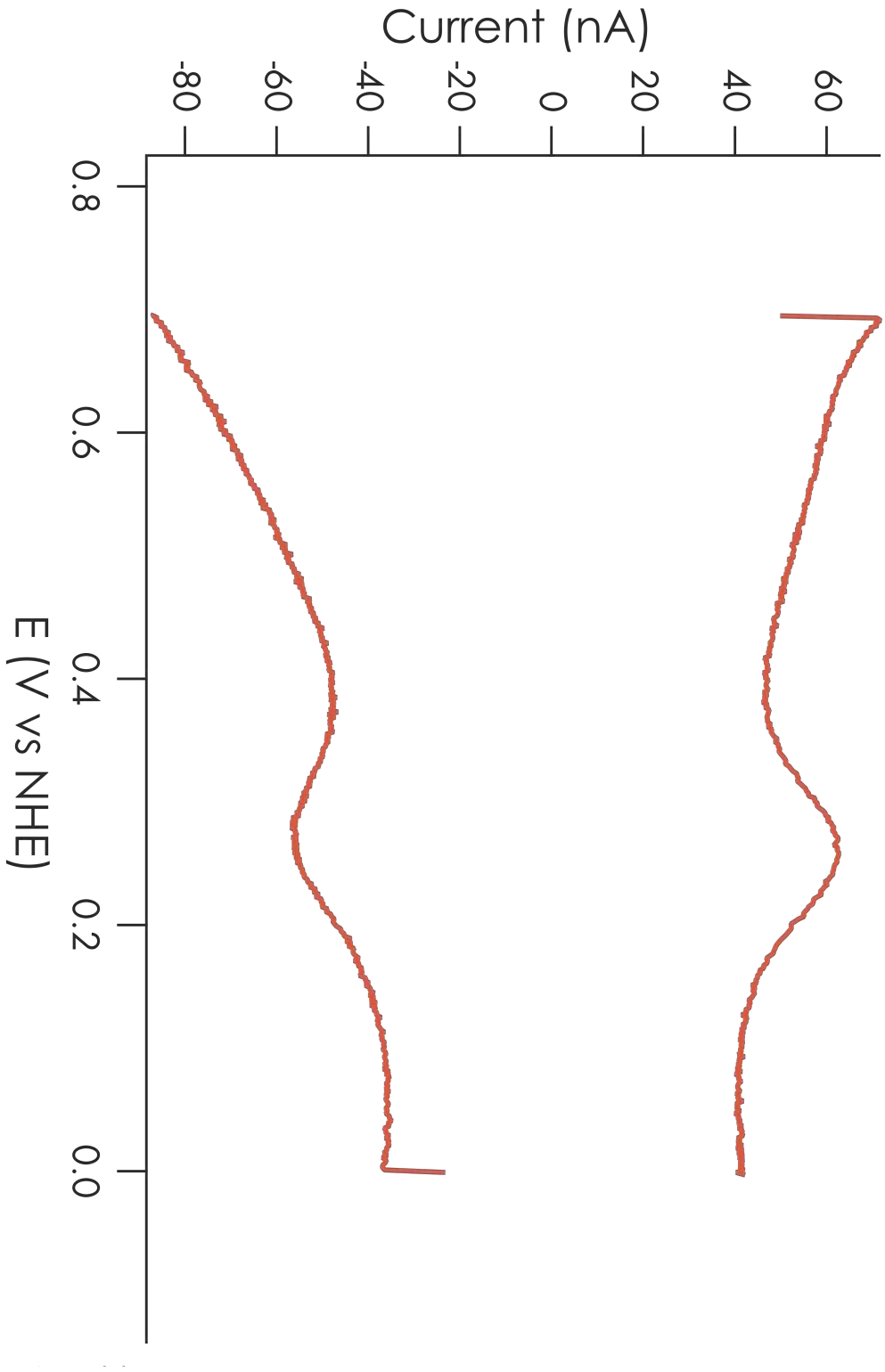
Current (nA)
-80
-60
-40
-20
0
20
40
60
0.8
0.6
0.4
0.2
0.0
E (V vs NHE)

Figure 2.14. a) Titration of 2 mL 8.5 μM Fe^{II}-cyt c_{551} in 100 mM HEPES pH 7.0 with 532 μM C112D/M121E azurin. **b)** Plot of [Fe^{III}] calculated by Eq. 2.2 versus [Cu^{II}] (concentrations corrected for volume) fit to Eq 2.1. K_{eq} was 3.69, giving a reduction potential of 289 mV vs NHE.

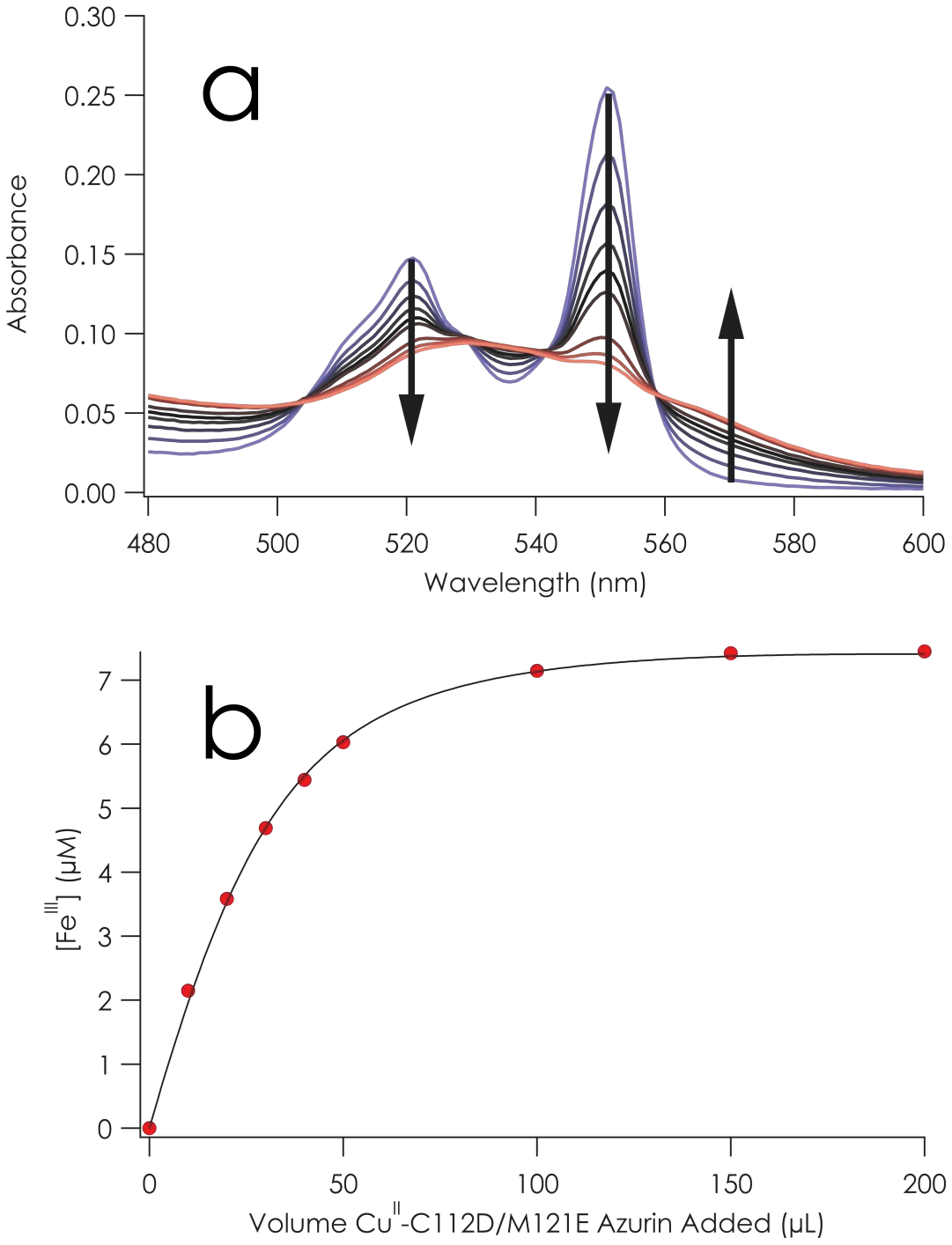
a
Absorbance
0.30
0.25
0.20
0.15
0.10
0.05
0.00
480
500
520
540
560
580
600
Wavelength (nm)
b
[Fe^III] (μM)
7
6
5
4
3
2
1
0
0
50
100
150
200
Volume Cu^II-C112D/M121E Azurin Added (μL)

Figure 2.15. CV of C112D/M121H azurin on SAM-modified Au(111) electrode in deaerated 10 mM NaP_i pH 7.0. CV was recorded under an Ar blanket at a scan rate of 50 mV/s and referenced to saturated Ag/AgCl (197 mV vs NHE). The CV is irreversible, but the estimated $E_{1/2}^{o} \sim 450$ mV vs NHE.

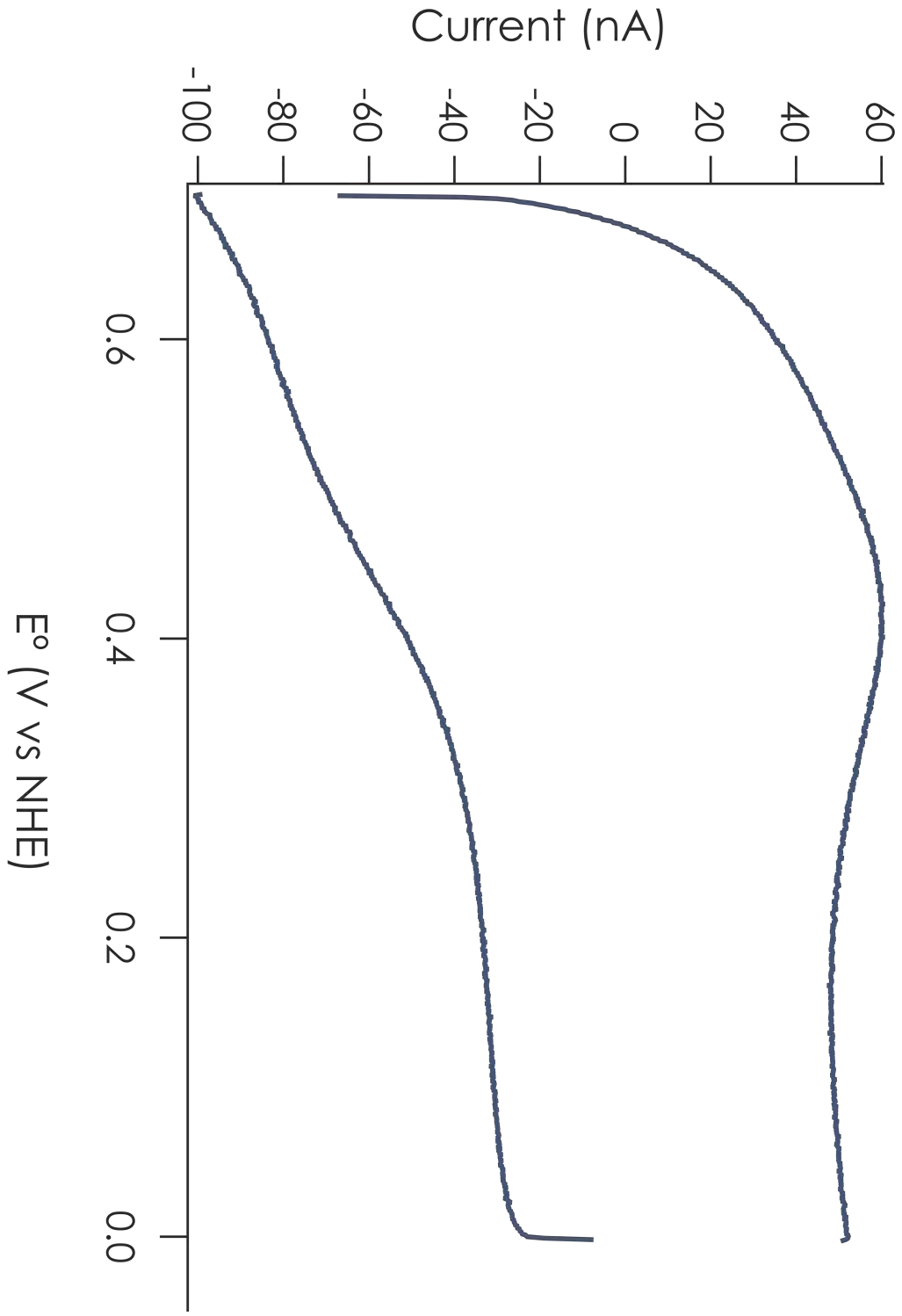
Current (nA)
-100
-80
-60
-40
-20
0
20
40
60
0.6
0.4
0.2
0.0
E° (V vs NHE)

Figure 2.16. a) Titration of 2.5 mL 20μM Fe^{II}-cyt c_{551} in 100 mM NaP_i pH 7.0 with 5.2 mM C112D/M121H azurin. **b)** Plot of [Fe^{III}] calculated by Eq. 2.2 versus [Cu^{II}] (concentrations corrected for volume) fit to Eq 2.1. K_{eq} was 20, giving a reduction potential of 332 mV vs NHE.

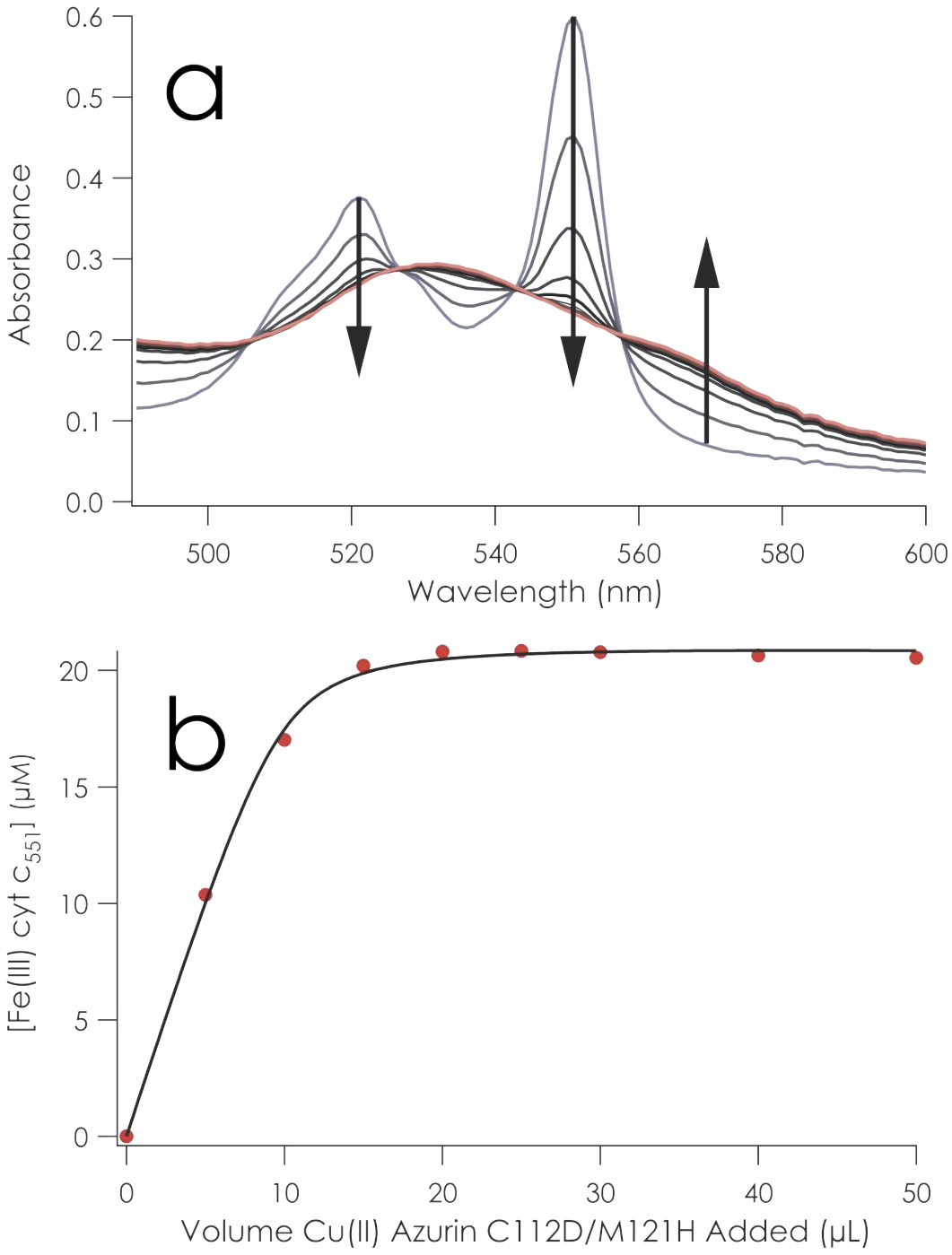
a
Absorbance
0.6
0.5
0.4
0.3
0.2
0.1
0.0
500
520
540
560
580
600
Wavelength (nm)
b
[Fe(III) cyt c551] (μM)
20
15
10
5
0
0
10
20
30
40
50
Volume Cu(II) Azurin C112D/M121H Added (μL)

Figure 2.17. CV of C112D/M121L azurin on SAM-modified Au(111) electrode in deaerated 10 mM NaP_i pH 7.0. CV was recorded under an Ar blanket at a scan rate of 50 mV/s and referenced to saturated Ag/AgCl (197 mV vs NHE). $E_{1/2}^{o}$ is 270 mV vs NHE.

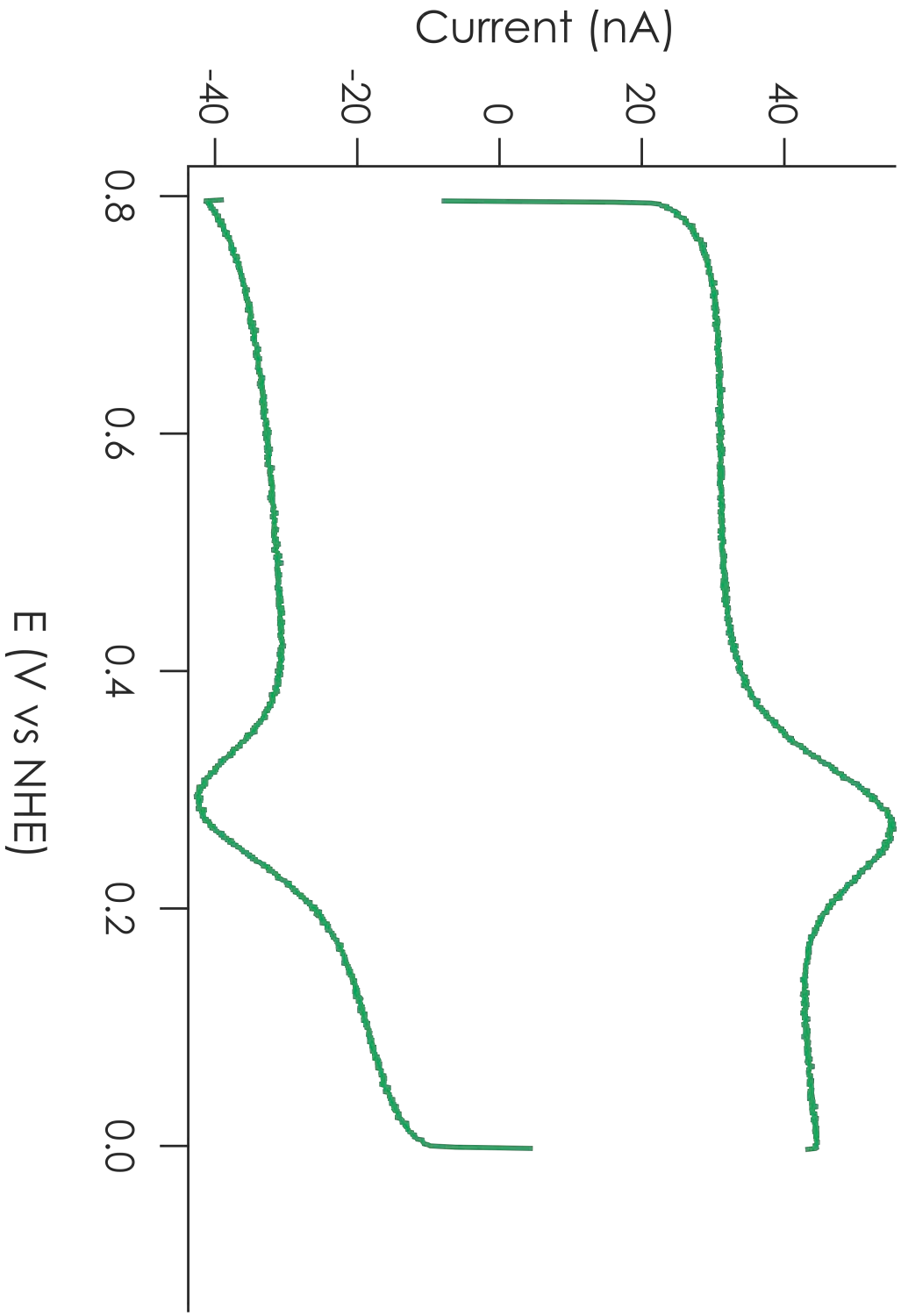
Current (nA)
-40
-20
0
20
40
0.8
0.6
0.4
0.2
0.0
E (V vs NHE)

Figure 2.18. a) Titration of 2 mL 8.45 μM Fe^{II}-cyt c_{551} in 100 mM NaP_i pH 7.0 with 1.63 mM C112D/M121L azurin. **b)** Plot of [Fe^{III}] calculated by Eq. 2.2 versus [Cu^{II}] (concentrations corrected for volume) fit to Eq 2.1. K_{eq} was 2.58, giving a reduction potential of 279 mV vs NHE.

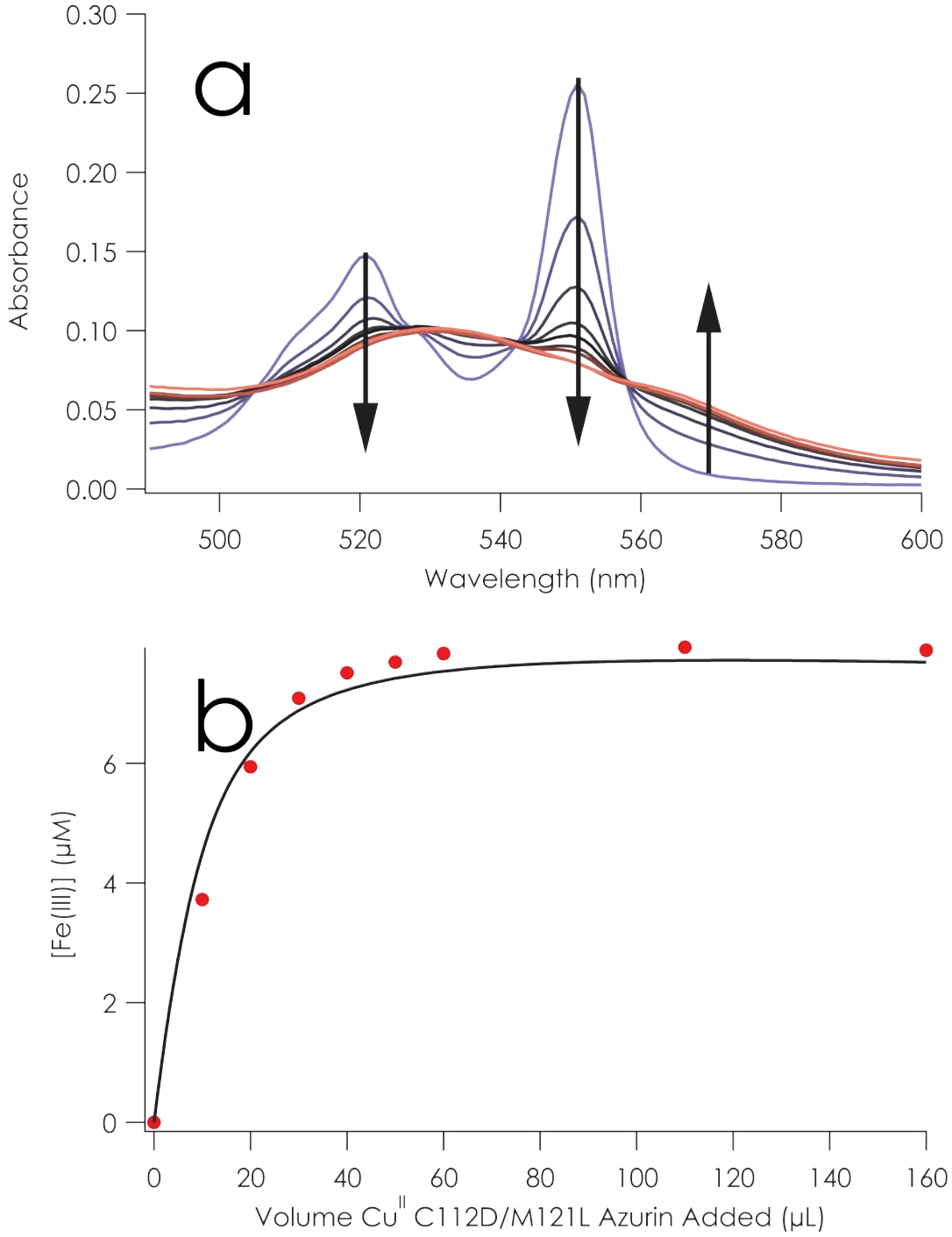
a
Absorbance
0.30
0.25
0.20
0.15
0.10
0.05
0.00
500
520
540
560
580
600
Wavelength (nm)
b
[Fe(III)] (μM)
6
4
2
0
0
20
40
60
80
100
120
140
160
Volume Cu^II C112D/M121L Azurin Added (μL)

Figure 2.19. pH dependence of the C112D/M121E azurin reduction potential (by cytc_{551} titrations in buffered aqueous solutions at 298 K). Error bars represent one standard deviation of three titrations.

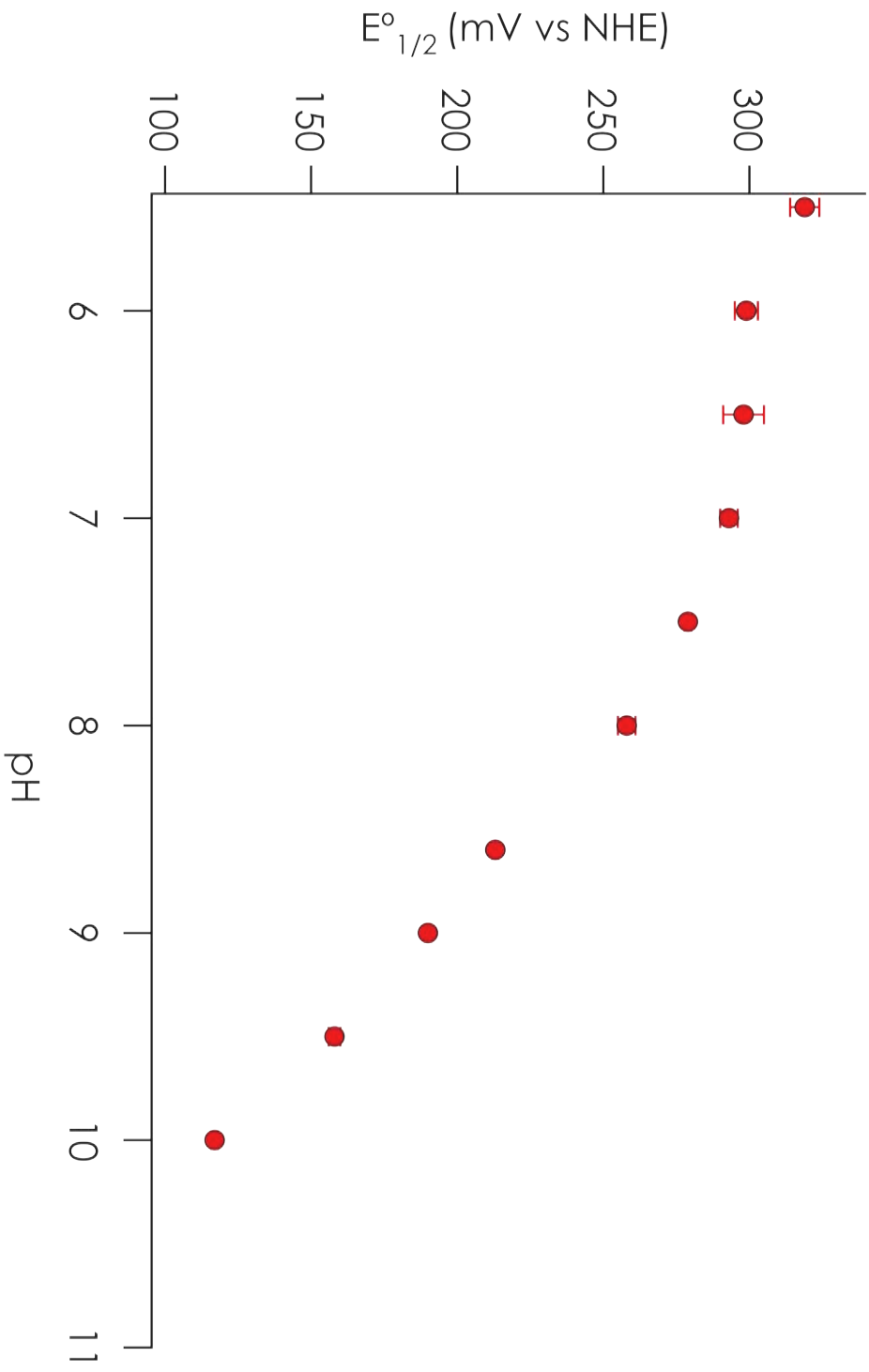
E°1/2 (mV vs NHE)
100
150
200
250
300
pH
6
7
8
9
10
11

Figure 2.20. EPR spectra of C112D/M121E azurin recorded in aqueous 77 K glass at pH 7.0 (50 mM HEPES containing 50% glycerol) at **a)** X-band (9.5 GHz) and **b)** Q-band (34 GHz). The X-band spectrum was recorded with a 6 G modulation amplitude at a microwave power of 2 mW. The Q-band spectrum was recorded with a 15.37 G modulation amplitude.

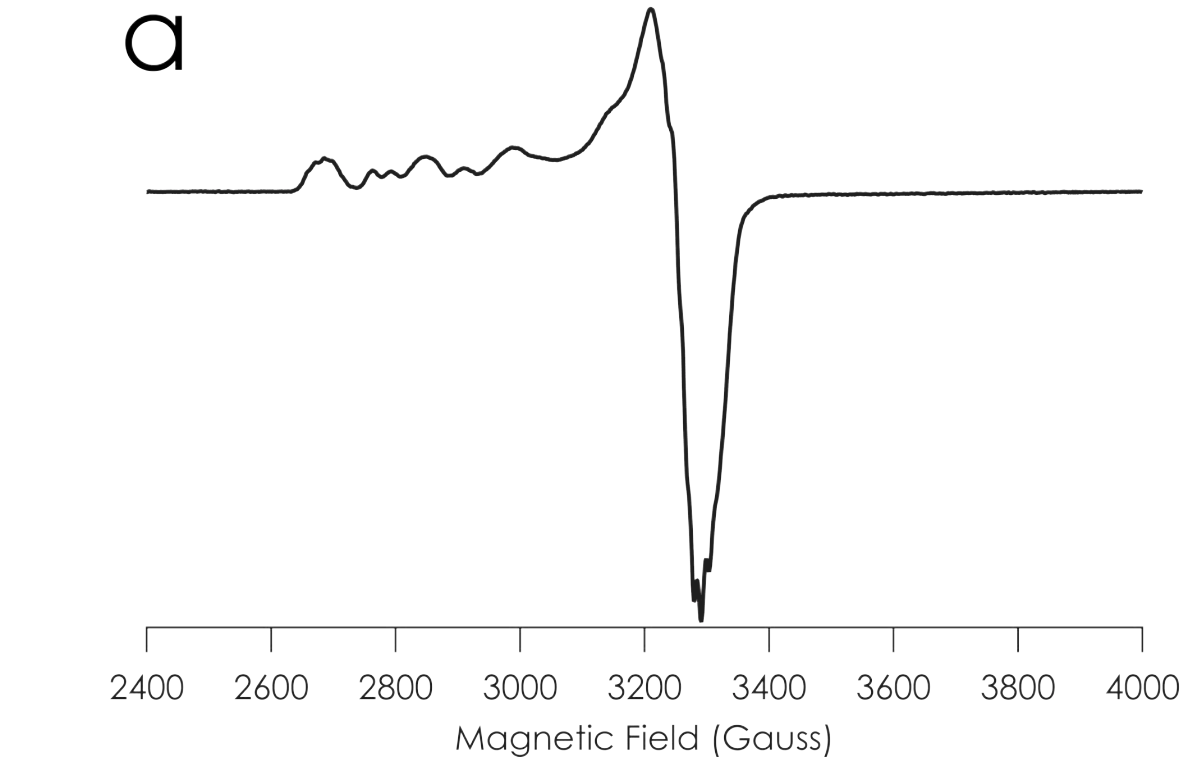
a
2400
2600
2800
3000
3200
3400
3600
3800
4000
Magnetic Field (Gauss)

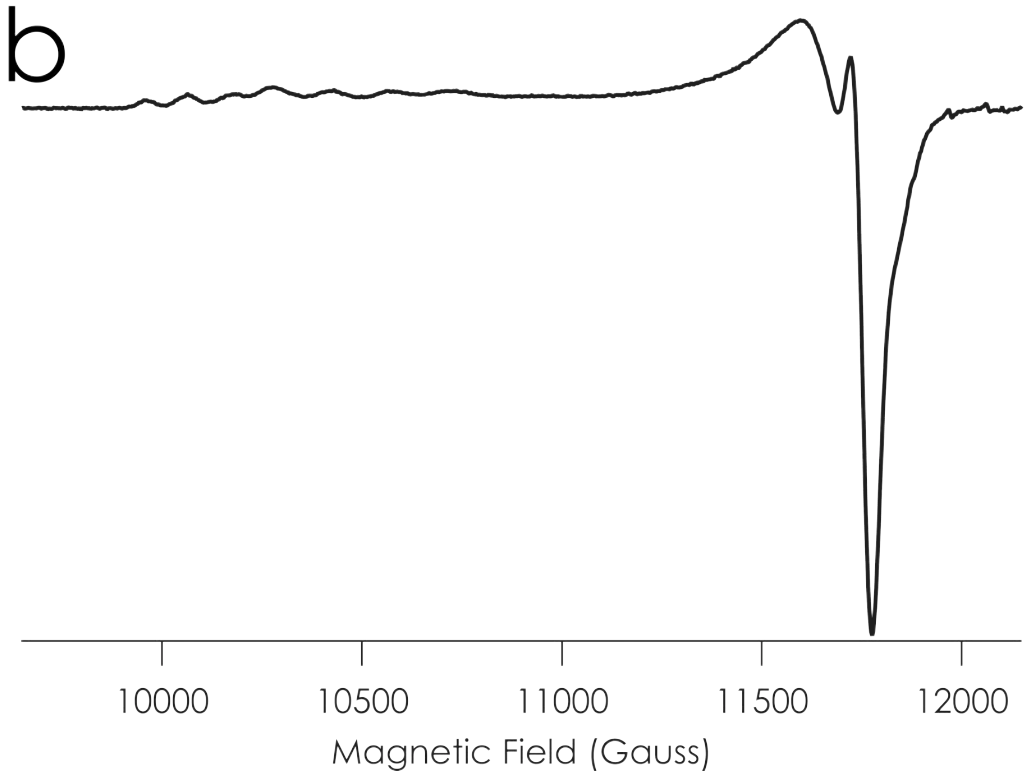
b
10000
10500
11000
11500
12000
Magnetic Field (Gauss)

Figure 2.21. X-band (9.5 GHz) EPR spectra of C112D/M121E between the pH range of 5.5 to 10.0 in aqueous 77 K glass (50 mM indicated buffer containing 50% glycerol). Spectra were recorded with a 6 G modulation amplitude and at a microwave power of 2 mW.

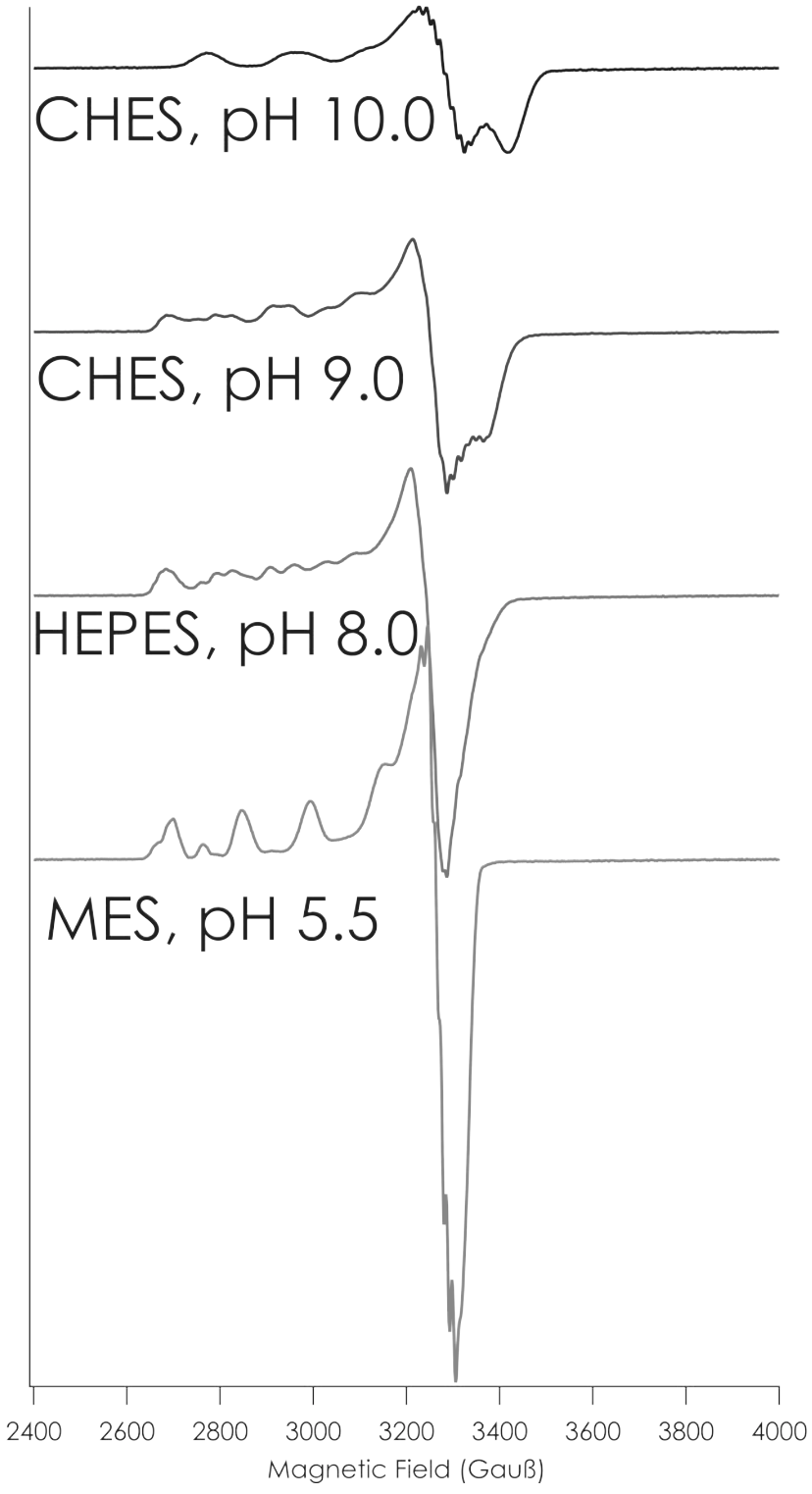
CHES, pH 10.0
CHES, pH 9.0
HEPES, pH 8.0
MES, pH 5.5
2400
2600
2800
3000
3200
3400
3600
3800
4000
Magnetic Field (Gauß)

Figure 2.22. X-band (9.5 GHz) EPR spectra of C112D/M121E azurin recorded in aqueous 77 K glass at pH 10.0 (50 mM CHES containing 50% glycerol, red) and at pH 5.5 (50 mM MES containing 50% glycerol, blue). The spectra were recorded with 6 G modulation amplitudes at 2 mW of microwave power. Results of SpinCount[23] simulations overlaid in gray.

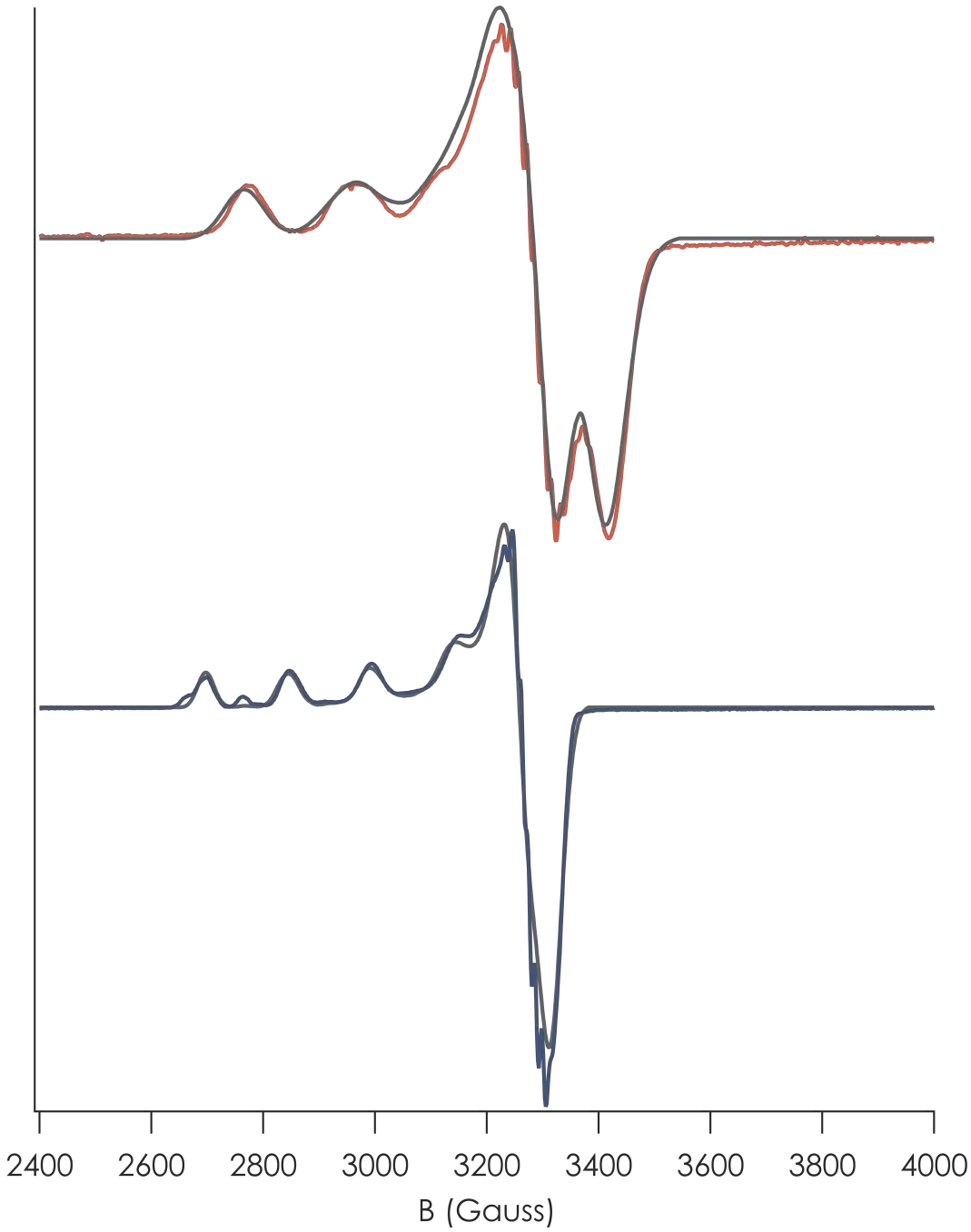
2400
2600
2800
3000
3200
3400
3600
3800
4000
B (Gauss)

Figure 2.23. Electronic absorption spectra of C112D/M121E azurin in 50 mM MES pH 5.5 (blue) and 50 mM CHES 10.0 (red) aqueous solutions at 298 K. The spectra are focused on the LF absorption band, which blue shifts ~ 7 kK on raising the pH from 5.5 to 10.0.

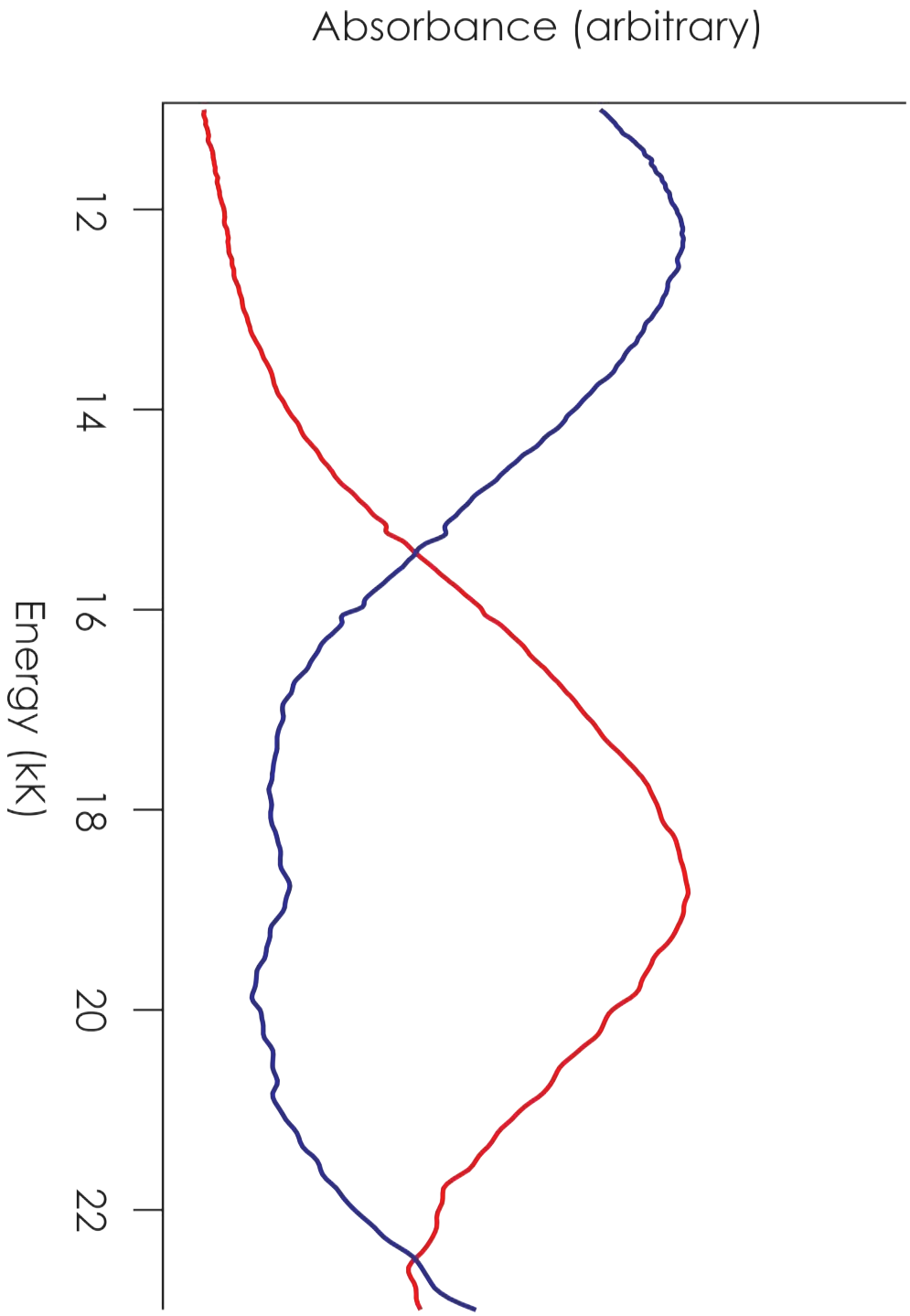
Absorbance (arbitrary)
Energy (kK)
12
14
16
18
20
22

Figure 2.24. Cu K-edge XAS of C112D/M121E azurin at pH 5.5 (blue, 50 mM MES), 7.0 (black, 50 mM HEPES), and 10.0 (red, 50 mM CHES) at 10 K. Spectra are the averages of two scans to K = 10 $Å^{-1}$. Inset: the 1s to 3d transition is highlighted. 2 scans were averaged for each spectrum, with absorbance normalized to the spline-corrected EXAFS region. Normalization error is taken as 5%. Each averaged scan corresponds to the first recorded per 1 x 10 mm spot.

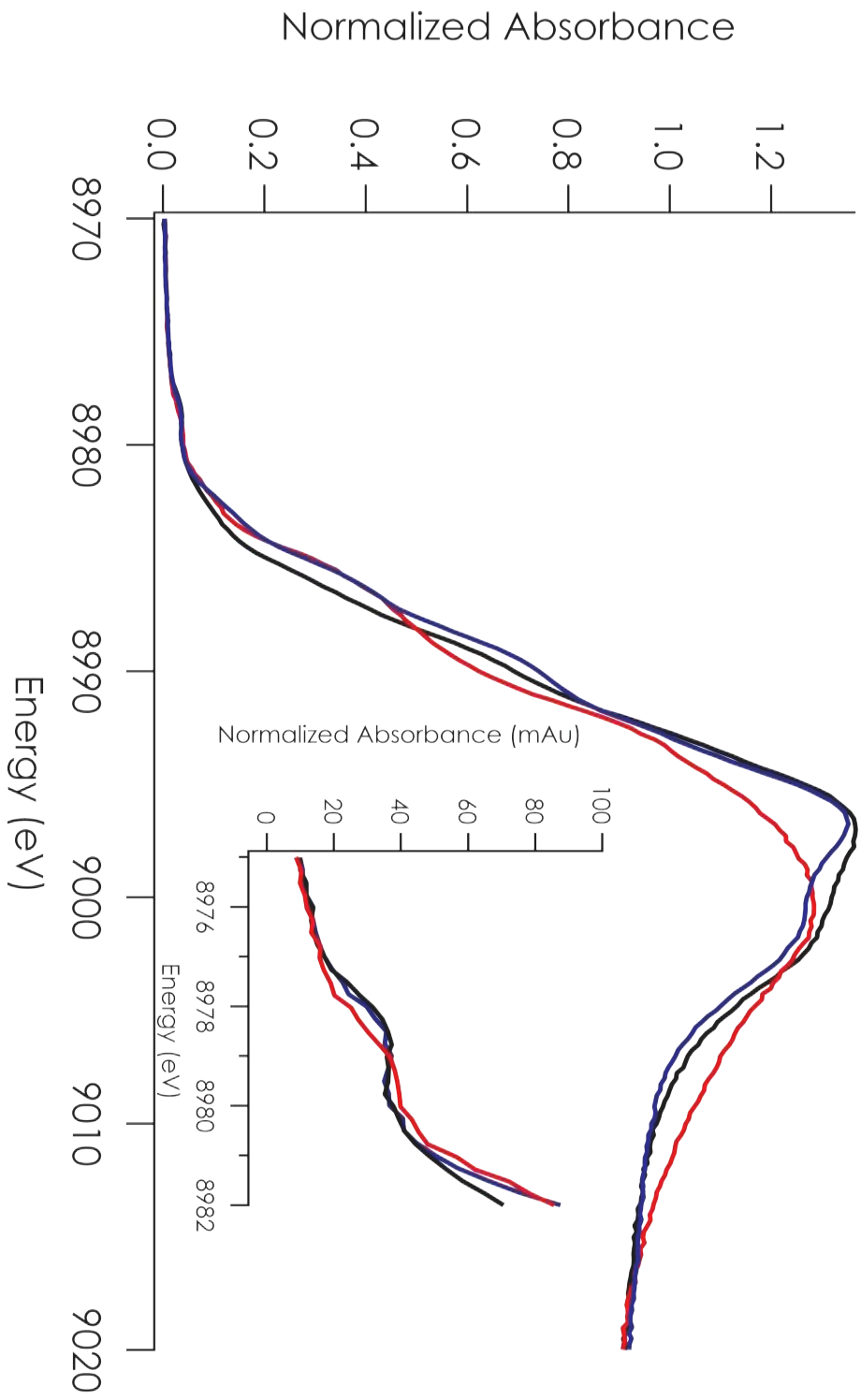
Normalized Absorbance
0.0
0.2
0.4
0.6
0.8
1.0
1.2
8970
8980
8990
9000
9010
9020
Energy (eV)
Normalized Absorbance (mAu)
0
20
40
60
80
100
8976
8978
8980
8982
Energy (eV)

Figure 2.25. Cu^{II} active-site region C112D/M121E azurin at pH 7.0 (2.1 Å, **a)** PDBID: 3NP3) and pH 9.0 (2.25 Å, **b)** PDBID: 3NP4). $2F_o$-F_c electron density maps are contoured at the 1σ level. Nitrogen atoms are blue; oxygen atoms are red.

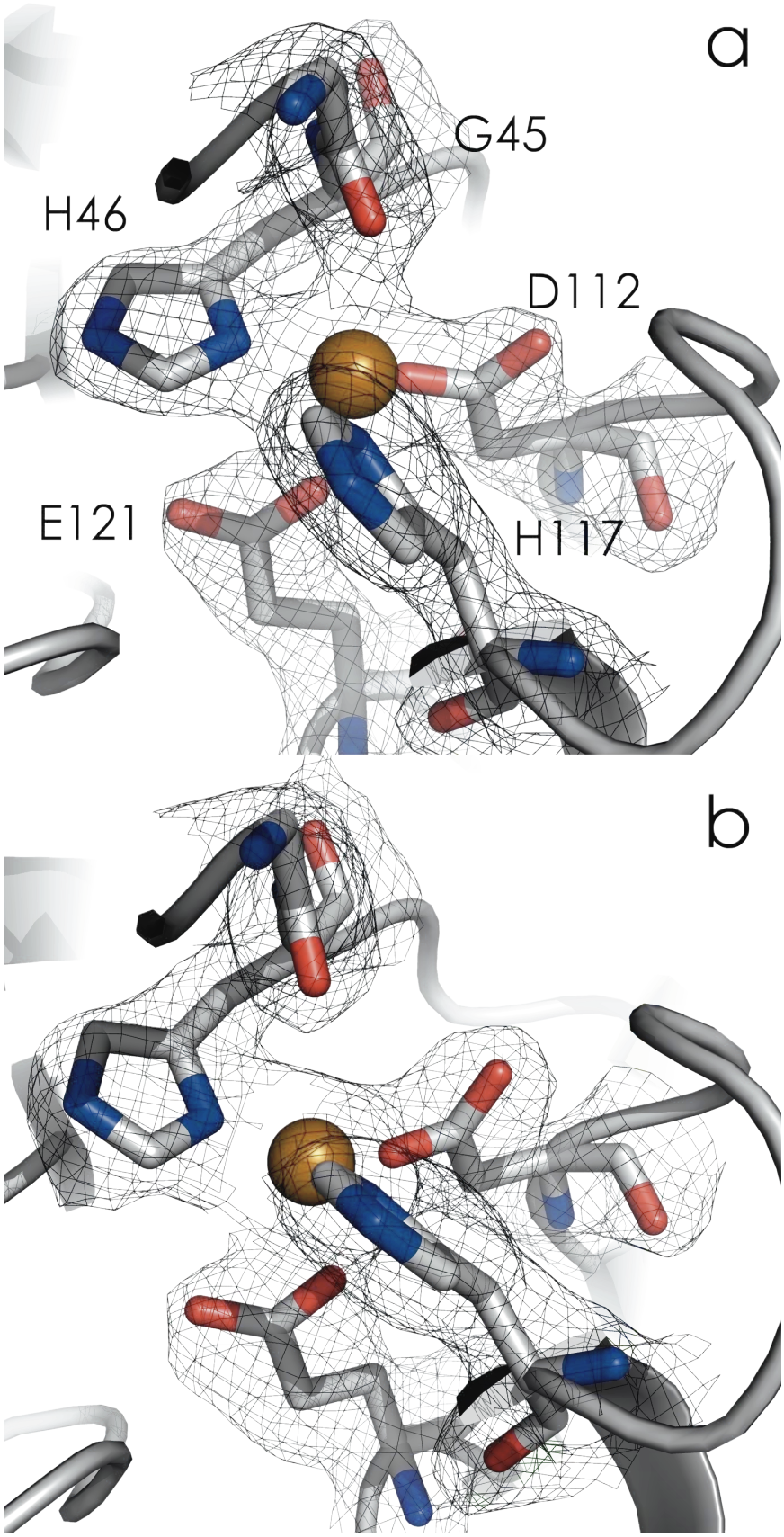
a
G45
H46
D112
E121
H117
b

Figure 2.26. Active-site region showing the H35-P36 interaction in C112D/M121E azurin at pH 7.0 (2.1 Å, a, PDBID: 3NP3) and pH 9.0 (2.25 Å, b, PDBID: 3NP4). $2F_o$-F_c maps are contoured at the 1σ level. Nitrogen atoms are blue; oxygen atoms are red.

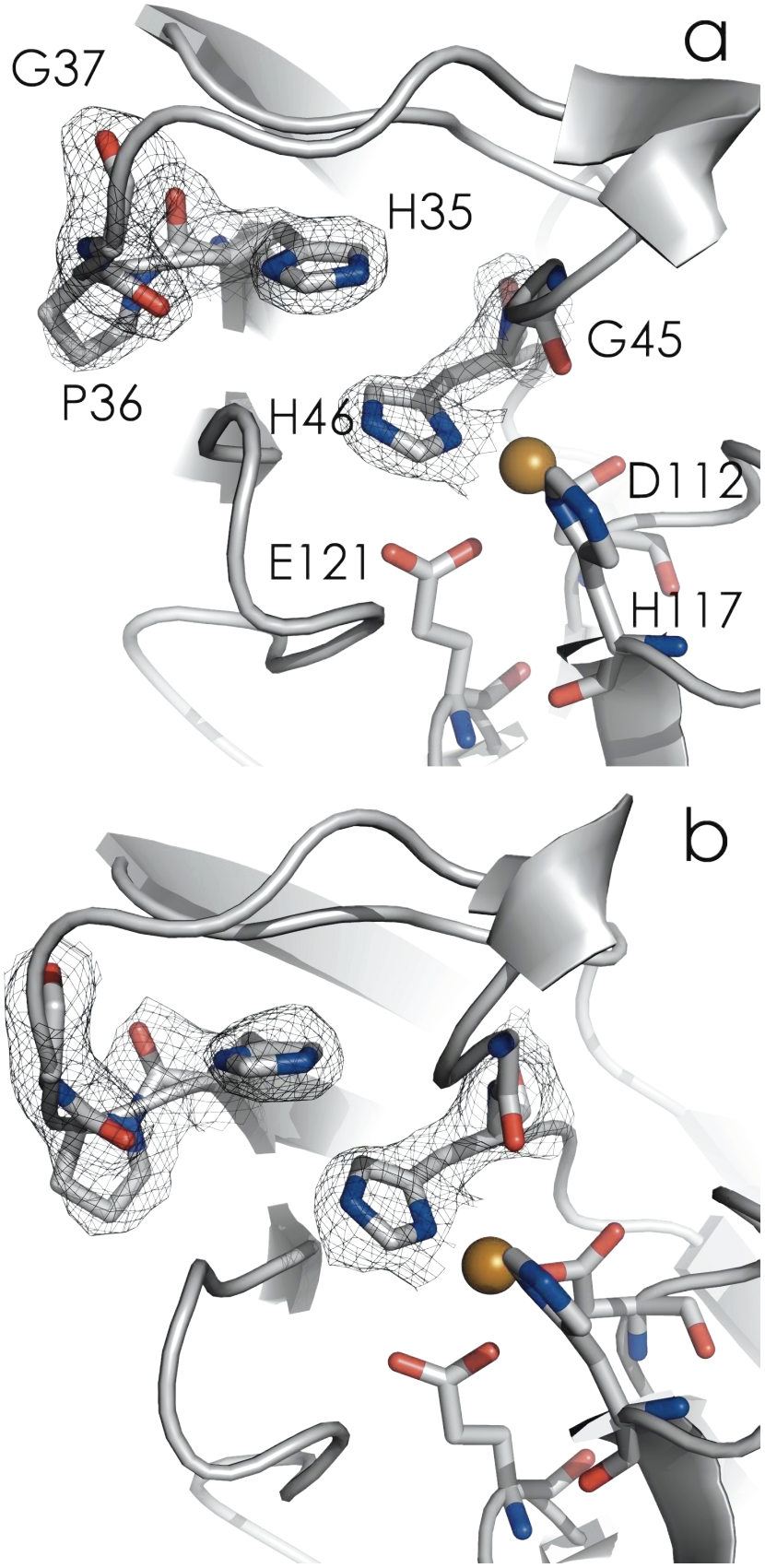
a
G37
H35
G45
P36
H46
D112
E121
H117
b

Figure 2.27. C_α structural alignment of pH 7.0 (2.1 Å, white, PDBID: 3NP3) and pH 9.0 (2.25 Å, periwinkle, PDBID: 3NP4) C112D/M121E azurin structures. Arrows are added for clarity to indicate the movement of H35 and H45 allowing ligation of Cu^{II} by E121.

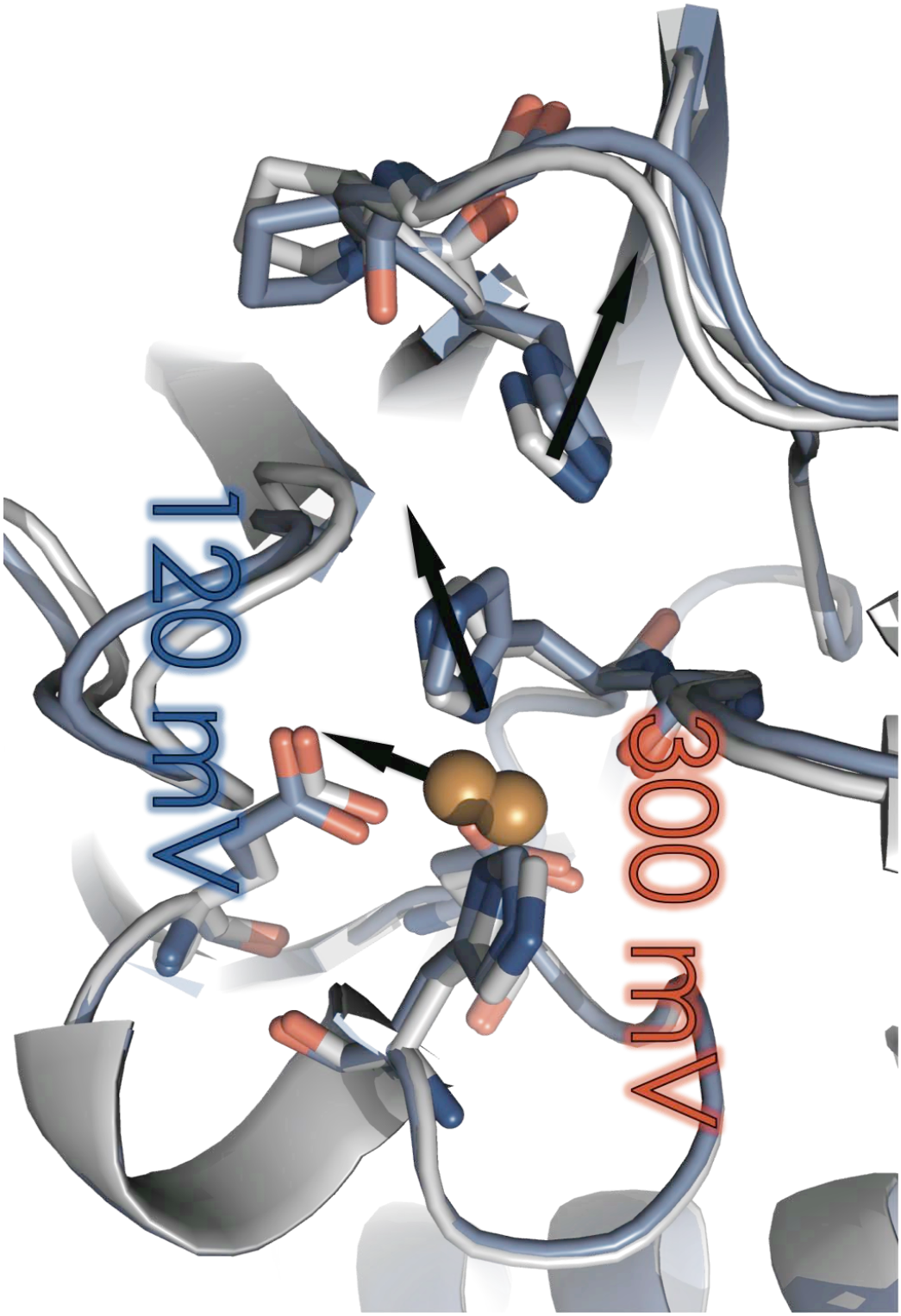
120mV
300 mV

Figure 2.28. 77 K frozen solution X-band (9.5 GHz) EPR spectra of C112D/M121H azurin in 50 mM Tris at indicated pH. Experimental spectra are blue, SpinCount simulations are gray. Spectra were recorded with 5 G modulation amplitude with 2 mW microwave power. With increasing pH, there is a decrease in g_z with a concomitant increase in $A_{||}$.

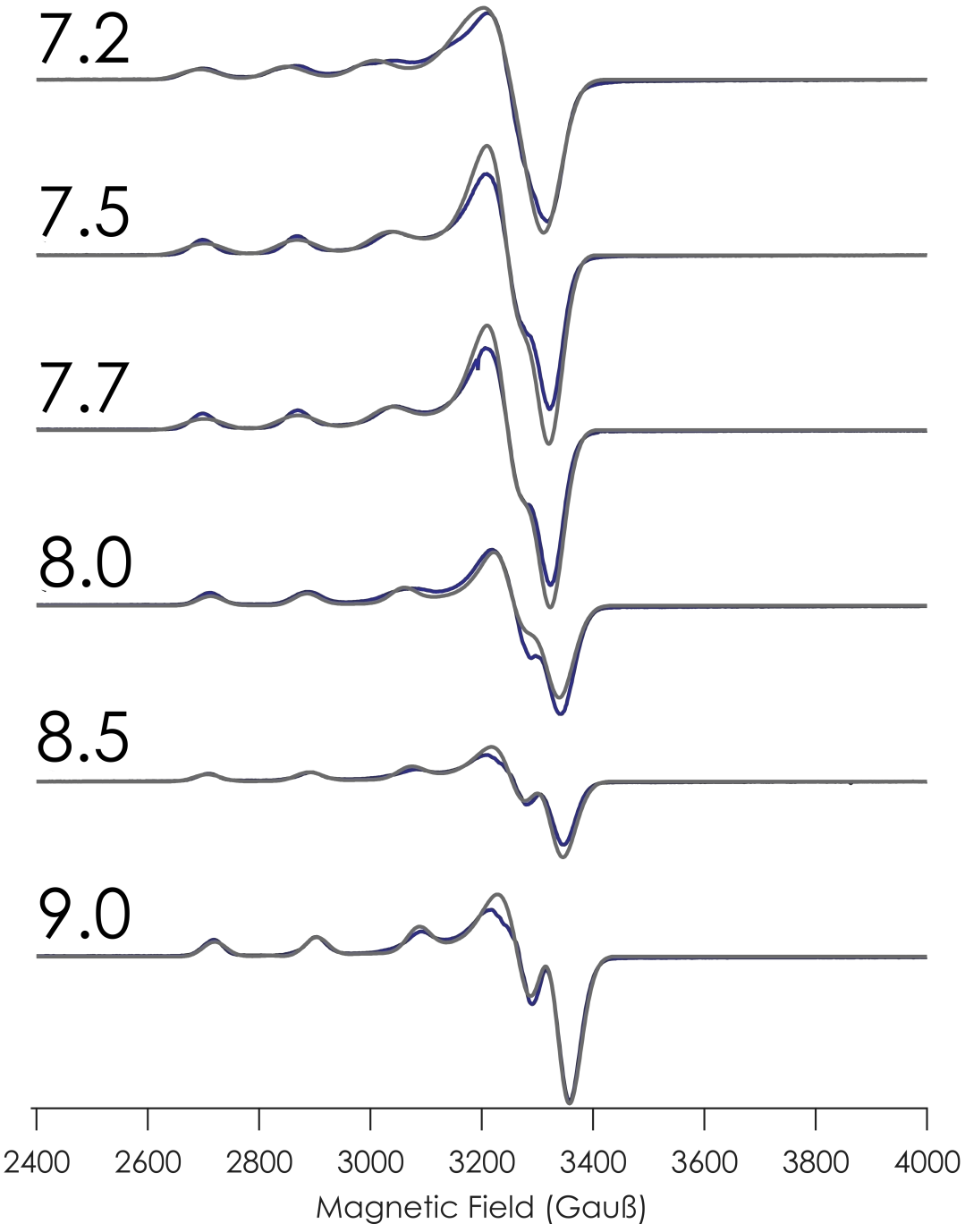
7.2
7.5
7.7
8.0
8.5
9.0
2400
2600
2800
3000
3200
3400
3600
3800
4000
Magnetic Field (Gauß)

Figure 2.29. Plot of g_z and $A_{||}$ for C112D/M121H azurin versus pH. Values extracted from SpinCount simulations of X-band (9.5 GHz) EPRs recorded in 77 K frozen 50 mM Tris solution. The simultaneous but inverse trends indicate that the increase in $A_{||}$ is attributable to an increasing spin dipolar term arising from a small deviation in g_z from g_e.

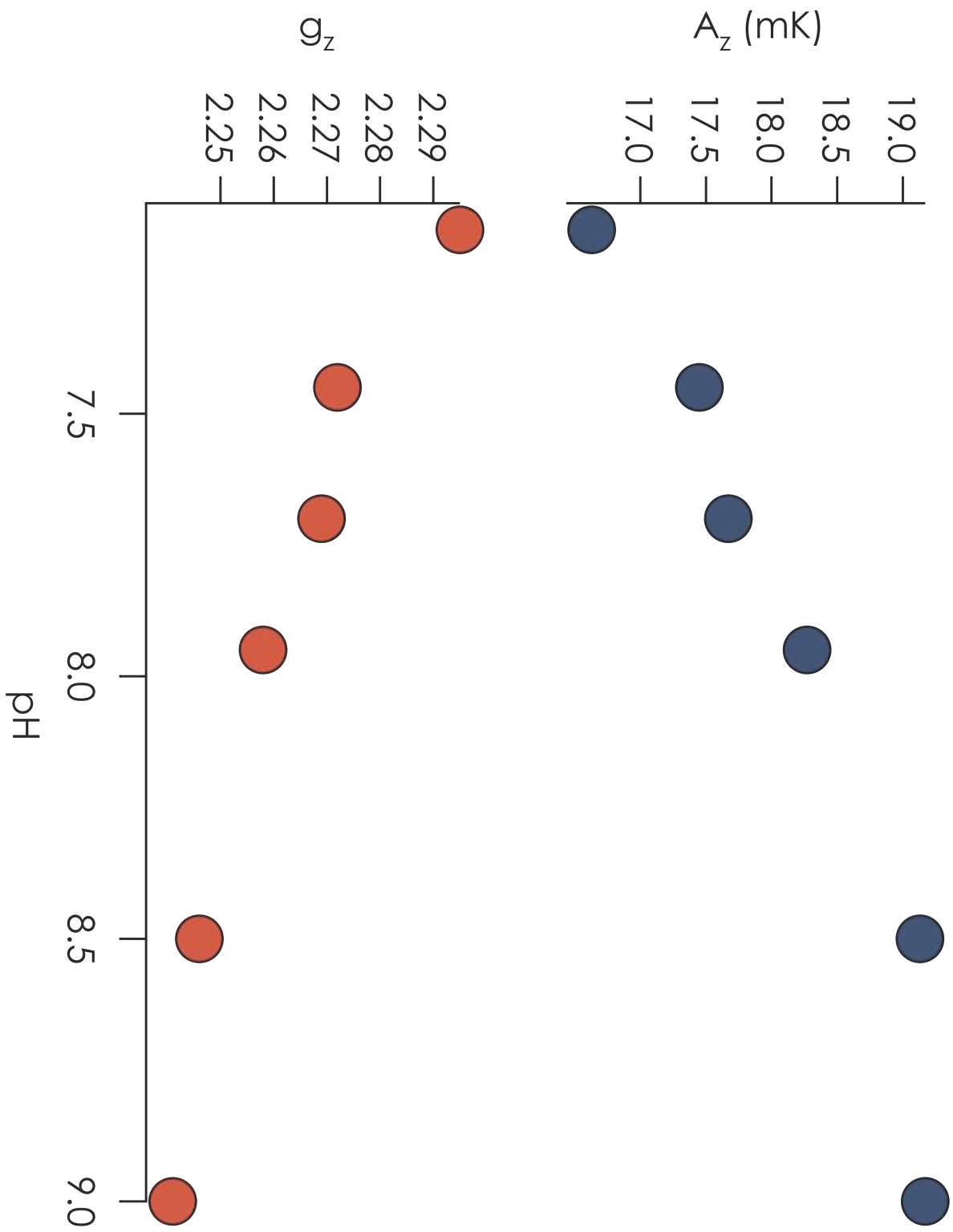
g_z
2.25
2.26
2.27
2.28
2.29
A_z (mK)
17.0
17.5
18.0
18.5
19.0
pH
7.5
8.0
8.5
9.0

Figure 2.30. Electronic absorption spectra of C112D/M121H in 50 mM Tris at indicated pH values at 298 K. The spectra are focused on the LF absorption band, which blue shifts ~ 2 kK as the pH is increased from 7.2 to 9.0.

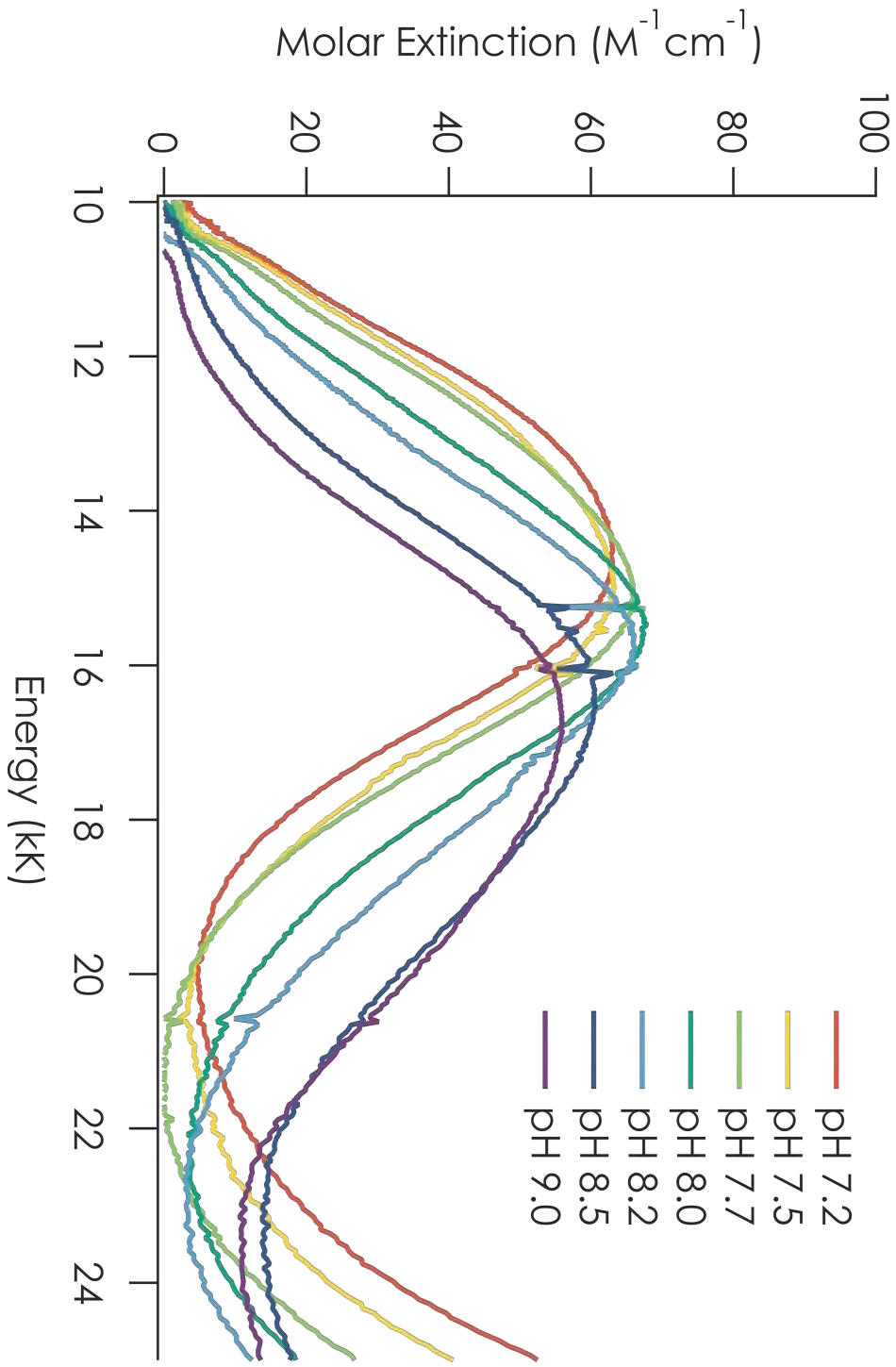
Molar Extinction ($M^{-1}cm^{-1}$)
0
20
40
60
80
100
Energy (kK)
10
12
14
16
18
20
22
24
pH 7.2
pH 7.5
pH 7.7
pH 8.0
pH 8.2
pH 8.5
pH 9.0

Figure 2.31. X-ray diffraction pattern of C112D/M121H azurin. 0.5º of oscillation was recorded. Diffraction is observed out to ~ 2.4 Å.

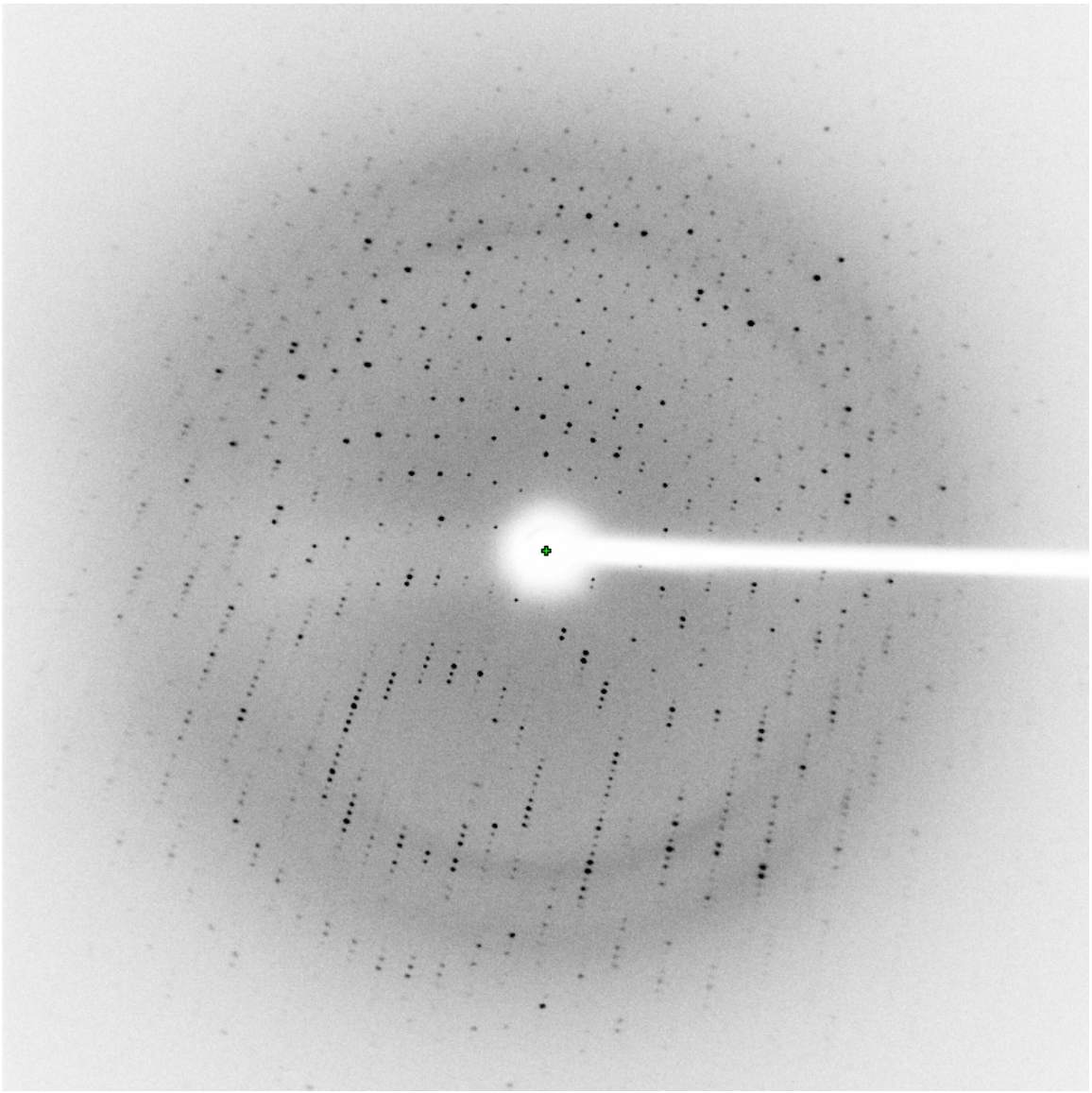

Figure 3.32. Cu K-edge XAS of C112D/M121H (blue) and C112D/M121E (red) azurin at pH 7.0 at 10 K. Inset: the 1s to 3d transition is highlighted. Negligible intensity change (within the 5% normalization error) in the 1s to 3d transition indicates that like E121 (based on evidence from crystallography), H121 is not coordinated at pH 7.0. Similar white-line structures support this assertion. 2 scans were averaged for each spectrum, with absorbance normalized to the spline-corrected EXAFS region. Normalization error is taken at 5%. Each averaged scan corresponds to the first recorded per 1 x 10 mm spot.

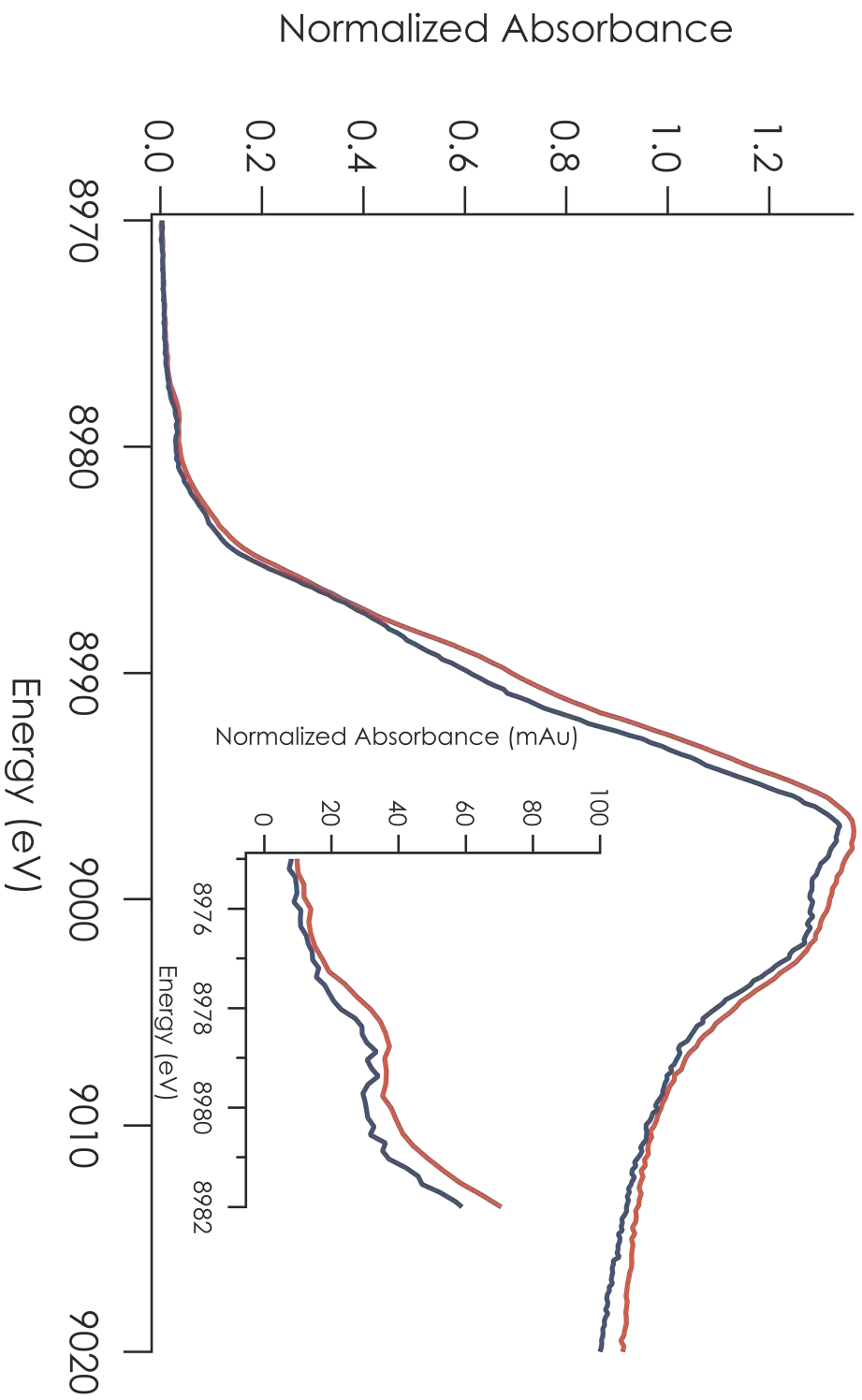
Normalized Absorbance
0.0
0.2
0.4
0.6
0.8
1.0
1.2
8970
8980
8990
9000
9010
9020
Energy (eV)
Normalized Absorbance (mAu)
0
20
40
60
80
100
8976
8978
8980
8982
Energy (eV)

Figure 3.33. Putative C112D/M121H Cu binding site built by C112D substitution to the *A. denitrificans* M121H azurin structure (PDBID: 1A4B). Model created in PyMol. Oxygen atoms are red, nitrogen atoms are blue.

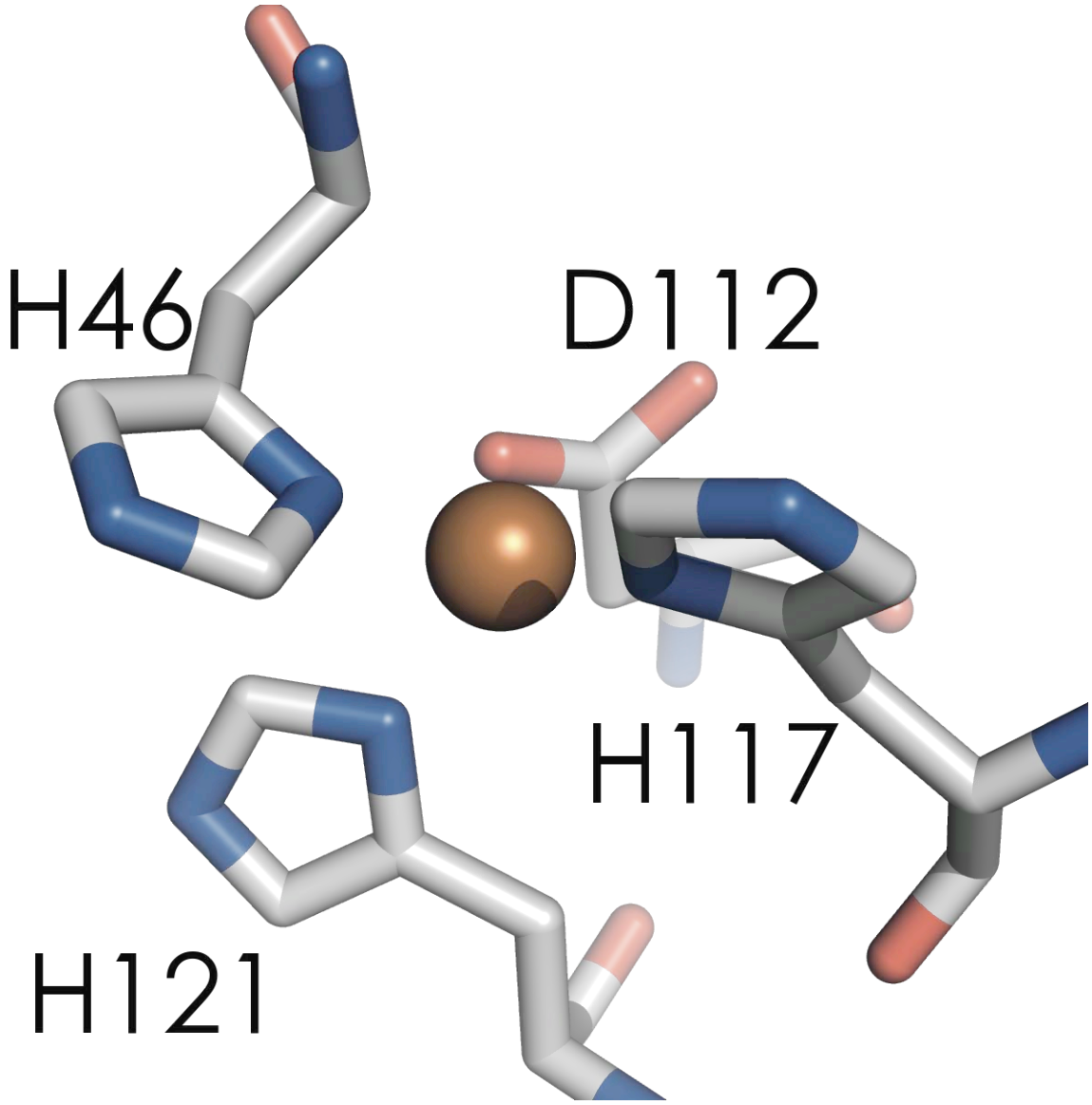
H46
D112
H117
H121

Figure 2.34. Cu^{II} K-edge EXAFS and Fourier transform thereof (blue) from C112D/M121H azurin. The best OPT fit to scattering paths calculated from the structural model by FEFF7 is overlaid in gray. This fit indicates a coordination by 3-4 N/O ligands at 1.99 Å, with one other N/O at 2.56 Å. This scatterer may be N_ε from H121, a non-coordinated carboxylate O from D112, or the G45 carbonyl O. Low-k residual likely corresponds to multiple-scattering paths that were not explicitly modeled.

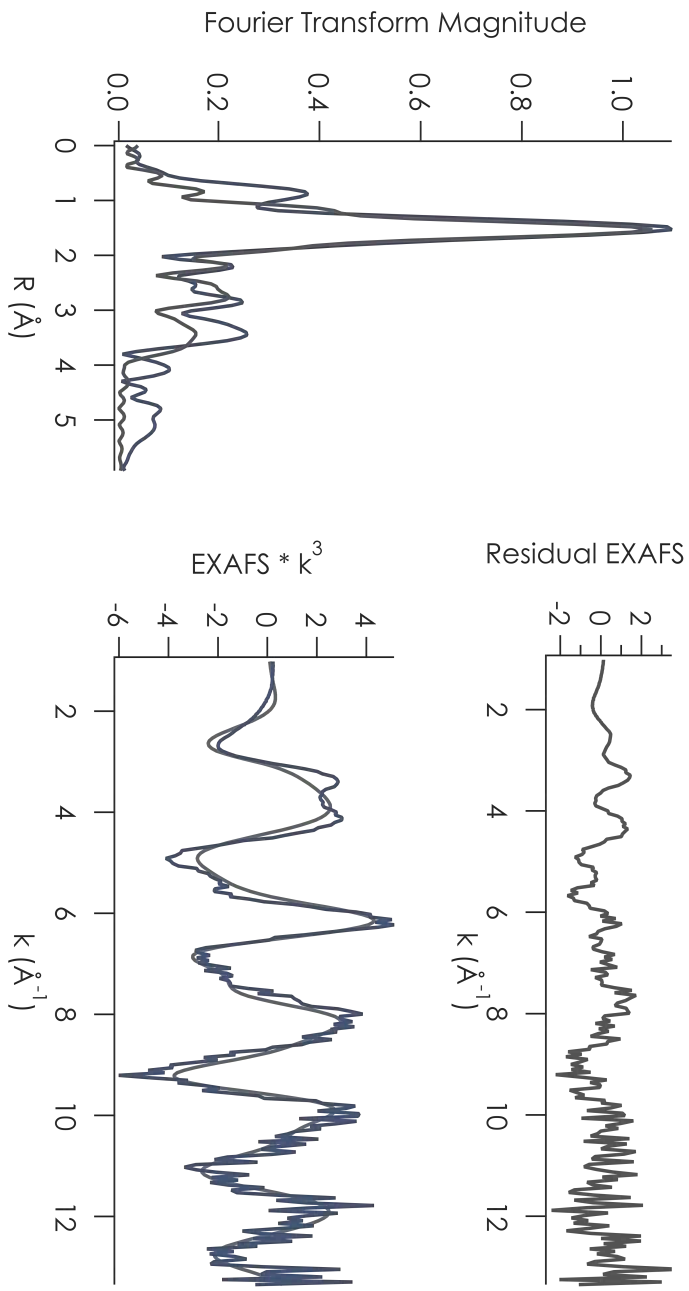
Fourier Transform Magnitude
0.0
0.2
0.4
0.6
0.8
1.0
0
1
2
3
4
5
R (Å)
EXAFS * k3
-6
-4
-2
0
2
4
2
4
6
8
10
12
k (Å-1)
Residual EXAFS
-2
0
2
2
4
6
8
10
12
k (Å-1)

APPENDIX 2-A

Gene sequences for C112D/M121X (X = E, H, L) azurins. These maps were made with Ape.

```
Tue Aug  3 04:45:30 2010
C112DM121E_Azurin.ape
Text Map
          40        50        60        70        80
         *         *         *         *         *
    34 ATGCTGCGTAAGCTGGCTGCAGTGTCTCTGCTGTCTCTGCTGTCTGCTCC
       M  L  R  K  L  A  A  V  S  L  L  S  L  L  S  A  P
       >>>
       Start
       >>>>>>>>>>>>>>>>>>>>>>>>>>>>>>>>>>>>>>>>>>>>>>>>>>>
       Periplasmic translocation leader sequence

          90        100       110       120       130
         *         *         *         *         *
    84 GCTGCTGGCTGCTGAATGCTCCGTTGATATCCAGGGTAATGATCAGATGC
        L  L  A  A  E  C  S  V  D  I  Q  G  N  D  Q  M  Q
       >>>>>>>>>>
       Periplasmic translocation leader sequence

          140       150       160       170       180
         *         *         *         *         *
   134 AGTTCAACACCAACGCCATCACCGTCGACAAGAGCTGCAAGCAGTTCACT
         F  N  T  N  A  I  T  V  D  K  S  C  K  Q  F  T

          190       200       210       220       230
         *         *         *         *         *
   184 GTTAACCTGTCTCACCCAGGTAACCTGCCGAAGAACGTTATGGGTCACAA
       V  N  L  S  H  P  G  N  L  P  K  N  V  M  G  H  N

          240       250       260       270       280
         *         *         *         *         *
   234 CTGGGTTCTGTCCACCGCGGCTGACATGCAAGGCGTTGTCACTGACGGTA
        W  V  L  S  T  A  A  D  M  Q  G  V  V  T  D  G  M

          290       300       310       320       330
         *         *         *         *         *
   284 TGGCTAGCGGTCTGGATAAAGACTACCTGAAGCCGGATGACTCTCGAGTT
         A  S  G  L  D  K  D  Y  L  K  P  D  D  S  R  V

          340       350       360       370       380
         *         *         *         *         *
   334 ATCGCCCACACCAAGCTGATCGGATCCGGTGAAAAAGACTCCGTTACTTT
       I  A  H  T  K  L  I  G  S  G  E  K  D  S  V  T  F

          390       400       410       420       430
         *         *         *         *         *
   384 CGACGTTTCCAAGCTTAAAGAAGGTGAACAGTACATGTTCTTCGATACTT
        D  V  S  K  L  K  E  G  E  Q  Y  M  F  F  D  T  F
                                                 >>>>>>>
                                                 Metal Binding Loop

          440       450       460       470       480
         *         *         *         *         *
   434 TCCCGGGCCACTCCGCGCTGGAAAAGGGTACCCTGACTCTGAAATAG
         P  G  H  S  A  L  E  K  G  T  L  T  L  K  *
                                                  >>>
                                                  Stop

       >>>>>>>>>>>>>>>>>>>>>>
       Metal Binding Loop
```

```
Tue Aug  3 04:36:35 2010
C112DM121H_Azurin.ape
Text Map
       20        30        40        50        60
             *         *         *         *         *
    19 ATGCTGCGTAAGCTGGCTGCAGTGTCTCTGCTGTCTCTGCTGTCTGCTCC
       M  L  R  K  L  A  A  V  S  L  L  S  L  L  S  A  P
       >>>
       Start
       >>>>>>>>>>>>>>>>>>>>>>>>>>>>>>>>>>>>>>>>>>>>>>>>>>
       Periplasmic translocation leader sequence

       70        80        90        100       110
             *         *         *         *         *
    69 GCTGCTGGCTGCTGAATGCTCCGTTGATATCCAGGGTAATGATCAGATGC
        L  L  A  A  E  C  S  V  D  I  Q  G  N  D  Q  M  Q
       >>>>>>>>>>
       Periplasmic translocation leader sequence

       120       130       140       150       160
             *         *         *         *         *
   119 AGTTCAACACCAACGCCATCACCGTCGACAAGAGCTGCAAGCAGTTCACT
         F  N  T  N  A  I  T  V  D  K  S  C  K  Q  F  T

       170       180       190       200       210
             *         *         *         *         *
   169 GTTAACCTGTCTCACCCAGGTAACCTGCCGAAGAACGTTATGGGTCACAA
       V  N  L  S  H  P  G  N  L  P  K  N  V  M  G  H  N

       220       230       240       250       260
             *         *         *         *         *
   219 CTGGGTTCTGTCCACCGCGGCTGACATGCAAGGCGTTGTCACTGACGGTA
        W  V  L  S  T  A  A  D  M  Q  G  V  V  T  D  G  M

       270       280       290       300       310
             *         *         *         *         *
   269 TGGCTAGCGGTCTGGATAAAGACTACCTGAAGCCGGATGACTCTCGAGTT
         A  S  G  L  D  K  D  Y  L  K  P  D  D  S  R  V

       320       330       340       350       360
             *         *         *         *         *
   319 ATCGCCCACACCAAGCTGATCGGATCCGGTGAAAAAGACTCCGTTACTTT
       I  A  H  T  K  L  I  G  S  G  E  K  D  S  V  T  F

       370       380       390       400       410
             *         *         *         *         *
   369 CGACGTTTCCAAGCTTAAAGAAGGTGAACAGTACATGTTCTTCGATACTT
        D  V  S  K  L  K  E  G  E  Q  Y  M  F  F  D  T  F
                                                >>>>>>>
                                                112-121 Metal Binding Loop

       420       430       440       450       460
             *         *         *         *         *
   419 TCCCGGGCCACTCCGCGCTGCACAAGGGTACCCTGACCCTGAAATAG
         P  G  H  S  A  L  H  K  G  T  L  T  L  K  *
       >>>>>>>>>>>>>>>>>>>>>>>                   >>>
       112-121 Metal Binding Loop                Stop
```

```
Tue Aug  3 04:51:55 2010
C112DM121L_Azurin.ape
Text Map
       50        60        70        80        90
             *         *         *         *         *
    49 ATGCTGCGTAAGCTGGCTGCAGTGTCTCTGCTGTCTCTGCTGTCTGCTCC
       M  L  R  K  L  A  A  V  S  L  L  S  L  L  S  A  P
       >>>
       Start
       >>>>>>>>>>>>>>>>>>>>>>>>>>>>>>>>>>>>>>>>>>>>>>>>>>
       Perpiplasmic translocation leader sequence

       100       110       120       130       140
             *         *         *         *         *
     99 GCTGCTGGCTGCTGAATGCTCCGTTGATATCCAGGGTAATGATCAGATGC
         L  L  A  A  E  C  S  V  D  I  Q  G  N  D  Q  M  Q
       >>>>>>>>>>
       Perpiplasmic translocation leader sequence

       150       160       170       180       190
             *         *         *         *         *
    149 AGTTCAACACCAACGCCATCACCGTCGACAAGAGCTGCAAGCAGTTCACT
          F  N  T  N  A  I  T  V  D  K  S  C  K  Q  F  T

       200       210       220       230       240
             *         *         *         *         *
    199 GTTAACCTGTCTCACCCAGGTAACCTGCCGAAGAACGTTATGGGTCACAA
       V  N  L  S  H  P  G  N  L  P  K  N  V  M  G  H  N

       250       260       270       280       290
             *         *         *         *         *
    249 CTGGGTTCTGTCCACCGCGGCTGACATGCAAGGCGTTGTCACTGACGGTA
         W  V  L  S  T  A  A  D  M  Q  G  V  V  T  D  G  M

       300       310       320       330       340
             *         *         *         *         *
    299 TGGCTAGCGGTCTGGATAAAGACTACCTGAAGCCGGATGACTCTCGAGTT
          A  S  G  L  D  K  D  Y  L  K  P  D  D  S  R  V

       350       360       370       380       390
             *         *         *         *         *
    349 ATCGCCCACACCAAGCTGATCGGATCCGGTGAAAAAGACTCCGTTACTTT
       I  A  H  T  K  L  I  G  S  G  E  K  D  S  V  T  F

       400       410       420       430       440
             *         *         *         *         *
    399 CGACGTTTCCAAGCTTAAAGAAGGTGAACAGTACATGTTCTTCGATACTT
         D  V  S  K  L  K  E  G  E  Q  Y  M  F  F  D  T  F
                                                  >>>>>>>
                                                  Metal Binding Loop

       450       460       470       480       490
             *         *         *         *         *
    449 TCCCGGGCCACTCCGCGCTGCTGAAGGGTACCCTGACCCTGAAATAG
          P  G  H  S  A  L  L  K  G  T  L  T  L  K  *
       >>>>>>>>>>>>>>>>>>>>>>>>                  >>>
       Metal Binding Loop                        Stop
```

APPENDIX 2-B

REDACTED ~~The initial characterization of azurins C112D/M121X (X = H, E, L) appeared as a Communication in *Inorganic Chemistry*, Volume 48 Issue 4, Pages 1278-1280. The communication is reproduced here with permission from the American Chemical Society.~~ REDACTED

Chapter 3

TYPE ZERO COPPER

INTRODUCTION

We had been testing the proposition that sulfur ligation is essential for the widespread electron transfer characteristics of type 1 proteins, as successful replacement of soft sulfur donors with hard ligands could greatly enhance protein lifetimes in catalytic processes involving dioxygen or other powerful oxidants. In preliminary work on the Mizoguchi *Pseudomonas aeruginosa* C112D azurin scaffold,[1-2] we found that the additional mutation M121L generates a protein with a high Cu(II/I) reduction potential. However, C112D/M121L azurin was anomalous; its spectroscopic properties and redox potential made it appear a hybrid of type 1 and type 2 copper proteins. However, it does not have a sulfur; this obviates the possibility of enhanced Cu-Sσ LMCT giving rise through Solomon's "coupled distortion" to the green type 1.5 copper site.[3-5] In accord with the lack of sulfur, the C112D/M121L Cu^{II} g_z is accordingly fairly high.[6] We shall now see through spectroscopic and structural investigations that C112D/M121L azurin, as well as the other constituents of the C112D/M121X (X = L, F, I) hydrophobic series are in a class unto their own. Moreover, we shall also behold their striking ET reactivity relative to C112D azurin. To do so, we again called upon the help of Keiko Yokoyama, but also recruited the X-ray expertise of Serena DeBeer, then at Stanford Synchrotron Lightsource (SSRL). Portions of this work have been published in *Nature Chemistry*.

MATERIALS AND METHODS

Site-Directed Mutagenesis

SDM was carried out as described in Chapter 2 using the following nucleotides:

C112D/M121F:

5'-CCCGGGCCACTCCGCGCTG**TTT**AAGGGTACCCTGACCCTGAAG-3';

C112D/M121I:

5'-CCCGGGCCACTCCGCGCTG**ATT**AAGGGTACCCTGACCCTGAAG-3'

Protein Overexpression and Purification

C112D/M121X (X = M, L, F, I) azurins were overexpressed and purified as described in Chapter 2. Purity was assessed by SDS-PAGE and ESI-MS. Reconstitution with Cu^{II} was conducted in 50 mM HEPES pH 7.0.

Spectroscopy

UV/vis, EPR, and X-ray absorption spectra were collected as described in Chapter 2. Co^{II} spectroscopy was not performed for the hydrophobic series.

Electrochemistry

Electrochemical measurements were conducted as in Chapter 2. ET rate constants from azurin-bound Cu through variable alkane chain-length SAMS were calculated from CV peak separations by the formalisms of Laviron.[7]

X-ray Crystallography

Crystal growth and diffraction were carried out as described in Chapter 2.

RESULTS

Protein Overexpression and Purification

Sequences of C112D/M121X (X = F, I) azurin are included in Appendix 3-A. C112D/M121X (X = L, F, I) azurins overexpressed in *E. coli*. Interestingly, populations of Zn^{II} C112D/M121F and C112D/M121I azurins were not observed (by Co^{II} assay) during HiPrep Q FF column chromatography (Figure 3.1). This implies lower metal affinity in these two proteins. Accordingly, Cu^{II} reconstituted C112D/M121X (X = L, F, I) azurins were observed to lose metal to pH 7.0 NaP_i buffer over time. While several experiments described below were conducted in NaP_i or Tris, effects from buffer competition were accounted for in their analysis. However, later holoprotein manipulation (Chapters 4-5) was conducted in non-coordinating HEPES buffer.* Apoprotein yields as measured by A_{280} were high, typically on the order of 40 mg homogeneous protein per liter of growth culture following size-exclusion chromatography (Figure 3.2). ESI-MS gave molecular masses for C112D/M121F: 13973 (calc), 13970.6 (exp); C112D/M121I: 13939 (calc), 13937.0 (exp) (Figure 3.3).

Structural Studies

Crystals of C112D/M121X (X=M,L,F,I) azurins diffracted to high resolution (reflections visible to 1.6 Å) despite the limitations of laboratory X-ray sources. This afforded higher-resolution data for C112D (compared to the 2.4 Å, 298 K structure), facilitating more meaningful comparisons among the series of mutants. In all cases, only one crystal proved necessary to collect > 95% complete datasets to high resolution. Structures were solved readily by molecular replacement, and coordinates were refined with the resolution limit set by evaluation of Wilson plots and scaling/merging statistics (Table 3.1). Coordinate error may be obtained from the estimated standard uncertainty (e.s.u.) in atomic positions as calculated by REFMAC5 from R_{work} and R_{free}.[8] As the e.s.u.'s represent an average uncertainty for each structure, Cu^{II} to ligand bond distances are expected to exhibit increased precision owing to lower thermal disorder (B-factors) relative to the entire atomic ensemble. Coordinates and structure factors have been deposited in the PDB. Cu oxidation state was verified by

* Although the author notes that the photoreactivity of HEPES leads to the formation of a brown solution uniquely in the case of Cu^{II}-C112D/M121L azurin. As such, HEPES solutions of azurins were kept out of light.

comparing inner-sphere bond distances from Cu K-edge EXAFS to the crystallographic coordinates (Table 3.2, Figure 3.4).

In all cases the proteins packed as monomers around a copper coordination complex consisting of the N-terminal alanine of one azurin molecule and H83 of a second, with the remaining coordination sites occupied by one molecule of Tris buffer and solvent (Figure 3.5). The protein tertiary structure remains unchanged among the four proteins, displaying the characteristic ß-sandwich motif exhibited by members of the cupredoxin family.[9]

The double mutants display striking differences within both their inner and outer copper coordination spheres as compared to the C112D protein (Figures 3.6-3.9, Table 3.3). In the inner-sphere case, the remarkable perturbations manifest themselves in the orientation and position of the oxygen-donor ligands. G45, heretofore regarded as weakly interacting due to its remoteness to Cu^{II} (2.6 to 3.1 Å), now appears to function as a *bona fide* ligand to the metal, with distances ranging from 2.55 Å in C112D/M121I to a record 2.35 Å in C112D/M121L. In this extreme case, the Cu(II) is distorted out of the NNO (H46-H117-D112) trigonal plane. The absence of M121 thioether ligation likely promotes metal ion bonding to the G45 oxygen lone pair.

The orientation of the D112 carboxylate and by extension the distance of the second oxygen from copper precludes assignment of this residue as a true bidentate ligand in any of the four proteins. This long-standing error may be attributable to ambiguity stemming from the modest (2.4 Å) resolution of the earlier C112D structure.[10] Interestingly, major reorganization of the outer-sphere coordination structure accompanies positioning of the monodentate carboxylate (Fig. 3.10). In C112D/M121L and C112D/M121F, the nonligating carboxyl oxygens form hydrogen bonds with the backbone amides of N47 and F114 in nearly symmetric 120º arrangement. In contrast, this oxygen in C112D and C112D/M121I only approaches F114 close enough for hydrogen bonding. Distances notwithstanding, these atoms likely do not participate in hydrogen bonding owing to unfavorable O-H-N angles.

The two hydrogen bonds to D112 in C112D/M121L provide further impetus for Cu^{II} to seek stabilization by bonding to the G45 carbonyl. This release of Cu^{II} from interaction with

position 121 and movement toward 45 allows D112 the freedom to rearrange and reconstitute the rack responsible for the spectroscopic and reactivity properties of naturally occurring type 1 proteins. Furthermore, it appears that this rearrangement of hydrogen bonds is modulated by the hydrophobic packing of residue 121 (Fig. 3.11). Specifically, I121 and F121 sterically clash with F15, causing a reorientation of this residue. In the extreme case of C112D/M121F, this clash forces F15 to adopt multiple conformations. By contrast, F15 remains unperturbed by L121. This interaction likely causes the structural rearrangement leading to reorientation of the N47-D112-F114 hydrogen bonding network.

A structure of C112D/M121L azurin was also solved following a soak of a crystal in pH 10.0 cryoprotectant solution (Table 3.4). This structure was not deposited in the PDB. At pH > 7, WT azurin undergoes a backbone flip of P36-G37 as H35 is deprotonated (Chapter 1); this rearrangment allows the P36 backbone amide to hydrogen bond with the imidazole nitrogen.[11] This structural perturbation is observed in the pH 10-soaked C112D/M121L structure, confirming an elevated pH in the crystal (Figure 3.12). No significant rearrangement is observed in the metal binding site (Figure 3.13).

UV/Vis Spectroscopy

Electronic absorption parameters for Cu^{II} C112D/M121X (X= F,I) azurins were evaluated by metal titrations (Figure 3.14-3.15, Table 3.5) Each holoprotein displays a LF absorption system with maxima near 12.5 kK nm, as well as shoulders at ~ 32 kK nm assigned to imidazole to Cu^{II} LMCT (Figure 3.16). The intensities of the LF features are very similar to one another and to C112D/M121L, though bandshapes and positions differ somewhat. Multiple bands comprise this system as evidenced by a shoulder at 11 kK and another distinct absorption feature resolving at < 10 kK. LMCT intensties vary across the series, indicative of differential Cu-N orbital overlap owing to varying degrees of tetrahedral distortion among the proteins.

X-ray Absorption Spectroscopy

Two familiar features are present in the Cu^{II} XANES of C112D/M121X (X=L,F,I) azurins (Figure 3.17).[12-13] The first is the weak 1s to 3d absorption at ~8979 eV. The intensity of this transition increases on going from C112D/M121I to C112D/M121F to

C112D/M121L, which appears to correlate with the Cu^{II} to G45 carbonyl oxygen bond distance. The data suggest that Cu^{II}-O(G45) bonding promotes Cu^{II} 4p mixing into the 3d ground state, although the lack of polarized single-crystal XAS data precludes definitive p-orbital assignment.

The azurins also show variation in the shoulder near 8987 eV, the so-called "shakedown" transition. The energy and intensity of this transition have been used as metrics of site covalency. Although the poorly resolved nature of this feature precludes quantitative analysis of any differences in band positions, the decreased intensities could indicate that there is a slight increase in site covalency for the C112D/M121X (X=L,F,I).

EPR Spectroscopy

EPR spectra for glassed C112D (Figure 3.18) and C112D/M121X (X=L,F,I) azurins were recorded at X-band (9.5 GHz) (Table 3.6, Figure 3.19). Superhyperfine coupling to ^{14}N is observed under the experiment conditions in C112D as has been reported previously.[1] The C112D/M121X (X= F,I) proteins share with C112D/M121L a dissimilarity to C112D, with elevated g_z, anisotropic $g_\perp$, and decreased $A_{||}$ values. Such spin parameters are typical for tetrahedral Cu^{II} complexes.[14-16] Despite narrow linewidths, superhyperfine structure is not resolved in the C112D/M121X (X=L,F,I) azurins, demonstrating diminished coupling of the unpaired electron to the histidines in each case.

The following expressions for g values apply to Cu(II) in a distorted tetrahedral ligand field:[17]

$$\Delta g_x = -\frac{2\lambda\kappa_x^2}{\Delta_{yz}} \tag{3.1a}$$

$$\Delta g_y = -\frac{2\lambda\kappa_y^2}{\Delta_{xz}} \tag{3.1b}$$

$$\Delta g_z = -\frac{8\lambda\kappa_z^2}{\Delta_{x^2-y^2}} \tag{3.1c}$$

where Δg_i is the difference between observed g values and the free electron $g_e = 2.0023$, Δ_{di} is the energy difference between ground and excited states formed by transitions to orbital $3d_i$, λ is the Cu^{II} spin-orbit coupling constant (taken to be -830 cm^{-1}), and κ_i represents the orbital reduction factor along axis *i*. This latter parameter provides a metric of Cu^{II} character in the ground state. These expressions also hold for distorted O_h, $3d_{x2-y2}$ ground state systems, although Δ_{di} terms are exchanged for Δg_x and Δg_y. These expressions assume a ground state wavefunction that lacks any d_{z2} character.

Assuming a perturbed D_{4h} geometry for the C112D protein, a κ of ~0.78 is in agreement with the band at 13.26 kK in the absorption spectrum (Fig. 3.16). Calculated LF splittings based on assignment of the corresponding bands in the spectra of the C112D/M121X (X=L,F,I) proteins as d_{x2-y2} to d_{xy} transitions are in accord with experiment only if κ is near 0.85, which is consistent with the disappearance of superhyperfine broadening on going from the C112D protein to the double mutants. The LF transitions in C112D/M121F and C112D/M121I azurins should be lower in energy than in C112D/M121L, contrary to observation. However, as shown in the case of $IrCl_6^{2-}$,[18-19] mixing of ligand orbitals into the metal ground state leads to angular momentum quenching and in turn a decrease in the orbital reduction factor. The shortening of the Cu^{II}-O(G45) bond increases oxygen 2p mixing into the ground state, which would lead to a smaller κ in C112D/M121L azurin relative to the C112D/M121F and C112D/M121I proteins. Differences in covalency predicted by the $\Delta\kappa$ of ~0.05 going from C112D to the double mutants and $\Delta\kappa$ ~ 0.01 between C112D/M121L and

C112D/M121F,I are likely to be small, in accord with the lack of substantial change in the ~8987 eV XANES shakedown transition.

Hyperfine splitting arises from Fermi contact, spin dipolar, and orbital dipolar terms (Chapter 1).[20] Mixing of $4p_z$ into the electronic ground state of tetrahedral Cu^{II} sites decreases the spin dipolar term, leading to smaller axial hyperfine splittings. In the absence of polarized single crystal XAS we cannot definitively assign the ~8979 eV feature to a transition to a specific 4p orbital. However, the 1s to 3d intensities show no definitive correlation with the $A_{||}$, likely ruling out a spin dipolar mechanism for the low $A_{||}$ of these azurins (Figure 3.20).

Differing $g_\perp$ anisotropies could indicate varying degrees of d_{z2} mixing, possibly attributable to a low-lying LF excited state in each of the proteins. This anisotropy has been parameterized according to (Eq. 3.2):

$$R_g = \frac{2\left(\Delta g_y - \Delta g_x\right)}{\Delta g_y + \Delta g_x} \tag{3.2}$$

R_g values were interpolated with the plot from Solomon and co-workers to estimate $\%d_{z2}$ character in the ground state wavefunction.[20] These values do not correlate with Cu(II)-O(G45) distances or, for that matter, any other observable.

EPR was recorded of C112D/M121L azurin to assess the capacity for exogenous ligand binding. Sodium azide and sodium cyanide were added stoichiometrically to 1 mM solutions of protein. Following a 30 minute incubation time the solutions were desalted and concentrated. EPR spectra from these samples are indistinguishable within error from the untreated sample, except that the intensity of the cyanide treated protein is diminished likely owing to metal abstraction from the active site (Figure 3.21). Thus, the C112D/M121L metal site does not accommodate exogenous ligands.

Electrochemistry

The $Cu^{II/I}$ reduction potentials of C112D/M121I and C112D/M121F azurins at pH 7.0 were measured by direct electrochemistry on SAM modified monocrystalline gold bead electrodes. From CV, the potential of C112D/M121I is 310 mV vs NHE (Figure 3.22). For C112D/M121F, which coupled poorly to the electrode, signals could only be observed by SWV; its $Cu^{II/I}$ reduction potential is also 310 mV (Figure 3.23). Given the competition for metal binding from the phosphate buffer, it is likely that better current amplitudes can be achieved through the use of a non-coordinating buffer such as HEPES.

CV experiments using SAM-modified gold bead electrodes afford not only reduction potentials but also electron transfer (ET) rates.[7,21-22] Cu-electrode ET rates ($\Delta G^{o} = 0$) were calculated for C112D, C112D/M121L, and C112D/M121I for several SAM chain lengths (Figure 3.24). We were not able to determine ET rates for the C112D/M121F protein (weak CV signals). Importantly, the copper centers of C112D/M121L and C112D/M121I exhibit markedly enhanced ET reactivities relative to that of C112D.

DISCUSSION

Clearly hydrophobicity is not the only factor operating in the reduction potential tuning of C112D/M121L and, by extension, C112D/M121X (X = F, I) azurins. The electronic structure is wildly perturbed relative to the C112D protein, a consequence of distortion toward tetrahedral geometry as the Cu^{II} seeks stabilization by the G45 carbonyl. The proteins display a host of spectroscopic features that in-and-of themselves fingerprint this peculiar class of proteins. However, the Peisach-Blumberg "truth table"[6] paints a more evocative picture. The C112D/M121L (X = L, F, I) azurins are plotted by their EPR parameters g_z and $A_{||}$ along with several other azurin variants (Figure 2.25). These proteins clearly segregate into distinct regions – type 1 proteins with very low $A_{||}$ and simultaneously low g_z; type 2 proteins with high $A_{||}$ yet maintaining low g_z, and appropriately type 1.5 in between, with low g_z but intermediate (~ 10 mK) $A_{||}$.

Off on their own are the C112D/M121X (X = L, F, I) azurins – high g_z, intermediate $A_{||}$. These azurins are not "intermediate" between type 1 and type 2 – absence of sulfur ligation obviates intensive visible charge transfer. They also appear to have some appreciable d_{z2} character in their ground state wavefunctions evidenced by $g_\perp$ anisotropy. More significantly (as we shall see!), they have a reconstituted outer coordination sphere – the rack[23] is back. The consequences of this outer-sphere rearrangement manifest themselves in apparently enhanced ET properties. So do we call a rack-constrained, protein-bound tetrahedral Cu^{II} coordinated by entirely hard-ligand donor atoms?

Type zero copper.

REFERENCES

1. a) Mizoguchi, T.J.; Di Bilio, A.J.; Gray, H.B.; Richards, J.H. *J. Am. Chem. Soc.* **1992**, *114*, 10076-10078. b) Mizoguchi, T.J. Ph.D. Thesis, California Institute of Technology, **1996**.
2. Lancaster, K.M.; Yokoyama, K.; Richards, J.H.; Winkler, J.R.; Gray, H.B. *Inorg. Chem.* **2009**, *48*, 1278-1280.
3. Ghosh, S.; Xie, X.; Dey, A.; Sun, Y.; Scholes, C.P.; Solomon, E.I. *Proc. Natl. Acad. Sci. U.S.A.* **2009**, *106*, 4969-4974.
4. Messerschmidt, A.; Prade, L.; Kroes, S.J.; Sanders-Loehr, J.; Huber, R.; Canters, G.W. *Proc. Natl. Acad. Sci. U.S.A.* **1998**, *95*, 3443-3448.
5. Clark, K.M.; Yu, Y.; Marshall, N.M.; Sieracki, N.A.; Nilges, M.J.; Blackburn, N.J.; van der Donk, W.A.; Lu, Y. *J. Am. Chem. Soc.* **2010**, *132*, 10091-10101.
6. Peisach, J.; Blumberg, W.E. *Arch. Biochem. Biophys.* **1974**, *165*, 691-708.
7. Laviron, E.; *J. Electroanal. Chem.* **1979**, *101*, 19-28.
8. Murshudov, G.N.; Vagin, A.A.; Dodston, E.J. *Acta Crystallogr., Sect D: Biol. Crystallogr.* **1997**, *53*, 240-255.
9. Engman, K.C.; Sandberg, A.; Leckner, J.; Karlsson, B.G. *Protein Sci.* **2004**, *13*, 2706-2715.
10. Faham, S.; Mizoguchi, T.J.; Adman, E.T.; Gray, H.B.; Richards, J.H.; Rees, D.C. *J. Biol. Inorg. Chem.* **1997**, *2*, 464-469.
11. Nar, H.; Messerschmidt, A.; Huber, R.; van de Kamp, M.; Canters, G.W. *J. Mol. Biol.* **1991**, *221*, 765-772.
12. Shadle, S.E.; Penner-Hahn, J.E.; Schugar, H.; Hedman, B.; Hodgson, K.O.; Solomon, E.I. *J. Am. Chem. Soc.* **1993**, *115*, 767-776.
13. DeBeer, S.; Kiser, C.N.; Mines, G.A.; Richards, J.H.; Gray, H.B.; Solomon, E.I.; Hedman, B.; Hodgson, K.O. *Inorg. Chem.* **1999**, *38*, 433-438.
14. Sharnoff, M. *J. Chem. Phys.* **1965**, *42*, 3383-3395.
15. Bates, C.A.; Moore, W.S.; Standley, K.J.; Stevens, K.W.H. *Proc. Phys. Soc.* **1962**, *79*, 73-83.
16. Bencini, A.; Gatteschi, D.; Zanchini, C. *J. Am. Chem. Soc.* **1980**, *102*, 5234-5237.
17. Mabbs, F.E.; Machin, D.J. *Magnetism and Transition Metal Complexes*, Dover: Mineola, 2008.
18. Gewirth, A.A.; Cohen, S.L.; Schugar, H.J.; Solomon, E.I. *Inorg. Chem.* **1987**, *26*, 1133-1146.
19. Stevens, K.W.H. *Proc. R. Soc. London, Ser. A* **1953**, *219*, 542-555.
20. Griffiths, J.H.E.; Owen, J. *Proc. R. Soc. London, Ser. A* **1954**, *226*, 96-111.
21. Fujita, K.; Nakamura, N.; Ohno, H.; Leigh, B.S.; Niki, K.; Gray, H.B.; Richards, J.H. *J. Am. Chem. Soc.* **2004**, *126*, 13954-13961.
22. Yokoyama, K.; Leigh, B.S.; Sheng, Y.; Niki, K.; Nakamura, N.; Ohno, H.; Winkler, J.R.; Gray, H.B.; Richards, J.H. *Inorg. Chim. Acta* **2008**, *361*, 1095-1099.'
23. George, G.N. *EXAFSPAK* (Stanford Synchrotron Radiation Lightsource, Stanford Linear Accelerator Center, Stanford University: Stanford, CA).
24. DeLeon, J.M.; Rehr, J.J.; Zabinsky, S.I.; Albers, R.C. *Phys. Rev. B* **1991**, *44*, 4146-4156.
25. Rehr, J.J.; DeLeon, J.M.; Zabinsky, S.I.; Albers, R.C. *J. Am. Chem. Soc.* **1991**, *113*, 5135-5140.
26. Golombek, A.P.; Hendrich, M.P. *J. Magn. Reson.* **2003**, *165*, 33-48.
27. Kroes, S.J.; Hoitink, C.W.G.; Andrew, C.R.; Ai, J.; Sanders-Loehr, J.; Messerschmidt, A.; Hagen, W.R.; Canters, G.W. *Eur. J. Biochem.* **1996**, *240*, 342-351.
28. Pascher, T.; Karlsson, B.G.; Nordling, M. Malmström, B.G.; Vänngård, T. *Eur. J. Biochem.* **1993**, *212*, 289-296.
29. Romero, A.; Hoitink, C.W.; Nar, H.; Huber, R.; Messerschmidt, A.; Canters, G.W. *J. Mol. Biol.* **1993**, *229*, 1007-1021.

Table 3.1. Crystallographic data collection statistics for C112D/M121X (X = M, I, L, F) azurin at pH 7.0 and 100 K.

	C112D	C112D/M121L	C112D/M121I	C112D/M121F
PDBID	3FQY	3FPY	3FQ1	3FQ2
Space Group	C 2 2 2_1	P 6_1 2 2	C 2 2 2_1	C 2 2 2_1
A (Å)	48.930	48.620	48.500	48.360
B (Å)	55.080	48.620	54.800	54.760
C (Å)	94.440	276.311	95.780	95.540
α	90°	90°	90°	90°
β	90°	90°	90°	90°
γ	90°	120°	90°	90°
Resolution	19.84 – 1.90 Å	24.22 – 2.1 Å	19.99 – 1.90 Å	18.12 – 1.91 Å
Reflections	9441 (677)	10944 (546)	10344 (715)	9230 (476)
Completeness	95.7% (92.60%)	93.6% (68.16%)	99.6% (100%)	95.6% (69.58%)
Multiplicity	3.5 (3.1)	8.3 (4.8)	4.1 (2.0)	3.5 (2.9)
I/σI	13.8 (2.4)	7.5 (2.9)	9.0 (3.7)	15.9 (9.1)
R_{work}	18.6% (24.7%)	17.5% (20.6%)	19.8% (24.6%)	20.0% (21.2%)
R_{free}	24.4% (34.5%)	23.6% (26.9%)	25.6% (28.3%)	24.5% (31.4%)
e.s.u. (R_{work})	0.168 Å	0.164 Å	0.170 Å	0.185 Å
e.s.u. (R_{free})	0.162 Å	0.168 Å	0.165 Å	0.165 Å

Table 3.2 C112D/M121X (X = L, F, I) Cu^{II} K-edge EXAFS simulations. EXAFS were fit in OPT[23] using paths calculated by FEFF7[24,25]. Coordination numbers (CN) were held constant while distances (R) and Debye-Waller factors (σ^2) were allowed to float. Error in distances are estimated to be 0.02-0.03 Å and 25% for coordination numbers. Fits were performed over the entire (0 to 6.0 Å) Fourier transform window. Goodness of fit is measured by F, defined as $\left[\left(\sum_i^n \left[k_i^3\left(\mathrm{EXAFS}_{\mathrm{obs}} - \mathrm{EXAFS}_{\mathrm{calc}}\right)_i\right]\right)^2 \Big/ n\right]^{1/2}$. F could be dramatically improved by data smoothing, but only fits to raw data are reported.

C112D/M121L Azurin

Fit Number	Path	CN	R(Å)	σ^2	F
1	Cu to N/O	3	1.96	0.00247	0.40
2	Cu to N/O	4	1.96	0.00395	0.37
3	Cu to N/O	4	1.96	0.00394	0.34
	Cu to C/N (MS)	8	4.17	0.00509	

C112D/M121F Azurin

Fit Number	Path	CN	R(Å)	σ^2	F
1	Cu to N/O	3	1.97	0.00208	0.43
2	Cu to N/O	4	1.97	0.0034	0.35
3	Cu to N/O	4	1.97	0.00288	0.30
	Cu to C/N (MS)	8	4.16	0.00603	

C112D/M121I Azurin

Fit Number	Path	CN	R(Å)	σ^2	F
1	Cu to N/O	3	1.98	0.00252	0.45
2	Cu to N/O	4	1.98	0.00388	0.40
3	Cu to N/O	4	1.97	0.00448	0.36
	Cu to C/N (MS)	8	4.13	0.00571	

Table 3.3. Selected interatomic distances (Å) and angles in the active sites of C112D/M121X (X = M, L, F, I) azurins.

	C11D	C112D/M121L	C112D/M121F	C112D/M121I
O(G45) - Cu	2.59	2.35	2.44	2.53
N_{δ}(H46) - Cu	2.05	1.94	1.97	1.98
$O_{\varepsilon 1}$(D112) - Cu	1.92	1.92	2.00	2.07
$O_{\varepsilon 2}$(D112) - Cu	2.80	3.42	3.27	3.05
N_{δ}(H117) - Cu	2.04	2.04	1.99	2.10
$O_{\varepsilon 2}$(E112) - N_{NH}(N47)	4.01	3.25	3.15	3.60
$O_{\varepsilon 2}$(E112) - N_{NH}(F114)	2.79	2.90	3.08	2.99
N_{NH}(F114)-$O_{\varepsilon 2}$(E112) - N_{NH}(N47)	117.82º	126.89º	123.96º	121.21º
C_{γ}(E112)-Oε2(E112) – N_{NH}(N47)	68.64º	103.79º	103.99º	82.34º
Cγ(E112)-Oε2(E112) – N_{NH}(F114)	166.67º	128.78º	130.96º	153.81º

Table 3.4. Crystallographic data collection statistics for C112D/M121L azurin at pH 10.0 and 100 K.

Space Group	P 6_1 2 2
A (Å)	48.028
B (Å)	48.028
C (Å)	279.154
α	90°
β	90°
γ	120°
Resolution	19.49 – 2.07 Å
Reflections	11471 (618)
Completeness	94.89% (73.77%)
Multiplicity	
I/σI	
R_{work}	19.31% (18.8%)
R_{free}	24.64% (29.0%)
e.s.u. (R_{work})	0.169 Å
e.s.u. (R_{free})	0.168 Å

Table 3.5. Electronic absorption data for C112D/M121X (X = M, L, F, I) azurins. Parenthetical values indicate error, which is reported as the standard deviation of three metal titrations.

	LF λ_{max}	LF ε_{max}	LMCT ε_{310}
C112D[1a]	13.26	97 $M^{-1}cm^{-1}$	1950 $M^{-1}cm^{-1}$
C112D/M121L	12.53(30)	96(1)	1650(20)
C112D/M121I	12.67(30)	99(5)	2000(30)
C112D/M121F	12.67(30)	90(10)	1450(20)

Table 3.6. Principal components of spin Hamiltonian g-tensor and ^{63,65}Cu (I = 3/2, 100% abundance) magnetic hyperfine tensor (A, mK) derived from SpinCount[26] simulations of 77 K aqueous glass X-band (9.5 GHz) EPR spectra of C112D/M121X (X = M, L, F, I). Linewidths were modeled entirely by the g-strain parameters, σ_g and σ_A. Base simulation linewidth was set to 5 G in keeping with a 5 G modulation amplitude used in the experiment.

	C112D	C112DM121L	C112DM121I	C112DM121F
g_x	2.063	2.047	2.043	2.054
g_y	2.063	2.116	2.101	2.100
g_z	2.311	2.381	2.386	2.386
σg_x	0.008	0.015	0.013	0.018
σg_y	0.008	0.008	0.021	0.011
σg_z	0.002	0.007	0.005	0.006
$A_{x,y}$ (mK)	0.07	1.65	0.25	0.18
A_z (mK)	14.89	10.32	10.18	10.36
$\sigma A_{x,y}$ (mK)	0.06	0.001	0.003	0.009
σA_z (mK)	0.17	0.10	0.10	0.09
R_g	0	0.87	0.83	0.62

Table 3.7. Principal components of spin Hamiltonian g-tensor and ^{63,65}Cu (I = 3/2, 100% abundance) magnetic hyperfine tensor (A, mK) Derived from SpinCount[26] simulations of 77 K frozen solution X-band (9.5 GHz) EPR spectra of C112D/M121L azurin treated with exogenous ligands. Linewidths were modeled entirely by the g-strain parameters, σ_g and σ_A. Base simulation linewidth was set to 5 G in keeping with a 5 G modulation amplitude used in the experiment.

	Untreated (NaP_i)	N_3^-	CN^-
g_x	2.046	2.039	2.033
g_y	2.114	2.114	2.109
g_z	2.388	2.388	2.385
σg_x	0.018	0.019	0.017
σg_y	0.029	0.021	0.019
σg_z	0.017	0.017	0.017
$A_{x,y}$ (mK)	0.400	0.549	0.644
A_z (mK)	9.97	9.95	10.18
$\sigma A_{x,y}$ (mK)	0.001	0.027	0.035
σA_z (mK)	0.07	0.08	0.12

Figure 3.1. FPLC chromatograms from the purification of C112D/M121X (X = **a)** F, **b)** I) azurin with HiPrep Q FF 16/10 column. In all cases the protein was in 10 mM DEA•Cl pH 9.0 buffer and loaded onto the column equilibrated with this buffer. Protein was run against a gradient from 0 to 40% 10 mM DEA•Cl containing 200 mM salt over 30 minutes at a flow rate of 5 mL/minute. Bands corresponding to apoazurin are marked with asterisks.

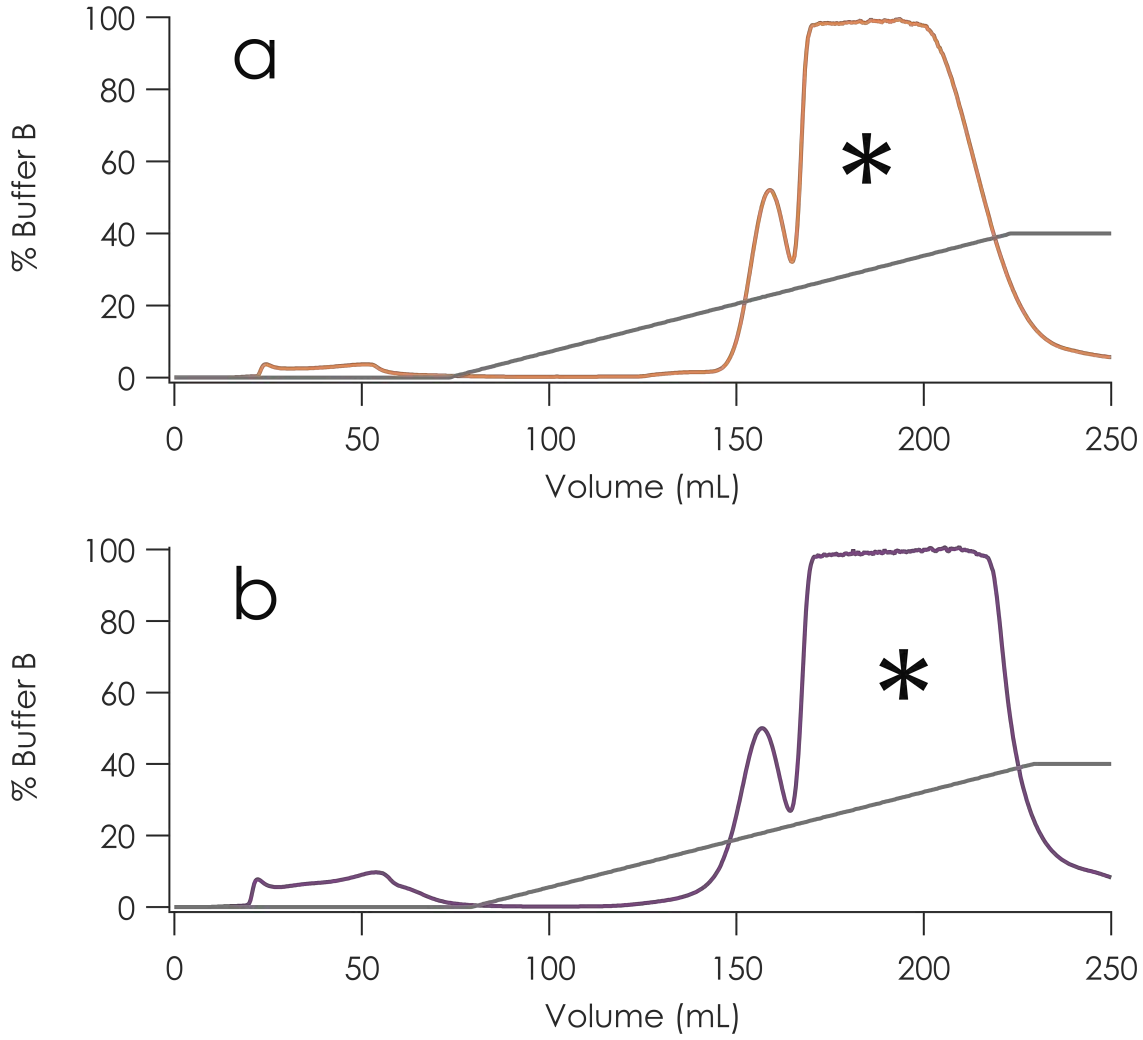
a
b
*
*
% Buffer B
Volume (mL)
0
20
40
60
80
100
0
50
100
150
200
250

Figure 3.2. FPLC chromatograms from the purification of apo C112D/M121X (X = F: a; I: b) azurin with HiLoad Superdex 75 16/60 column. In all cases the protein was in 50 mM Tris pH 7.5 buffer containing 150 mM NaCl and loaded onto the column equilibrated with this buffer. Bands corresponding to apoazurin are marked with asterisks.

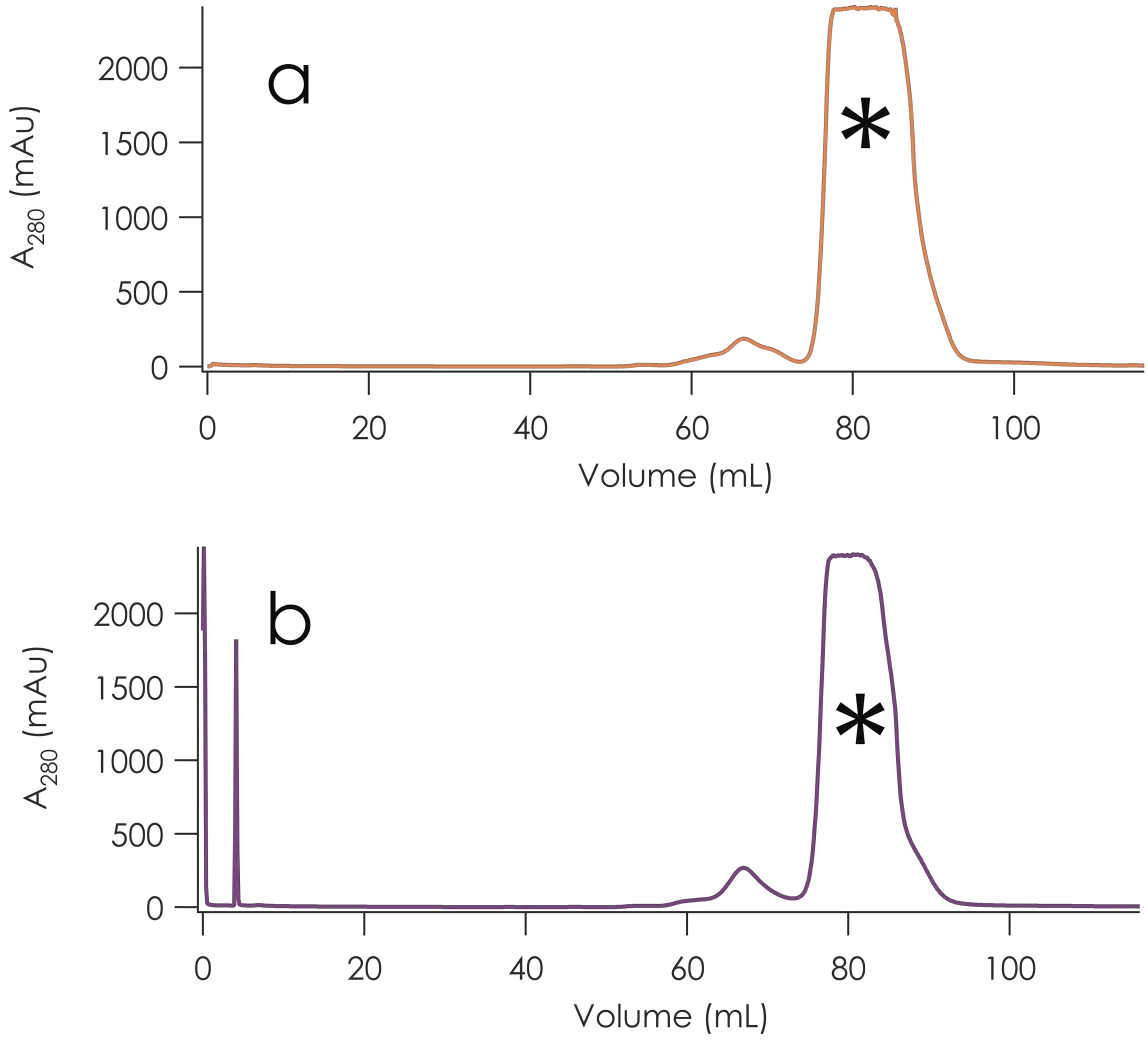
a
b
*
*
2000
1500
1000
500
0
A_{280} (mAu)
0
20
40
60
80
100
Volume (mL)

Figure 3.3. ESI-MS of C112D/M121X (X = **a)** F, calc: 13973; **b)** I, calc: 13939) azurins.

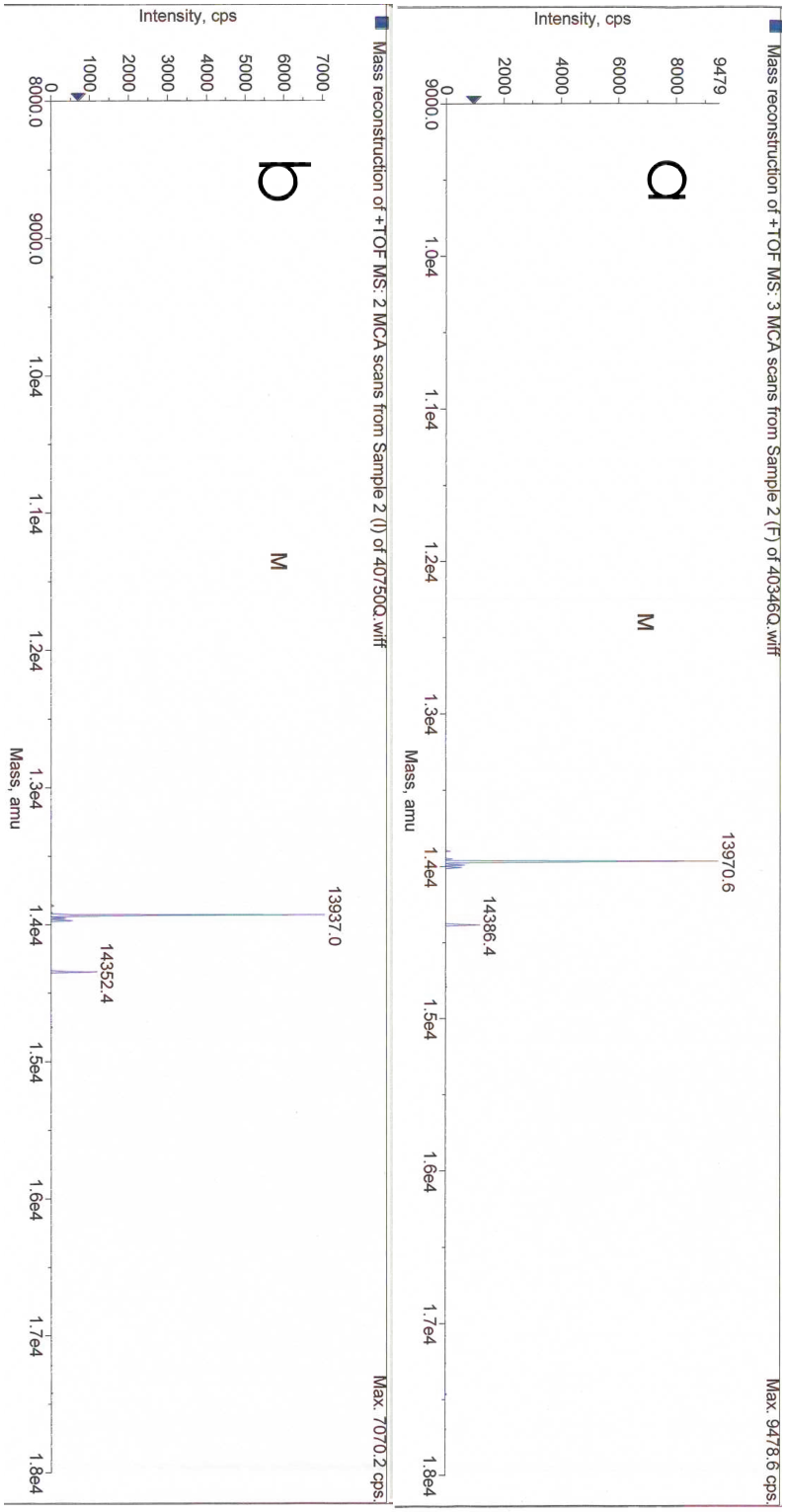
Mass reconstruction of +TOF MS: 3 MCA scans from Sample 2 (F) of 40346Q.wiff
Max. 9478.6 cps.
Intensity, cps
9479
8000
6000
4000
2000
0
Q
M
13970.6
14386.4
9000.0
1.0e4
1.1e4
1.2e4
1.3e4
1.4e4
1.5e4
1.6e4
1.7e4
1.8e4
Mass, amu
Mass reconstruction of +TOF MS: 2 MCA scans from Sample 2 (I) of 40750Q.wiff
Max. 7070.2 cps.
Intensity, cps
7000
6000
5000
4000
3000
2000
1000
0
b
M
13937.0
14352.4
8000.0
9000.0
1.0e4
1.1e4
1.2e4
1.3e4
1.4e4
1.5e4
1.6e4
1.7e4
1.8e4
Mass, amu

Figure 3.4. Cu^{II} K-edge EXAFS and Fourier transform thereof from C112D/M121X (X = **a)** L, **b)** F, **c)** I) azurins. The best OPT[23] fits to scattering paths calculated from the structural model by FEFF7 are overlaid in gray. Low-k residual likely corresponds to multiple-scattering paths that were not explicitly modeled.

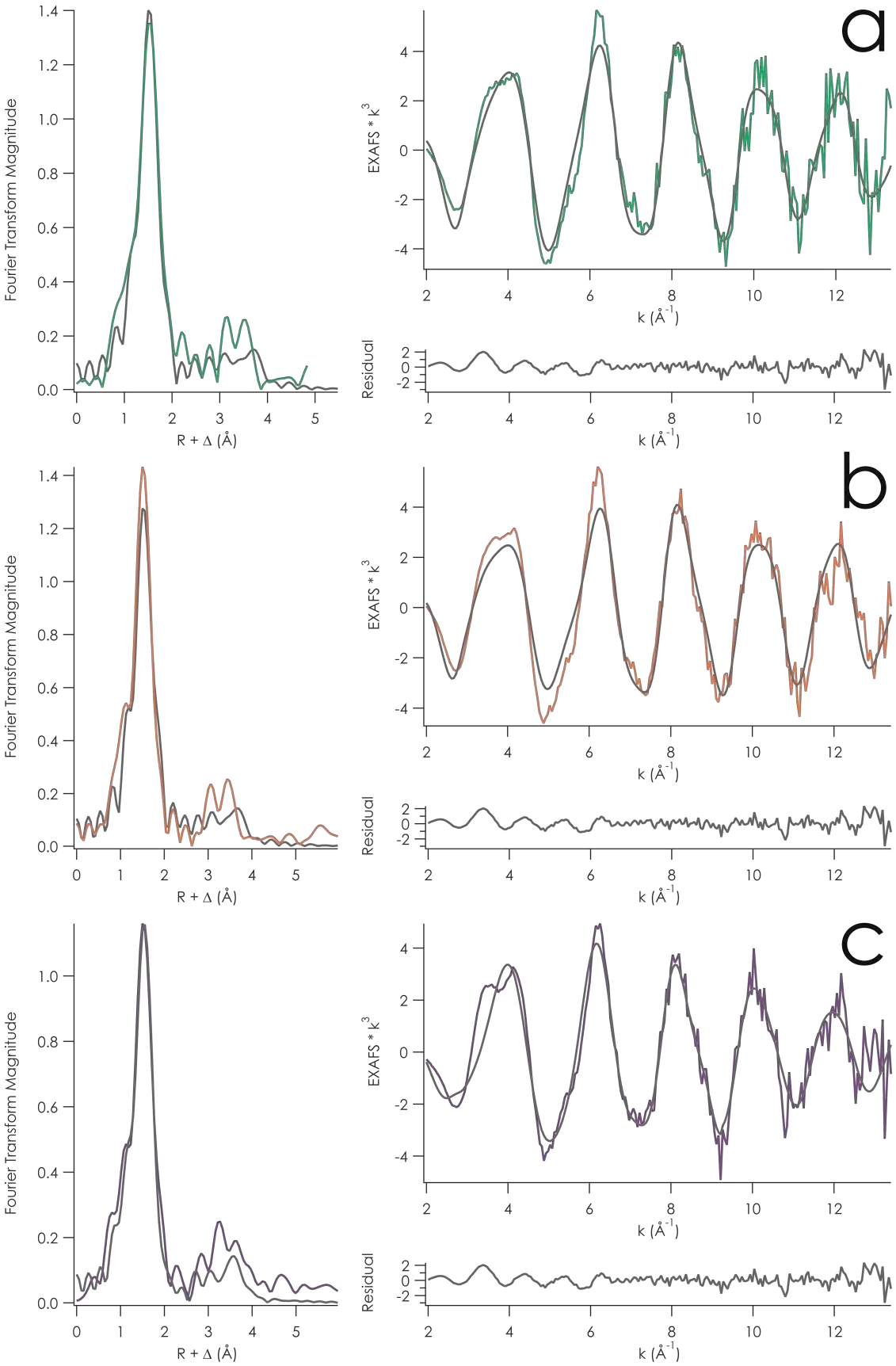
a
b
c
Fourier Transform Magnitude
R + Δ (Å)
EXAFS * k^3
k (Å^-1)
Residual

Figure 3.5. Secondary Cu^{II} binding site in C112D (**a)**, 1.9 Å, PDBID: 3FQY), C112D/M121L (**b)**, 2.1 Å, PDBID: 3FPY), C112D/M121F (**c)**, 1.9 Å, PDBID: 3FQ2), and C112D/M121I (**d)**, 1.9 Å, PDBID: 3FQ1) azurins. Crystal contacts are mediated by this quinary complex of Cu coordinated by two azurins (N1 from one and H83 from a second), a molecule of Tris buffer, and a water. Oxygen atoms are red; nitrogen atoms are blue.

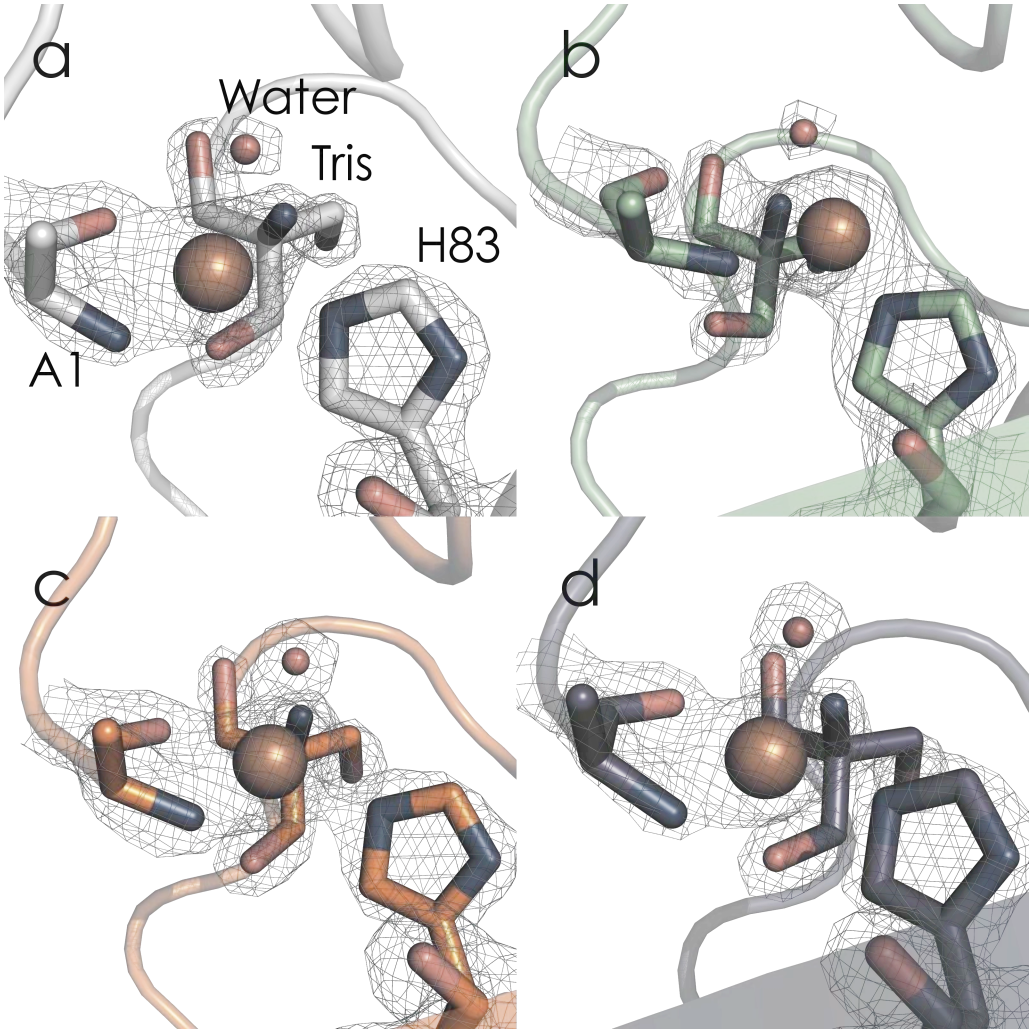
a
Water
Tris
H83
A1
b
c
d

Figure 3.6. Active site region of 1.9 Å C112D azurin crystal structure (PDBID: 3FQY). The $2F_o$-F_c electron density map is overlaid at a level of 2σ. Nitrogen atoms are blue, oxygen atoms are red, sulfur atoms are yellow. Cu-O(D112) distances are 1.92 and 2.80 Å, indicating that coordination is not properly bidentate, though there is likely some weak interaction with the more distant O.

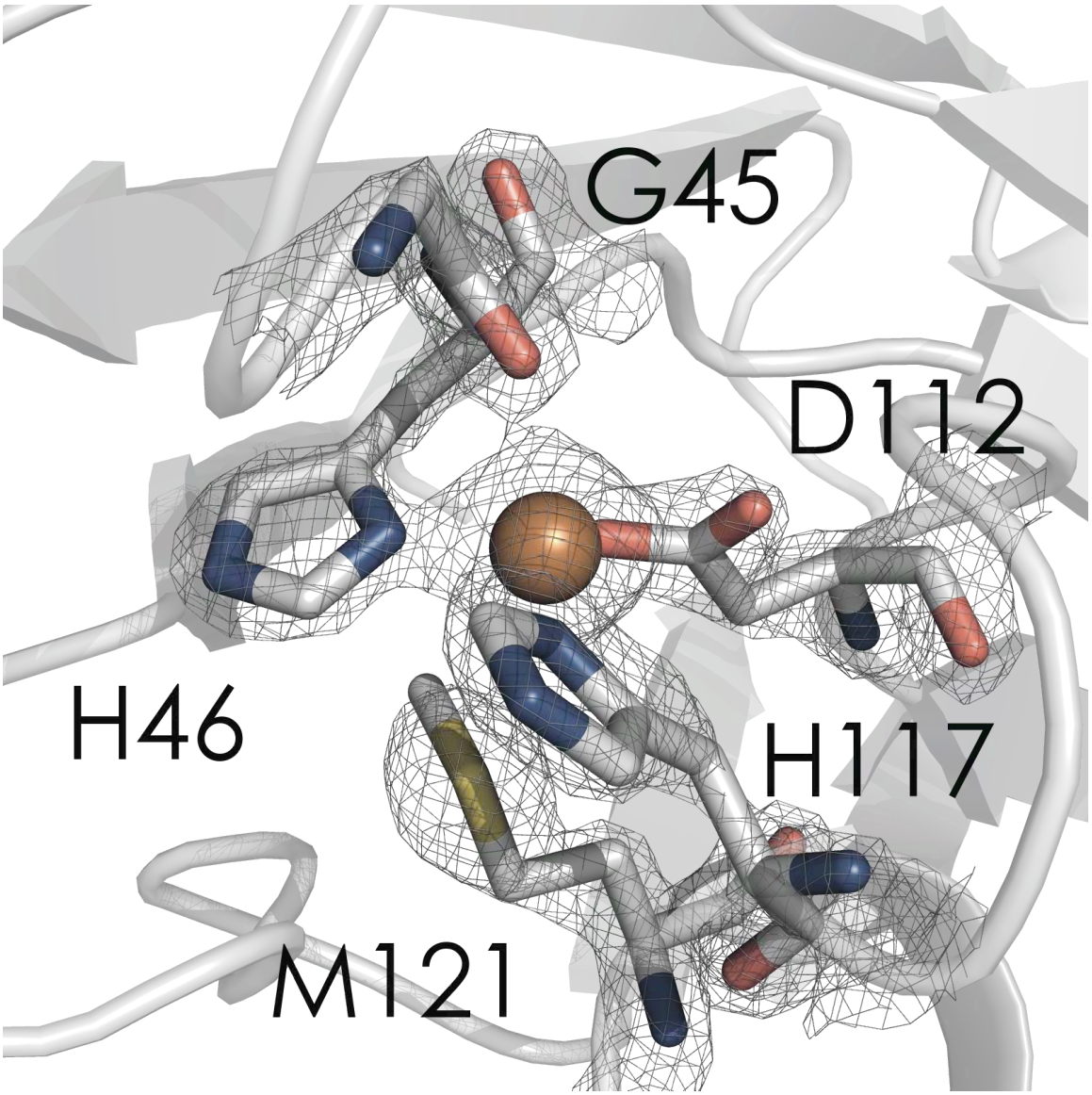
G45
D112
H46
H117
M121

Figure 3.7. Active site region of 2.1 Å C112D/M121L azurin crystal structure (PDBID: 3FPY). The $2F_o$-F_c electron density map is contoured at a level of 2σ. Nitrogen atoms are blue, oxygen atoms are red.

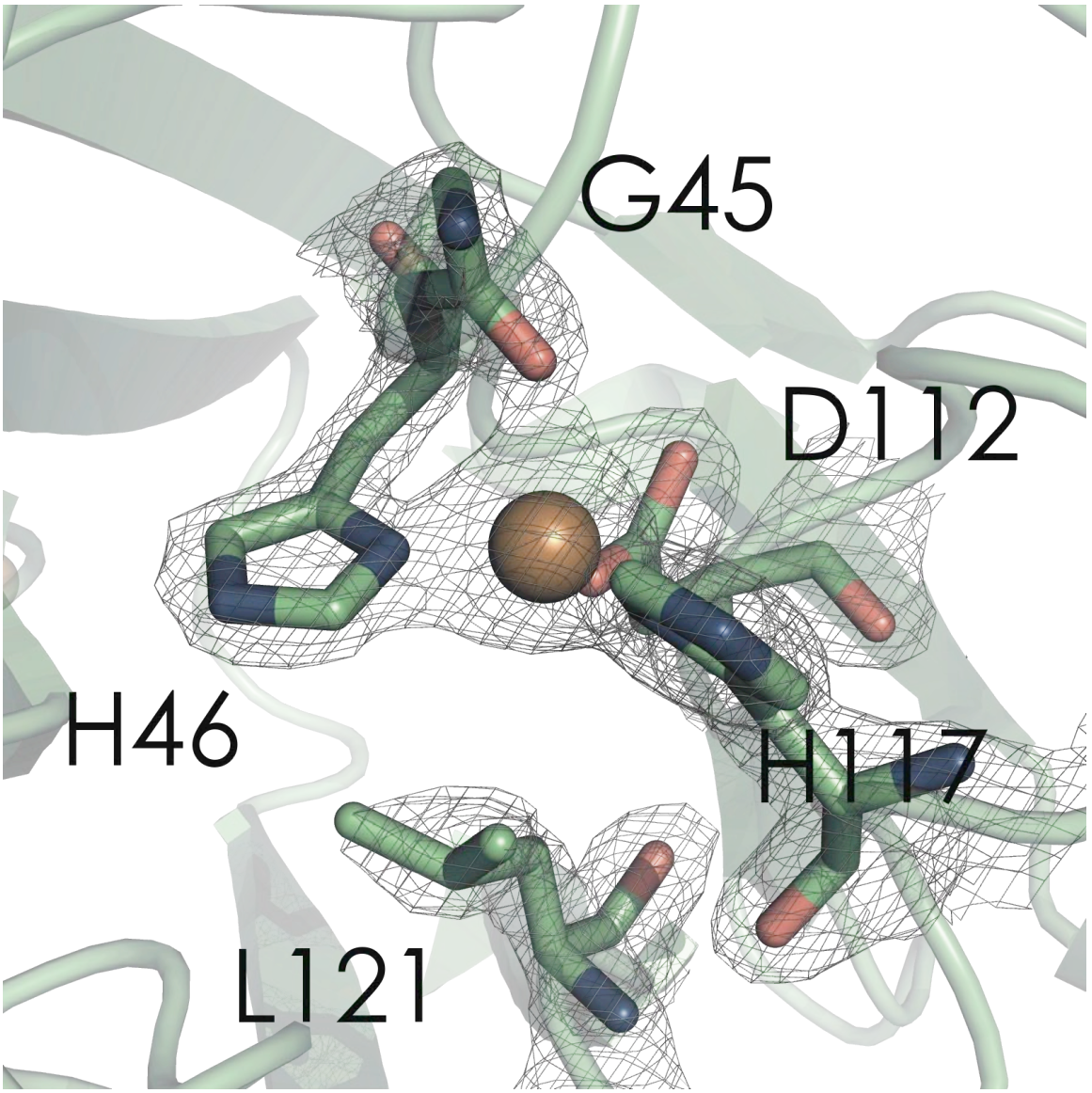
G45
D112
H46
H117
L121

Figure 3.8. Active site region of 1.91 Å C112D/M121F azurin crystal structure (PDBID: 3FQ2). The $2F_o$-F_c electron density map is contoured at a level of **a)** 2σ and **b)** 1 σ. F121 is disordered, suggesting lower active site rigidity compared to C112D and C112D/M121L azurin. Nitrogen atoms are blue, oxygen atoms are red.

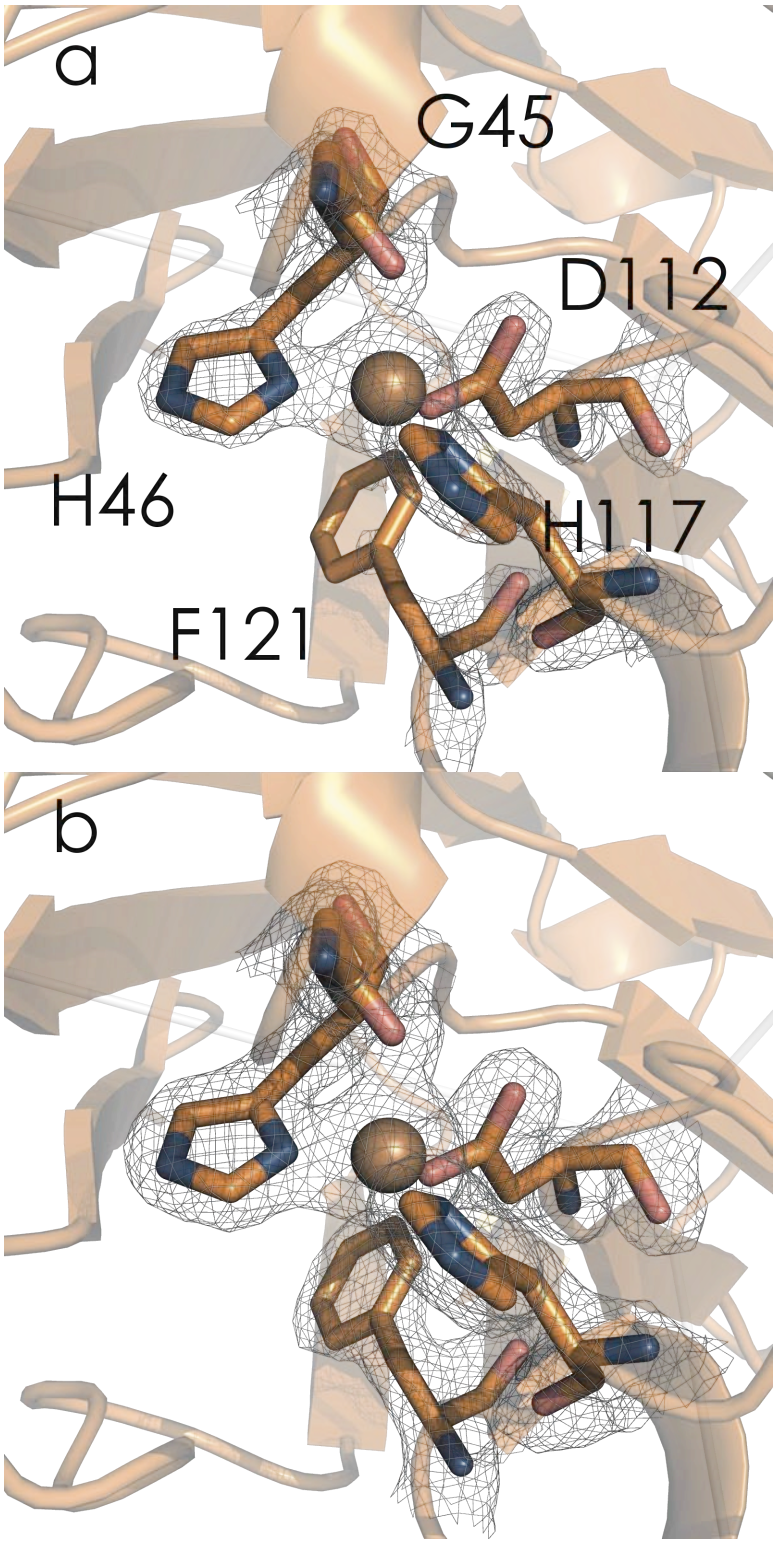
a
G45
D112
H46
H117
F121
b

Figure 3.9. Active site region of 1.9 Å C112D/M121I azurin crystal structure (PDBID: 3FQ1). The $2F_o$-F_c electron density map is overlaid at a level of **a)** 2σ and **b)** 1 σ. I121 is disordered, suggesting lower active site rigidity compared to C112D and C112D/M121L azurin. Nitrogen atoms are blue, oxygen atoms are red.

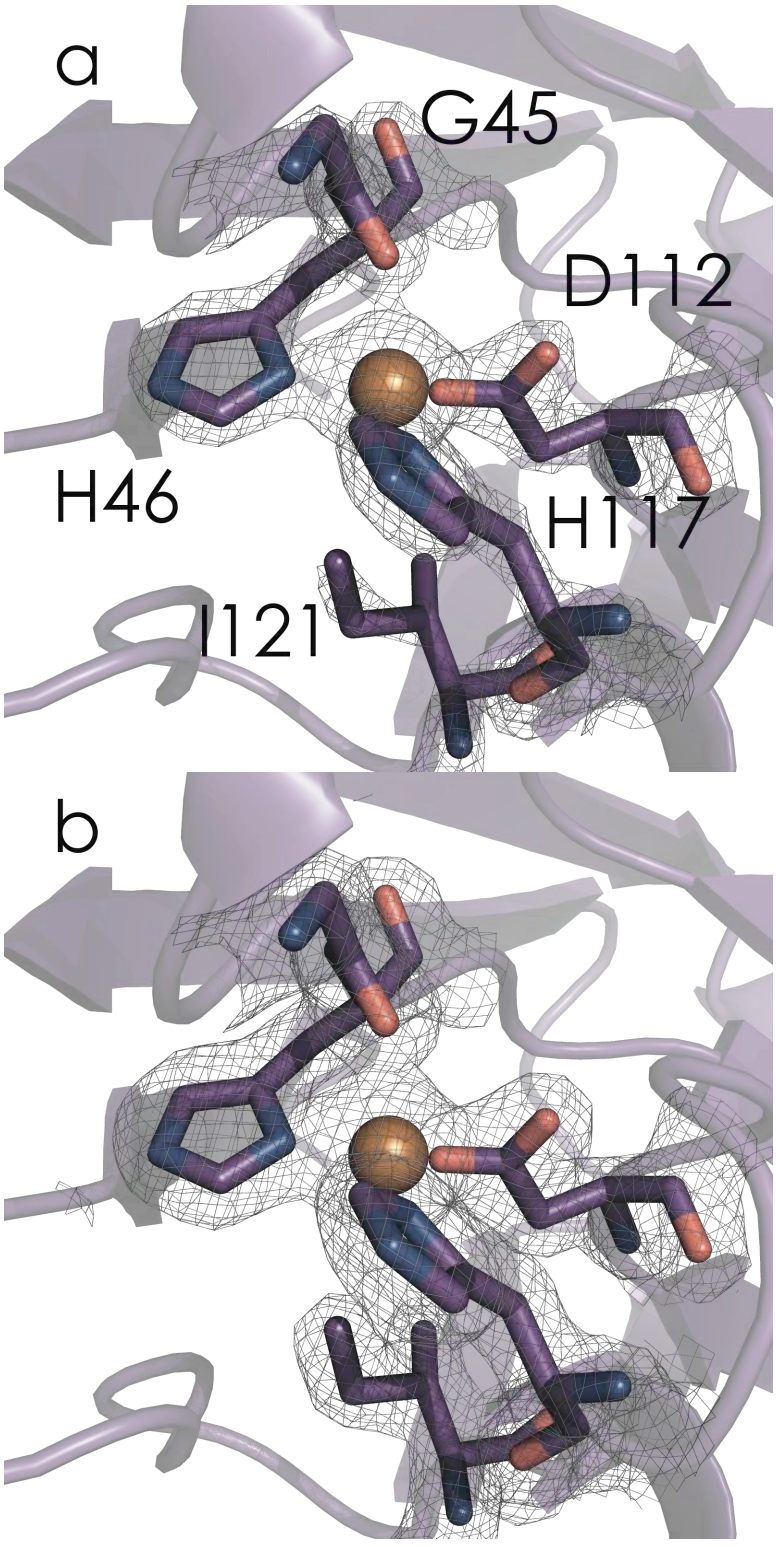
a
G45
D112
H46
H117
I121
b

Figure 3.10. Outer coordination spheres of Cu^{II} in C112D (**a**, 1.9 Å, PDBID: 3FQY), C112D/M121L (**b**, 2.1 Å, PDBID: 3FPY), C112D/M121F (**c**, 1.9 Å, PDBID: 3FQ2), and C112D/M121I (**d**, 1.9 Å, PDBID: 3FQ1) azurins are highlighted with bond distances shown in Å for heteroatoms involved in the hydrogen bonding 'rack' network of the wild-type protein. N-O-N bond angles are **a)** 117.82º, **b)** 126.89º, **c)** 123.96º, **d)** 121.21º Nitrogen atoms are blue, oxygen atoms are red.

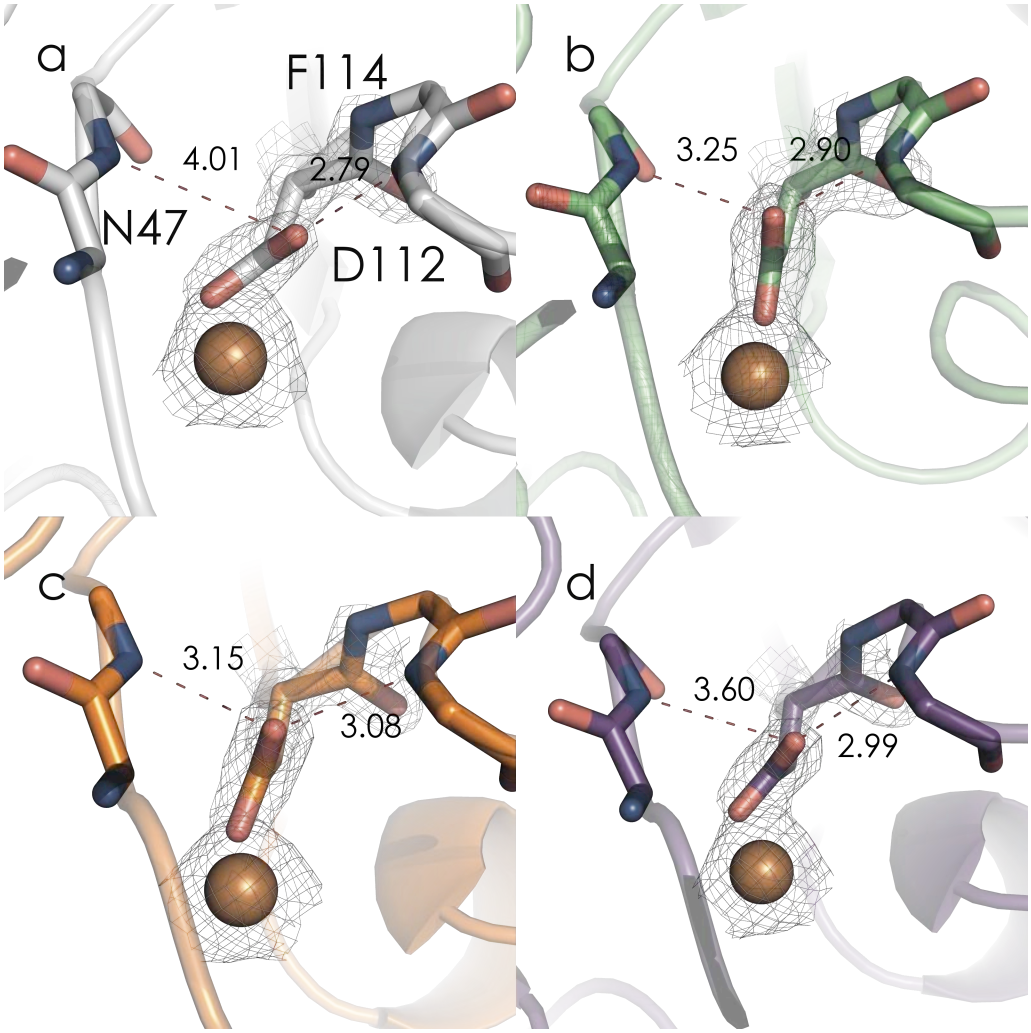
a
F114
4.01
2.79
N47
D112
b
3.25
2.90
c
3.15
3.08
d
3.60
2.99

Figure 3.11. Hydrophobic packing between F15 and X121 in C112D/M121L (**a**, 2.1 Å, PDBID: 3FPY), C112D/M121F (**b**, 1.9 Å, PDBID: 3FQ2), and C112D/M121I (**c**, 1.9 Å, PDBID: 3FQ1). $2F_o$-F_c electron density maps are contoured at the 1σ level. This residue experiences steric clash with F121 and I121. In the case of F121 this leads to the F15 sidechain adopting multiple conformations. F15 is unperturbed in C112D and C112D/M121L; this destabilizing interaction possibly explains the decresed metal affinity of C112D/M121X (X = F, I) azurins. A C_α structural alignment of C112D/M121X (X = M, I, L, F) is displayed in **d)**. Nitrogen atoms are blue, oxygen atoms are red.

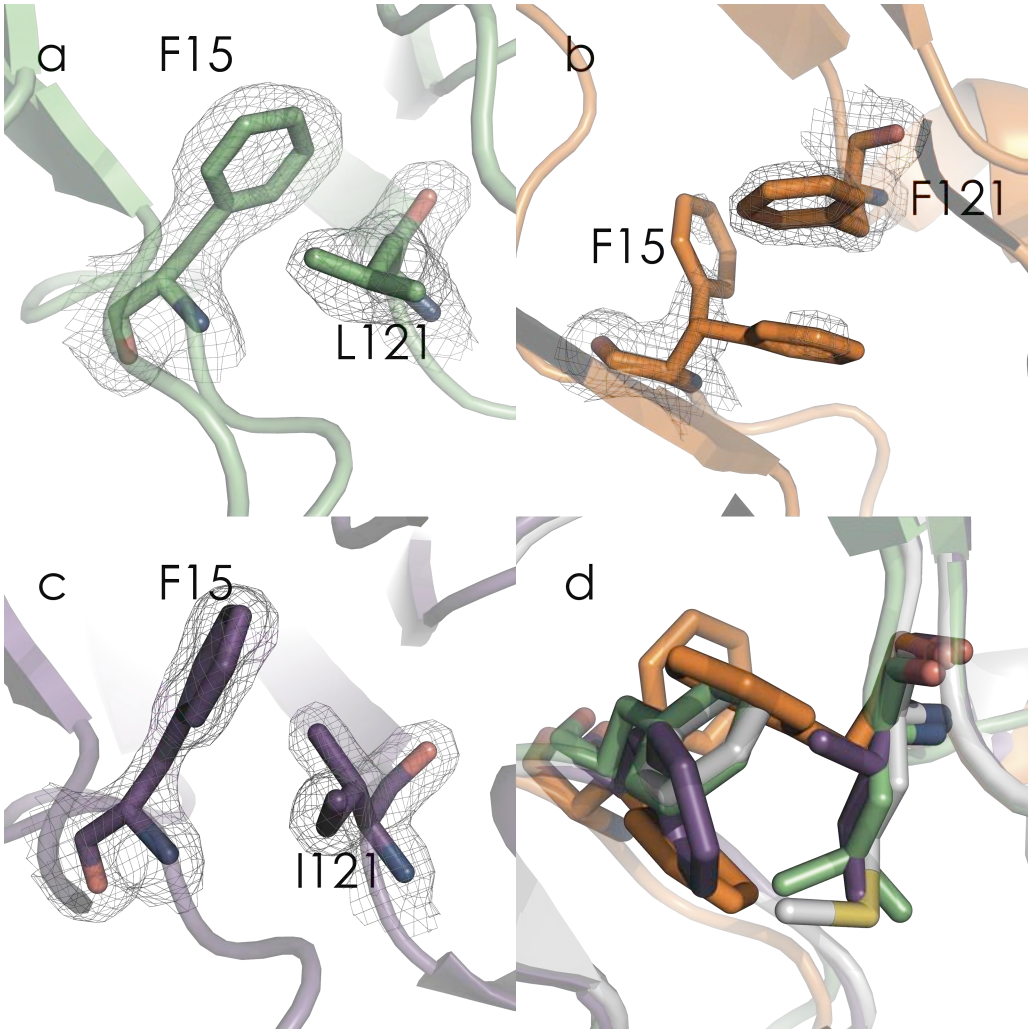
a
F15
L121
b
F121
F15
c
F15
I121
d

Figure 3.12. P36/G37 backbone flip mediated by H35 protonation state as seen by comparing the structure of C112D/M121L azurin at pH 7.0 (**a)**, 2.1 Å, PDBID:3FPY) and pH 10.0 (**b)**, 2.1 Å, undeposited). Hydrogen bonds to N_{H35} are marked with dashed red lines for clarity. $2F_o$-F_c electron density maps are contoured at the 2σ level. A C_α structural alignment is displayed in **c)**.

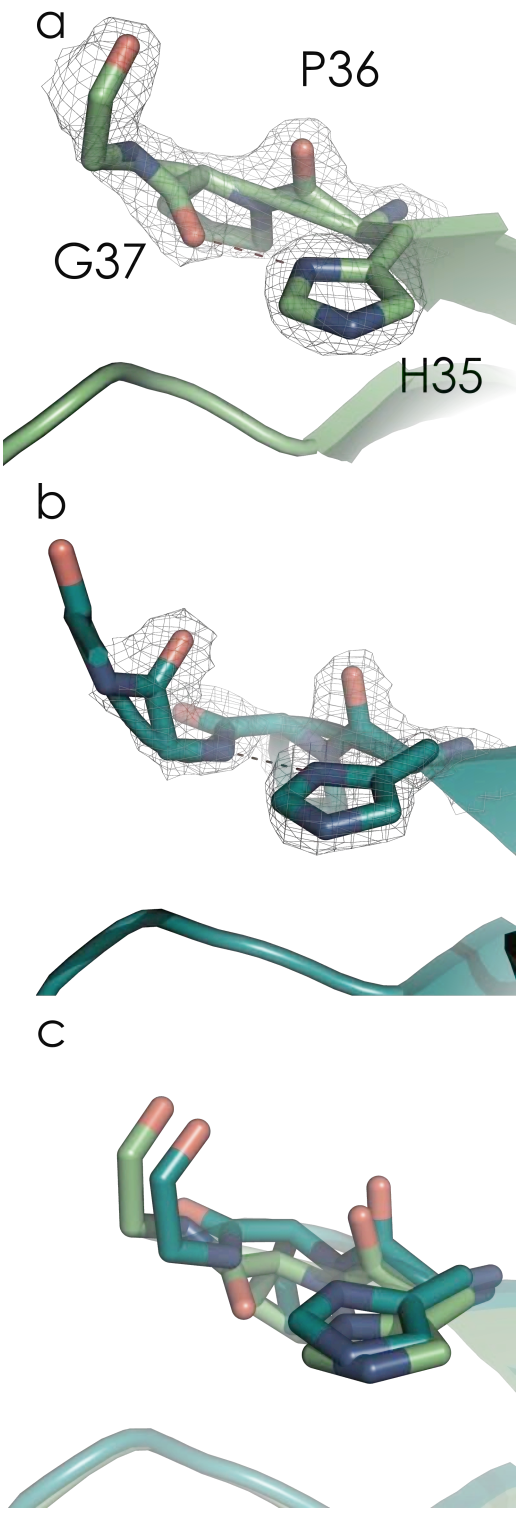
a
P36
G37
H35
b
c

Figure 3.13. **a)** Equatorial and **b)** axial views of C_α overlay of C112D/M121L azurin crystal structures at pH 7.0 (green, 2.1 Å, PDBID: 3FPY) and 10.0 (teal, 2.1 Å, undeposited). The active site is unperturbed by the H35-mediated P36/G37 backbone flip.

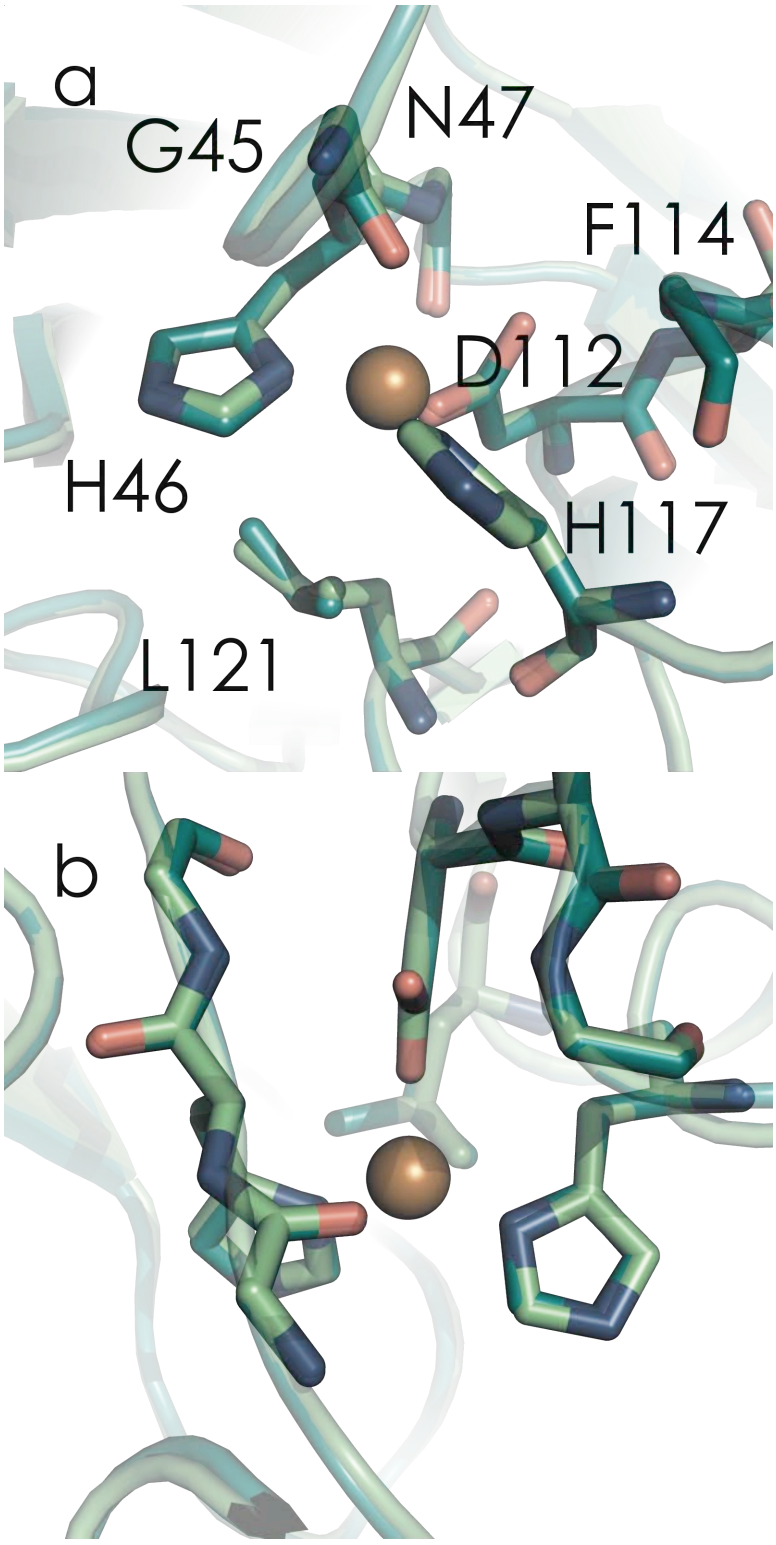
a
G45
N47
F114
D112
H46
H117
L121
b

Figure 3.14. Titration of 1 mL of 836 μM apo C112D/M121F azurin with 10 μL aliquots of 10.18 mM $CuSO_4$ in 100 mM Tris pH 7.0. Tris competes for Cu^{II} binding; using the experimentally determined extinction for Cu^{II}-Tris (ε = 48 $M^{-1}cm^{-1}$), the Cu^{II}-azurin concentration was corrected ratiometrically, giving ε_{310} = 1700 and ε_{789} = 90 $M^{-1}cm^{-1}$.

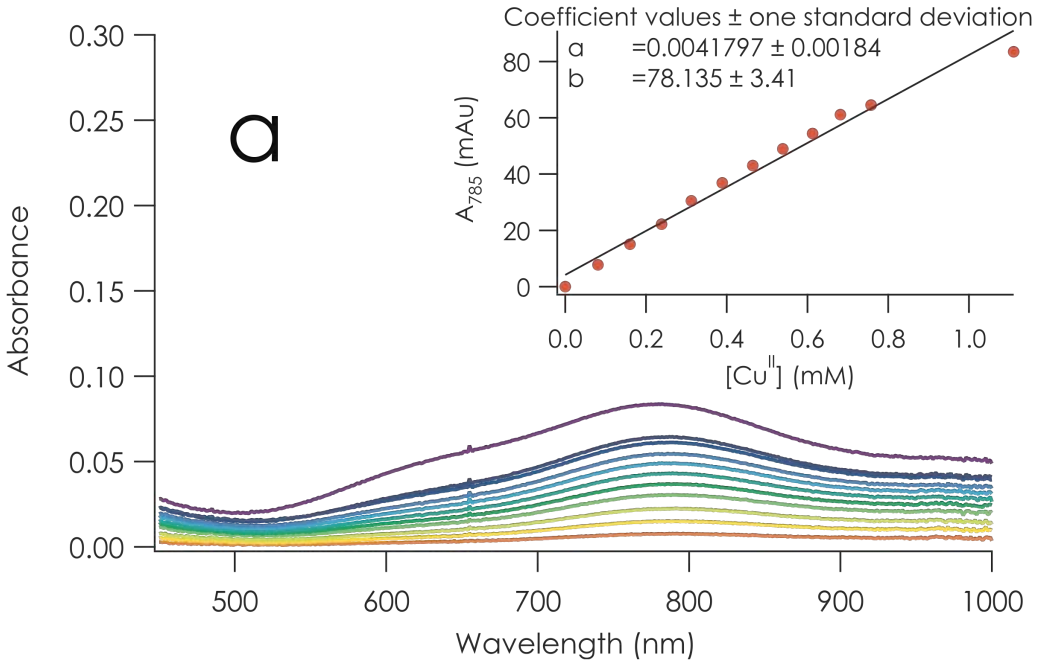
a
Absorbance
Wavelength (nm)
Coefficient values ± one standard deviation
a =0.0041797 ± 0.00184
b =78.135 ± 3.41
A785 (mAu)
[CuII] (mM)

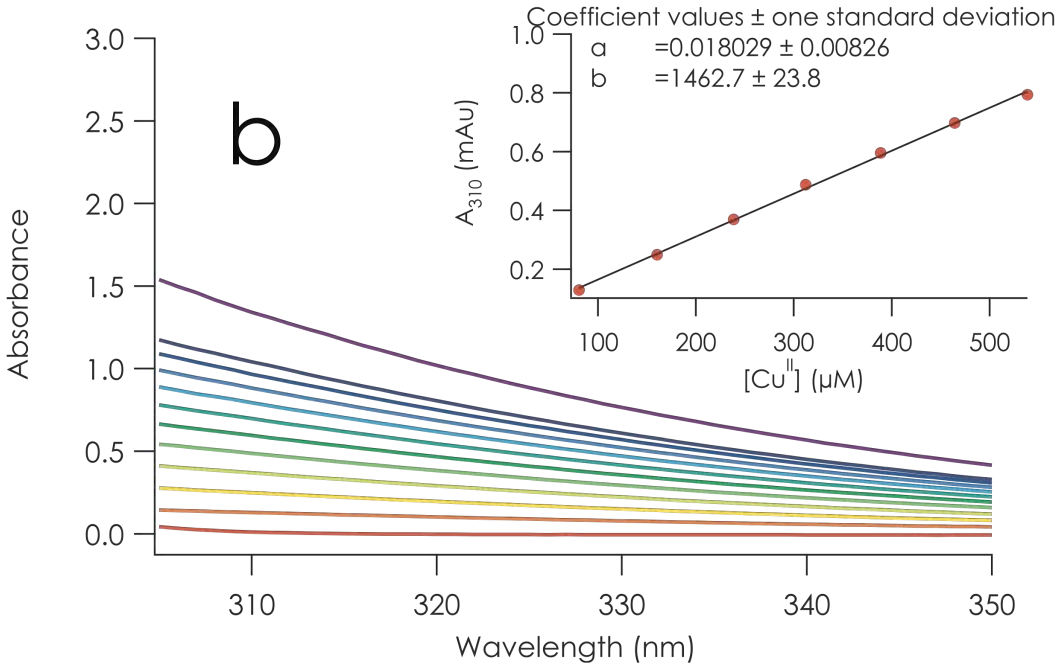
b
Absorbance
Wavelength (nm)
Coefficient values ± one standard deviation
a =0.018029 ± 0.00826
b =1462.7 ± 23.8
A310 (mAu)
[CuII] (μM)

Figure 3.15. Titration of 1 mL of 400 μM apo C112D/M121I azurin with 50 μL aliquots of 1.018 mM $CuSO_4$ in 100 mM Tris pH 7.0. Tris competes for Cu^{II} binding; using the experimentally determined extinction for Cu^{II}-Tris (ε = 48 $M^{-1}cm^{-1}$), the Cu^{II}-azurin concentration was corrected ratiometrically, giving ε_{310} = 2000 and ε_{789} = 99 $M^{-1}cm^{-1}$.

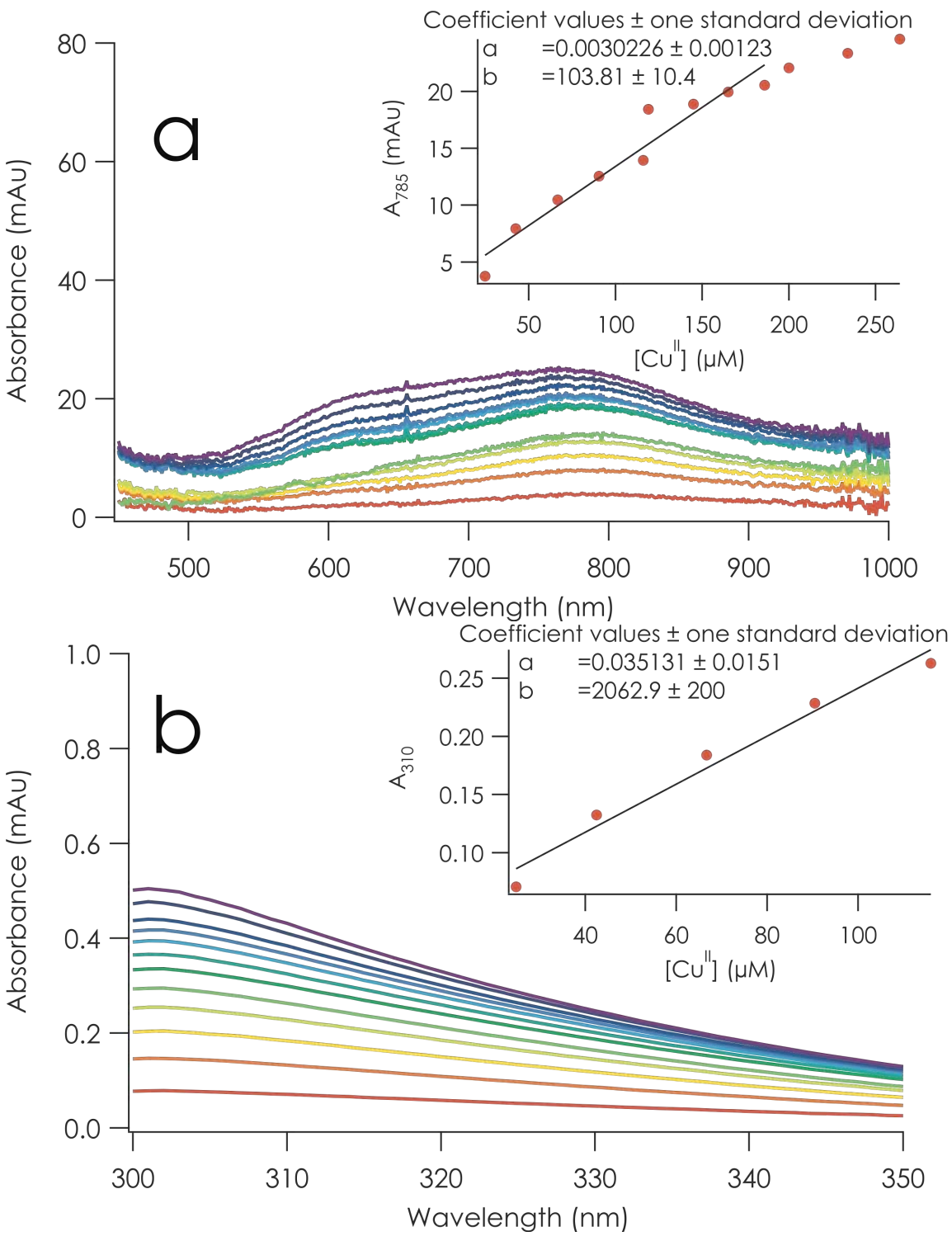
a
Coefficient values ± one standard deviation
a =0.0030226 ± 0.00123
b =103.81 ± 10.4
A785 (mAu)
[Cu^II] (μM)
Absorbance (mAu)
Wavelength (nm)
b
Coefficient values ± one standard deviation
a =0.035131 ± 0.0151
b =2062.9 ± 200
A310
[Cu^II] (μM)
Absorbance (mAu)
Wavelength (nm)

Figure 3.16. Electronic absorption spectra of C112D/M121X (X = M, black; L, green; F, orange; I, purple) showing the LF absorption systems. The C112D/M121X (X = L, F, I) azurins show a second resolved band at E < 10 kK, as well as a possible shoulder at 11 kK.

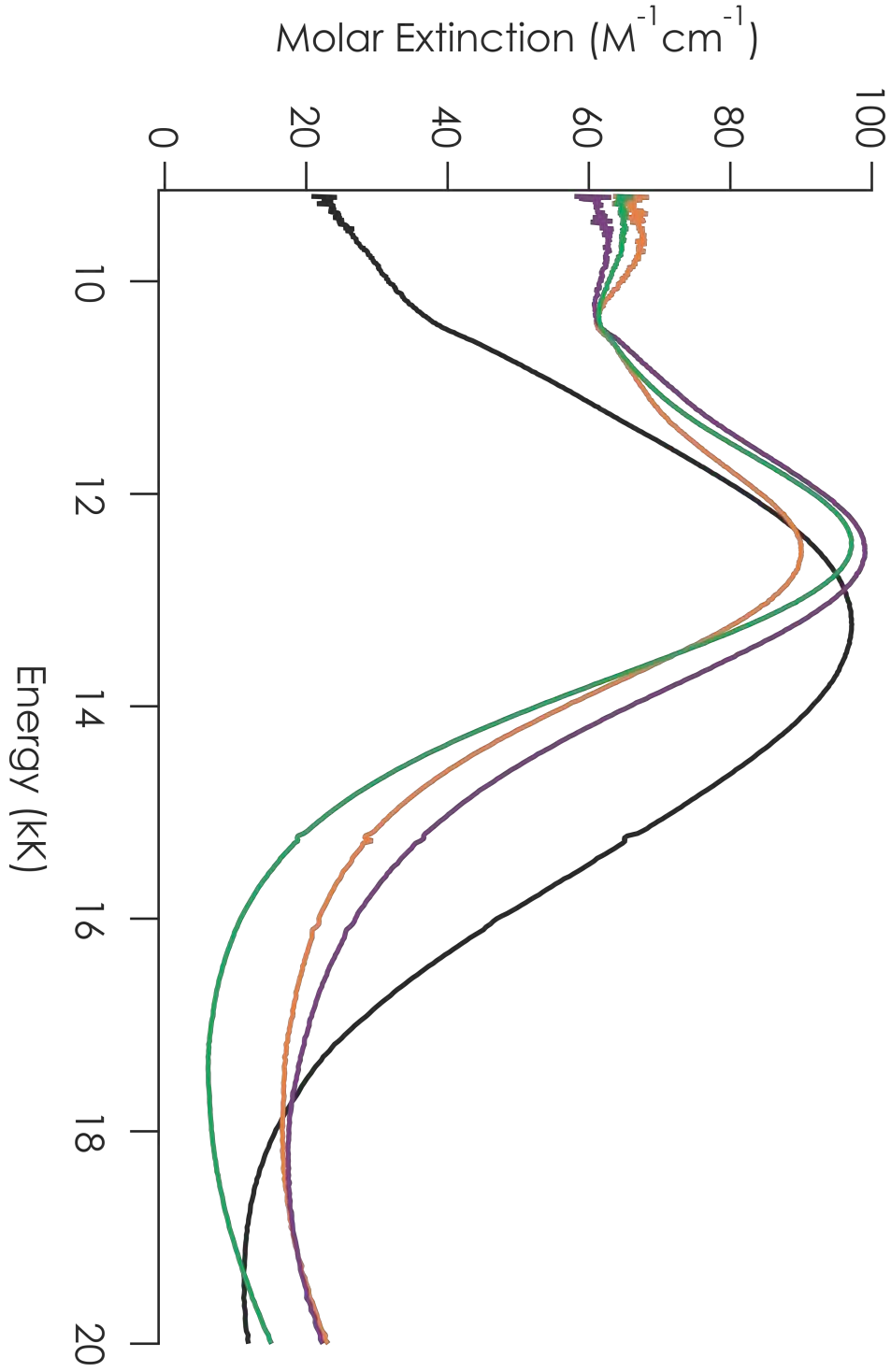
Molar Extinction ($M^{-1}cm^{-1}$)
0
20
40
60
80
100
Energy (kK)
10
12
14
16
18
20

Figure 3.17. Cu K-edge XAS of C112D/M121X (X = M, black; L, green; F, orange; I, purple) azurin at pH 7.0 at 10 K. Spectra are the averages of four scans to K = 13.5 $Å^{-1}$. Bottom left inset: the 1s to 3d transition is highlighted. Top left inset: 1s to 3d transition intensity is plotted against Cu-O(G45) distance. Error in the distances are likely overestimated given crystallographic thermal factors for the active site. Top right inset: the first derivative spectra are shown, indicating very small energy changes in 1s to 3d absorption energy. Absorbance is normalized to the spline-corrected EXAFS region. Normalization error is taken as 5%. Each averaged scan corresponds to the first recorded per 1 x 10 mm spot.

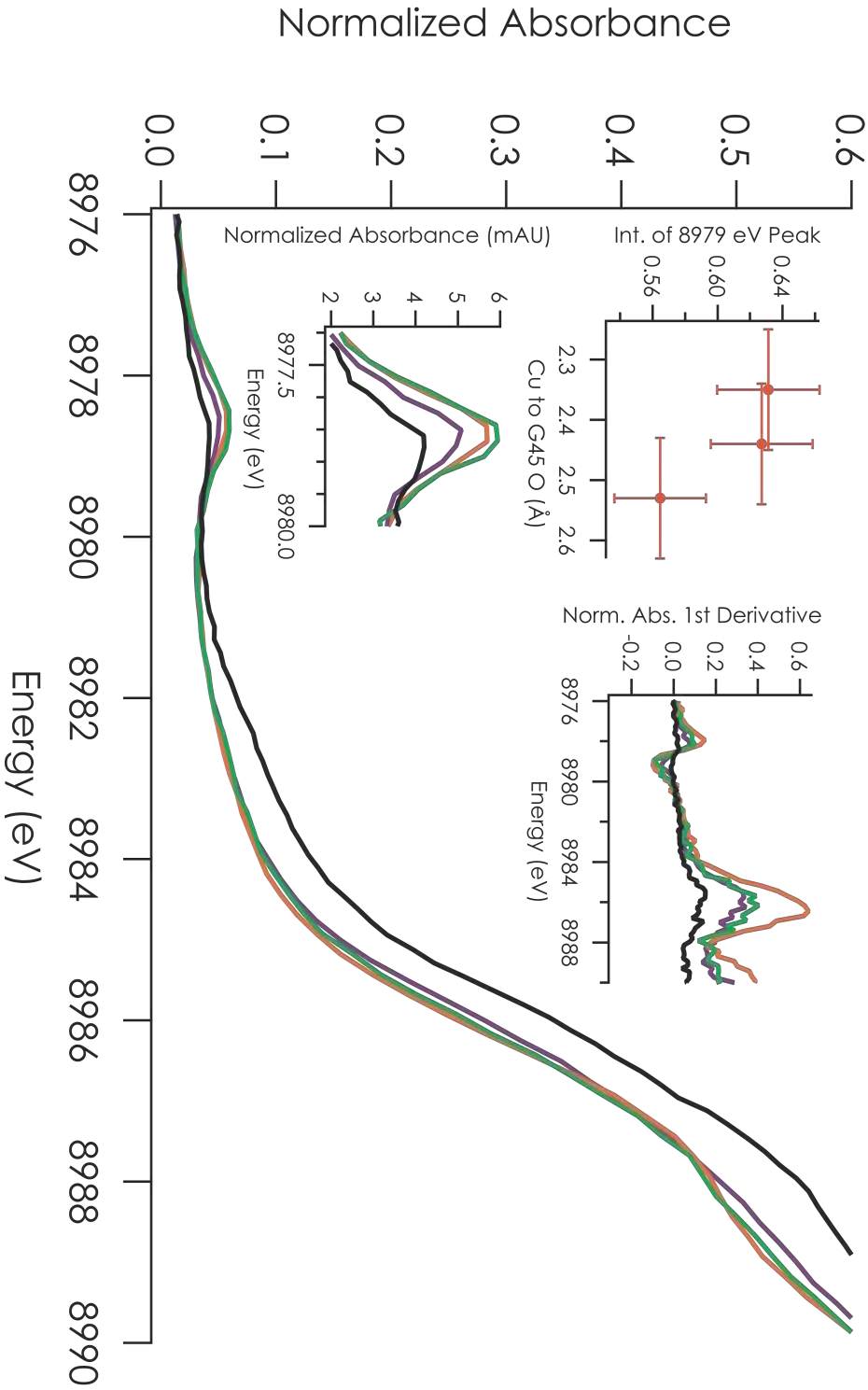
Normalized Absorbance
0.0
0.1
0.2
0.3
0.4
0.5
0.6
8976
8978
8980
8982
8984
8986
8988
8990
Energy (eV)
Normalized Absorbance (mAU)
2
3
4
5
6
8977.5
8980.0
Energy (eV)
Int. of 8979 eV Peak
0.56
0.60
0.64
2.3
2.4
2.5
2.6
Cu to G45 O (Å)
Norm. Abs. 1st Derivative
-0.2
0.0
0.2
0.4
0.6
8976
8980
8984
8988
Energy (eV)

Figure 3.18. X-band (9.5 GHz) EPR spectra of C112D azurin in 77 K glass (100 mM NaP_i pH 7.0, 50% glycerol). The lowest field feature of $A_{||}$ is highlighted, showing ^{14}N superhyperfine features. The SpinCount[26] simulation is overlaid in dashed gray. Spectra were recorded with a 5 G modulation amplitude at a microwave power of 2 mW.

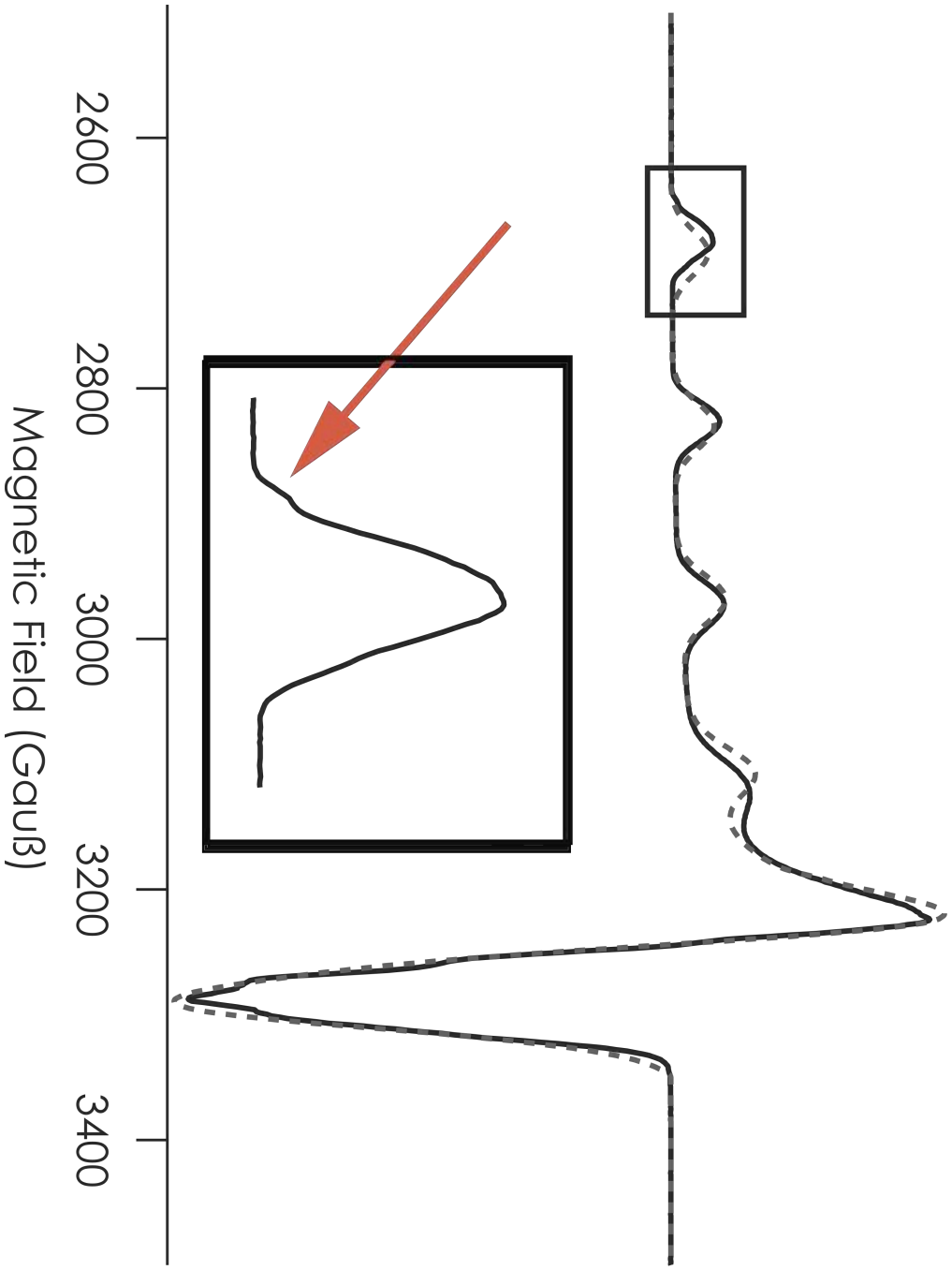
2600
2800
3000
3200
3400
Magnetic Field (Gauß)

Figure 3.19. X-band (9.5 GHz) EPR spectra of C112D/M121X (X = L, **a)**; F, **b)**; I, **c)**) azurin in 100 mM NaP_i pH 7.0 50% glyercol. SpinCount[26] simulations are overlaid in dashed gray. Spectra were recorded with a 5 Gauss modulation amplitude at a microwave power of 2 mW.

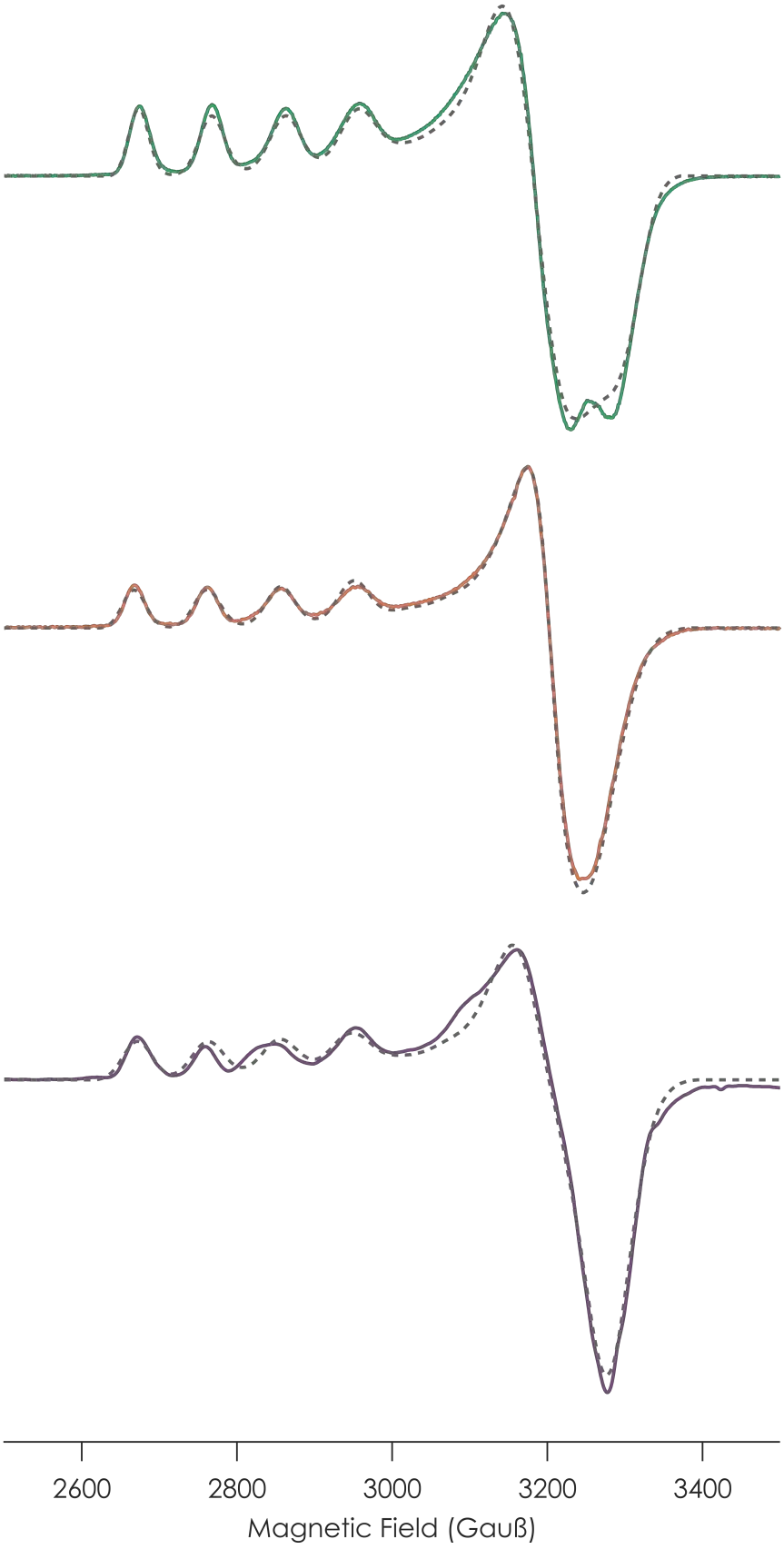
2600
2800
3000
3200
3400
Magnetic Field (Gauß)

Figure 3.20. Plot of $A_{||}$ versus 1s to 3d XANES intensity for C112D/M121X (X = L, green; F, orange; I, purple) azurins. Error in XANES intensity arises from 5% normalization error, error in $A_{||}$ arises from A-strain. The data show that the narrow hyperfine is independent of the XANES intensity; *i.e.* the spin-dipolar term is not predominantly operative in lowering $A_{||}$ relative to type 2 copper.

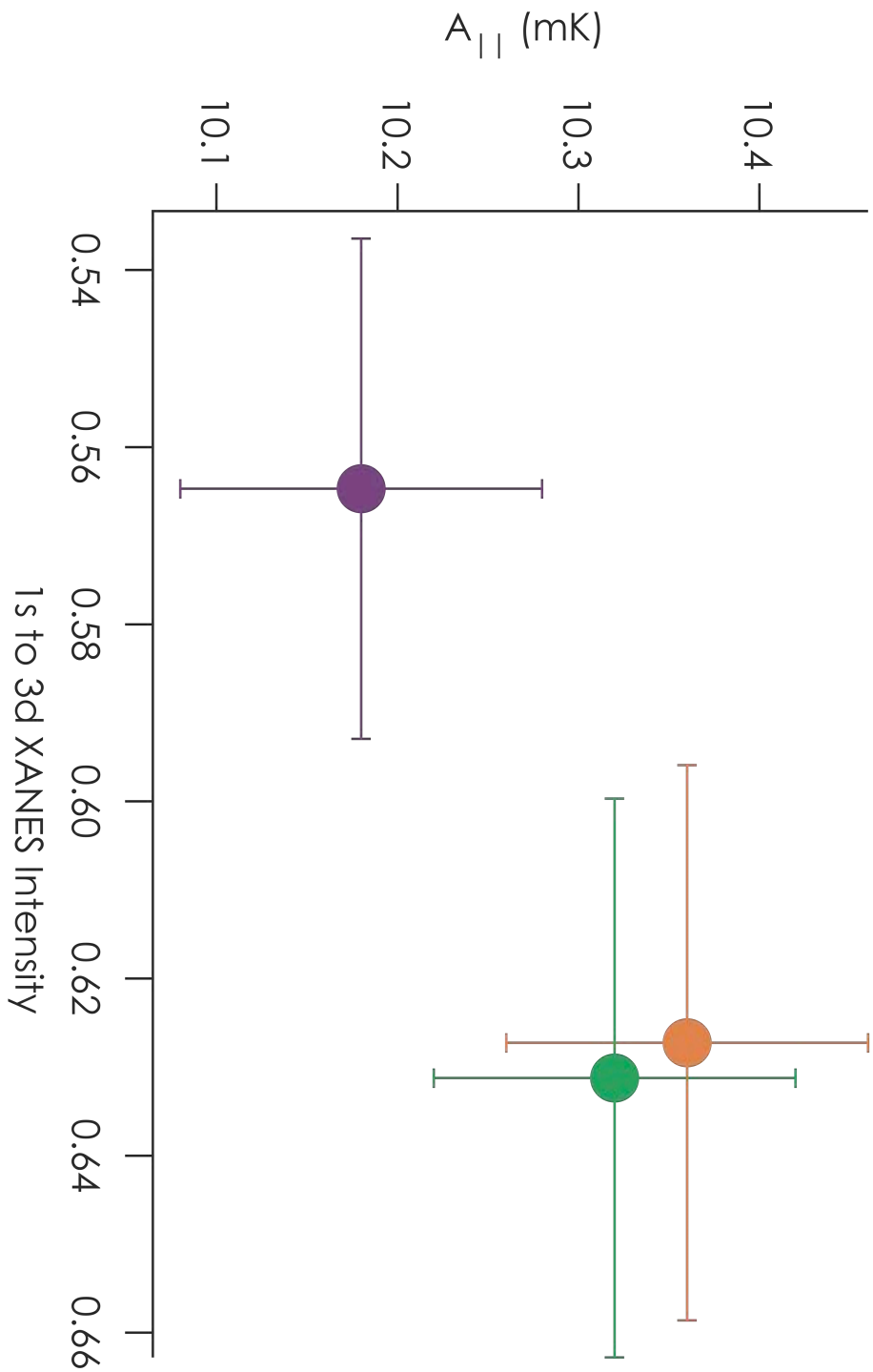
A|| (mK)
10.1
10.2
10.3
10.4
0.54
0.56
0.58
0.60
0.62
0.64
0.66
1s to 3d XANES Intensity

Figure 3.21. 77 K frozen solution X-band (9.5 GHz) EPR spectra of 1 mM C112D/M121L azurin in **a)** 100 mM NaP_i pH 7.0, **b)** 100 mM NaP_i containing 1 mM NaN_3, and **c)** 100 mM NaP_i containing 1 mM NaCN. SpinCount[26] simulations are overlaid in dashed gray. Spectra were recorded with a 5 G modulation amplitude at a microwave power of 2 mW.

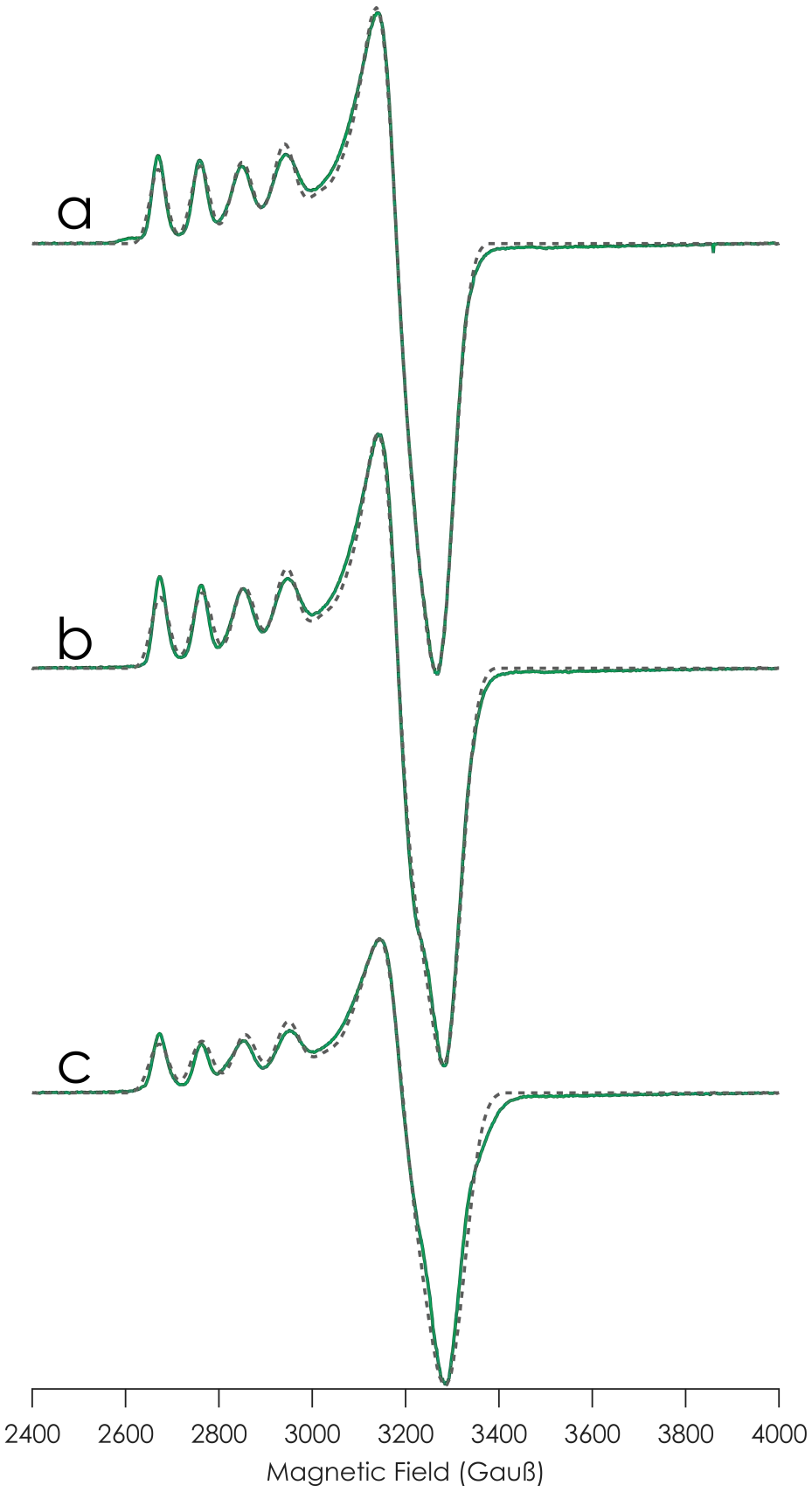
a
b
c
2400
2600
2800
3000
3200
3400
3600
3800
4000
Magnetic Field (Gauß)

Figure 3.22. CV of C112D/M121I azurin on 1:1 CH_3:OH-terminated alkanethiol SAM-modified Au(111) electrode in deaerated 10 mM NaP_i pH 7.0. CV was recorded under an Ar blanket at a scan rate of 50 mV/s and referenced to a saturated Ag/AgCl (197 mV vs NHE). $E_{1/2}^{o}$ is 310 mV vs NHE.

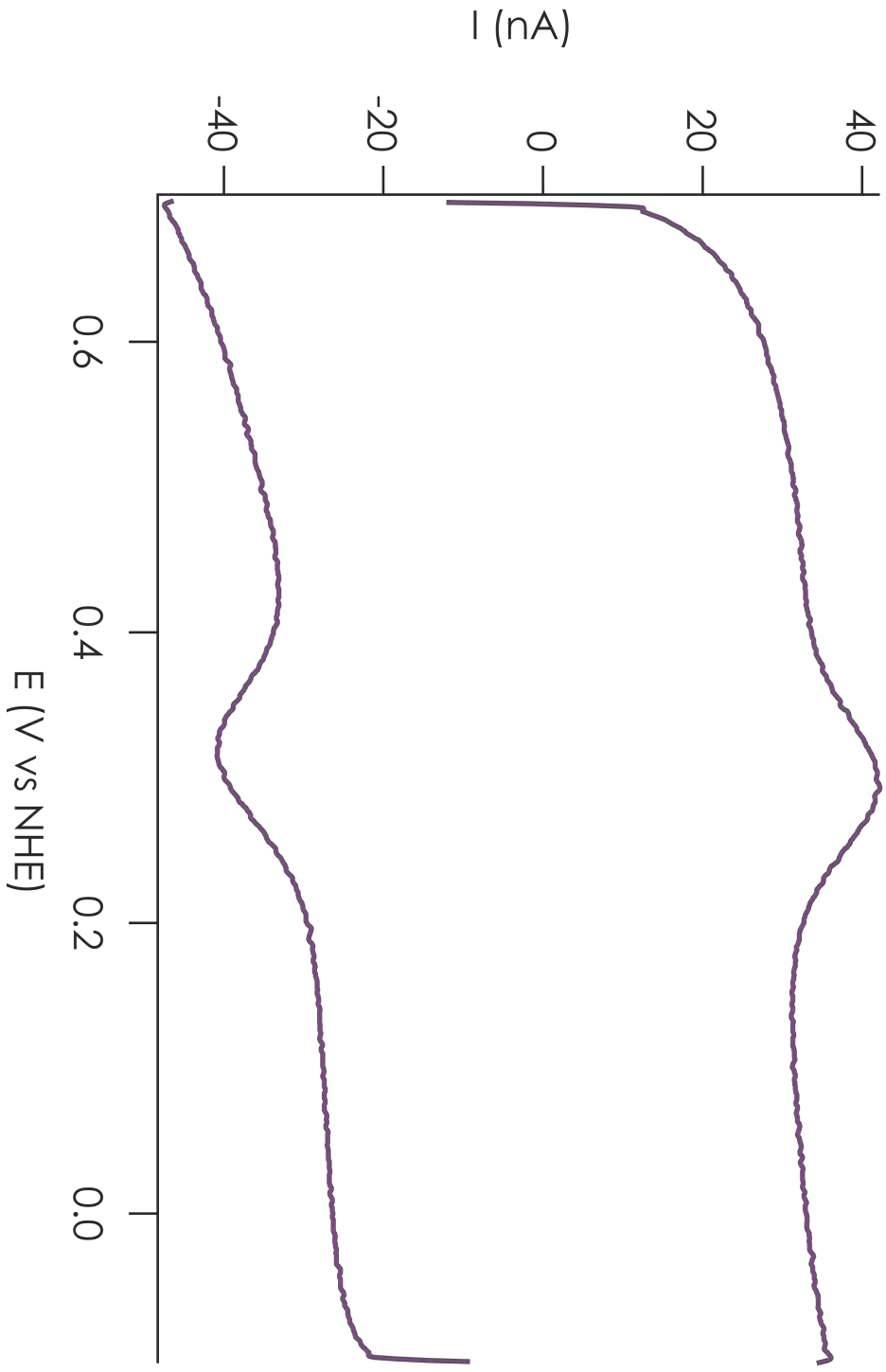
I (nA)
-40
-20
0
20
40
0.6
0.4
0.2
0.0
E (V vs NHE)

Figure 3.23. SWV of C112D/M121F azurin on 1:1 CH_3:OH-terminated alkanethiol SAM-modified Au(111) electrode in deaerated 10 mM NaP_i pH 7.0. SWV was recorded under an Ar blanket with a square wave frequency of 8 Hz and referenced to saturated Ag/AgCl (197 mV vs NHE). $E_{1/2}°$ is 310 mV vs NHE.

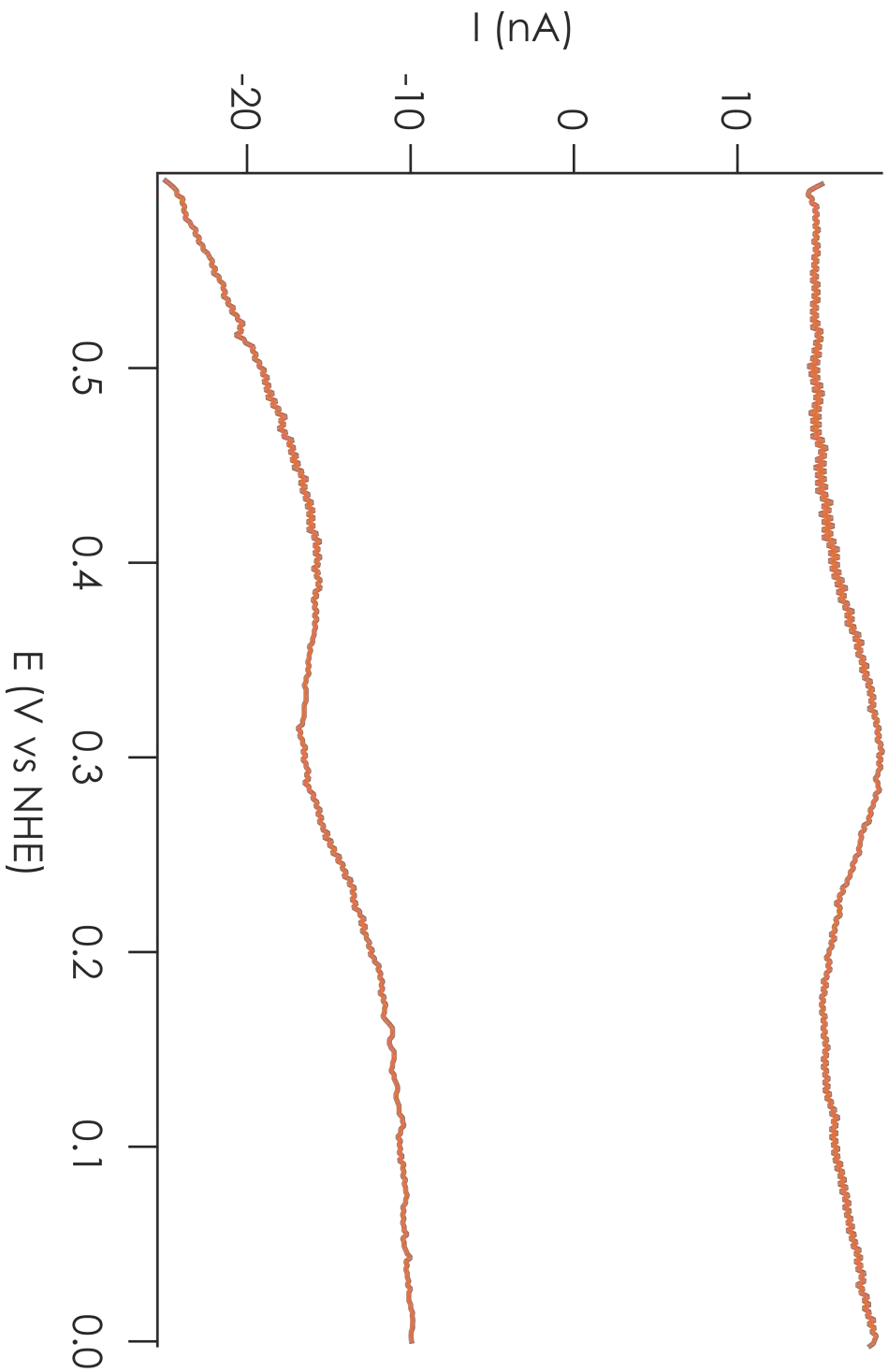
I (nA)
-20
-10
0
10
0.5
0.4
0.3
0.2
0.1
0.0
E (V vs NHE)

Figure 3.24. SAM chain-length dependence Cu to electrode ET rates obtained for C112D (black), C112D/M121L (green), and C112D/M121I (purple) azurins. WT azurin (blue) is also plotted for reference. Linear fit of the log of k_{ET} to the chain length within the region of dependence shows a three order-of-magnitude drop in ET rate on going from WT to C112D azurin, however an order-of-magnitude gain in rate is achieved from C112D to C112D/M121L azurin.

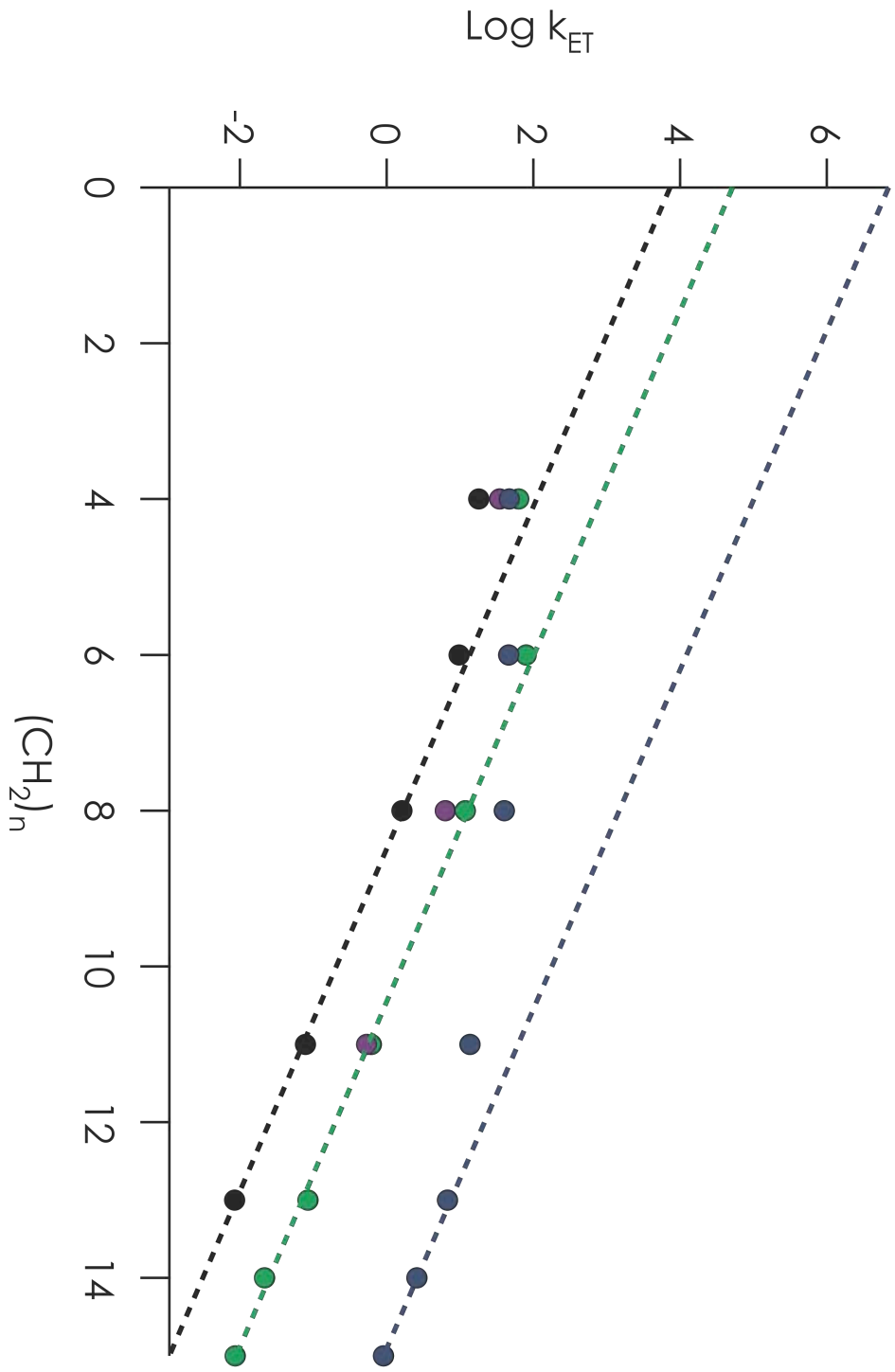
Log k_{ET}
-2
0
2
4
6
0
2
4
6
8
10
12
14
$(CH_2)_n$

Figure 3.25. Peisach-Blumberg plot of several azurin mutants demonstrating segregation into type 1 (blue circles), type 2 (light blue squares), type 1.5 (green diamond), and type zero (light green triangles). Literature values are reproduced for EPR parameters of M121H,[27] WT,[28] and M121Q[29] azurins. M121L, N47D, and N47Q azurin EPR parameters come from unpublished work with Keiko Yokoyama.

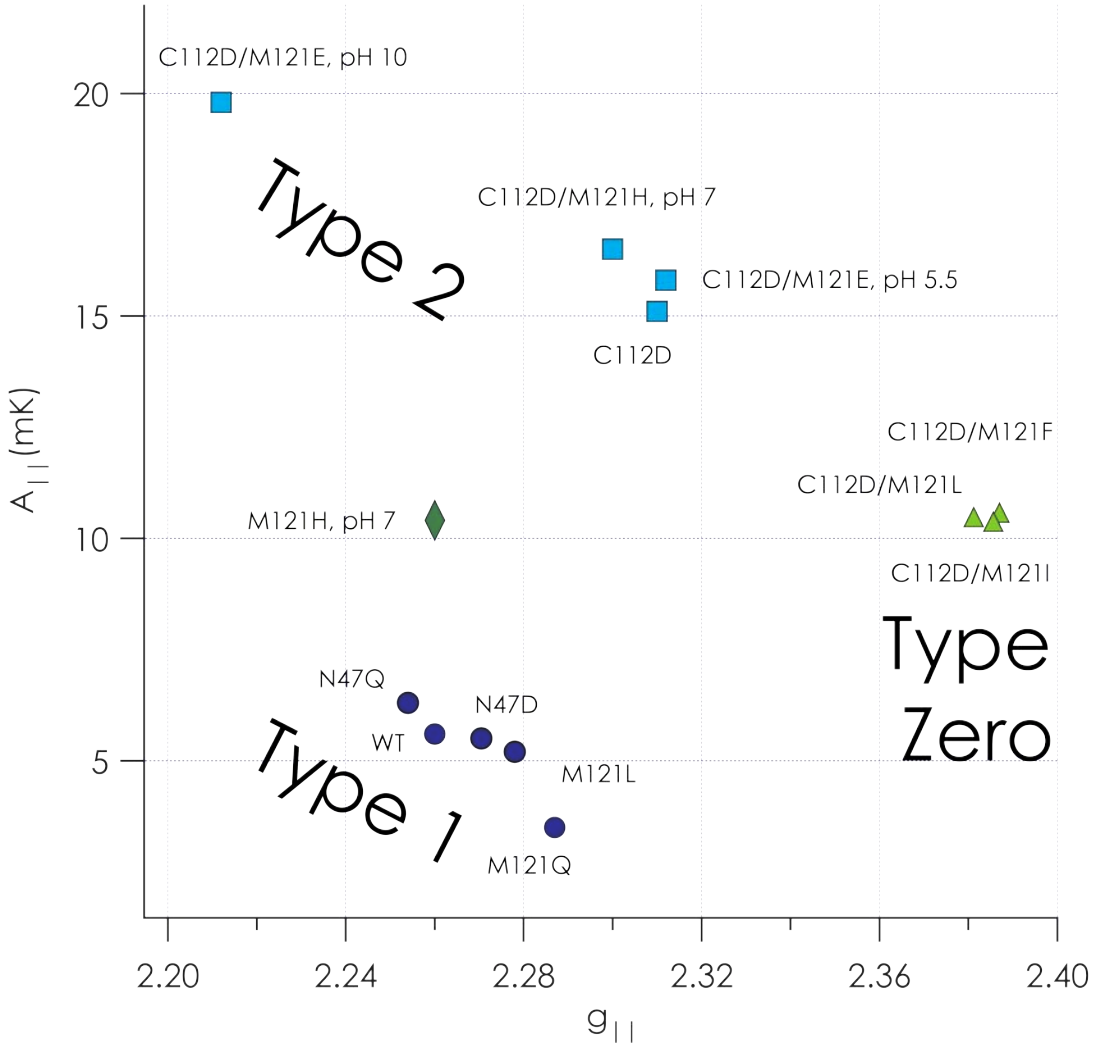
C112D/M121E, pH 10
C112D/M121H, pH 7
C112D/M121E, pH 5.5
C112D
C112D/M121F
C112D/M121L
M121H, pH 7
C112D/M121I
N47Q
N47D
WT
M121L
M121Q
Type 2
Type 1
Type Zero
20
15
10
5
2.20
2.24
2.28
2.32
2.36
2.40
A|| (mK)
g||

APPENDIX 3-A

The DNA sequences of C112D/M121X (X = F, I) azurins are included in this appendix. Maps were generated in Ape.

```
Tue Aug  3 07:05:13 2010
C112DM121F_Azurin.ape
Text Map
       50        60        70        80        90
         *         *         *         *         *
    49 ATGCTGCGTAAGCTGGCTGCAGTGTCTCTGCTGCCTCTGCTGTCTGCTCC
       M  L  R  K  L  A  A  V  S  L  L  P  L  L  S  A  P
       >>>
       Start
       >>>>>>>>>>>>>>>>>>>>>>>>>>>>>>>>>>>>>>>>>>>>>>>>>>
       Periplasmic translocation leader sequence

       100       110       120       130       140
         *         *         *         *         *
     99 GCTGCTGGCTGCTGAATGCTCCGTTGATATCCAGGGTAATGATCAGATGC
        L  L  A  A  E  C  S  V  D  I  Q  G  N  D  Q  M  Q
       >>>>>>>>>>
       Periplasmic translocation leader sequence

       150       160       170       180       190
         *         *         *         *         *
    149 AGTTCAACACCAACGCCATCACCGTCGACAAGAGCTGCAAGCAGTTCACT
          F  N  T  N  A  I  T  V  D  K  S  C  K  Q  F  T

       200       210       220       230       240
         *         *         *         *         *
    199 GTTAACCTGTCTCACCCAGGTAACCTGCCGAAGAACGTTATGGGTCACAA
       V  N  L  S  H  P  G  N  L  P  K  N  V  M  G  H  N

       250       260       270       280       290
         *         *         *         *         *
    249 CTGGGTTCTGTCCACCGCGGCTGACATGCAAGGCGTTGTCACTGACGGTA
        W  V  L  S  T  A  A  D  M  Q  G  V  V  T  D  G  M

       300       310       320       330       340
         *         *         *         *         *
    299 TGGCTAGCGGTCTGGATAAAGACTACCTGAAGCCGGATGACTCTCGAGTT
          A  S  G  L  D  K  D  Y  L  K  P  D  D  S  R  V

       350       360       370       380       390
         *         *         *         *         *
    349 ATCGCCCACACCAAGCTGATCGGATCCGGTGAAAAAGACTCCGTTACTTT
       I  A  H  T  K  L  I  G  S  G  E  K  D  S  V  T  F

       400       410       420       430       440
         *         *         *         *         *
    399 CGACGTTTCCAAGCTTAAAGAAGGTGAACAGTACATGTTCTTCGATACTT
        D  V  S  K  L  K  E  G  E  Q  Y  M  F  F  D  T  F
                                                 >>>>>>>
                                                 Metal Binding Loop

       450       460       470       480       490
         *         *         *         *         *
    449 TCCCGGGTCACTCCGCACTGTTTAAGGGTACCCTGACTCTGAAATAG
          P  G  H  S  A  L  F  K  G  T  L  T  L  K  *
       >>>>>>>>>>>>>>>>>>>>>>>                  >>>
       Metal Binding Loop                       Stop
```

```
Tue Aug  3 07:00:27 2010
C112DM121I_Azurin.ape
Text Map
          50        60        70        80        90
                *         *         *         *         *
    46 ATGCTGCGTAAGCTGGCTGCAGTGTCTCTGCTGTCTCTGCTGTCTGCTCC
       M  L  R  K  L  A  A  V  S  L  L  S  L  L  S  A  P
       >>>
       Start
       >>>>>>>>>>>>>>>>>>>>>>>>>>>>>>>>>>>>>>>>>>>>>>>>>>>
       Periplasmic translocation leader sequence

          100       110       120       130       140
                *         *         *         *         *
    96 GCTGCTGGCTGCTGAATGCTCCGTTGATATCCAGGGTAATGATCAGATGC
        L  L  A  A  E  C  S  V  D  I  Q  G  N  D  Q  M  Q
       >>>>>>>>>>
       Periplasmic translocation leader sequence

          150       160       170       180       190
                *         *         *         *         *
   146 AGTTCAACACCAACGCCATCACCGTCGACAAGAGCTGCAAGCAGTTCACT
         F  N  T  N  A  I  T  V  D  K  S  C  K  Q  F  T

          200       210       220       230       240
                *         *         *         *         *
   196 GTTAACCTGTCTCACCCAGGTAACCTGCCGAAGAACGTTATGGGTCACAA
       V  N  L  S  H  P  G  N  L  P  K  N  V  M  G  H  N

          250       260       270       280       290
                *         *         *         *         *
   246 CTGGGTTCTGTCCACCGCGGCTGACATGCAAGGCGTTGTCACTGACGGTA
        W  V  L  S  T  A  A  D  M  Q  G  V  V  T  D  G  M

          300       310       320       330       340
                *         *         *         *         *
   296 TGGCTAGCGGTCTGGATAAAGACTACCTGAAGCCGGATGACTCTCGAGTT
         A  S  G  L  D  K  D  Y  L  K  P  D  D  S  R  V

          350       360       370       380       390
                *         *         *         *         *
   346 ATCGCCCACACCAAGCTGATCGGATCCGGTGAAAAAGACTCCGTTACTTT
       I  A  H  T  K  L  I  G  S  G  E  K  D  S  V  T  F

          400       410       420       430       440
                *         *         *         *         *
   396 CGACGTTTCCAAGCTTAAAGAAGGTGAACAGTACATGTTCTTCGATACTT
        D  V  S  K  L  K  E  G  E  Q  Y  M  F  F  D  T  F
                                                 >>>>>>>
                                                 Metal Binding Loop

          450       460       470       480       490
                *         *         *         *
   446 TCCCGGGCCACTCCGCGCTGATTAAGGGTACCCTGACTCTGAAATAG
         P  G  H  S  A  L  I  K  G  T  L  T  L  K  *
       >>>>>>>>>>>>>>>>>>>>>>>>                   >>>
       Metal Binding Loop                         Stop
```

APPENDIX 3-B

The classification of the C112D/M121X (X = L, F, I) azurins as type zero copper proteins was published as a research article in *Nature Chemistry*, Volume 1, Pages 711-715. The article is reproduced here with permission from Nature Publishing Group.

nature chemistry

ARTICLES

PUBLISHED ONLINE: 1 NOVEMBER 2009 | DOI: 10.1038/NCHEM.412

Type-zero copper proteins

Kyle M. Lancaster[1], Serena DeBeer George[2,3], Keiko Yokoyama[1], John H. Richards[1]* and Harry B. Gray[1]*

Many proteins contain copper in a range of coordination environments, where it has various biological roles, such as transferring electrons or activating dioxygen. These copper sites can be classified by their function or spectroscopic properties. Those with a single copper atom are either type 1, with an intense absorption band near 600 nm, or type 2, with weak absorption in the visible region. We have built a novel copper(II) binding site within structurally modified *Pseudomonas aeruginosa* azurins that does not resemble either existing type, which we therefore call 'type zero'. X-ray crystallographic analysis shows that these sites adopt distorted tetrahedral geometries, with an unusually short Cu–O (G45 carbonyl) bond. Relatively weak absorption near 800 nm and narrow parallel hyperfine splittings in electron paramagnetic resonance spectra are the spectroscopic signatures of type zero copper. Cyclic voltammetric experiments demonstrate that the electron transfer reactivities of type-zero azurins are enhanced relative to that of the corresponding type 2 (C112D) protein.

One of the hallmarks of bioinorganic chemistry is the adaptation by proteins of a few transition metals to a host of functions spanning the range from structural to reactive[1]. Copper proves especially adept at meeting these biochemical demands and typically requires only ligands provided by the host protein. In a wide range of coordination environments, copper acts as an electron-transfer agent, activates dioxygen and scavenges reactive oxygen species, to cite only a few of its biological roles[2–4].

Copper sites in proteins have been classified according to their spectroscopic and functional properties[5]. A type-1 or blue copper site is so-named for an intense absorption band near 600 nm ($\varepsilon \sim 5{,}000\ M^{-1}\ cm^{-1}$) attributable to the cysteine S π to Cu(II) $d_{x^2-y^2}$ charge transfer. The highly covalent interaction between this thiolate ligand and Cu(II) also gives rise to drastically reduced parallel hyperfine splitting ($A_{\|}$) in the electron paramagnetic resonance (EPR) spectrum of a type-1 protein[6]. Blue copper sites behave as highly efficient electron-transfer agents, and their reduction potentials span a wide range (200 to 1,000 mV versus normal hydrogen electrode (NHE)). By contrast, type-2 sites do not exhibit intense bands in their visible absorption spectra, display $A_{\|}$ values resembling aqueous Cu(II) ions, and often have low reduction potentials. They do, however, combine with antiferromagnetically coupled (type 3) dicopper sites to form catalytically active trinuclear clusters capable of dioxygen activation[4,7]. Cu_A represents a case of delocalized binuclear copper related to type 1 but involving two cysteine ligands; it functions as another copper-based electron-transfer site in several proteins[8].

We have been testing the proposition that sulfur ligation is essential for the widespread electron-transfer functions of type-1 proteins, as successful replacement of soft sulfur donors with hard ligands could greatly enhance protein lifetimes in catalytic processes involving dioxygen or other powerful oxidants. In preliminary work on the Mizoguchi *Pseudomonas aeruginosa* C112D azurin scaffold[9,10], we found that the additional mutation M121L generates a protein with a high Cu(II/I) reduction potential as well as type-1 EPR parameters[11]. We also constructed C112D/M121F and C112D/M121I mutants that exhibit similar EPR behaviour; although, as in C112D/M121L, the intense charge transfer absorption is absent owing to coordination that previously has not appeared in the catalogue of copper sites. We call these unique constructs 'type zero' copper proteins.

Results

Structures. Crystals of C112D/M121X (X = L,F,I) azurins diffracted to high resolution (reflections visible to 1.6 Å) despite the limitations of laboratory X-ray sources. We took advantage of this unexpected windfall by collecting higher-resolution data for C112D to facilitate more meaningful comparisons among the series of mutants. In all cases, only one crystal proved necessary to collect >95% complete datasets to high resolution. Structures were solved readily by molecular replacement, and coordinates were refined with the resolution limit set by evaluation of Wilson plots and scaling/merging statistics (Supplementary Table S1). Coordinate error may be obtained from the estimated standard uncertainty (e.s.u.) in atomic positions as calculated by REFMAC5 from R_{work} and R_{free} (ref. 12). As the e.s.u. values represent an average uncertainty for each structure, Cu(II)-to-ligand bond distances are expected to show increased precision owing to lower thermal disorder (B-factors) relative to the entire atomic ensemble[13]. Coordinates and structure factors have been deposited in the Protein Data Bank. The oxidation state of copper was verified by comparing inner-sphere bond distances from Cu K-edge extended X-ray absorption fine structure (EXAFS) to the crystallographic coordinates (Supplementary Table S2 and Fig. S1).

In all cases the proteins packed as monomers around a copper coordination complex consisting of the N-terminal alanine of one azurin molecule and the H83 of a second, with the remaining coordination sites occupied by one molecule of Tris buffer and solvent. The protein tertiary structure remains unchanged among the four proteins, displaying the characteristic β-sandwich motif exhibited by members of the cupredoxin family[14].

The double mutants display striking differences within both their inner and outer copper coordination spheres compared with the C112D protein. In the inner-sphere case, the remarkable perturbations manifest themselves in the orientation and position of the oxygen-donor ligands. G45, previously regarded as weakly interacting owing to its remoteness to Cu(II) (2.6 to 3.1 Å), now appears to function as a true ligand to the metal, with distances ranging from

[1]Beckman Institute, California Institute of Technology, Pasadena, California 91125, USA, [2]Stanford Synchrotron Radiation Lightsource, SLAC National Accelerator Laboratory, Stanford University, Menlo Park, California 94025, USA, [3]Department of Chemistry and Chemical Biology, Cornell University, Ithaca, New York 14853, USA. *e-mail: jhr@caltech.edu; hbgray@caltech.edu

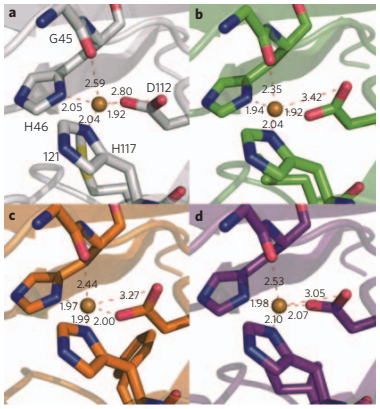

Figure 1 | The distorted tetrahedral coordination sphere of C112D/M121X (X = L,F,I) azurins features a relatively short Cu–O(G45 carbonyl) bond. **a–d**, The Cu(II) binding sites of C112D (**a**, 1.9 Å, PDBID: 3FQY), C112D/M121L (**b**, 2.1 Å, PDBID: 3FPY), C112D/M121F (**c**, 1.9 Å, PDBID: 3FQ2), and C112D/M121I (**d**, 1.9 Å, PDBID: 3FQ1) azurins are displayed with Cu–heteroatom bond distances indicated in Å. Oxygen atoms are red; nitrogen atoms are blue.

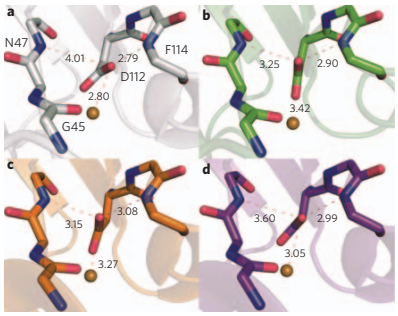

Figure 2 | The position of D112 shifts among the proteins, leading to variations in hydrogen bonding to the carboxylate. a–d, Secondary coordination spheres of Cu(II) in C112D (**a**, 1.9 Å, PDBID: 3FQY), C112D/M121L (**b**, 2.1 Å, PDBID: 3FPY), C112D/M121F (**c**, 1.9 Å, PDBID: 3FQ2), and C112D/M121I (**d**, 1.9 Å, PDBID: 3FQ1) azurins are highlighted with bond distances shown in Å for heteroatoms involved in the hydrogen bonding 'rack' network of the wild-type protein. Oxygen atoms are red; nitrogen atoms are blue.

2.55 Å in C112D/M121I to a record 2.35 Å in C112D/M121L (Fig. 1). In this extreme case, the Cu(II) is distorted significantly out of the NNO (H46–H117–D112) trigonal plane. The absence of M121 thioether ligation probably promotes metal ion bonding to the G45 oxygen lone pair.

The orientation of the D112 carboxylate, and by extension the distance of the second oxygen from copper, precludes assignment of this residue as a true bidentate ligand in any of the four proteins (Supplementary Fig. S3). We attribute this long-standing error to ambiguity stemming from the modest (2.4 Å) resolution of the earlier C112D structure[15]. Interestingly, major reorganization of the outer-sphere coordination structure accompanies positioning of the monodentate carboxylate (Fig. 2). In C112D/M121L, the nonligating carboxyl oxygen forms hydrogen bonds with the backbone amides of N47 and F114 in a near-perfect 120° arrangement. In contrast, this oxygen in C112D, C112D/M121I, and C112D/M121F makes a hydrogen bond only with F114. The two hydrogen bonds to D112 in C112D/M121L provide further impetus for Cu(II) to seek stabilization by bonding to the G45 carbonyl. This release of Cu(II) from interaction with position 121 and movement towards 45 allows D112 the freedom to rearrange and reconstitute the sterically constrained ('rack' or 'entatic') state responsible in part for the spectroscopic and reactivity properties of naturally occurring type 1 proteins[16]. Furthermore, it appears that this rearrangement of hydrogen bonds is modulated by the hydrophobic packing of residue 121 (Supplementary Fig. S2). Specifically, I121 and F121 sterically clash with F15, causing a reorientation of this residue. In the extreme case of C112D/M121F, this clash forces F15 to adopt multiple conformations. By contrast, F15 remains unperturbed by L121. This interaction may cause the structural rearrangement, which leads to reorientation of the N47–D112–F114 hydrogen bonding network.

Electronic absorption spectra. Each of the C112D and C112D/M121X (X = L,F,I) azurins displays a ligand-field absorption band near 800 nm, as well as a shoulder at ~310 nm corresponding to imidazole-to-Cu(II) charge transfer (ligand-to-metal charge transfer; LMCT) (Supplementary Fig. S4, Table 1). The intensities of the ligand-field features are very similar in the four proteins, although bandshapes and positions differ somewhat. Comparison of the hydrogen bond network between D112 and the backbone amide protons of N47 and F114 suggests that the withdrawal of electron density from the D112 carboxylate by these hydrogen bonds accounts for the lower ligand-field splitting in the C112D/M121L protein. LMCT intensities vary across the series, suggestive of differential Cu–N orbital overlap owing to varying degrees of tetrahedral distortion among the proteins.

X-ray absorption spectra. Two features are present in the Cu(II) X-ray absorption near-edge structure (XANES) of C112D/M121X (X = L,F,I) azurins (Fig. 3, Supplementary Fig. S5). The first is a weak absorption at ~8,979 eV that is assigned as a 1*s* to 3*d* transition. Formally forbidden in octahedral geometry, this feature, which gains intensity upon geometric distortion, has been used as a metric of 4*p* mixing into 3*d* ground states[6]. The intensity of this transition increases on going from C112D/M121I to C112D/M121F to C112D/M121L, which appears to correlate with the Cu(II) to G45 carbonyl oxygen bond distance. The data suggest that Cu(II)–O(G45) bonding promotes Cu(II) 4*p* mixing into the 3*d* ground state.

The second feature is a shoulder near 8,987 eV, which has been previously assigned as a 'shakedown' transition owing to an orbital contraction on promotion of core electrons to valence shells[17]. The energy and intensity of this transition have been used as metrics of site covalency. Although the poorly resolved nature of this feature precludes quantitative analysis of any differences in band positions,

Table 1 | Electronic absorption data.

	Ligand field λ_{max} (nm)	Ligand field ε_{max} (M^{-1} cm^{-1})	LMCT ε_{310} (M^{-1} cm^{-1})
C112D[10]	754	97	1,950
C112D/M121L	798(2)	96(1)	1,650(20)
C112D/M121I	789(2)	99(5)	2,000(30)
C112D/M121F	789(2)	90(10)	1,450(20)

NATURE CHEMISTRY DOI: 10.1038/NCHEM.412

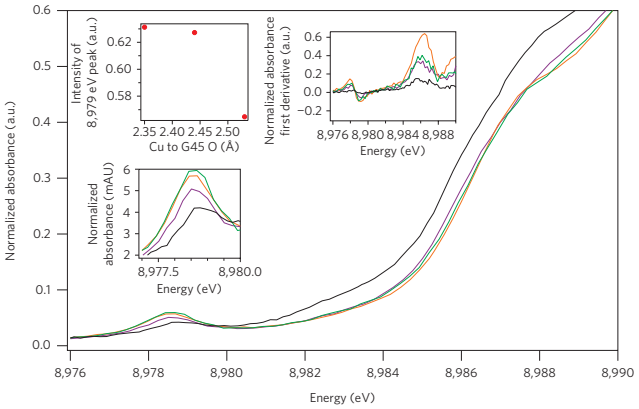

Figure 3 | XANES of C112D (black) and C112D/M121X (X = L, green; F, orange; I, purple) azurins with focus on the 8,979 eV and 8,987 eV pre-edge features. Intensity of the 1*s* to 3*d* 8,979 eV absorption (highlighted by the bottom-left inset) appears to correlate with the Cu(II) to G45–O bond distance as shown in the upper-left inset. The first derivative of the absorption spectrum (upper-right inset) indicates that the ~8,987 eV 'shakedown' energy does not vary within the resolution limits of the instrumentation.

the decreased intensities could indicate that there is a slight increase in site covalency for the C112D/M121X (X = L,F,I) proteins.

EPR spectra. EPR spectra for C112D and C112D/M121X (X = L,F,I) azurins were recorded at X-band (9.5 GHz) (Table 2, Supplementary Fig. S6). The C112D protein displays spin parameters characteristic of type-2 copper[5]. Previously reported superhyperfine coupling to ^{14}N is visible as unresolved broadening in the perpendicular region of the spectrum. The C112D/M121X (X = L,F,I) proteins differ markedly from C112D, with elevated g_z and decreased $A_{\|}$ values. Such spin parameters are typical for tetrahedral Cu(II) complexes[5]. Despite narrow linewidths, C112D/M121X (X = L,F,I) derivatives appear not to exhibit superhyperfine structure in their EPR spectra, suggesting diminished coupling of the unpaired electron to the ligating imidazole nitrogens in each case.

The $g_{\perp}$ anisotropy (R_g) is given by[18]:

$$R_g = \frac{2(\Delta g_y - \Delta g_x)}{(\Delta g_y + \Delta g_x)} \quad (1)$$

Factors affecting R_g include splitting between d_{xz} and d_{yz}, differences in the orbital reduction factors, and mixing of d_{z^2} into the Cu(II) ground state[19]. C112D/M121L displays the largest $g_{\perp}$ anisotropy, followed by C112D/M121I and C112D/M121F.

The following expressions for g values apply to Cu(II) in a distorted tetrahedral ligand field[20]:

$$\Delta g_x = -\frac{2\lambda\kappa_x^2}{\Delta d_{yz}} \quad (2a)$$

$$\Delta g_y = -\frac{2\lambda\kappa_y^2}{\Delta d_{xz}} \quad (2b)$$

$$\Delta g_z = -\frac{8\lambda\kappa_z^2}{\Delta d_{x^2-y^2}} \quad (2c)$$

where Δg_i is the difference between observed g values and the free electron $g_e = 2.0023$, Δd_i is the energy difference between ground and excited states formed by transitions to orbital $3d_i$, λ is the Cu(II) spin–orbit coupling constant (taken to be –830 cm^{-1}), and κ_i represents the orbital reduction factor along axis *i*. This latter parameter provides a metric of Cu(II) character in the ground state. These expressions also hold for a distorted O_h geometry, which has a $3d_{x^2-y^2}$ ground state, although Δd_i terms are exchanged for Δg_x and Δg_y.

Assuming a perturbed D_{4h} geometry for the C112D protein, a κ of ~0.78 is in agreement with the band at ~750 nm in the absorption spectrum (Supplementary Fig. S7). Calculated ligand-field splittings based on assignment of the corresponding bands in the spectra of the C112D/M121X (X = L,F,I) proteins as $d_{x^2-y^2}$ to d_{xy} transitions are in accord with experiment only if κ is near 0.85, which is consistent with the disappearance of superhyperfine broadening on going from the C112D protein to the double mutants. The ligand-field transitions in C112D/M121F and C112D/M121I azurins should be lower in energy than in C112D/M121L, contrary to observation. However, as shown in the case of $IrCl_6^{2-}$ (refs 21,22), mixing of ligand orbitals into the metal ground state leads to angular momentum quenching and in turn a decrease in the orbital reduction factor. The shortening of the Cu(II)–O(G45) bond increases oxygen 2*p* mixing into the ground state, which would lead to a smaller κ in C112D/M121L azurin relative to the C112D/M121F and C112D/M121I proteins. Differences in covalency, predicted by the $\Delta\kappa$ of ~0.05 going from C112D to the double mutants and a $\Delta\kappa$ of ~0.01 between C112D/M121L and C112D/M121F,I are likely to be small, in accord with the lack of substantial change in the ~8,987 eV XANES shakedown transition.

The axial hyperfine splitting arises from Fermi contact, spin dipolar and orbital dipolar terms. Mixing of $4p_z$ into the electronic ground state of tetrahedral Cu(II) sites decreases the spin dipolar term, leading to smaller axial hyperfine splittings. In the absence of polarized single-crystal X-ray absorption spectroscopy we cannot definitively assign the ~8,979 eV feature to a transition to a specific 4*p* orbital. The lack of correlation between ~8,979 eV intensity and the $A_{\|}$ values suggests that other mechanisms account for the diversity among the azurins. Differing $g_{\perp}$ anisotropies indicate varying degrees of d_{z^2} mixing, possibly attributable to a low-lying ligand-field excited state in each of the proteins.

Table 2 | EPR parameters from SpinCount simulations.

	g_x	g_y	g_z	σg_x	σg_y	σg_z	$A_{x,y}$ (mK)	A_z (mK)	$\sigma A_{x,y}$ (mK)	σA_z (mK)	R_g
C112D	2.063	2.063	2.311	0.008	0.008	0.002	0.07	14.89	0.06	0.17	0
C112D/M121L	2.047	2.116	2.381	0.015	0.008	0.007	1.65	10.32	0.001	0.10	0.87
C112D/M121I	2.043	2.101	2.386	0.013	0.021	0.005	0.25	10.18	0.003	0.10	0.83
C112D/M121F	2.054	2.100	2.386	0.018	0.011	0.006	0.18	10.36	0.009	0.09	0.62
WT[39]	2.059	2.059	2.259					5.0			

EPR spectra were simulated with *g*- and *A*-strain (σg, σA) included as fitting parameters to account for conformational heterogeneity in the glassed samples. Anisotropy in $A_{x,y}$ was not modelled due to the resolution limits of operating at X-band. Select parameters for wild-type azurin are included as a type 1 reference. Units are dimensionless unless otherwise indicated.

Electron transfer. We measured the Cu(II) reduction potentials of C112D/M121I and C112D/M121F azurins at pH 7.0 by direct electrochemistry on self-assembled monolayer (SAM)-modified monocrystalline gold bead electrodes (Supplementary Fig. S8). From both cyclic voltammetry and square wave voltammetry (SWV), the potential of C112D/M121I is 310 mV versus NHE (Supplementary Fig. S9). For C112D/M121F, which couples poorly to the electrode, the SWV Cu(II) reduction potential is also 310 mV.

Cyclic voltammetry experiments using SAM-modified gold bead electrodes afford not only reduction potentials but also electron-transfer rates[23]. Cu(II/I)-electrode electron-transfer rates ($\Delta G^\circ = 0$) were calculated for C112D, C112D/M121L, and C112D/M121I for several SAM chain lengths (Fig. 4). We were not able to determine electron-transfer rates for the C112D/M121F protein (weak cyclic voltammetry signals). Importantly, the copper centres of C112D/M121L and C112D/M121I exhibit enhanced electron-transfer reactivities relative to that of C112D, consistent with the lower Cu(II/I) reorganization associated with a sterically constrained active site[16].

Discussion

Type-zero copper proteins display marked similarities to their type-1 counterparts, especially in the striking resemblance of the F114-D112-N47 hydrogen bond network of C112D/M121L to that found in the sterically constrained native state[16,24]. The intensity of the 1*s* to 3*d* XAS transition and the narrow axial hyperfine splitting in EPR spectra are type-1 properties, whereas the absence of intense visible LMCT is a hallmark of type-2 proteins. Type-zero copper features a relatively short Cu(II)–O(G45) bond as part of near-tetrahedral coordination with accompanying narrow axial hyperfine splittings and relatively high reduction potentials. We suggest that 4*p* mixing accounts for much of the decreased axial hyperfine splitting relative to type 2 copper; and we conclude that the electronic ground state of type zero copper is Cu $3d_{xy}$ coupled to a low-lying d_{z^2}-based excited state.

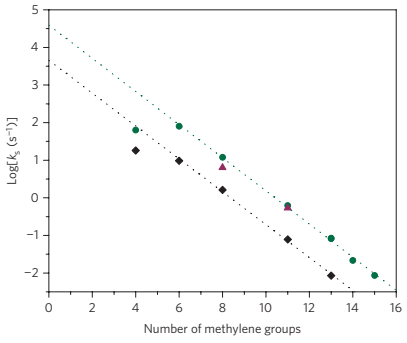

Figure 4 | Cu(II/I)-electrode electron-transfer rates (k_s) obtained for C112D (black), C112D/M121L (green), and C112D/M121I (purple) azurins from analysis of cyclic voltammetry data (Au–SAM electrochemistry). Type-zero azurins demonstrate significant rate enhancement relative to the type 2 C112D protein.

Copper proteins have received much attention recently as components of fuel cells based on biological materials[25–28]. Many of these studies have evaluated the efficacy of dioxygen reduction by multicopper oxidases as cathodes in such devices. Microscopic reversibility suggests that tuning reduction potentials in engineered multicopper oxidases could facilitate the oxidation of water to dioxygen. Such systems would be susceptible to irreversible deactivation of catalytic activity by oxidation of cysteine in their type-1 copper centres. Type-zero copper, with enhanced electron transfer reactivity relative to type-2 copper, offers a very promising alternative if reduction potentials in the 1 V range can be achieved.

Materials and Methods

Crystallography. Crystal growth procedures are available in the Supplementary Information. All X-ray diffraction experiments were carried out at the Caltech Molecular Observatory. Crystals were removed from wells and incubated in a cryoprotectant solution consisting of 30% ethylene glycol, 25% PEG 4000, 100 mM lithium nitrate, 10 mM copper sulfate and 100 mM Tris pH 7.0 for several minutes. During this time the large crystals fragmented along their long axes. Individual fragments were mounted on loops and immediately placed under a 100 K nitrogen cryostream. 1.54 Å X-rays were generated using a Rigaku rotating anode source. Oscillation images were recorded following determination of crystal parameters in a manner to maximize completeness of the data sets. Images were recorded on a Rigaku Raxis IV ++ detector operated with CRYSTALCLEAR.

Reflections were integrated and processed using iMOSFLM[29]. Data were scaled and merged using SCALA[30]. Structures were solved by the method of molecular replacement as implemented in program MOLREP[12] using the 2.4 Å structure of azurin C112D (PDBID: 1AG0) as a search model. The MOLREP output was then used for model building with ARP/wARP[31], with a single coordinate randomization included to alleviate any possible model bias. Maximum likelihood restrained refinement was carried out using the program REFMAC5[12].

Electronic absorption spectroscopy. Samples for UV/Vis spectra were concentrated to ~2 mM and exchanged into 100 mM sodium phosphate pH 7.0, with spectra recorded on a HP 8453 diode array spectrophotometer. Extinction coefficients were determined by titration of apoprotein with analytically prepared copper(II) sulfate. For NIR measurements, proteins were exchanged into 100 mM sodium phosphate pH 7.0 (uncorrected) in D_2O. NIR spectra were recorded on a Thermo Nicolet 6700 Fourier transform infrared spectrometer.

EPR spectroscopy. Samples for X-band EPR experiments were prepared by exchanging concentrated (~2 mM) protein into 100 mM sodium phosphate pH 7.0 containing 38% glycerol. Samples were glassed by rapid freezing in liquid nitrogen. X-band data were collected at 77 K on a Bruker EMX Biospin fitted with a cold finger. EPR spin parameters were simulated using the SPINCOUNT[32] package.

X-ray spectroscopy. Cu K-edge XAS, including EXAFS data, were collected at the Stanford Synchrotron Radiation Lightsource at beam line 7-3 under ring conditions of 3 GeV and 60–100 mA. A Si(220) double-crystal monochromator was used for energy selection and a Rh-coated mirror (set to an energy cutoff of 13 keV) was used for harmonic rejection. Internal energy calibration was performed by assigning the first inflection point of a Cu foil spectrum to 8,980.3 eV. Samples were exchanged into 100 mM sodium phosphate pH 7.0 with 38% glycerol and concentrated to ~3 mM. Proteins were loaded into 2 mm Lucite XAS cells with 38 μm Kapton windows and glassed by rapid immersion in liquid nitrogen. Data were collected in fluorescence mode (using a Canberra Ge 30-element array detector) with the sample maintained at 10 K in an Oxford liquid helium flow cryostat. To minimize photoreduction of Cu(II), the incident beam intensity was attenuated by a factor of ~3 with a four-layer aluminium Reynolds filter. Data were collected from 8,900 to

9,694 eV ($k = 13.5$ Å^{-1}) to reduce collection time and thus sample photoreduction. Photoreduction was monitored by following the growth of the 8,984 eV pre-edge feature indicative of Cu(I) formation. Four scans per spot were deemed to yield an acceptably oxidized sample (~20% Cu(I)), with a total of 16 scans being performed per protein. Scans were averaged and processed using the MAVE and PROCESS modules of the EXAFSPAK software package[33]. Background subtractions were achieved using PYSPLINE[34]. For XANES analysis, only the first scans per spot were averaged. XRD coordinates for the azurins were used to generate models for path calculation by FEFF7[35,36]. Relevant paths were then optimized by least-squares fitting in the OPT package of EXAFSPAK.

Electrochemistry. Detailed procedures for SAM-modified monocrystalline gold bead electrode preparation, azurin immobilization and electrochemical measurements have been reported previously[22,37]. 20 mM sodium phosphate pH 7.0 served as the electrolyte for electrochemical measurements. Electron-transfer rate constants were obtained by analysis of cyclic voltammetry peak separations[38].

Received 5 May 2009; accepted 15 September 2009; published online 1 November 2009

References

1. Gray, H. B. Biological inorganic chemistry at the beginning of the 21st century. *Proc. Natl Acad. Sci. USA* **100,** 3563–3568 (2003).
2. Gradinaru, C., Crane, B. R., Abrahamsson, M. L. & Gray, H. B. Electron transfer in metalloproteins (blue copper azurin). *Biophys. J.* **86,** 473A (2004).
3. Roberts, S. A. *et al.* Crystal structure and electron transfer kinetics of CueO, a multicopper oxidase required for copper homeostasis in Escherichia coli. *Proc. Natl Acad. Sci. USA* **99,** 2766–2771 (2002).
4. Palmer, A. E. *et al.* Spectroscopic characterization and O-2 reactivity of the trinuclear Cu cluster of mutants of the multicopper oxidase Fet3p. *Biochemistry* **41,** 6438–6448 (2002).
5. Solomon, E. I., Szilagyi, R. K., DeBeer George, S. & Basumallick, L. Electronic structures of metal sites in proteins and models: Contributions to function in blue copper proteins. *Chem. Rev.* **104,** 419–458 (2004).
6. Solomon, E. I. Spectroscopic methods in bioinorganic chemistry: Blue to green to red copper sites. *Inorg. Chem.* **45,** 8012–8025 (2006).
7. Lee, S. K. *et al.* Nature of the intermediate formed in the reduction of O_2 to H_2O at the trinuclear copper cluster active site in native laccase. *J. Am. Chem. Soc.* **124,** 6180–6193 (2002).
8. Hay, M., Richards, J. H. & Lu, Y. Construction and characterization of an azurin analog for the purple copper site in cytochrome c oxidase. *Proc. Natl Acad. Sci. USA* **93,** 461–464 (1996).
9. Mizoguchi, T. J., Di Bilio, A. J., Gray, H. B. & Richards, J. H. Blue to type 2 binding. Copper(II) and cobalt (II) derivatives of a Cys112Asp mutant of *Pseudomonas aeruginosa* azurin. *J. Am. Chem. Soc.* **114,** 10076–10078 (1992).
10. Mizoguchi, T. J. *Probing the role of the active site cysteine of azurin by site-directed mutagenesis*. PhD thesis, California Institute of Technology (1996).
11. Lancaster, K. M., Yokoyama, K., Richards, J. H., Winkler, J. R. & Gray, H. B. High-potential C112D/M121X (X = M, E, H, L) *Pseudomonas aeruginosa* azurins. *Inorg. Chem.* **48,** 1278–1280 (2009).
12. Murshudov, G. N., Vagin, A. A. & Dodson, E. J. Refinement of macromolecular structures by the maximum-likelihood method. *Acta Crystallogr. D* **53,** 240–255 (1997).
13. Vaguine, A. A., Richelle, J. & Wodak, S. J. SFCHECK: a unified set of procedures for evaluating the quality of macromolecular structure-factor data and their agreement with the atomic model. *Acta Crystallogr. D* **55,** 191–205 (1999).
14. Engman, K. C., Sandberg, A., Leckner, J. & Karlsson, B. G. Probing the influence on folding behavior of structurally conserved core residues in P-aeruginosa apo-azurin. *Protein Sci.* **13,** 2706–2715 (2004).
15. Faham, S. *et al.* Role of the active-site cysteine of *Pseudomonas aeruginosa* azurin. Crystal structure analysis of the Cu^{II}(Cys112Asp) protein. *J. Biol. Inorg. Chem.* **2,** 464–469 (1997).
16. Gray, H. B., Malmstrom, B. G. & Williams, R. J. P. Copper coordination in blue proteins. *J. Biol. Inorg. Chem.* **5,** 551–559 (2000).
17. DeBeer, S. *et al.* X-ray absorption spectra of the oxidized and reduced forms of C112D azurin from Pseudomonas aeruginosa. *Inorg. Chem.* **38,** 433–438 (1999).
18. Hitchman, M. A., Olson, C. D. & Belford, R. L. Behavior of in-plane g-tensor in low-symmetry d^1 and d^9 systems with application to copper and vanadyl chelates. *J. Chem. Phys.* **50,** 1195–1203 (1969).
19. Gewirth, A. A., Cohen, S. L., Schugar, H. J. & Solomon, E. I. Spectroscopic and theoretical studies of the unusual electron-paramagnetic-resonance parameters of distorted tetrahedral cupric sites - correlations to X-ray spectral features of core levels. *Inorg. Chem.* **26,** 1133–1146 (1987).
20. Mabbs, F. E. & Machin, D. J. *Magnetism and Transition Metal Complexes* (Dover Publications, 2008).
21. Stevens, K. W. H. On The magnetic properties of covalent XY_6 complexes. *Proc. R. Soc. Lond. A* **219,** 542–555 (1953).
22. Griffiths, J. H. E. & Owen, J. Complex hyperfine structures in microwave spectra of covalent iridium compounds. *Proc. R. Soc. Lond. A* **226,** 96–111 (1954).
23. Fujita, K. *et al.* Mimicking protein-protein electron transfer: Voltammetry of *Pseudomonas aeruginosa* azurin and the Thermus thermophilus Cu-A domain at omega-derivatized self-assembled-monolayer gold electrodes. *J. Am. Chem. Soc.* **126,** 13954–13961 (2004).
24. Ghosh, S., Xie, X., Dey, A., Sun, Y., Scholes, C. P. & Solomon, E. I. Thermodynamic equilibrium between blue and green copper sites and the role of the protein in controlling function. *Proc. Natl Acad. Sci. USA* **106,** 4969–4974 (2009).
25. Miura, Y. *et al.* Direct electrochemistry of CueO and its mutants at residues to and near Type I Cu for oxygen-reducing biocathode. *Fuel Cells* **9,** 70–78 (2009).
26. Tsujimura, S., Miura, Y. & Kano, K. CueO-immobilized porous carbon electrode exhibiting improved performance of electrochemical reduction of dioxygen to water. *Electrochimica Acta* **53,** 5716–5720 (2008).
27. Miura, Y. *et al.* Bioelectrocatalytic reduction of O-2 catalyzed by CueO from *Escherichia coli* adsorbed on a highly oriented pyrolytic graphite electrode. *Chem. Lett.* **36,** 132–133 (2007).
28. Blanford, C. F., Foster, C. E., Heath, R. S. & Armstrong, F. A. Efficient electrocatalytic oxygen reduction by the 'blue' copper oxidase, laccase, directly attached to chemically modified carbons. *Faraday Discuss.* **140,** 319–335 (2008).
29. Leslie, A. G. W. Recent changes to the MOSFLM package for processing film and image plate data. *Joint CCP4 + ESF-EAMCB Newsletter on Protein Crystallography* **26** (1992).
30. CCP4. The CCP4 suite: programs for protein crystallography. *Acta Crystallogr. D* **50,** 760–763 (1994).
31. Cohen, S. X. *et al.* ARP/wARP and molecular replacement: the next generation. *Acta Crystallogr. D* **64,** 49–60 (2008).
32. Golombek, A. P. & Hendrich, M. P. Quantitative analysis of dinuclear manganese(II) EPR spectra. *J. Magn. Reson.* **165,** 33–48 (2003).
33. George, G. N. *EXAFSPAK* (Stanford Synchrotron Radiation Laboratory, Stanford Linear Accelerator Center, Stanford University).
34. Tenderhold, A. *PySpline* (Stanford Synchrotron Radiation Laboratory, Stanford Linear Accelerator Center, Stanford University).
35. DeLeon, J. M., Rehr, J. J., Zabinsky, S. I. & Albers, R. C. Abinitio curved-wave X-ray-absorption fine-structure. *Phys. Rev. B* **44,** 4146–4156 (1991).
36. Rehr, J. J., DeLeon, J. M., Zabinsky, S. I. & Albers, R. C. Theoretical X-ray absorption fine-structure standards. *J. Am. Chem. Soc.* **113,** 5135–5140 (1991).
37. Yokoyama, K. *et al.* Electron tunneling through Pseudomonas aeruginosa azurins on SAM gold electrodes. *Inorg. Chim. Acta* **361,** 1095–1099 (2008).
38. Laviron, E. General expression of the linear potential sweep voltammogram in the case of diffusionless electrochemical systems. *J. Electroanal. Chem.* **101,** 19–28 (1979).
39. Pascher, T., Karlsson, B. G., Nordling, M., Malmstrom, B. G. & Vanngard, T. Reduction potentials and their pH dependence in site-directed-mutant forms of azurin from *Pseudomonas aeruginosa*. *Eur. J. Biochem.* **212,** 289–296 (1993).

Acknowledgements

We thank B. Brunschwig for assistance with Fourier transform infrared spectroscopy, Z. Gates and L. Thomas for assistance with X-ray diffraction data collection, and M. Day and J. Kaiser for discussions of crystal structural analyses. We thank E. Solomon for helpful comments on electronic structural formulations, and Y. Sheng for assistance with protein expression and purification. Stanford Synchrotron Radiation Lightsource operations are funded by DOE(BES). The Structural Molecular Biology program is supported by NIH (NCRR BMTP) (Grant Number 5 P41 RR001209)N and DOE(BER). This work was supported by NIH DK019038(HBG), Stanford GCEP, and NSF CHE-0802907. The Caltech Molecular Observatory is supported by the Gordon and Betty Moore Foundation.

Author contributions

K.M.L. and H.B.G. conceived and designed the experiments; K.M.L., S.D.G., and K.Y. performed the experiments; K.M.L., S.D.G., K.Y., and H.B.G. analysed the data, K.M.L., S.D.G., J.H.R., and H.B.G. co-wrote the paper.

Additional information

Supplementary information accompanies this paper at www.nature.com/naturechemistry. Reprints and permission information is available online at http://npg.nature.com/reprintsandpermissions/. Correspondence and requests for materials should be addressed to J.H.R. and H.B.G.

Chapter 4

THE ELECTRONIC STRUCTURE OF TYPE ZERO COPPER

INTRODUCTION

The type zero story now becomes more interesting from not only a scientific perspective, but also a literary one. The *dramatis personae* exploded around July 2009 as type zero went from spectroscopic curiosity to an international research effort enlisting the expertise of spectroscopists and theoreticians the world over. As with the "blue copper protein question," there was one initial spectroscopic feature that commanded attention: the peculiar EPR. Why was the hyperfine lowered so dramatically - was there enhanced covalency in the site? Why the $g_{\perp}$ anisotropy – was it substantial d_{z2} mixing in the ground state?

As a reviewer on the type zero SSRL proposal, Alejandro Vila was intrigued by the potential paramagnetic NMR behavior of these proteins that bound "type 1 copper in the absence of sulfur ligation," and as such reserved a month of instrument time on Argentina's biggest magnet to put type zero to the test. Of course, this required also the reservation of a month of María Eugenia "Ogi" Zaballa's time, as well. Israel Pecht (a central figure in the azurin saga whose contributions to type zero will be illuminated when we conclude with ET studies) brought these proteins to the attention of Daniella Goldfarb; she in turn recruited the computational assistance of Frank Neese (independently alerted to type zero by Serena DeBeer) to interpret reams of EPR data collected with her student Alexey Potapov. Frank also supplied the MPI – Mülheim MCD spectrometer in order to probe the type zero ligand field. Stephen Sproules would shortly join the fray, serving as spectroscopic ambassador to the Gray Nation by providing access to EPR at Q- and S-bands.

We shall now combine spectra recorded in Argentina, Israel, and Germany with German computational studies. The resulting electronic structural picture of type zero, in comparison with the type 2 C112D azurin, reveals that an effect as subtle as carboxylate orientation can result in dramatic perturbations to electronic structure.

MATERIALS AND METHODS

Protein Overexpression and Purification

Natural isotopic abundance C112D/M121X (X = M, L, F, I) *Pseudomonas aeruginosa* azurins were expressed and purified as outlined in Chapter 2. C112D/M121A azurin was kindly provided by Yuling Sheng.

Uniformly labeled $^{13}C/^{15}N$ C112D/M121X (X = M, L, F, I, A) and WT azurins were expressed using isotopically-enriched M9 minimal media by a modified literature procedure.[1] Starter cultures of BL21(DE3) *E. coli* transformed with plasmids encoding the desired azurin were grown in 50 mL of LB containing 100 μg/mL ampicillin cultures that were inoculated from single colonies grown on LB/agar plates. These cultures were grown overnight with shaking at 37 ºC. Cells were harvested by centrifugation at 5000 R PM with a Beckman JA-17 rotor for 10 minutes and resuspended in 20 mL fresh LB medium. 10 mL of this suspension was used to inoculate 2 L of LB medium containing 50 μg/mL ampicillin. This culture was grown with shaking at 37 ºC until an OD_{600} of 0.8 was reached. At this point, the culture was pelleted by centrifugation at 3750 x g for 8 minutes. Cells were transferred into 2 x 4 L baffled Fernbach flasks, each containing 500 mL of minimal media made with $^{15}NH_4Cl$-containing M9 salts, 2g U-^{13}C glucose (Cambridge Isotopes), and 100 μg/mL ampicillin. The full minimal media recipe is included as Appendix 4-A. These cultures were grown with shaking at 37 ºC for one hour. The temperature was then lowered to 32 ºC, ß-D-isopropylthiogalactopyranoside was added to 0.8 mM, and overexpression was then allowed to proceed for 7 hours.

Cells were harvested by centrifugation at 3750 x g for 10 minutes. Cells were resuspended in 100 mL of 20% sucrose solution containing 300 mM Tris (pH 8.1) and 1 mM EDTA and allowed to osmotically equilibrate for 45 minutes. Cells were then spun down at 7000 RPM for 20 minutes. Periplasmic extrusion was effected by resuspension in 30 mL ice-cold 500 μM $MgCl_2$; the material was transferred to a 150 mL beaker with a magnetic stir bar and allowed to

stir at 4 ºC for ten minutes. Contaminating genomic DNA was digested with DNaseI and RNase A if the mixture became viscous. The material was then spun at 12000 RPM in a Beckman JA-17 rotor for 30 minutes. Purification at this point followed the typical method (Chapters 2-3), although a Q FF FPLC column is substituted for the initial Q FF batch column; purification on the Superdex 75 size-exclusion column was run with 50 mM HEPES pH 7.0 containing 150 mM NaCl. This column was run covered in aluminum foil.

CW EPR Spectroscopy

S-band and Q-band spectra were measured using a Bruker ESP-300E spectrometer with an S-band loop-gap resonator (Bruker design ER4118SPT with custom improvements) or a Bruker Q-band cavity (ER5106QT), both with Bruker flexline support and an Oxford Instruments helium cryostat (CF935). Microwave frequencies were measured with a Hewlett-Packard frequency counter (HP5352P), and the field control was calibrated with a Bruker NMR field probe (ER035M). Spectra were simulated in SPINCOUNT. Samples for CW EPR were prepared in 50 mM HEPES pH 7.0 containing 50% glycerol.

Pulsed EPR Spectroscopy

W-band (95 GHz) measurements were performed by Alexey Potapov and Daniella Goldfarb on an in-house built spectrometer at the Weizmann Institute of Science in Rehovot, Israel. W-band echo detected EPR (ED-EPR) spectra were recorded using the two-pulse echo sequence, $\pi/2$-τ-π-τ-echo, where the microwave (μw) pulse lengths were $t_{\pi/2}$ =20 ns and t_{π}= 40 ns; and the inter-pulse delay τ of 550 ns.

W-band ENDOR spectra were measured using the Davies ENDOR pulse sequence, π-t-$\pi/2$-τ-π-τ- - echo, with a radio frequency (RF) π pulse applied during the time interval t. For measurements of ^{1}H ENDOR spectra the parameters were: $t_{\pi/2}$ =100 ns, t_{π} =200 ns, τ =400 ns and t_{rf} = 25 μs, for ^{15}N and ^{13}C the parameters were $t_{\pi/2}$ = 100 ns, t_{π} = 200 ns, τ =400 ns and t_{rf} = 40 μs. The ^{2}H ENDOR spectra were measured using the Mims ENDOR sequence $\pi/2$-τ-$\pi/2$-t-$\pi/2$-τ- - - echo, with a RF pulse applied during the time interval t. The experimental conditions were $t_{\pi/2}$ = 20 ns, τ = 550 ns (typical τ value that place the blind spots well outside the spectral range) and t_{rf} = 45 μs. All ENDOR spectra were recorded using the random acquisition mode, with one shot for each point and the total number of scans was

varied in the range 100-1500 depending on the signal to noise (S/N). The overall repetition time was 13-14 ms, which accounts for the instrumental overhead stemming from the time required for the data transfer from ADC to SpecMan.

W-band ELDOR detected NMR was measured with a pulse sequence π_{pump}-t- $\pi_{obs}/2$- τ-π_{obs}- echo where the subscripts pump and obs indicate different frequencies. In this experiment the frequency of the observe (obs) pulses is fixed at ν_1 and the frequency of the pump pulse, ν_2, is varied. The spectra are presented using the scale of $\Delta\nu=\nu_1-\nu_2$. The length of the $\pi_{obs}/2$ and π_{obs} pulses were 100/200 ns respectively τ was equal to 400 ns. The μw field strength of the pump pulse was ~2.5 MHz, which for the π_{pump} pulse of 10 μs yields a nominal flip angle of 5π.

W-band HYSCORE spectra were measured with the $\pi/2$-τ-$\pi/2$-t_1-π-t_2-$\pi/2$-τ-echo sequence where t_1 and t_2 are varied and echo intensity is monitored. The length of the $\pi/2$ and π pulses was 12.5 and 25 ns respectively; the length of interval τ is given in the figure captions. The starting value for t_1 and t_2 was 50 ns and it was incremented in 12.5 ns steps to obtain a 90 x 90 dataset. Background decay was removed by subtracting a 2nd order polynomial, the resulting data was zero filled to 512 points, apodized by a sine-bell function in both dimensions and 2D fast Fourier transformed to obtain a final spectra, shown in magnitude mode. For all W-band measurements the temperature was 8 K.

X-band pulsed EPR measurements were carried out on a Bruker ELEXSYS E580 spectrometer. The HYSCORE sequence employed $\pi/2$ and π pulses of 12 and 24 ns respectively, t1 and t2 were incremented in 48 ns steps, 128 points were collected in each dimension, the length of interval τ is given in the figure captions. The data were treated as described for the W-band HYSCORE spectra. For all X-band measurements the temperature was 10 K.

NMR Spectroscopy

Samples for NMR spectroscopy were prepared in 50 mM HEPES pH 7.0 buffer that was either 10 or 99% D_2O. Samples were concentrated to ~2-3 mM.

NMR spectra were recorded on a Bruker Avance II NMR Spectrometer at IBR – CONICET, Rosario, Argentina operating at a frequency of 600.13 MHz. ^{1}H spectra were acquired with a triple-resonance (TXI) probehead. ^{1}H spectra were recorded with a $\pi/2$ pulse preceded by presaturation of the water signal and diamagnetic region. The spectra window was ~ 100 kHz; total recycle time was ~ 200 ms. Spectra were apodized with ~ 40 Hz of exponential line broadening.

Saturation transfer difference (STD) ^{1}H spectra were acquired by the MicroNOE pulse sequence (Appendix 4-B). Samples were reduced to ~ 10-20% Cu^{I} by addition of appropriate stoichiometric amounts of ascorbate.

Directly detected ^{13}C NMR spectra were acquired with a broadband observe probehead tuned at the proper frequency, using an excitation pulse of 6.9 μs at 88.67 W. Inverse gated decoupling was applied during acquisition of ^{13}C spectra. For ^{13}C experiments, the carrier frequency was varied to ensure that putative paramagnetic signals did not arise due to frequency offsets.

MCD Spectroscopy

Samples for MCD were prepared by adding glycerol to ~50% to C112D/M121X (X = M, L, F, I, A) azurins in 100 mM HEPES, pH 7.0. Proteins were added to MCD cells and repeatedly frozen at 77 K until optically clear glassing was achieved. MCD spectra were obtained at MPI – Mülheim, Germany, at liquid He temperatures (5 and 10 K) on a Jasco J-715 (200–1060 nm) with an extended S-20 and S-1 photomultiplier tube (Hammamatsu). The J-500C spectrometer was equipped with an Oxford Instruments SM4-11 T superconducting magnet/cryostat. Spectra were recorded at ±1, ±3, ±5, and ±7 T.

Computational Methods

Calculations were performed by Mahesh Sundararajan and Frank Neese at U. Bonn, Germany using the Orca quantum chemistry suite.[2] Calculations were based on the following five X-ray structures: 4AZU = WT, 3FQY = C112D, 3FPY = C112D/M121L, 3FQ1 = C112D/M121I, 3FQ2 = C112D/M121F. QM/MM partitioning is shown as Figure 4.1, where the QM region comprised the Cu ligands as well as residues 47, 114, and 121; thus the outer coordination

sphere is preserved. Geometries were optimized in the presence of protein point charges (~2 x 10^4) using the BP86 functional[3] in conjunction with the Ahlrich's def2-SV(P) basis set. All geometry optimizations incorporated scalar relativistic effects (ZORA).[4]

The B3LYP functional[5] was used in conjunction with the CP(PPP)[6] basis for EPR calculations. The EPR-II basis[7] was selected for the nitrogen and oxygen atoms, the IGLO-II basis[8] for sulfur atoms, and def2-SV(P) was used to treat the remaining atoms. For all EPR calculations, scalar relativistic ZORA single point calculations were performed, employing a model potential derived for atomic ZORA calculations. In these calculations, the basis sets were uncontracted. The integration accuracy for Cu was additionally increased and three steep s-functions with exponents 3, 9, and 27 times larger than the exponent of the steepest s-function in the CP(PPP) basis set were added. Nuclear quadrupole coupling constants e^2qQ/h (NQCs) of ^{14}N nuclei were calculated from the electric field gradients V employing a nuclear quadrupole moment Q (^{14}N) of 0.02 barn. In addition, the asymmetry parameters of the quadrupole tensors were calculated as $\eta = (V_{xx}-V_{yy})/V_{zz}$ in a coordinate system with $|V_{zz}| \geq |V_{yy}| \geq |V_{xx}|$.

EPR properties were predicted using coupled perturbation Kohn-Sham theory for the g-tensor and the spin orbit coupling (SOC) operator was treated by the spin-orbit mean-filed (SOMF) approximation according to the Breit-Pauli operator.[9] Fermi contact terms and spin-dipole contributions to the hyperfine coupling contributions were obtained as expectation values over the B3LYP ground state spin density. First-order HFPCs were calculated for ^1H and ^{14}N, while spin-orbit contributions were taken into account for Cu.

Calculations at Caltech were performed using TITAN on a Windows XP 64 workstation (GlaDOS). TITAN was used to add protons to minimal active site regions from the 3D structures as well as to geometry optimize these protons by energy minimization.

THEORETICAL BACKGROUND

NMR of Paramagnetic Species

Typically, chemists use NMR as a staple characterization technique to glean structural information about diamagnetic species. The introduction of a paramagnetic center can complicate analysis of an NMR spectrum, but this complication in turn can yield valuable information about the electronic and molecular structure of the molecule under observation. It manifests in shifts of resonances outside their typical diamagnetic envelope (this envelope being 12 to -2 ppm for ^{1}H's) with concomitant broadening of signals on the order of several kHz. This broadening often results in the obliteration of measurable signals. The shifts are referred to as "contact shifts," and they arise due to summed contributions from Fermi contact (δ_{con}) and dipolar (pseudocontact) (δ_{dip}) terms added to the diamagnetic chemical shift (δ_{dia}) (Eq 4.1):[10]

$$\delta_{obs} = \delta_{con} + \delta_{dip} + \delta_{dia} \tag{4.1}$$

The first of these terms provides a measure of direct electron delocalization over the nucleus of interest, while the second can be used to glean structural information about the paramagnetic center. The magnitude of δ_{con} in ppm is given by Eq (4.2):[10-11]

$$\delta_{con} = 10^6 x \left[\frac{g_{av}\mu_B S(S+1)}{3\gamma_N k_B T} \right] x \frac{A}{\hbar} \tag{4.2}$$

where g_{av} is the average of the three principal components of the g-tensor, μ_B is the Bohr magneton, S is the electronic spin, k_B is Boltzmann's constant, $\hbar$ is Planck's constant divided by 2π, T is the temperature in Kelvin, γ_N is the gyromagnetic ratio of the observed nucleus, and A is the isotropic Fermi contact hyperfine coupling constant in MHz. The magnitude of δ_{pc} is given by Eq (4.3):[10-11]

$$\delta_{dip} = \frac{\mu_o \mu_B^2 S(S+1)}{36\pi k_B T r^3} x\left[\left(3\cos^2\theta - 1\right)\left[g_z^2 - \frac{1}{2}\left(g_x^2 + g_y^2\right)\right] + \frac{3}{2}\left(g_y^2 - g_x^2\right)\left(\sin^2\theta\cos 2\phi\right)\right] \quad (4.3)$$

where μ_o is the vacuum permeability, r is the distance between the paramagenetic center and the nucleus, g_i are the principal components of the g-tensor, θ is the angle between the z component of the g-tensor and the nucleus, and φ is the angle between the x component of the g-tensor and the nucleus. Exploring the θ and φ parameter space at r = 3.5 Å (an estimated moderate value for the distance to nuclei experiencing contact shifting in systems of present interest) and using the EPR parameters for C112D/M121L azurin (Chapter 3) reveals that contributions in Eq. (4.2) arising from $g_\perp$ anisotropy are minimal (0 – 3.5 ppm at $\theta = \pi/2$) and can be reasonably ignored in subsequent treatments (Figure 4.2).

In addition to being shifted outside of the diamagnetic envelope, resonances proximal to paramagnetic centers experience broadening. Again, this broadening possesses contributions from Fermic contact and pseudocontact terms. The full-width at half-maximum (FWHM), $\Delta\omega_{1/2}$ of an NMR peak is given by Eq. (4.4):

$$\Delta\omega_{1/2} = \frac{1}{\pi T_2} \quad (4.4)$$

where T_2 is the spin-spin or latitudinal relaxation time of an isolated spin; thus, the coupling of nuclear spins with electron spins leads to shorter nuclear spin relaxation times. The Fermi contact effect on T_2 is given by Eq. (4.5):* [10-11]

$$T_2^{-1} = \frac{1}{3} S(S+1)\left(\frac{A}{\hbar}\right)^2 \left(\tau_e + \frac{\tau_e}{1 + \left(\omega_s - \omega_I\right)^2 \tau_e^2}\right) \quad (4.5)$$

* Rigorously, the Fermi contact contribution to T_2^{-1} is also a function of τ_M, the chemical exchange lifetime, which will be assumed to be negligible for systems contained herein.

where τ_e is the electron spin relaxation time, and ω_S and ω_I are the electron and nuclear Larmor frequencies, respectively. Thus, with increasing magnetic fields the Fermi contact contribution to linewidth reduces to Eq. (4.6):

$$T_{2,con}^{-1} = \frac{1}{3} S(S+1)\left(\frac{A}{\hbar}\right)^2 \tau_e \tag{4.6}$$

Thus, greater electron delocalization over a ligand in a paramagnetic metal complex results in increasingly broadened NMR peaks. This can be somewhat mitigated by recording spectra at higher field, as has been demonstrated for plastocyanin.[12] The pseudocontact contribution to NMR linewidth is approximated by Eq. (4.7):[10-11]

$$T_{2,dip}^{-1} = \frac{4}{3}\left(\frac{\mu_o}{4\pi}\right)^2 \frac{\gamma_N^2 g_e^2 \mu_B^2 S(S+1)}{r^6} \tau_e \tag{4.7}$$

where g_e is the g value of a free electron. Again there are contributions from molecular rotation speed and the Larmor frequencies of nuclear and electronic spins, but these are insignificant compared to τ_e. With a knowledge of τ_e and in cases of zero to minimal metal-ligand covalency, linewidths of paramagnetically shifted signals can be used to glean distances to nuclei proximal to paramagnetic metal centers.

The value of τ_e is a major determinant of the observability of paramagnetically shifted NMR signals at typical protein NMR operating frequencies (600 – 900 MHz), with short relaxation times being required for successful spectroscopy. Values span several orders of magnitude, with $\tau_e = 10^{-11}$-10^{-13} s for so-called "shift agents" (used as structural probes to shift location-specific residues without significantly affecting observability) and $\tau_e \geq 10^{-8}$ s for typical aqueous Cu^{II} species. However, type 1 copper and Cu_A sites have been shown to have $\tau_e \leq 10^{-10}$ s. Plotting the distance dependence of Eq (4.7) for S = ½ systems and using Eq. (4.4) to convert to linewidth reveals the extent to which dipolar broadening can shroud nuclei in an NMR experiment (Figure 4.3).

The theory for electron spin relaxation time is complicated. Qualitatively, the presence of low-lying excited states has been invoked as a mechanism of τ_e enhancement.[10,13] Expressions for the electronic spin-spin ($T_{2,e}$) and spin-lattice ($T_{1,e}$) relaxation times reveal contributions from both g- and A-tensor anisotropy, with greater anisotropy conferring faster relaxation times.[10] This correlation has been observed experimentally, whereupon going from azurin to plastocyanin to stellacyanin (with increasing values of R_g, Eq. (3.2), sharper NMR peaks are observed.[14] In these cases the EPR parameter anisotropies are ascribed to the mixing of d_{z2} character into the ground state wavefunctions, implying small excitation energies to the d_{z2}-based LF state.[15]

We now see that from linewidths and calibration to prior BCP NMR studies, we can estimate τ_e in copper proteins. Moreover, while the very observability immediately implies the presence of low-lying excited states, the variable linewidths among related paramagnetic species can be used to gauge the relative energy gaps to these states within a series. Finally, through temperature dependence we may narrow this energy gap yet further. The temperature dependence of δ_{con} for a nucleus *k* is given by Eq. (4.8):

$$\delta_{con,k} = \frac{1}{T} \times \frac{f_{k,1} + f_{k,2} e^{(-\Delta E / k_B T)}}{1 + e^{(-\Delta E / k_B T)}} \tag{4.8}$$

In short, deviations of δ_{con} from inverse linear temperature dependence (Curie behavior) implies the presence of low-lying ($\Delta E \leq 0.8$ kK) excited states.

Magnetic Circular Dichroism

We shall treat MCD in only the most rudimentary fashion, as analysis of the C112D/M121X (X = M, L, F, I, A) azurins proved very simple. A summary of the discussion by Johnson is presented.[16]

The most basic theoretical approach to MCD dispersion is the rigid shift (RS) approach. RS assumes validity of the Born-Oppenheimer and Franck-Condon approximations and that spectral bandshape is unaffected by the Zeeman interaction with the applied magnetic field. RS MCD dispersion is given by Eq (4.9):

$$\Delta A(X \rightarrow Y) = \gamma\left\{-A_1\left(\frac{\partial f}{\partial E}\right) + \left(B_0 + \frac{C_0}{k_B T}\right) f\right\} \beta H b l \tag{4.9}$$

where X and Y are the states involved in the transition, γ is a spectroscopic constant, f is a normalized line shape function dependent on the transition energy $E_{XY} = E_Y - E_X$ and the incident photon energy, E; A_1, B_0, and C_0 are parameters that depend on the electric dipole selection rules for the absorption of circularly polarized light. These parameters give rise to the so-called *A*, *B*, and *C* term contributions to MCD spectra. Such terms can be identified readily via their spectroscopic behavior. A terms are dispersive and temperature independent, *B* terms are absorption shaped and temperature independent, and C terms are absorption shaped and temperature dependent.

We shall concern ourselves only with *C* terms. As mentioned, they can be distinguished by their temperature dependence. Their identification can be complicated by their appearance as closely-spaced transitions with opposite signs; these dispersive features are referred to as "pseudo-*A*" terms, but can be identified by their temperature dependence. Another feature of *C* terms is that in cases where Zeeman splitting is smaller than the bandwidth (applicable to our systems under discussion), the *C*-term will exhibit absorption shaped dispersion with the maximum at the same energy as the absorption maximum – it will allow identification of the transition energies within, *e.g.* our LF manifold.

Pulsed EPR

While the resulting hyperfine couplings provided by pulsed EPR techniques are quantities that may be readily understood (as they indicate degree of electron delocalization over nuclei proximal to a paramagnetic center), getting from point A to B is somewhat involved. However, a theoretical description of pulsed EPR as written by Daniella and Alexey for a forthcoming electronic structure report will be reproduced here to facilitate better understanding. Further discussion may be found in the chapter of Chasteen and Snetsinger.[17]

The energy level diagram for an electron spin S=1/2, coupled to one ^{14}N (I=1) nucleus is shown in Fig. 4.4. The nuclear frequencies within the α (M_S=1/2) and the β (M_S=-1/2) electron spin manifolds are ν^{α}_{sq1}, ν^{α}_{sq2} , ν^{α}_{dq} and ν^{β}_{sq1}, ν^{β}_{sq2} , ν^{β}_{dq} respectively. The notation sq

corresponds to single quantum transitions and dq to double quantum transitions. To first order

$$\nu^{\alpha}_{sq1,2} = \nu_{14N} - A/2 \pm P \tag{4.10}$$

$$\nu^{\beta}_{sq1,2} = \nu_{14N} + A/2 \pm P$$

where A and P are the orientation dependent hyperfine and nuclear quadrupole couplings, respectively and ν_{14N} is the ^{14}N Larmor frequency. There are three types of methods that can be used to measure nuclear frequencies in paramagnetic systems, ENDOR, ESEEM and ELDOR-detected (ED) NMR. While ENDOR is based in the excitation of allowed EPR ($\Delta M_S=\pm1$, $(\Delta M_I=0)$ and NMR ($\Delta M_S=0$, $(\Delta M_I=\pm1)$ transitions, the other two methods rely on the excitation of allowed and forbidden ($\Delta M_S=\pm1$, $(\Delta M_I=\pm1)$ EPR transitions and does not involve excitation of nuclear transitions as in ENDOR. In this work we have used all three methods.

When the hyperfine coupling happens to be equal to twice the nuclear Larmor frequency ($A=2\nu_{14N}$) a special situation is encountered called the cancellation condition. This means that the nuclear Zeeman interaction almost cancels the hyperfine interaction in one of the manifolds (depending on the sign of A). The nuclear quadrupole interaction is not cancelled and dictates the frequencies in low-frequency manifold, which are close to the nuclear quadrupole frequencies (NQR). The NQR frequencies are often referred to as ν_0, ν_-, ν_+, where $\nu_0 + \nu_- = \nu_+$ and are given by:

$$\nu_0 = 2K\eta, \qquad \nu_- = K(3-\eta), \qquad \nu_+ = K(3+\eta) \tag{4.11}$$

where $K=e^2Qq/4h$. Here e is the electronic charge, eq is the electric field gradient across the nucleus along the z axis, and Q is the nuclear quadrupole moment. The double quantum transition frequency of the other manifold is given by:

$$\nu_{dq} = 2[(\nu_{14N} + A)^2 + K^2(3+\eta)]^{1/2} \tag{4.12}$$

For $\eta \sim 0$ $\nu_0 = 0$ and $\nu_+ = \nu_-$ and only one NQR line is observed, whereas for $\eta \sim 1$, $\nu_0 \sim \nu_- \sim 1/2\nu_+$ and two frequencies appear, in the general case $0<\eta<1$ three lines are expected. The single quantum frequencies of the other manifold depend on both the ^{14}N hyperfine and quadrupole couplings, whereas the double quantum transition frequency does not depend on the quadrupole interaction to first order. The cancellation condition is often sought because the modulation depth in this case is very large and the hyperfine and quadrupole couplings can be easily determined.

RESULTS

Protein Overexpression and Purification

Column chromatography of $^{15}N/^{13}C$ azurins proceeded identically to natural abundance isotopologs (Chapters 2-3). ESI-MS of ^{15}N C112D/M121L azurin showed a major peak corresponding to a species weighing 14094.8 amu in an early preparation (Figure 4.5). The calculated, monoisotopic molecular weight for the ^{15}N isotopolog assuming average isotopic abundance for all remaining atoms is 14102.5. Secure with the ability to achieve >99% isotopic enrichment, copious U-^{13}C glucose was expended toward the production of $^{15}N/^{13}C$ azurins. ESI-MS of these proteins were not recorded, though NMR and EPR experiments revealed satisfactory isotopic enrichment.

CW EPR Spectroscopy

Among the type zero proteins discussed thus far, the only remarkable differences in spectroscopic properties are the $g_\perp$ anisotropies; $A_{||}$ values are consistently ~ 10 mK, g_z is consistently ~ 2.38. We can add C112D/M121A to the collection at this point; like C112D/M121L it displays well-resolved $g_\perp$ anisotropy in its X-band spectrum (Table 4.1, Figure 4.6). To more precisely define all of these quantities and thus facilitate more quantitative discussion, EPR spectra were recorded for C112D/M121X (X = M, L, F) at S (3.4 GHz) and Q (34 GHz) bands. The g-tensor is field dependent; the A-tensor is not. As such this

approach allows a separation of spectroscopic features arising from the hyperfine and g components.

Reassuringly, g- and A- parameters extracted from simulations of X-band EPR data (Chapter 3) simulate well the S- and Q-band spectra (Table 4.2). The C112D azurin EPR is nearly perfectly $g_{||} > g_{\perp}$ axial with $R_g = 0.17$ (Figure 4.7). The type zero azurins are indeed anisotropic in $g_{\perp}$, with the C112D/M121F mutant (Figure 4.8) possessing a lower R_g (Eq 3.2) of .60 as compared to 0.79 for C112D/M121L (Figure 4.9). Assuming isoenergetic excitations to d_{xz} and d_{yz} excited states, this translates to ~ 0.75% d_{z2} mixing into the C112D/M121F ground state wavefunction and ~ 1.5% into that of C112D/M121L.[15] The origin of this anisotropy and its consequences have been subsequently probed by a variety of methods (*vide infra*).

MCD Spectroscopy

Not surprisingly the MCD spectra of the type zero azurins C112D/M121X (X = L, F, I, A) are quite different from that of C112D azurin (Figure 4.10). Unfortunately circumstances prohibited quantification of protein concentrations (both the rush to prepare samples for the journey as well as desperate attempts to produce glasses), so $\Delta\varepsilon$ values are not reported. However, ample information concerning the electronic structure of the proteins may yet be extracted.

First, the 10-13 kK bands gain substantial magnetic dipole intensity over the 32.25 kK nm shoulders, consistent with their assignment to LF and CT transitions, respectively. The intensities of these bands are all inversely temperature dependent (Figure 4.11). Thus the dispersive band in the type zero spectra may be assigned as a pseudo-A convolution of C-terms, and the C112D band also assigned as a C-term. Gaussian deconvolution of these bands results gives a best fit to the type zero spectra with three bands within the dispersive feature (Figure 4.12-4.15, Table 4.3). For the C112D spectrum, one or two bands fit acceptably (Figure 4.16, Table 4.3).

The type zero Cu^{II} LF transitions observed by MCD are isoenergetic across the series of mutants explored. This indicates differences in R_g arise not due to energy differences of

transitions to d_{xz} and d_{yz} based excited states but rather are primarily attributable to variable amounts of d_{z2} character mixed into the ground state wavefunctions (*vide supra*). This in turn implies that the energy of the excited state with the highest degree of d_{z2} character is not very far above the ground state.

Unfortunately the Mülheim MCD did not allow probing to energies lower than 9 kK. Attempts to observe this low-lying LF band by near-infrared spectroscopy were unsuccessful, despite valiant attempts by Theis Brock-Nannestad using Jesper Bendix's Cary-5E spectrometer at the Univeristy of Copenhagen. We thus turned to the indirect approach of paramagnetic NMR spectroscopy.

NMR Spectroscopy

Generally the long relaxation times ($\tau_e \sim 10^{-9}$-10^{-8} s) of the unpaired spins in mononuclear Cu^{II} complexes preclude their study by NMR.[18] Long τ_e values are not universal to paramagnetic species – compounds with low-lying excited states such as high-spin Co^{II}, low-spin Fe^{III}, etc. afford mechanisms by which the τ_e can be accelerated. Type 1 copper proteins also possess low-lying excited states, ~ 5 kK; as such they have τ_e values near 10^{-10} s.[18] This enabled the Canters group to observe paramagnetically shifted ^{1}H resonances for ligands directly coordinated to blue copper.[13] We have reproduced the NMR spectrum of Cu^{II} WT azurin to afford ready comparison to the C112D and C112D/M121X (X = L, F, I, A) mutants (Figure 4.17).

C112D, as a type 2 copper protein, is devoid of paramagnetically shifted resonances in its ^{1}H NMR spectrum. However, resonances are visible outside the diamagnetic envelope in the type zero azurins (Figure 4.19). While C112D/M121X (X = L, I, A) azurins show many paramagnetically shifted resonances, only one signal is observed for C112D/M121F. The C112D/M121X (X = L, I, A) spectra generally show more features and narrower linewidths than WT azurin, demonstrating that these type zero proteins possess τ_e's as short as type 1 copper.

The temperature dependence of paramagnetically shifted resonances can reveal the presence of low lying (0.2 – 0.8 kK) excited states (*vide supra*).[19-20] The temperature dependence

of the paramagnetically shifted resonances of C112D/M121L azurin was recorded from 5 to 30 ºC (Figure 4.19). The resonances all follow Curie behavior, indicating an absence of thermally accessible excited states.

NMR can also be used to map electron delocalization over nuclei proximal to a paramagnetic center. In order to do so, resonance identity needed to be established. The downfield region of the 90% H_2O C112D/M121L spectrum was fit to 5 Lorentzian functions to pinpoint chemical shifts and to quantify linewidths (Figure 4.20). Recording spectra in 90% H_2O and 99% D_2O permitted initial assignment of resonances A and C in C112D/M121L to exchangeable protons, these likely being N_ε protons from H117 and H46, respectively (Figure 4.21, Table 4.4). Sequence specificity of these assignments is based on linewidth as the solvent-exposed exchangeable proton of H117 is more likely to experience chemical exchange broadening with the D_2O added to lock the NMR; the substantially larger FWHM of resonance A (9400 vs 1300 Hz for C) strongly suggests it corresponds to this residue. This experiment also revealed resonance B, masked by the solvent exchangeable signals. Resonance B was included in the Lorentzian fits to the 90% H_2O spectrum.

More complete assignment required STD experiments. Electrochemically determined ET rates for type zero azurins (Chapter 3) suggest that ESE should be sufficiently rapid to allow observation of saturation transfer; in the case of C112D/M121L (Figure 4.22) resonances D and E were assigned to ring protons of H46/H117 and resonance B was assigned to a $C_ß$ proton of D112. These assignments are based on previously determined values for azurin as well as statistics from BMRB for aspartate ß protons.[21] STD was not observed for C112D/M121X (X = I, F) azurins, though this was likely a result of suboptimal experimental conditions.

With these tentative assignments, estimates were made of δ_{dip} contributions. Without a C112D/M121A structure, analysis was limited to the C112D/M121L protein. The z-axis of the magnetic g-tensor was assumed to be parallel to the Cu-O(G45) bond; single-crystal EPR experiments with wild-type protein have shown this axis to be ~ 5º deviant from this line (Chapter 1). This amounts to at most a 1 ppm error (at 3.5 Å) in estimating δ_{dip}. Proton

distances were calculated using an active site model to which protons had been added. Bond lengths and geometries of these protons were optimized by energy minimization, freezing all heavier atoms. Using Eq. (4.3) (ignoring contributions from ϕ), values for δ_{dip} were calculated for the assigned protons. Finally, Eqs. (4.1-4.2) were applied to calculate hyperfine couplings $A/\hbar$ (Table 4.4).

Immediately apparent is an asymmetry in the hyperfine couplings to histidine protons. This has been observed consistently in BCP EPR and NMR studies (Chapter 1). Furthermore, it appears that there is substantial delocalization over the D112 C_{β} protons ($A/\hbar$ = 0.058 mK). ^{13}C NMR was pursued as an attempt to determine whether there is increased electron delocalization over the D112 carboxylates in type zero centers relative to the imidazoles. Paramagnetically shifted resonances could be observed in all C112D/M121X (X = L, F, I, A) azurins, but attempts to assign these resonances by STD were unsuccessful (Figure 4.23).

Pulsed EPR Spectroscopy[*]

Pulsed EPR was pursued to further map the electron delocalization of the type zero copper sites. Importantly, these techniques are applicable to type 2 copper proteins, enabling direct comparison of C112D/M121X (X = L, F) to C112D azurin.

The W-band echo detected (ED) EPR spectra of C112D/M121X (X = M, L, F) azurins are shown in Figure 4.24. The g-values extracted from the apparent features in the spectrum are presented in Table 4.5. Generally they agree well with those determined from CW EPR measurements, with small differences attributable to the increased linewidth of the W-band spectra arising from unresolved $^{63,65}Cu$ hyperfine couplings and g-strain. Small inaccuracies in the W-band field sweep may also contribute to the minor discrepancies. The spectra of the double mutants show some wiggles that are attributed to nuclear modulation effects, the depths of these effects vary with the magnetic field.[22]

^{14}N hyperfine couplings of directly bound N_{δ} of the histidine ligands. The hyperfine couplings to coordinated ^{14}N were first probed by W-band ED-NMR. The advantage of ED-NMR over

[*] The following section was written by Alexey Potapov and Daniella Goldfarb as a contribution to a manuscript in preparation. It has been edited by KML.

W-band ^{14}N ENDOR lies in its better S/N, particularly for cases with substantial forbidden transitions that occur when the hyperfine coupling and the nuclear Larmor frequency are comparable. The presence of significant quadrupolar interactions contribute further to the mixing of the nuclear states, increasing the transition probabilities of the forbidden transitions. It has been shown to be highly effective at W-band for ^{14}N hyperfine couplings around 20 MHz (ref). The disadvantage of this experiment is its low resolution, which is determined by the electron spin phase memory time.[23] In the case of broad lines, as often observed for ^{14}N, this disadvantage becomes less critical.

Figure 4.25 shows a series of ED-NMR spectra of the C112D mutant recorded at several field positions within the EPR spectrum. The spectrum measured at 32890 G, $g_{\perp}$, shows two pairs of lines, at 4.2 and 8.6 MHz, and 23.7 and 28.3 MHz. At this field, ν_{14N} is 10.17 MHz, meaning that there are two possible assignments for these lines. One possibility is that all four signals belong to one type of nuclei where one sees all four $\nu^{\alpha,\beta}_{sq1,2}$ lines. In this case A = 32.4 MHz and P = 2.2 MHz. In short, the N_{δ} of the two histidines have the same hyperfine and qudrupole couplings. The second possibility is that these lines belong to two types of nuclei: one with A_1 = 27.9 MHz (the 4.2 and 23.7 MHz lines) and the other with A_2 = 36.9 MHz (the 8.6 and 28.3 MHz lines). In this case, the quadrupolar couplings are not resolved. As the observer field decreases, the peak frequencies decrease and the splitting within the high and low frequency doublet components is reduced (see spectrum recorded at 31160 G). At lower fields the quality of the spectra is low, although the peaks at 7 and 22.7 MHz are clear.

We have carried out ED-NMR on uniformly labeled $^{13}C/^{15}N$ C112D samples to distinguish between the two above alternatives. At 32890 G, for the case of identical ligated nitrogens a $A(^{15}N)$ =45.4 MHz is expected and a doublet should appear at 8.4 MHz and 36.9 MHz, whereas for the anisotropic coupling two doublets corresponding to $A_1(^{15}N)$ = 39.1 MHz and $A_2(^{15}N)$ = 51 MHz are expected with doublets appearing at 5.3 and 33.8 MHz and 11.6 and 40.1 MHz, respectively. The ED-NMR spectrum recorded at 32890 G shows a peak at 33.8 MHz and the ENDOR spectrum shows a broad signal in the 40-44 MHz range (Figure 4.28a), supporting the case of inequivalently coupled nitrogens. The S/N of the ^{15}N ED-NMR

spectrum is much lower because forbidden transitions are less intense due to the absence of nuclear quadrupole interactions that contribute to the mixing of the nuclear states.

The ED-NMR spectra of C112D/M121L azurin were recorded at several fields along the EPR spectrum (Figure 4.25). They show a broad line at 20 MHz and a shoulder at ~5 MHz. The ED-NMR of the $^{15}N/^{13}C$ sample (Figure 4.26b) shows two peaks at 27 and 33 MHz. The latter may overlap with ^{13}C signals at 32.5 MHz (see Fig. 26a). The 27 MHz line corresponds to $A(^{15}N)$= 26 MHz and $A(^{14}N)$= 18.5 MHz and a signal at 19.2 MHz. This line is also very clear in the W-band ENDOR spectrum (Figure 29b). The second line would give $A(^{14}N) \sim 27$ MHz and a signal at 23.5 MHz. Both of these cases are within the linewidth of the ^{14}N ED-NMR signal. This shows that for C112D/M121L the two coordinated histidines ^{14}N are inequivalent. The spectra of C112D/M121F are similar, showing a single narrower peak at 20 MHz and a weak signal at 40 MHz assigned to ν^{β}_{dq}. This inequivalence is apparent also in some of the C112D/M121L ED-NMR spectra. Here the low frequency peak, corresponding the $\nu^{\alpha}_{sq1,2}$ frequencies of the other manifold is not resolved. From the 20 MHz signal we obtain $A \sim 20$ MHz and there should be a second line at ~0 MHz (ignoring the quadrupolar interaction). Since the position of ^{14}N lines does not vary with the magnetic field, the hyperfine anisotropy is not substantial.

To further confirm this assignment we carried out W-band HYSCORE (hyperfine sublevel correlation spectroscopy) measurements, where we expect to resolve the low frequency component. HYSCORE is a two dimensional correlation experiment where cross-peaks appear between nuclear frequencies in different electron spin manifolds, namely ($\nu^{\alpha}_{sq1,2}$, $\nu^{\beta}_{sq1,2}$), ($\nu^{\alpha}_{sq1,2}$, ν^{β}_{dq}) and (ν^{α}_{dq}, ν^{β}_{dq}) and their symmetric counterparts. Goldfarb and co-workers have already shown in a number of studies that W-band HYSCORE is particularly useful for observing ^{14}N hyperfine couplings around 20 MHz, which at W-band are within the cancellation condition, $|A| \sim 2\nu_{14N}$.[24]

W-band HYSCORE spectra of C112D/M121F were recorded at the g_y position (32420 G) with two different τ-values (Figure 4.28a,b). A number of cross peaks appear in both (+,+) and (-,+) quadrants. The frequencies of the peaks and their assignments are listed in Table 4.6. In an earlier work on ascorbate oxidase Goldfarb and coworkers have determined that $A > 0$

for the directly bound nitrogen and therefore we assign the low frequency signals to the α manifold.[25] The frequencies of $sq_{1,2}^{\beta}$ are in good agreement with those observed in the ED-NMR spectrum and their resolution allows estimating the quadrupolar splitting 2P ~ 2.5 MHz. Similar to the ED-NMR the signals of the N_{ε} of the two different histidines are not resolved. The HYSCORE spectra of C112D/M121L were in general similar to those of C112D/M121F, showing most of the signal at the (-,+) quadrant, indicating a slightly larger A value for at least one of the ^{14}N. This is consistent with the ED-NMR of this sample that showed a broader peak. Spectra measured also at $g_{||}$ were better resolved but no significant shifts were observed. The observed frequencies are summarized in Table 4.7 as well. The quality of the HYSCORE spectra of C112D is lower than that of the other mutant because the couplings are further away from the cancellation condition (Figure 4.28c). One cross peak is observed in the (-,+) quadrant (see Table 2), consistent with our earlier assignment. We could not observe any cross peaks involving the 28 MHz signal, which does appear on the (+,+) diagonal. Table 3 lists the hyperfine couplings obtained from these measurements.

^{13}C hyperfine couplings. To further characterize the first shell ligands of type zero Cu^{II} we carried out W-band ENDOR measurements on the ^{15}N, ^{13}C enriched samples, focusing on the ^{13}C region. The spectra shown in Figure 4.28b present the small coupling region and consist of several doublets centered around the Larmor frequency of ^{13}C, ν_{13C}, revealing marked differences between C112D and C112D M121F/L. While the largest hyperfine coupling observed in the ENDOR spectrum of C112D is ~ 5 MHz, for the C112D/M121L/F mutants that have rather similar spectra, it is ~ 9 MHz. It is difficult, however, to assign the observed couplings to any particular nucleus, since the signals may arise from various ^{13}C nuclei such as the carboxyl of aspartate, imidazole carbons, *etc.* We have also recorded the X-band HYSCORE spectrum of C112D at $g_{\perp}$. It exhibits two ridges running perpendicular to the main diagonal with hyperfine couplings of A ~ 2.5-5 MHz and A ~ 2.5-4 MHz. Furthermore there are poorly resolved ridges around the ν_{13C} due to more distant ^{13}C nuclei. The presence of two inequivalent carbon nuclei with close couplings is consistent with W-band ^{13}C-ENDOR spectra, where the line shape may not be simulated with only one nucleus. The ^{13}C hyperfine couplings observed for an equatorial carboxylate ligand in a $Cu(Histidine)_2$ complex are A=(-5.0, -2.9, -1.4) MHz[26] and therefore part of the signals observed can be tentatively assigned to

the D112 carboxylate ligand. The other couplings in this range are likely first neighbor ^{13}C nuclei to the coordinated N_δ of the histidine ligands.

Figure 4.28a shows the region of large ^{13}C couplings. Here again there is clear difference between the type 2 and type zero spectra. The spectra of C112D/M121L and C112D/ M121F exhibit ^{13}C couplings of up to 22 MHz. From the lineshape of the positive side of the spectra (high frequency end) of both mutants we can estimate $A_\perp \sim$ 15 MHz and $A_{||} \sim$ 22 MHz. We exclude the possibility that this broad line is a $^{63,65}Cu$ line because for the C112D/M121L mutant these are expected to appear around 2 and 67 MHz (neglecting the nuclear quadrupole interaction) for ^{63}Cu (69% natural abundance) based on the $A_\perp(^{63,65}Cu) = 14.2$ G obtained from simulations of the CW X-band EPR spectrum (Chapter 3). For C112D the ^{13}C signals severely overlap with the ^{15}N signals and therefore the assignment is ambiguous. Nonetheless, we can safely estimate that the ^{13}C coupling does not exceed 15 MHz for this sample. For C112D $A_\perp(^{63,65}Cu) = 1.5$ G and the ^{63}Cu lines are expected at 37 ± 4 MHz. Hence the broad feature observed for C112D could have contributions from ^{63}Cu.

^{14}N hyperfine couplings of the remote nitrogens. In order to detect any weakly coupled ^{14}N nuclei such as the remote N_ε of the histidine ligands or the backbone ^{14}N's of G45 or D112 we have also performed X-band HYSCORE measurements that are known to be particularly useful for the detection of nitrogens in Cu^{II} binding sites of proteins.[27] At X-band frequencies the cancellation condition for ^{14}N applied for A ~ 2MHz. The HYSCORE spectra of the three mutants were recorded at maximum echo intensity ($g_\perp$ for C112D and g_y for the other two). All three are quite similar showing a set of three cross peaks of the type ($\nu^\beta_{sq1,\ sq2,\ dq}$, ν^α_{dq}) (assuming A > 0). The cross peaks indicate a significant broadening of the ν^α_{dq} line that seems to consist of two peaks. This broadening is also apparent in spectra recorded at the g_{zz} ($g_{||}$ for C112D), where the range of selected orientations is considerably narrower and it suggests that it arises from two resolved types of ^{14}N. In Table 4.8 we summarize the frequencies of all peaks observed and their assignments. Here $\eta \sim 1$ and therefore only two NQR lines are observed. In a few spectra a combination line at $\nu^\beta_{dq}+\nu^\beta_{sq1,2}$ ($\nu_{0,-}+\nu_{+}$) is evident, arising from the presence of two coupled nuclei.[28] From the NQR frequencies we obtain that e^2Qq/h = 1.52 MHz, similar to values reported in the literature.[29] In fact the HYSCORE spectra are very similar to that of azurin, except that it lacks the cross peaks arising from a backbone ^{14}N

assigned to C112;[30] its absence confirms this earlier assignment. Using Eq. 4.12, K = 0.38 and η = 1 we estimate A_a=1.7-1.9 MHz and A_b=1.3-1.6 MHz for all three mutants for the two histidines remote nitrogens. These are well within the range observed for type 1 and type 2 Cu^{II} in other proteins. X-band HYSCORE of the enriched $^{15}N/^{13}C$ C112D sample (Figure 4.29) shows ^{15}N cross peaks with a width that corresponds to A(^{15}N) = 1.6-2.5 MHz and the same is observed for the W-band ENDOR in this region (Figure 4.30a). This corresponds to A(^{14}N) = 1.1-1.8 MHz, in agreement with the above estimation. We have also measured the W-band Mims ENDOR spectrum of the natural abundance and the $^{15}N/^{13}C$ labeled C112D/M121F sample in the $^{14}N/^{15}N$ Larmor frequency region (Figure 4.30b). Here, a sharp ^{15}N doublet with a splitting of 2.2 MHz is observed in the enriched sample. This spectrum indicates that the two $^{15}N_\varepsilon$ have the same hyperfine couplings for this particular set of selected orientation (at g_y). The ^{15}N 2.2 MHz hyperfine coupling corresponds to a ^{14}N coupling of 1.6 MHz. Interestingly, this value is just between the estimates of A_a and A_b. The orientation selection at maximum echo at X-band is different and therefore one can resolve the two different nitrogens.

^1H hyperfine couplings. To complete the picture of the spin density distribution in type zero Cu^{II} we have measured the ^1H ENDOR spectra, searching for unusually large hyperfine couplings, beyond those expected from the point-dipole approximation that may indicate some large spin density on the ligands. The W-band orientation selection spectra of the three mutants are presented in Figure 4.31. The largest couplings, $A_{||}$ ~ 11-12 MHz, are observed for C112D/M121L/F as the $g_{||}$ position is approached. For C112D the maximum splitting, ~ 12 MHz is observed in the center of the powder pattern. There are many protons and it is rather difficult to assign them. However examination of the crystal structures of C112D and C112D/M121L can help assigning those with the largest couplings. The nearby protons are listed in Table 5.

The most likely candidate for the closest proton with the largest hyperfine coupling is the proton attached to C_α of H46 (Table 4.9). We can facilitate these assignments by identifying solvent-exchangeable protons. For that we have also performed ENDOR experiments on samples partially enriched with D_2O. The proton ENDOR spectra with and without D_2O are

compared in Figure 4.34. The spectra reveal the disappearance of lines at ± 2 MHz upon addition of D_2O. These spectra are further compared with the ^2H ENDOR spectra, presented in the ^1H frequency scale obtained by multiplying by γ_H/γ_D. The disappearing features coincide with lines in deuteron ENDOR spectrum. The distance to those exchangeable protons as estimated using the dipole-dipole approximation is ~ 3.4 A., the line most probably belonging to one of the exchangeable amide protons.

The proton couplings observed are those expected from dipolar interactions and do not reveal any large unexpected spin density that would be manifested by a large isotropic hyperfine coupling as observed for the cysteine β-protons in type 1 copper. In addition no significant differences were observed in the maximum width of the spectra between single and double mutants. The spectra of the two C112D/M121L/F mutants are rather similar, while they differ considerably from C112D.

Calculations

Calculations were performed to assist the assignment of hyperfine couplings from NMR/EPR, as well as to elucidate the electronic structural origin of the observed spectroscopic features in the type 2 and type zero azurins. As mentioned, clear monodentate coordination is observed in the type zero azurins, while in the case of C112D azurin there is some ambiguity regarding the extent of interaction between the Cu^{II} and $O_{\varepsilon 2}$ of D112 (Table 4.10). In QM/MM optimized structures, for both C112D/M121L and C112D/M121F azurins, monodentate D112 coordination is found to be more stable by ~ 20 kJ/mol. In the case of C112D and C112D/M121I, bidentate coordination mode was found to be ~15 kJ/mol more stable than monodentate coordination. For the bidentate C112D and C112D/M121I structures, 100% spins were observed; for the monodentate C112D/M121L and C112D/M121F structures, only 75% spin density was observed near Cu, while the remaining 25% spin delocalized near D112 amide linkages. Constrained bidentate QM/MM geometry optimizations were then performed on these two azurins.

Calculated g- and A-tensors from both monodentate and bidentate QM/MM structures are presented in Table 4.9. Agreement is marginal, although clear trends may be observed. First, the experimental anisotropy in g-values of the type zero proteins are better reproduced

by the monodentate optimized structures. The C112D $g_{\perp}$ isotropy is only reproduced by the bidentate D112 structure. The experimental drop in $^{63/65}$Cu $A_{||}$ on going from type 2 to type zero requires bidentate D112 coordination for C112D azurin, with monodentate coordination for the type zero proteins.

DISCUSSION

Like their wild-type progenitor, the C112D/M121X (X = M, L, F, I, A) azurins have been subjected to a battery of spectroscopic probes and theoretical methods. Unfortunately, at this point only a semi-quantitative description of the electronic structure has emerged.

First we shall address the narrow hyperfine splitting. While the pulsed EPR detected a not-insubstantial ^{13}C coupling of ~24 MHz in the C112D/M121X (X = L, F) azurins compared to ~12 MHz for the largest ^{13}C coupling in C112D, this hardly approaches the value that would be expected in the presence of metal-ligand covalency akin to WT azurin's Cu^{II}-S(C112) bond.[31] Moreover, the calculated XAS for these azurins indicates that what 4p-mixing exists is hardly of the magnitude required (~12%) to produce the narrow hyperfine splitting. Thus, the narrow hyperfine splitting is almost entirely attributable to spin-dipolar effects.

The $g_{\perp}$ anisotropy is attributable to d_{z2} mixing into the ground state wavefunction. MCD spectra show as many as 3 isoenergetic LF excitations. However, calculated MCD spectra suggest that there may only be 2 LF transitions visible for the type zero mutants within the experimentally observed window (35 kK > E > 9 kK). Nevertheless, the linewidths of paramagnetically shifted NMR signals show a clear trend with the anisotropy of the $g_{\perp}$, ultimately being obliterated from observation in the C112D/M121F mutant, suggesting that the lowest-lying state is at variable excitation energy within the type zero series. The temperature dependence behavior of the type zero NMR puts a lower limit of 0.8 kK for low-lying LF excitations.

Interestingly, the calculations indicate a requirement for monodentate D112 coordination in order account for type zero spectroscopic features. The orientation of D112 appears to be controlled by the packing of residue 121. It is unclear whether freedom of Cu^{II} from the constraint of south-pole ligation and thus its movement toward G45 leads to D112's carboxylate reorientation, or whether effects from hydrophobic packing in the south pole region propagate to the D112 reorientation. In either case, the reorientation seems to be stabilized by hydrogen bonding from the amide nitrogens of N47 and F114. Structural alignment of C112D with C112D/M121L reveals that the positions of these moieties are unperturbed by axial substitution.

Possibly, the alignment of D112 to receive hydrogen bonds from the classical "rack" results in a shift of polarization of electron density within this carboxylate moiety. These interactions may result in a perturbation of the energy landscape of the ligand, with stabilization of the sp^2 resonance form of the non-coordinated oxygen, leading to larger sp^3 character of the coordinated oxygen and thus deeper penetration into the singly occupied Cu^{II} molecular orbital.

Alternatively, as with WT azurin, the strengthened axial interactions with G45 may result in analogous behavior to the "coupled distortion" exhibited by type 1 copper.[32-33] Increased overlap with orbitals at the north pole may rotate the frontier d_{x2-y2} orbital, shifting the character of the interaction with D112 O to either predominantly σ or π character. In this manner a further parallel may be drawn between type zero and type 1: proteins within either regime display characteristic spectroscopic perturbations arising from their degrees of tetrahedral distortion. Of course the electronic structural nature of both the C112D and the type zero Cu-O bonds will require elucidation to test this hypothesis.

Establishing the actual effects of hydrogen bonding on the electronic structure of the D112 ligand and thus the effects when coordinated to Cu^{II} will require further study. Considering the parallels with the WT protein, it is not unreasonable that N47 and F114 should exert some control over the spectroscopic properties of type zero centers. Now, however, we shall see that in addition to conferring distinguishing spectroscopic properties, the restoration of the rack to sulfur-free mononuclear copper binding sites also imparts function.

REFERENCES

1. Marley, J.; Lu, M.; Bracken, C. *J. Biomol. NMR* **2001**, *20*, 71-75.
2. Neese, F.; Becker, U.; Ganyushin, D.; Hansen, A.; Liakos, D. G.; Kollmar, C.; Kossmann, S.; Petrenko, T.; Reimann, C.; Riplinger, C.; Sivalingam, K.; Valeev, E.; Wezisla, B.; Wennmohs, F. ORCA, version 2.7.0b; University of Bonn: Bonn.
3. a) Becke, A. D. *Phys. Rev. A* **1988**, *38,* 3098; b) Perdew, J. P. *Phys. Rev. B* **1986**, *33,* 8822.
4. a) van Lenthe, E.; Baerends, E.J.; Snijders, J.G. *J. Chem. Phys.* **1993**, *99*, 4597-4610. b) van Wllen, C. *J. Chem. Phys.* **1998**, *109,* 392.
5. a) Becke, A. D. *J. Chem. Phys.* **1993**, *98,* 5648. b) Lee, C., Yang, W., and Parr, R. G. *Phys. Rev. B* **1988** *37* 785
6. a) Neese, F. *Inorg. Chim. Acta* **2002**, *337,* 181. b) Sinnecker, S., Slep, L. D, Bill, E., and Neese, F. *Inorg. Chem.* **2005**, *44,* 2245
7. V. Barone, in *Recent Advances in Density Functional Methods, Part I*, Ed. D. P. Chong, World Scientific Publ. Co., Singapore, **1996**.
8. Kutzelnigg, W., Fleischer, U., and Schnidler, S. The IGLO-Method: Ab Initio Calculation and Interpretation of NMR Chemical Shifts and Magnetic Susceptibilities. In *NMR Basic Principles and Progress*; Springer Verlag: Berlin/Heidelberg, **1991**; pp 165− 262.
9. Neese, F. *J. Chem. Phys.* **2005**, *122*, 34107.
10. *Solution NMR of Paramagnetic Molecules. Applications to Metallobiomolecules and Models.* Bertini, I.; Luchinat, C.; Parigi, G., Eds.; Current Methods in Inorganic Chemistry 2; Elsevier: Amsterdam, **2001**.
11. Golding, R.M.; Stubbs, L.C. *J. Magn. Reson.* **1979**, *33*, 627-647.
12. Bertini, I.; Ciurli, S.; Dikiy, A.; Gasanov, R.; Luchinat, C.; Martini, G.; Safarov, N. *J. Am. Chem. Soc.* **1999**, *121*, 2037-2046.
13. Kalverda, A.P.; Salgado, J.; Dennison, C.; Canters, G.W. *Biochemistry* **1996**, *35*, 3085-3092.
14. Bertini, I.; Fernández, C.O.; Karlsson, B.G.; Leckner, J.; Luchinat, C.; Malmström, B.G.; Nersissian, A.M.; Pierattelli, R.; Shipp, E.; Valentine, J.S.; Vila, A.J. *J. Am. Chem. Soc.* **2000**, *122*, 3701-3707.
15. Gewirth, A.A.; Cohen, S.L.; Schugar, H.J.; Solomon, E.I. *Inorg. Chem.* **1987**, *26*, 1133-1146.
16. Johnson, M.K. CD and MCD Spectroscopy. In *Physical Methods in Bioinorganic Chemistry: Spectroscopy and Magnetism.* Que, L. Jr., Ed. University Science Books: Sausalito, **2000**, pp 233-286.
17. Chasteen, N.D.; Snetsinger, P.A.; ESEEM and ENDOR Spectroscopy. In *Physical Methods in Bioinorganic Chemistry: Spectroscopy and Magnetism.* Que, L. Jr., Ed. University Science Books: Sausalito, **2000**, pp 187-232.
18. Banci, L.; Pierattelli, R.; Vila, A.J. *Adv. Protein Chem.* **2002**, *60*, 397-449.
19. Bertini, I.; Bren, K.L.; Clemente, A.; Fee, J.A.; Gray, H.B.; Luchinat, C.; Malmström, B.G.; Richards, J.H.; Sanders, D.; Slutter, C.E. *J. Am. Chem. Soc.* **1996**, *118*, 11658-11659.
20. Fernandez, C.O.; Cricco, J.A.; Slutter, C.E.; Richards, J.H.; Gray, H.B.; Vila, A.J. *J. Am. Chem. Soc.* **2001**, *123*, 11678-11685.
21. Biological Magnetic Resonance Data Bank. http://www.bmrb.wisc.edu/
22. Modulation effects on W-band.
23. Schosseler, P.; Wacker, T.; Schweiger, A. *Chem. Phys. Lett.* **1994**, *224*, 319-324.
24. Höfer, P.; Gruff, A.; Nebenführ, H.; Mehring, M. *Chem, Phys. Lett.* **1986**, *132*, 279-282.
25. Potapov, A.; Pecht, I.; Goldfarb, D. *Phys. Chem. Chem. Phys.* **2010**, *12*, 62-65.
26. Baute, D.; Arieli, D.; Neese, F.; Zimmerman, H.; Weckhuysen, B.M.; Goldfarb, D. *J. Am. Chem. Soc.* **2004**, *126*, 11733-11745.
27. Van Doorslaer, S.; Cereghetti, G.M.; Glockshuber, R.; Schweiger, A. *J. Phys. Chem. B* **2001**, *105*, 1631-1639.
28. McCracken, J.; Pember, S.; Benkovic, S. J.; Villafranca, J. J.; Miller, R. J.; Peisach, J. *J. Am. Chem. Soc.* **1988**, *110*, 1069.
29. Coremans, J.W.A.; Poluektov, O.G.; Groenen, E.J.J.; Canters, G.W.; Nar, H.; Messerschmidt, A. *J. Am. Chem. Soc.* **1997**, *119*, 4726-4731.
30. Kofman, V.; Farver, O.; Pecht, I.; Goldfarb, D. *J. Am. Chem. Soc.* **1996**, *118*, 1201-1206.

31. Fittipaldi, M.; Warmerdam, G.C.M.; de Waal, E.C.; Canters, G.W.; Cavazzini, D.; Rossi, G.L.; Huber, M.; Groenen, E.J.J. *ChemPhysChem* **2006**, *7*, 1286-1293.
32. Clark, K.M.; Yu, Y.; Marshall, N.M.; Sieracki, N.A.; Nilges, M.J.; Blackburn, N.J.; van der Donk, W.A.; Lu, Y. *J. Am. Chem. Soc.* **2010**, *132*, 10093-10101.
33. Ghosh, S.; Xie, X.; Dey, A.; Sun, Y.; Scholes, C.P.; Solomon, E.I. *Proc. Natl. Acad. Sci. U.S.A.* **2009**, *106*, 4969-4974.
34. Golombek, A.P.; Hendrich, M.P.; *J. Magn. Reson.* **2003**, *165*, 33-48.

Table 4.1. Principal components of spin Hamiltonian g-tensor and ^{63,65}Cu (I = 3/2, 100% abundance) magnetic hyperfine tensor (A, mK) derived from SpinCount[34] simulations of 77 K frozen aqueous glass X-band (9.5 GHz) EPR spectra of C112D/M121A azurin. Linewidths were modeled by strain parameters, σ_g and σ_A; these are indicated by parenthetical values alongside their corresponding parameters.

$\mathbf{g_x}$	2.0422
$\mathbf{g_y}$	2.1242
$\mathbf{g_z}$	2.3774
$\mathbf{\sigma g_x}$	0.0201
$\mathbf{\sigma g_y}$	0.0177
$\mathbf{\sigma g_z}$	0.0131
$\mathbf{A_x(mK)}$	2.45
$\mathbf{A_y(mK)}$	1.68
$\mathbf{A_z(mK)}$	10.47
$\mathbf{\sigma A_x(mK)}$	0.01
$\mathbf{\sigma A_y(mK)}$	0.01
$\mathbf{\sigma A_z(mK)}$	0.09
$\mathbf{R_g}$	1.01

Table 4.2. Principal components of spin Hamiltonian g-tensor and ^{63,65}Cu (I = 3/2, 100% abundance) magnetic hyperfine tensor (A, mK) derived from SpinCount[34] simulations of 60 K frozen aqueous glass S- (3.4 GHz) and Q- EPR spectra of C112D/M121X (X = M, L, F) azurin.

X	g_x	g_y	g_z	A_x(mK)	A_y(mK)	A_z(mK)	R_g
M	2.0608	2.0719	2.3165	0.51	0.17	15.06	0.17
L	2.0522	2.117	2.3878	1.62	0.81	10.5	0.79
F	2.0559	2.1015	2.3899	0.25	1.06	10.08	0.6

Table 4.3. Gaussian deconvolution of 7 T, 5 K MCD spectra of C112D/M121X (X = M, L, F, I, A) azurins. Deconvolution was performed using the multipeak fitting package in Igor.

3 Peak Fitting			2 Peak Fitting		
C112D/M121L					
Position	**FWHM**	**Normalized Amplitude**	**Position**	**FWHM**	**Normalized Amplitude**
10007	1194	0.85	10026	1327	0.37
12874	749	-1.00	13172	675	-1
13698	1044	-0.70			
C112D/M121F					
Position	**FWHM**	**Normalized Amplitude**	**Position**	**FWHM**	**Normalized Amplitude**
10056	1097	0.91	10071	1214	0.70
12910	722	-1.00	13178	987	-1
13730	1045	-0.64			
C112D/M121I					
Position	**FWHM**	**Normalized Amplitude**	**Position**	**FWHM**	**Normalized Amplitude**
10088	1104	0.89	10113	1227	0.65
12848	745	-1.00	13132	1048	-1
13680	1067	-0.67			
C112D/M121A					
Position	**FWHM**	**Normalized Amplitude**	**Position**	**FWHM**	**Normalized Amplitude**
10042	1293	0.77	10089	1580	0.59
12953	771	-1.00	13230	1175	-1
13929	1192	-0.60			

2 Peak Fitting			1 Peak Fitting		
C112D					
Position	**FWHM**	**Normalized Amplitude**	**Position**	**Width**	**Normalized Amplitude**
14056	991	-0.61	14800	1545	-1
15215	1440	-1.00			

Table 4.4. Paramagnetically shifted NMR signals and calculated hyperfine interactions for C112D/M121L.

Resonance	Assignment	δ_{obs}	FWHM (Hz)	δ_{dip}	δ_{dia}	A with dip (MHz)	A without dip(MHz)	A with dip (mK)	A without dip (mK)
A	H117/H46 NH	62.15	9400	-1 / -2	6.91	1.87 / 1.84		.062 / .061	
B	D112 Cß	52.07	3000	-1	2.7	1.74		0.058	
C	H117/H46 NH	44.00	1300	-1 / -2	5.92	1.28 / 1.25		.043 / .042	
D	H117/H46 Ring	30.74	1500	-5 /0	8.6/7.2	0.64 / 0.59	0.81 / 0.77	.021 / .020	.027 / .026
E	H117/H46 Ring	28.09	600	-5 /0	8.6/7.2	0.55 / 0.50	0.72 / 0.68	.018 / .017	.024 / .023
F	Exchangeable Amide?	19.76	2400	~ 0	?	?			
G	H46 Ca	-5.65	1000	?	?	?			

Table 4.5. Principal components of the g-tensor of C112D/M121X (X = M, L, F) azurins measured by W-band (95 GHz) EPR, compared to X-band (9.5 GHz) values.

X	g_{xx}, g_{yy}, g_{zz} (W-band)	g_{xx}, g_{yy}, g_{zz} (X-band)
M	2.08, 2.08, 2.31	2.063,2.063, 2.311
L	2.07, 2.10, 2.38	2.04, 2.116, 2.381
F	2.07, 2.09, 2.41	2.054, 2.10, 2.386

Table 4.6. The assignment and frequencies observed (MHz) in the W-band (95 GHz) HYSCORE spectra of C112D/M121X (X = M, L, F) azurins. Because of the powder characteristic of the sample, particularly when the experiment is carried out at g_y where many molecular orientations contribute to the signal, a range of individual frequencies that cover the range of frequencies covered by the different cross peaks are given.

X	F	L	M
$(\nu^{\beta}_{sq1}, \nu^{\alpha}_{sq1})$	[(17.5-18, 1.5-1.7)]	[18, (1.5-2)]	[(24-25), (2-7)]
$(\nu^{\beta}_{sq2}, \nu^{\alpha}_{sq1})$	[(19.6-21), (1.5-1.7)]	[(20-23),(1.5-2)]	
$(\nu^{\beta}_{sq2}, \nu^{\alpha}_{sq2})$	[19.5, 3.5]	[(20-23),3.5]	
$(\nu^{\beta}_{sq2}, \nu^{\alpha}_{dq})$	[(19.2-21), (4.8-5)]	[(20-23), (4.5-5)]	

Table 4.7. Summary of all the hyperfine couplings obtained for C112D/M121X (X = M, L, F) azurins by pulsed EPR in MHz.

* Determined from W-band ELDOR detected NMR

% Determined from W-band HYSCORE

& Determined from W-band ENDOR

X-band HYSCORE

X	M	L	F
^{14}N (His)-direct	A_1 =27.9[*,%] A_2 =36.9[*]	A_1= A_2=15-28[*,%]	A_1= A_2=20[*,%]
^{15}N (His)-direct	A_1 =39[*,&] A_2 =52[&]	A_1=27-28*[,&] A_2~38[*]	
^{13}C – (OC)		$A_{\perp}$~15[&] $A_{\|\|}$~24 MHz	$A_{\perp}$~15[&] $A_{\|\|}$~24 MHz
^{14}N (His)-remote	A_a~1.5[#] A_b=1.7-1.8	A_a=1.4-1.6[#] A_b=1.8-1.9	A_a=1.3-1.4[#] A_b=1.7-1.9
^{15}N (His)-remote	1.55-2.55[#,&]		A_1= A_2=2.2[&]

Table 4.8. The assignment and frequencies observed (MHz) in the X-band HYSCORE spectra of C112D/M121X (X = M, F, L). NQR notations are in parentheses.

X	F		L		M	
	$g_{\perp}$	$g_{\|\|}$	$g_{\perp}$	$g_{\|\|}$	$g_{\perp}$	$g_{\|\|}$
ν^{α}_{dq}, $\nu^{\beta}_{sq1,2}$ ($\nu_{0,-}$) (a) ν^{α}_{dq}, $\nu^{\beta}_{sq1,2}$ ($\nu_{0,-}$) (b)	4.2,0.7 3.4,0.8	4.0,0.6 3.6,0.6	4.3,0.7 3.5,0.8	 3.8,0.7	4.1,0.7 3.7,0.7	4.0,0.8 3.7,1.0
ν^{α}_{dq}, ν^{β}_{dq} (ν_{+}) (a) ν^{α}_{dq}, ν^{β}_{dq} (ν_{+}) (b)	4.2,1.5 3.6,1.5	4.0,1.5 3.6,1.5	4.3,1.5 3.5,1.6	4.1, 1.7 3.7,1.7	4.1,1.5 3.7,1.6	4.0,1.7 3.7,1.8
(ν^{α}_{dq}, ν^{β}_{dq}+$\nu^{\beta}_{sq1,2}$ ($\nu_{0,-}$ + ν_{+}) (a) (ν^{α}_{dq}, ν^{β}_{dq}+$\nu^{\beta}_{sq1,2}$ ($\nu_{0,-}$ + ν_{+}) (b)		4.0,2.2 3.6,2.2				

Table 4.9. Summary of the Cu-H distances obtained from the crystal structures (C112D: 3FQY; C112D/M121L: 3FPY) and the corresponding dipolar coupling $T_{\perp}=1/2T_{||}$.

C112D/M121L	r, Å	$T_{\perp}$, MHz	**C112D**	r, Å	$T_{\perp}$, MHz
L121	2.828	3.4885	M121	3.189	2.4328
H1: H46	2.924	3.1561	H46 ring	3.259	2.2794
H2: H117	3.225	2.3523	H1 ring H117	3	2.9222
F114	3.876	1.355	F114	2.868	3.3446
F114	3.063	2.7456	F114	3.635	1.6427
H2: chain H117	3.013	2.8846	H1 chain H117	3.326	2.1444
H2: chain H117	3.455	1.9131	H1 chain H117	3.303	2.1895
C_{α} (H46)	2.668	4.1545	C_{α} (H46)	2.403	5.6861

Table 4.10. Total energies of geometry optimized structures and corresponding EPR parameters for C112D/M121X (X = M, L, F, I) azurins calculated by Mahesh Sundararajan and Frank Neese according to bidentate and monodentate D112 coordination modes. EPR parameters are also reported as calculated using X-ray structures. Calculations were performed using Orca.[2] Hyperfine coupling constants are reported in mK.

C112D

	X-ray	Monodentate	Bidentate	Experiment (Q and S-band)
ΔE (kJ mol^{-1})		+18	0	
g_1	2.035	2.042	2.061	2.0608
g_2	2.114	2.119	2.064	2.0719
g_3	2.283	2.237	2.199	2.3165
A_1 (Cu)	-6.37	-6.17	0.80	0.51
A_2 (Cu)	8.31	10.1	1.36	0.17
A_3 (Cu)	9.93	10.5	17.9	15.06

C112D/M121L

	X-ray	Monodentate	Bidentate	Experiment (Q and S-band)
ΔE (kJ mol^{-1})		0	+13	
g_1	2.085	2.075	2.051	2.0522
g_2	2.123	2.136	2.01	2.117
g_3	2.357	2.323	2.248	2.3878
A_1 (Cu)	3.9	4.45	1.03	1.62
A_2 (Cu)	4.33	6.09	6.01	0.81
A_3 (Cu)	5.77	-7.49	-14.2	10.5

C112D/M121F

	X-ray	Monodentate	Bidentate	Experiment (Q and S-band)
ΔE (kJ mol^{-1})		0	+8	
g_1	2.096	2.066	2.047	2.0559
g_2	2.122	2.091	2.137	2.1015
g_3	2.351	2.252	2.256	2.3899
A_1 (Cu)	3.37	1.96	-1.69	0.25
A_2 (Cu)	5.2	2.24	5.95	1.06
A_3 (Cu)	5.73	-13.7	-13.2	10.08

C112D/M211I

	X-ray	Monodentate	Bidentate	Experiment (X-band)
ΔE (kJ mol^{-1})		+14	0	
g_1	2.087	2.092	2.068	2.043
g_2	2.105	2.105	2.08	2.101
g_3	2.303	2.318	2.229	2.386
A_1 (Cu)	2.73	2.89	4.26	0.25
A_2 (Cu)	4.57	5.29	4.6	0.25
A_3 (Cu)	-5.37	-6.67	13.6	10.18

Figure 4.1. QM/MM partitioning of azurin. h denotes a link atom.

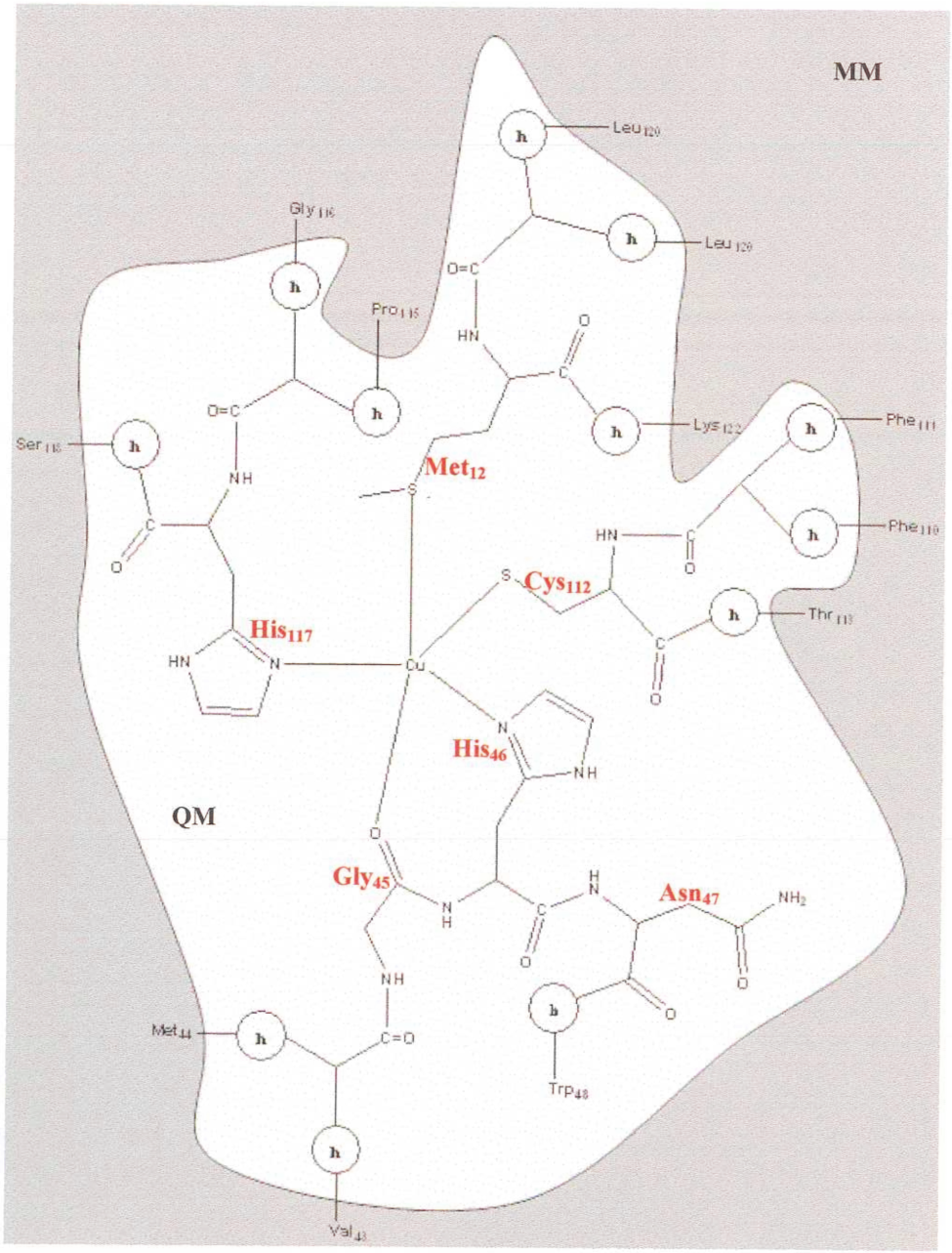
MM
QM
Leu120
Leu120
Gly116
Pro115
Ser118
Met12
Lys122
Phe111
Phe110
Cys112
Thr113
His117
His46
Gly45
Asn47
NH2
Met44
Trp48
Val43

Figure 4.2. Pseudocontact shifts at 3.5 Å calculated using the principal components of the Cu^{II} C112D/M121L azurin g-tensor.

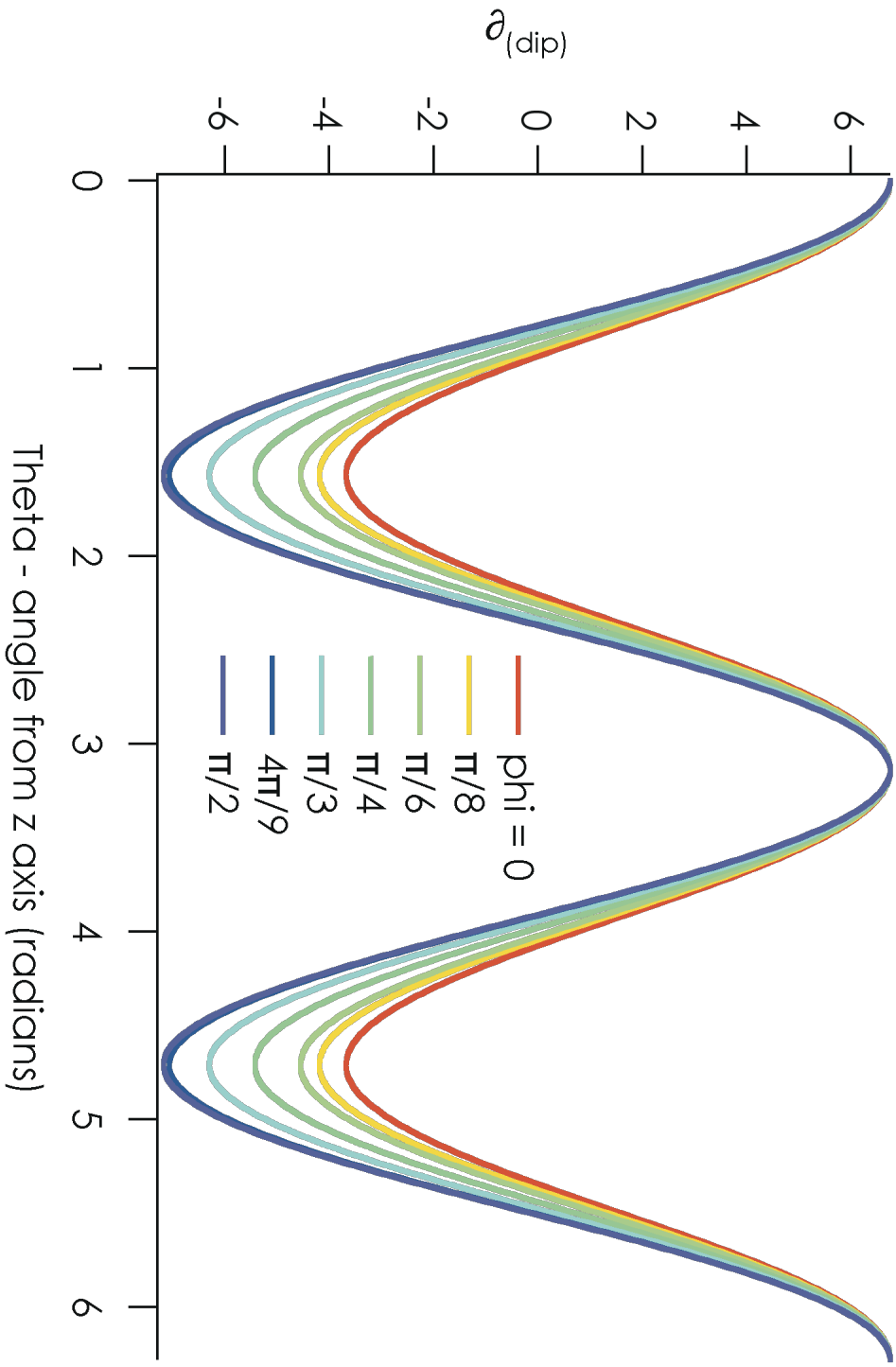
∂(dip)
6
4
2
0
-2
-4
-6
0
1
2
3
4
5
6
Theta - angle from z axis (radians)
phi = 0
π/8
π/6
π/4
π/3
4π/9
π/2

Figure 4.3. Pseudocontact contributions to linewidths in pNMR following Eq. (4.7). Linewidths are plotted as a function of distance from the paramagnetic center. Different curves represent functions through four orders of magnitude of τ_e.

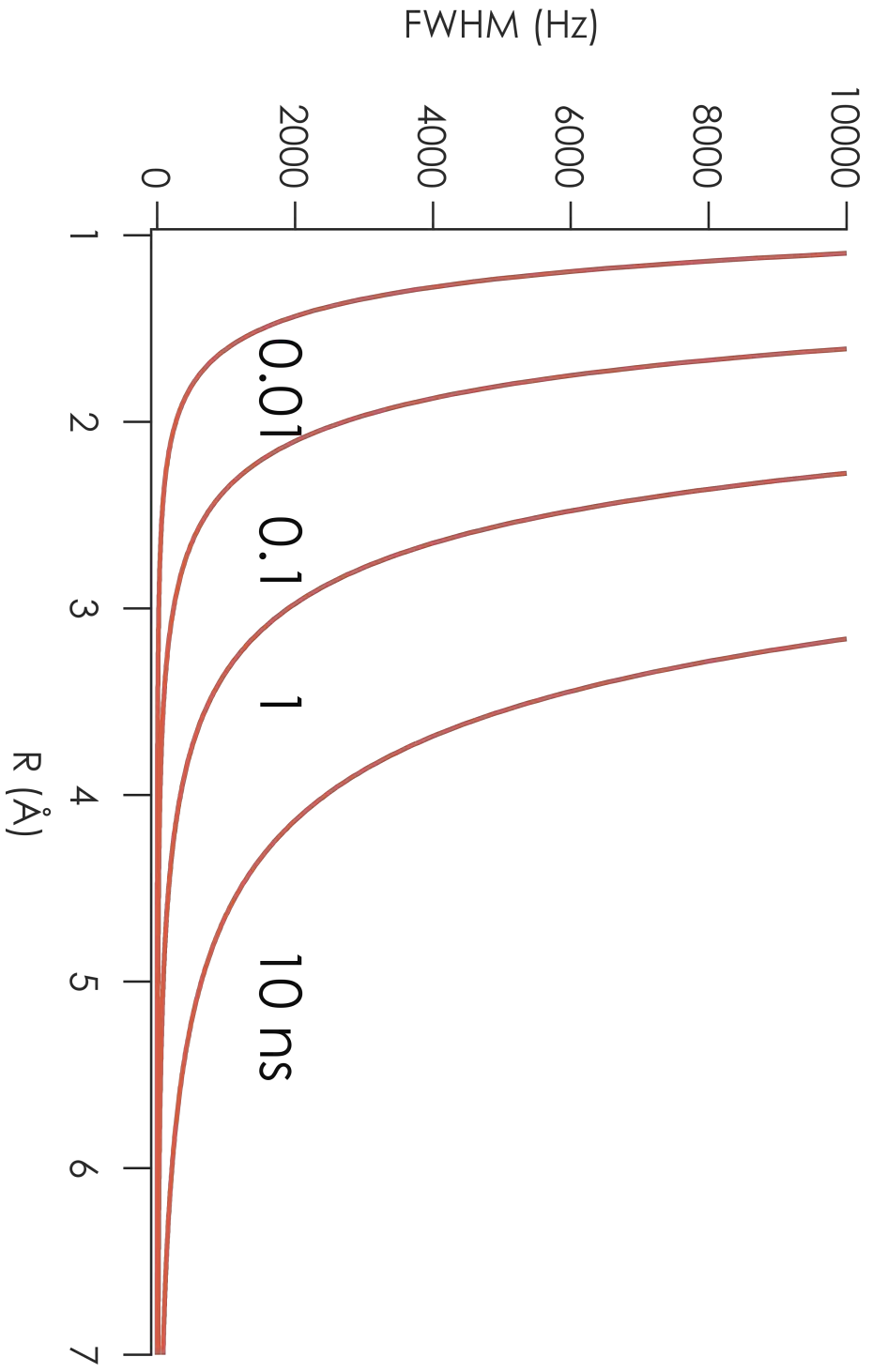
FWHM (Hz)
0
2000
4000
6000
8000
10000
R (Å)
1
2
3
4
5
6
7
0.01
0.1
1
10 ns

Figure 4.4. Energy level diagram for S= ½ with ^{14}N.

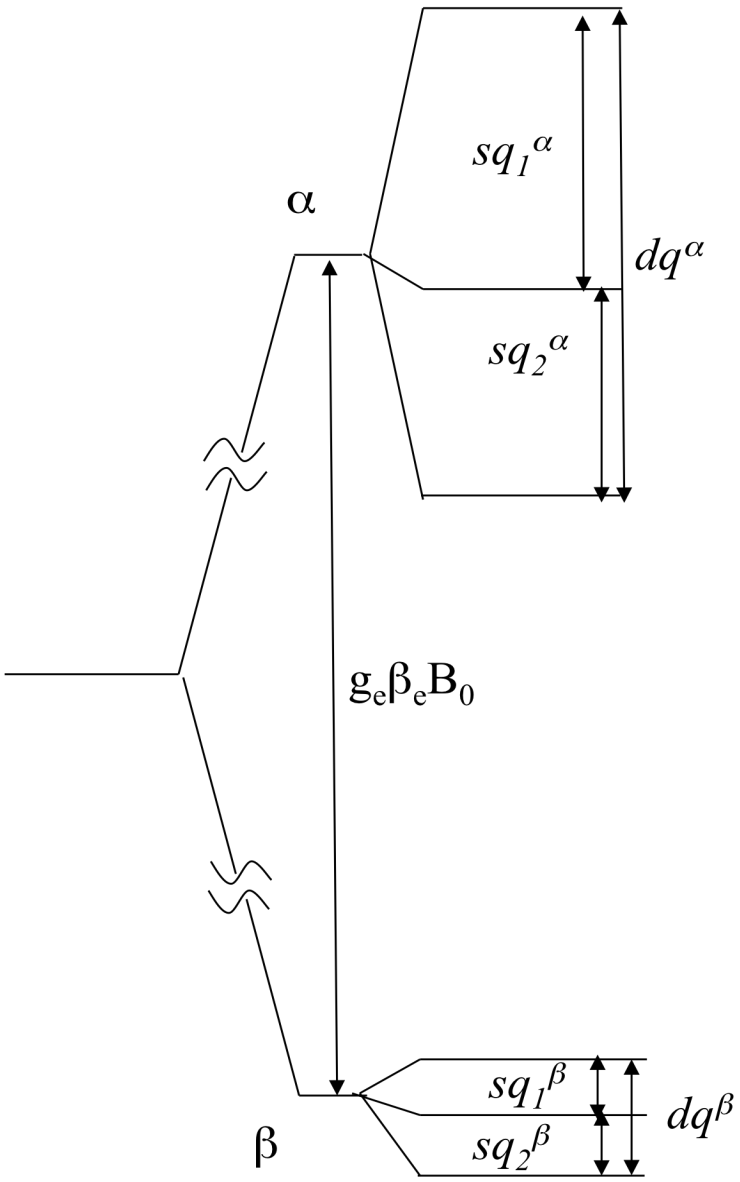
sq_1^{α}
α
dq^{α}
sq_2^{α}
$g_e\beta_e B_0$
sq_1^{β}
dq^{β}
sq_2^{β}
β

Figure 4.5. ESI-MS of ^{15}N-C112D/M121L azurin.

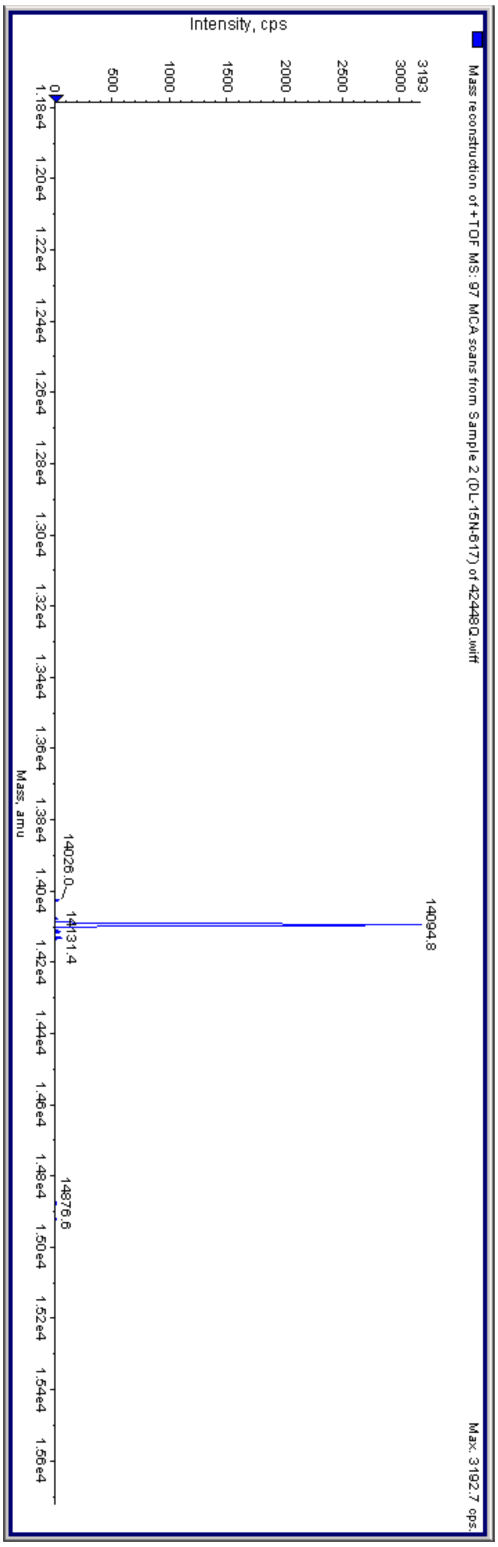
Mass reconstruction of +TOF MS: 97 MCA scans from Sample 2 (DL-15N-617) of 424480.wiff
Intensity, cps
3193
3000
2500
2000
1500
1000
500
0
1.18e4
1.20e4
1.22e4
1.24e4
1.26e4
1.28e4
1.30e4
1.32e4
1.34e4
1.36e4
1.38e4
1.40e4
1.42e4
1.44e4
1.46e4
1.48e4
1.50e4
1.52e4
1.54e4
1.56e4
Mass, amu
14026.0
14131.4
14094.8
14876.6
Max. 3192.7 cps.

Figure 4.6. X-band (9.5 GHz) EPR spectra of C112D/M121A azurin in 77 K glass (50 mM HEPES pH 7.0, 50% glycerol). SpinCount[34] simulation is overlaid in dashed gray. This spectrum was recorded with a 5 G modulation amplitude at a microwave power of 6.3 mW.

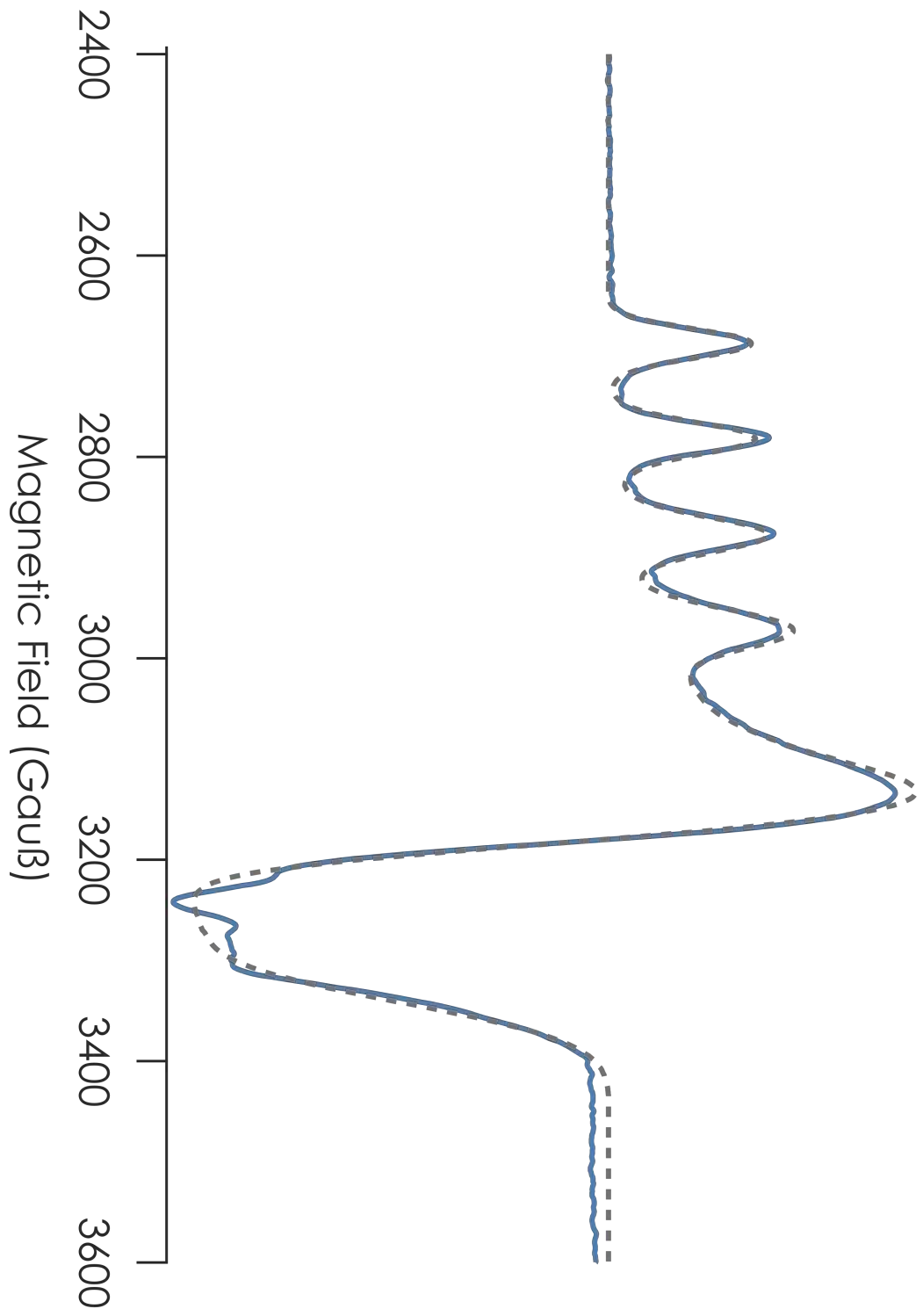
2400
2600
2800
3000
3200
3400
3600
Magnetic Field (Gauß)

Figure 4.7. S-band (**a)**, 3.4 GHz) and Q-band (**b)**, 34 GHz) EPR spectra of C112D azurin in 60 K aqueous glass (50 mM HEPES pH 7.0, 50% glycerol). SpinCount[34] simulations are overlaid in dashed gray. Inset in **a)**: $A_{||}$ feature showing 5 lines with spacing 10 G (0.10 mK), indicating superhyperfine coupling to 2 equivalent ^{14}N nuclei.

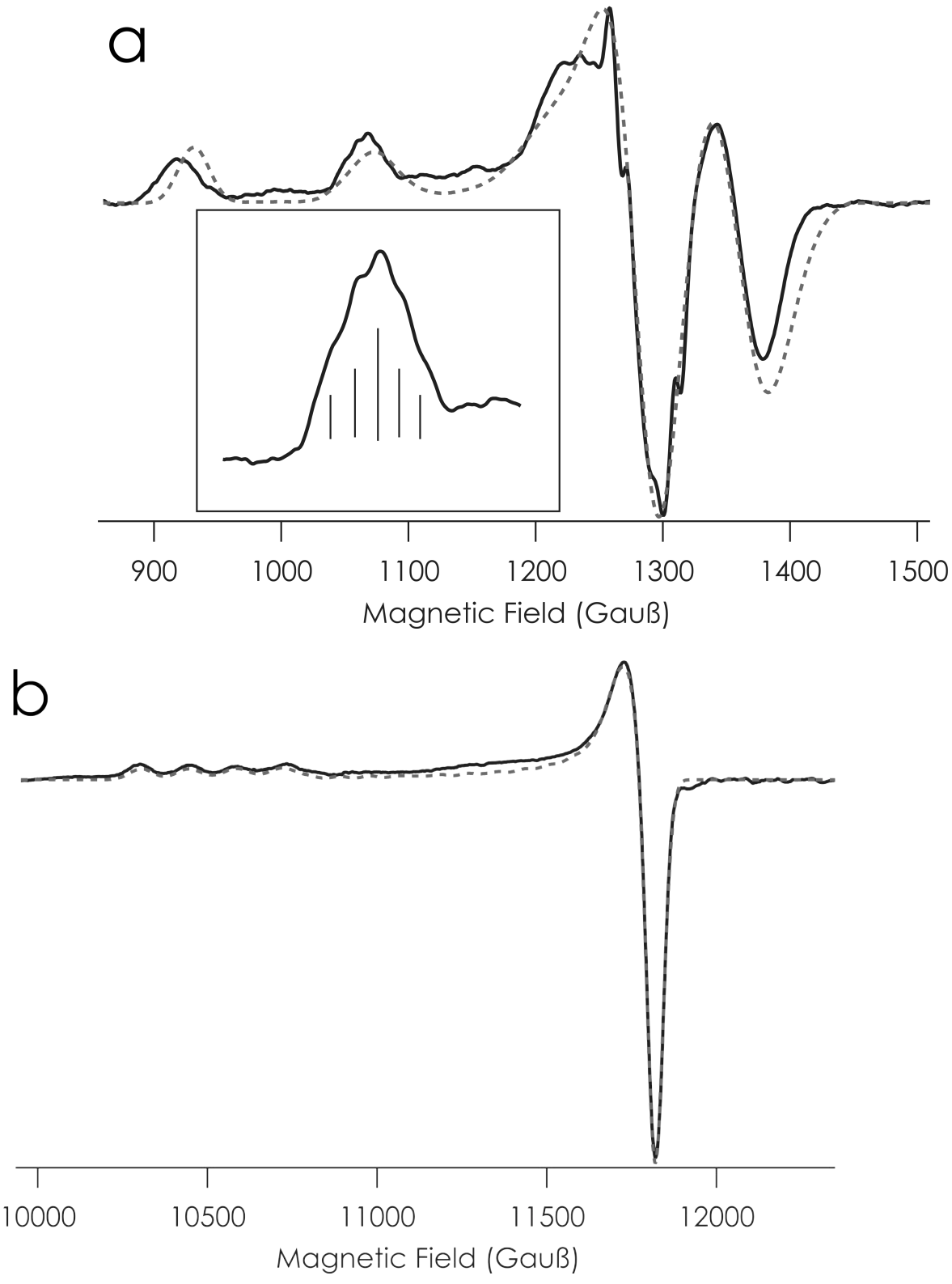
a
900
1000
1100
1200
1300
1400
1500
Magnetic Field (Gauß)
b
10000
10500
11000
11500
12000
Magnetic Field (Gauß)

Figure 4.8. S-band (**a)**, 3.4 GHz) and Q-band (**b)**, 34 GHz) EPR spectra of C112D/M121F azurin in 60 K aqueous glass (50 mM HEPES pH 7.0, 50% glycerol). SpinCount[34] simulations are overlaid in dashed gray.

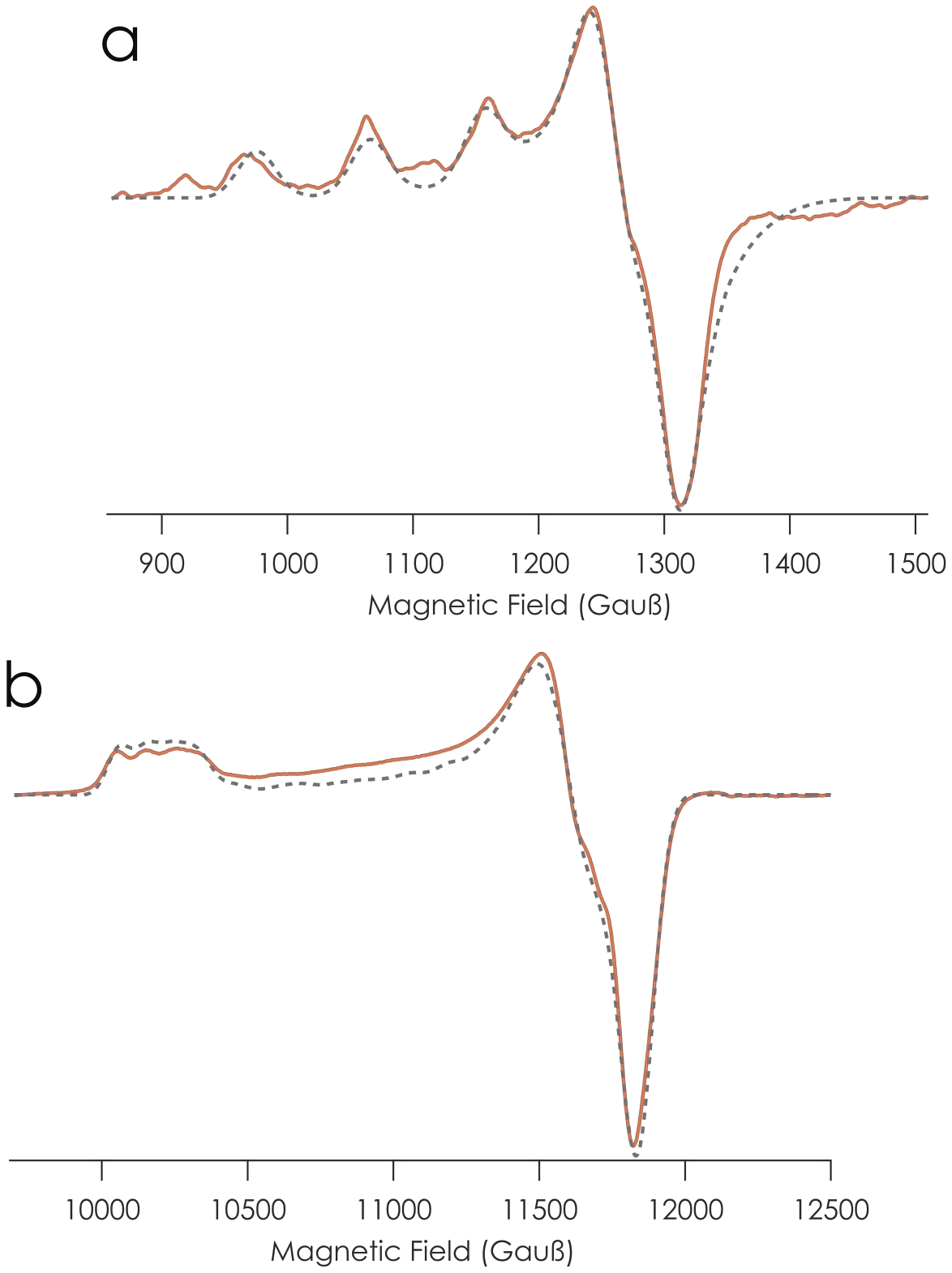
a
900
1000
1100
1200
1300
1400
1500
Magnetic Field (Gauß)
b
10000
10500
11000
11500
12000
12500
Magnetic Field (Gauß)

Figure 4.9. S-band (**a)**, 3.4 GHz) and Q-band (**b)**, 34 GHz) EPR spectra of C112D/M121L azurin in 60 K aqueous glass (50 mM HEPES pH 7.0, 50% glycerol). SpinCount[34] simulations are overlaid in dashed gray.

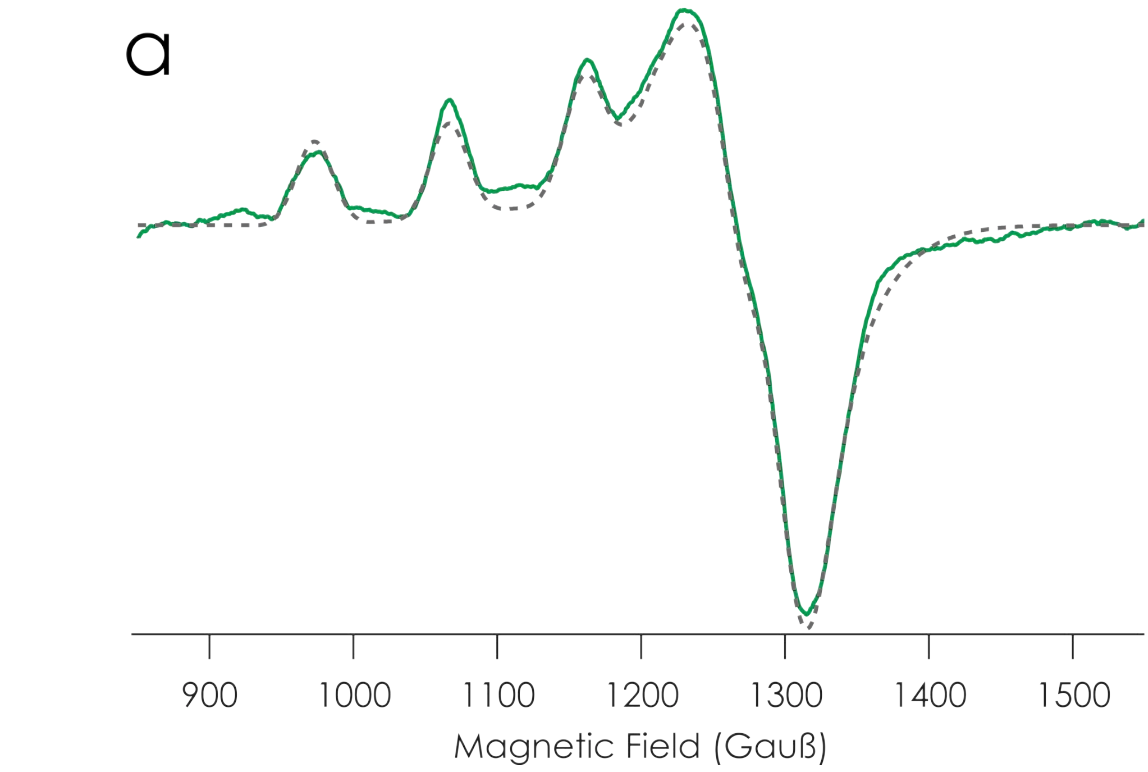
a
900
1000
1100
1200
1300
1400
1500
Magnetic Field (Gauß)

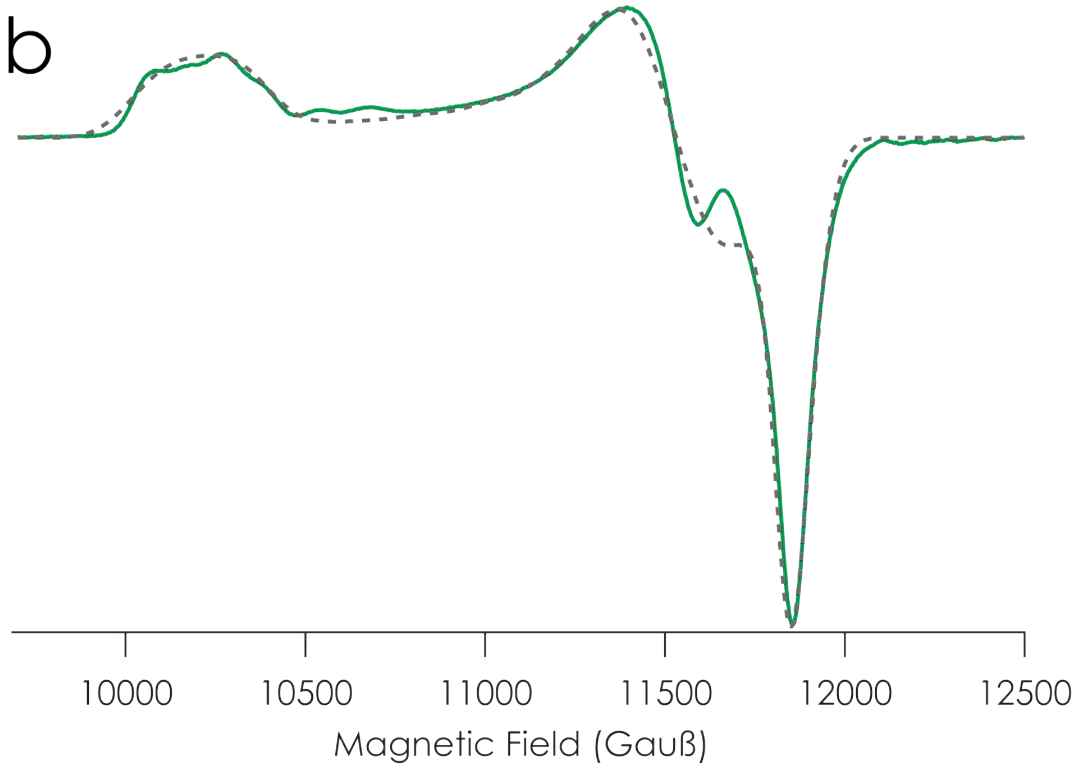
b
10000
10500
11000
11500
12000
12500
Magnetic Field (Gauß)

Figure 4.10. MCD spectra of C112D/M121X (X = M, black; L, green; F, orange; I, purple; A, teal). Spectra recorded at a magnetic field strength of 7 Tesla at 5 K in 50 mM HEPES pH 7.0 glass.

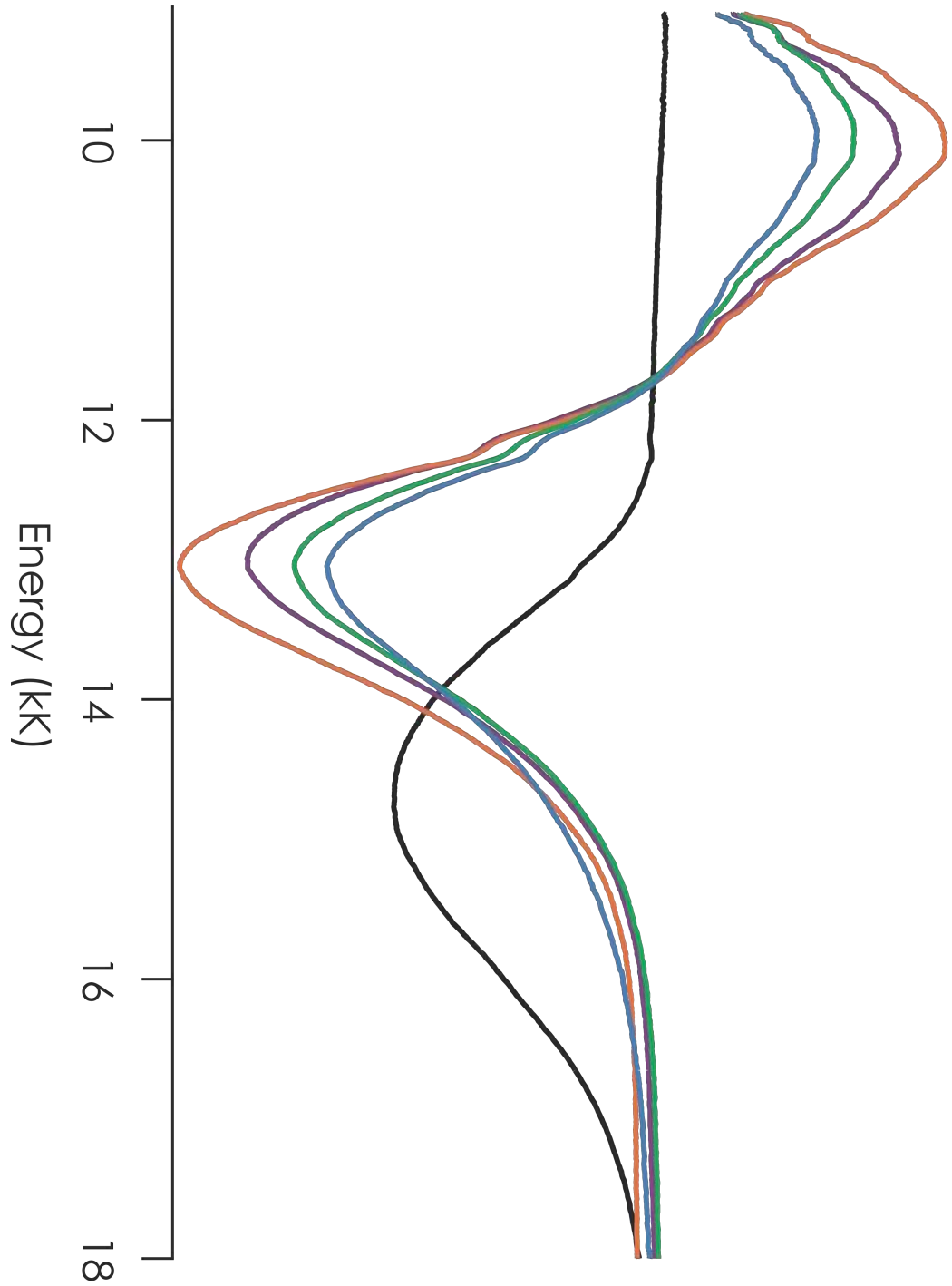
10
12
14
16
18
Energy (kK)

Figure 4.11. MCD spectra of C112D/M121L azurin at **a)** 5 K (solid) and **b)** 10 K (dashed). Assignment of the E ≤ 15 kK peaks to LF transitions is confirmed by their substantial magnetic dipole enhancement over the LMCT band at ~ 32 kK. All peaks show inverse temperature dependence, indicating they are *C* terms of the total MCD dispersion. Spectra recorded in 50 mM HEPES pH 7.0 glass.

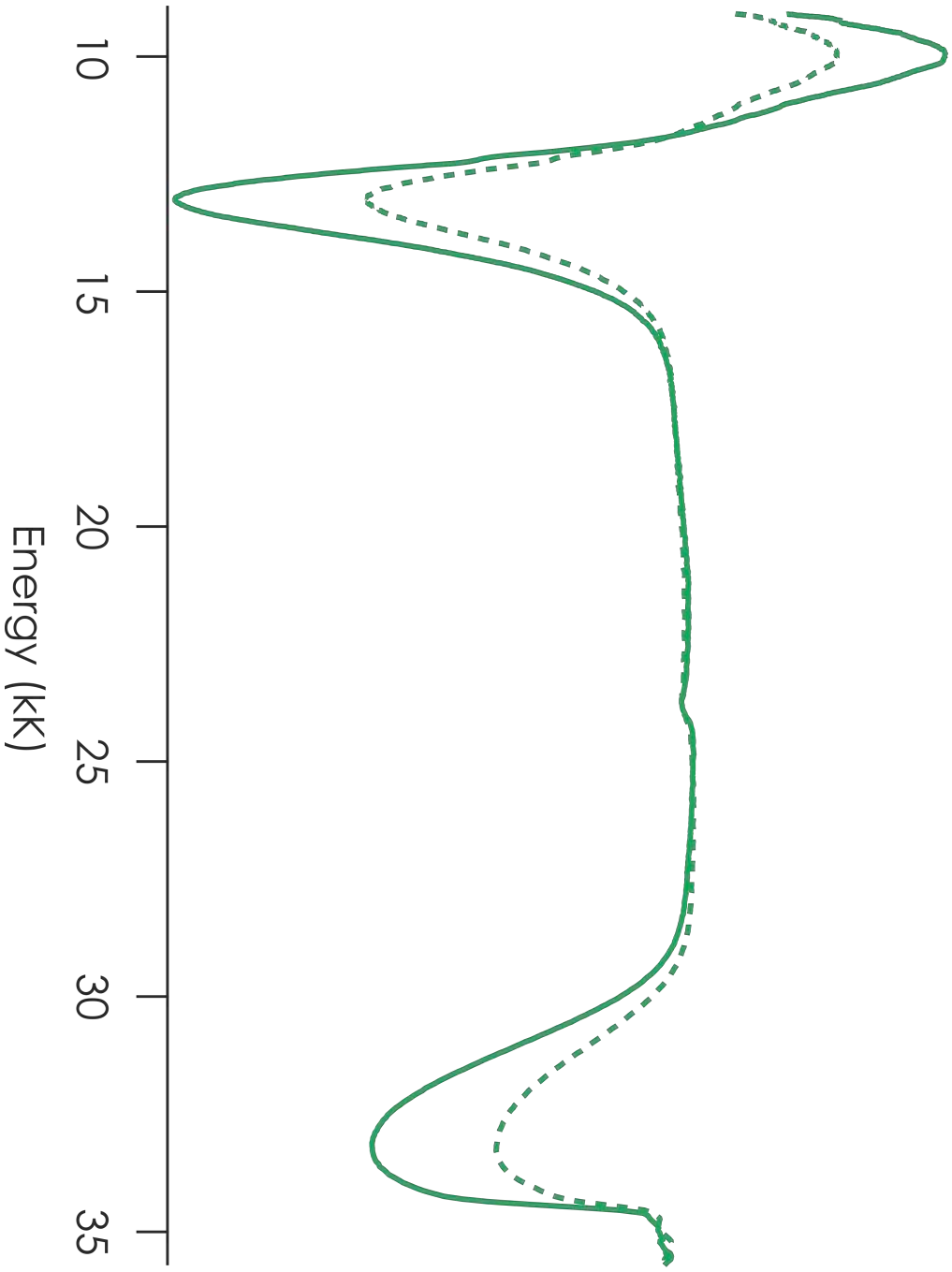
10
15
20
25
30
35
Energy (kK)

Figure 4.12. Gaussian deconvolution of the 7T, 5K MCD spectrum of C112D/M121L azurin with **a)** 2 bands and **b)** 3 bands.

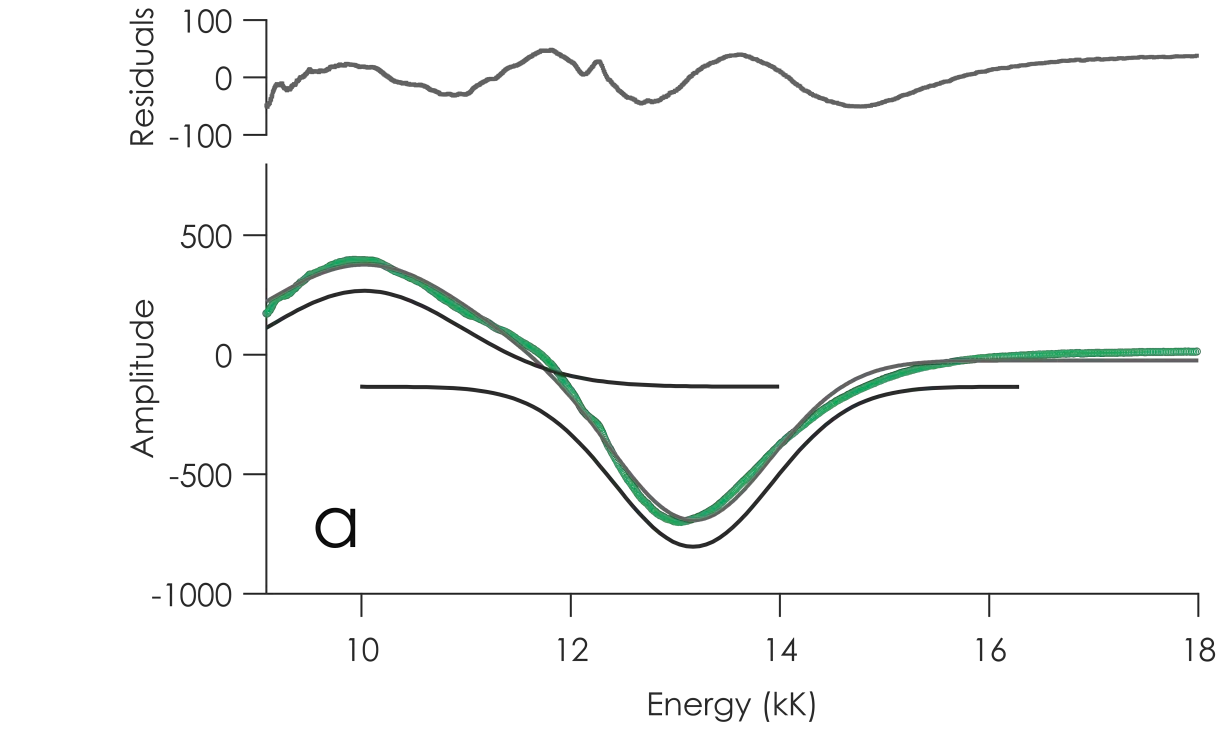
Residuals
100
0
-100
Amplitude
500
0
-500
-1000
a
10
12
14
16
18
Energy (kK)

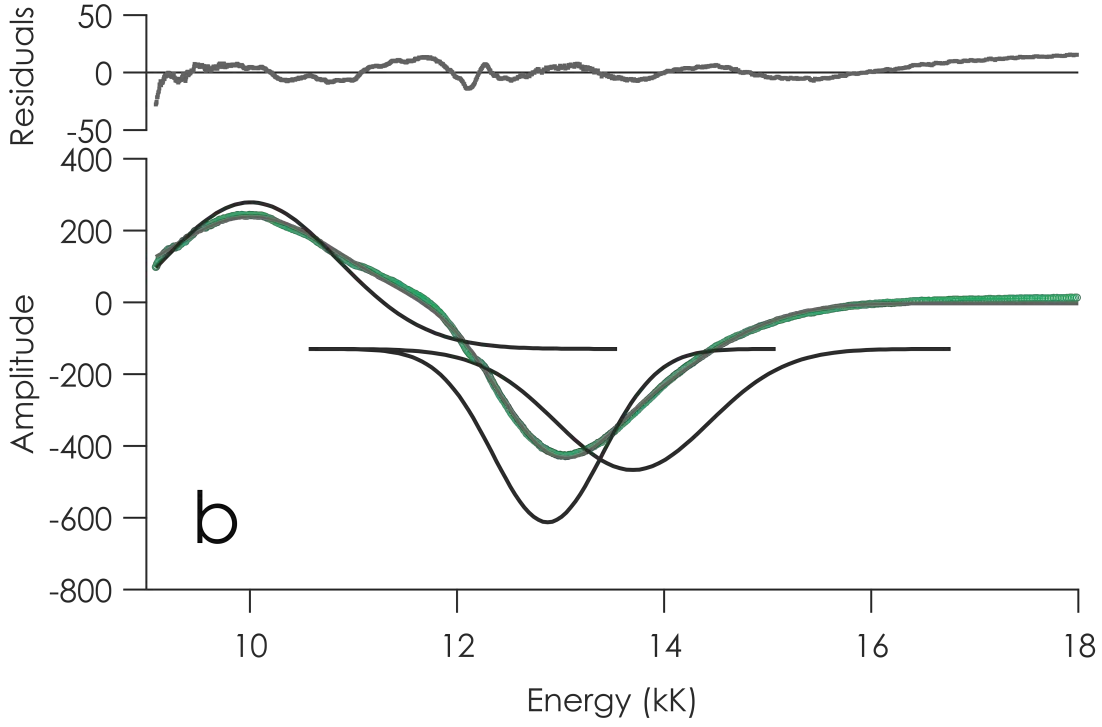
Residuals
50
0
-50
Amplitude
400
200
0
-200
-400
-600
-800
b
10
12
14
16
18
Energy (kK)

Figure 4.13. Gaussian deconvolution of the 7T, 5K MCD spectrum of C112D/M121F azurin with **a)** 2 bands and **b)** 3 bands.

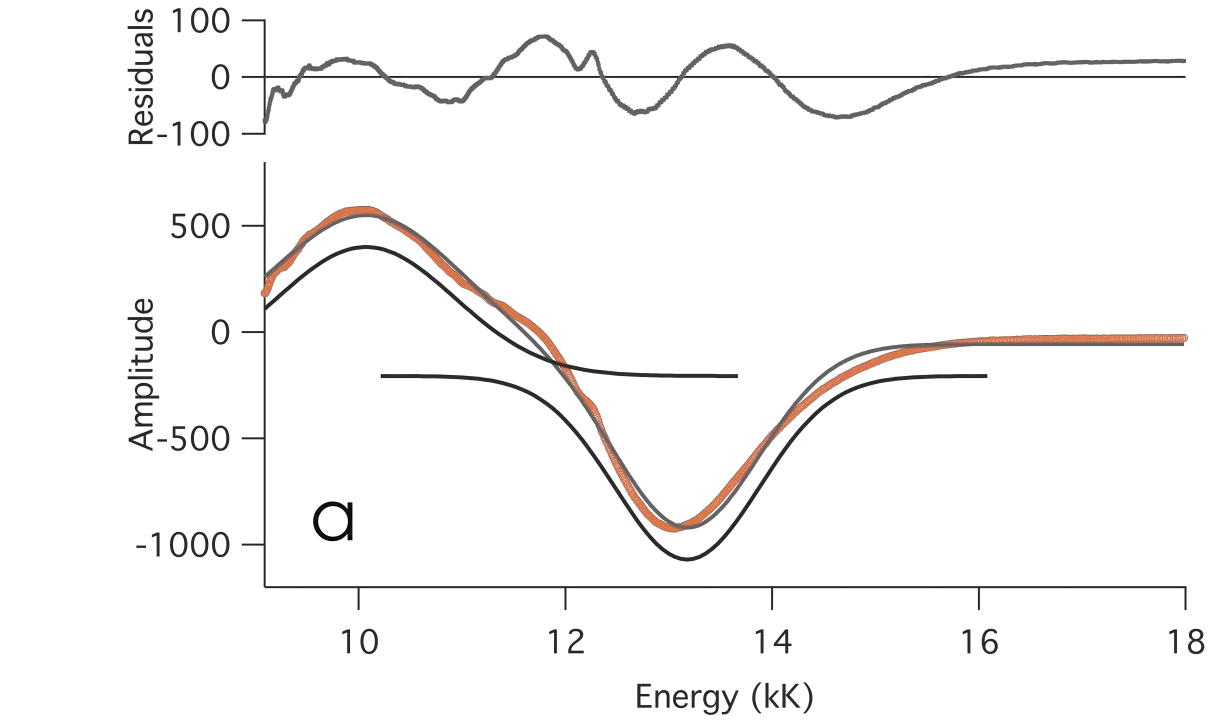
Residuals
100
0
-100
Amplitude
500
0
-500
-1000
a
10
12
14
16
18
Energy (kK)

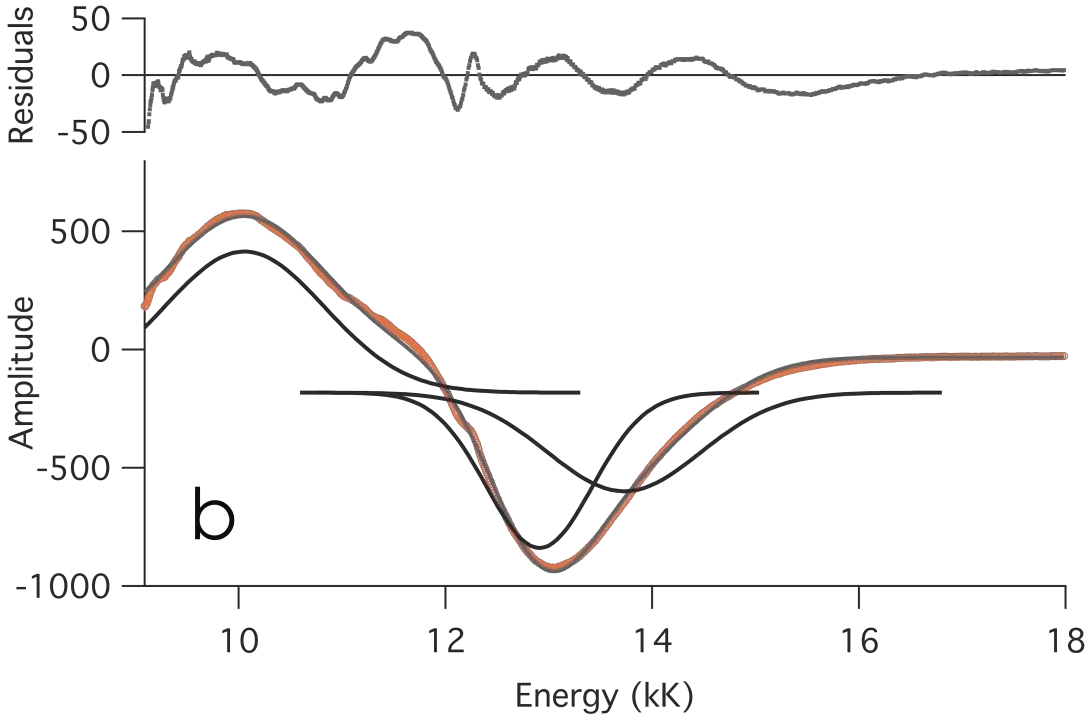
Residuals
50
0
-50
Amplitude
500
0
-500
-1000
b
10
12
14
16
18
Energy (kK)

Figure 4.14. Gaussian deconvolution of the 7T, 5K MCD spectrum of C112D/M121I azurin with **a)** 2 bands and **b)** 3 bands.

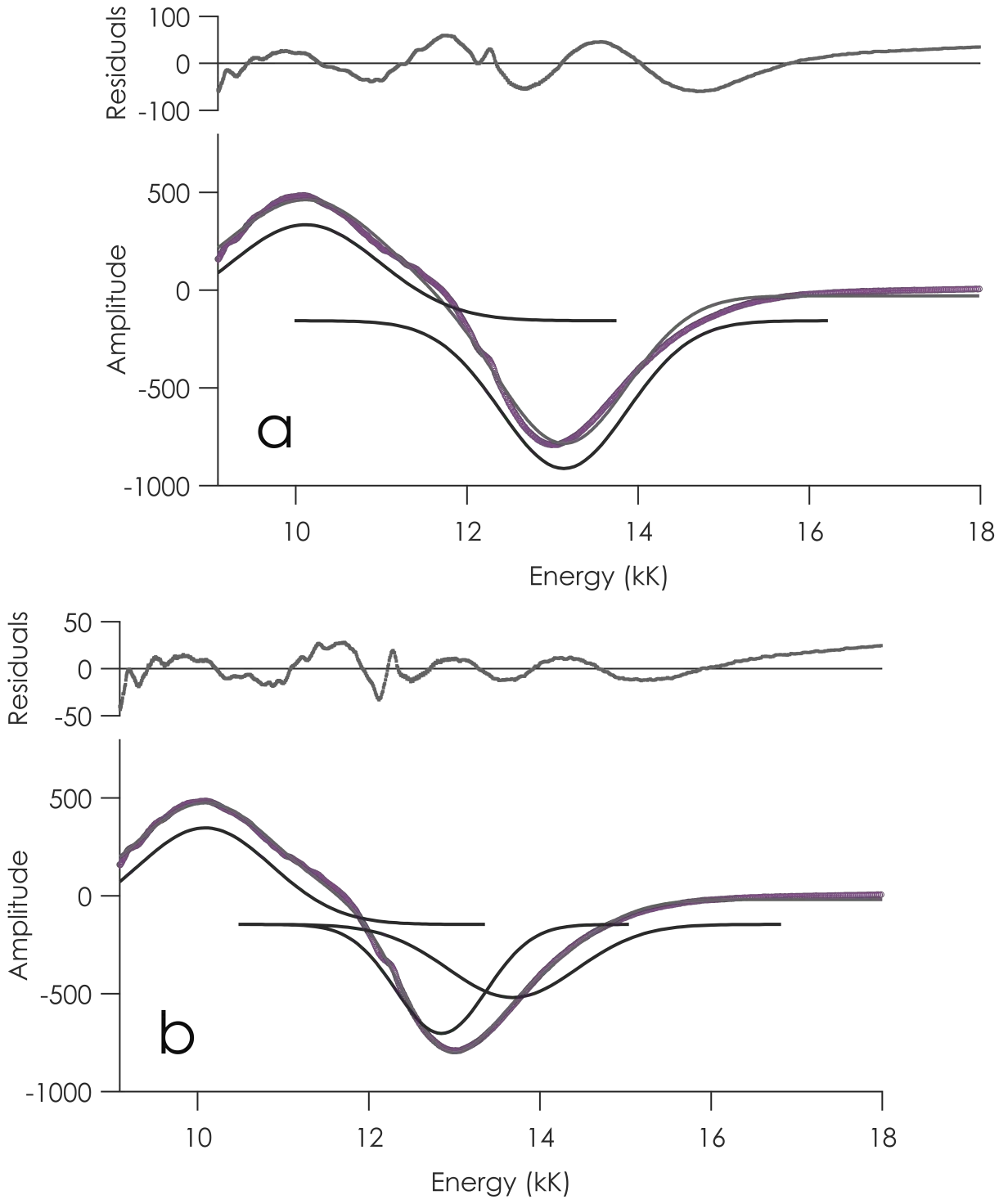
Residuals
100
0
-100
Amplitude
500
0
-500
-1000
a
10
12
14
16
18
Energy (kK)
Residuals
50
0
-50
Amplitude
500
0
-500
-1000
b
10
12
14
16
18
Energy (kK)

Figure 4.15. Gaussian deconvolution of the 7T, 5K MCD spectrum of C112D/M121A azurin with **a)** 2 bands and **b)** 3 bands.

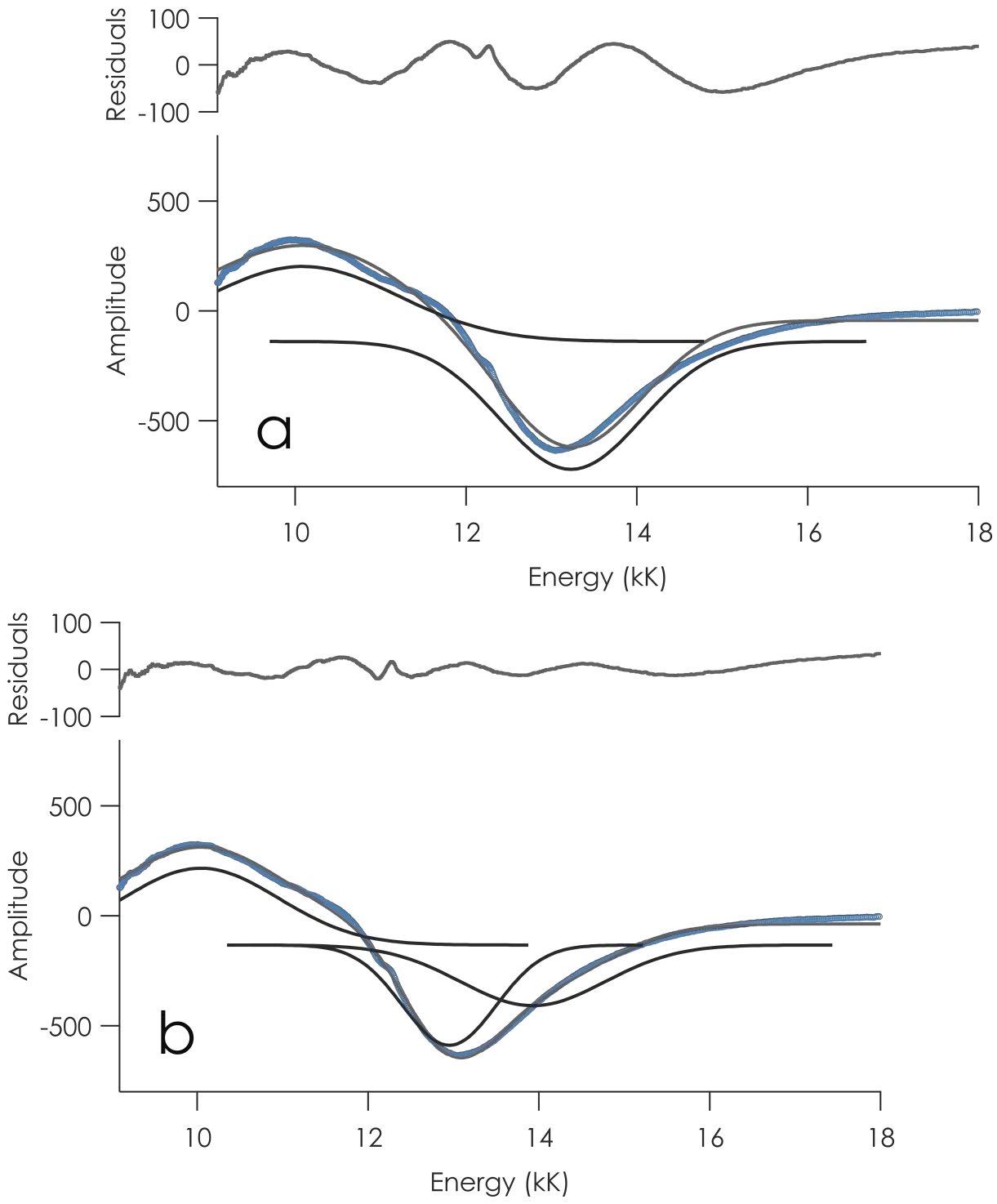
Residuals
100
0
-100
Amplitude
500
0
-500
a
10
12
14
16
18
Energy (kK)
Residuals
100
0
-100
Amplitude
500
0
-500
b
10
12
14
16
18
Energy (kK)

Figure 4.16. Gaussian deconvolution of the 7T, 5K MCD spectrum of C112D azurin with **a)** 1 bands and **b)** 2 bands.

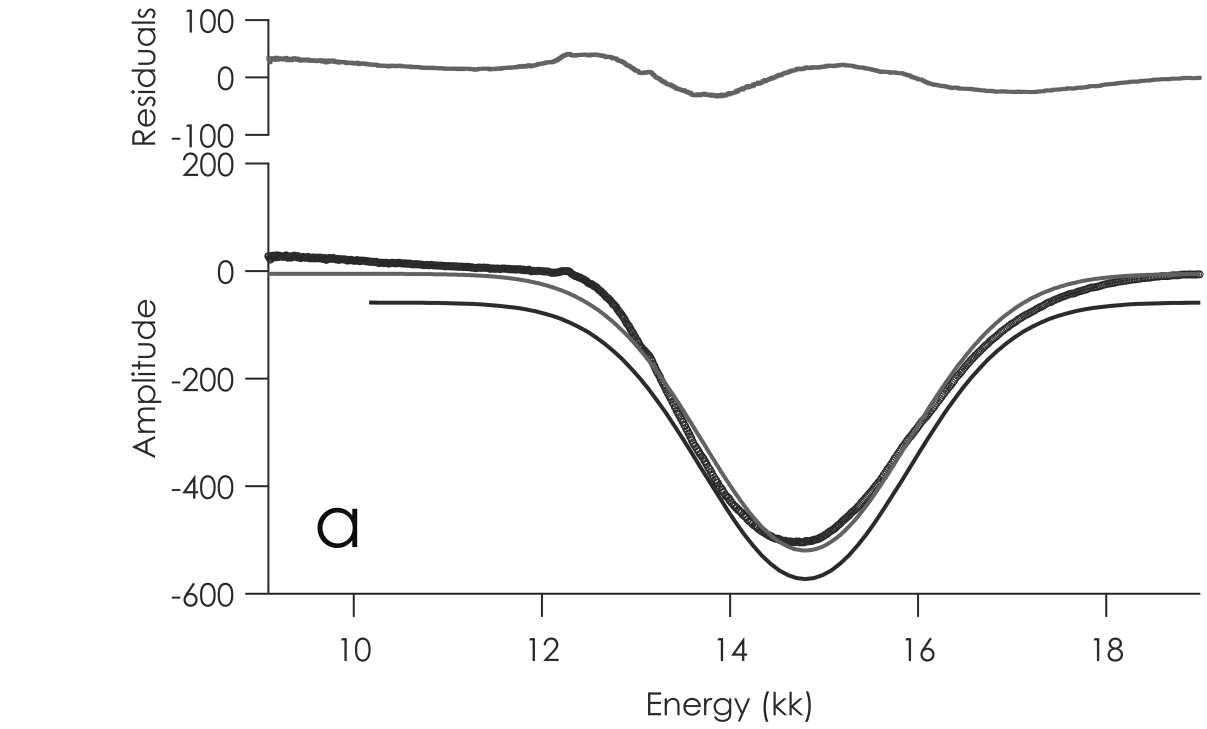
Residuals
100
0
-100
200
0
-200
-400
-600
Amplitude
a
10
12
14
16
18
Energy (kk)

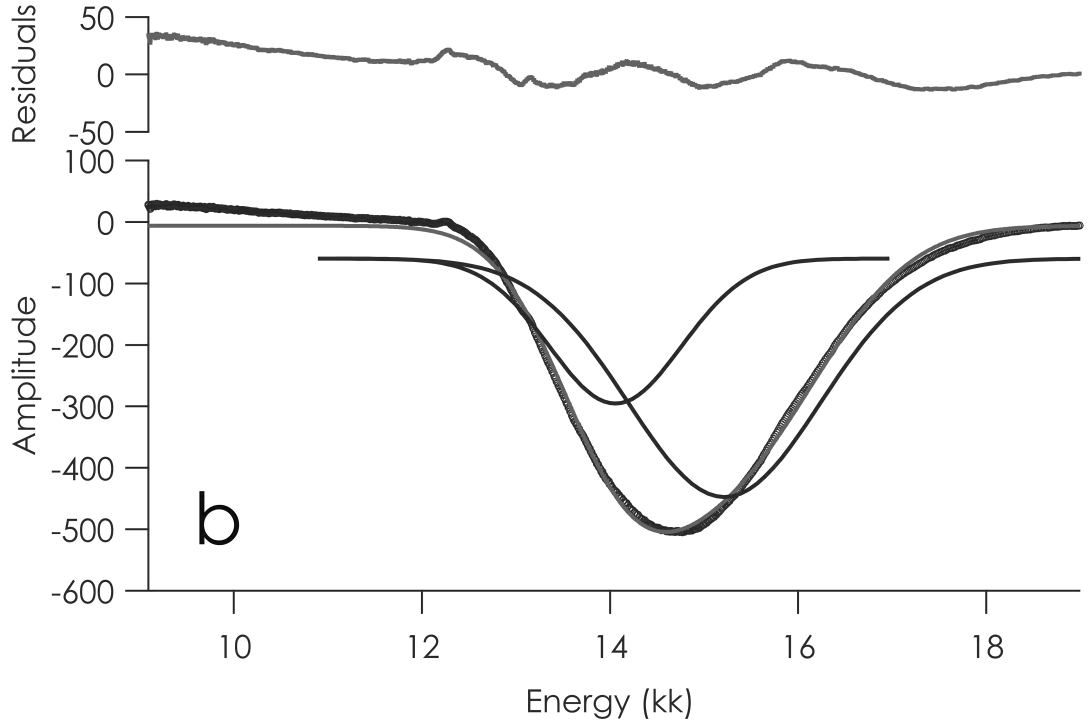
Residuals
50
0
-50
100
0
-100
-200
-300
-400
-500
-600
Amplitude
b
10
12
14
16
18
Energy (kk)

Figure 4.17. Downfield region of the 600 MHz ^{1}H NMR spectrum of WT *P. aeruginosa* azurin. Spectrum recorded and provided by María-Eugenia Zaballa. Peaks are labeled with assignments from Reference 14.

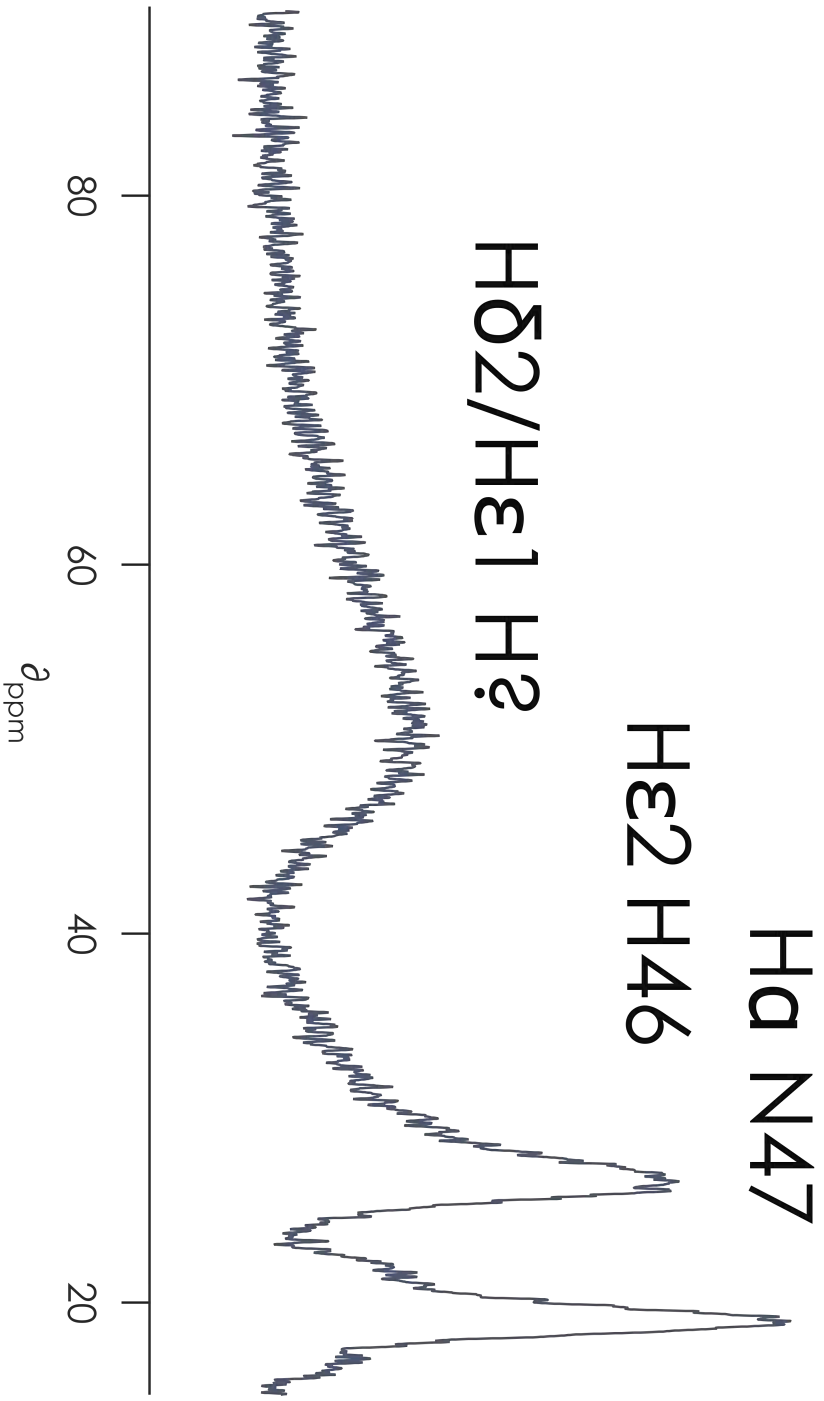
Hα N47
Hε2 H46
Hδ2/Hε1 H?
80
60
40
20
δppm

Figure 4.18. Downfield paramagnetic regions of the 600 MHz ^{1}H NMR spectra of C112D/M121X (X = L, green; A, light blue; I, purple; F, orange) azurins. Spectra were recorded at 298 K in 100 mM NaP_i pH 7.0 containing 10% D_2O. The peak observed in the C112D/M121F azurin spectrum very likely arises due to dipolar broadening; contact shifted residues accordingly are broadened beyond observability.

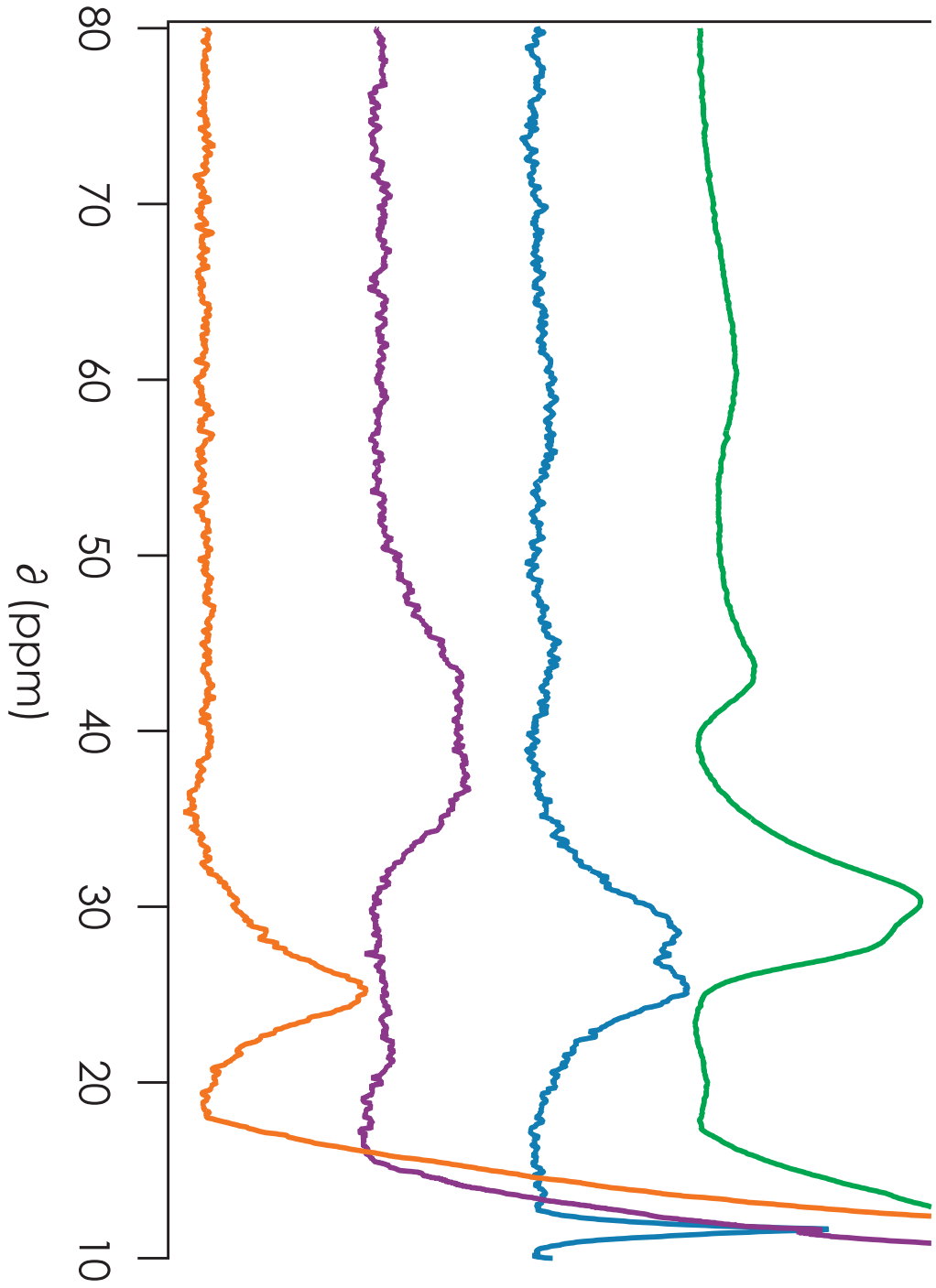
80
70
60
50
40
30
20
10
δ (ppm)

Figure 4.19. Temperature dependence of the paramagnetically shifted ^{1}H resonances of C112D/M121L azurin recorded at 600 MHz across the temperature range from 5 to 35 ºC. All observed paramagnetically shifted resonances obey Curie behavior, excluding the possibility of thermally accessible excited states proximal in the type zero electronic structure. Spectra recorded at 298 K in 100 mM NaP_i pH 7.0 containing 10% D_2O except for the ~55 ppm (298 K) resonance, which was recorded in 100 mM NaP_i pH 7.0 (corrected for D_2O) in 99% D_2O.

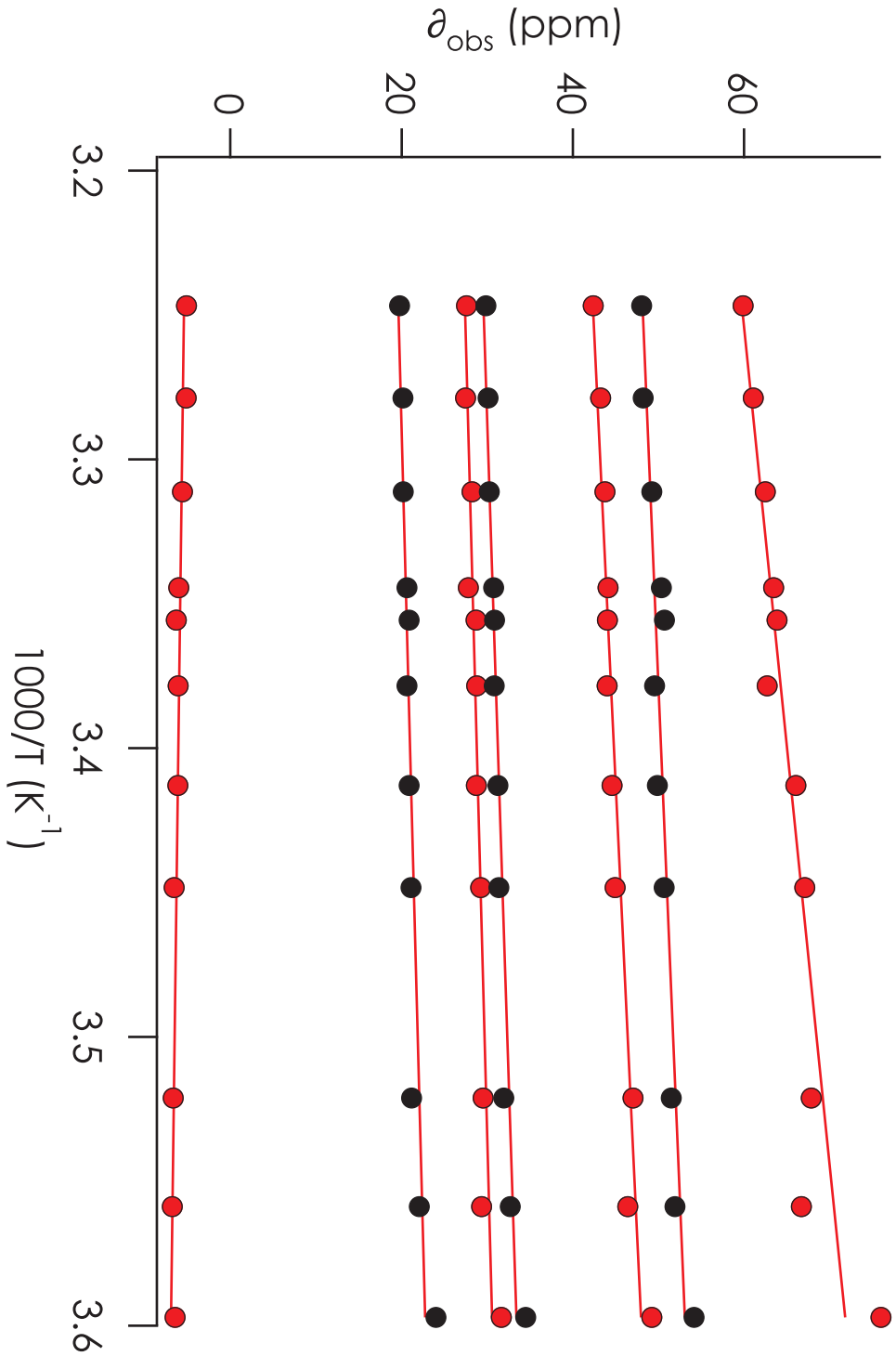
∂_{obs} (ppm)
0
20
40
60
3.2
3.3
3.4
3.5
3.6
1000/T (K^{-1})

Figure 4.20. Lorentzian deconvolution of the downfield paramagnetic region of the 600 MHz ^{1}H NMR spectrum of C112D/M121L. Spectrum recorded at 298 K in 100 mM NaP_i pH 7.0 containing 10% D_2O.

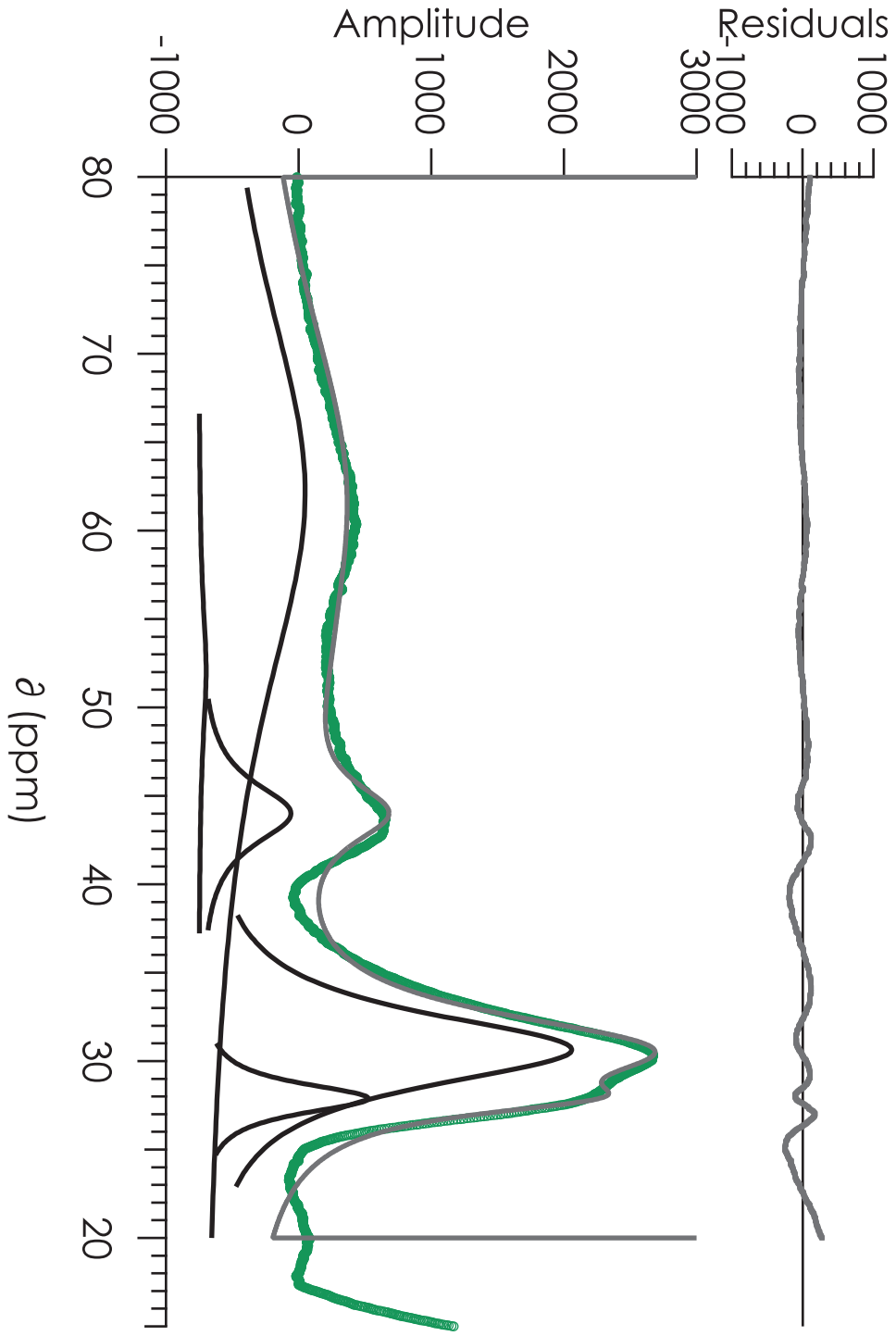
Amplitude
Residuals
-1000
0
1000
2000
-1000
3000
0
1000
80
70
60
50
40
30
20
∂ (ppm)

Figure 4.21. 600 MHz ^{1}H NMR spectrum of C112D/M121L azurin in 100 mM NaP_i pH 7.0 containing 10% H_2O (solid) and 100 mM NaP_i pH 7.0 (corrected) in 99% D_2O (dashed).

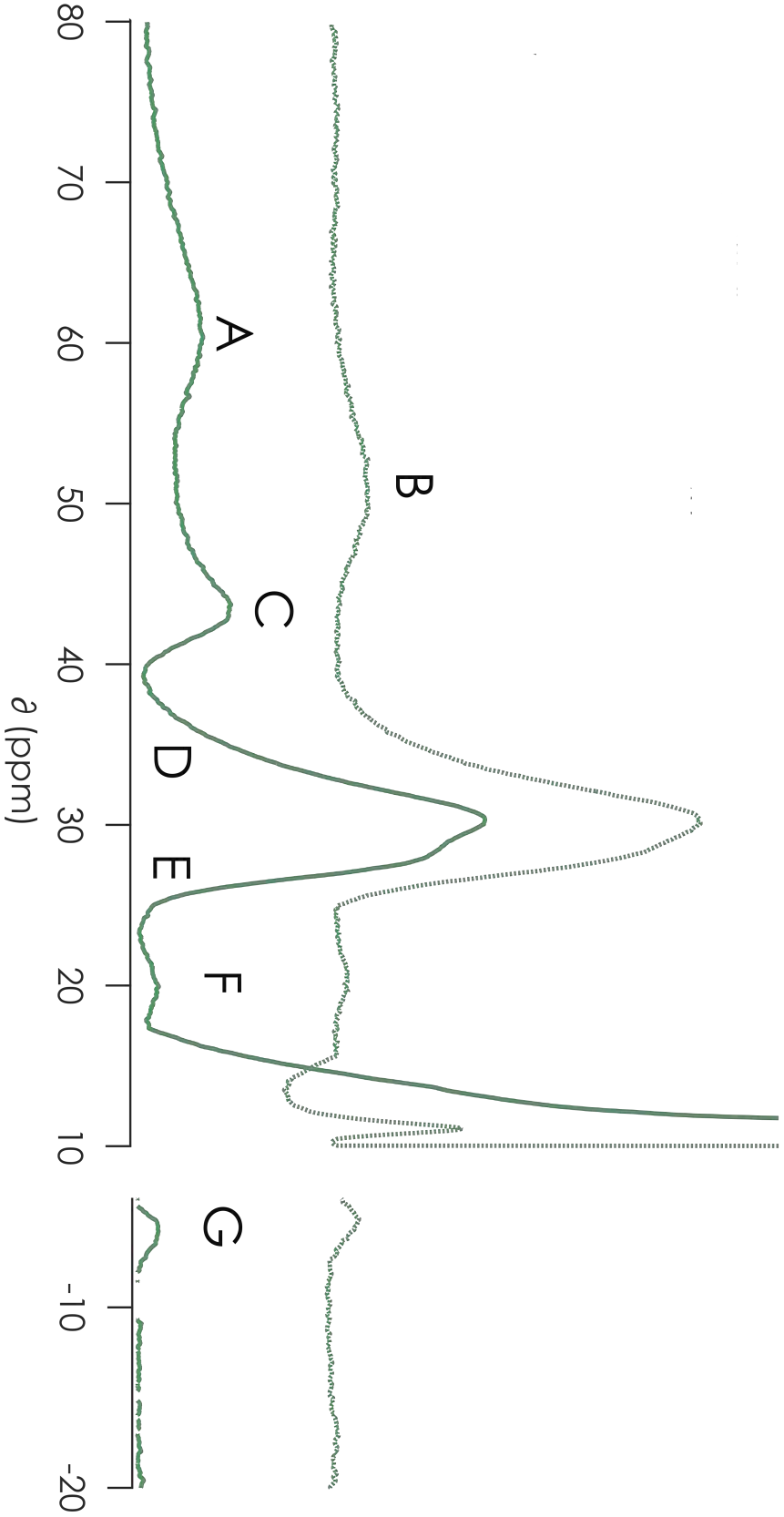
80
70
60
50
40
30
20
10
-10
-20
δ (ppm)
A
B
C
D
E
F
G

Figure 4.22. 600 MHz ^{1}H STD spectra of C112D/M121L azurin. **a)** Saturation at 30 ppm reveals two imidazole ring protons at 7.21 and 8.60 ppm. **b)** Saturation at 54 ppm reveals an aspartate C_{β} proton at 2.70 ppm. This latter saturation also magnetized the 30 ppm feature, again producing saturation transfer to the 7.21 and 8.60 ppm imidazole ring protons.

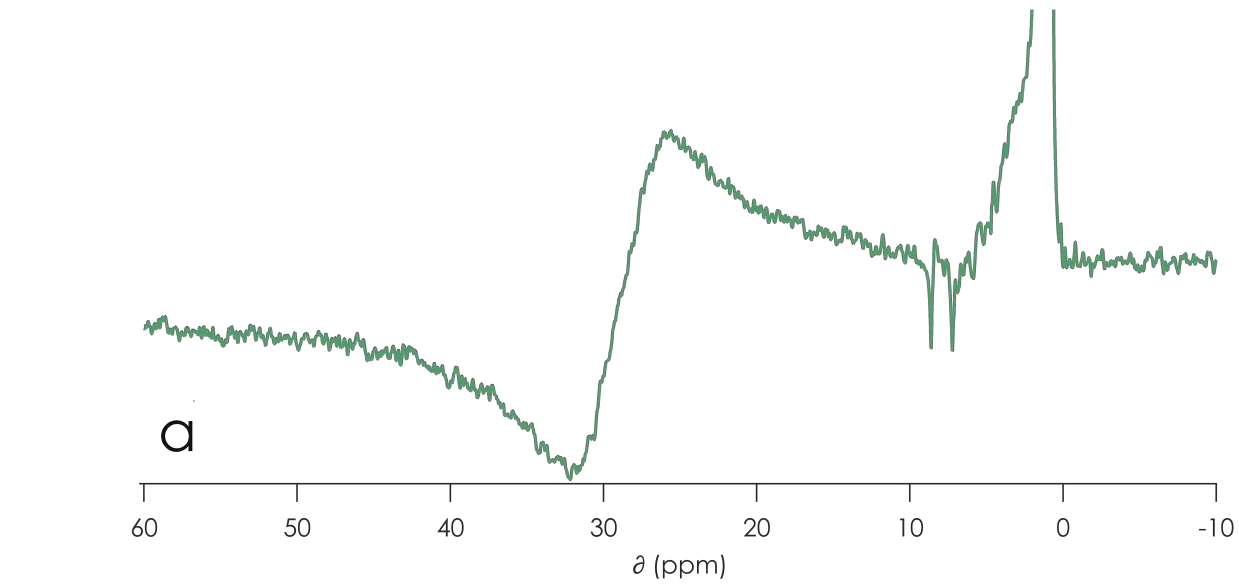
a
60
50
40
30
20
10
0
-10
∂ (ppm)

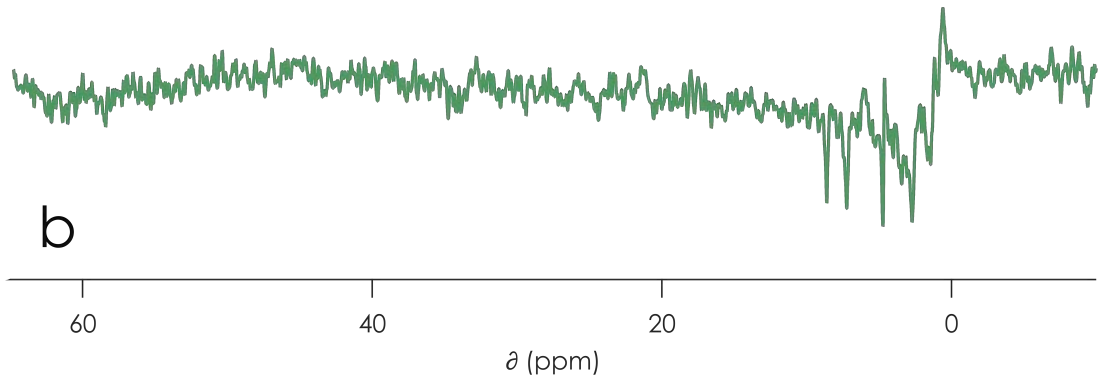
b
60
40
20
0
∂ (ppm)

Figure 4.23. Directly detected paramagnetic ^{13}C NMR spectra (600 MHz ^{1}H operating frequency) of C112D/M121X (X = L, green; A, light blue; I, purple; F, orange) azurins. Spectra were recorded in 50 mM HEPES pH 7.0 containing 10% D_2O.

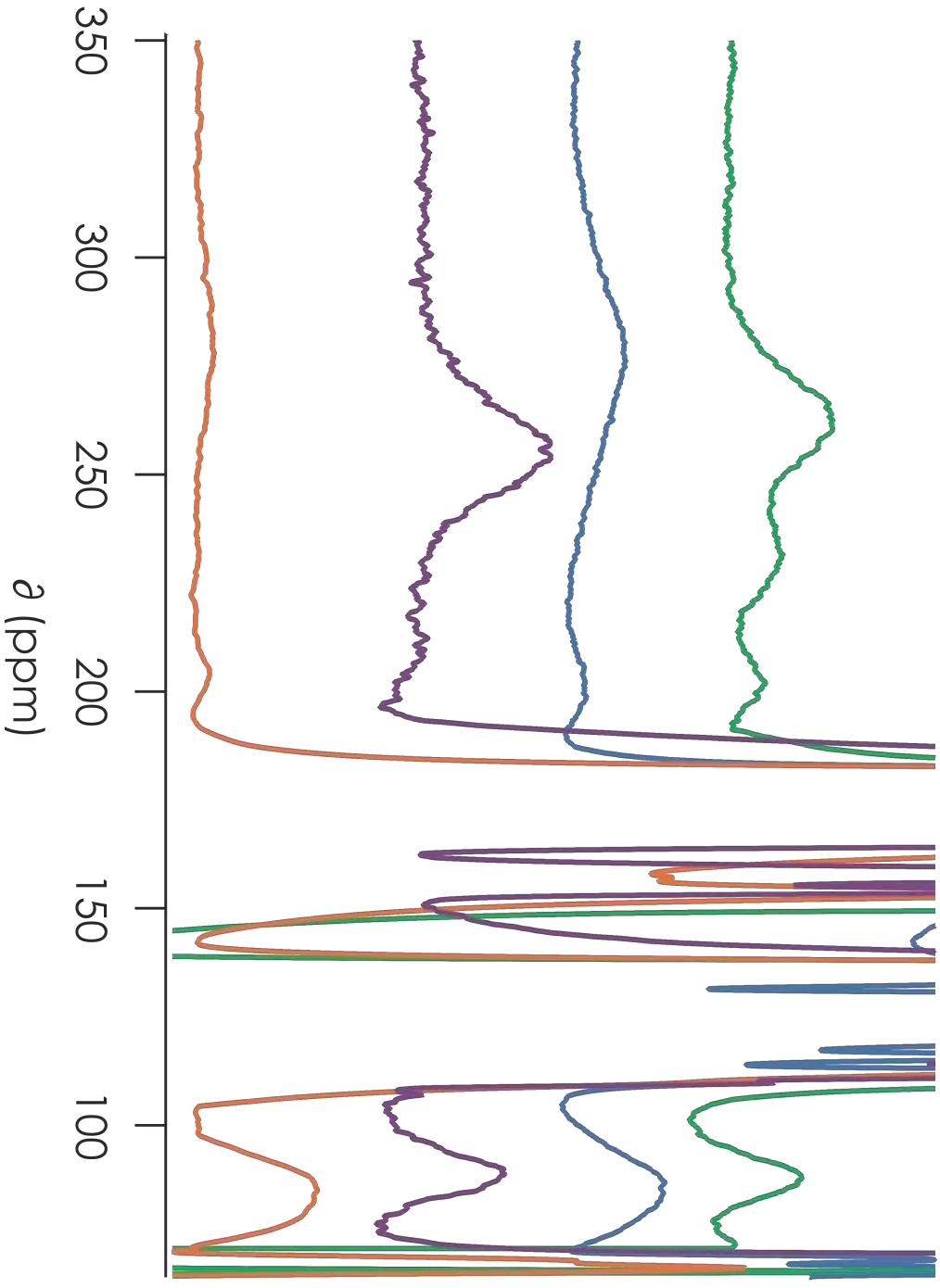
350
300
250
200
150
100
δ (ppm)

Figure 4.24. W-band (95 GHz) echo detected EPR spectra of the C112D/M121X (X = M, L, F) azurins measured in 8 K pH 7.0 frozen solution.

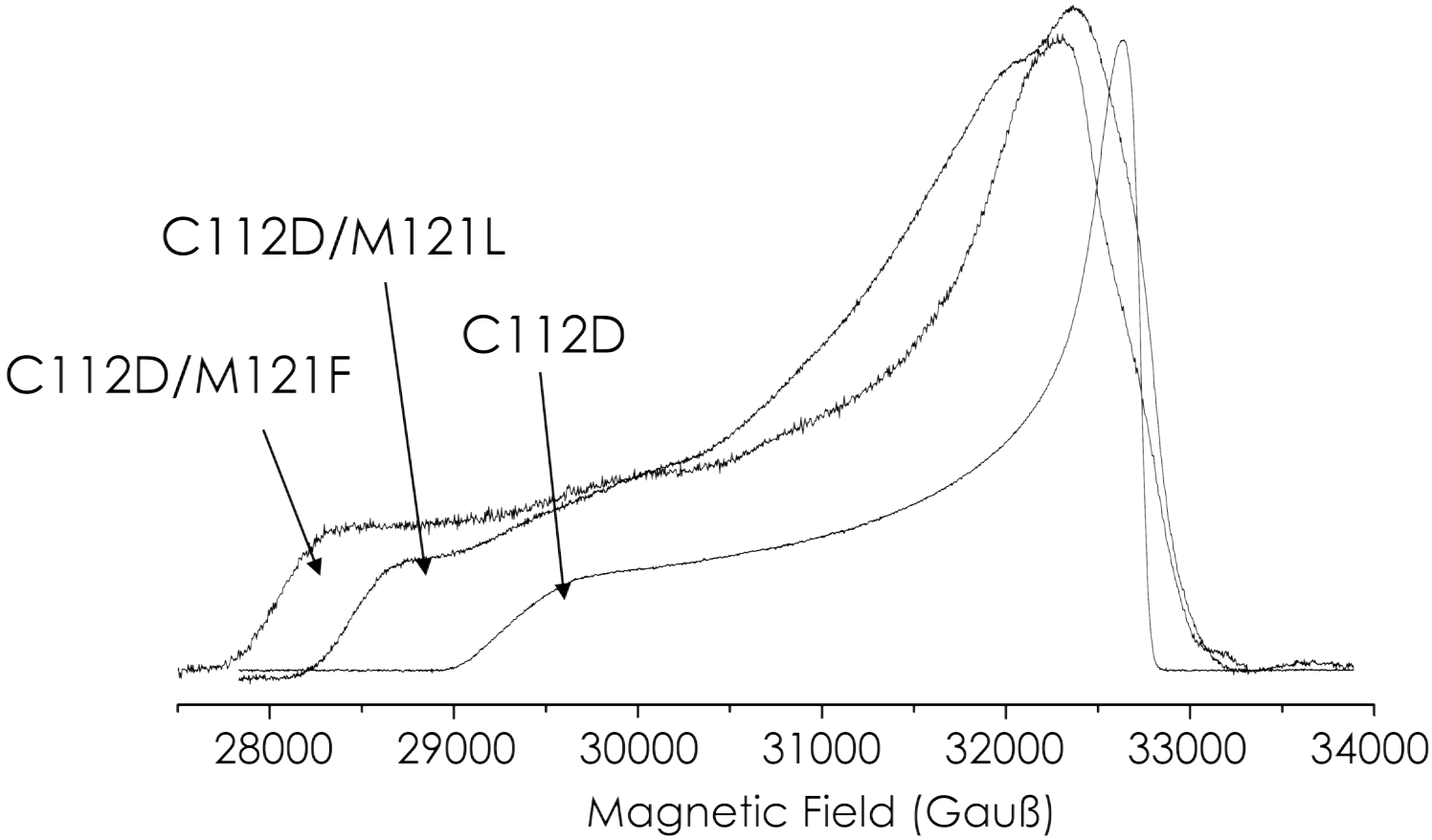
C112D/M121L
C112D
C112D/M121F
28000
29000
30000
31000
32000
33000
34000
Magnetic Field (Gauß)

Figure 4.25. ED-Detected NMR spectra of C112D/M121X (X = M, L, F) azurins measured at different magnetic field strengths through the EPR spectrum.

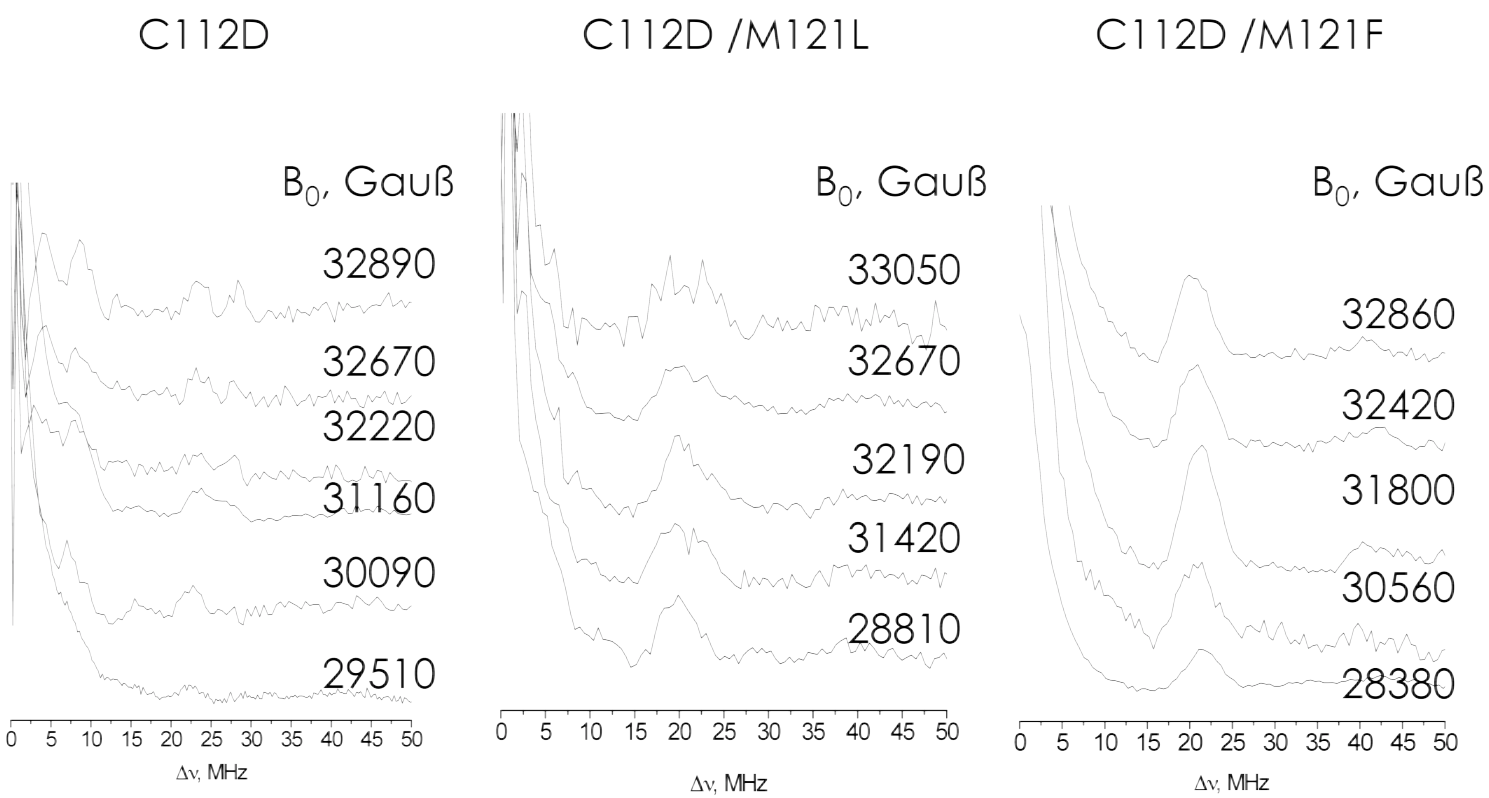
C112D
C112D /M121L
C112D /M121F
B0, Gauß
32890
32670
32220
31160
30090
29510
B0, Gauß
33050
32670
32190
31420
28810
B0, Gauß
32860
32420
31800
30560
28380
0 5 10 15 20 25 30 35 40 45 50
Δν, MHz
0 5 10 15 20 25 30 35 40 45 50
Δν, MHz
0 5 10 15 20 25 30 35 40 45 50
Δν, MHz

Figure 4.26. (a) W-band ENDOR of $^{13}C/^{15}N$ enriched C112D recorded at B=32890 G. (b) ED-NMR of $^{13}C/^{15}N$ enriched C112D/M121L recorded at B=32670 G.

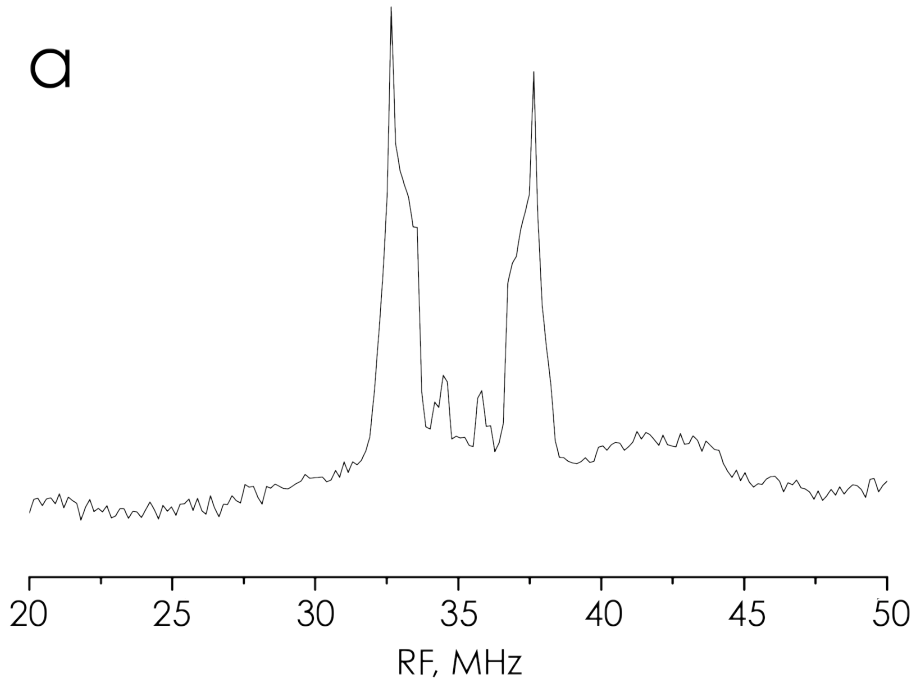
a
20
25
30
35
40
45
50
RF, MHz

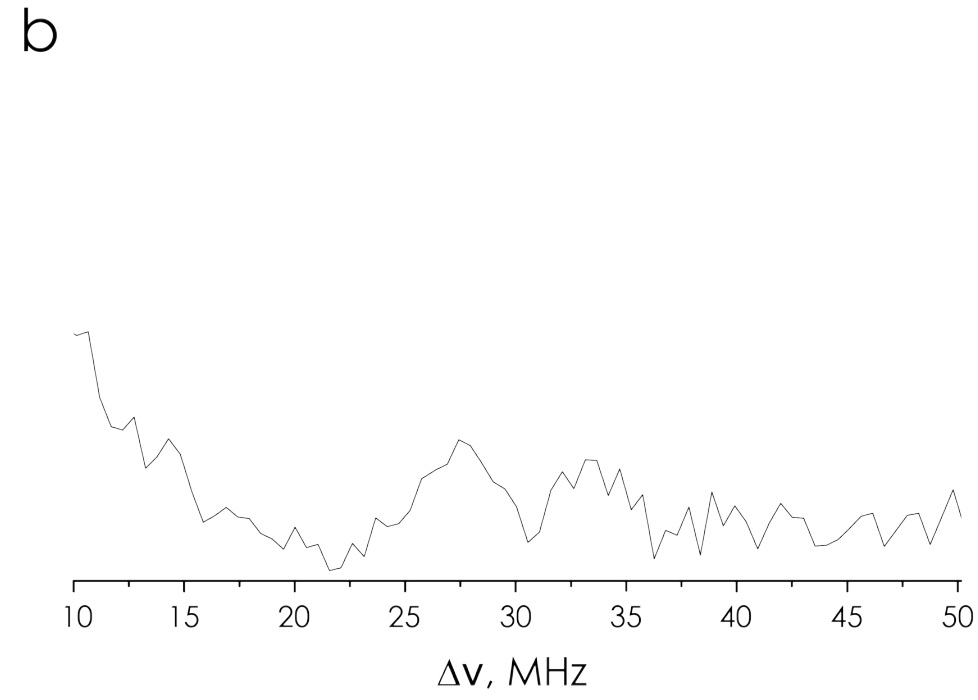
b
10
15
20
25
30
35
40
45
50
Δν, MHz

Figure 4.27. W-band HYSCORE spectra of C112D/M121F recorded at B=32420 G recorded with two different τ-values marked on the Fig. (a,b) and of C112D measured at 32890 G and τ=137.5. The strong signals on the diagonal of the (-,+) quadrant are noise.

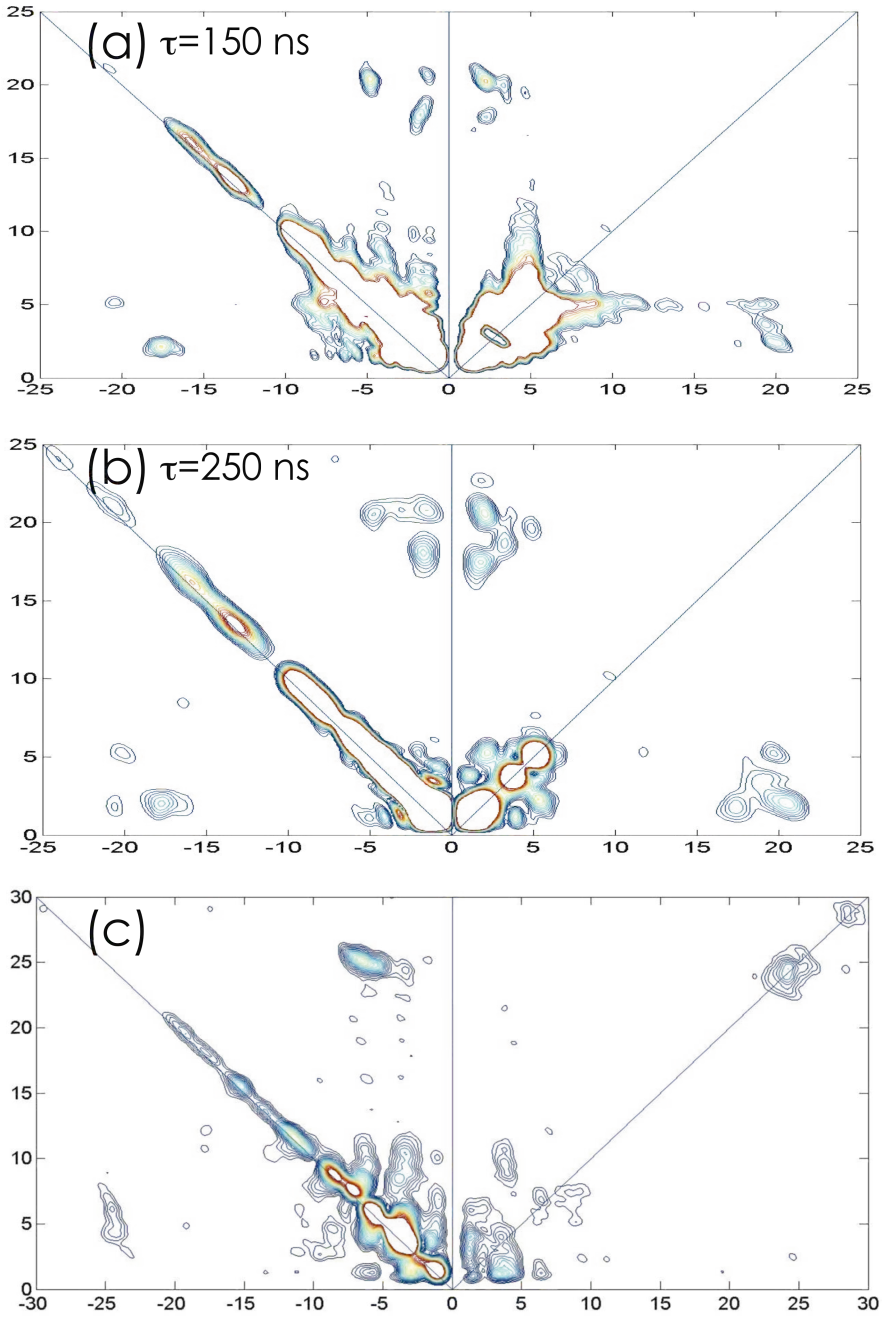
(a) τ=150 ns
(b) τ=250 ns
(c)

Figure 4.28. W-band Davies ENDOR of $^{15}N/^{13}C$ enriched samples of C112D/M121X (X = M, black; L, green; F, orange) at the position of maximum signal (g_{yy}, $g_{\perp}$). **a)** Shows the region of the large couplings obtained with t_{inv}=100 ns and **b)** shows the small coupling region obtained with t_{inv}=200 ns.

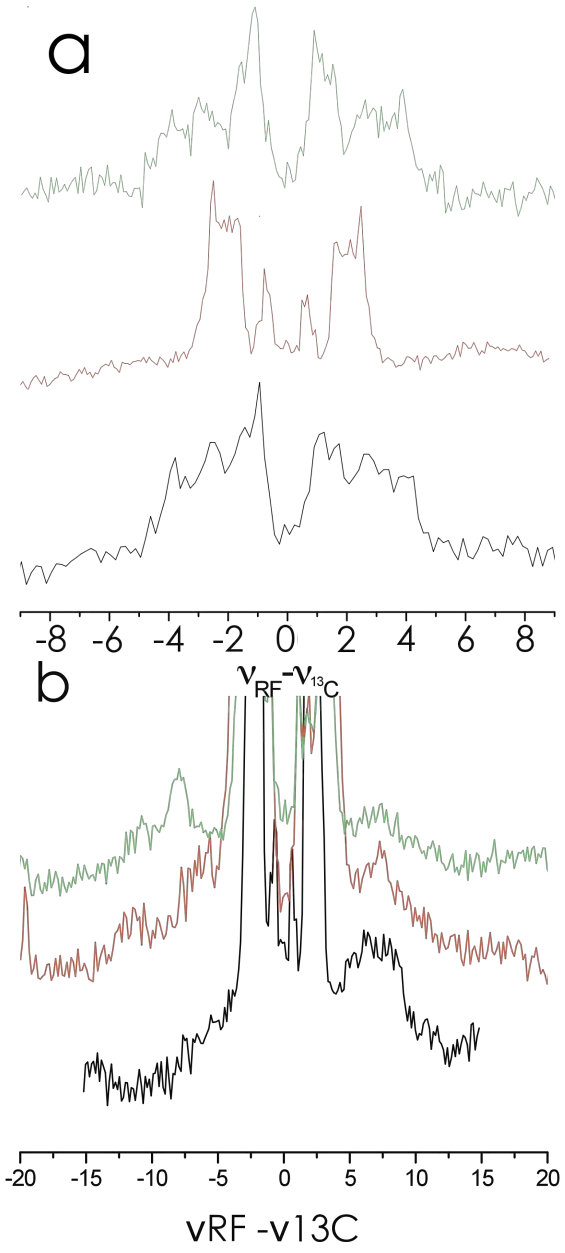
a
-8 -6 -4 -2 0 2 4 6 8
b
ν_{RF}-$\nu_{^{13}C}$
-20 -15 -10 -5 0 5 10 15 20
vRF -v13C

Figure 4.29. X-band HYSCORE spectrum of fully enriched $^{15}N/^{13}C$ C112D azurin recorded at 3300 G.

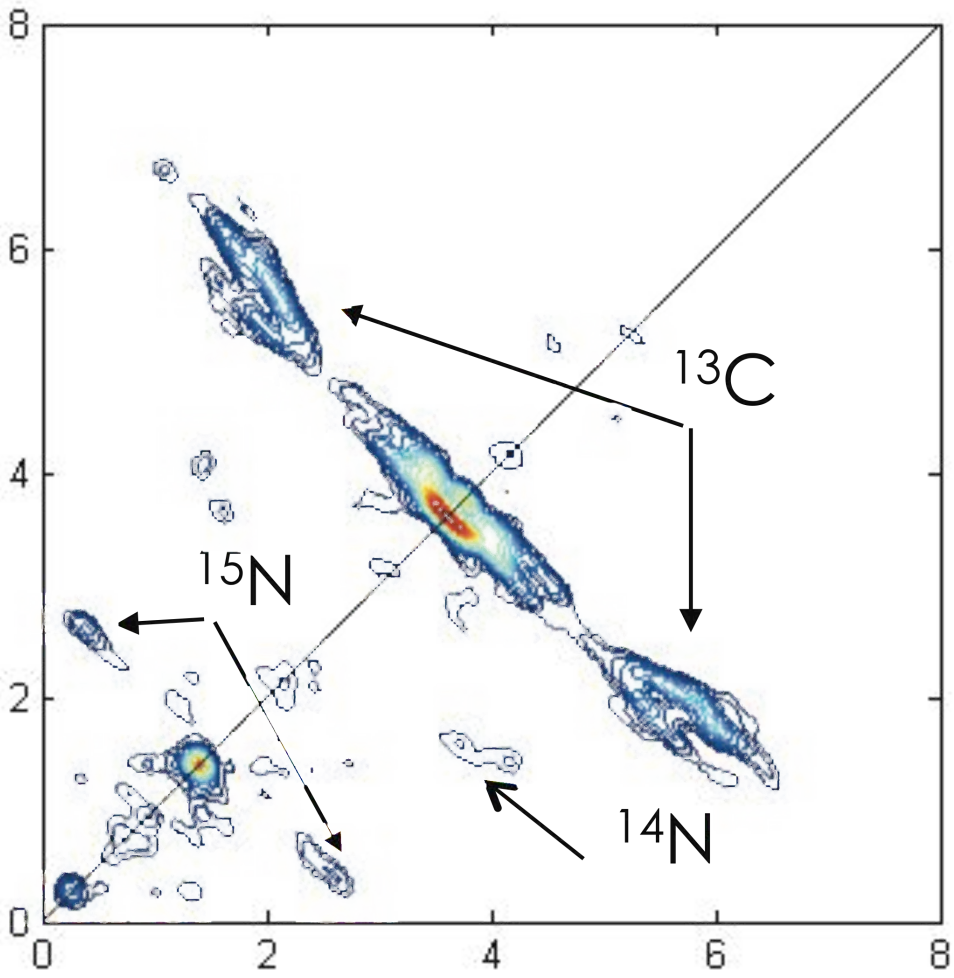
8
6
4
2
0
0
2
4
6
8
^{13}C
^{15}N
^{14}N

Figure 4.30. a) W-band Davies ENDOR spectrum of fully enriched $^{15}N/^{13}C$ C112D azurin recorded at 32860 G. **b)** W-band Mims ENDOR spectrum fully enriched $^{15}N/^{13}C$ C112D/M121F azurin compared with that of the natural abundance sample recorded at 32420 G.

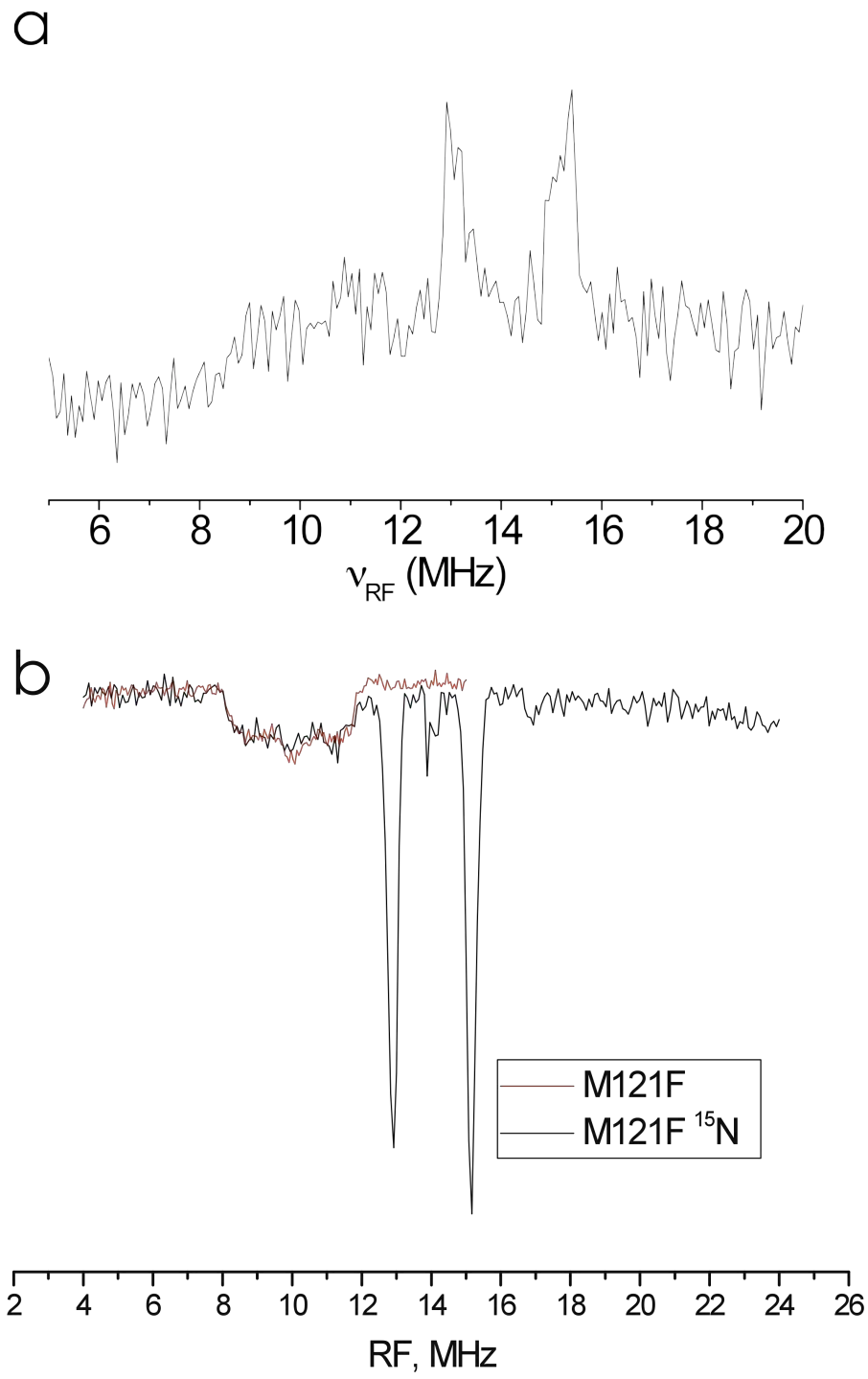
a
6
8
10
12
14
16
18
20
ν_{RF} (MHz)
b
M121F
M121F ^{15}N
2
4
6
8
10
12
14
16
18
20
22
24
26
RF, MHz

Figure 4.31. W-band ^{1}H Davies ENDOR spectra of C112D/M121X (X = M, L, F – indicated) measured at different magnetic fields within the EPR spectrum. The dotted lines trace the largest couplings.

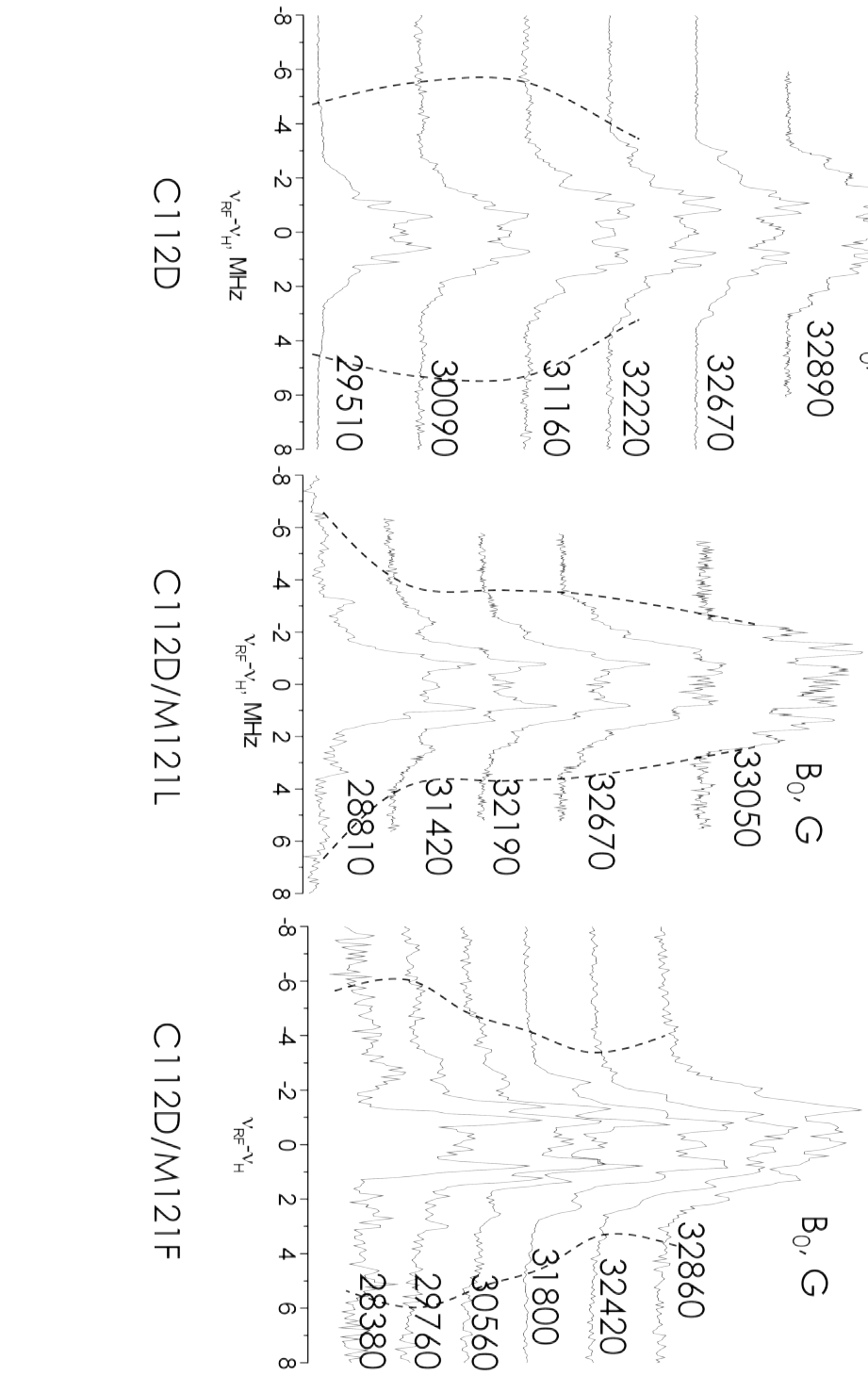
B0, G
32890
32670
32220
31160
30090
29510
νRF-νH, MHz
C112D
B0, G
33050
32670
32190
31420
28810
νRF-νH, MHz
C112D/M121L
B0, G
32860
32420
31800
30560
29760
28380
νRF-νH
C112D/M121F

APPENDIX 4

The following recipe details the preparation of minimal media for the growth of isotopically enriched protein. It was acquired from the Cambridge MRC site:

http://www.mrc-lmb.cam.ac.uk/ms/methods/protein/nmr.html

5x M9 Salts

Per liter, add

64 g $Na_2HPO_4 \cdot 7\ H_2O$
15 g KH_2PO4
2.5 g NaCl
5.0 g NH_4Cl – Either ^{15}N or ^{14}N

Stir to dissolve and autoclave.

To prepare media: (sterile technique!)

Measure 700 mL sterile MQ-H_2O
Add 200 mL 5x M9 salts
    2 mL 1 M $MgSO_4$
    20 mL 20% glucose – ^{12}C or ^{13}C as necessary
    100 μL 1 M $CaCl_2$
    1 mL 40 mg/mL thiamine
    10 mL 100 mg/L biotin
Adjust to 1 L with sterile MQ-H_2O. Serves millions.

Chapter 5

ELECTRON TRANSFER REACTIVITY OF TYPE ZERO COPPER

INTRODUCTION

Spectroscopic and theoretical evidence proposed a role for the crystallographically observed N47-D112-F114 hydrogen bond network in giving rise to the electronic structure of type zero copper. However, we have also noted that such networks have also been implicated in establishing the low ET reorganization energies characteristic of blue copper sites. We will now see by EXAFS that the type zero site undergoes minimal structural perturbation upon reduction to Cu^{I}. Moreover, we shall confirm the consequences of this behavior as we incorporate the efforts of Scot Wherland, Ole Farver, and Israel Pecht – names long associated with the azurin story – in a multifaceted investigation of the ET kinetics of C112D/M121L azurin and its comparison to those of the type 2 C112D variant.

MATERIALS AND METHODS

Materials

All chemicals were used as obtained. Milli-Q water (18.2 MΩ) was used in the preparation of all buffers and solutions.

Protein Expression and Purification

Both C112D and C112D/M121L *P. aeruginosa* azurins were expressed and purified as described in Chapter 3. As recombinantly expressed azurins are isolated with a substantial Zn^{II} population,[1-2] this material was reserved and purified separately. The wild-type (WT) protein was expressed in a similar fashion, but was purified by a divergent procedure; following isolation from cellular debris, 1:10 volume of 100 mM $CuSO_4$ was added to the periplasmic fraction. Metalation was allowed to proceed for 30 minutes, after which time 1:10 volume of 500 mM ammonium acetate pH 4.5 was added to the solution and the pH was adjusted to 4.6

using glacial acetic acid. Acid-precipitated contaminants were removed by centrifugation. The crude blue solution was repeatedly concentrated in an Amicon cell fitted with a YM-10 membrane and diluted with 50 mM ammonium acetate at pH 4.5 to remove low-molecular weight contaminants and adjust the ionic strength of the solution. This material was applied to a HiLoad SP Sepharose 26/10 FPLC column and eluted by a pH gradient using 50 mM ammonium acetate at pH 9.0. Portions of this material were then dialyzed against 100 mM potassium phosphate, containing 500 mM potassium cyanide, at pH 8.0 to remove contaminating Zn^{II}. Cyanide was removed by repeated dialysis against 50 mM Tris at pH 7.5. The holoprotein was reconstituted by two, one-hour dialyses against 50 mM Tris pH 7.5 containing 10 mM $CuSO_4$. Excess Cu^{II} was removed by dialysis against 15 mM sodium acetate pH 4.6. Protein was purified to homogeneity on a MonoS 10/10 cation exchange column by a gradient from 15 to 300 mM sodium acetate at pH 4.6.

P. aeruginosa cytc_{551} was expressed as described in Chapter 2.

Stopped-Flow Kinetics

Kinetics data were collected by KML at Pomona College on E.J. Crane's Applied Photophysics SX20 stopped-flow spectrometer equipped with a photodiode array detector and a thermostated circulating water bath under constant argon sparge. The instrument was flushed with dithionite, followed by deoxygenated buffer prior to data collection. Proteins were reduced by incubation for approximately one hour in a solution of 40 mM sodium ascorbate in 100 mM sodium phosphate at pH 8.0. Reduced proteins were subsequently exchanged into experimental buffers by PD-10 desalting column in an anaerobic chamber and inserted into a glass tonometer that was then sealed from the atmosphere. Measurements were repeated at least three times at each concentration of oxidized protein. Data was collected at 5 ºC intervals from 10 to 30 ºC. 1024 data points were collected on a logarithmic timescale. Temperatures were allowed to equilibrate for ten minutes prior to measurements. Data were analyzed by two methods. In the first, direct numerical integration and non-linear least squares fitting of a bimolecular, reversible process was conducted by Scot Wherland using the Kintecus package.[3] In this approach, the forward rate constant and the initial concentration of WT azurin were optimized. The reverse rate constant was maintained at the value calculated

from the forward rate constant and the equilibrium constant. In the second, data were treated as corresponding to a pseudo-first order process and fit to a single exponential in Igor; linear fits to concentration dependences were used to calculate second-order rate constants. The validity fitting to a single exponential under our regime of concentrations and rate constants has also been demonstrated analytically Darvey and Ninham.[4] Acceptable fits to the integrated bimolecular reversible reaction, with the assumed equilibrium constant, could only be achieved with a consistently lower-than-measured intitial concentration of WT azurin (the limiting reactant); extracted rate constants were within 5% of the values from the pseudo first-order treatment. In all cases the data fit well to single exponentials; as such values from this treatment are reported.

X-ray Absorption Spectroscopy

Cu^{I} K-edge X-ray absorption spectra (XAS) including extended X-ray absorption fine structure (EXAFS) were collected at the Stanford Synchrotron Radiation Lightsource at beam line 9-3 under ring condition of 3 GeV and 200 mA. A Si(220) double-crystal monochromator was used for energy selection and a Rh-coated mirror (set to an energy cutoff of 13 keV) was used for harmonic rejection. Internal energy calibration was performed by assigning the first inflection point of a Cu foil spectrum to 8980.3 eV. Following reduction in similar fashion to stopped-flow samples, proteins were exchanged into 50 mM HEPES at pH 7.0 containing 40% glycerol. Proteins were loaded into 2 mm Delrin XAS cells with 38 micron Kapton windows and glassed by rapid immersion in liquid nitrogen. Data were collected in fluorescence mode (using a Canberra Ge 30-element array detector) with the sample maintained at 10 K in an Oxford liquid helium flow cryostat. Data were collected from 8900 to 9857 eV ($k = 15$ $Å^{-1}$). 10 scans were averaged and processed using the MAVE and PROCESS modules of the EXAFSPAK[5] software package. Background subtractions were achieved using PYSPLINE.[6] XRD coordinates for C112D/M121L azurin (PDBID: 3FPY) were used to generate models for path calculation by FEFF7.[7-8] Relevant paths were then optimized by least-squares fitting in the OPT package of EXAFSPAK.

Pulse Radiolysis

Time-resolved measurements were performed by Ole Farver and Israel Pecht using the pulse-radiolysis (PR) system based on the Varian V-7715 linear accelerator at the Hebrew University

in Jerusalem, Israel, employing 5 MeV accelerated electrons. All experiments were performed under anaerobic conditions between 8 and 45 ºC at pH 7.0 in nitrous oxide saturated solutions containing 100 mM formate and 10 mM phosphate. Protein concentrations were in the range from 40 to 60 μM. Pulse widths of 1.0 μs produce ~ 15 μM CO_2^- radicals, as determined by independent dosimetry measurements. Pulse widths of 0.3 μs were used, yielding ~ 4-5 μM CO_2^- radicals. A 1x1 cm Suprasil (HELLMA®) cuvette was used, with three light passes which result in an overall optical path-length of 3 cm. A 150 W xenon lamp produced the analyzing light beam together with a Bausch & Lomb double grating monochromator. An appropriate optical filter with cut-off at 385 nm was used to reduce photochemical and light scattering effects. The data acquisition system consisted of a Tektronix 390 A/D transient recorder attached to a PC. The temperature of the reaction solutions in the cuvette was controlled by a thermostated circulating system, and continuously monitored by a thermocouple attached to the cuvette. Reactions were generally performed under pseudo-first order conditions, with at least 10-fold excess of oxidized protein over reducing radicals. In each experiment 2,000 data points were collected, divided equally between two different time ranges. Usually the processes were recorded over at least three half-lives. The formation and decay of the $RSSR^-$ radical was followed at 410 nm (ε_{410} = 10,000 M^{-1} cm^{-1}).[9] Each individual measurement was repeated at least three times at each temperature, with data collection repeated at least four times. The data were analyzed by fitting to a sum of exponentials using a nonlinear least squares program written in MATLAB®.

RESULTS

Spectra and Structures

XAS of C112D and C112D/M121L azurins were recorded at 10 K in pH 7.0 buffered solution (Figure 5.1). Previous analysis of the Cu^{I} X-ray absorption near edge spectrum (XANES) of C112D azurin compared the energy and intensity of the ~8985 eV pre-edge feature to corresponding values for three- and four-coordinate model complexes.[10] This feature in the C112D/M121L pre-edge spectrum is shifted roughly to 1 eV higher energy (from 8985.7 eV to 8986.6 eV), with a concomitant decrease in intensity. It is likely that Cu^{I} in C112D/M121L azurin retains all four ligands during redox cycling in contrast to C112D, which was shown to undergo ligand loss upon reduction of Cu^{II} to Cu^{I}.

In the same study, an analysis of C112D azurin EXAFS indicated a 0.2 Å expansion of the Cu equatorial ligands upon reduction to Cu^{I}. EXAFS data for Cu^{I} C112D/M121L azurin were collected to $k = 15$ $Å^{-1}$, although signal to noise precluded fitting beyond 14.5 $Å^{-1}$ (Figure 5.2). Data were fitted to models of increasing complexity (Table 5.1). Repeated attempts to force coordination spheres with four equidistant ligands resulted in damped Debye-Waller coefficients and degraded F-factors. Best fits were achieved explicitly modeling the Cu^{I}-O(G45) and Cu^{I}-Oε_2(D112) pairs as distinct scattering paths.

Our data indicate only minor changes to the crystallographically determined and EXAFS-verified Cu^{II} structure. The largest of these appears to be an expansion of the Cu-O(G45) axial interaction from 2.35 to 2.45 Å. This bond lengthening suggests an electrostatic component to this interaction that is mitigated upon reduction of the Cu charge from +2 to +1. No significant changes in the Cu-N/O bond distances of the equatorial ligand set were found. These studies suggest that the higher ET reactivity of C112D/M121L azurin relative to C112D is attributable to lower active site reorganization during redox cycling.

Reactivity

Bimolecular ET kinetics data were obtained from stopped-flow mixing experiments in which oxidized C112D and C112D/M121L azurins were mixed with the reduced wild-type

protein. Direct measurements of electron self exchange (ESE) by the widely-used NMR method are intractable owing to the longer electron spin relaxation time of type 2 copper (Chapter 4) making comparison to C112D impossible; furthermore, low extinction coefficients lead to unacceptable uncertainty in determination of the low concentrations required for the technique.[11-12] ET was monitored at 630 nm (Figure 5.3).

Equilibrium constants were calculated using the 298 K reduction potential of C112D (180 mV) and C112D/M121L (281 mV) azurins evaluated by redox titrations with cytochrome c_{551} (Chapter 2) and a value of 304 mV for WT azurin.[13] These solution measurements were found to be more precise than electrode measurements, and it should be noted that the values found by the technique are within the error of the previously published values. These potentials give equilibrium constants at 298 K for the reduction of C112D by WT of 0.0082 and for the reduction of C112D/M121L of 0.41. Excess concentrations of the mutant azurins were mixed to establish pseudo first-order kinetics conditions. Owing to the rapid reaction times, lower concentrations of C112D/M121L azurin were required; however, the reaction equilibrium constant being near unity, exponential kinetics could still be observed even when near-equal concentrations of reactants were mixed.[4] Plots of rate constants extracted from single exponential fits as a function of oxidized azurin concentration were found to be linear (Figure 5.4); the second order rate constants k_{12} were extracted from linear fits to these plots. Activation parameters were calculated from temperature dependences of the rate constants from 10 to 30º C (Table 5.2, Figure 5.5).

Notably, the C112D/M121L protein displays a two order-of-magnitude increase in the rate constant for reaction with WT azurin over that for C112D at 298 K, with k_{12} = 31,100 $M^{-1}s^{-1}$ compared to 338 $M^{-1}s^{-1}$. The temperature dependences of these rate constants show that the greater reactivity of C112D/M121L is attributable to activation enthalpy, which within error is decreased substantially (12.6 kJ mol^{-1}) relative to C112D azurin. The activation entropies for the two proteins are virtually identical.

Intramolecular electron transfer kinetics were measured by pulse radiolysis (PR). PR produced CO_2^- radicals were shown to reduce the disulfide bridge as well as the Cu^{II} site of the

two azurins. As the type 2 and type zero Cu^{II} sites exhibit relatively weak absorptions in the visible region, only formation and decay of disulfide radical could be followed. A protein-concentration dependent increase in absorption was monitored at 410 nm in the microsecond time range for both mutants, reflecting $RSSR^{-}$ radical anion formation assigned to the direct, second order reduction by the CO_2^{-} radicals. This fast, diffusion controlled bimolecular reaction was followed by slower processes in the millisecond time range reflecting the $RSSR^{-}$ reoxidation (Figure 5.6). The observed rate constants of this process were found to be independent of both protein and CO_2^{-} radical concentrations, characteristic for an intramolecular process, namely intramolecular ET from the disulfide radical ion to Cu^{II} center. Control reactions with Zn^{II} azurins do not undergo this process (Fig 5.7). The temperature dependence of this process was examined for both azurin mutants in the 4 to 45° C range at pH 7.0 (Table 3, Figure 5.8).

In stark contrast to rate constants determined by stopped flow and electrochemical (Chapter 3) measurements, the rate constant of ET from C3/C26 $RSSR^{-}$ is found to be slower by a factor of two for C112D/M121L compared to C112D azurin. A marked drop is again observed in the activation enthalpy, but this is overcome by a substantially less favorable activation entropy.

DISCUSSION

The semiclassical ET theory for reactions between spatially fixed and oriented donors and acceptors provides a framework for analysis of rate constants, Eq. (5.1):[14]

$$k_{ET} = \sqrt{\frac{4\pi^3}{h^2 \lambda k_B T}} H_{AB}^2 \exp\left\{ -\frac{\left(\Delta G^\circ + \lambda\right)^2}{4\lambda k_B T} \right\} \tag{5.1}$$

In Eq. (1), h is Planck's constant, k_B is Boltzmann's constant, T is the temperature (K), H_{AB} is the electronic coupling between reactants, ΔG^o is the driving force for the electron transfer, and λ is the reorganization energy. When the driving force of the reaction equals the total reorganization energy the rate constant reaches its maximum value, k_{MAX}. H_{AB}^2 decays exponentially with the separation distance; as such we can estimate k_{MAX} by Eq. (5.2)

$$k_{MAX} = 1 \times 10^{13} \exp\left\{ -\beta (r - r_0) \right\} \ s^{-1} \tag{5.2}$$

where r is the donor-acceptor distance and r_0 is the value of r for donor and acceptor in direct (van der Waals) contact; the generally accepted value for r_0 is 3.0 Å. A time table for activationless electron tunneling in β-sheet proteins predicts a coupling decay constant, $\beta = 1.1$ Å^{-1}.[15] This value has been shown to be as high as ß = 1.6 Å^{-1} for tunneling through water molecules.[16] λ for donors and acceptors can be determined by the Marcus cross-relation Eq. (5.3):

$$\lambda_{TOT} = \frac{\lambda_D}{2} + \frac{\lambda_A}{2} \tag{5.3}$$

where λ_{TOT} is the total reorganization energy for the ET reaction.

To treat the bimolecular data with and thus to obtain estimates of ET parameters from Eqs. 1 and 2 we must first convert the second-order rate constants to first-order values (Eq. 5.4):

$$k_{ese} = K_A \times k_{ET} \tag{5.4}$$

where K_A, the ET complex association constant, is taken to be 1 M^{-1}.[11-12] Extensive study has demonstrated that azurin electron self-exchange (ESE) occurs through H117, and that the ET complex is mediated by a hydrophobic patch surrounding this residue.[17] The 3D structure of *P. aeruginosa* WT azurin exhibits interprotein crystallographic contacts in this region.[18] Moreover, two water molecules bridge the two H117 sidechains. These have been shown to enhance the coupling between the coppers in ESE.[19] The ET reaction of reduced WT azurin with oxidized mutants should approximate ESE, as such C_α structural alignment of C112D and C112D/M121L azurins with WT azurin was used to model the bimolecular ET complex (Figure 5.9). Importantly, the bridging water molecule is conserved in the mutant structures. Direct Cu-Cu distances are 14.68 and 14.75 Å from WT to C112D and C112D/M121L azurin, respectively.

Electron transfer rates were calculated with ß = 1.0 to 1.65 and with variable λ's for the bimolecular ET reactions taking the Cu-Cu separations for r (Figure 5.10). A λ of 0.82 eV is used for WT azurin in Eq. (5.3) to calculate λ_{TOT}.[20]

The value of ß for ET between two azurin molecules lies between the values for ET through protein backbone (1.1 $Å^{-1}$) and through water (1.6 $Å^{-1}$). The value of ß for each reaction is assumed to be invariant given identical (within error) values of $\Delta S^{‡}$ for the reactions. Within this range, agreement with experimentally determined rates requires λ = 1.6 – 2.4 eV for C112D and λ = 0.4 – 1.2 eV for C112D/M121L. A lower λ for C112D/M121L is supported by the lower $\Delta H^{‡}$ as well as the structural similarity of the Cu^{II} and Cu^{I} sites.

We can narrow the ranges for λ. The Marcus cross-relationship can also be used to estimate ESE rates for the azurin mutants (Eq. 5.5):[14]

$$k_{12} = \sqrt{K_{12} k_{11} k_{22} f_{12}} \quad (5.5)$$

In Eq. (1), k_{12} is the observed second-order rate constant for the reaction between species 1 and 2, K_{12} is the equilibrium constant of this reaction (calculated using the reduction potentials of the reactants), k_{ii} values are the self-exchange rate constants, and f_{12} is taken to be 1. A value of 1 x 10^6 $M^{-1}s^{-1}$ is used for WT azurin ESE.[11-12] Eq. (5.5) gives ESE rate constants of 1.4 x 10^1 $M^{-1}s^{-1}$ for C112D azurin and 2.4 x 10^3 $M^{-1}s^{-1}$ for C112D/M121L azurin. ESE among the WT and two azurin variants will be dominated by λ. Slight differences in coupling of H117 to Cu may impact ESE; by EPR (Chapters 3 and 4) C112D is found to have greater electron delocalization its equatorial imidazoles than C112D/M121L. Notwithstanding, C112D azurin ESE is very slow. Thus, the decreased ESE rate constant for C112D/M121L relative to WT azurin suggests a modestly elevated λ ~ 0.8 – 1.0 eV; meanwhile, the dramatically reduced C112D ESE rate constant further supports a highly elevated λ. A λ of 0.8 – 1.0 eV for C112D/M121L azurin best fits experimental data with ß of 1.3-1.4, seemingly appropriate for ET that is half through imidazole and half through water. These values of ß require a λ of 2.1 - 2.3 eV for C112D azurin. This latter value is consistent for $Cu^{II/I}$ reorganization in unconstrained complexes, for exampled the λ of Cu(1,10-phenanthroline)$_2$ is 2.4 eV and the λ of unfolded WT azurin is estimated to be approximately the same.[21-22]

Having honed estimates for λ, we may now turn to the PR data. ET from the disulfide to the Cu^{II} in WT azurin has been demonstrated to proceed through two pathways (Figure 8).[23] The first pathway follows the backbone from C3 to N10 whereupon the electron passes through a hydrogen bond from N10 to H46 for entry into the Cu^{II}. The second pathway involves several hydrogen bonds and a through-space jump from V31 to W48, with the electron ultimately entering Cu^{II} through C112. The high covalency of the Cu-S(C112) bond affords this pathway equal weight to the H46 pathway.[23] This covalency is likely abolished by the C112D mutation, leaving the H46 pathway as the only viable route for ET for C112D and C112D/M121L azurin.

The activation parameters for the PR ET lend further support to a lower λ in C112D/M121L azurin than in C112D. λ has been estimated as ~ 1.2 eV for the azurin disulfide.[20] Using λ =

0.8 – 1.0 eV for C112D/M121L azurin, with $r\text{-}r_o$ = 23.8 Å and $-\Delta G^o$ = 0.691 eV, agreement with experimental data is found with ß = 1.2 $Å^{-1}$. With λ = 2.1 – 2.3 eV for C112D azurin and $r\text{-}r_o$ = 23.2 Å at $-\Delta G^o$ = 0.590 eV, ß = 0.9 $Å^{-1}$ is required to match experimental data. A larger ß for C112D/M121L PR ET is consistent with an increased $\Delta S^{\ddagger}$ relative to C112D. The physical origin of the decreased coupling is puzzling. C_α structural alignment of C112D with C112D/M121L azurin reveals almost-perfect superimposability of the ß-strands from C3 to N10. The N10 hydrogen bond to H46 is slightly longer in C112D/M121L at 2.84 Å than C112D at 2.58 Å, though this would not result in such a dramatic attenuation of ET coupling. Differences in coupling of Cu to histidines are unlikely to strongly influence the PR ET, as such effects would have arisen in the bimolecular ET reaction. There may be enhanced coupling of of Cu^{II} to D112 in the double mutant, leading to the establishment of pathway interference for electron transfer.[24] Metal-ligand covalency in the type zero copper site is still under investigation (Chapter 4).

REFERENCES

1) Karlsson, B.G.; Pascher, T.; Nordling, M.; Arvidsson, R.H.A.; Lundberg, L.G. *FEBS Lett.* **1989**, *246*, 211-217.
2) Nar, H.; Huber, R.; Messerschmidt, A.; Fillippou, A.C.; Barth, M.; Jaquinod, M.; van de Kamp, M.; Canters, G.W. *Eur. J. Biochem.* **2005**, *205*, 1123-1129.
3) Ianni, J. C. *Kintecus*, version 3.96; **2010**; http://www.kintecus.com.
4) Darvey, I.G.; Ninham, B.W. *J. Chem. Phys.* **1967**, *46*, 1626-1645.
5) George, G.N. *EXAFSPAK* (Stanford Synchrotron Radiation Lightsource, Stanford Linear Accelerator Center, Stanford University.)
6) Tenderholt, A. *PySpline*, version 1.1; **2006**; http://sourceforge.net/projects/pyspline.
7) DeLeon, J.M.; Rehr, J.J.; Zabinsky, S.I.; Albers, R.C. *Phys. Rev. B* **1991**, *44*, 4146-4156.
8) Rehr, J.J.; DeLeon, J.M.; Zabinsky, S.I.; Albers, R.C. *J. Am. Chem. Soc.* **1991**, *113*, 5135-5140.
9) Klapper, M.H.; Faraggi, M. *Q. Rev. Biophys.* **1979**, *12*, 465-519.
10) DeBeer, S.; Kiser, C.N.; Mines, G.A.; Richards, J.H.; Gray, H.B.; Solomon, E.I.; Hedman, B.; Hodgson, K.O. *Inorg. Chem.* **1999**, *38*, 433-438.
11) Groeneveld, C.M.; Canters, G.W. *Eur. J. Biochem.* **1985**, *153*, 559-564.
12) Groeneveld, C.M.; Canters, G.W. *J. Biol. Chem.* **1988**, *263*, 167-173.
13) Rosen, P.; Pecht, I. *Biochemistry* **1976**, *15*, 775-786.
14) Marcus, R.A.; Sutin, N. *Biochim. Biophys. Acta* **1985**, *811*, 265-322.
15) Gray, H.B.; Winkler, J.R. *Biochim. Biophys. Acta* **2010**, *1797*, 1563-1572.
16) Ponce, A.; Gray, H.B.; Winkler, J.R. *J. Am. Chem. Soc.* **2000**, *122*, 8187-8191.
17) Van Pouderoyen, G.; Mazumdar, S.; Hunt, N.I.; Hill, H.A.O.; Canters, G.W. *Eur. J. Biochem.* **1994**, *222*, 583-588.
18) Nar, H.; Messerschmidt, A.; Huber, R.; van de Kamp, M.; Canters, G.W. *J. Mol. Biol.* **1991**, *221*, 765-772.
19) Mikkelsen, K.V.; Skov, L.K.; Nar, H.; Farver, O. *Proc. Natl. Acad. Sci. U.S.A.* **1993**, *90*, 5443-5445.
20) Di Bilio, A.J.; Hill, M.G.; Bonander, N.; Karlsson, B.G.; Villahermosa, R.M.; Malmström, B.G.; Winkler, J.R.; Gray, H.B. *J. Am. Chem. Soc.* **1997**, *119*, 9921-9922.
21) Augustin, M.A.; Yandell, J.K. *Inorg. Chem.* **1979**, *18*, 577-583.
22) Winkler, J.R.; Wittung-Stafshede, P.; Leckner, J.; Malmström, B.G.; Gray, H.B. *Proc. Natl. Acad. Sci. U.S.A.* **1997**, *94*, 4246-4249.
23) Farver, O.; Pecht, I. *J. Biol. Inorg. Chem.* **1997**, *2*, 387-392.
24) Regan, J.J.; Di Bilio, A.J.; Langen, R.; Skov, L.K.; Winkler, J.R.; Gray, H.B.; Onuchic, J.N. *Chem. Biol.* **1995**, *2*, 489-496.

Table 5.1. EXAFS Simulations. EXAFS were fit in OPT[5] using paths calculated by FEFF7.[7-8] Coordination numbers (CN) were held constant while distances (R) and Debye-Waller factors (σ^2) were allowed to float. Error in distances are estimated to be 0.02-0.03 Å and 25% for coordination numbers. Fits were performed over the entire (0 to 6.0 Å) Fourier transform window. Goodness of fit is measured by F, defined as

$$[(\sum_i^n [k_i^3(\mathrm{EXAFS_{obs}} - \mathrm{EXAFS_{calc}})_i])^2 / n]^{1/2}$$

Fit Number	Path	CN	R(Å)	s^2	F
1	Cu to N/O	3	1.96	0.00697	0.43
2	Cu to N/O	4	1.969	0.00956	0.47
3	Cu to N/O	3	1.95	0.00695	0.37
	Cu to N/O	1	2.45	0.00521	
4	Cu to N/O	4	1.95	0.00954	0.42
	Cu to N/O	1	2.45	0.00553	
5	Cu to N/O	3	1.95	0.00697	0.32
	Cu to N/O	1	2.45	0.00512	
	Cu to N/C (MS)	4	4.17	0.0031	
6	Cu to N/O	4	1.95	0.00956	0.37
	Cu to N/O	1	2.45	0.00538	
	Cu to N/C (MS)	4	4.17	0.00305	
7	Cu to N/O	4	1.95	0.00955	0.36
	Cu to N/O	1	2.44	0.00539	
	Cu to N/O	1	3.28	0.00617	
	Cu to N/C (MS)	4	4.16	0.0029	
8	Cu to N/O	3	1.95	0.00694	0.3
	Cu to N/O	1	2.45	0.00486	
	Cu to N/O	1	3.28	0.00594	
	Cu to N/C (MS)	4	4.16	0.00299	
9	Cu to N/O	1	1.94	0.00154	0.29
	Cu to N/O	1	2.06	0.00246	
	Cu to N/O	1	1.91	0.00577	
	Cu to N/O	1	2.46	0.00495	
	Cu to N/O	1	3.28	0.00628	
	Cu to N/C (MS)	4	4.17	0.00323	

Table 5.2. Temperature-dependent stopped flow kinetics data and activation parameters.

	C112D	**C112D/M121L**
k_{12} – 284 K, $M^{-1}s^{-1}$	111	13600
k_{12} – 288 K, $M^{-1}s^{-1}$	158	18600
k_{12} - 293 K, $M^{-1}s^{-1}$	212	23651
k_{12} - 298 K, $M^{-1}s^{-1}$	338	31100
k_{12} - 303 K, $M^{-1}s^{-1}$	455	41500
$\Delta H^{\ddagger}$ (kJ mol^{-1})	50.9 ± 2.1	38.3 ± 1.5
$\Delta S^{\ddagger}$ (J mol^{-1} K^{-1})	-26.4 ± 7.4	-30.6 ± 5.4

Table 5.3. Temperature dependent PR data and activation parameters.

	C112D	**C112D/M121L**
k_{PR} – 281 K, s^{-1}	35	
k_{PR} – 283 K, s^{-1}	54	37
k_{PR} - 286 K, s^{-1}	45	
k_{PR} - 290 K, s^{-1}	112	52
k_{PR} - 297 K, s^{-1}	123	61
k_{PR} - 309 K, s^{-1}	228	99
k_{PR} - 315 K, s^{-1}	329	110
$\Delta H^{\ddagger}$ (kJ mol^{-1})	34.8 ± 4.0	22.6 ± 1.0
$\Delta S^{\ddagger}$ (J mol^{-1} K^{-1})	-88 ± 8	-135 ± 4

Figure 5.1. Cu K-edge X-ray absorption spectra of Cu^{I} C112D (black) and C112D/M121L (green) azurins in glassed pH 7.0 aqueous solution at 10 K. Normalization error is estimated to be ~ 5%.

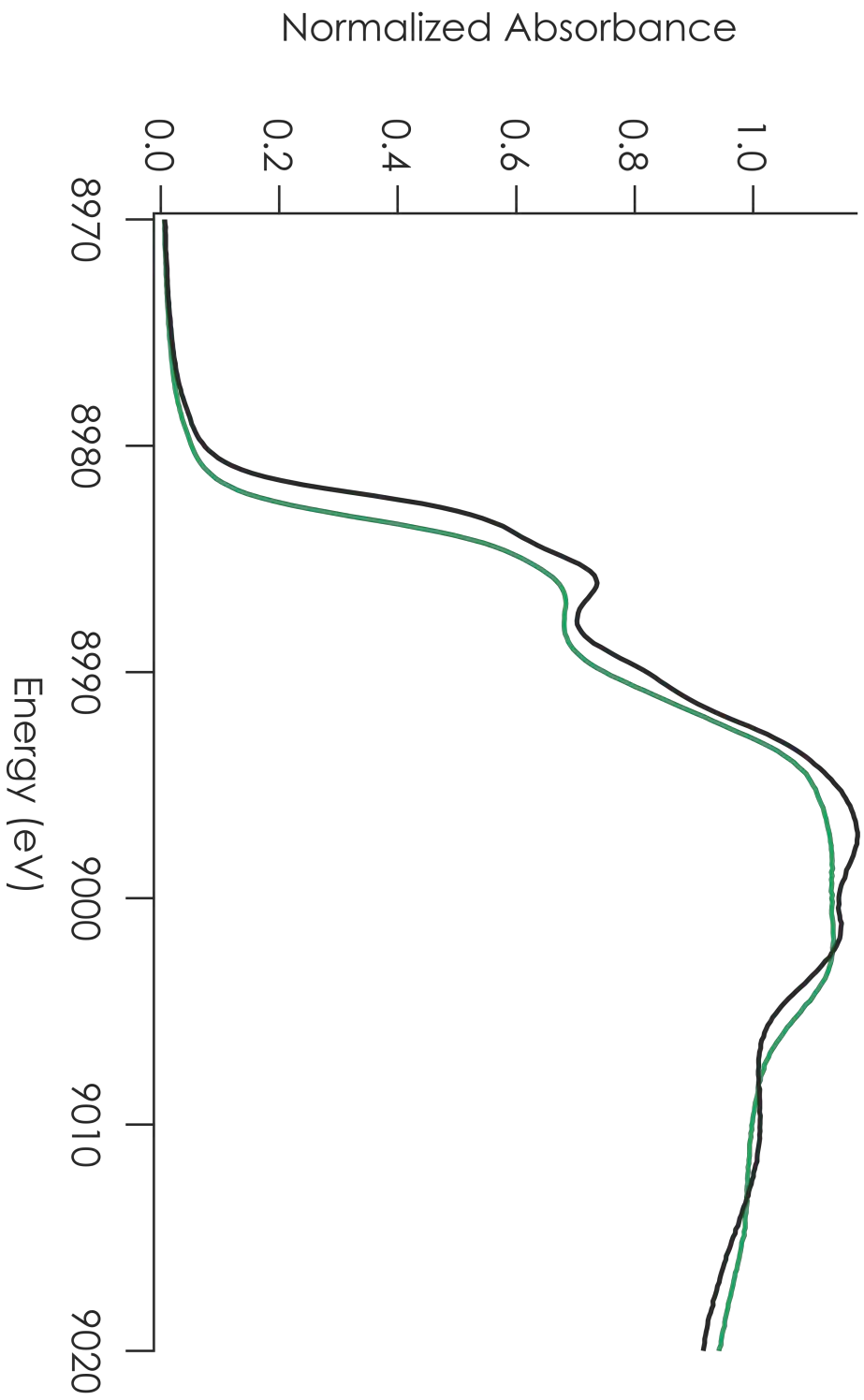
Normalized Absorbance
0.0
0.2
0.4
0.6
0.8
1.0
Energy (eV)
8970
8980
8990
9000
9010
9020

Figure 5.2. EXAFS of Cu^{I} C112D/M121L azurin in pH 7.0 glassed aqueous solution at 10 K. The green traces correspond to experimental data, while gray traces represent simulated data from fit number 9 (Table 5.1).

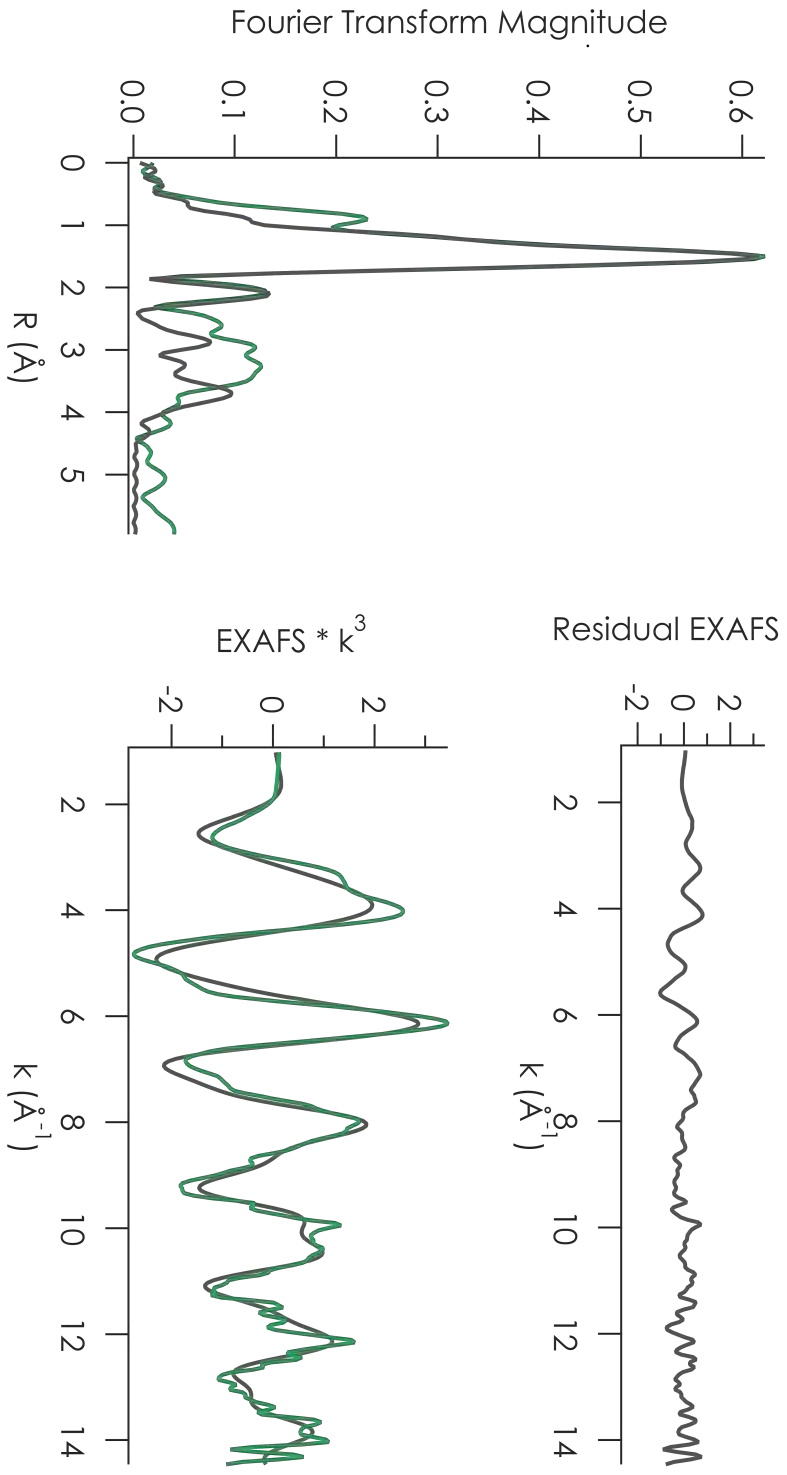
Fourier Transform Magnitude
0.0
0.1
0.2
0.3
0.4
0.5
0.6
0
1
2
3
4
5
R (Å)
EXAFS * k3
-2
0
2
2
4
6
8
10
12
14
k (Å-1)
Residual EXAFS
-2
0
2
2
4
6
8
10
12
14
k (Å-1)

Table 5.3. Transient absorption traces at 630 nm of **a)** 20 μM Cu^{I} WT azurin mixed with 424 μM Cu^{II} C112D azurin and **b)** 17 μM Cu^{I} azurin mixed with 270 μM Cu^{II} C112D/M121L azurin. Both traces represent reactions at 25 ºC in 100 mM NaP_i pH 7.0.

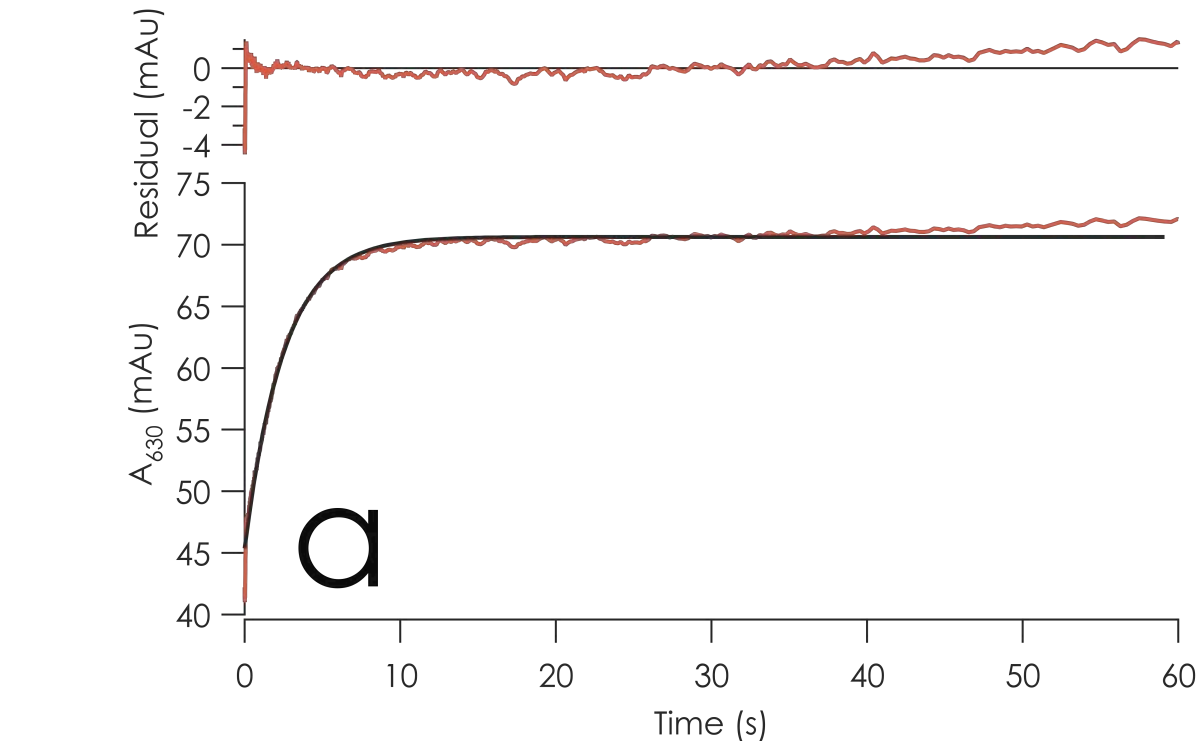
Residual (mAu)
0
-2
-4
75
70
65
60
55
50
45
40
A_{630} (mAu)
a
0
10
20
30
40
50
60
Time (s)

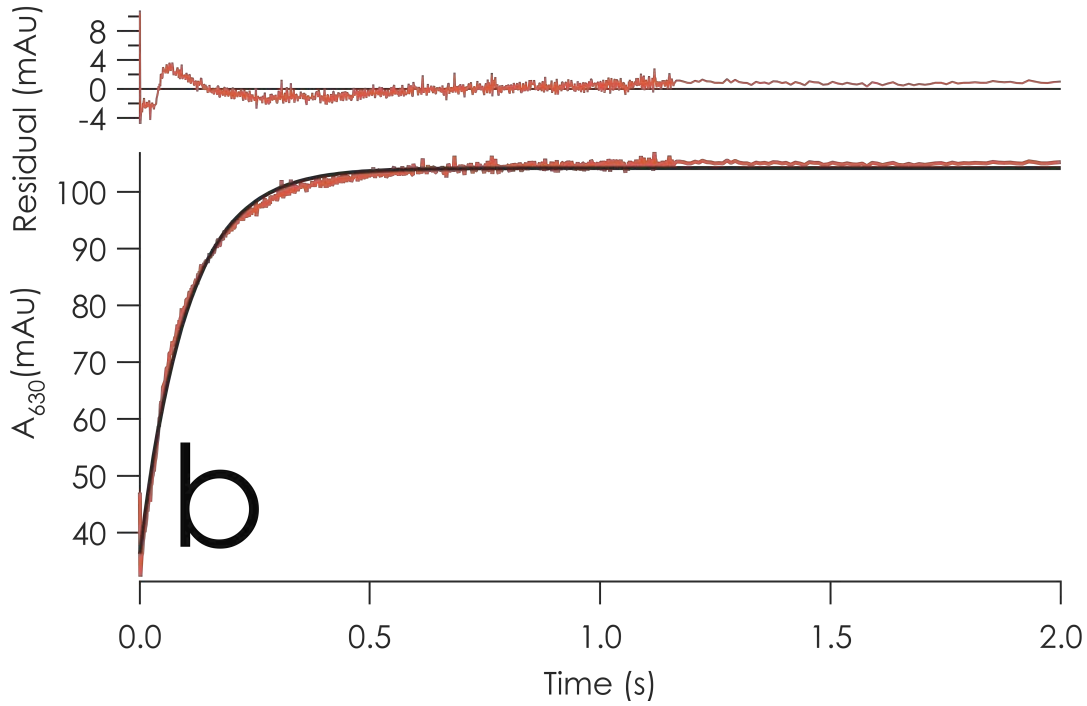
Residual (mAu)
8
4
0
-4
100
90
80
70
60
50
40
A_{630}(mAu)
b
0.0
0.5
1.0
1.5
2.0
Time (s)

Figure 5.4. Concentration dependence of pseudo first order rate constants for reactions of Cu^{I} WT azurin with Cu^{II} **a)** C112D and **b)** C112D/M121L azurins in 100 mM NaP_i pH 7.0 at 10, 15, 20, 25, and 30 ºC.

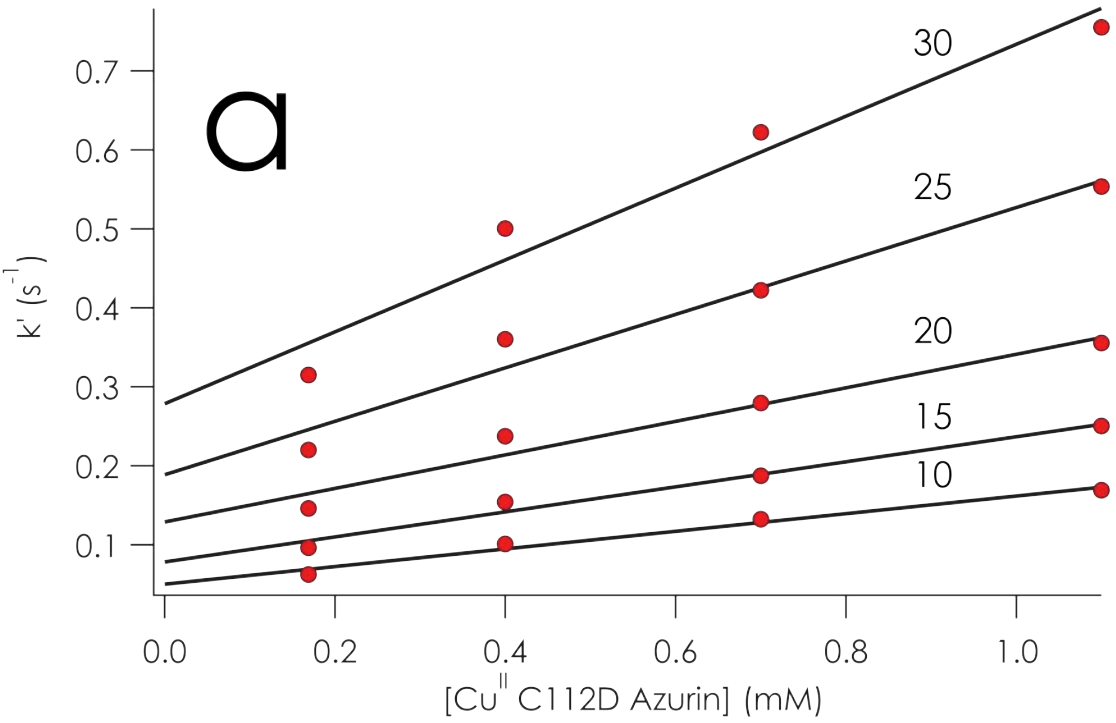
a
0.7
0.6
0.5
0.4
0.3
0.2
0.1
k' (s-1)
30
25
20
15
10
0.0
0.2
0.4
0.6
0.8
1.0
[CuII C112D Azurin] (mM)

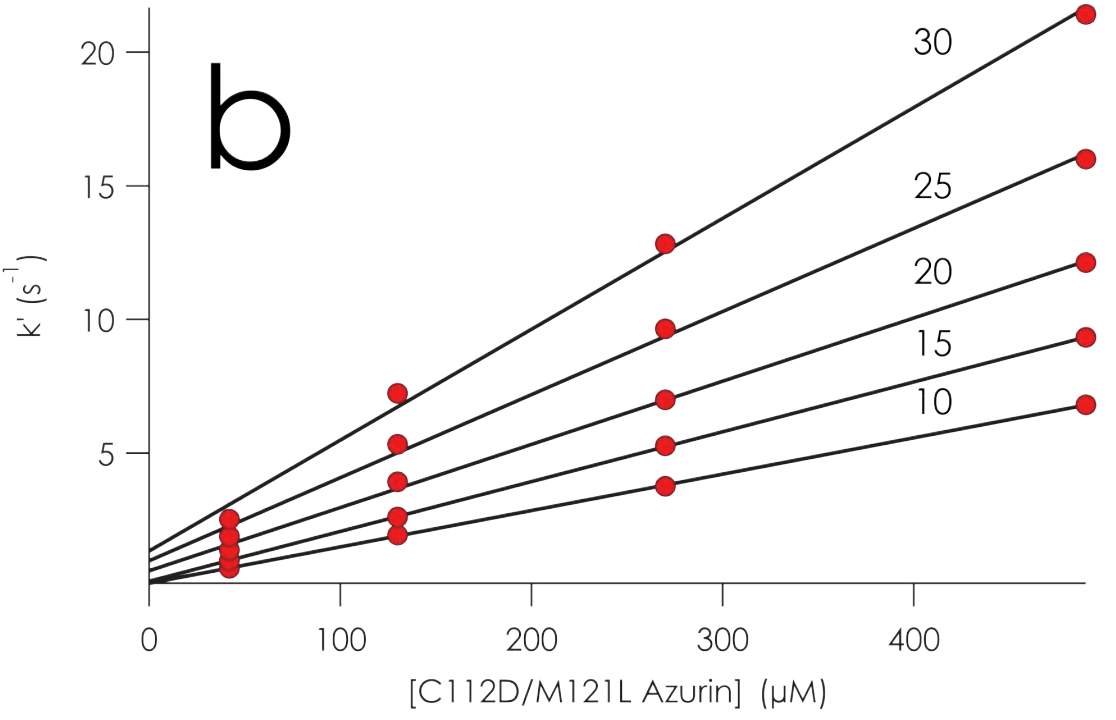
b
20
15
10
5
k' (s-1)
30
25
20
15
10
0
100
200
300
400
[C112D/M121L Azurin] (μM)

Figure 5.5. Temperature dependences of bimolecular rate constants for reaction of WT azurin with C112D and C112D/M121L mutants.

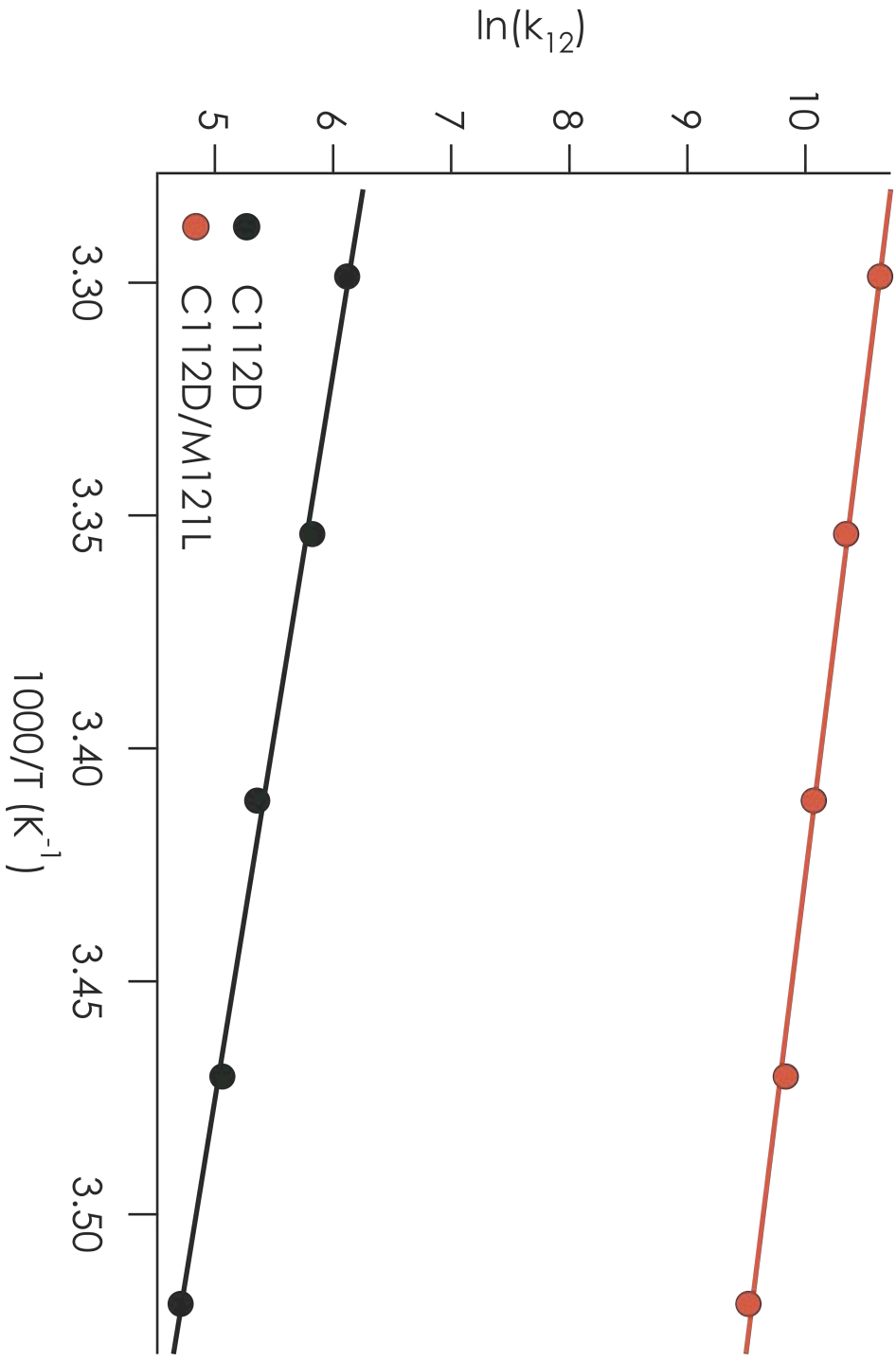
ln(k12)
10
9
8
7
6
5
C112D
C112D/M121L
3.30
3.35
3.40
3.45
3.50
1000/T (K-1)

Figure 5.6. Transient absorption at 410 nm following 0.3 μs pulse of 10 mM NaP_i/100 mM sodium formate pH 7.0 solutions of **a)** 40.5 μM C112D azurin at 35 ºC and **b)** 60 μM C112D/M121L azurin at 17 ºC. Fits corresponding to formation of $RSSR^-$ and its subsequent decay by dismutation ($8.2 \pm 2 \times 10^6$ $M^{-1}s^{-1}$, measured with Zn^{II} protein) and ET to Cu^{II} are overlaid in black.

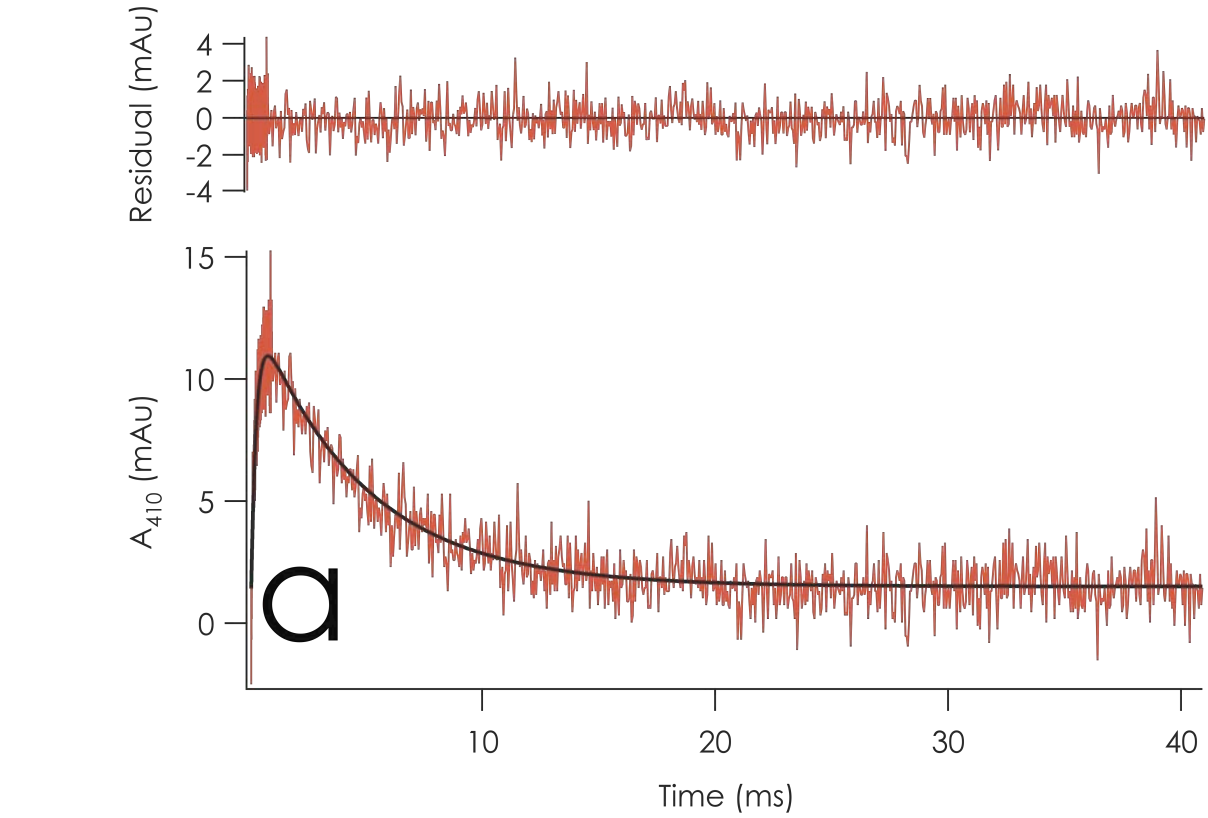
Residual (mAu)
4
2
0
-2
-4
A_{410} (mAu)
15
10
5
0
a
10
20
30
40
Time (ms)

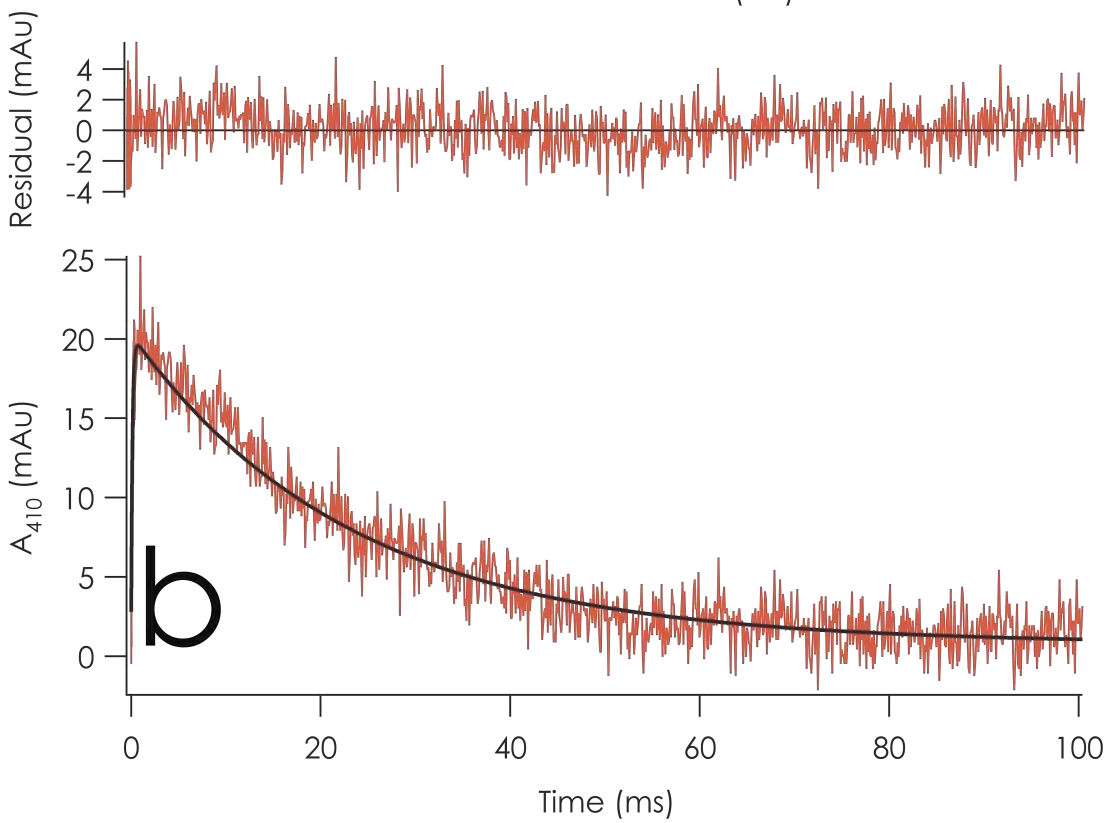
Residual (mAu)
4
2
0
-2
-4
A_{410} (mAu)
25
20
15
10
5
0
b
0
20
40
60
80
100
Time (ms)

Figure 5.7. Transient absorption at 410 nm following 0.3 μs pulse of 10 mM NaP_i/100 mM sodium formate pH 7.0 solutions of **a)** 60 μM Zn^{II} C112D azurin at 10 ºC and **b)** 50 μM Zn^{II} C112D/M121L azurin at 10 ºC. Fits corresponding to formation of $RSSR^-$ and its subsequent decay by dismutation ($8.2 \pm 2 \times 10^6$ $M^{-1}s^{-1}$) are overlaid in black.

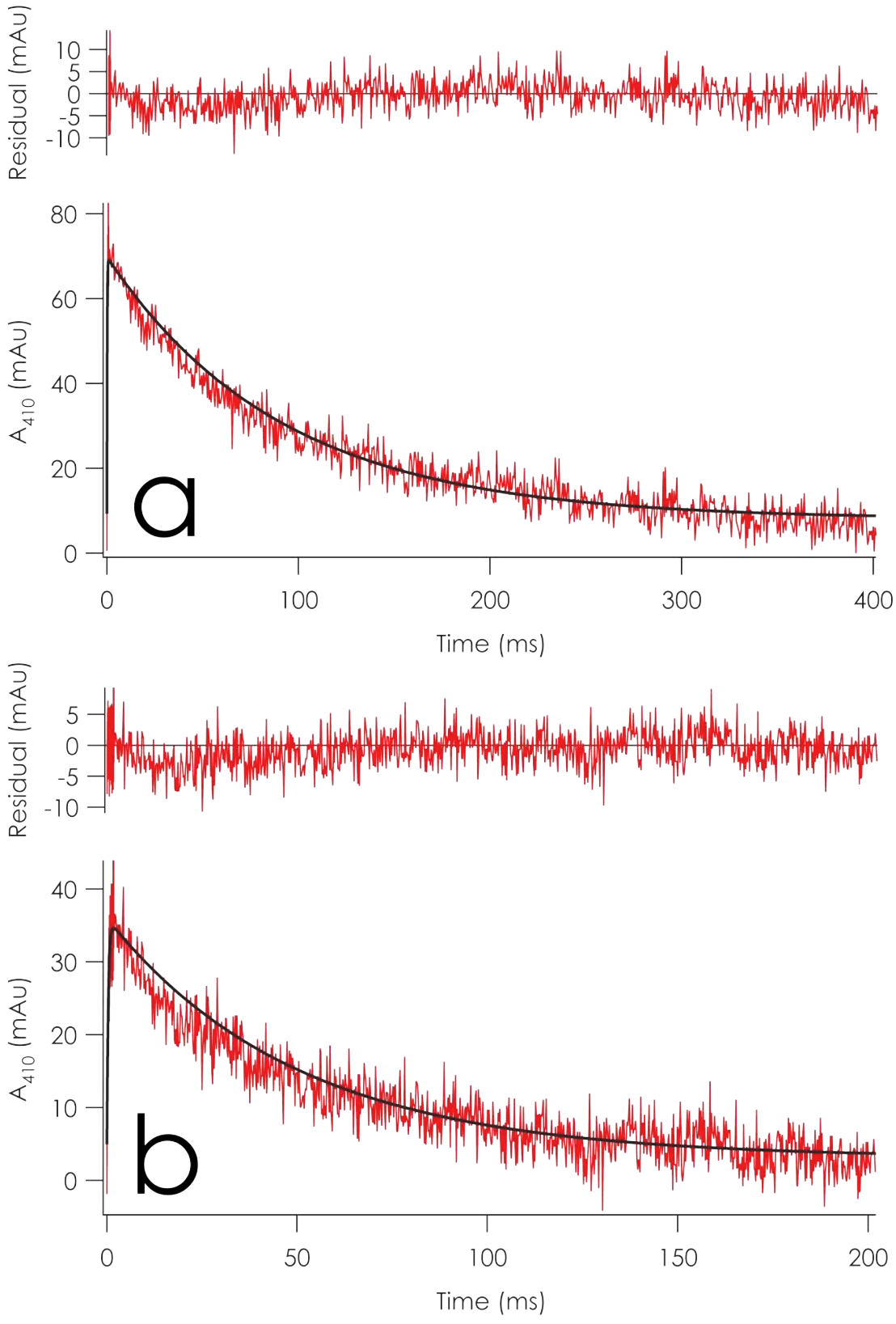
Residual (mAu)
10
5
0
-5
-10
A410 (mAu)
80
60
40
20
0
a
0
100
200
300
400
Time (ms)
Residual (mAu)
5
0
-5
-10
A410 (mAu)
40
30
20
10
0
b
0
50
100
150
200
Time (ms)

Figure 5.8. Temperature dependence of the ET reaction from pulse-radiolytically generated $RSSR^{-}$ to Cu^{II} at pH 7.0.

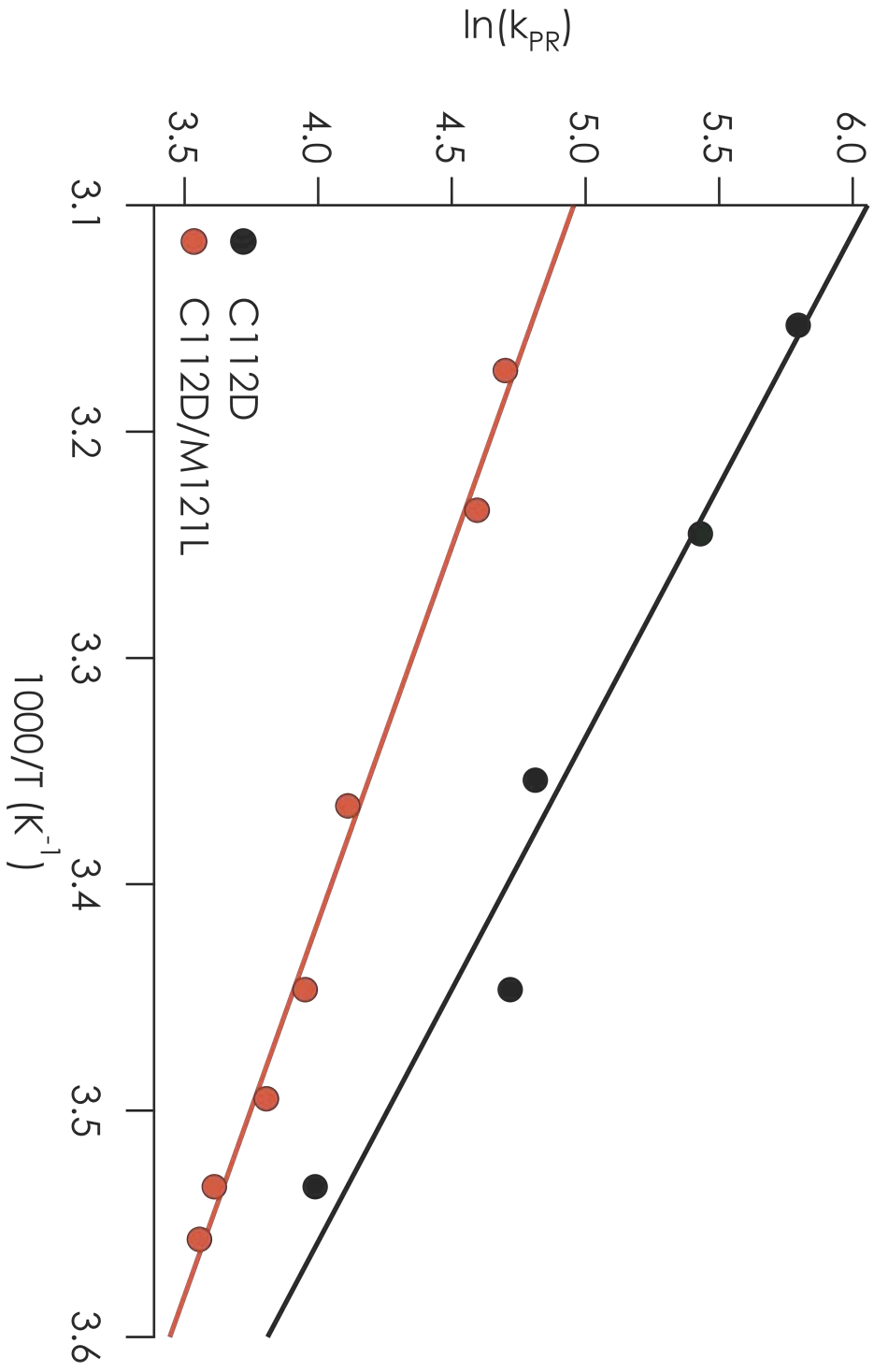
ln(k_PR)
6.0
5.5
5.0
4.5
4.0
3.5
3.1
3.2
3.3
3.4
3.5
3.6
1000/T (K^-1)
C112D
C112D/M121L

Figure 5.9. Model ET complex for reaction of WT azurin (PDBID: 4AZU) with **a)** C112D (PDBID: 3FQY) and **b)** C112D/M121L (PDBID: 3FPY) azurins. $2F_o$-F_c electron density maps are contoured at 2σ over the active sites and corresponding bridging water of the mutant azurins. Nitrogen atoms are blue, oxygen atoms are red.

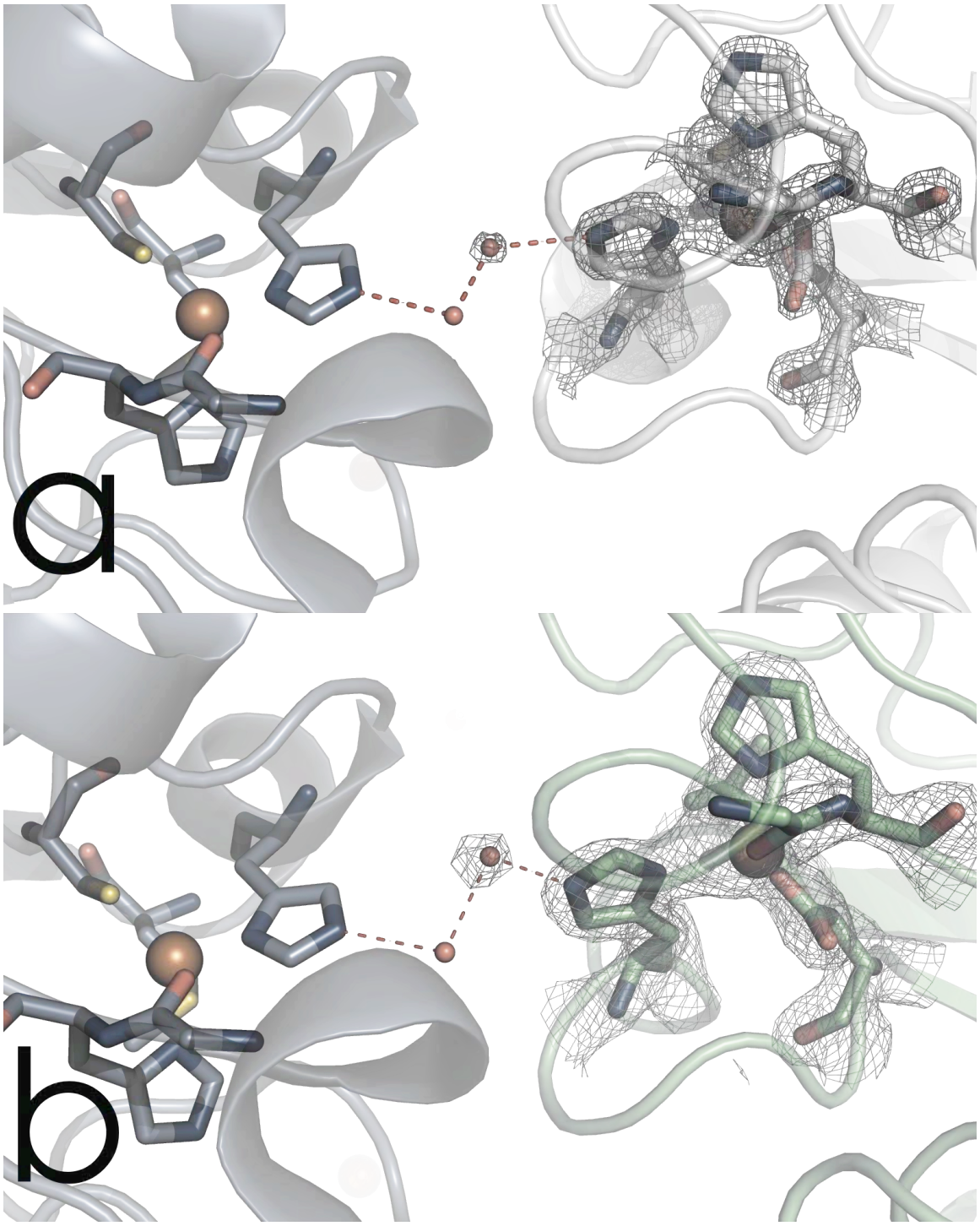
a
b

Figure 5.10. ß-dependence of electron transfer between WT and **a)** C112D azurin with λ = 1.6-2.4 eV ($-\Delta G^o$ = 0.124 eV, $r\text{-}r_o$ = 11.69 Å) **b)** C112D/M121L azurin with λ = 0.4 – 1.2 eV ($-\Delta G^o$ = 0.23 eV, $r\text{-}r_o$ = 11.75 Å) at 298 K. The red lines are the experimentally determined rate constants for ET through the encounter complex from Eq. (5.4).

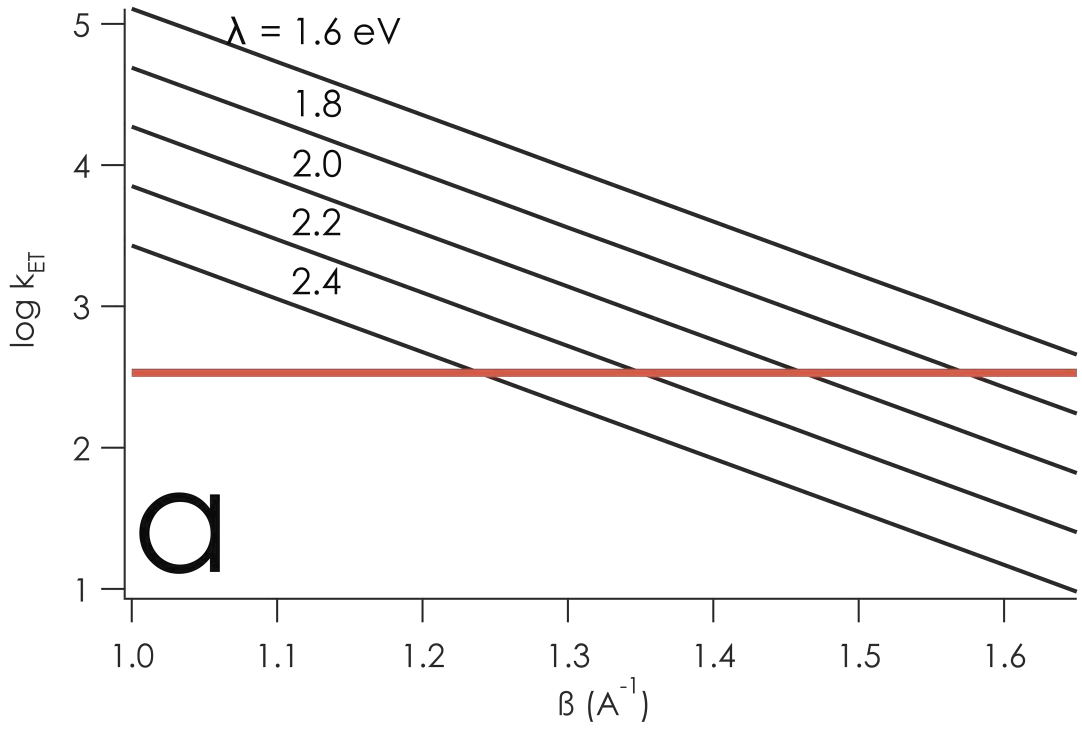
λ = 1.6 eV
1.8
2.0
2.2
2.4
a
log k_{ET}
5
4
3
2
1
1.0
1.1
1.2
1.3
1.4
1.5
1.6
ß (A^{-1})

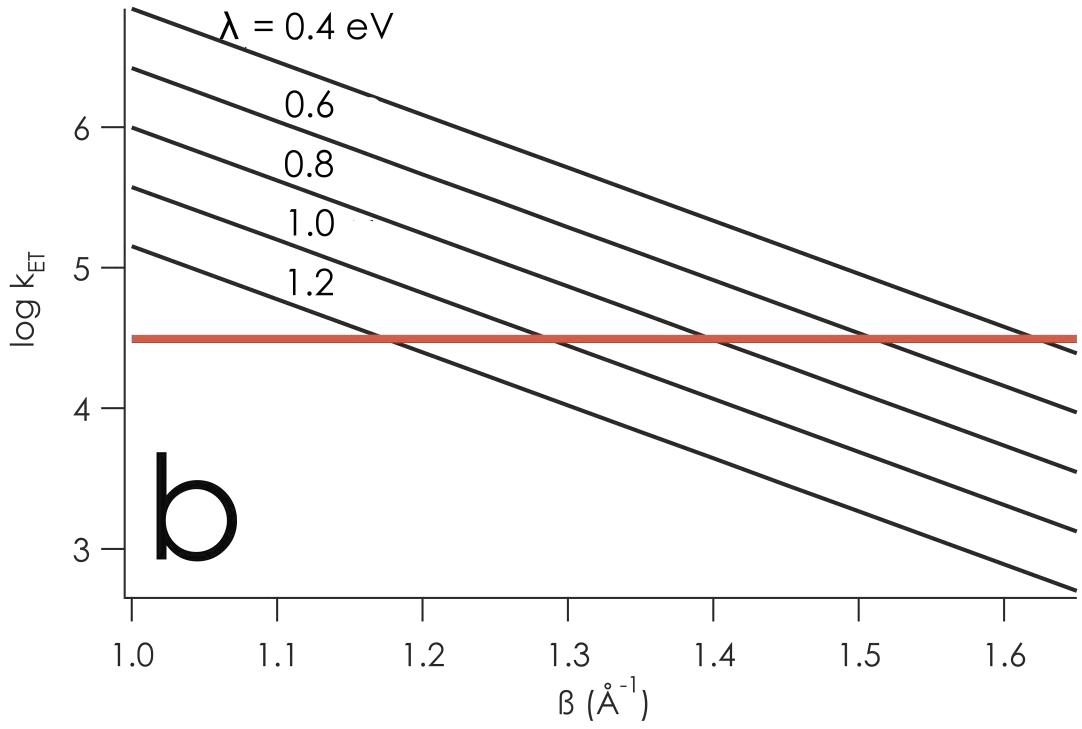
λ = 0.4 eV
0.6
0.8
1.0
1.2
b
log k_{ET}
6
5
4
3
1.0
1.1
1.2
1.3
1.4
1.5
1.6
ß ($Å^{-1}$)

Figure 5.11. Calculated pathways for ET from the sulfur of C3 to the copper center in WT *P. aeruginosa* azurin (PDBID: 4AZU). The "H46 pathway" (magenta) is likely to be the major route of electron flow in the C112D and C112D/M121L azurins. The "W48 pathway" features many non-bonded contacts, but is operative in WT azurin owing to high Cu-S(C112) covalency. Oxygen atoms are red, nitrogen atoms are blue, sulfur atoms are yellow.

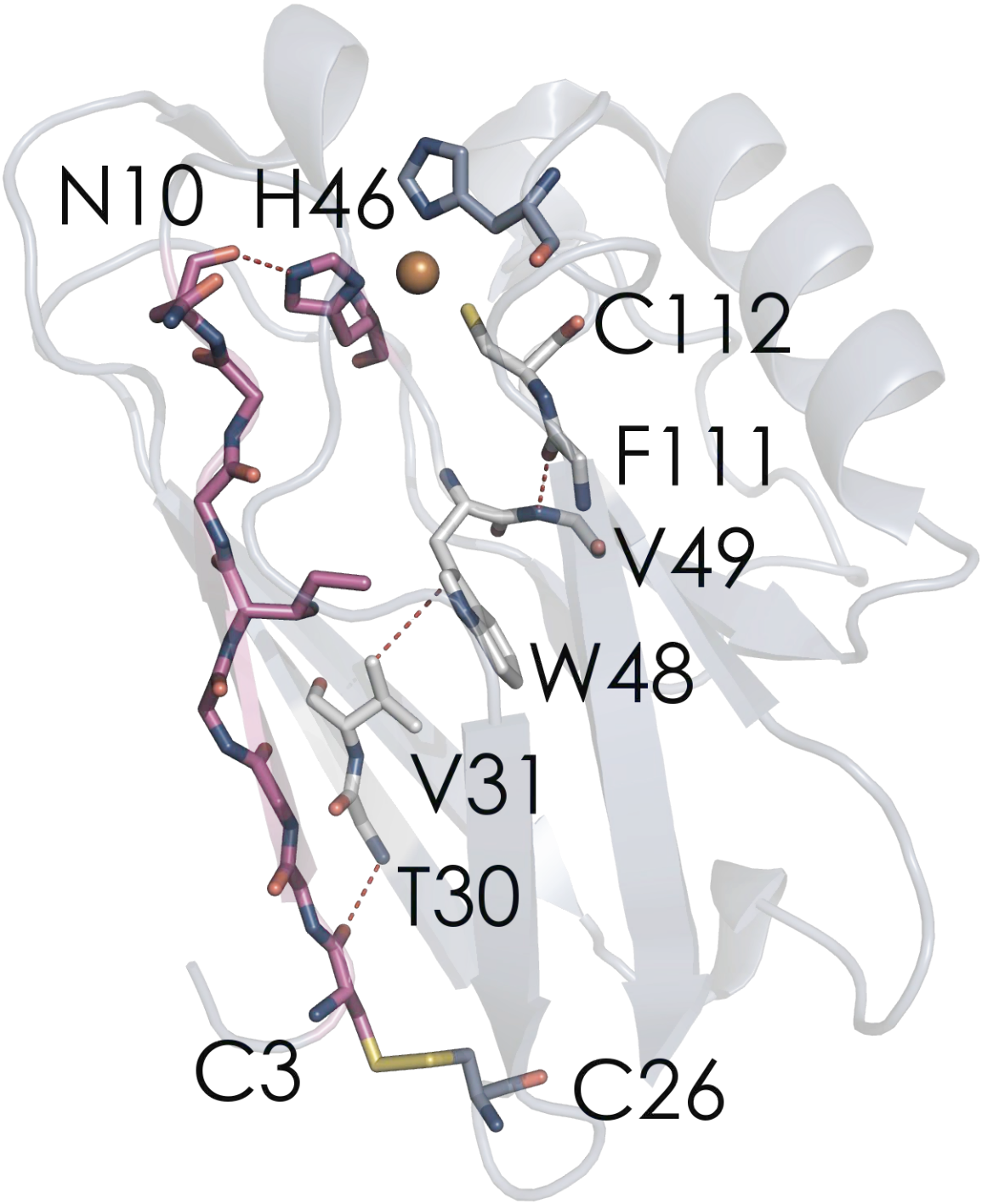
N10
H46
C112
F111
V49
W48
V31
T30
C3
C26

Figure 5.12. ß-dependence of electron transfer between $RSSR^-$ and Cu^{II} in **a)** C112D azurin with λ = 2.1-2.3 eV ($-\Delta G^o$ = 0.590 eV, r-r_o = 23.2 Å) **b)** C112D/M121L azurin with λ = 0.8 – 1.0 eV ($-\Delta G^o$ = 0.691 eV, r-r_o = 23.8 Å) at 298 K. The red lines are the experimentally determined rate constants for ET measured by PR.

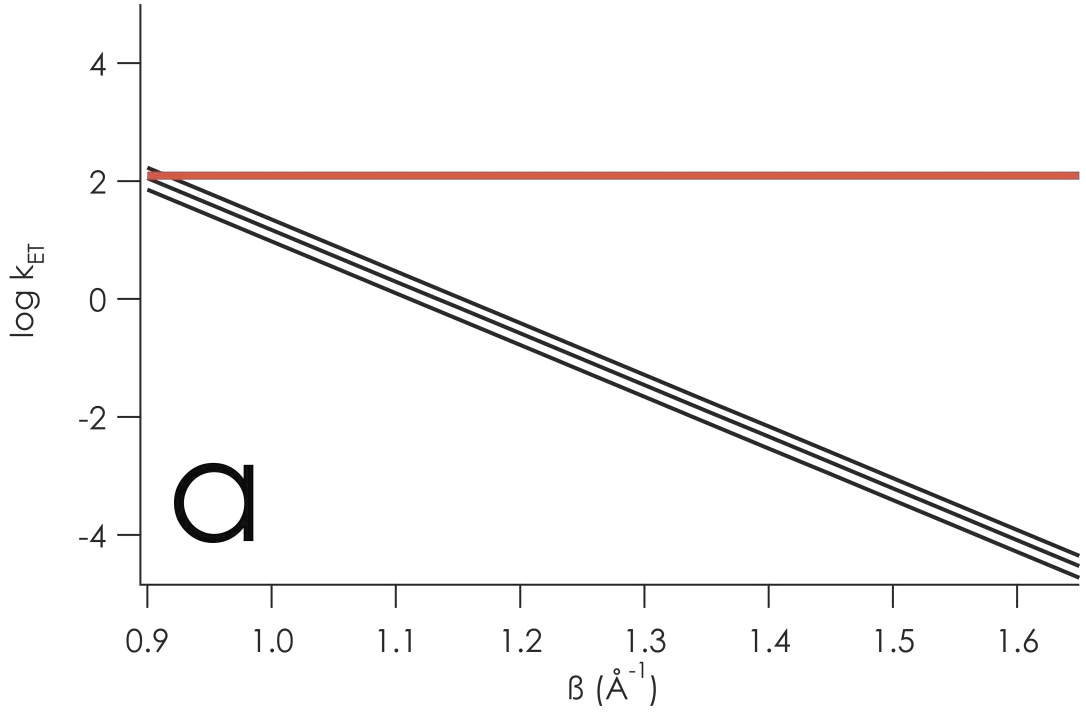
4
2
0
-2
-4
log k_{ET}
a
0.9
1.0
1.1
1.2
1.3
1.4
1.5
1.6
ß (Å^{-1})

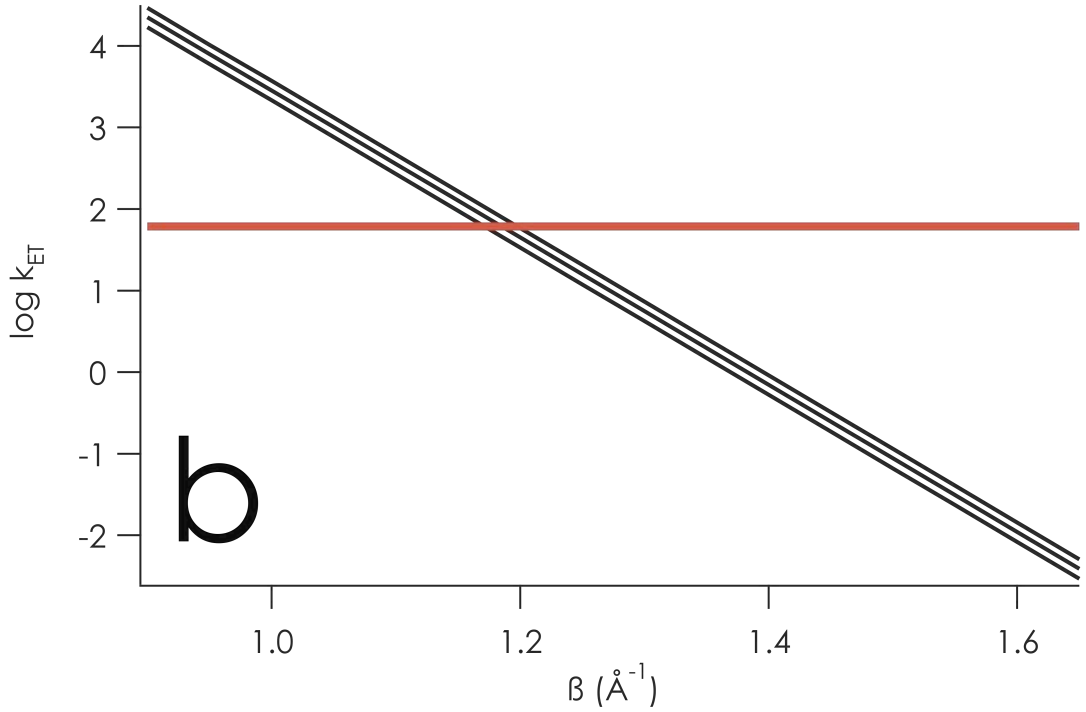
4
3
2
1
0
-1
-2
log k_{ET}
b
1.0
1.2
1.4
1.6
ß (Å^{-1})

Epilogue

There is a great divide in our understanding separating a protein's primary structure from its function. Indeed, no substantial ground is closed with the tertiary structure as a starting point. The addition of cofactors, even as simple as transition metal ions, confounds this understanding yet further. For example, we have seen that the simple yet elegant correlation established by Yi Lu between site hydrophobicity and the reduction potential of type 1 *P. aeruginosa* azurins is not operative in all copper proteins. Indeed, the installation of a Cu^{II}-stabilizing negatively charged glutamate residue as seen in the C112D/M121E azurin first *elevates* the reduction potential of the bound Cu^{II} before both the hydrophobicity and the electrostatics effect their attenuating influences. This arises due to structural constraints imposed upon the inner coordination sphere by the distant H35/P36 backbone torsional rotation, which in turn exerts constraints upon H46 that are ultimately responsible for a "rack" effect hindering the binding of E121 to Cu^{II}. Unfortunately the absence of structural evidence precludes at this point the extension of this argument to the C112D/M121H azurin, but its structure will not remain forever elusive. However, we have shown in at least one case that substantial (~ 200 mV) elevation of site reduction potential can be achived by the outer coordination sphere structurally impeding coordination of a "perfectly good" ligand to Cu^{II}.

In cases where we need not have been concerned about installing potentially complicating new axial interactions, we found that azurin's G45 carbonyl presents itself as a now strongly-interacting ligand; so much so that it effects such dramatic structural rearrangement that the Cu^{II} adopts a wholly divergent electronic structure. The C112D/M121X (X = L, F, I, A) azurins present as cases of hard ligand-bound, proteinaceous tetrahedral Cu^{II}. In addition to elevated (~ 300 mV vs NHE) reduction potentials, these proteins also exhibit narrow EPR hyperfine splitting ($A_{||}$ ~ 10 mK) and $g_{\perp}$ anisotropy (R_g ~ 0.8). These features arise not only due to the tetrahedral coordination geometry, but also because of the rack-constrained monodentate coordination of D112.

This coordination constraint imparts functional enhancement on the type zero copper proteins over their type 2 counterpart C112D. A variety of kinetics approaches have been combined to show a substantial decrease in the reorganization energy of the C112D/M121L

azurin compared to C112D. However, the effects on electron transfer of perturbations to electronic coupling between the metal and its ligands have yet to be firmly established.

Nevertheless, protein engineers have now been afforded greater freedom in the design of functional metalloproteins. High-potential copper proteins with efficient electron transfer properties are no longer limited to the domain of the sulfur-containing type 1 proteins. The range of these reduction potentials has yet to be explored – N47 and F114 mutants, whose additive effects on reduction potentials in type 1 proteins have been demonstrated, have not been tested within the type zero framework. Moreover, the possibility exists for the installation of type zero sites into BCPs such as rusticyanin, whose hydrophobicity results in one of the higher potentials of the cupredoxins.

Functional behavior of type zero copper within a metalloenzyme should also be explored. While not yet found in nature, the fact that these cofactors exhibit markedly efficient electron transfer properties obviates any excuse for their exclusion within functional catalytic molecules. The multicopper oxidases immediately exemplify a testbed for this proposition: the mutation of the type 1 site within *E. coli*'s copper efflux oxidase to a type zero site should be straightforward. From there, catalytic behavior may be tested either chemically or electrochemically. With sufficiently high reduction potentials, the type zero site affords the possibility of engineering a multicopper oxidase to perform the reverse reaction; that is, the oxidation of water. Key to this proposition, however, is that catalytic activity will not be compromised by the irreversible oxidation of the type 1 thiolate and the consequent removal of the functional Cu cofactor.

Proteins are molecules rife with subtlety, metalloproteins even more so. Ultimately it will require the identification and parameterization of many interactions within and without the inner coordination sphere such as those described herein before humanity attains the mastery over the elements that we require before we best Nature at her own game. She will continue to roll the dice, but she cannot bend the rules such as we can – and the more rules we learn, the more bending to be done.

APPENDIX 5

Now and again I traded an FPLC for a fume hood. Many of these masquerades as a synthetic inorganic chemist produced little more than colorful waste bottles, however in a few cases interesting molecules emerged. While explorations into iridium dithiolenes and pyridylimidazoles remain in their infancy at this point, James Gerken, Alec Durrell, and Joshua Palmer and I managed to construct a study out of two pyridylimidazole complexes of ruthenium. James is credited with the improved synthesis of 4-pimH, Alec assisted with photophysics, and Joshua ran the electrochemistry. DFT calculations could not have been run without the help of WINKLER, our Linux "cluster." This "review" appeared in 2010 in Volume 254 of *Coordination Chemistry Reviews* and is reproduced here with permission from Elsevier B.V.

Coordination Chemistry Reviews 254 (2010) 1803–1811

Contents lists available at ScienceDirect

Coordination Chemistry Reviews

journal homepage: www.elsevier.com/locate/ccr

Review

Electronic structures, photophysical properties, and electrochemistry of ruthenium(II)$(bpy)_2$ pyridylimidazole complexes

Kyle M. Lancaster[a], James B. Gerken[b], Alec C. Durrell[a], Joshua H. Palmer[a], Harry B. Gray[a,*]

[a] Beckman Institute, California Institute of Technology, 1200 E California Blvd, Pasadena, CA 91125, USA
[b] Department of Chemistry, University of Wisconsin-Madison, Madison, WI 53706, USA

Contents

ARTICLE INFO

Article history:
Received 20 August 2009
Accepted 9 April 2010
Available online 24 April 2010

Keywords:
Ruthenium
Pyridylimidazoles
Photophysics
Cyclic voltammetry

ABSTRACT

The properties of Ru^{II} complexes involving the imidazole moiety are discussed. Complexes $[Ru(bpy)_2(L)]^{2+}$ [bpy = 2,2′-bipyridine, L = 2-(2′-pyridyl)imidazole (2-pimH) and 4-(2′-pyridyl)imidazole (4-pimH)] have been synthesized and fully characterized. Reduction potentials are 0.76 V vs. Fc^+/Fc^0 for both complexes in acetonitrile solution, and the deprotonated complexes undergo irreversible electrochemical oxidation at 0.38 V vs. Fc^+/Fc^0. Density functional theory (DFT) calculations suggest that oxidation of the protonated complexes is primarily metal-based and that of the deprotonated complexes is ligand-centered. The pK_a of the 4-pimH complex was found to be 9.7 ± 0.2; the pK_a of the 2-pimH complex is 7.9 ± 0.2. Luminescence lifetimes (L = 4-pimH, 277 ns; 2-pimH, 224 ns; $4pim^-$, 40 ns; $2pim^-$, 34 ns in 5% methanol/water solution) combined with quantum yield data and acid–base behavior suggest that the non-coordinated imidazole nitrogen tunes deactivation pathways.

1. Introduction

The complexes of ruthenium with bidentate, L_2-type heteroaromatic ligands exhibit rich photochemistry arising mainly from excited state electron-transfer reactions [1–5]. Among the panoply of such ligands, pyridylimidazoles are of interest because complexes of the two isomers, 4-(2′-pyridyl)-imidazole (4-pimH) and 2-(2′-pyridyl)-imidazole (2-pimH) (Fig. 1) should allow further investigation and discussion of the effects of subtle differences in structure on the chemical properties of this molecular family. Moreover, the presence of non-coordinated, ionizable amines opens avenues of investigation into excited state acid–base behavior and proton-coupled electron transfer (PCET).

PimH isomeric differences were first described by Holmes et al. in a series of papers on association constant measurements and calorimetry of the reactions of 2-pimH and 4-pimH with various first-row transition elements [6–8]. These observations showed a general trend of weaker binding by 2-pimH than 4-pimH, with both being less strongly binding than bpy, a trend attributed to decreasing π-acceptor strength [7]. Holmes et al. [9] and Lions et al. [10] also noted an increase in the acidity of the pimH amine proton on complexation to metals, but did not quantify the change in pK_a.

* Corresponding author.
E-mail address: hbgray@caltech.edu (H.B. Gray).

0010-8545/$ – see front matter © 2010 Published by Elsevier B.V.
doi:10.1016/j.ccr.2010.04.005

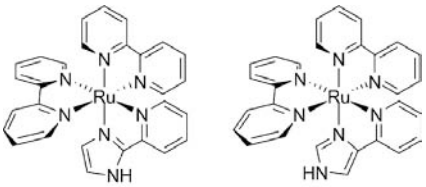

1 2

Fig. 1. Structures of $Ru(bpy)_2$ 2-pimH (**1**) and 4-pimH (**2**) complexes.

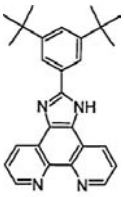

3

Fig. 2. Structure of 2-(3,5-di-*tert*-butylphenyl)imidazo[4,5-*f*]-[1,10]-phenanthroline.

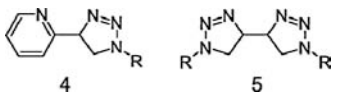

4 5

Fig. 3. Structures of 2′-(1,2,3-triazol-4-yl)pyridine (**3**) and 4,4′-bis(triazole) (**4**).

Later, Boggess and Martin reported a pK_a range of 8–10 for various $[M(2\text{-pimH})_3]^{2+}$ complexes and 13.4 for the free ligand [11]. Herein, we review the literature on Ru-pimH complexes with an emphasis on their photophysics and electrochemistry, and report an extension of Haga's work [12,13] on $[Ru(bpy)_2(2\text{-pimH})]^{2+}$ (**1**) including comparison to the heretofore unreported $[Ru(bpy)_2(4\text{-pimH})]^{2+}$ (**2**).

2. Properties of Ru^{II} complexes with pyridylimidazole and related ligands

Ru(II) complexes of 2-pimH, for which facile ligand syntheses exist, have been more extensively studied than those of 4-pimH. An enantiomerically enriched material was produced by synthesizing the homoleptic complex $[Ru(2\text{-pimH})_3]^{2+}$ [14–17] in the presence of (+)tartrate; its circular dichroism spectrum is similar to that of resolved $[Ru(bpy)_3]^{2+}$ aside from a change in sign indicative of either a reversed Cotton effect or a shift from Δ to Λ as the favored enantiomer [14]. Cooling $[Ru(2\text{-pimH})_3]^{2+}$ to 77 K revealed photoluminescence; Braun et al. attributed its absence at room temperature to rapid ^{3}MLCT (metal to ligand charge transfer) to ^{3}MC (metal-centered) relaxation [15]. Braun observed the $Ru^{III/II}$ couple, however, no electrochemical reduction of $[Ru(2\text{-pimH})_3]^{2+}$ is observable in acetonitrile, which speaks to the high-lying LUMO of the complex [15]. A cathodic shift of the $Ru^{III/II}$ couple by 0.92 V was observed on full deprotonation of this complex [17]. Comparison of this shift with the 0.38 V cathodic shift observed by Haga on deprotonation of $[Ru(bpy)_2(2\text{-pimH})]^{2+}$ led the investigators to conclude that the stabilization of the higher oxidation state in the deprotonated homoleptic complex is mostly of electrostatic origin.

A detailed experimental and theoretical investigation has been reported on the effects of protonation states of a distal, non-coordinated imidazole motif on the electrochemistry and photophysics of $Ru(bpy)_2$(PhenImHPh) [PhenImHPh = 2-(3,5-di-*tert*-butylphenyl)imidazo[4,5-*f*]-[1,10]phenanthroline (**3**), Fig. 2] [18]. The investigators indicate that though the imidazole nitrogen atoms are not directly coordinated to the ruthenium, their protonation states dramatically perturb the excited state lifetimes of the molecule. Moreover, acid–base behavior allowed assignment of excited state localization to either the bpy or PhenImHPh ligands that was supported by theoretical results.

The isomeric complex $[Ru(tpy)(bpy)imidazole]^{2+}$ and some derivatives have been prepared [19]; their reported photophysical properties have not been extensively interpreted but are broadly similar to **1** and **2** (*vide infra*) with differences due to the more extensively conjugated terpyridine ligand. Other monopyridylimidazole Ru complexes have been prepared with η^5-cyclopentadienyl and phosphine [20], η^6-benzene and chloride [21], and bis(β-diketonato) [22] ligands. The $[Ru(2\text{-pimH})(\beta\text{-diketonato})_2]$ complexes display rich hydrogen atom transfer (HAT) chemistry at the free imidazole nitrogen that depends on the electronic nature of the ancillary ligands [22]. The general trends are as expected, with the more electron-withdrawing β-diketonate raising the MLCT energy, oxidation potential, and N–H bond dissociation energy (BDE) of the complex while lowering its pK_a.

The absorption spectra and reduction potentials of $[RuL_3]^{2+}$ complexes featuring 2′-(1,2,3-triazol-4-yl)pyridine (**4**) and 4,4′-bis(triazole) (**5**) ligands (Fig. 3) have recently been reported [23]. The MLCT absorption energies of each complex correlate well with the separation of their first anodic and cathodic reduction potentials; this provides experimental corroboration of the electronic structural picture adopted for Ru polypyridine complexes possessing a largely metal-based HOMO beneath low-lying unoccupied ligand orbitals. Similarly, the properties of $Ru(bpy)_{3-x}L_x^{2+}$ (*vide supra*) ($x = 0$–3) complexes show systematic shifts as the bpy ligands are replaced with less donating 2,2′-bipyrazine and 2,2′-bipyrimidine ligands [24]. The $d\pi \rightarrow \pi^*$ absorptions undergo bathochromic shifting with increasing number of bpy ligands, behavior that is correlated with a decrease in $Ru^{III/II}$ potentials. The optimization of a ruthenium bis-(methylbenzimidazole)pyridine complex for surface-tethered electrocatalytic water oxidation is an elegant demonstration of the application of redox tuning via ligand selection [25].

Despite the electronic tunability afforded by triazole, bipyrimidine, and bipyrazine, this set of ligands has the deficiency of being very weak bases at the distal nitrogen, as is exemplified by the pK_a values of 0.0 and 2.5 for the corresponding $[Ru(NH_3)_5(C_4H_4N_2)]^{3+}$ complexes [26,27]. $[Ru(bpy)_2(bpm)]^{2+}$ and $[Ru(bpy_2)(bpz)]^{2+}$ show excited state pK_a shifts indicative of MLCT states involving the bipyrimidine or bipyrazine [24]; however, sequential protonation of ruthenium bipyrazine complexes requires strongly acidic conditions (>50% H_2SO_4) and leads to quenching of the luminescence [28]. In contrast, free imidazole has a pK_a of 14.2 [29] and its metal complexes are more acidic [30], leading to proton transfers under mild conditions. A similar shift has been observed in 2-pimH complexes [9–11].

Consequently, ruthenium complexes of pimH are of interest as they can undergo both acid–base and redox chemistry, (PCET) [31–33] and other hydrogen-bonding mediated interactions *via* the distal imidazole nitrogen. For example, the HAT kinetics of $Ru^{II}(acac)_2$(2-pimH) have recently been reported [34]. Intriguingly, the self-exchange reaction shows a k_H/k_D of only 1.5 despite a much higher kinetic isotope effect (KIE) of 23 in the reaction with 2,2,6,6-tetramethyl-piperidine-1-oxyl (TEMPO). If the proton source is a hydroxyl rather than an imidazole ligand, as is the case

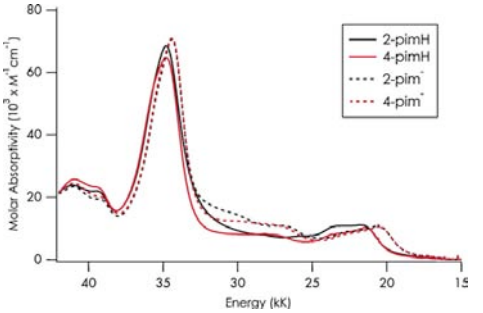

Fig. 4. Absorption spectra of $[Ru(bpy)_2(L)]^{2+}$ and $[Ru(bpy)_2(L–H^+)]^+$ in 5% $MeOH/H_2O$ solution at room temperature.

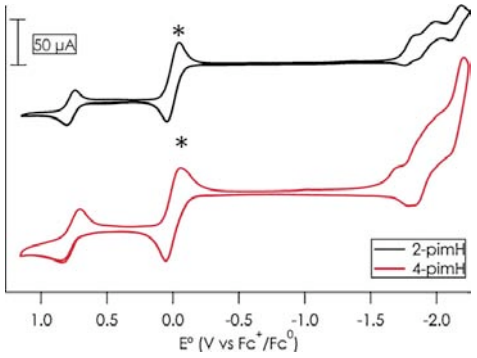

Fig. 5. CVs of 1.5 mM $[Ru(bpy)_2(L)]^{2+}$ in acetonitrile solution at room temperature. Scan rate is 0.1 V/s. Ferrocene was added to sample solutions as an internal standard (Fc^+/Fc^0 wave indicated by an asterisk).

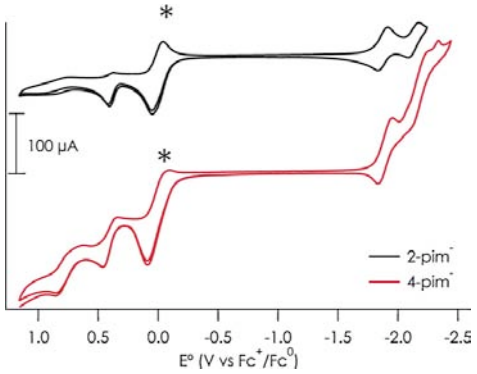

Fig. 6. CVs of 1.5 mM $[Ru(bpy)_2(L^-)]^+$ in acetonitrile solution at room temperature. Deprotonated complexes were generated *in situ* by dropwise addition of concentrated sodium methoxide solution. Scan rate is 0.1 V/s. Ferrocene was added to sample solutions as an internal standard (Fc^+/Fc^0 wave indicated by an asterisk).

for $[Ru^{III}(bpy)_2(py)OH]^{2+}$, the self-exchange rate is similar, and also has a small KIE [35]. This suggests that the imidazole N–H bond in the 2-pimH system behaves similarly to a hydroxyl ligand in some respects. The UV–vis spectrum and electrochemistry of **1** are also sensitive to added heterocyclic bases, with the shifts attributed to hydrogen bonding [13], although PCET could reasonably explain the data. Although pyridyl–benzimidazole complexes are beyond the *sensu stricto* scope of this work, very interesting reactions between the excited state of $[Ru^{II}(bpy)_2(2\text{-pbim}^-)]^+$ (2-pbim$^-$ = 2-(2-pyridyl)benzimidazolate) and quinols with $k_D > k_H$ have been reported [36]. These observations have been explained in the context of PCET theory as arising from coupling of the electronic and proton vibrational states leading to nonadiabatic reactions [37]. In the case of $Ru(bpy)_2$(PhenImHPh), with both imidazole nitrogen atoms available for protonation and hence three protonation states possible, electron transfer in the mono- and deprotonated states is primarily from the extensively conjugated imidazole-bearing ligand [18].

Despite the abundance of studies involving 2-pimH, there is almost no discussion of 4-pimH, particularly with respect to photophysics and PCET. We attribute this absence to relative synthetic accessibility (the 2-pimH ligand is readily synthesized *via* a modification of the procedure of Radziszewski [38,39]). While many routes to the acquisition of the 4-pimH ligand have been developed since its initial synthesis [40], we chose to modify the method of Wang and Schwabacher [41] in order to more easily isolate the ligand as the dihydrochloride salt. Pyridylimidazoles in hand, ligand exchange with $Ru(bpy)_2Cl_2$ [42] to form **1** and **2** was accomplished using methods typical for $[Ru(bpy)_2L]^{2+}$ complexes, with isolation effected by precipitation of the PF_6^- salts.

3. Absorption spectra

Spectra of $Ru(bpy)_2(L)$ (L = 2-pimH, 4-pimH) were recorded in dichloromethane (Fig. 3, Table 1) and 5% methanol/water (Fig. 4) solutions. The lowest energy band of **2**, attributable to MLCT, is slightly (~0.15 kK) red shifted relative to that of **1**. A more substantial difference in both energy and intensity is exhibited in the next higher-energy MLCT band (23.47, **1**; 23.70 kK, **2**). Interestingly, these ~20 kK MLCT systems appear to merge upon deprotonation of the complexes, suggesting that either the deprotonated pyridylimidazoles are isoelectronic donors, or that ligand energy levels are reordered such that these low-lying MLCT systems become largely bipyridyl-based. Scant changes are observed upon transfer of the complexes to a nonpolar solvent.

4. Redox properties

Cyclic voltammograms (CVs) for **1** and **2** were recorded in acetonitrile solution (Fig. 5). Each complex displays one reversible wave at 0.76 V vs. Fc^+/Fc^0, corresponding to the $Ru^{III/II}$ redox couple. Separation between the anodic and cathodic current peaks for this process is similar (~0.08 V) to that of the Fc^+/Fc^0 wave, supporting the assignment of this feature to a one-electron redox process. Two waves observed at highly negative potentials are attributable to ligand-centered reduction and are analogous to the behavior observed for $[Ru(bpy)_3]^{2+}$ [24]. Precise assignment of the redox loci are not straightforward as in the case of $[Ru(bpy)_2(bpx)]^2$ (bpx = 2,2′-bipyridmidine, 2,2′-bipyrazine).

A concentrated solution of sodium methoxide was added dropwise to electrolyte-containing acetonitrile solutions of each complex with CVs recorded between additions (Fig. 6). Disappearance of the $Ru^{III/II}$ couple in the protonated complexes tracks with appearance of a new, irreversible oxidation wave cathodically shifted to 0.38 V vs. Fc^+/Fc^0. The electrochemical behavior as well as the results of our DFT calculations (*vide infra*) indicate that this new

Table 1
Electronic absorption[a] features of $Ru(bpy)_2(L)^{2+}$.

L	5% MeOH/H_2O pH 3 ν_{max} ($\varepsilon \times 10^{-3}$ M^{-1} cm^{-1})	5% MeOH/H_2O pH 12 ν_{max} ($\varepsilon \times 10^{-3}$ M^{-1} cm^{-1})	Dichloromethane ν_{max} ($\varepsilon \times 10^{-3}$ M^{-1} cm^{-1})
(2-pimH)	23.47 (10.5), 21.51 (11.0)	22.83 (8.00), 20.49 (10.70)	23.47 (10.60), 21.51 (12.10)
(4-pimH)	27.40 (8.30), 23.70 (7.80), 21.37 (10.20)	26.88 (9.80), 22.94 (7.00), 20.41 (10.20)	27.40 (8.80), 23.53 (8.00), 21.37 (10.90)

[a] Absorption energies are reported in kilokaisers. Uncertainties in band positions are ±0.05 kK. Extinction coefficients are correct to within 5% based on triplicate analysis.

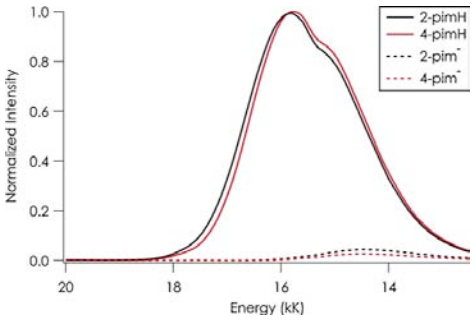

Fig. 7. Emission spectra of 10 μM $[Ru(bpy)_2(L)]^{2+}$ and $[Ru(bpy)_2(L)]^{+}$ (dotted lines) in degassed 5% methanol/water solution at room temperature. Excitation at 21.28 kK (21.05 kK long-pass filter). Spectral intensity corrected by λ^2_{nm} following conversion to energy units.

wave arises not from cathodic shifting of the $Ru^{III/II}$ potential but rather from a redox process occurring on the deprotonated pim^- ligand.

5. Excited state properties

Emission spectra in aqueous solution were obtained by 21.28 kK excitation of each of the 4 complexes (Fig. 7, Table 2). The protonated complexes exhibit intense emissions that upon deprotonation are red-shifted by ~1.3 kK and quenched 12-fold in **1** and 8-fold in **2**. The band shapes and positions of the protonated states of the complexes are slightly different, likely owing to differences in excited state structural perturbations. Energy differences between the $E_{0,0}$ and ν_{max} of the protonated complexes are not quantifiable within experimental error. Red-shifted emission spectra of the deprotonated complexes are likely attributable to increased π donation from the more electron-rich pim^- ligands. These shifts have been investigated by DFT calculations (*vide infra*).

Emission spectra also were recorded in deuterated solvent. In 5% CD_3OD/D_2O, the dedeuterated forms of **1** and **2** are quenched 14- and 13-fold relative to the deuterated complexes. Interestingly, both deuterated and dedeuterated states of **2** emit more strongly than those of **1**, suggesting a role for solvent and/or vibrational quenching of the complexes, likely at the distal amine the 4-pimH ligand.

Luminescence lifetime measurements were performed to probe the role of the non-coordinating imidazole nitrogen in deactivating the excited complexes (Table 3). In addition to decreased emission intensity, the lifetimes are considerably reduced upon deprotonation. While this behavior could be a consequence of the energy-gap law [43], we posit that it arises due to a change in character of the emissive state from ^{3}MLCT to ^{3}LLCT (*vide infra*). In protic solvent, **1** and **2** exhibit 7-fold increased emission decay rates upon deprotonation to $\mathbf{1}^-$ and $\mathbf{2}^-$. In deuterated solvent the lifetimes of both **1** and **2** increase in both protonation/deuteration states. Complex **2** exhibits longer lifetimes than **1** in all cases and presents a larger isotope effect (1.8 vs. 1.4). The observed isotope effects suggest that some combination of solvent hydrogen-bonding effects and N–H/D stretching contribute to excited state deactivation in these systems.

Table 2
Steady-state emission features[a] of $[Ru(bpy)_2(L)]^{2+}$.

L	5% MeOH:H_2O ν_{max} pH 3 (Φ_{em})	5% MeOH:H_2O ν_{max} pH 12 (Φ_{em})
2-pimH	15.82 (0.008)	14.49 (0.0003)
4-pimH	15.77 (0.013)	14.49 (0.0003)

[a] Emission energies are reported in kilokaisers. Quantum yields of emission (Φ_{em}) were calculated using $Ru(bpy)_3Cl_2$ as a standard.

Table 3
$[Ru(bpy)_2(L)]^{2+}$ luminescence lifetimes.[a].

Solvent	Lifetime (ns)			
	2-pimH	2-pim^-	4-pimH	4-pim^-
5% MeOH/H_2O	224	34	277	40
5% MeOD/D_2O	305	63	502	78

[a] Excitation at 21.46 kK (10 ns, pulsed Nd:YAG laser), emission detected at 15.38 kK, (protonated complexes) and 14.08 kK (deprotonated complexes), sample concentrations 10 μM, pH 3 for protonated and pH 12 for deprotonated complexes.

Radiative (k_r) and non-radiative (k_{nr}) rate constants for the protonated complexes in aqueous solutions were calculated from Eqs. (1) and (2):

$$\Phi = \varphi_{isc}\frac{k_r}{k_r + k_{nr}} = \varphi_{isc}k_r\tau_m \quad (1)$$

$$k_{nr} = \frac{1}{\tau_m} - k_r \quad (2)$$

where τ_m is the measured lifetime and φ_{isc} is the efficiency of intersystem crossing. Assuming $\varphi_{isc} = 1$ (all observed emission is phosphorescence), rate constants are: **1**, $k_r = 3.6 \times 10^4$ s^{-1}, $k_{nr} = 4.4 \times 10^6$ s^{-1}; **2**, $k_r = 4.7 \times 10^4$ s^{-1}, $k_{nr} = 3.6 \times 10^6$ s^{-1}. The faster non-radiative decay and decreased solvent isotope effect of **1** suggests a role for pimH-based non-radiative states that are populated with differing efficiencies between the two isomers. There is a similarity of this behavior to the divergent solvent isotope effects on the lifetimes of $[Ru(bpy)_3]^{2+}$ and $[Ru(phen)_3]^{2+}$ observed by Sriram and Hoffman [44], which were attributed to decay by differing relative amounts of non-radiative relaxation and upconversion to the triplet ligand field state. By analogy, quenching by upconversion appears to be more important relative to non-radiative relaxation in **1** than in $\mathbf{1}^-$, **2**, or $\mathbf{2}^-$.

6. Acid–base behavior

UV/vis monitored pH titrations reveal that **1** and **2** have strikingly differing acidities (pK_a of 7.9 ± 0.2 for **1**, 9.7 ± 0.2 for **2**). Spectroscopic and electrochemical parameters being approximately equal between the complexes, we suggest that the increased distance (calculated 4.14 Å for **1**, 4.27 Å for **2**, *vide infra*) between the acidic amine and the metal center of **2** is largely responsible for the decreased acidity of the molecule. Excited state pK_a values were approximated through use of the Förster cycle (**3**) [45], rather than the method of Sun and Hoffman [46], which requires pK_a measurements of the ground state of an oxidation state that mimics the

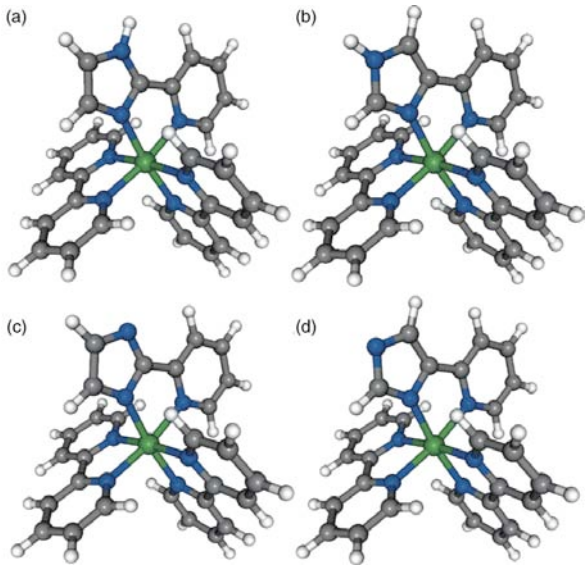

Fig. 8. Optimized gas-phase molecular structures of (a) **1**, (b) **2**, (c) $\mathbf{1}^-$, and (d) $\mathbf{2}^-$.

charge distribution of the excited state.

$$\Delta pK_a = pK_a - pK_a^* = \frac{E_{HA} - E_{A^-}}{2.3RT} \quad (3)$$

E_{HA} and E_{A^-} are the excited to ground state energy gaps ($E_{0,0}$) of the protonated and deprotonated complexes, respectively. R is the gas constant and T is the temperature (Kelvin). Estimation of $E_{0,0}$ as the initial rise of emission intensity results in approximately equivalent (~0.4 pK_a units) shifts towards greater acidity upon excitation. The photoacidic shift indicates that the long-lived emissive states of the molecules are bpy-rather than pimH-^{3}MLCT states. Population of pimH-based excited states, on the other hand, would transfer electron density to the non-coordinated amine, resulting in photobasicity, as observed with bipyrimidine and bipyrazine ligands (Table 4) [24,28,46]. These shifts in pK_a are substantial relative to the minor shifts in the case of **1** and **2**, as rather than tuning the acid–base properties by a coulombic interaction between the formally Ru^{III} and the imidazole, electron density is directly contributed to the ionizable nitrogen that stabilizes protonation. Similar behavior has been observed in the case of the non-coordinated imidazole in $Ru(bpy)_2$(PhenImHPh) [18].

7. Theory

The application of DFT and time-dependent DFT (TDDFT) to the electronic structures of ground and excited states of transition metal complexes has been demonstrated as a valuable complement to experiment [50,51]. In the present case, calculations were performed using ORCA [52]. Molecular geometries were optimized in the gas phase (Fig. 8), with electronic structures subsequently calculated at these stationary points. The highest-occupied molecular orbital (HOMO) for both protonated molecules consists of a predominantly (~80% by Löwdin population analysis) Ru $4d_{z2}$ metal-centered (MC) orbital. The lowest unoccupied molecular orbital (LUMO) is a ligand-centered (LC) π^* orbital delocalized primarily over both bpy ligands. The computed gas-phase HOMO–LUMO gap calculated is 3.42 eV for both molecules. Modeling of solvation by water with COSMO [53] results in minor alterations to the electronic structures (Fig. 9). The HOMO–LUMO gaps shrink to 3.35 eV. pimH-based MOs exhibit the greatest perturbation upon inclusion of solvation into the calculations. There are minimal effects from solvation on the calculated molecular structures, as has been observed previously in calculations of the electronic structures of Ru(II) polyimine complexes [51].

Deprotonation leads to dramatic perturbation of the calculated ground-state electronic structure. The gas-phase HOMO–LUMO gaps shrink to 2.45 eV (**1**) and 2.61 eV (**2**). The HOMO of each molecule becomes a largely pim$^-$-based M–L delocalized orbital. Thus, a ligand-centered redox locus may be implicated in the CVs of the deprotonated complexes (*vide supra*). The LUMO remains a bpy-centered ligand state, though with quite asymmetric population between the two bpy ligands. The metal-centered orbitals of $\mathbf{1}^-$ display larger energy gaps than those of $\mathbf{2}^-$, presumably owing to a stronger ligand field due to closer proximity of the distal $N^{\delta-}$ (calculated 4.16 Å for $\mathbf{1}^-$ vs. 4.31 Å for $\mathbf{2}^-$). The effect of COSMO modeled solvation is far more dramatic on the MO energies of the deprotonated complexes, likely due to charge localization on the deprotonated imidazole (Fig. 10). The HOMO–LUMO gaps increase to 3.01 eV (**1**) and 3.10 eV (**2**). This increase arises from greater

Table 4
Ruthenium diimine complex ground and excited state acidities.

Compound	pK_a	pK_a^*	Reference
1	7.9	7.5	This work
2	9.7	9.3	This work
$Ru(bpy)(bpz)_2^{2+}$	−0.72	3.5	[47]
$Ru(bpy)_2(bpm)^{2+}$	−2.9	1.95	[48]
$Ru(bpz)_3^{2+}$	−2.2	2.0	[28]
$Ru(bpm)_3^{2+}$	−1.0	2.2	[49]

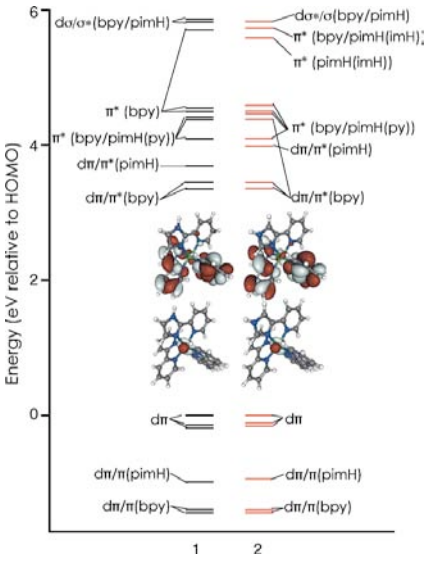

Fig. 9. Energy diagram for complexes **1** and **2** in solution (water, COSMO) with orbitals plotted on a scale normalized to the HOMO. Frontier orbital pictures are displayed.

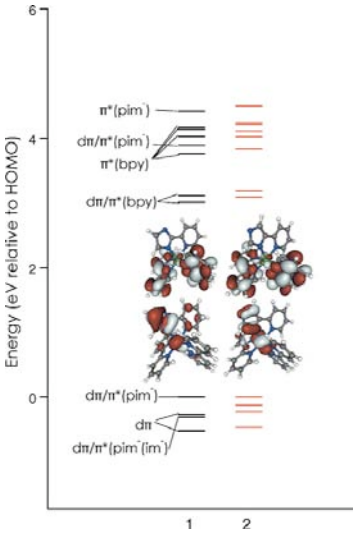

Fig. 10. Energy diagram of complexes $\mathbf{1}^-$ and $\mathbf{2}^-$ in solution (water, COSMO) with orbitals plotted on a scale normalized to the HOMO. Frontier orbital pictures are displayed.

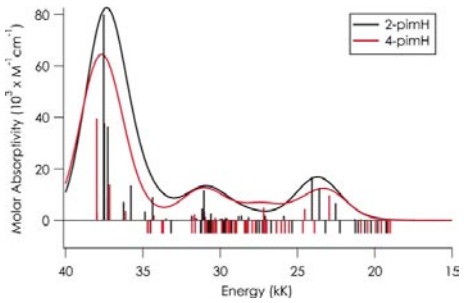

Fig. 11. TDDFT-calculated absorption spectrum of $Ru(bpy)_2L^{2+}$. Triplet excitations are plotted along the negative *y*-axis with arbitrary normalized intensity.

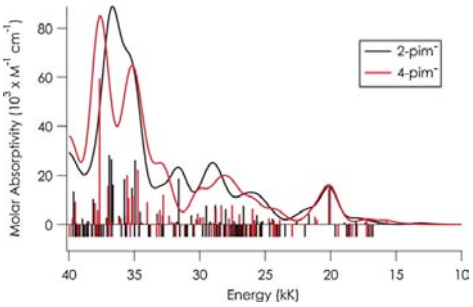

Fig. 12. TDDFT-calculated absorption spectrum of $Ru(bpy)_2L^{+}$ complexes. Triplet excitations are plotted along the negative *y*-axis with arbitrary normalized intensity.

destabilization of the LUMO relative to the HOMO upon inclusion of solvation.

From the optimized structures, TDDFT calculations were performed incorporating the COSMO solvation model with water chosen as the solvent (Fig. 11, Table 5). For simplicity, only singlet transitions were included in the spectra as triplet excitations can be expected to be minor contributors to the absorption spectra. Singlet energies and intensities accord with experiment. The calculations suggest that the broad absorption spectra are attributable to large numbers of ^{1}MLCT and ^{1}LLCT excited states. The spectrum of **1** arises from multi-component transitions; notably, many low-energy singlet and triplet excitations include contributions that are pimH-localized. Transitions in the spectrum of **1** arising purely from promotions to pimH-centered ^{1}LC states are conspicuously absent. However, pure pimH transitions are predicted for **2**; notably this transition gives rise to the intense absorption band at ~27 kK that is absent in the spectrum of **1**. Thus we suggest that the greater energy separations between pimH-based LC excited states and bpy-based LC excited states disfavor internal conversion to and subsequent pimH NH-based excited state deactivation of **2**, resulting in its longer emission lifetime.

The theoretical spectra of the deprotonated complexes are also in accord with experiment (Fig. 12). Almost double the number of singlet excited states are predicted between the intense, low energy 20 kK MLCT and the 40 kK LLCT system. As differences between excited state lifetimes measured for the deprotonated complexes are near the level of instrumental error, we have not made a thorough analysis of their calculated spectra in order to explain their relative photophysical properties.

Table 5
TDDFT-calculated singlet transitions for **1** and **2**.

1			
Transition energy[a]	Oscillator strength	Transition class[b]	Dominant transition orbitals
22.54	0.047	MLCT	dπ-bpy(π*), dπ-pimH(π*)
23.59	0.087	MLCT	dπ-bpy(π*), dπ-pimH(π*)
24.06	0.116	MLCT	dπ-bpy(π*), dπ-pimH(π*)
31.05	0.081	MLCT	dπ-bpy(π*)
34.37	0.063	LLCT	bpy(π)-pimH(π*), pimH(π)-pimH(π*)
35.77	0.094	LLCT	bpy(π)-pimH(π*), pimH(π)-pimH(π*)
37.54	0.553	LLCT	pimH(π)-bpy(π*), bpy(π)-bpy(π*)
2			
22.95	0.135	MLCT	dπ-bpy(π*)
24.53	0.060	MLCT	dπ-bpy(π*)
27.19	0.067	MLCT	dπ-pimH(π*)
31.03	0.048	MLCT	dπ-bpy/pimH(π*)
31.08	0.037	MLCT	dπ-bpy(π*)
37.99	0.548	LLCT	bpy(π)-pimH(π*), bpy(π)-bpy(π*)

[a] Transition energies in kK.
[b] Transitions are assigned in either the strict MLCT or LLCT limits; in many cases there is some orbital contribution from the metals that would technically classify the transitions as metal to metal/ligand charge transfers (MMLCT).

The lowest-lying triplet excited states of the protonated complexes accord with experiment; they are calculated as 19.16 kK for **1** and 19.00 kK for **2**. These excited states are entirely Ru 4d to bpy ^{3}MLCT in nature, consistent with the observed acid–base behavior. The lowest-lying triplet excited states of the deprotonated complexes also agree with experiment; these are calculated as 16.79 kK for $\mathbf{1}^-$ and 16.94 kK for $\mathbf{2}^-$. In this case the excited states are pimH to bpy ^{3}LLCT. Thus the energy-gap law cannot be applied as an explanation for the dramatically reduced quantum yields of the deprotonated complexes [54]. Rather, we suggest some combination of poor electronic coupling between the bpy and pimH ligands and efficient non-radiative deactivation by distal N^--solvent interactions as factors contributing to the weak emission.

8. Conclusions

The separations between the anodic and first cathodic electrochemical waves of **1** and **2** in both protonation states correlate with the lowest energy electronic absorption observed in each spectrum, as predicted by theory for redox processes with minimal reorganization [55]. The emission energies correlate with redox properties observed for other Ru-diimine complexes [15]. However, the observed photoacidity of Ru-pimH contrasts with the photobasicity observed for Ru(bpz) and Ru(bpm) by Meyer [24], Lever [28], and Hoffman [46], supporting the conclusion that the ^{3}MLCT excited states of 1 and 2 are bpy-centered. Complexes **1** and **2** display divergent acid–base and photophysical behaviors despite being largely indistinguishable spectroscopically and electrochemically. The former is attributable to the relative position of the acidic proton relative to the metal center and hence the electron localization in the ring [24]. The latter has been shown by DFT including TDDFT to arise from variable mixing of pimH-based MOs into singlet and triplet excited states, likely leading to the enhanced non-radiative decay observed for **1**. Due to the more sterically accessible N–H of 4-pimH relative to its well-studied isomer, along with the slower non-radiative relaxation of its ruthenium complexes, we suggest that molecules based on those reported herein could find potential use in studies of proton transfer and proton-coupled electron transfer. Tuning of photoacidities through substitutions on the bpy and pimH rings should be a straightforward means to synthesize a collection of Ru(II)-based photoacids.

9. Syntheses

All reagents were obtained from Sigma–Aldrich and used without further purification. Solvents for electronic absorption and emission measurements were of spectroscopic grade. $Ru(bpy)_2Cl_2$ (**6**) was prepared according to a published procedure [42].

2-(2′-pyridiyl)imidazole (2-pimH) (**7**) was prepared according to a published procedures [39].

4-tosyl-5-(2-pyridyl)oxazoline (8): Tosylmethyl isocyanide (0.975 g) was suspended in absolute ethanol. Pyridine-2-carboxaldehyde (0.5 mL) was added with stirring. Freshly crushed sodium cyanide (0.026 g) was added and the mixture was allowed to stir for 30 min. The product was filtered and washed with 20 mL of 1:1 ethyl ether:hexanes. The product was allowed to air-dry to give 1.219 g of an odorless tan powder, m.p. 121–124 °C. The proton NMR spectrum (300 MHz, $CDCl_3$, TMS reference) gave peaks at 2.458 ppm (s, 3H), 5.590 ppm (dd, 5.77, 1.65 Hz, 1H), 6.072 ppm (d, 5.63 Hz, 1H), 7.160 ppm (dd, 1.65, 0.41 Hz, 1H), 7.295 ppm (dd, 4.81, 1.24 Hz, 1H), 7.321 ppm (dd, 4.81, 1.09 Hz, 1H), 7.385 ppm (dd, 8.51, 0.69 Hz, 2H), 7.450 ppm (dm, 7.83 Hz, 1H), 7.759 ppm (td, 7.83, 1.79 Hz, 1H), 7.880 ppm (dm, 8.24 Hz, 2H), 8.645 ppm (ddd, 4.81, 1.65, 0.83 Hz, 1H). The proton decoupled ^{13}C NMR spectrum (75 MHz, $CDCl_3$, TMS reference) gave peaks at 22.001, 79.617, 90.559, 122.346, 124,346, 129.787, 130.080, 133.582, 137.445, 145.802, 150.479, 155.571, and 159.182 ppm.

4-(2′-pyridyl)imidazole (9): 8 (1.210 g) was dissolved in a resealable pressure tube with 40 mL of anhydrous ammonia-saturated methanol. The mixture was heated to 90–110 °C for 18 h and allowed to cool to room temperature. The solvent was removed by rotary evaporation and the remaining material was purified by chromatography on silica gel in 9:1 methylene chloride:hexanes to give 0.330 g of a dark brown oil with an odor of burnt butter. The oil was dissolved in isopropyl alcohol, acidified with hydrochloric acid, and precipitated as the dihydrochloride salt with acetone. The proton NMR spectrum (600 MHz, CD_3OD, solvent reference) gave peaks at 7.228 ppm (ddd, 7.37, 6.62, 1.72 Hz, 1H), 7.690 ppm (s, 1H), 7.784 ppm (d, 1.06 Hz, 1H), 7.807 ppm (td, 6.47, 0.89 Hz, 1H), 7.864 ppm (br d, 7.37 Hz, 1H), 8.472 ppm (br d, 6.32 Hz, 1H). The proton decoupled ^{13}C NMR spectrum (150 MHz, CD_3OD, solvent reference) gave peaks at 120.815, 123.205, 123.257, 137.759, 137.840, 150.026, 150.121, and 166.237 ppm.

$[Ru(bpy)_2(2\text{-pimH})](PF_6)_2$ (1): 0.520 g of **7** was combined with 0.145 g **4** and 0.040 g LiCl in 80 mL of a 3:1 absolute ethanol:water

mixture and heated at reflux for 4 h. A few drops of 37% HCl were added to effect complete isolation as the protonated complex. Ethanol was removed by rotary evaporation. 0.736 g of KPF_6 dissolved in a minimal amount of water was added to the red-orange solution to separate a dark red powder. The solid was filtered in a medium porosity frit and washed 3× each with 25 mL of water and 25 mL ethyl ether. The solid was dried by suction. The proton NMR spectrum (600 MHz, CD_2Cl_2, solvent reference) gave peaks at 6.471 ppm (s, 1H), 7.304 ppm (t, 7.20 Hz, 1H), 7.380 ppm (t, 7.20 Hz, 1H), 7.465 ppm (m, 4H), 7.539 ppm (d, 5.40 Hz, 1H), 7.724 ppm (d, 6.00 Hz, 1H), 7.793 ppm (d, 5.40 Hz, 2H), 7.839 ppm (d, 5.40 Hz, 1H), 8.007 ppm (dd, 8.4 Hz, 7.8 Hz, 2H), 8.050 ppm (t, 7.20 Hz, 3H), 8.270 ppm (d, 7.80 Hz, 1H), 8.367 ppm (t, 7.20 Hz, 2H), 8.414 ppm (t, 7.20 Hz 2H), 11.780 ppm (br, s, 1H). ESI MS m/z (calc) = 558.6 for $C_{28}H_{23}N_7Ru$; m/z (obs) = 558.3. Elemental analysis (single) (calc) C = 39.6, H = 2.70, N = 11.5, Ru = 11.91; (found) C = 39.86, H = 2.90, N = 11.52, Ru = 11.8.

$[Ru(bpy)_2(4\text{-}pimH)](PF_6)_2 \cdot H_2O$ (2): Preparation of **2** proceeded the same as **1** using **9** as the ligand, though the material required additional purification. The red solid isolated following filtration of the PF_6 workup was applied to a silica gel column, washed with **1** column volume each of acetone, acetone containing 10% of a 10% saturated KNO_3 solution, and finally eluted with acetone containing 40% of a 10% saturated KNO_3 solution. Acetone was stripped by rotary evaporation from the pool of **2**, KPF_6 was added to crash out product. This material was collected on a fine porosity fritted glass funnel and washed with water and ether. The proton NMR spectrum (600 MHz, CD_2Cl_2, solvent reference) gave peaks at 7.205 ppm (t, 6.32 Hz, 1H), 7.275 ppm (s, 1H), 7.350 ppm (t, 6.53 Hz, 1H), 7.460 ppm (m, 3H), 7.493 ppm (t, 6.51 Hz, 1H), 7.707 ppm (d, 5.54 Hz, 1H), 7.804 ppm (d, 5.30 Hz, 1H), 7.876 ppm (m, 2H), 7.920 ppm (d, 7.87 Hz, 1H) 7.955 ppm (br s, 2H), 7.997 ppm (t, 7.82 Hz, 1H), 8.050 ppm (m, 3H), 8.345 ppm (d, 8.16 Hz, 1H), 8.375 ppm (d, 8.17 Hz, 1H), 8.415 ppm (d, 7.85 Hz, 2H), 11.192 ppm (br s, 1H). ESI MS m/z (calc) = 558.6 for $C_{28}H_{23}N_7Ru$; m/z (obs) = 558.3. Elemental analysis (single) (calc) C = 39.6, H = 2.70, N = 11.5, Ru = 11.91, loss on drying (H_2O) 2.07%; (found) C = 40.0, H = 3.04, N = 11.2, Ru = 11.77, loss on drying (H_2O) 2.07%.

10. Spectroscopic methods

Absorption spectra were recorded on a Hewlett Packard HP8453 diode array spectrophotometer. Samples for emission studies were prepared by 10× cycles of pump-purge with dry argon. Steady state emission spectra were recorded on a Jobin Yvon Spex Fluorolog-3-11. Sample excitation was achieved via a xenon arc lamp with a single monochromator providing wavelength selection. Right angle light emission was sorted using a single monochromator and fed into a Hammamatsu R928P photomultiplier tube with photon counting. Signal from scattered light was minimized using short and long pass filters where appropriate. Time-resolved measurements were conducted at the Beckman Institute Laser Resource Center. Laser excitation was achieved using 8 ns pulses at 355 nm from a Spectra-Physics Quanta-Ray Q-switched Nd:YAG laser (3rd harmonic) operating at 10 Hz to pump an optical parametric oscillator (OPO Spectra-Physics Quata-Ray MOPO-700) which was used to achieve laser pulses at 466 nm. Luminescence decays were detected using a Hamamatsu R928 PMT and recorded on a Tektronix model TDS-620A oscilloscope.

11. Electrochemical methods

CVs were measured using an edge-plane pyrolytic graphite electrode as the working electrode, platinum coil as the counter electrode, and a silver wire as a quasi-reference electrode. Ferrocene was added as an internal standard. Measurements were conducted under an argon atmosphere on 1 mM acetonitrile solutions containing 0.1 M tetrabutylammonium hexafluorophosphate as a supporting electrolyte. Measurements were made with a Model 660 Electrochemical Workstation (CH-Instrument, Austin).

12. Computational methods

DFT calculations including TDDFT were performed using the ORCA computational chemistry package [52]. Geometries were optimized for gas-phase molecules using the B3LYP hybrid functional with def2-TZV(P) [56] basis set. Relativistic effects were included using a zeroth-order approximation (ZORA) [57]. For TDDFT calculations, the conductor-like screening model (COSMO) [49] was included using dielectric parameters for water. For all calculations the RIJCOSX approximation [58–60] was employed with standard integration grids. Calculated absorption spectra were produced by summation of 3 kK full width at half maximum gaussians centered on the stick spectra with intensities proportional to oscillator strengths.

Acknowledgements

We thank Jay Winkler and Theis Brock-Nannestad for discussions. We thank Tony Vlček for a critical reading of this manuscript. We also thank John D. Roberts and Brian Stoltz for the kind loan of reagents and equipment. This work was supported by the NSF Center for Chemical Innovation (Powering the Planet, CHE-0802907 and CHE-0947829), the Arnold and Mabel Beckman Foundation, and CCSER (Gordon and Betty Moore Foundation).

References

[1] A.A. Vlček Jr., Coord. Chem. Rev. 200–202 (2000) 933.
[2] C.R. Bock, T.J. Meyer, D.G. Whitten, J. Am. Chem. Soc. 96 (1974) 4710.
[3] C. Creutz, N. Sutin, Inorg. Chem. 15 (1976) 496.
[4] O. Johansen, A. Launikonis, A.W.H. Mau, Aust. J. Chem. 33 (1980) 1643.
[5] J.J. Concepcion, J.W. Jurss, M.K. Brennaman, P.G. Hoertz, A.O.T. Patrocinio, N.Y.M. Iha, J.L. Templeton, T.J. Meyer, Acc. Chem. Res. 42 (2009) 1954.
[6] W.J. Eilbeck, F. Holmes, G.G. Phillips, A.E. Underhill, J. Chem. Soc. A (1967) 1161.
[7] W.J. Eilbeck, F. Holmes, J. Chem. Soc. A (1967) 1777.
[8] W.J. Eilbeck, F. Holmes, G. Phillips, J. Chem. Soc. A (1970) 689.
[9] F. Holmes, K.M. Jones, E.G. Torrible, J. Chem. Soc. (1961) 4790.
[10] B. Chiswell, F. Lions, B.S. Morris, Inorg. Chem. 3 (1964) 110.
[11] R.K. Boggess, R.B. Martin, Inorg. Chem. 13 (1974) 1525.
[12] M. Haga, Inorg. Chim. Acta 75 (1983) 29.
[13] M. Haga, A. Tsunemitsu, Inorg. Chim. Acta 164 (1989) 137.
[14] J.G.D.M. Atton, R.D. Gillard, Transition Met. Chem. 6 (1981) 351.
[15] G. Orellana, M.L. Quiroga, A.M. Braun, Helv. Chim. Acta 70 (1987) 2073.
[16] G. Orellana, C. Alvarez-Ibarra, M.L. Quiroga, Bull. Soc. Chim. Belg. 97 (1988) 731.
[17] G. Stupka, L. Gremaud, A.E. Williams, Helv. Chim. Acta 88 (2005) 487.
[18] A. Quaranta, F. Lachaud, C. Herrero, R. Guillot, M.-F. Charlot, W. Leibl, A. Aukauloo, Chem. Eur. J. 13 (2007) 8201.
[19] X.-J. Yang, F. Drepper, B. Wu, W.-H. Sun, W. Haehnel, C. Janiak, Dalton Trans. (2005) 256.
[20] K. Pachhunga, B. Therrien, K.A. Kreisel, G.P.A. Yap, M.R. Kollipara, Polyhedron 26 (2007) 3638.
[21] H. Mishra, R.J. Mukherjee, Organomet. Chem. 691 (2006) 3545.
[22] A. Wu, J. Masland, R.D. Swartz, W. Kaminsky, J.M. Mayer, Inorg. Chem. 46 (2007) 11190.
[23] J.T. Fletcher, B.J. Bumgarner, N.D. Engels, D.A. Skoglund, Organometallics 27 (2008) 5430.
[24] D.P. Rillema, G. Allen, T.J. Meyer, D. Conrad, Inorg. Chem. 22 (1983) 1617.
[25] Z. Chen, J.J. Concepcion, J.W. Jurss, T.J. Meyer, J. Am. Chem. Soc. 131 (2009) 15580.
[26] P. Ford, de F.P. Rudd, R. Gaunder, H. Taube, J. Am. Chem. Soc. 90 (1968) 1187.
[27] A. Albert, P.J. Taylor, J. Chem. Soc. Perkin Trans. II (1989) 1903.
[28] R.J. Crutchley, N. Kress, A.B.P. Lever, J. Am. Chem. Soc. 105 (1983) 1170.
[29] G. Yagil, Tetrahedron 23 (1967) 2855.
[30] P.J. Morris, R.B. Martin, J. Am. Chem. Soc. 92 (1970) 1543.
[31] M.H.V. Huynh, T.J. Meyer, Chem. Rev. 107 (2007) 5004.
[32] J.M. Mayer, Annu. Rev. Phys. Chem. 55 (2004) 363.
[33] J. Rosenthal, D.G. Nocera, Acc. Chem. Res. 40 (2007) 543.
[34] A. Wu, J.M. Mayer, J. Am. Chem. Soc. 130 (2008) 14745.
[35] J.R. Bryant, J.M. Mayer, J. Am. Chem. Soc. 125 (2003) 10351.
[36] J.L. Cape, M.K. Bowman, D.M. Kramer, J. Am. Chem. Soc. 127 (2005) 4208.

[37] M.K. Ludlow, A.V. Soudackov, S. Hammes-Schiffer, J. Am. Chem. Soc. 131 (2009) 7094.
[38] B. Radziszewski, Chem. Ber. 15 (1882) 2706.
[39] T.I.A. Gerber, E. Hosten, P. Mayer, Z.R. Tshentu, J. Coord. Chem. 59 (2006) 243.
[40] G.R. Clemo, T. Holmes, G.C. Leith, J. Chem. Soc. (1938) 753.
[41] F. Wang, A.W. Schwabacher, Tetrahedron Lett. 40 (1999) 4779.
[42] B.P. Sullivan, D.J. Salmon, T.J. Meyer, Inorg. Chem. 17 (1978) 3334.
[43] J.R. Lakowicz, Principles of Fluorescence Spectroscopy, 3rd ed., Springer, New York, 2006.
[44] R. Sriram, M.Z. Hoffman, Chem. Phys. Lett. 85 (1982) 572.
[45] T.H. Förster, Z. Electrochem. 54 (1950) 42.
[46] H. Sun, M.Z. Hoffman, J. Phys. Chem. 97 (1993) 5014.
[47] K.A. Goldsby, T.J. Meyer, Inorg. Chem. 23 (1984) 3002.
[48] Md.K. Nazeeruddin, K. Kalyanasundaram, Inorg. Chem. 28 (1989) 4251.
[49] M. Hunziker, A. Ludi, J. Am. Chem. Soc. 99 (1977) 7370.
[50] A.A. Vlček Jr., S. Zális, Coord. Chem. Rev. 251 (2007) 258.
[51] E. Jakubikova, W. Chen, D.M. Dattelbaum, F.N. Rein, R.C. Rocha, R.L. Martin, E.R. Batista, Inorg. Chem. 48 (2009) 10720.
[52] F. Neese, U. Becker, D. Ganyushin, A. Hansen, D.G. Liakos, C. Kollmar, S. Kossmann, T. Petrenko, C. Reimann, C. Riplinger, K. Sivalingam, E. Valeev, B. Wezisla, F. Wennmohs, ORCA, version 2.7.0b, University of Bonn, Bonn.
[53] A. Klamt, G.J. Schüürmann, Chem. Soc. Perkin Trans. 2 (1993) 799.
[54] D.J. Stufkens, A.A. Vlček Jr., Coord. Chem. Rev. 177 (1998) 127.
[55] A.A. Vlček, Electrochim. Acta 13 (1968) 1063.
[56] D.A. Pantazis, X.Y. Chen, C.R. Landis, F. Neese, J. Chem. Theory Comput. 4 (2008) 908.
[57] C. van Wuellen, J. Chem. Phys. 109 (1998) 392.
[58] F. Neese, F. Wennmohs, A. Hansen, U. Becker, Chem. Phys. 356 (2009) 98.
[59] S. Kossman, F. Neese, Chem. Phys. Lett. 481 (2009) 240.
[60] F. Neese, J. Comput. Chem. 24 (2003) 1740.